

**GEOLOGICAL EVOLUTION AND METALLOGENETIC  
RELATIONSHIPS OF THE FARALLON NEGRO VOLCANIC  
COMPLEX, NW ARGENTINA**

Anne M. Sasso

A thesis submitted to the Department of Geological Sciences  
in conformity with the requirements for  
the degree of Doctor of Philosophy

*Queen's University  
Kingston, Ontario, Canada  
August, 1997*

copyright © by Anne M. Sasso, 1997



National Library  
of Canada

Acquisitions and  
Bibliographic Services

395 Wellington Street  
Ottawa ON K1A 0N4  
Canada

Bibliothèque nationale  
du Canada

Acquisitions et  
services bibliographiques

395, rue Wellington  
Ottawa ON K1A 0N4  
Canada

*Your file Votre référence*

*Our file Notre référence*

The author has granted a non-exclusive licence allowing the National Library of Canada to reproduce, loan, distribute or sell copies of this thesis in microform, paper or electronic formats.

The author retains ownership of the copyright in this thesis. Neither the thesis nor substantial extracts from it may be printed or otherwise reproduced without the author's permission.

L'auteur a accordé une licence non exclusive permettant à la Bibliothèque nationale du Canada de reproduire, prêter, distribuer ou vendre des copies de cette thèse sous la forme de microfiche/film, de reproduction sur papier ou sur format électronique.

L'auteur conserve la propriété du droit d'auteur qui protège cette thèse. Ni la thèse ni des extraits substantiels de celle-ci ne doivent être imprimés ou autrement reproduits sans son autorisation.

0-612-22508-9



**Frontispiece:** Early morning vista towards Sierra Durazno (horizon) from the Bajo de la Alumbraera plant site, north of Bajo de la Alumbraera. The hills in the foreground are underlain by breccias of the Main Farallón Negro Stratovolcano.

**"It's *nature* not *nurture*, porphyry copper deposits are *born*, they are not *made*."**

A.H. Clark



## ABSTRACT

The 700 km<sup>2</sup> region encompassing the Farallón Negro Volcanic Complex and associated outlying intrusive centres represents the locus of the greatest metal endowment currently recognized in Argentina. It is host to two world-class deposits (Bajo de la Alumbrera and Agua Rica), two producing mines (Capillitas and Farallón Negro - Alto de la Blenda), five additional porphyry Cu-Au prospects (Bajo de Agua Tapada, Bajo el Durazno, Bajo de San Lucas, Bajo las Juntas and Bajo las Pampitas) and an epithermal Au-Ag prospect (Cerro Atajo).

The early volcanic history of the region is characterized by the extrusion from discrete centres from 12.56 to 8.51 Ma of basalt, basaltic andesite and dacite flows of the *Farallón Negro Group*. These precursor volcanic events were subsequently covered by flows and breccias of the Main Farallón Negro Stratovolcano, centred on Alto de la Blenda, which erupted from *ca.* 8.51 to 7.49 Ma, but with the minor extrusion of pyroclastics persisting as late as 6.72 Ma. The stratocone-building event was accompanied by intrusive activity, of the *Farallón Negro Intrusive Suite*, which peaked between 6.8 and 8.6 Ma and continued until 5.2 Ma with the emplacement of dacite and rhyolite dykes representing the terminal stages of magmatic activity in the region. Porphyry Cu-Au and epithermal Au-Ag alteration-mineralization formed early in this terminal stage.

The geochemical continuum represented by the Farallón Negro high-K calc-alkaline and shoshonite suites strongly suggests that they originated from a common source. Whereas shoshonitic units represent some of the oldest dated units at Farallón

Negro, they are interbedded with high-K calc-alkaline units. The absence of features commonly interpreted to be indicative of magma mixing (*e.g.*, sieve-textured plagioclase) in the shoshonites suggests a lesser involvement of deep-crustal MASH processes for the more potassic members. This would imply either thinner crust at the time of eruption and/or rapid emplacement of shoshonitic melts with minimal crustal interaction. The calc-alkaline melts show evidence for mixing and may have experienced greater interaction with the lower crust through slower magma ascent and/or longer crustal residence time. They were erupted quasi-continuously throughout the igneous history at Farallón Negro.

The igneous rocks of the Farallón Negro region were emplaced in a pull-apart basin related to coalescing zones of transtension, nucleated at the intersection of N-S striking faults and the NE-trending dextral Tucumán Transfer Zone. Initiation of the localized extension occurred in a stress regime dominated by E-W compression related to the convergence of the Nazca and South American Plates. A reorientation of stress regimes at *ca.* 8.0 Ma, evident from the NW orientation of the Aguila dyke swarm, heralds the overriding of the subduction-related stresses by NW-SE directed stresses related to the uplift of the *Puna*.

The study-area delimits the eastern extension of a transect of Chile and Argentina centred at *ca.* 27° S which hosts a definable, world-class, concentration of Cu-Au deposits. It constitutes the northern boundary of a distinct Cu-Au metallogenetic sub-province. A unique geodynamic setting is also proposed for this latitude. Tears in the subducted slab, possibly nucleated on inhomogeneities in the oceanic crust related to the Easter Island volcanic chain, allowed asthenosphere to traverse the slab and rise into the

overlying mantle wedge. This provided higher heat flow and possibly allowed greater devolatilization of the subducted slab, which is inferred to have resulted in the generation of melts which record the Middle Miocene arc broadening at this latitude.

The coincidence of a unique geodynamic environment with the unusually intense Cu-Au metallogenetic signature of this transect implies a significant and fundamental role of "provenance" in the formation of ore deposits at this latitude.

## ACKNOWLEDGEMENTS

If one of the goals of a Ph. D. is to expand one's horizons and promote an exchange of ideas which transcends barriers of culture, language and international frontiers, among others, then the experience of my doctorate has been a glorious success. This has been built on the friendship, assistance and unconditional generosity of many people, Canadian, American, Argentine, Australian and Chilean. And, as with any undertaking of this magnitude, contributions have come in many forms, from many sources, and if I have forgotten to mention anyone in the lengthy section that follows, I am deeply sorry for that omission.

This thesis began and will end at Queen's University in Canada. I am indebted to my advisors, Drs. Alan H. Clark and Edward Farrar, for their support and encouragement throughout my time in Kingston. Alan Clark is especially thanked for his untiring editing of this manuscript; our discussions during the "writing up" period were invaluable in defining the salient points of this study. I must also acknowledge Alan's acute insight into human nature and the personality traits of his students: he quickly learnt which buttons to push, and while I didn't always appreciate his 'button pushing', it usually resulted in times of heightened learning and creativity.

This research was supported financially by both the School of Graduate Studies and Research and the Department of Geological Sciences at Queen's University, and by Natural Sciences and Engineering Research Council of Canada grants to Drs. Clark and Farrar. I was the recipient of one of the first H.E. McKinstry Scholarships from the

Society of Economic Geologists, for which I am grateful. This research would not have been possible without the generous support of the exploration industry. M.I.M. Exploration Pty. Ltd., American Resource Corporation, B.H.P. Minerals Ltd., Placer Dome Sud America Ltd. and Minera Alumbra are thanked for their interest in the project, for their contributions and for the "hands-off" nature of their involvement in the scientific aspects of the research.

There are many in the Department of Geological Sciences who deserve thanks for their help and assistance. I am indebted to Dr. Doug Archibald for his extreme patience with my geochronological bumbling and neanderthal computer skills (O.K.: C... colon... backslash... what??!) and for his hand-holding through the intimidating, "big science" world of laser beams and mass spectrometers (and those funky goggles!) that is the Laser  $^{40}\text{Ar} - ^{39}\text{Ar}$  lab. I would like to thank Dr. Dugald Carmichael for the use of his microscope and his unfailing enthusiasm in helping me to identify "mystery green minerals". Dr. Brian Mackenzie provided helpful advice on approaching companies for sponsorship and contacts made while working for Brian on his Economic Guidelines for Mineral Exploration industry short course were instrumental in securing some of the support for this project. Dr. Bob Mason, "Dad" from my Minex days, is thanked for his "no-nonsense" advice and encouragement. I always felt ready to take on the world after a pep-talk from Bob!

Many of my fellow graduate students at Queen's provided moral support and technical assistance throughout my thesis. In particular, however, I would like to thank Amabel Ortega and Ted Doughty for the oral transmission of the "Secrets of

Geochronological Mineral Separation Sutra"; Dr. Hamish Sandeman, the target of all my geochem and geochron data interpretation angst, for his unending patience; Marian Warren, Dave Love and the "Alberta Crude" (including Cooley and Newfy Dave) for sharing their thesis writing and submission tips - they had already made the mistakes so I didn't have to! Jerry Grant kindly ran some "last minute" laser step-heating age determinations on key samples when he would have much rather been kayaking. Conversations (and cappuccinos) with Annette McIlroy helped to clarify many of the organizational aspects for the most effective presentation of the thesis data and information, and were very enjoyable. The assistance of Tom Ullrich has been instrumental in the completion of this study. His prowess in computerized drafting resulted in many of the impressive diagrams contained in this thesis. His friendship, help and hard work will not soon be forgotten.

The field research would not have been possible without the permission and cooperation of Yacimientos Mineros de Agua de Dionysio (Y.M.A.D.). In particular, Farallón Negro mine manager, Emilio Prado, and geologists, Nicholas Montenegro and Mari Carrizo are to be thanked for their graceful accommodation of a couple of gringos who just appeared out of nowhere one day! All became friends, and once I was able to communicate effectively in Spanish, they and their families contributed to the enjoyment of my time in the Farallón Negro community. Time spent on the outcrop and looking at core with Mari Carrizo, at Farallón Negro while she was with Y.M.A.D., at Alumbrera with Minera Alumbrera and at Cerro Atajo with Placer Dome, was always instructive. Nino and Sulema Salgado are also thanked for their hospitality at Farallón Negro. The

"boys in the galpón" and the "ladies in the JICA" are fondly remembered for all the laughter - and for the empanada-making lessons.

Jay Harrington, David Braxton and Cristian Jofre are thanked for their companionship and assistance in the field. Dave Braxton adopted the project as his own, and never have I seen a more enthusiastic field assistant. His knowledge, energy and superhuman sampling skills were invaluable during what proved to be the critical field season for this work.

There are many others in Argentina who deserve thanks for their help and assistance. Jack Crawford, formerly with American Resource Corp., was extremely generous with logistical assistance during the first year of study. There are very few exploration managers who would loan their 4 wheel-drive vehicle to a couple of students from Canada for months on end! Time spent in the field with Nivaldo Rojas of B.H.P. was very instructive and most enjoyable. Agua Rica geologist Claudio Deveaux has always cheerfully answered all of our questions and has been very accommodating during our site visits. An afternoon of philosophical geological armwaving in John Mortimers' (B.H.P.) office in Andalgalá will be remembered. A phone conversation with John and a fax from Dr. Martin Leake (B.H.P.) were very helpful in understanding the evolution of the Agua Rica deposit. Steve Brown of M.I.M. provided excellent taxi service during the second field season. His humour in the face of Argentine-Australian cultural differences is appreciated. Peter Forrestal, M.I.M. - Minera Alumbrera, appeared to tolerate us and was always very accommodating of our requests to "borrow the truck for the weekend"! He also generously shipped a significant portion of the Farallón Negro

Volcanic Complex to Kingston. The brief time spent in the field with John Proffett was illuminating. His detailed maps of Bajo de la Alumbrera are the most intricate, beautiful, and mind-blowing exercises in patience that I have witnessed. John, you are my geological mapping hero!

Also in Argentina, Dr. José Sosa Gomez and his colleagues at the Universidad Nacional de Tucumán were always happy to see us when a break was needed from field work. Discussions with José were useful in beginning to unravel aspects of the structural evolution of the Farallón Negro region. Dr. Eduardo Llambías, of CONICET, was very gracious in discussing aspects of his work on rocks of the Farallón Negro region and over the course of the study has continued with encouragement and provided information whenever it was requested.

I seem to have spent a fair amount of my time in Argentina in the company of Tim Coughlin from the University of Queensland, Australia. His aussie-surfer high-energy and wild geological armwaving antics have been great fun. Field trips to both our thesis areas have been instructive. Ongoing e-mail conversations have helped greatly to clarify, and occasionally to confuse, the structural evolution of northwestern Argentina.

Joe Piekenbrock, originally with Placer Dome and now with a small Canadian junior exploration company, has been an unfailing source of encouragement and support. Joe is solely responsible for the existence of Chapter 4: without his interest in the chemistry of my rocks, it is unlikely that any analyses would have been completed. His ideas about geology, exploration and the philosophy of life have made for memorable discussions. His house in Santiago and the warmth of his family continue to be a personal



sanctuary to which I can escape when South America becomes overwhelming.

Thanks are also extended to Dr. John Guilbert who was instrumental in securing support from M.I.M. Dr. Vic Wall of M.I.M. was generous in his support and the sharing of ideas. A field trip to Argentina, organized by Vic in the fall of 1995, provided a wonderful experience to discuss my emerging ideas about the geology of the Farallón Negro region. Ilmars Gemuts, formerly of Argentina Mineral Development, always demonstrated keen interest in the ideas emerging from this project. Dr. Rick Allmendinger, Ben Brooks and other members of the Cornell Andes Project generously shared their time and ideas during several visits to Ithaca. Tim Gubbels of Earth Sat. Corp. was very helpful early in the study in providing printed TM imagery and in sharing fieldwork "tips" gained during his doctoral research in Bolivia. Henry Truebe of the Alpine Exploration Group was very helpful with all questions relating to the interpretation of TM imagery and went out of his way to provide me with information. Emmanuelle Renard, formerly with El Misti Gold, took a bumbled version of my geological map and worked some magic on it to produce the version presented in Chapter 2, for this, I am very grateful.

Anne-Marie Pichette was a glamorous model in the *défilé* of the 1995 summer collection of lab coats and protective breathing apparati. She cut many thin sections, crushed, pulverized and sieved many of my samples, and was a great help in accelerating the geochronological mineral separation process.

The last section of the thesis on ore genesis would not have been nearly as well accomplished were it not for a last minute pep talk by Laurel Fagervik on applying

aspects of athletic competition, particularly competitive rowing and cycling, to daily life.

I am indebted to Joe Bartolino of Newmont, one of my classmates in the Minex program at Queen's, who originally suggested the idea of a Ph. D. and who encouraged me to pursue it.

I would also like to thank Dr. Tom Skulski of the G.S.C. I have not seen or spoken to Tom in several years but he first introduced me to volcanology and patiently endured all my neophyte questions during a summer in the St. Elias mountains in the Yukon. He, along with James Brennan and Dr. Don Francis, unwittingly influenced the path of my career in geology far more than they could ever have imagined possible.

My parents and family have provided support and encouragement in all my endeavours. Upon hearing that I had decided to do a Ph.D., my brother, Steve, said that I was his intellectual hero. That is more important than anything that anyone else has to say about this project. Finally, Steve Ilg, friend and coach, has said: "All I know, is that when you're done learning, you're DONE!" I'm not done learning, Steve, and I'm certainly not done with living, but I am done with this thesis!

## TABLE OF CONTENTS

	page
Frontispiece	ii
Quotation	iii
Abstract	iv
Acknowledgements	vii
Table of Contents	xiv
List of Figures	xxi
List of Tables	xxvii
 <b>CHAPTER 1: Introduction</b>	 <b>1</b>
Previous Geological Research	2
Present Investigation	5
Location of, and Access to, the Study-Area	6
Scope of the Investigation	6
Thesis Organization	10
Original Contributions	11
 <b>CHAPTER 2: Geological Setting of the Farallón Negro Volcanic Complex</b>	 <b>13</b>
Regional Tectonic Setting	13
Sierras Pampeanas	24
Regional Geology	36
Crystalline Basement	41
Suncho Formation	41
Buey Muerto Schists	42
Capillitas Granite	42
Mylonites	46
Planation of the Crystalline Basement	46
El Morterito Formation	50
Farallón Negro Volcanic Complex	54
Araucanense Formation	55
Punaschotter Formation	56
Lithostratigraphic Nomenclature	60
Existing Nomenclature	60
Proposed Nomenclature	62
Local Geology of the Farallón Negro Volcanic Complex	65
Main Farallón Negro Stratovolcano	66
Volcanic Stratigraphy	66
Intrusive Stratigraphy	96
Arroyo Alumbrera Andesite	100

Durazno Andesite	101
Sierra Durazno Dykes	105
Las Casitas Rhyolite	105
La Chilca Andesite	110
Aguila Dykes	115
Alto de la Blenda Monzonite	116
Agua Tapada Dacite	119
Macho Muerto Dacite	122
Los Leones Rhyolite	122
Vis Vis	125
Sierra Durazno	128
Western Flanks of Sierra Durazno	128
Eastern Flanks of Sierra Durazno	129
Cerro Atajo	130
Capillitas	133
Agua Rica	134
Synthesis	134

### **CHAPTER 3: Mineralization Associated with the Farallón Negro**

<b>Volcanic Complex</b>	138
Review of Metallogenetic Concepts	139
Metallogeny: Background	139
Metallogeny: Terminology	
Cu and Au Metallogeny of the 26° to 18° S transect of the Central	
Andes	143
Previous work	144
This study	146
Mineral Deposits of the Farallón Negro Volcanic Complex	155
Bajo de la Alumbraera	156
Location and Access	156
Previous Work - Discovery History	156
Geological Relationships	162
Nomenclature of Prophyries	163
Intrusive Units	166
Alteration-Mineralization	169
Structure	184
Agua Rica	185
Location and Access	185
Previous Work - Discovery History	185
Geological Relationships	189
Alteration-Mineralization	197
Geologic Evolution of the Agua Rica deposit	208
Capillitas	211

Location and Access	211
Previous Work	211
Geological Relationships	214
Mineralization	221
Farallón Negro - Alto de la Blenda	222
Location and Access	222
Previous Work	222
Geological Relationships	223
Mineralization	224
Characteristics of porphyry Cu-Au systems at Farallón Negro	227
Relationships between porphyry Cu-Au and Epithermal Au-Ag mineralization	
at Farallón Negro	235
Background	235
Examples	236
Farallón Negro District	239
 <b>CHAPTER 4: Petrology and Whole-rock Geochemistry of the</b>	
<b>Farallón Negro Volcanic Complex</b>	241
Previous work	242
Analytical techniques	244
Presentation of data	245
Chemical classification	246
Shoshonites	251
Background	251
Shoshonites at Farallón Negro	252
Abundance of major and minor elements in the Farallón Negro Volcanic	
Complex	262
Incompatible element (including REE) signatures at Farallón Negro	267
Petrography	272
Comparison to selected regional volcanic suites	292
Major and trace elements	292
Comparison to shoshonitic suites in other regions of the Central Andes	314
Argentine shoshonite suites	317
Pocho	317
San Gerónimo and Cerro Negro de Chorillos	320
Peruvian shoshonite suites	321
Linga Group	321
Picotani Group	322
Cerro Moromoroni Formation	323
Tacaza Group	324
11 Ma shoshonites	325
Sillapaca Group	325
Quaternary shoshonites	325

Bolivian Shoshonite suites	326
Abaroa Formation	326
SW Bolivian shoshonite suite	327
Major and trace elements of Central Andean shoshonitic suites	327
Episodes of shoshonitic volcanism in the Central Andes	352
20 - 31 Ma	352
8 - 13 Ma	353
5 - 6 Ma	353
Quaternary	354
Petrogenesis of Farallón Negro rocks	355
 <b>CHAPTER 5: <math>^{40}\text{Ar}/^{39}\text{Ar}</math> Geochronology of the Farallón Negro Volcanic Complex</b>	 358
Previous work	358
Comparison of results with previous dating studies	358
$^{40}\text{Ar}/^{39}\text{Ar}$ Dating Techniques	365
Background	365
Analytical method	369
The Dating Study	373
Round 1	373
Round 2	376
Round 3	377
Recommendations for future dating studies involving young samples	377
Final round of dating	379
The presentation of analytical data	379
Mineral pairs	387
Synthesis of results	394
Volcanic Units	401
Intrusions	407
Alteration-mineralization	430
Bajo de la Alumbraera	430
Agua Rica	444
Bajo de Agua Tapada	449
Bajo el Durazno	452
Cerro Atajo	457
Other alteration centres	460
Summary	461
 <b>CHAPTER 6: Conclusions</b>	 465
Integrated Tectono-magmatic model for the evolution of the Farallón Negro	465
Volcanic Complex	465
Subduction-related effects	465

Puna-related effects	467
Crustal inhomogeneities	468
NW and NE-trending orogen-oblique faults	468
Tucumán Transfer Zone	471
N-S-trending faults	473
Local structures	480
Presentation of a model for the structural evolution of the Farallón Negro region	488
Magmatic evolution of the Farallón Negro region	502
Arc broadening <i>versus</i> arc migration	502
Implications for the geodynamics and petrogenesis of the Farallón Negro region	514
A model for the mid-Miocene arc broadening at the latitude of Farallón Negro	522
Ore-genetic and metallogenetic implications	527
Ore genesis and metallogenesis of the deposits of the Farallón Negro region	532
Process <i>versus</i> provenance in the Farallón Negro camp	535
<b>REFERENCES</b>	541
<b>APPENDIX A. Metallic Mineral Deposits of the Farallón Negro</b>	
<b>Volcanic Complex not Documented in Chapter 3</b>	568
Cerro Atajo	569
Location and Access	569
Previous Work	569
Geological Relationships	574
Structure	575
Mineralization	577
Bajo de Agua Tapada	577
Location and Access	577
Previous Work	580
Geological Relationships	580
Mineralization	587
Bajo el Durazno	591
Location and Access	591
Previous Work	591
Geological Relationships	594
Structure	601
Mineralization	601
Bajo de San Lucas	604
Location and Access	604
Previous Work	607
Geological Relationships	607

Structure	614
Mineralization	614
Bajo las Pampitas	615
Location and Access	615
Previous Work	618
Geological Relationships	618
Structure	625
Mineralization	625
Bajo la Chilca	626
Location and Access	626
Previous Work	629
Geological Relationships	629
Structure	629
Bajo las Juntas	632
Location and Access	632
Previous Work	632
Geological Relationships	632
Mineralization	635
Bajo de Tampa Tampa	638
Location and Access	638
Previous Work	638
Geological Relationships	638
Bajo del Espanto	639
Location and Access	639
Previous Work	639
Geological Relationships	640
Structure	640
Bajo de los Jejenes	640
Location and Access	640
Previous Work	643
Geological Relationships	643
Structure	643
Mineralization	
<b>APPENDIX B. Whole-rock geochemical data for igneous rocks of the Farallón Negro Volcanic Complex</b>	<b>647</b>
<b>APPENDIX C. CIPW Norms</b>	<b>679</b>
<b>APPENDIX D. Duplicate Whole-Rock Analyses</b>	<b>685</b>
<b>APPENDIX E. Published Whole-Rock Geochemistry</b>	<b>693</b>



<b>APPENDIX F. Petrography of selected samples</b>	<b>702</b>
<b>APPENDIX G. Published whole-rock geochemistry from the Andean shoshonite suites</b>	<b>715</b>
<b>APPENDIX H. <math>^{40}\text{Ar}/^{39}\text{Ar}</math> laser microprobe geochronological data</b>	<b>745</b>
<b>Vita</b>	<b>841</b>

## List of Figures

### Chapter 1

Fig. 1-1	Location map of the Farallón Negro region	8
----------	---	---

### Chapter 2

Fig. 2-1	Regional tectonic setting	15
Fig. 2-2	Curvature of the South American - Nazca plate boundary	18
Fig. 2-3	Regional morphological characteristics of the <i>Puna</i>	21
Fig. 2-4	Regional morphological characteristics of the <i>Puna</i>	21
Fig. 2-5	Location of the Easter Hot Line	23
Fig. 2-6	Young volcanoes in the Ojos del Salado region	26
Fig. 2-7	Physiographic provinces of northwestern Argentina	28
Fig. 2-8	Field characteristics of the <i>Sierras Pampeanas</i>	31
Fig. 2-9	Morphology of the <i>Sierras Pampeanas</i>	33
Fig. 2-10	Generalized regional geology map	38
Fig. 2-11	Geological map of the Farallón Negro - Capillitas District	40
Fig. 2-12	Lithological characteristics of the Capillitas Granite	45
Fig. 2-13	Field characteristics of the planate basement surface	48
Fig. 2-14	Field characteristics of the El Morterito Formation	53
Fig. 2-15	Lithological characteristics of the Punaschotter Formation	58
Fig. 2-16	Generalized geological map of the Main Farallón Negro Stratovolcano	68
Fig. 2-17	Lateral distribution of facies in the Volcán de Fuego, Guatemala	71
Fig. 2-18	Range in clast sizes of breccias of the Farallón Negro Volcanic Complex	76
Fig. 2-19	Field characteristics of the Proximal Volcaniclastic Facies	78
Fig. 2-20	Field characteristics of volcanic flows	81
Fig. 2-21	Field characteristics of a flow-banded rhyolite	83
Fig. 2-22	Field characteristics of poorly-welded andesite tuffs	86
Fig. 2-23	Field characteristics of the Medial Volcaniclastic Facies	88
Fig. 2-24	Field characteristics of lahars in the Medial Volcaniclastic Facies	91
Fig. 2-25	Regional field characteristics of volcanic units on the periphery of the Main Farallón Negro Stratovolcano	93
Fig. 2-26	Field characteristics of the Distal Volcaniclastic Facies	95
Fig. 2-27	Lithological characteristics of the Arroyo Alumbrera Andesite	103
Fig. 2-28	Field characteristics of the Sierra Durazno Dykes	107
Fig. 2-29	Field and lithological characteristics of the Las Casitas Rhyolite	109
Fig. 2-30	Field relationships of basaltic dykes cutting the Las Casitas Rhyolite body	112
Fig. 2-31	Field and lithological characteristics of the La Chilca Andesite	114

Fig. 2-32	Petrographic characteristics of the Alto de la Blenda Monzonite	118
Fig. 2-33	Field and lithological characteristics of the Ague Tapada Dacite	121
Fig. 2-34	Field and lithological characteristics of the Macho Muerto Dacite	124
Fig. 2-35	Field and lithological characteristics of the Durazno Andesites at VisVis	127
Fig. 2-36	Field characteristics of rhyolite intrusives at Cerro Atajo	132
Fig. 2-37	Locations and stratigraphic relationships of dated volcanic samples	136

### Chapter 3

Fig. 3-1	Cu-Au metallogeny of the Central Andes	148
Fig. 3-2	Cu-Au metallogenetic sub-province of northern Chile and Argentina	151
Fig. 3-3	Location map of the Farallón Negro deposits	158
Fig. 3-4	Field characteristics of the Bajo de la Alumbrera deposit	160
Fig. 3-5	Geological map of Bajo de la Alumbrera	168
Fig. 3-6	Alteration map of Bajo de la Alumbrera	172
Fig. 3-7	Field and lithologic characteristics of potassic alteration at Bajo de la Alumbrera	174
Fig. 3-8	Lithologic characteristics of <i>early</i> quartz-magnetite alteration at Bajo de la Alumbrera	177
Fig. 3-9	Lithologic characteristics of "B" veins at Bajo de la Alumbrera	179
Fig. 3-10	Lithologic characteristics of massive chalcopyrite "B" veins at Bajo de la Alumbrera	181
Fig. 3-11	Lithologic characteristics of late "D" veins at Bajo de la Alumbrera	183
Fig. 3-12	Location of mineralized centres and important drainages at the Agua Rica deposit	187
Fig. 3-13	Geological map of the Agua Rica deposit	191
Fig. 3-14	Field characteristics of the Agua Rica deposit	193
Fig. 3-15	Field and lithologic characteristics of breccias at Agua Rica	196
Fig. 3-16	Alteration map of the Agua Rica deposit	199
Fig. 3-17	Field and microscopic characteristics of quartz-alunite alteration at Agua Rica	201
Fig. 3-18	Microscopic characteristics of potassic alteration at Agua Rica	204
Fig. 3-19	Generalized cross-section through the Agua Rica deposit	206
Fig. 3-20	Field characteristics of the Capillitas deposit	213
Fig. 3-21	Geological map of the Capillitas deposit	217
Fig. 3-22	Lithologic characteristics of flow-banded rhyolite tuff at Capillitas	219
Fig. 3-23	Lithologic characteristics of dacite porphyry dykes at Capillitas	219
Fig. 3-24	Field characteristics of the Farallón Negro Au-Ag mine	226
Fig. 3-25	Comparison of alteration zoning at other porphyry centres at Farallón Negro	231
Fig. 3-26	Megascopic characteristics of quartz-magnetite alteration-mineralization	233

## Chapter 4

Fig. 4-1	Total alkalies vs. $\text{SiO}_2$ diagram for rocks of the Farallón Negro Volcanic Complex	248
Fig. 4-2	AFM diagram for rocks of the Farallón Negro Volcanic Complex	250
Fig. 4-3	$\text{K}_2\text{O}$ vs. $\text{SiO}_2$ diagram for rocks of the Farallón Negro Volcanic Complex	254
Fig. 4-4	Location map for shoshonites from the Farallón Negro Volcanic Complex	259
Fig. 4-5	Harker variation diagrams for major elements vs. $\text{SiO}_2$	261
Fig. 4-6	Harker variation diagrams for minor elements vs. $\text{SiO}_2$	265
Fig. 4-7	"Spider diagram" for high-K calc-alkaline series rocks	269
Fig. 4-8	"Spider diagram" for shoshonite series rocks	271
Fig. 4-9	Microscopic characteristics of plagioclase	277
Fig. 4-10	Petrographic characteristics of clinopyroxene	279
Fig. 4-11	Petrographic characteristics of hornblende (A)	282
Fig. 4-12	Petrographic characteristics of hornblende (B)	284
Fig. 4-13	Petrographic characteristics of biotite and quartz	286
Fig. 4-14	Macroscopic characteristics of magma-mixing textures	289
Fig. 4-15	Nemarski differential interference contrast microscopy photomicrographs of plagioclase	291
Fig. 4-16	Location map of Miocene volcanic centres in the Sierras Pampeanas	294
Fig. 4-17	Geological map of the Pocho volcanic centre	299
Fig. 4-18	Geological map of the San Luis volcanic centre	301
Fig. 4-19	Total alkalies vs. $\text{SiO}_2$ diagram for rocks from Farallón Negro, Pocho and San Luis	304
Fig. 4-20	AFM diagram for rocks from Farallón Negro, Pocho and San Luis	306
Fig. 4-21	$\text{K}_2\text{O}$ vs. $\text{SiO}_2$ diagram for rocks from Farallón Negro, Pocho and San Luis	308
Fig. 4-22	Comparative REE plots for rocks from Farallón Negro and Pocho	311
Fig. 4-23	$\text{Ba/La}$ vs. $\text{La/Yb}$ diagram for regional volcanic suites	313
Fig. 4-24	$\text{Ba/Ta}$ vs. $\text{La/Ta}$ diagram for regional volcanic suites	316
Fig. 4-25	Location map of Andean shoshonite suites	319
Fig. 4-26	Total alkalies vs. $\text{SiO}_2$ diagram for rocks of the Andean shoshonite suite	329
Fig. 4-27	AFM diagram for rocks of the Andean shoshonite suite	331
Fig. 4-28	$\text{K}_2\text{O}$ vs. $\text{SiO}_2$ diagram for rocks of the Andean shoshonite suite	333
Fig. 4-29	$\text{TiO}_2$ vs. $\text{SiO}_2$ diagram for rocks of the Andean shoshonite suite	335
Fig. 4-30	$\text{MgO}$ vs. $\text{SiO}_2$ diagram for rocks of the Andean shoshonite suite	339
Fig. 4-31	$\text{Cr}$ vs. $\text{SiO}_2$ diagram for rocks of the Andean shoshonite suite	341
Fig. 4-32	Location map of Main and Inner Arcs	343
Fig. 4-33	$\text{Ba/La}$ vs. $\text{La/Yb}$ diagram for rocks of the Andean shoshonite suite	345
Fig. 4-34	$\text{Ba/Ta}$ vs. $\text{La/Ta}$ diagram for rocks of the Andean shoshonite suite	347

## Chapter 5

Fig. 5-1	Calibration curve for can 141	372
Fig. 5-2	Representative degassing spectra for FAR 324	381
Fig. 5-3	Representative degassing spectra for FAR 176	384
Fig. 5-4	Representative degassing spectra for FAR 65	386
Fig. 5-5	Histogram of new laser microprobe $^{40}\text{Ar}$ - $^{39}\text{Ar}$ ages	400
Fig. 5-6	Sample location map of volcanic rocks dated in this study	405
Fig. 5-7	Sample location map of intrusive rocks dated in this study	411
Fig. 5-8	Step-wise degassing spectra for FAR 327	414
Fig. 5-9	Location map of intrusive rocks dated from the Agua Rica deposit	417
Fig. 5-10	Location map of intrusive rocks dated from the Bajo el Durazno prospect	419
Fig. 5-11	Location map of intrusive rocks dated from the Bajo de San Lucas prospect	422
Fig. 5-12	Location map of intrusive rocks dated from the Bajo de la Alumbra deposit	425
Fig. 5-13	Location map of intrusive rocks dated from the Bajo de Agua Tapada prospect	428
Fig. 5-14	Location map of intrusive rocks dated from the Capillitas deposit	432
Fig. 5-15	Sample location map of altered rocks dated in this study	436
Fig. 5-16	Location map of altered rocks dated from the Bajo de la Alumbra deposit	438
Fig. 5-17	Comparison of $^{40}\text{Ar}$ - $^{39}\text{Ar}$ degassing spectra from hydrothermally-altered samples at Bajo de la Alumbra	443
Fig. 5-18	Location map of altered rocks dated from the Agua Rica deposit	446
Fig. 5-19	Location map of altered rocks dated from the Bajo el Durazno prospect	454
Fig. 5-20	Location map of altered rocks dated from the Cerro Atajo prospect	459
Fig. 5-21	Schematic illustration of the temporal evolution of the Farallón Negro Volcanic Complex	463

## Chapter 6

Fig. 6-1	Orthogonal structural fabric of the basement of NW Argentina	470
Fig. 6-2	N-S structural fabric of northwestern Argentina	475
Fig. 6-3	Proposed Tertiary rift zone in northwestern Argentina	478
Fig. 6-4	Field characteristics of the Bola del Atajo fault zone	482
Fig. 6-5	Field characteristics of footwall synclines related to high-angle reverse faults	484
Fig. 6-6	Calculated transport directions on basement blocks	486
Fig. 6-7	Structural evolution model for the Farallón Negro Volcanic Complex	491

Fig. 6-8	Proposed model for the clockwise rotation of the Sierra Durazno block	500
Fig. 6-9	Physiographic provinces of northwestern Argentina	508
Fig. 6-10	Proposed mechanism of lithospheric delamination	511
Fig. 6-11	Geological compilation maps of volcanic units in the 26° - 28° S transect	518
Fig. 6-12	Compilation of selected geochronological results for volcanic units in the 26° - 28° S transect	520
Fig. 6-13	Proposed model for the development of tears on the subducted slab at the latitude of Farallón Negro	526
Fig. 6-14	Process-dominated model of ore-genesis	531
Fig. 6-15	Compilation of selected geochronological results for Cu and/or Au deposits in the 26° - 28° S transect	534

## Appendix A

Fig. A-1	Location map of the Farallón Negro deposits	571
Fig. A-2	Field characteristics of Cerro Atajo	573
Fig. A-3	Geological map of Cerro Atajo	576
Fig. A-4	Field characteristics of the Cerro Atajo vein systems	579
Fig. A-5	Geological map of Bajo de Agua Tapada	582
Fig. A-6	Field characteristics of Bajo de Agua Tapada	584
Fig. A-7	Alteration facies of Bajo de Agua Tapada	586
Fig. A-8	Lithological characteristics of jasperoid veins at Bajo de Agua Tapada	589
Fig. A-9	Field characteristics of Bajo el Durazno	593
Fig. A-10	Geological map of Bajo el Durazno	596
Fig. A-11	Lithological characteristics of quartz-magnetite alteration at Bajo el Durazno	598
Fig. A-12	Alteration facies of Bajo el Durazno	600
Fig. A-13	Field and lithological characteristics of phyllic alteration at Bajo el Durazno	603
Fig. A-14	Field characteristics of Bajo de San Lucas	606
Fig. A-15	Geological map of Bajo de San Lucas	609
Fig. A-16	Lithological characteristics of magnetite alteration at Bajo de San Lucas	611
Fig. A-17	Alteration facies of Bajo de San Lucas	613
Fig. A-18	Field characteristics of Bajo las Pampitas	617
Fig. A-19	Geological map of Bajo las Pampitas	620
Fig. A-20	Lithological characteristics of quartz-magnetite alteration at Bajo las Pampitas	622
Fig. A-21	Lithological characteristics of dacite porphyry at Bajo las Pampitas	624
Fig. A-22	Field characteristics of Bajo la Chilca	628

Fig. A-23	Lithological characteristics of quartz-carbonate veins at Bajo la Chilca	631
Fig. A-24	Geological map of Bajo las Juntas	634
Fig. A-25	Alteration facies at Bajo las Juntas	637
Fig. A-26	Field characteristics of Bajo del Espanto	642
Fig. A-27	Geological and alteration facies map of Bajo de los Jejenes	645

## **Appendix B**

Fig. B-1	Location map for geochemical samples	652
----------	--------------------------------------	-----

## List of Tables

### Chapter 2

Table 2-1	Sedimentary characteristics of non-marine volcanoclastic deposits	73
Table 2-2	Temporal sequence of intrusive events in the Main Farallón Negro Stratovolcano	99

### Chapter 3

Table 3-1	Definitions of metallogensis-related terms	141
Table 3-2	Subdivision of intrusive bodies at Bajo de la Alumbrera	165

### Chapter 4

Table 4-1	Classification of Farallón Negro shoshonites	256
Table 4-2	Summary of mineralogical relationships of rocks of the Farallón Negro Volcanic Complex	274
Table 4-3	Comparison of the major and trace element chemistry of Farallón Negro and regional suites	296
Table 4-4	Salient geological characteristics of the Andean shoshonite suites	350

### Chapter 5

Table 5-1	Comparison of conventional K-Ar dates by McBride and new $^{40}\text{Ar} - ^{39}\text{Ar}$ dates	361
Table 5-2	Comparison of published K-Ar dates from Capillitas and Cerro Atajo with new $^{40}\text{Ar} - ^{39}\text{Ar}$ dates	364
Table 5-3	Comparison of biotite and hornblende mineral-pair ages	389
Table 5-4	Comparison of sericite and whole-rock pair ages	393
Table 5-5	Compilation of new laser microprobe $^{40}\text{Ar} - ^{39}\text{Ar}$ ages for rocks of the Farallón Negro Volcanic Complex	396
Table 5-6	New laser microprobe $^{40}\text{Ar} - ^{39}\text{Ar}$ ages for volcanic rocks of the Farallón Negro Volcanic Complex	403
Table 5-7	New laser microprobe $^{40}\text{Ar} - ^{39}\text{Ar}$ ages for intrusive rocks of the Farallón Negro Volcanic Complex	409
Table 5-8	New laser microprobe $^{40}\text{Ar} - ^{39}\text{Ar}$ ages for altered rocks of the Farallón Negro Volcanic Complex	434
Table 5-9	New laser microprobe $^{40}\text{Ar} - ^{39}\text{Ar}$ ages for rocks from Bajo de la Alumbrera	440



Table 5-10	New laser microprobe $^{40}\text{Ar}$ - $^{39}\text{Ar}$ ages for rocks from Agua Rica	448
Table 5-11	New laser microprobe $^{40}\text{Ar}$ - $^{39}\text{Ar}$ ages for rocks from Bajo de Agua Tapada	451
Table 5-12	New laser microprobe $^{40}\text{Ar}$ - $^{39}\text{Ar}$ ages for rocks from Bajo el Durazno	456

## Chapter 6

Table 6-1	Geographical and geophysical data for volcanic arcs at convergent plate margins	504
-----------	--	-----

## Appendix B

Table B-1	Sample locations	648
Table B-2	Whole-rock geochemical analyses listed by sample number	653
Table B-3	Trace and REE analyses	660
Table B-4	Whole-rock geochemical analyses listed by rock-type	664

## Appendix C

Table C-1	CIPW norms	680
-----------	------------	-----

## Appendix D

Table D-1	Duplicate sample analyses	686
Table D-2	Duplicate standard analyses	691

## Appendix E

Table E-1	Whole-rock geochemical data from Dostal <i>et al.</i> (1977)	694
Table E-2	Whole-rock geochemical data from Caelles (1979)	696
Table E-3	Whole-rock geochemical data from Allison (1986)	698
Table E-4	Whole-rock geochemical data from Kay <i>et al.</i> (1988)	700

## Appendix G

Table G-1	Whole-rock geochemical data from Pocho	716
Table G-2	Whole-rock geochemical data from San Gerónimo	719
Table G-3	Whole-rock geochemical data from Chorillos	722
Table G-4	Whole-rock geochemical data from La Poma	724
Table G-5	Whole-rock geochemical data from the Picotani Group	726
Table G-6	Whole-rock geochemical data from Cerro Moromoroni	728
Table G-7	Whole-rock geochemical data from the Tacaza Group	731
Table G-8	Whole-rock geochemical data from SW Bolivia	734
Table G-9	Whole-rock geochemical data from the Abaroa Formation	736
Table G-10	Whole-rock geochemical data from the Sillapaca Group	738
Table G-11	Whole-rock geochemical data from the 11 Ma shoshonites	741
Table G-12	Whole-rock geochemical data from the Linga Group	743

## CHAPTER 1

### INTRODUCTION

In the past several years Argentina has emerged as one of the most attractive areas in which to conduct exploration for mineral deposits. With little historical mining activity, vast areas that are relatively under-explored and the extension of highly prospective geological units and mineralization environments from known ore districts in contiguous Chile (*e.g.*, the Maricunga and El Indio Au belts) into Argentina, international exploration companies have been turning to Argentina in the hopes of discovering the next "supergiant" deposit. No area has generated greater interest than the Farallón Negro region of Catamarca Province, NW Argentina. It is host to the Bajo de la Alumbrera Cu-Au deposit (owned 50% by M.I.M. Exploration Pty. Ltd., and 25% each by North Ltd. and Rio Algom) which is scheduled to begin production in late-1997 and to the large B.H.P. Minerals Intl. Exploration Inc. (70%) and Northern Orion (30%) Agua Rica Cu-Au-Mo prospect, as well as to several other porphyry Cu-Au and epithermal Au-Ag centres. These deposits occur within and near the 700 km<sup>2</sup> Farallón Negro Volcanic Complex, which comprises the deeply eroded remnants of an enormous stratovolcano, together with a series of small outlying intrusive and/or volcanic centres. The porphyry copper deposits and vein systems in the district are markedly enriched in gold: thus, the Bajo de la Alumbrera Cu-Au-(Mo) deposit displays the highest recorded Au content (0.65 g/t) among significant Central Andean porphyry copper systems (Sillitoe, 1979).

The Farallón Negro deposits occur at the easternmost limit of a transect of the Central Andes, arbitrarily delimited by latitudes 26° and 28° S, which also includes the

gold-rich porphyries of the Maricunga camp and the Au-rich El Salvador and Potrerillos porphyry copper deposits in Chile (Clark *et al.*, 1976; Colley *et al.*, 1989). This transect remains the locus of all presently-known significant Au-bearing porphyry copper deposits in the Andes (with the exception of Andacollo, at latitude 30° 15' S).

The Neogene Farallón Negro Volcanic Complex constitutes an ideal setting in which to study the temporal, spatial and genetic relationships of volcanism, hypabyssal intrusion and magmatic-hydrothermal mineralization, and to evaluate their relationships in the context of the regional tectonic development of a convergent plate boundary environment, the Central Andes. It represents the easternmost magmatic-hydrothermal event confirmed in the Andean arc at this latitude (Clark *et al.*, 1976). However, as renewed mapping efforts by the Argentine federal and provincial surveys are progressing, additional volcanic centres of similar age and general tectonic setting are becoming better known (*e.g.*, Las Animas volcanic centre: González *et al.*, 1989; González, 1990; San Lorenzo volcanic complex: González, 1995; O. González, pers. comm., 1995; El Alisal volcanic complex: Martínez and Chipulina, 1996). The present thesis is predicated on the concept that clarification of the age relationships and setting of the Farallón Negro Volcanic Complex will aid in the evaluation of these, possibly similar, volcanic complexes as potential hosts to economic mineralization.

### **Previous Geological Research**

The regional geology of the area surrounding and including the Farallón Negro Volcanic Complex was first systematically mapped by González Bonorino in 1945

(published in 1950). That author briefly described the distribution and nature of the volcanic and intrusive units, which he grouped as *El Complejo Volcánico*, and their relationship to the regional stratigraphy. Peirano (1945) had previously briefly described units from the central area of the Volcanic Complex. The geology and structure of the Farallón Negro region were described in a number of reports prior to 1970 (*inter alia*, Quartino, 1960; Sister, 1963), but the only published detailed study of the geology of the Farallón Negro Volcanic Complex is provided by Llambias (1970, 1972), who outlined the history of the area as follows:

- 1) Block faulting of the crystalline basement, resulting in the formation of a tectonic depression which was to focus the Cenozoic volcanism;
- 2) Eruption of igneous breccias and tuffs of largely andesitic composition;
- 3) Emplacement of dykes, sills, andesitic and basaltic flows, and andesite domes peripheral to the complex, possibly controlled by a caldera margin;
- 4) Passive emplacement of a central monzonite intrusion;
- 5) Intrusion of granodiorite porphyry stocks with associated porphyry copper type mineralization; intrusion of a radial dyke swarm of andesitic to dacitic composition; and the emplacement of a NW-SE-trending belt of small quartz andesite to dacite and rhyodacite stocks; and
- 6) Intrusion of minor rhyolite domes and dykes, and the emplacement of rhodochrosite-Au-Ag veins, with minor local Cu, Pb and Zn.

This remains the most comprehensive study of the field relationships in the Farallón Negro Volcanic Complex, although local details of the volcanic stratigraphy in the Bajo

de la Alumbra area are documented by J.M. Proffett (1994, 1995).

In the 1970's, the Central Andean Metallogenetic Project, a co-operative program directed by Drs. A.H. Clark and E. Farrar of Queen's University, contributed a significant body of information on the geology, petrology, major and minor element geochemistry, geochronology and magmatic and tectonic evolution of the Farallón Negro region and its mineral occurrences (Caelles *et al.*, 1971; Clark and Zentilli, 1972; McBride, 1972; McNutt *et al.*, 1979; McBride *et al.*, 1976; Clark *et al.*, 1976; Dostal *et al.*, 1977; Clark, 1977; Zentilli and Dostal, 1977; Caelles, 1979). Specifically, the work of Caelles (*op. cit.*) generated the first published geochemical analyses of rocks of the Farallón Negro Volcanic Complex and provided the foundation for the first radiometric dating study of samples from the Farallón Negro area, conducted by McBride (1972).

Various aspects of the region have also been treated in more general studies devoted to porphyry copper genetic models and surveys of the metallogenesis of Argentina and western South America in general (Stoll, 1964; Figueroa, 1971; Sillitoe, 1973b, 1976, 1977, 1979, 1981, 1989, 1992; Ramos, 1977; Malvicini and Llambias, 1982; Sillitoe and Bonham, 1984; Clark and Arancibia, 1995). The setting of the Farallón Negro deposits was extensively relied upon in Sillitoe's (1973b) seminal paper addressing the characteristic features of the tops and bottoms of porphyry copper deposits.

Various aspects of the mineral occurrences hosted in rocks of the Farallón Negro Volcanic Complex are described in numerous published and unpublished reports. These are referred to in more detail in the individual ore deposit descriptions included in Chapter 3. The most significant recent contributions include: three M.Sc. theses at the University

of Arizona on Bajo de la Alumbrera (Stults, 1985), Bajo de Agua Tapada (Suchomel, 1985) and Bajo el Durazno (Allison, 1986); an exhaustive description of the mineralogy of the Capillitas deposit by Márquez Zavalía (1988); and ongoing mapping of the Bajo de la Alumbrera deposit and environs by J.M. Proffett (1994, 1995).

### **Present Investigation**

The evolution of exploration interest in the Farallón Negro area, reflecting exploration in Argentina as a whole, is mirrored by the level of interest in, and logistical support for, this study by international exploration companies. However, the writer's initial 1993 field season was funded solely by American Resource Corporation (through its Argentine subsidiary, Recursos Americanos Argentinos S.A.), an American junior exploration company which no longer has interests in Argentina. International Musto Explorations Ltd., a Vancouver-based venture company, and B.H.P. Minerals Inc., although not formally involved at that time, also provided logistical support. Research in 1994 was supported by M.I.M. Exploration Pty. Ltd., Placer Dome Sud America Ltd., American Resource Corp. and B.H.P. Minerals Inc., but much of the logistical support for the 1994 field season was provided by Minera Alumbrera Ltd., which at that time was owned jointly by M.I.M. and Musto. Support for ongoing research in 1995 was provided by M.I.M., B.H.P. and American Resource Corp. Analytical studies have been funded largely by N.S.E.R.C. grants to A.H. Clark and E. Farrar.

### ***Location of, and Access to, the Study-Area***

The Farallón Negro area (Fig. 1-1) is situated in the Hualfin District of Belén Department, Catamarca Province, northwestern Argentina, the centre of district lying at *ca.* latitude 27° 15' S, longitude 66° 30' W. It is located approximately 175 to 225 km to the east of the Main Andean Cordillera (*Cordillera Principal*) and straddles the boundary between the *Puna* physiographic and tectonic province to the north and the *Sierras Pampeanas* to the south. The area is about 1100 km northwest of Buenos Aires and 6 hours by paved and graded dirt roads from the nearest airport at Tucumán. Many of the mineralized centres can be reached using four-wheel-drive vehicles via dirt roads, but much of the area is accessible only on foot or horseback. The establishment of backpacking and four-wheel-drive access camps was necessary for work in more remote areas.

The area is rugged and sparsely vegetated, and is very similar in topography and vegetation to the Arizona-Sonora desert of the southwestern United States. Elevations range from 2400 m to 5450 m a.s.l. at Cerro Nevado del Candado in the Sierra de Aconquija. The arid climate is characterised by extreme daily temperature variations in the austral winter months and an annual rainfall of approximately 200 mm.

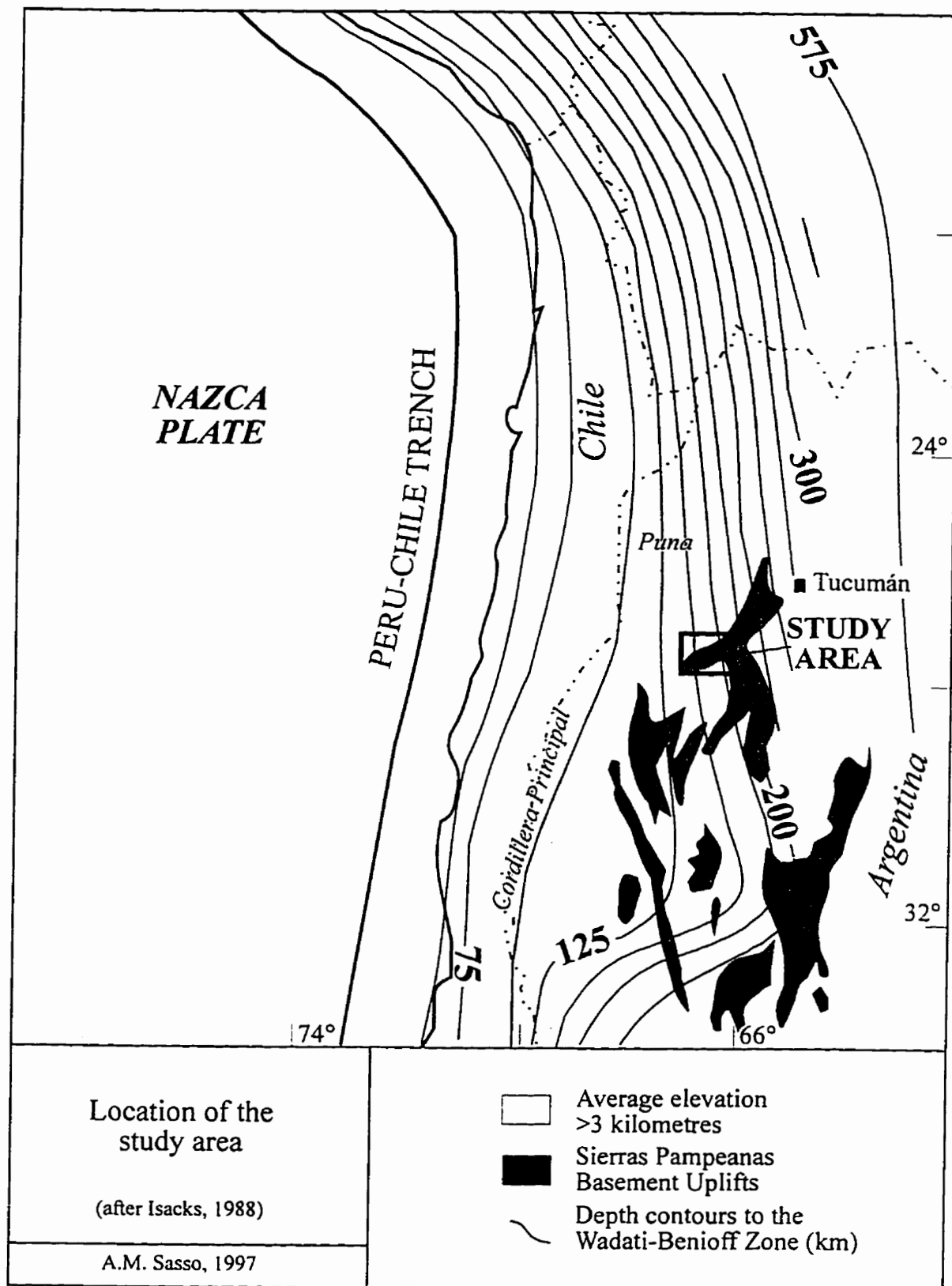
### ***Scope of the Investigation***

Field work for this thesis was initiated during three months of the austral winter of 1993. The initial focus of the study was the investigation of the ore deposits located in the Farallón Negro and Capillitas districts, with particular emphasis on the ages and



**Figure 1-1.**

Location of the study-area in relation to the Peru-Chile Trench, *Cordillera Principal*, *Puna* and *Sierras Pampeanas*. The dip of the subducting slab is indicated by the depth contours on the Wadati-Benioff zone (after Isacks, 1988). Farallón Negro is located in the transition zone between steep subduction to the north and shallow subduction to the south.



duration of the mineralizing systems and the relationships between the porphyry Cu-Au and epithermal Au-Ag mineralization facies. To this end, all mineralized centres in the region were visited and sampled for petrological and geochronological study. Observations during that field season and, particularly, the acquisition of 1:250 000 and 1:50 000 digital enlargements of a thematic mapper (TM) image for the area, led to a revised agenda for the second field program. During June to September, 1994, the scope of the study was expanded to develop a better understanding of the overall evolution of the Farallón Negro Volcanic Complex, to interpret the structural history of the area, and to evaluate the role of structure in controlling the emplacement of mineral deposits. Therefore, a greater emphasis was placed on the igneous petrology of the volcanic complex and on the regional distribution of volcanic units. This necessitated the preparation of a regional 1:50 000 geological map encompassing the area of the Farallón Negro Volcanic Complex and extending to the east to include the Agua Rica deposit and, to the south, to approximately 6.5 km beyond the confluence of the Vis Vis, Jaci-Yaco and El Tigre rivers. Volcanic and intrusive units and hydrothermal alteration assemblages were sampled for ongoing petrological and geochronological studies.

The purpose of the thesis is therefore fourfold: i) to document the petrology and age relationships of the igneous rocks of the Farallón Negro Volcanic Complex in order to provide a geochemical and temporal framework for the study of the timing and duration of mineralized centres; ii) to apply these data to the evaluation of the relationships between the porphyry Cu-Au and epithermal Au-Ag mineralization facies; iii) to construct a model linking the observed patterns of Cu-Au mineralization at Farallón Negro to the

tectonic development of the region; and iv) to evaluate the implications of this model for the metallogenetic evolution of this transect of the Central Andes.

### ***Thesis Organization***

The geological setting of the Farallón Negro Volcanic Complex is described in Chapter 2, in which the regional tectonic context, regional geology, and the local geology of the Farallón Negro Volcanic Complex are documented as a basis for developing an understanding of the environment in which the volcanic complex and its contained ore deposits were emplaced.

Aspects of the metallogenesis of the Central Andes relevant to the Farallón Negro District are reviewed in Chapter 3. Descriptions of the mineralized centres provide the basis for a general discussion of the characteristics of Cu-Au porphyry systems at Farallón Negro and for discussion of the relationships between the porphyry Cu-Au and epithermal Au-Ag deposits of the region.

In Chapter 4, the petrographic and geochemical aspects of the volcanic and associated intrusive rocks of the Farallón Negro Volcanic Complex are described, including a comparison with volcanic rocks from other areas of northwestern Argentina and a comparison of the Farallón Negro shoshonite suite to other potassium-rich rocks of the Central Andes. This provides the basis for the elucidation of the petrogenetic evolution of the Farallón Negro Volcanic Complex.

The results of the  $^{40}\text{Ar}/^{39}\text{Ar}$  geochronological study are presented in Chapter 5. The new data establish a firm time-frame for the evolution of the area and for the development

of mineralization.

Chapter 6 constitutes the integration of the above data and the development of new models for the structural evolution of the Farallón Negro Volcanic Complex and to explain the mid-Miocene arc broadening at the latitude of the study-area. It focuses on the petrogenetic evolution of the complex, as outlined in Chapter 4, within the temporal framework of volcanism, intrusion and alteration/mineralization established in Chapter 5. This chapter further integrates the relationships between the porphyry and epithermal mineralization environments and the evolution of the Farallón Negro Volcanic Complex and mineral deposits, this relationship is then discussed within the broader context of the regional metallogenetic evolution of this transect of the Central Andes. Finally the long-standing ore-genetic and metallogenetic debate of provenance *versus* process is briefly evaluated in relation to the two major deposits of the district, Bajo de la Alumbrera and Agua Rica.

### ***Original Contributions***

The original contributions of this thesis include:

- i) the development of a system of formal lithostratigraphic nomenclature for igneous rocks of the Farallón Negro region and the definition of the new *Farallón Negro Group*, *Farallón Negro Intrusive Suite*, *Sierras Pampeanas Supergroup* and *Sierras Pampeanas Intrusive Supersuite*;
- ii) the definition and delimitation of a Central Andean Cu-Au metallogenetic sub-province;

- iii) the presentation and interpretation of a significant body of new geochemical and geochronological data;
- iv) the development of new laser  $^{40}\text{Ar} - ^{39}\text{Ar}$  techniques for the dating of young samples;
- v) the development of a new model for the emplacement and structural evolution of the Farallón Negro Volcanic Complex; and
- vi) the development of a model to explain the Middle Miocene arc broadening at the latitude of the study-area.

## CHAPTER 2

### GEOLOGICAL SETTING AND ANATOMY OF THE FARALLON NEGRO VOLCANIC COMPLEX

#### Regional Tectonic Setting

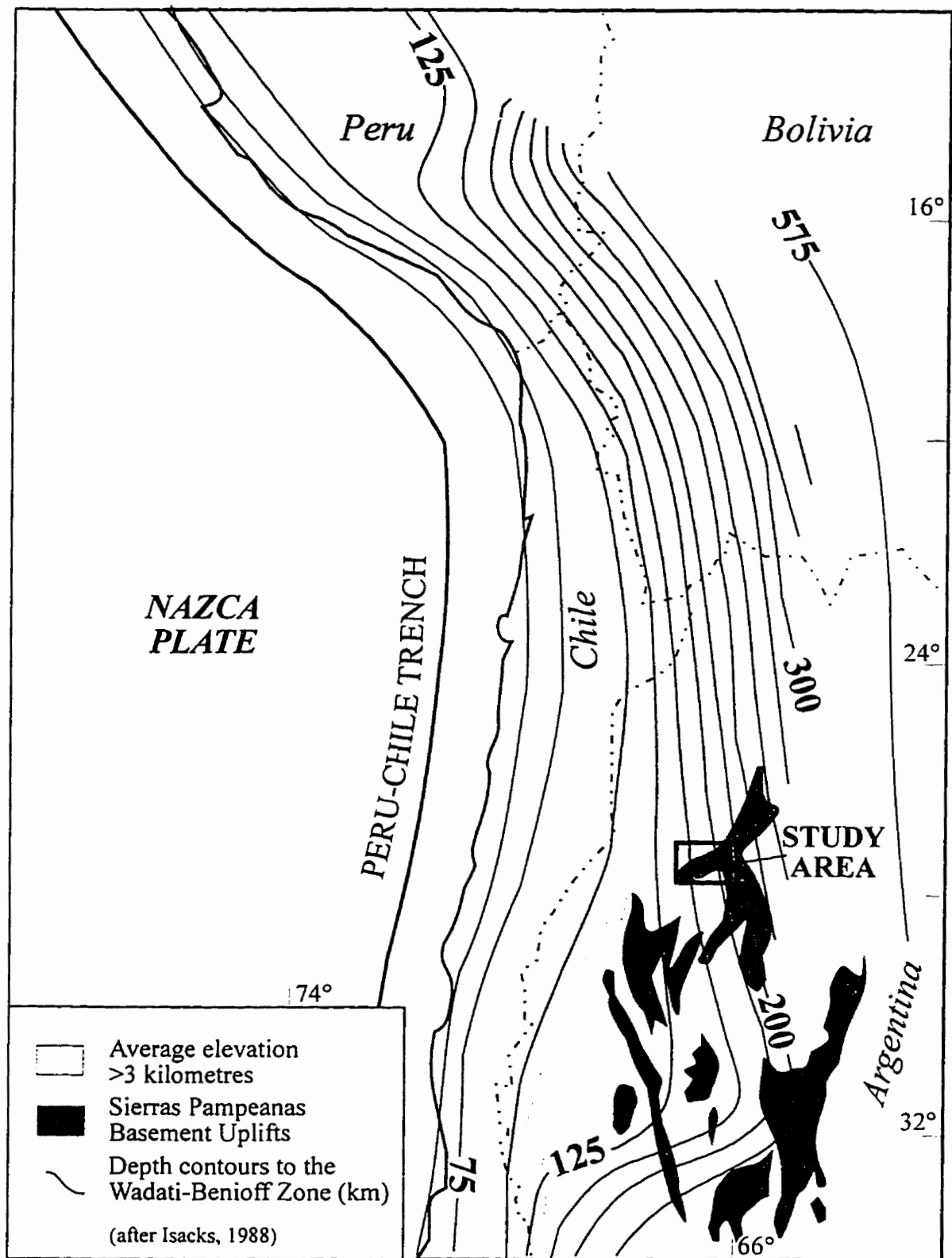
The Andes as a whole have experienced continuous subduction over a 200 m.y. period, and are often cited as a type-example of an orogen generated at a continental margin (Dewey and Bird, 1970; James, 1971). However, abrupt discontinuities along the length of the extant Andean volcanic arc do not conform to the classic subduction model. The approximately 4,500 km - long orogen has been subdivided into the Northern, Central and Southern Volcanic Segments, or Zones, which are separated by regions lacking modern volcanic activity. This apparent segmentation in the South American plate is mirrored by domains of similar scale in the subducting Nazca plate (Fig. 2-1), delimited by major along-strike variations in the dip of the Wadati-Benioff zone. The segments between latitudes 2° and 15° S (Peru) and 28° to 33° S (central Chile and Argentina) have low angles of inclination of about 5° to 10° and exhibit no Quaternary volcanism. In contrast, the three other segments, at 0° to 2° S (Ecuador), 15° to 24° S (northern Chile) and 33° to 45° S (southern Chile), have steeper dips of about 25° to 30° and are characterized by active volcanism (Barazangi and Isacks, 1976; Jordan *et al.*, 1983; Bevis and Isacks, 1984).

The dip of the subducted plate is inferred from the location of earthquake hypocentres, which clearly delimit the location of the steeply- and shallowly-dipping segments but generally do not allow precise definition of the transition zones between slab

**Figure 2-1.**

Configuration of the hanging wall of the subducted Nazca Plate based on depth contours to the Wadati-Benioff seismic zone (after Isacks, 1988). The locations of the study-area and the *Sierras Pampeanas* are also shown.

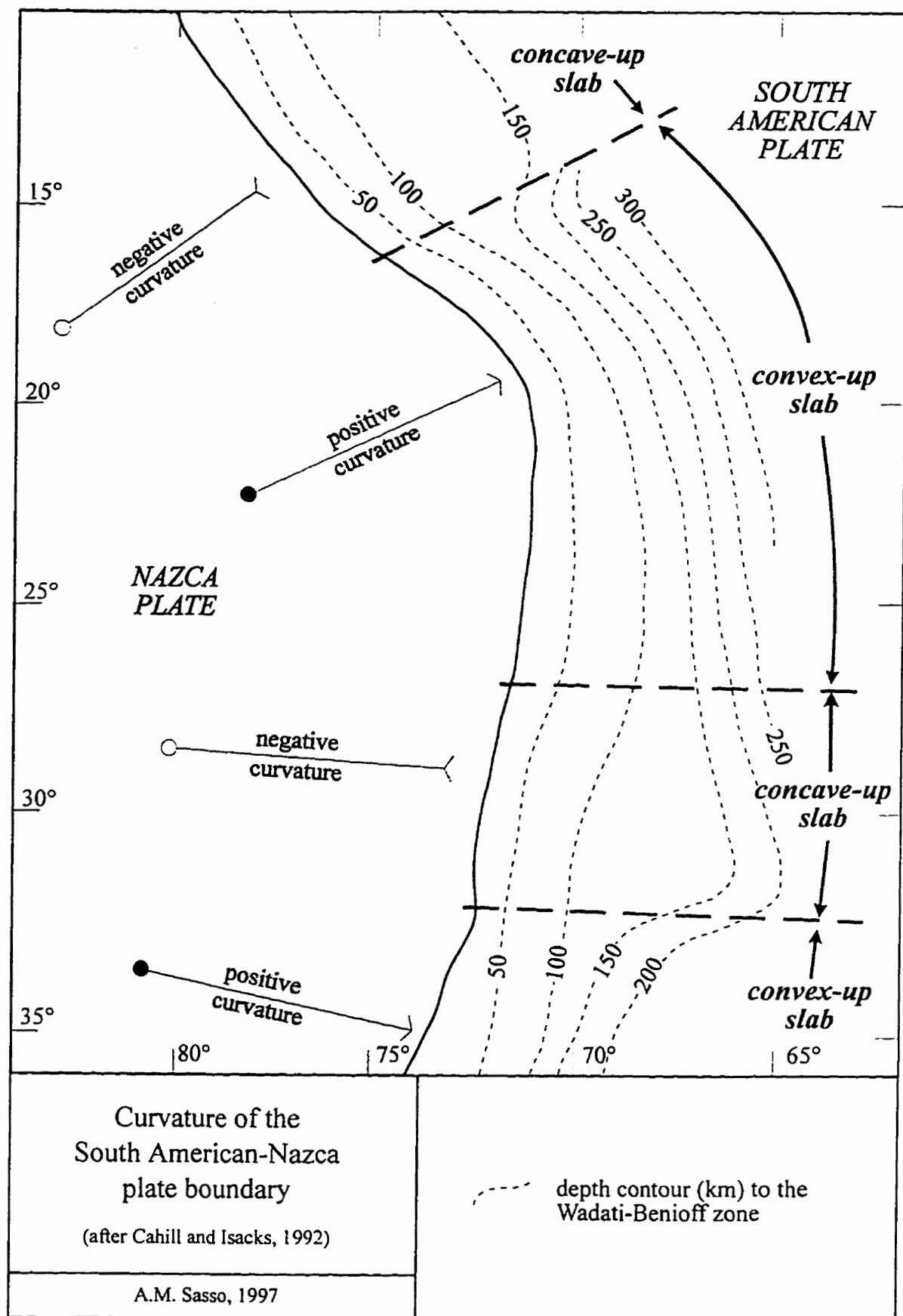




segments. These were initially interpreted as tears in the descending plate (Barazangi and Isacks, 1976). However, later re-analysis of the seismic data and more accurate contouring of the Benioff Zone allowed further refinement of the geometry of the subducted slab and revealed its smooth curvature in the transition zones (Bevis and Isacks, 1984; Cahill and Isacks, 1985). An updated compilation of earthquake locations and focal mechanism solutions by Cahill and Isacks (1992) confirmed the previously-inferred occurrence of sharp flexures in the subducting plate at the transition zones at approximately 15° S beneath southern Peru and at 33° S beneath Chile and Argentina, but also revealed a gradual, southward flattening of the plate at the transition zone centred at 27° S. The area of study overlies this transition, which is marked by a large, seismically quiescent region from 25°30' S to 27°30' S. This gap in seismicity has persisted as long as reliable seismic recording stations have been established (Jordan *et al.*, 1983; Cahill and Isacks, 1992). Jordan *et al.* (*op. cit.*) concluded, on the basis of the continuity of forearc and magmatic arc features, that the major change from steep to flat subduction occurs at approximately 27° S. Cahill and Isacks (1992) proposed that tears may exist in the vicinity of this transition zone. These are not interpreted to be major segment-bounding faults but rather small gaps lying within the surface of the curved subducting plate. These authors also observed a direct relationship between the configuration of vertical curvature in the subducted slab, *i.e.*, concave-up in regions of flat subduction and convex-up in steeply-dipping segments, and the gross lateral curvature in the South America-Nazca Plate margin, *i.e.*, convex-seaward and concave-seaward, respectively (Fig. 2-2). They concluded that the South American Plate itself may have played an important role in

**Figure 2-2.**

Relationship between the configuration of the vertical curvature in the subducted plate with the lateral curvature in the South America - Nazca Plate margin (after Cahill and Isacks, 1992).



determining subduction angle. It was postulated that variable shortening rates along the plate margin, as proposed by Isacks (1988), may be responsible for the shape of the plate margin: in regions of lesser shortening, more of the convergence between the plates is taken up through subduction, resulting in an increase in the convexity of the margin.

Many longitudinal changes in Andean tectonic style coincide with major segment boundaries, suggesting a direct relationship between subducted plate geometry and structures developed in the overriding plate. The transition zone centred at 27° S overlaps with many geological, geophysical and topographic discontinuities. Thus, the area of study and the 27° S transition zone overlap the boundary between the *Puna* physiographic and tectonic province to the northwest and the *Sierras Pampeanas* to the south (Fig. 2-1). The *Puna*, the southern extension of the Peruvian/Bolivian *Altiplano*, is a high plateau with an average elevation of 4,000 m and characterized by centripetal drainage basins with extensive saline deposits or *salares* (Fig. 2-3). N-S trending mountain ranges rise 1-2 km above the plateau. This region has experienced Cenozoic volcanism, felsic flows being overlain by andesitic stratovolcanoes, and the youngest volcanic episode generating monogenetic basaltic cones (Fig. 2-4). The northern part of the *Sierras Pampeanas* overlies the Benioff zone transition. The *Sierras Pampeanas* are characterized by irregular basement blocks bounded by moderately- to steeply-dipping reverse faults, and will be discussed in greater detail in a subsequent section.

The transition zone at 27° S (Fig. 2-5) is further marked by the shoaling and offset of the Peru-Chile Trench, the interruption of major morphological features of the Andean Cordillera and Coastal Ranges, longitudinal features to the north giving way to transverse

*Regional morphological characteristics of the Puna.*

**Figure 2-3.**

The *Puna* is characterized by centrally-drained basins which commonly contain saline lakes or *salares*. The view shows a small unnamed saline lake on the SW margin of the Cerro Galán Caldera, a relic of a much larger lake that occupied the floor of the caldera prior to its resurgence. The hills on the horizon were formed by the resurgence of the central part of the caldera to the present elevation of 6100 m a.s.l. View to the NE.

**Figure 2-4.**

Young monogenetic cones are widespread on the *Puna*. View to the south of small mafic scoria cones and lavas of the Antofagasta de la Sierra valley developed along regional north-south striking faults to the west of Cerro Galán.

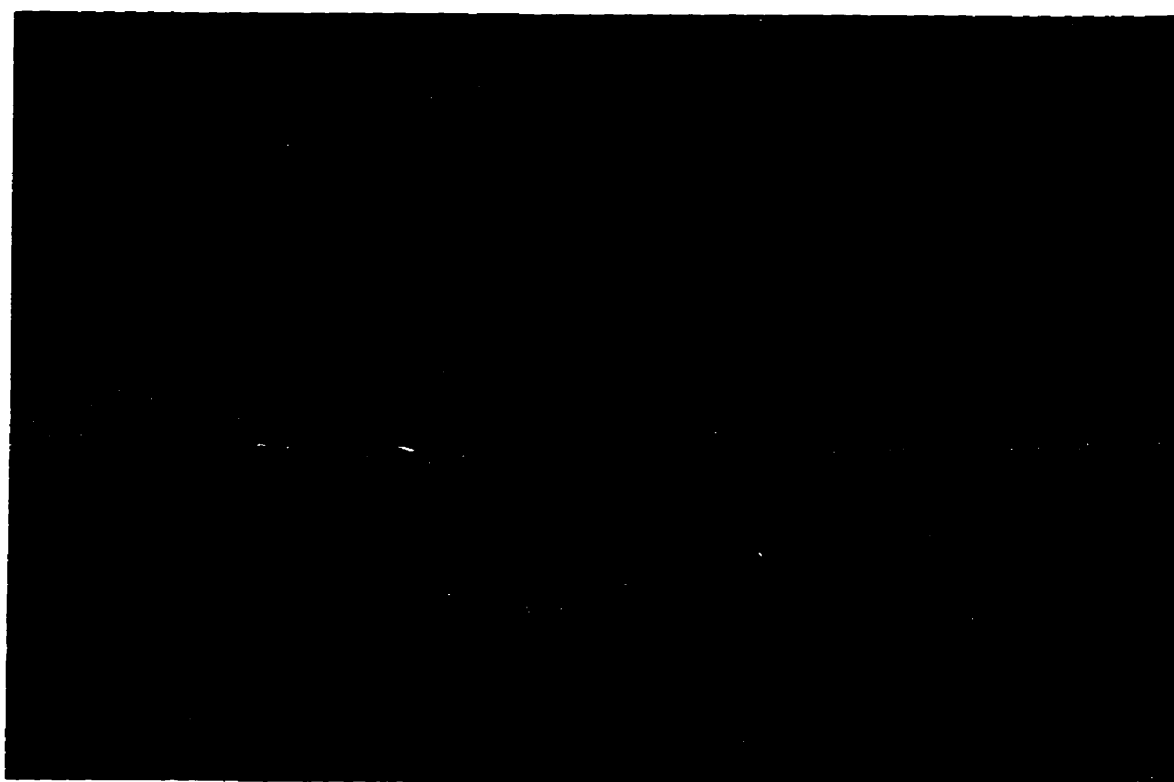
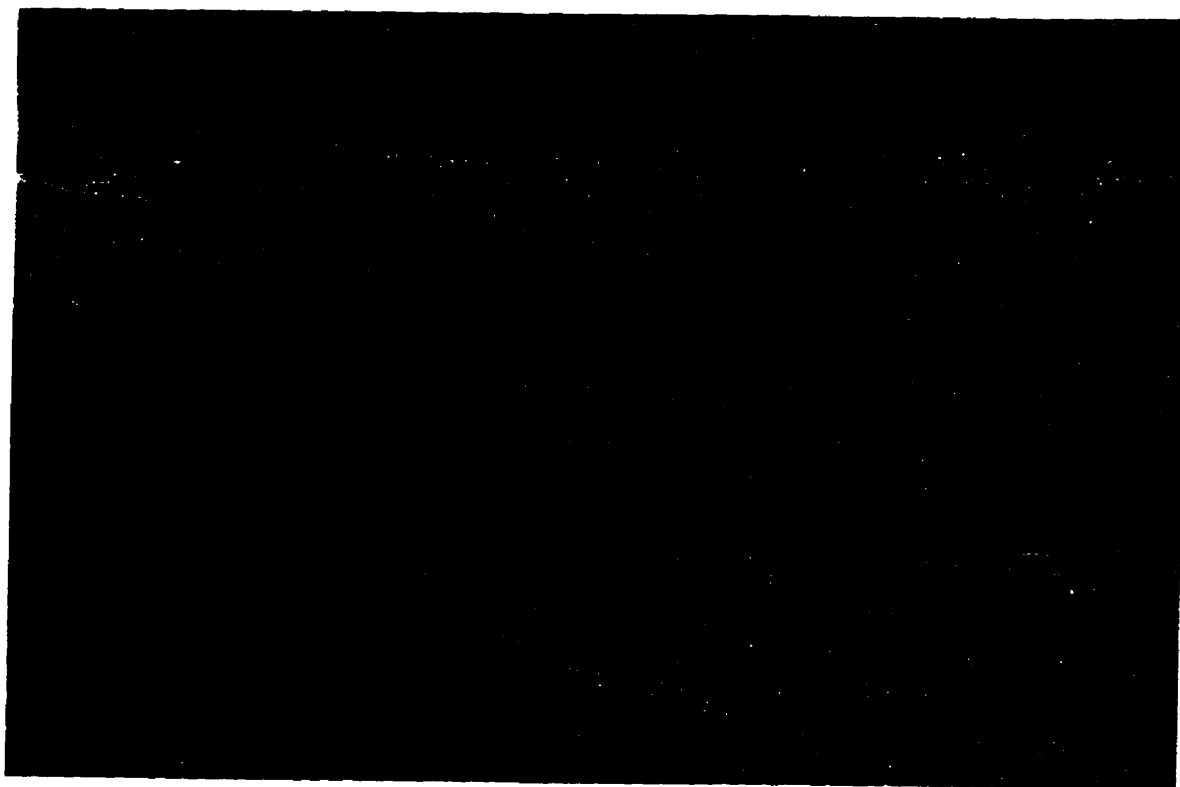
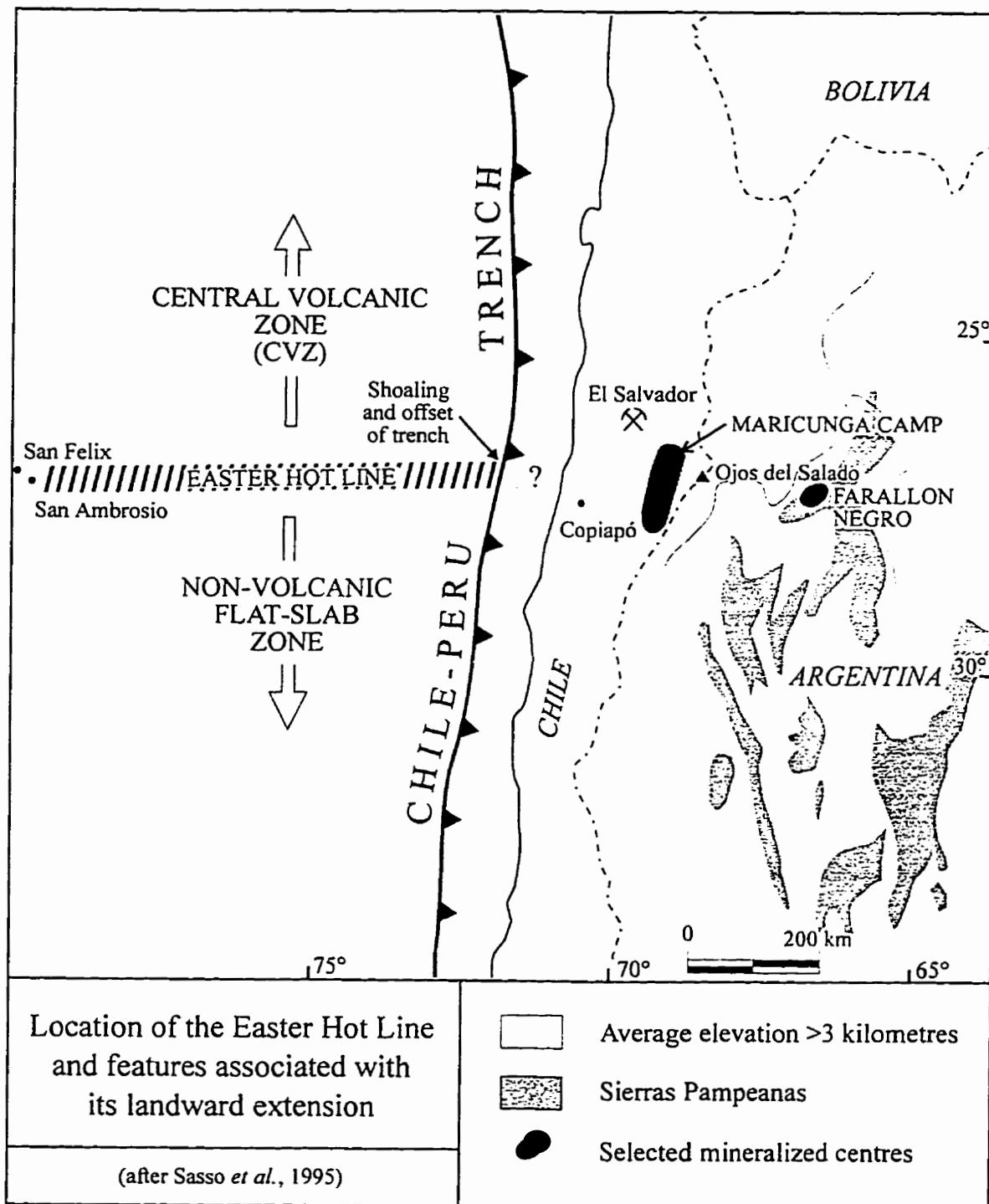


**Figure 2-5.**

East-west alignment of morphological, seismic and volcanic discontinuities associated with the landward extension of the Easter Hot Line. Also shown are the locations of the Eocene El Salvador porphyry Cu-Mo-Au centre, the Oligo-Miocene Maricunga Au-Ag district and the Farallón Negro area.





features to the south, and a 50 km E-W displacement of the Andean continental divide (highlighted by the jog in the Chile-Argentina frontier). Pleistocene-to-Recent volcanoes occur along and to the north of the 27° S transition but are absent to the south. The transition is marked by an E-W-trending line of young volcanoes in the Ojos del Salado volcanic chain (Fig. 2-6), which includes Ojos del Salado itself, which at 6,885 m a.s.l. is the highest volcano in the world. This alignment of features, termed the Ojos del Salado lineament by Zentilli (1974), is inferred to be the on-land manifestation of the Easter Hot Line, a Pliocene-to-Recent submarine volcanic chain on the Nazca Plate (Zentilli, *op. cit.*; Bonatti *et al.*, 1977; Baker *et al.*, 1987). Caelles (1979) recognized the continuation of the lineament into Argentina as an 80 km long east-west belt of Miocene-Pliocene volcanism in the Farallón Negro area. The Easter Hot Line has produced a chain of volcanic islands and seamounts over 6,000 km long, approximately 200 km wide, and roughly centred at latitude 27° S, supposedly delimiting a "mantle hot line" superimposed on the Nazca Plate. Bonatti *et al.* (1977) suggested that either the activity created by this hot line may have been able to cut across the subduction zone to act on the mantle beneath western South America, or that subduction of anomalous lithospheric material may cause anomalies in the Benioff zone which would be reflected on the overlying plate.

### ***Sierras Pampeanas***

The *Sierras Pampeanas* represent one of the main physiographic provinces of northwestern Argentina (Fig. 2-7). This province is dominated by NNW-trending mountain ranges underlain largely by Paleozoic crystalline basement and bounded by high-angle

**Figure 2-6.**

*Young volcanoes in the Ojos del Salado region,  
Chile and Argentina.*

**A.** View to the ESE across the eastern Maricunga Belt of northern Chile. The volcanoes on the horizon are Miocene basaltic andesitic-to-dacitic stratocones of the Wheelwright Volcanic Group. These peaks form the southwest rim of the Wheelwright Caldera. The road leading to Paso de San Francisco, a major E-W pass across the Andes, is located in the valley to the right (south) of the high peaks. The green lake in the centre of view is Laguna Santa Rosa. The white saline deposits extending to the left and hidden by the slopes of Volcán de Maricunga (foreground) represent the southern extension of the Salar de Maricunga. The road that veers right (south) out of the field of view provides access to the Marte, Lobo and Refugio gold deposits as well as to other prospects in the southern Maricunga Belt.

**B.** View to the WSW (from Argentina) of the Pleistocene 6610 m a.s.l. Volcán de Incahuasi (cloud-covered peak) in the Ojos del Salado Volcanic Chain. The Paso de San Francisco lies out of the field of view to the right.

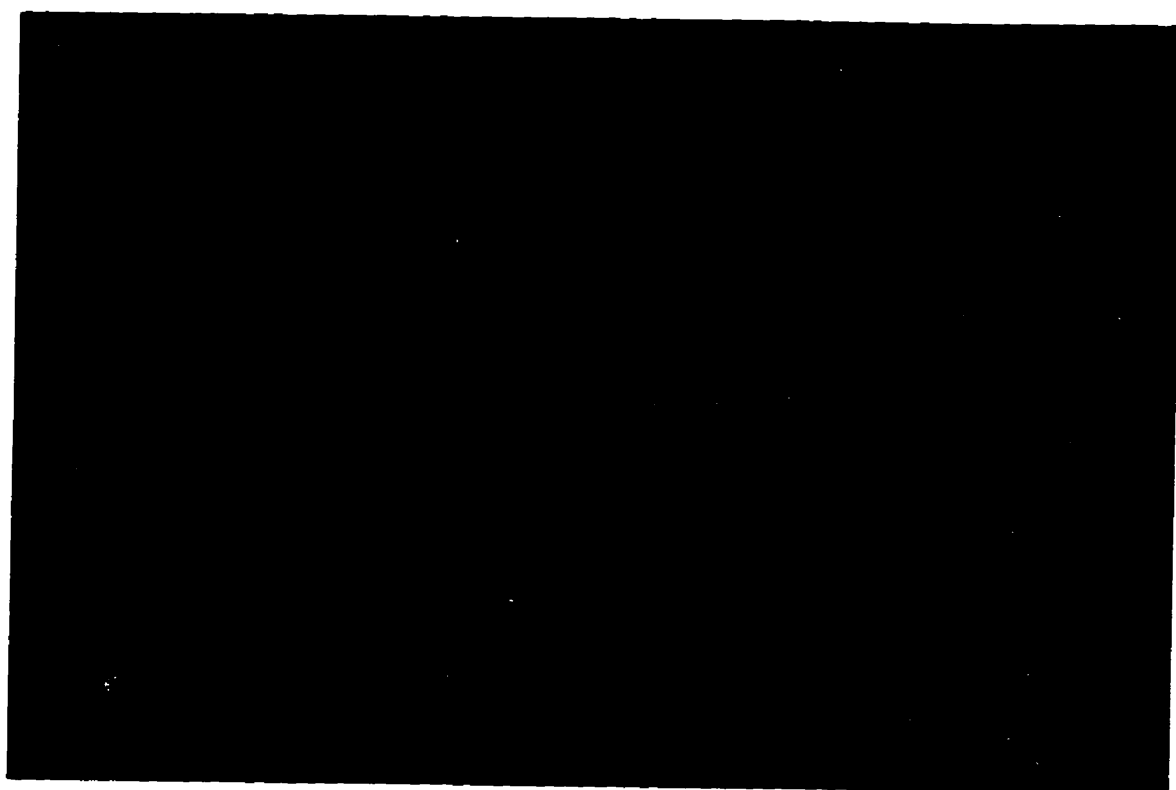
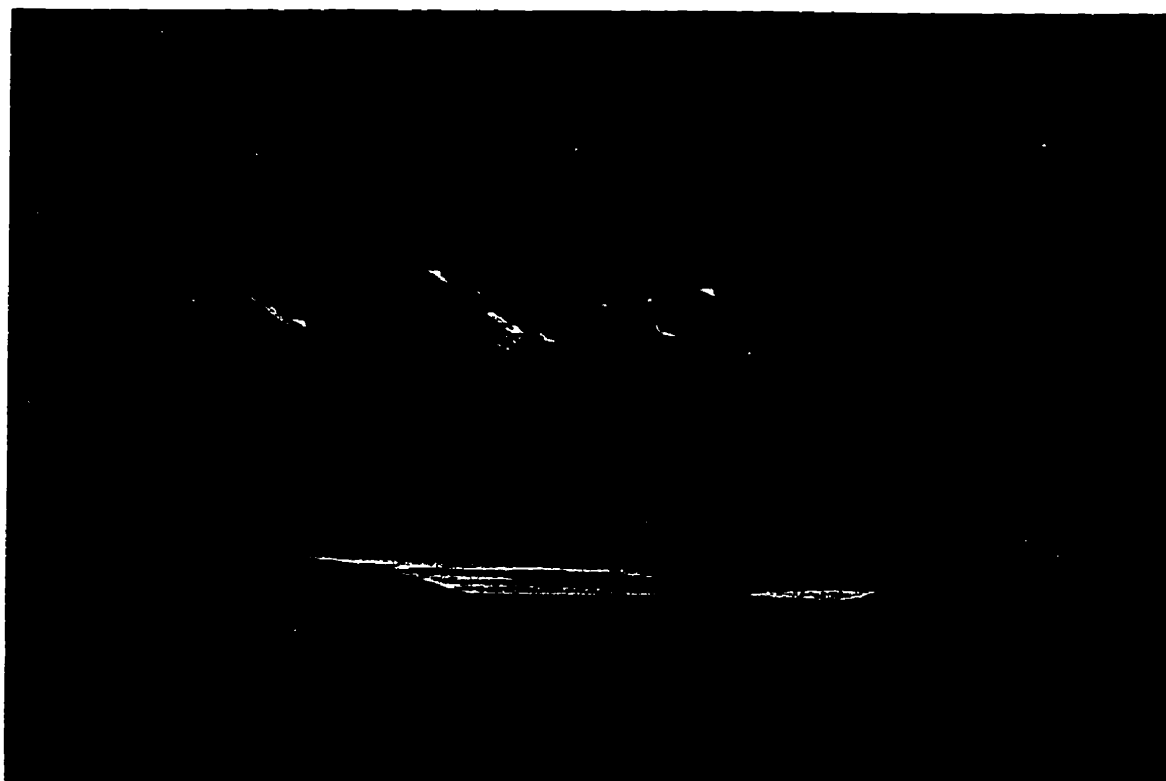
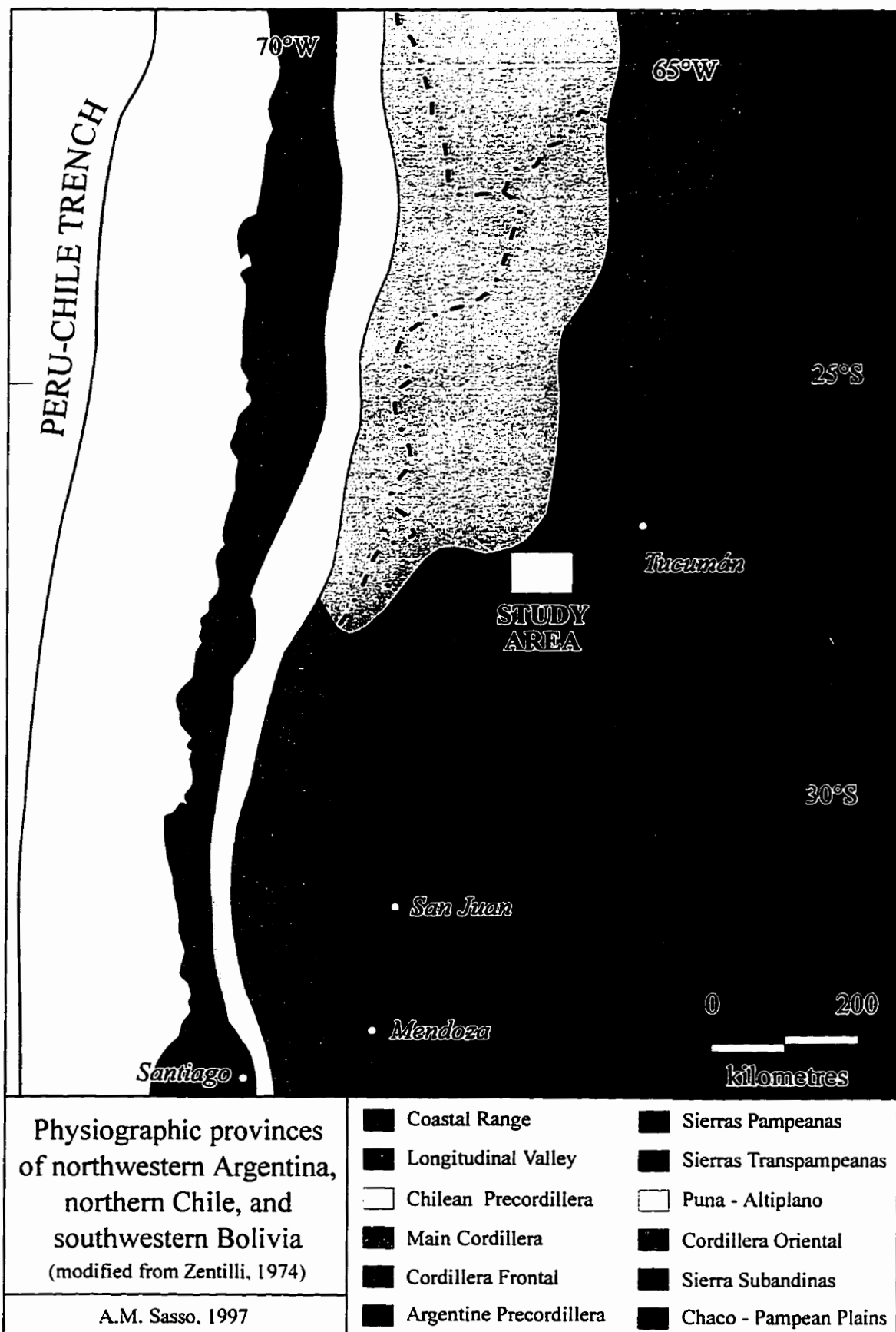


**Figure 2-7.**

Physiographic provinces of northwestern Argentina, northern Chile and southwestern Bolivia. The study-area is located at the boundary between the *Puna* province and the northern *Sierras Pampeanas* (modified from Zentilli, 1974).



reverse faults (Fig. 2-8). Analogies have been made with the "thick-skinned" Laramide uplifts of the western United States (Allmendinger *et al.*, 1983; Jordan *et al.*, 1983 and 1986). The timing of principal deformation in the Pampean Ranges is poorly constrained, but is thought to be Pliocene-to-Pleistocene (Jordan *et al.*, 1983). The mountain ranges commonly attain elevations of 2,000 to 4,000 m, locally rising to 6,000 m a.s.l., and are separated by broad, axially- and internally-drained basins. The latter are partially filled with Neogene and Quaternary sedimentary sequences which attain thicknesses of 4,000 m. The presently amagmatic *Sierras Pampeanas* experience shallow crustal seismicity. The earthquake focal mechanisms indicate E-W horizontal compression, but the nodal planes trend NNW, parallel to the tectonic grain of the ranges, suggesting the influence of pre-existing basement structures and lithologies on the young uplift event (Eremchuk *et al.*, 1981; Chinn and Isacks, 1983; Jordan *et al.*, 1983).

To the northwest, the *Sierras Pampeanas* exhibit a physiographic transition to the *Puna* (González Bonorino, 1950b), while the elevations of the ranges and intervening basin floors decrease from west to east. The *Puna* boundary is characterized by a series of *en echelon* structural blocks (Allmendinger, 1986). To the northeast, the *Sierras Pampeanas* grade into the southern extension of the *Cordillera Oriental*, a transition marked by the Santa Bárbara province, a small, Neogene, west-verging, thrust belt which constitutes the southern termination of a Cretaceous rift basin (Mon, 1979; Salfity, 1982; Jordan *et al.*, 1983; Grier *et al.*, 1991). The *Sierras Pampeanas* are bordered to the west by the *Precordillera*, representing a low-angle thrust belt, and grade eastwards into the flat, low-lying *Pampas* (Fig. 2-9). The southern limit of the *Sierras Pampeanas* coincides

**Figure 2-8.**

*Field characteristics of the Sierras Pampeanas in the Farallón Negro region.*

**A.** The Sierra de las Cuevas, located to the northeast of the Main Farallón Negro Stratovolcano, is a block of granitic basement which has undergone uplift along a NE-striking, NW-dipping high-angle reverse fault which lies approximately at the break of slope. View to the NW from the alluvial outwash plain north of Quebrada de Pozos Verde.

**B.** The Sierra de Aconquija (horizon), located to the northwest of the Main Farallón Negro Stratovolcano, was uplifted along a NNW-striking, ESE-dipping high-angle reverse fault. The fault trace is hidden by the low hills incised into Tertiary sediments (middle ground) in the southern Santa María Valley.

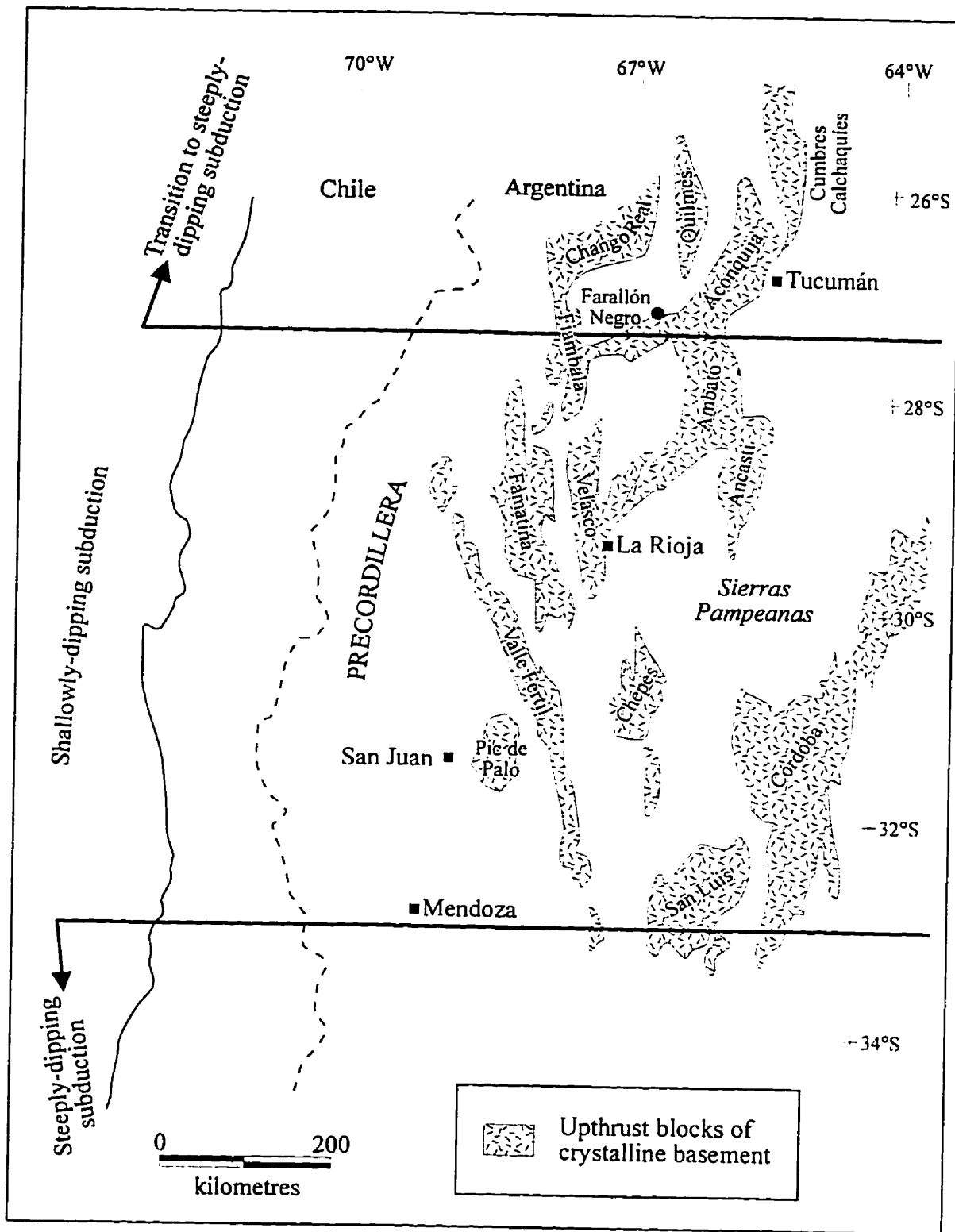




**Figure 2-9.**

*Morphology of the Sierras Pampeanas.*

The main *Sierras Pampeanas* overlie the domain of shallowly-dipping subduction. Their southern limit broadly coincides with the abrupt change in the angle of subduction located at approximately 33° S. The northern *Sierras Pampeanas* extend north into the transition zone to steeply-dipping subduction.



approximately with the southern boundary of the flat-slab subduction segment in San Luis and Mendoza Provinces. The northern boundary of the *Sierras Pampeanas* extends well into the transition zone north of 27° S. The Sierra de Famatina and Sierra de Narváez, in the northwest quadrant of the province (Fig. 2-9), are sometimes referred to as the *Sierras Traspampeanas* (Harrington, 1956; Turner, 1962). This distinction is made because of the abundance of low-grade metamorphic rocks and sedimentary rocks present in these ranges, but Caelles (1979) questions the significance of these relationships.

The morphological consistency of the *Sierras Pampeanas* physiographic province is attributed to the degree of rigidity of the basement units (Mon, 1972). The strength of the granitic and high-grade metamorphic schist and gneiss underlying the ranges is envisaged to have resulted in the formation of high-angle reverse faults as opposed to the thrusting and folding observed in the basement metagreywackes and phyllites of the Puncoviscana Formation in the provinces to the north. The range-bounding faults commonly strike parallel to the dominant basement schistosity, which is oriented NNW or NNE (González Bonorino, 1950b). The southern half of the Sierra Aconquija and the Sierra Chango Real, however, have orientations distinct from the rest of the *Sierras Pampeanas*, and González Bonorino (*op. cit.*) attributed their NE-SW orientation, parallel to the southern *Puna* boundary, to the predominance of granitic rocks in these ranges. The Pampean Ranges are generally asymmetric, being bounded on one side, commonly the western, by a steep reverse fault, but with a gently-sloping surface on the opposite side, disappearing beneath the Cenozoic basin-fill. On the basis of these relationships, González Bonorino (1950a and 1950b) inferred that the steeply-dipping faults flatten at depth, but

this interpretation has yet to be confirmed by seismic reflection data.

Several models have been advanced to explain the tectonic development of the *Sierras Pampeanas*. Salfity *et al.* (1984) proposed that faulting was contemporaneous with the final uplift phase of the Andean system, which is interpreted to have become pronounced during the Pliocene and is thought to have climaxed in the Early Pleistocene (Mon, 1972; 1976; Caminos, 1979). However, geochronological investigations in the Sierra de Famatina (McBride, 1972; Losada-Calderón *et al.*, 1994; Losada-Calderón and McPhail, 1996) demonstrate that uplift had there commenced by the latest Miocene, at 5 to 6 Ma, and that it persisted, episodically, at least into the Early Pliocene. New  $^{40}\text{Ar}$ - $^{39}\text{Ar}$  laser microprobe data generated by the present study are similarly interpreted (Chapter 5) to reveal uplift of the Capillitas and Aconquija ranges between 5.0 and 5.5 Ma. In another model, basement uplifts and associated low-angle subduction have resulted from the oblique subduction of the buoyant Juan Fernandez Ridge since 13 Ma, when it was overridden by the South American Plate (Pilger, 1981; 1984). In this model, the southward migration of the subducted ridge, as suggested by global Nazca-South America Plate reconstructions, would have resulted in time-transgressive development of the Pampean Ranges, with increasingly younger uplift to the south. However, this temporal-spatial relationship has not been supported by studies of the timing of deformation in the *Sierras Pampeanas* (e.g., Tabbutt *et al.*, 1987, 1988; Reynolds, 1987; Strecker *et al.*, 1989).

In general, the area of the *Sierras Pampeanas* corresponds to the region underlain by the flat-slab segment between 27° and 33° S, implying a strong correlation between the

styles of subduction and of structural development of the overriding plate (Allmendinger *et al.*, 1983; Cahill and Isacks, 1985). However, the northerly Sierra Quilmes and Sierra Cumbres Calchaquíes ranges (Fig. 2-9), extend well into the transition zone, where the Wadati-Benioff zone is becoming gradually steeper to the north. Strecker (1987) proposed an alternative model for the development of the northern *Sierras Pampeanas* which is independent of shallow subduction. He suggested that this region is underlain by thermally-thinned lithosphere which is the result of the formation of a broad asthenospheric wedge between the relatively shallowly-subducting oceanic slab and the overriding plate in the transition from steep to flat slab segments. Uplift of the ranges was thus a result of shortening of a mechanically weakened basement. This model accounts for the similarity in the morphologies of the uplifted blocks overlying the transition zone and the flat slab. This morphology is fundamentally controlled by the similar lithological and structural predisposition of the basement in both areas (Strecker, *op. cit.*; Strecker *et al.*, 1989).

### **Regional Geology**

The generalized regional geology of the broader Farallón Negro district is depicted in figure 2-10. The local geology mapped during this study is presented as figure 2-11; hereinafter the area encompassed by the latter map is referred to as the "study-area".

**Figure 2-10.**

Generalized regional geology of the study-area. Compiled from Jordan and Allmendinger (1986), Allmendinger (1986) and the present study. Note the areal relationships between the Farallón Negro volcanic centre and the southern boundary of the *Puna*, and to the regional change of strike of the Neogene uplifted blocks between the Sierras de Aconquija and Ambato.

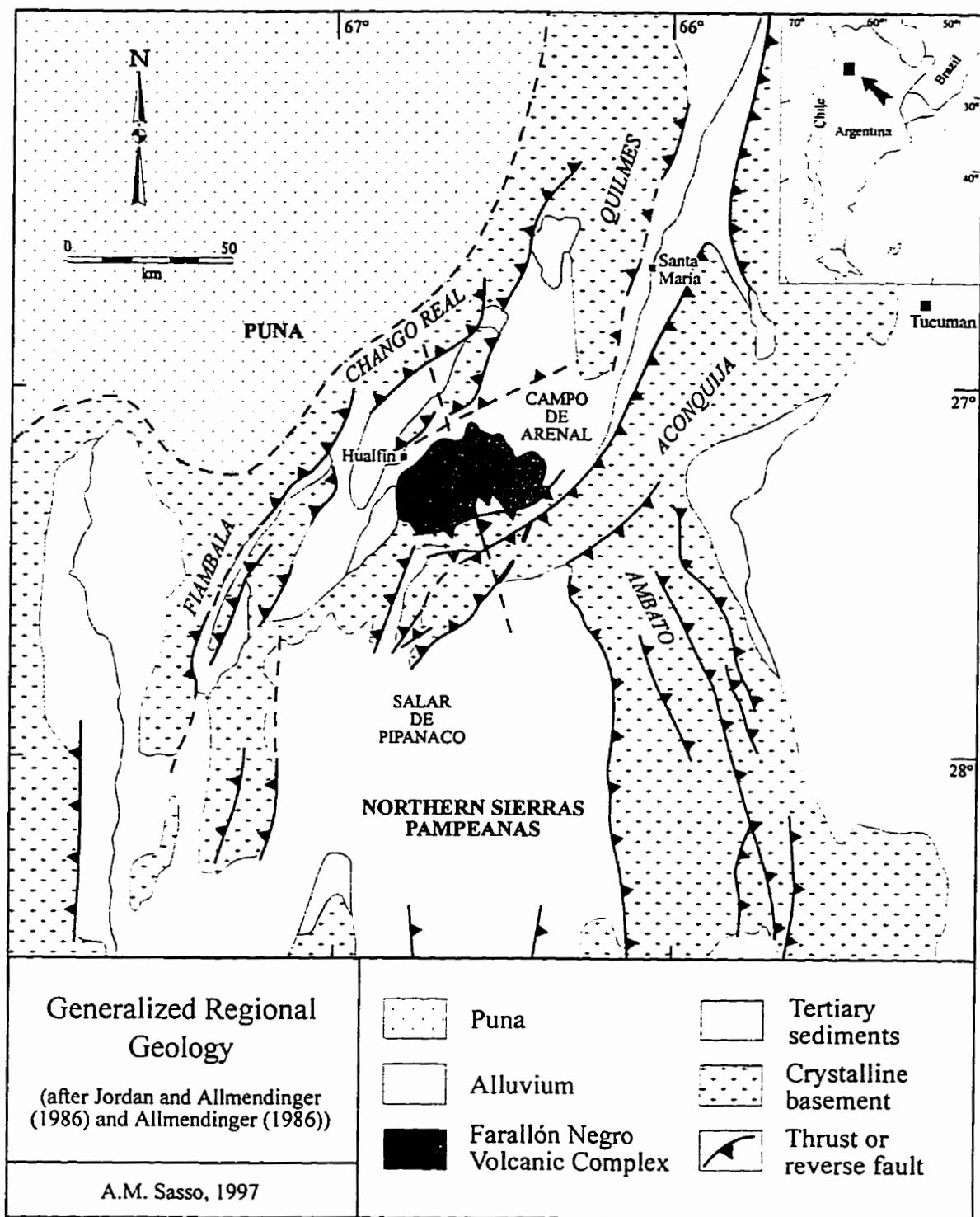
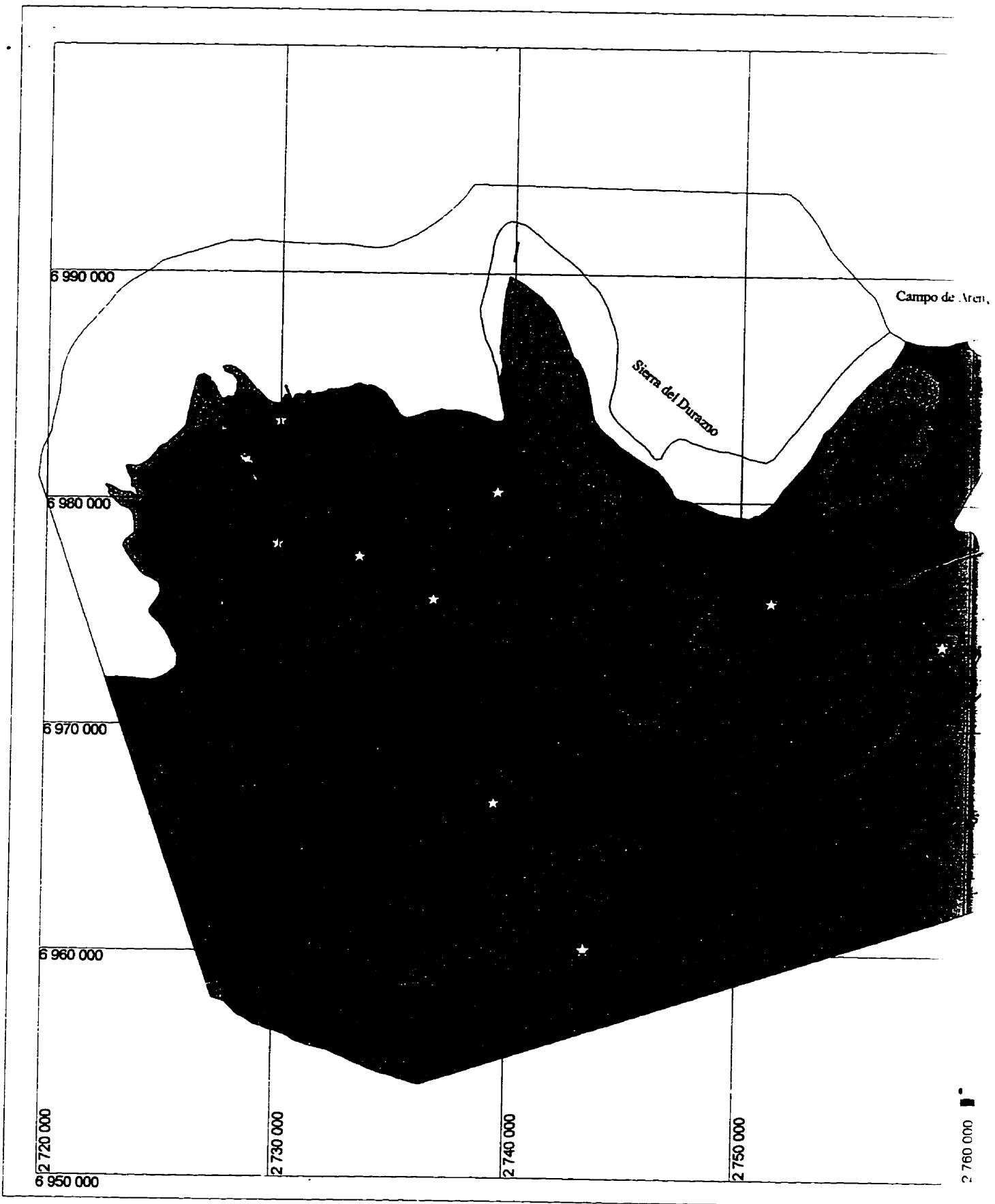




**Figure 2-11.**

Geological map of the Farallón Negro - Capillitas District.

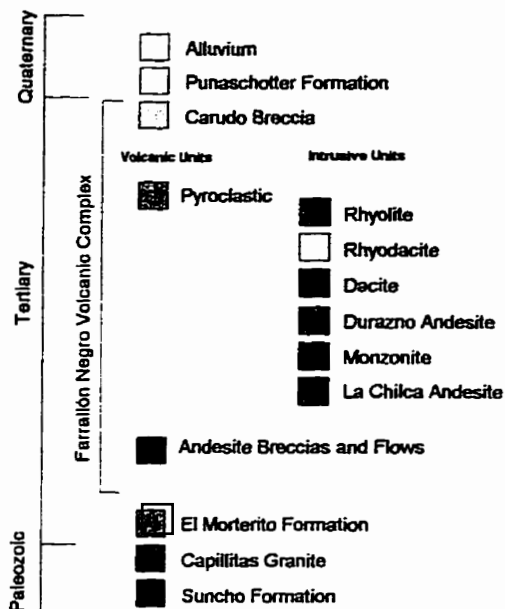




umpo de Arenal



## Legend



## Symbols

Reverse fault :  
observed (solid)  
inferred (dashed)

Normal fault :  
observed (solid)  
inferred (dashed)

Deposit

**Geological Map of Farallón Negro  
Capillitas District  
Catamarca Province, Argentina.**

Anne M. Sasso.

May, 1997

Base : Digital Enlargement of Landsat TM image.



## ***Crystalline Basement***

### **Suncho Formation**

The oldest rocks in the area are deep-water, flysch-type (meta-) sediments. This unit was defined by Mirré and Aceñolaza (1972) and corresponds to the "Slates of the Sierra de la Ovejera and Ampujaco" (*Pizarras de la Sierra de la Ovejera y Ampujaco*) of González Bonorino (1950a).

The unit consists of an homogeneous succession of pelites and arenites. The rhythmic banding of the sequence is well exposed in the Vis Vis Valley. Colour varies from pale- and greenish-grey to dark-green, with red oxidized zones associated with alteration along faults. The unit has undergone penetrative deformation and isoclinal folding. The base of the formation is not exposed and hence its thickness is uncertain. The top is seen locally as an erosional surface overlain by Tertiary sediments (e.g., San Lucas area: Durand, 1982). Regional metamorphism of the lower greenschist facies affected these units and was overprinted by contact metamorphism which accompanied the emplacement of the Capillitas Batholith.

The presence of *Oldhamia* ichnofossils (Mirré and Aceñolaza, 1972; Durand, 1982) indicates an Early Cambrian age of deposition, and this unit has been correlated with the Puncoviscana Formation in the *Cordillera Oriental* (Aceñolaza and Toselli, 1978) on the basis of lithological similarities and trace fossils. A K-Ar age of 424 Ma was determined by McBride (1972) for a sample of phyllite from the Vis Vis valley. This age may have been reset by the intrusion of the Capillitas Granite and may represent an age of intrusion rather than regional metamorphism.

### Buey Muerto Schists

This unit crops out in the northeast corner of the map-area along the western flanks of the Sierra de Aconquija, and also forms roof-pendants in the Capillitas Batholith. It was defined by González (1978) and is equivalent to the Aconquija Schists (*esquistos del Aconquija*) of González Bonorino (1950a). These strata are generally of higher metamorphic grade than the Suncho Formation and comprise banded schists of quartz-biotite-plagioclase-muscovite and quartz-microcline-andesine-hornblende-biotite compositions. Ptigmatic segregations of quartz occur locally. The colour varies from greyish-black to dark-grey.

This unit has not been dated by radiometric methods and trace fossils have not been reported. Aceñolaza *et al.* (1982) tentatively correlate it with the Suncho Formation. It is herein suggested that this unit represents a lateral facies equivalent of the Suncho Formation as a whole, or possibly of a lower member of the latter, and it has therefore been grouped with the Suncho Formation in figure 2-11. The high grade of metamorphism may be due to the greater uplift of the units to the east of the Río Vis Vis relative to those to the west (see below).

### Capillitas Granite

González Bonorino (1951) concluded that all granitic outcrops within the Capillitas and Andalgalá 1:200,000 map-sheets constitute a single intrusive body, the Capillitas Batholith, the largest granitoid complex in the northwestern *Sierras Pampeanas*.

Textures in the granite vary from porphyritic to equigranular. Grain-size ranges

from fine- to coarse-grained, with microcline crystals in the porphyritic facies attaining lengths of 10-15 cm (Fig. 2-12). The rocks consist of plagioclase, quartz and alkali feldspar with accessory biotite, sillimanite, muscovite, cordierite, zircon, apatite, rutile and ilmenite. Chlorite, muscovite and kaolinite occur as alteration products. The granites are peraluminous and calc-alkaline (Caelles, 1979), and range in composition from syenogranite in the south-western portion of the study-area (Durand, 1982) to monzogranite to the east (Indri, 1979).

Simple pegmatites, composed of quartz, microcline, muscovite and tourmaline, are common in the granites. Pegmatite swarms with graphic granite textures are notable in the Sierra de Capillitas to the northeast of the Capillitas Mine and in the anticlinal dome to the north of Cerro Atajo and Capillitas. Lamprophyre dykes locally intrude the granitic and metamorphic basement.

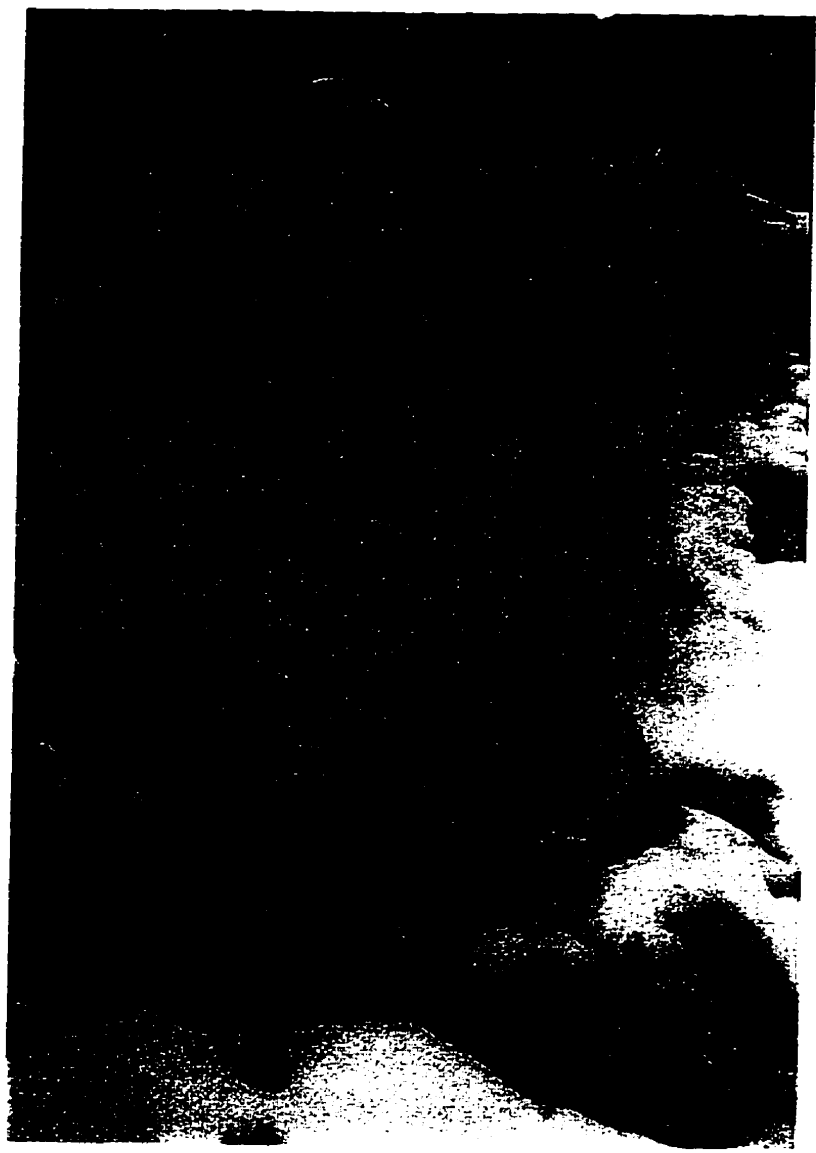
In the Sierra de Ovejera, Durand (1982) classified the batholith as epizonal with a maximum depth of emplacement of 5 km, on the basis of the lack of foliation and the sharp contacts with the metamorphic host. González Bonorino (1950a) describes abundant xenoliths of the metamorphic envelope which have been variably assimilated, and attributes these to an emplacement mechanism involving "piecemeal stoping". There are numerous mafic, microgranitic bodies (enclaves) which record magma commingling and mixing (A.H. Clark, pers. comm., 1994).

McBride *et al.* (1975) determined Ordovician K-Ar ages for the granites which range from 423 to 471 Ma. Aceñolaza *et al.* (1982) suggest that the plutonism was associated with the Famatinian Orogeny, part of the Famatinian Cycle which extended



**Figure 2-12.**

Lithological characteristics of the porphyritic facies of the Capillitas Granite. Coarse microcline phenocrysts are observed in a coarsely crystalline matrix which consists of plagioclase, quartz, microcline and biotite. The outcrop is located in the Sierra Aconquija, along the access road to the Agua Rica deposit.



from the Late Cambrian to the Late Devonian.

### Mylonites

Llambías (1972) noted the distinct difference in metamorphic grade and composition between the units in the high hills to the east of the Río Vis Vis and those exposed in the river valley and to the west. The former are gneissic migmatites and potassium feldspar-megacrystic granites and may represent deeper portions of the basement than the slates and phyllites exposed further west. Llambías invoked a north-northwest-striking fault to account for the difference in metamorphic grade. This offset must have pre-dated the emplacement of the Farallón Negro Volcanic Complex (see below).

The north-northwest discontinuity is marked by a well-developed zone of mylonitization of the granite. Up to 400 m wide, this runs along the western margin of Bola del Atajo and wraps around its northern side. The mylonite zone comprises gneisses, schists, mylonites and ultramylonites, the degree of deformation increasing from east to west. González Bonorino (1950a) suggests an age between Ordovician and Paleogene for the mylonites.

### *Planation of the crystalline basement*

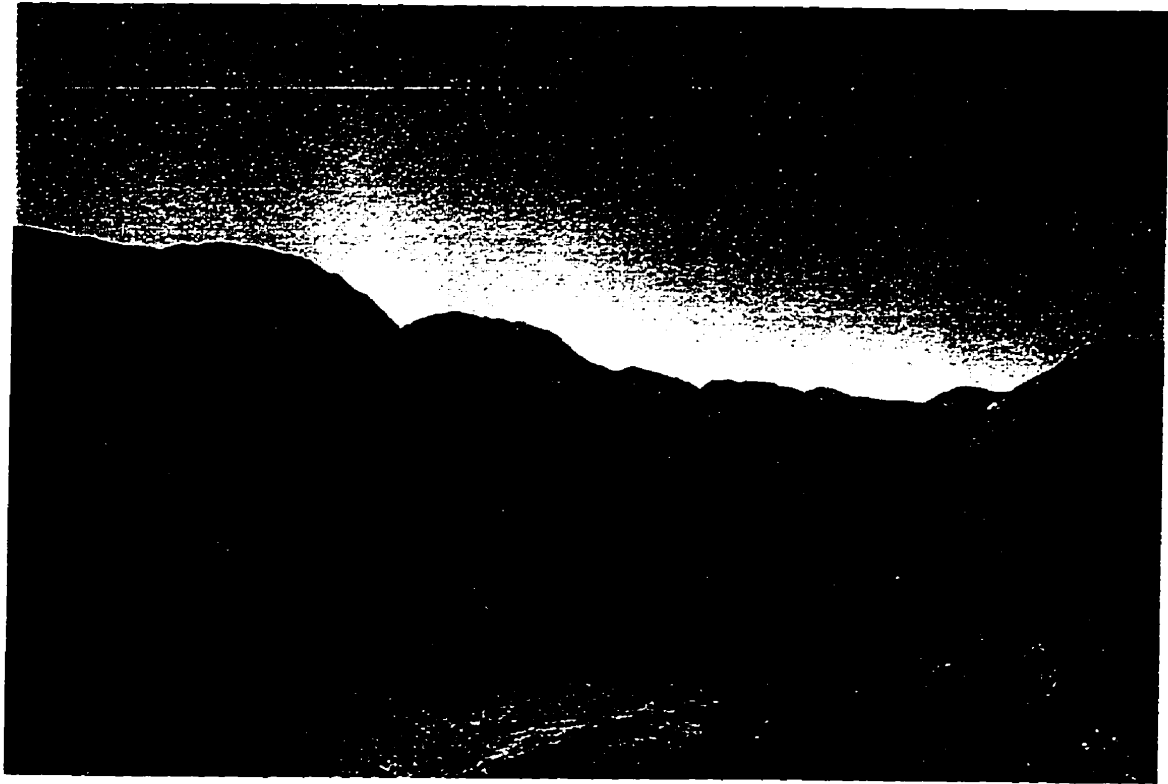
Throughout the *Sierras Pampeanas* an extensive planate surface is developed on the basement rocks (Fig. 2-13). The age of this surface is poorly constrained. In the study-area, it must be younger than the intrusion of the Capillitas Batholith and older than the

**Figure 2-13.**

*Field characteristics of the planate basement surface.*

**A.** Exposure of the planate surface on the south-eastern slope of Bola del Atajo (view to the east-northeast). The steeply-dipping surface is underlain by granite and overlain by red sediments of the El Morterito Formation (right foreground).

**B.** Exposure (right) of the planate surface on the south-eastern slope of the Sierra de Capillitas (view to the west-southwest). Strata of the El Morterito Formation (left-foreground) overlie the planated granitic basement. Bluish-grey outcrops in erosional gullies in the ridge on the near horizon are andesitic breccias of the Farallón Negro Volcanic Complex. Rock-cut pediment surfaces of probable mid-Miocene age are developed on the volcanic strata (sub-horizontal surfaces in the centre of view - near horizon and on the left horizon).



El Morterito Formation (see below), *i.e.*, between the Late Silurian and Middle Miocene. The consistent morphology of the surface throughout the *Sierras Pampeanas* has led many researchers to conclude that it represents a formerly continuous "peneplain" (González Bonorino, 1950b, 1951; Turner, 1971). Jordan *et al.* (1989) presented thermochronometric data from the Sierras de Córdoba, Velasco, and Ancasti, in the eastern and central *Sierras Pampeanas*, which suggested slow denudation of the basement during the Mesozoic and Cenozoic, and noted that the planated surface is diachronous by more than 300 m.y. Fission-track cooling ages of apatite crystals,  $^{40}\text{Ar}/^{39}\text{Ar}$  ages of potassium feldspars, and the K-Ar age of a muscovite were interpreted to demonstrate slow cooling of the crust since the end of the Paleozoic. Stratigraphic data indicate that the planated surface formed after the middle Paleozoic, but that elevations close to sea-level were not attained before the Neogene. On the basis of the present distribution of Upper Paleozoic and Triassic strata and paleogeographic reconstruction of facies distributions, Jordan *et al.* (*op. cit.*) concluded that during the deposition of these rocks the eastern *Sierras Pampeanas* constituted a mountainous region with intermontane basins to the east and west and that pronounced local relief existed across basin margins in the central and western *Sierras Pampeanas*.

Expansive planated surfaces are documented in the Chilean Andes at these latitudes. The Atacama Pediplain (Clark *et al.*, 1967; Sillitoe *et al.*, 1968), a dominant landform over an extensive area on the western flanks of the Andean Cordillera, is interpreted to have formed rapidly (A.H. Clark, pers. comm., 1997) between 9.15 and 12.6 Ma (Clark *et al.*, *op. cit.*). The formation of this surface records a period of significant

uplift and erosion to the west of the Farallón Negro region. Whether the continental divide attained sufficient altitude at this time to have generated erosional events as far east as the study area is unclear. However, the deposition of the thick El Morterito sediments which, in the vicinity of Farallón Negro, were derived from the granitic basement (Bossi *et al.*, 1993), records a period of significant uplift and erosion. Given the semi-arid environment that probably existed in the Miocene, the erosion would have been dominated by the development of pediplains rather than canyon incision. Valley pediments are developed in volcanic strata in the Capillitas Valley, south of the Capillitas deposit (Figs. 2-11 and 2-13b). These surfaces are sub-horizontal and indicate periods of uplift and erosion. The timing of their formation is poorly constrained. The surfaces are incised into a section of volcanic units which includes a 9.17 Ma dacite flow. Their sub-horizontal attitude would suggest an age of formation post-dating the major uplift event responsible for the formation of the *Sierras Pampeanas* which tilted the plateau basement surface up to 30° (see figure 2-13). Strecker *et al.* (1987) document a series of pediment surfaces in the Santa María Valley which formed between 2.5 and 0.3 Ma. The rock-cut pediments observed in the Capillitas Valley may be contemporaneous with those of the Santa María Valley, but more detailed field work will be necessary to resolve this relationship.

### ***El Morterito Formation***

This unit (Figs. 2-10 and 2-11) was first described by Turner (1962; 1973) as a series of continental red beds, including conglomerates, sandstones and siltstones,

cropping out to the west of the Sierra de Cajón, in the Laguna Blanca map-sheet. Aceñolaza *et al.* (1982) correlated these strata with the El Calchaquense (González Bonorino, 1950a) in the Sierra de Capillitas and surrounding areas, on the basis of lithological and stratigraphic similarities. The nomenclature varies from map-sheet to map-sheet but the term *Calchaquense* has been applied to all Cenozoic red-bed sequences exposed in northwestern Argentina. An effort is underway (Bossi *et al.*, 1993; C. Muruaga, pers. comm., 1994) to rationalize the stratigraphic nomenclature. The El Morterito Formation corresponds to Bossi *et al.*'s "Sequence I" in the Santa María - Hualfin Neogene basin (Fig. 2-10).

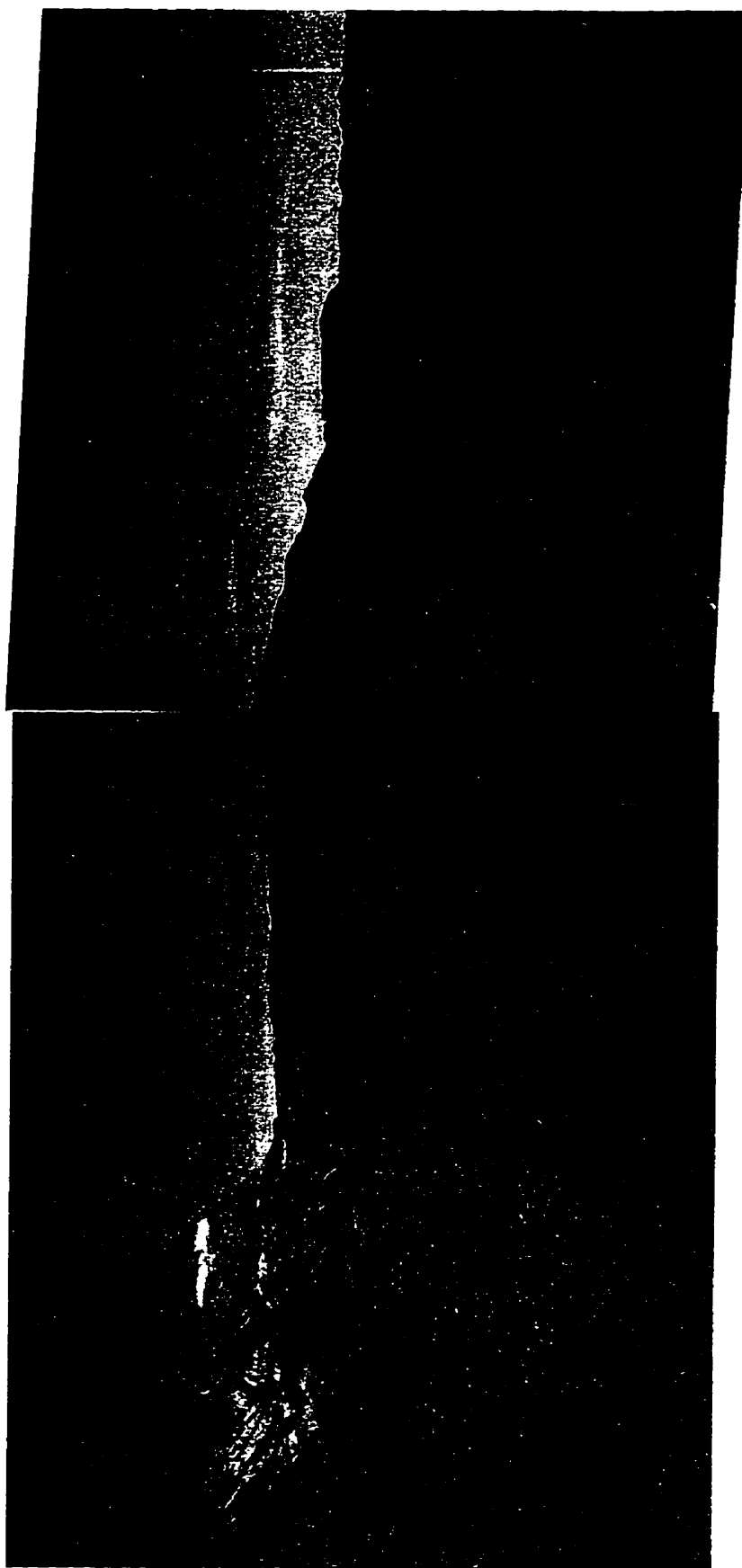
The unit is fairly homogeneous, but may be subdivided into lower and upper sequences. The former is primarily a series of polymictic conglomerates with a fine, red, sandstone matrix and intercalated red, micaceous, fine-to-medium-grained sandstones and finely-laminated siltstones (Fig. 2-14). The upper sequence is pale-buff in colour and consists of fine-grained calcareous sandstones with thin, grey, limey horizons. It is generally absent in the vicinity of the Farallón Negro Volcanic Complex. Intercalations of pyroclastic material and volcanic detritus become more common with proximity to the volcanic edifice. Sedimentation was probably characterized by short periods of intense, "flash flood", deposition, alternating with extended periods of relative quiescence. This unit is inferred to have attained a thickness of 1500 m (Bossi *et al.*, 1993), but outcrops are limited in the area of the present study. They rest disconformably on the planate basement surface (Fig. 2-13b) and did not achieve significant thickness before the onset of volcanism. Thicknesses range from approximately 20 m in the Capillitas area to 63 m



**Figure 2-14.**

*Field characteristics of the El Morterito Formation.*

View to the south along the axis of a broad anticline in the foothills of the Sierra Durazno. These outcrops are of the lower part of the formation and consist of interbedded sandstones, siltstones and conglomerates. The paler units on the slopes to the left are tuffaceous horizons which mark the transition from the El Morterito Formation to volcanic units of the Farallón Negro Volcanic Complex. A thin basaltic flow (not discernible at this scale) crops out at the base of the cliff band at the left of the field of view and is overlain by thick volcanoclastic gravels of the Punaschotter Formation (*Distal Volcanoclastic Facies*).



in the Sierra Durazno area (Bossi *et al.*, 1993).

Turner (1962, 1973) assigned this unit a Miocene age on the basis of vertebrate and invertebrate fossils. I found vertebrate fossils at several localities in the Sierra Durazno area. The stratigraphic position, underlying the Farallón Negro Volcanic Complex, also predicates a Middle Miocene or older age. An age of 13 Ma for initiation of sedimentation in the basin is suggested by Bossi *et al.* (1993) based on radiometric dating (technique not specified) of a tuff from the base of the sequence.

The nomenclature for this unit is vague, correlation between published sections is not straightforward, and the calculated rates of sedimentation, preserved section thicknesses and available geochronological data are often mutually conflicting. Discrepancies may be due to several factors, including errors in the estimation of sedimentation rates and the time of initial sedimentation, an older age for the initiation of volcanism than previously thought, and a slower rate of sedimentation during the early stages of the development of the basin. Alternatively, these discrepancies could reflect the focussing of volcanism in a pull-apart basin-type setting (Sasso *et.al.*, 1995). In this case, the continued stretching of the centre of the basin, followed by rupture and eruption of volcanics to form a new floor would result in the earlier strata being confined to the attenuated margins of the structure (Crowell, 1974). This is the preferred interpretation and will be elaborated upon in Chapter 6.

#### ***Farallón Negro Volcanic Complex***

Over much of the map-area, the volcanic rocks of the Farallón Negro Volcanic

Complex overlie the El Morterito sediments. The volcanic and hypabyssal rocks will be discussed in detail separately below.

### ***Araucanense Formation***

This unit has not been recognized in the study-area but is included herein for the sake of completeness. First described by González Bonorino (1950a), it is equivalent to the El Cajón Formation of Turner (1962, 1973) and has been assigned to the upper portion of the Sequence II of Bossi *et al.* (1993). It is one of the most intensely studied units in the Andean Cordillera due to its abundant and diverse vertebrate fauna (Allmendinger, 1986).

It consists of a sequence of buff, fine-to-medium-grained, commonly cross-bedded and tuffaceous sandstones, conglomerate lenses and beds, with numerous tuff horizons. The erosion of the Farallón Negro volcanic edifice, probably the highest then-existing topographic feature, resulted in the deposition of the thick sequences of reworked conglomerate and volcanic breccia forming the base of the formation (Bossi *et al.*, 1993). It has been dated using both magnetic reversal stratigraphy and conventional potassium-argon geochronology. Butler *et al.* (1984) calculated ages of 7.5 Ma and 6.4 Ma, respectively, for the lower and upper boundaries of a 2400 m thick section at Puerto de Corral Quemado, approximately 35 km west-southwest of the Farallón Negro area. The geochronological data, in conjunction with the magnetic reversal stratigraphy, indicate a very consistent rate of sedimentation of 56 cm/1,000 yr (Butler *et al.*, *op. cit.*). The unit is almost 4000 m thick in the section between Hualfín and Corral Quemado

(approximately 15 km to the north of Farallón Negro), with approximately 660 m of conformable section preserved above the highest tuff dated (Allmendinger, 1986). Allmendinger (*op. cit.*) applied the rate of sedimentation calculated by Butler *et al.* (*op. cit.*) to the remainder of the section to estimate an age of approximately 2.35 Ma for the uppermost-exposed unit in the area.

### ***Punaschotter Formation***

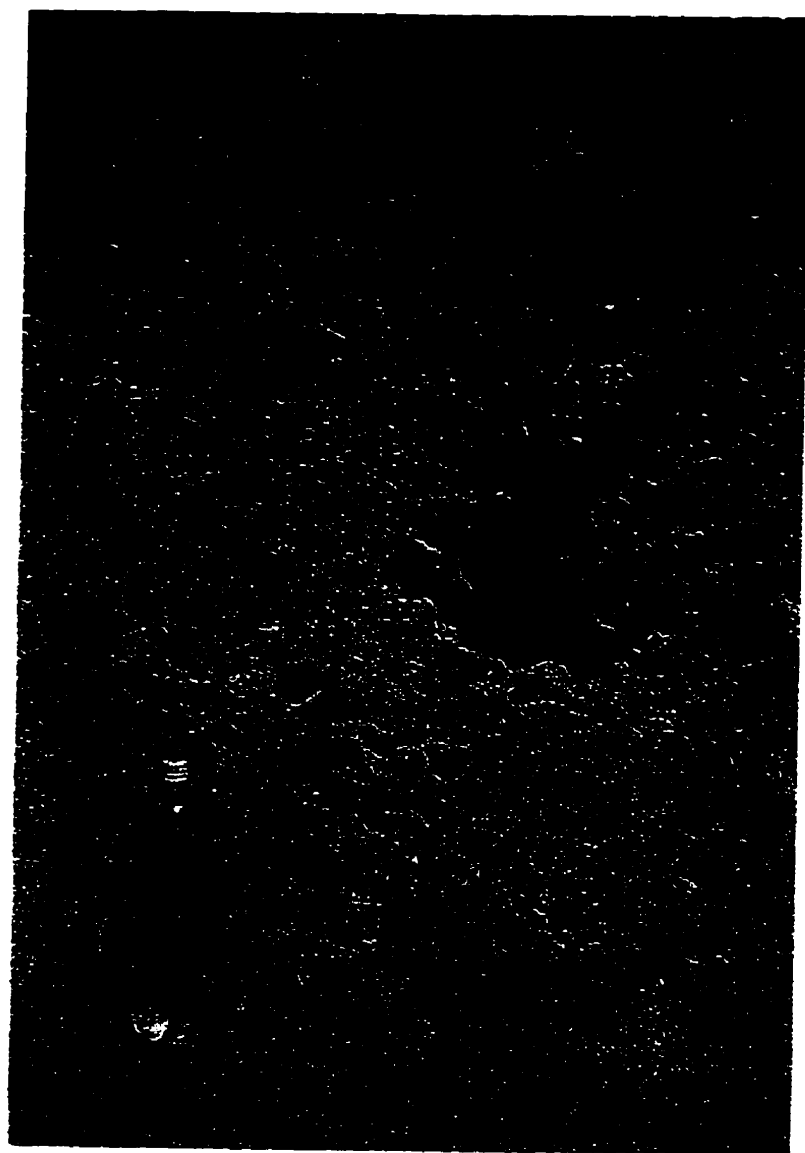
Overlying all other rocks in the Farallón Negro region with slight unconformity or disconformity, this succession of alluvial and colluvial deposits was first described by Penck (1920) at the southern extremity of the *Puna* in the region of the Bolsón de Fiambalá. Allmendinger (1986) correlated similar boulder conglomerates in the Sierra de Hualfin - Sierra Las Cuevas area with this unit. Bossi *et al.* (1993) equate the Punaschotter strata with their Sequence III in the Sierra Durazno.

In the vicinity of the Farallón Negro Volcanic Complex, the unit consists of a boulder conglomerate of almost exclusively volcanic provenance (Fig. 2-15). Clasts are rounded and the sediment is clast-supported, with a sandy matrix of similar composition. The thickness is estimated at 200 m in the Sierra Durazno. Paleocurrent features indicating a northeasterly flow direction and the clast compositions both indicate a provenance in the area of Alto de la Blenda (Bossi *et al.*, 1993; Fig. 2-11). Bossi *et al.* also concluded that this unit was deposited prior to the uplift of the Sierra Durazno; the latter event is interpreted to be Pleistocene in age, but no basis is given for this conclusion.

**Figure 2-15.**

*Lithological characteristics of the Punaschotter  
Formation.*

Boulder conglomerates with rounded clasts of predominantly volcanic provenance located on the far-eastern flank of the Sierra Durazno approximately 10 km NNE of Cerro Atajo. These gravels were deposited by braided stream systems on the flanks of the stratovolcano and represent the Distal Volcaniclastic Facies (see below). An andesitic tuff overlying these outcrops yielded an age of 8.75 Ma.



In areas remote from the Farallón Negro Volcanic Complex, the unit consists of a boulder conglomerate of granitic and subordinate metasedimentary clasts, locally interbedded with medium-to-coarse sandstone. North of the study-area the thickest sequences of the gravels are located in structural lows between basement horsts (Allmendinger, 1986). Topographic relief resulting from deformation and uplift of the basement prior to the deposition of the Punaschotter probably controlled the deposition of the unit.

No direct evidence exists for the age of this unit. Locally it must be younger than the Araucanense Formation for which, as previously noted, Allmendinger (1986) calculated a minimum age of *ca.* 2.35 Ma. That author therefore inferred an early Quaternary age for the Punaschotter. However, andesitic tuffs interbedded with gravels assigned to a unit equivalent to the Punaschotter by Bossi *et al.* (1993; see above) in the Sierra Durazno yielded ages of 8.75 and 6.72 Ma (this study), clearly contradicting the age proposed by Allmendinger (1986). In the immediate vicinity of the Farallón Negro Volcanic Complex these gravels are herein interpreted to represent the Distal Volcaniclastic Facies associated with the formation of the Main Farallón Negro Stratovolcano (see below) and thus were forming during volcanism, as is indicated by the interbedded tuffs. The name Punaschotter has been retained herein, but it is suggested that its application to the gravels directly overlying and exhibiting lateral transitions to rocks of the Farallón Negro Volcanic Complex may be misleading. More detailed field investigation will be required to resolve the classification of these units.



## **Lithostratigraphic Nomenclature**

### ***Existing Nomenclature***

The rocks of the Farallón Negro region were first documented in the mapping of the Capillitas 1:100,000 map-sheet by González Bonorino (1950a). He briefly described the distribution and nature of the volcanic and intrusive units and their relationship to regional stratigraphy, grouping them as *El Complejo Volcánico* ("Volcanic Complex"). It is assumed that this represented the formal recognition of a distinct lithostratigraphic unit. The most detailed descriptions of the volcanic and intrusive units of the region are those of Llambías (1970; 1972). He defined the *El Grupo Volcanico Farallón Negro* ("Farallón Negro Volcanic Group") to include the volcanic and associated hypabyssal intrusive units within the "Area de Reserva del distrito mineralizado Yacimientos Mineros Agua de Dionisio", an area bounded approximately to the north and west by the limit of outcropping volcanic units, to the south by the Quebrada de San Buenaventura, and to the east by Bola del Atajo and an unnamed fault responsible for the uplift of the Sierra Durazno (Fig. 2-11). Llambías noted the existence of other nearby Tertiary volcanic centres at Vis Vis, Capillitas, and Cerro Atajo, and suggested that they were once part of a larger, continuous volcanic outcrop which underwent tectonic segmentation and variable uplift and erosion.

Local exposures of volcanics on neighbouring map-sheets have been correlated with the rocks of the Farallón Negro district, largely on the basis of their stratigraphic position, *i.e.*, overlying red beds of the Calchaquense (or El Morterito) Formation but overlain by the Araucanense Formation. These include: the El Aspero Formation, exposed

on Hoja 11d, Laguna Blanca (Turner, 1973) and Hoja 12c, Laguna Helada (Ruiz Huidobro, 1975); Tertiary eruptives in Hoja 13c, Fiambalá (González Bonorino, 1972); the El Zarzo Formation, Hoja 11e, Santa María (Ruiz Huidobro, 1972); volcanic breccia, Hoja 12e, Aconquija (González Bonorino, 1951); the El Aspero Formation, Hoja 10e, Cafayate (Navarro Garcia, 1982); and possibly the more remote Cerro Rosillo Andesite Formation (Maisonave, 1973) in Hoja 13b, Chaschuil (mapped by Turner, 1967). These tentative correlations imply the existence of a much more extensive Tertiary volcanic province than is now evident, but its original volume and continuity remain uncertain.

The El Aspero Formation was first defined by Turner (1973) in the Laguna Blanca map-sheet immediately northwest of the study-area. He combined the El Morterito Formation (equivalent to the Calchaquense Formation), El Aspero Formation and El Cajón Formation (equivalent to the Araucanense Formation) to establish the *Grupo El Bolsón* (El Bolsón Group), to which he attributed a Late Tertiary age. The El Aspero Formation was considered to be temporally equivalent to the *Complejo Volcánico* of González Bonorino (1950a). A southerly provenance in the Farallón Negro region was postulated for the rocks of the El Aspero Formation.

In the Laguna Blanca map-sheet, Bossi *et al.* (1993) proposed a change in the stratigraphic rank of the El Aspero *Formation* of Turner (1973) to the El Aspero *Member* on the basis of its lenticular character and its disappearance to the south in the Puerta de Corral Quemado area. However, they do not indicate to which formation, *viz.* El Morterito or El Cajón, the Member would belong. The bottom of the sequence is defined by conglomerates of volcanic origin which are overlain by andesitic breccias and flows. Its

top is marked by volcanic conglomerates, pelites and medium-grained sandstones. A sample (FAR 285) of the volcanic breccia which crops out in the Villa Vil valley was investigated during this study. Its geochronological (Chapter 5), geochemical and petrographic (Chapter 4) characteristics are indistinguishable from those of the andesite breccias of the Farallón Negro Volcanic Complex and it is interpreted (see Chapters 4 and 5) to represent a cogenetic flow of this complex, albeit possibly a distal one. I therefore disagree with the demotion in rank proposed by Bossi *et al.* (1993) for these strata, because this does not take into consideration the broader relationships of this unit in the regional stratigraphy beyond the Laguna Blanca map-sheet, and appears to ignore the existence of the approximately 700 km<sup>2</sup> of outcropping volcanic units in the Farallón Negro region only 20 km south. I also disagree with the inclusion of the El Aspero Formation in the El Bolsón Group as proposed by Turner (1973). A revision of the lithostratigraphic nomenclature of the volcanic and associated intrusive units of the northern *Sierras Pampeanas* is clearly necessary.

### ***Proposed Nomenclature***

Volcanic and intrusive units crop out over a broad area in the Farallón Negro region and represent the highly dissected remnants of the largest Tertiary eruptive centre in the *Sierras Pampeanas* of northwestern Argentina. These units are referred to herein as the Farallón Negro Volcanic Complex, in the sense of González Bonorino (1950a). This lithostratigraphic assemblage includes the Main Farallón Negro Stratovolcano, as mapped by Llambías (1970; 1972), and isolated occurrences of volcanic rocks at Vis Vis,

Las Juntas, Capillitas and Cerro Atajo. These centres have been structurally separated from one another by the high-angle reverse faulting event which resulted in the uplift of the *Sierras Pampeanas* ranges; it is considered that, at the time of their emplacement, they may have formed a large, coherent, volcanic edifice. The term Volcanic Complex was retained in this study and used in this text, because mapping of the volcanic stratigraphy was beyond the scope of this project. However, the detailed research of J.M. Proffett (1994; 1995) on the Bajo de la Alumbrera deposit and surrounding area has defined an informal sequence of mappable units within the volcanic stratigraphy. Formations may be erected in the future.

I therefore suggest that formal lithostratigraphic nomenclature be developed for these rocks. Accordingly, I suggest that volcanic rocks of the Farallón Negro Volcanic Complex be accorded the rank and name of *Farallón Negro Group*, in partial agreement with Llambías (1970; 1972), and the associated hypabyssal intrusive units be assigned to the *Farallón Negro Intrusive Suite*, which may be subdivided into a number of lithodemes. The name, Farallón Negro, is maintained as it is well established and the mine-site of Farallón Negro is centrally located within the largest outcropping domain of the rocks under consideration. It is implicit in this scheme that Turner's (1973) "El Bolsón Group" be rejected. The El Morterito and El Cajón Formations may each be worthy of group status, but revision of the nomenclature of these units is not undertaken herein.

I would also suggest that the volcanic and intrusive suites mapped at Las Animas and El Alisal in the Sierra de Aconquija, 95 and 115 km to the northeast, respectively, represent broadly cogenetic assemblages and, although confirmation through more detailed

geochronological, geochemical and petrographic studies of these suites is necessary, would tentatively include them in the Farallón Negro Group.

Further afield, the rocks of the Pocho area, Córdoba Province, approximately 460 km south of Farallón Negro, are contemporaneous and exhibit geochemical features similar to those of the rocks of the Farallón Negro Group (see Chapter 4). I would suggest that the volcanic and intrusive rocks of this area be formally designated the Pocho Volcanic Complex (with a rank equivalent to that of a group), inferred to be correlative in age with the Farallón Negro Group and Intrusive Suite. It could moreover be argued that the broadly contemporaneous San Luis volcanics and the isolated outcrops on the neighbouring map-sheets mentioned above are also correlative with units of the Farallón Negro Group.

In the light of the extent of this Tertiary volcanic province in NW Argentina, I define a new stratigraphic assemblage, the *Sierras Pampeanas Supergroup*, to embrace all volcanic units of Mio-Pliocene age exposed in the northern *Sierras Pampeanas*. The cogenetic subvolcanic intrusives are assigned to the *Sierras Pampeanas Intrusive Supersuite*. The most extensive outcrops of the volcanic strata and the greatest diversity in composition of associated intrusive rocks are encountered in the Farallón Negro region.

The northeastern limit of the proposed supergroup is uncertain, and ongoing mapping by the provincial governments continues to document previously unknown volcanic centres, but it is probable that magmatic rocks in the San Lorenzo region (*ca.* 225 km northeast of Farallón Negro) represent broadly correlative assemblages. It is argued that the northwestern limit of the supergroup be defined by the southern margin

of the *Puna*. The southern limit incorporates the Pocho and San Luis centres, *ca.* 460 and 660 km south of Farallón Negro. The possible extension of volcanism of this age further southward has not been investigated.

In the *Sierras Pampeanas*, lithological units have been formally defined as Formations but few workers have sought to provide higher-rank lithostratigraphic units: the El Bolsón Group of Turner (1973; see above) and Santa María Group of Ruiz Huidobro (1972) are exceptions in the immediate vicinity of Farallón Negro. The name *Sierras Pampeanas* is proposed for the new supergroup as it has not been previously used with lithostratigraphic connotations in northwestern Argentina and the volcanic units which comprise the Supergroup are defined as occurring within the *Sierras Pampeanas* physiographic province.

### **Local Geology of the Farallón Negro Volcanic Complex**

Rocks of the Farallón Negro Volcanic Complex form a series of discontinuous outcrops over an area of approximately 700 km<sup>2</sup>. The exposures now define several discrete centres, *e.g.*, the Main Farallón Negro Stratovolcano, Vis Vis, Cerro Atajo, Capillitas and Agua Rica, which have been separated by movement along high-angle reverse faults (Fig. 2-11). It is thought that these outcrops may originally have formed a large, continuous volcanic field, with several eruptive centres. To clarify the spatial relationships between the isolated outcrops of volcanic units, a 1 : 50,000 scale map of the area was prepared. Contacts and structures were mapped in the field on approximately 1 : 50,000 scale air photographs and then transferred onto a photographic print of a 1 :

50,000 scale digital enlargement of a TM image for the area (Path 231, Row 79, 25 August, 1986). This map has been reduced and is presented as figure 2-11. It is argued that this map is an improvement on the 1 : 250,000 scale map presented by González Bonorino (1950a), but does not provide the detail within the Main Farallón Negro Stratovolcano shown on the 1 : 20,000 map of Llambías (1970), a generalized version of which is presented as figure 2-16.

### ***Main Farallón Negro Stratovolcano***

#### **Volcanic Stratigraphy**

This represents the most areally extensive series of volcanic outcrops in the study-area and comprises the bulk of the Farallón Negro Volcanic Complex. The dominant extrusive units are andesitic volcanic breccias. An internally consistent stratigraphy has not been established in previous mapping studies. Llambías defined a centrally-located series of *Brechas Moradas* ("purple breccias"), distinguished by an igneous matrix, purple-grey colour and poorly-stratified nature, and the peripherally-located *Brechas Polimícticas* ("polimictic breccias"), *i.e.*, extrusive breccias with locally variable clast composition. Proffett (1994, 1995) has recently documented five stratigraphic units in the immediate vicinity of the Bajo de la Alumbra deposit. The 500 m thick section mapped by Proffett incorporates the oldest sample from the Farallón Negro Volcanic Complex dated in this study, a 12.6 Ma hornblende-phyric basaltic-andesite from his "Lower Andesite Unit", suggesting that this area may expose the deepest levels of the volcanic edifice.

In a detailed study of the Volcán de Fuego, Guatemala, Vessell and Davies (1981)

**Figure 2-16.**

Generalized geological map of the Main Farallón Negro Stratovolcano, simplified from Llambías (1970).





document the lateral variations in volcanic and volcanoclastic facies associated with the construction of a large continental andesitic stratovolcano. They recognized four facies which are mutually gradational with increasing distance from the vent, viz. Volcanic Core; Proximal Volcanoclastic; Medial Volcanoclastic; and Distal Volcanoclastic. A cartoon of the lateral distribution of the facies is presented herein as figure 2-17 and their sedimentary characteristics are summarized in Table 2-1. The Volcanic Core Facies at Fuego consists of interbedded lavas, airfall ash and colluvium. The proximal Volcanoclastic Facies is characterized by matrix- and grain-supported breccias formed by glowing debris avalanches. These breccias are distinguished by poor sorting, extreme variations in grain-size and variable bed thickness, are rarely heterolithologic and are of limited lateral continuity. They grade downslope into lahars (debris-flows) of the Medial Volcanoclastic Facies. The matrix- and grain-supported laharic breccias are poorly sorted, with large variations in grain-size. Individual flows are recorded as poorly-defined beds. The Distal Volcanoclastic Facies is characterized by a wide range of lithologies, with sedimentary structures and textures typical of braided or meandering fluvial systems.

Broadly similar relationships are observed in the volcanic and volcanoclastic stratigraphic units of the Farallón Negro Volcanic Complex. The volcanic successions of continental stratovolcanoes are inherently variable (Cas and Wright, 1988), and thus the relationships observed at Farallón Negro depart, at times significantly, from those described for the Volcán de Fuego.

The *Volcanic Core Facies* and the *Proximal Volcanoclastic Facies* appear to be conflated at Farallón Negro. They are represented by interbedded breccias, basaltic-to-

**Figure 2-17.**

Cartoon of the lateral distribution of volcanic and sedimentary facies related to the formation of the Volcán de Fuego stratovolcano, Guatemala (from Vessell and Davies, 1981).

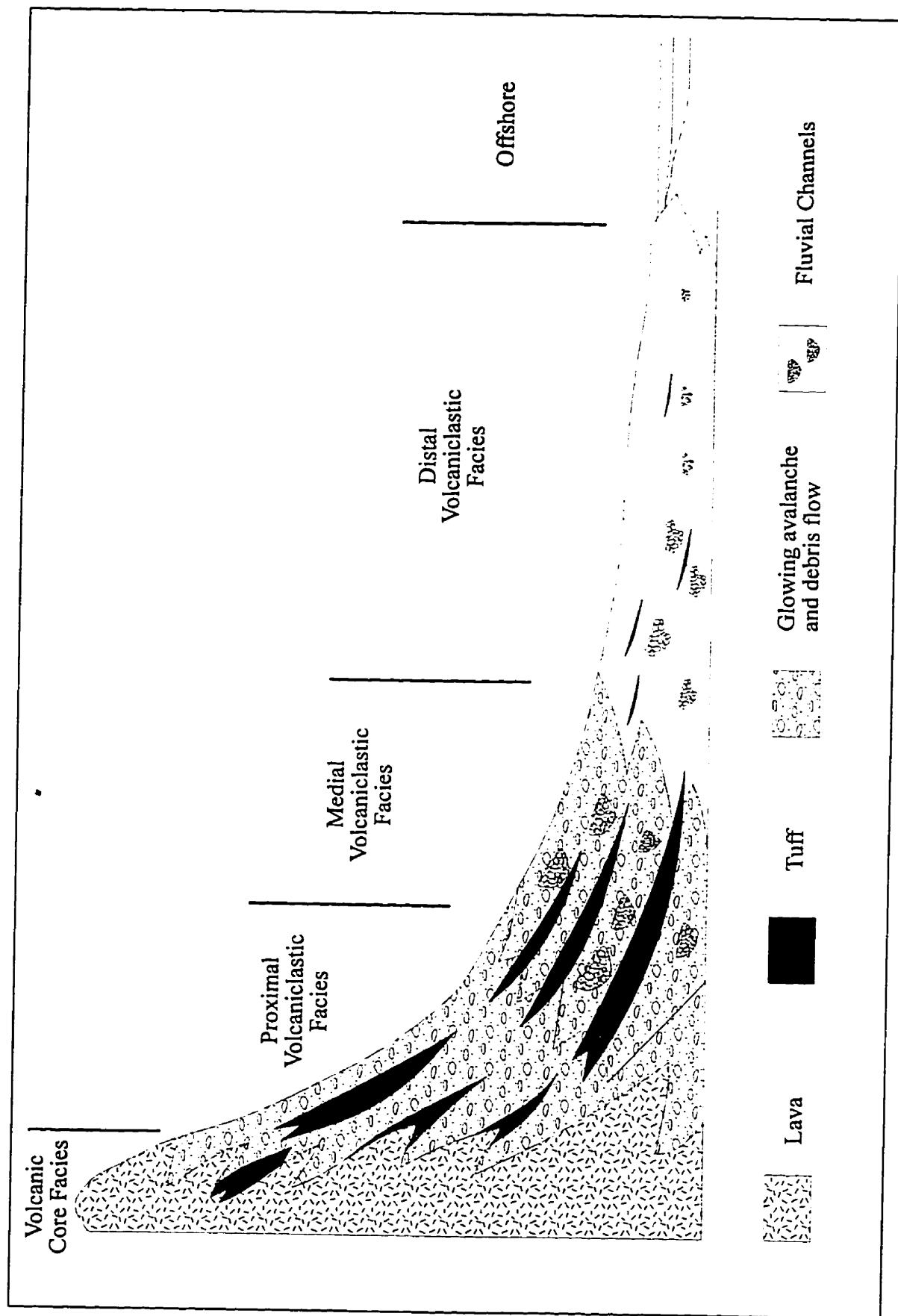


**Table 2-1.**

Sedimentary characteristics of non-marine volcanoclastic deposits from an active andesitic continental stratovolcano, the Volcán de Fuego, Guatemala (from Vessell and Davies, 1981).

SEDIMENTARY CHARACTERISTICS	GLOWING AVALANCHES	DEBRIS FLOWS	FLUVIAL DEPOSITS
BASE	Non-erosive	Non-erosive	Erosive
FABRIC	Matrix- Supported	Matrix- Supported	Grain- Supported
GRAIN SIZE	Boulders-to- sand	Boulders-to- sand	Boulders-to- sand
VERTICAL GRAIN SIZE CHANGE	No change	No change	Variable
SORTING	Very poorly sorted	Very poorly sorted	Very poorly sorted
SEDIMENTARY STRUCTURE	None	Faint parallel bedding	Generally structureless, locally cross-bedded
DOWNFLOW CHANGES IN INDIVIDUAL BEDS	Thickness constant or may decrease. No change in grain-size, sorting or roundness	Thickness decreases. No change in grain-size, sorting or roundness	Thickness and grain-size decrease. Sorting and roundness increase.
ASSOCIATED DEPOSITS	Thick airfall ash beds and debris flows.	Thin airfall ashbeds, glowing avalanche deposits and coarse-grained fluvial deposits.	Rare, thin airfall ashbeds. Lahars and rare glowing avalanche deposits.

dacitic flows and, locally, thin, very fine-grained, volcanoclastic lenses which may represent brief erosional episodes on the flanks of the stratovolcano. Minor welded tuffaceous units are also observed. The majority of the breccias encountered in the central portion of the Complex conform to descriptions of *alloglastic volcanic breccias* (Parsons, 1969; Allison, 1986), such as are typical of vent or cone complex facies and derived by underground brecciation of previously consolidated flows, breccias and intrusive rocks of the volcanic edifice. Clasts of previously brecciated and solidified material are observed, suggesting that multiple, successive brecciation events may have been common. Basement rocks may also be affected and variably absorbed basement xenoliths are seen, if rarely, within the Complex. Such breccias are subsequently intruded into the vent walls or are erupted as breccia flows (Parsons, 1969). The alloglastic breccia flows defined by Parsons (*op. cit.*) are herein interpreted to be equivalent to the glowing avalanche deposits of Vessell and Davies (1981). The majority of breccias observed at Farallón Negro are breccia flows, although some breccia intrusions are encountered. The former are characterized by an absence of sorting or bedding, great variety in fragment size and angular-to-rounded fragment shapes. Fragments in the breccias of the Farallón Negro Volcanic Complex range in size from millimeters to several meters (Fig. 2-18). The breccias are commonly thick and unstratified. They are heterolithic, although the main variations in the fragments are in texture, colour, degree of weathering, and type and percent of phenocrysts, rather than in the overall composition of fragments (Fig. 2-19). Breccia units are commonly characterized by a predominant clast-type, e.g., hornblende-phyric andesite, and the matrix material is similar in composition to the dominant clast-

**Figure 2-18.**

*Illustration of the range in clast size in breccias of the Farallón Negro Volcanic Complex.*

**A. Proximal Volcaniclastic Facies** breccia flows from south of Quebrada de la Chilca in the central area of the Main Farallón Negro Stratovolcano. Clasts, *e.g.*, left of field assistant, may attain widths of several metres. Stratification is marked by thin layers of very fine-grained material, interpreted to separate successive breccia flow events.

**B. Proximal Volcaniclastic** breccia flow from Bajo el Espanto which demonstrates the fine-grained nature of clasts in some flows. Dark-grey clasts are of the metasedimentary Suncho Formation (basement).



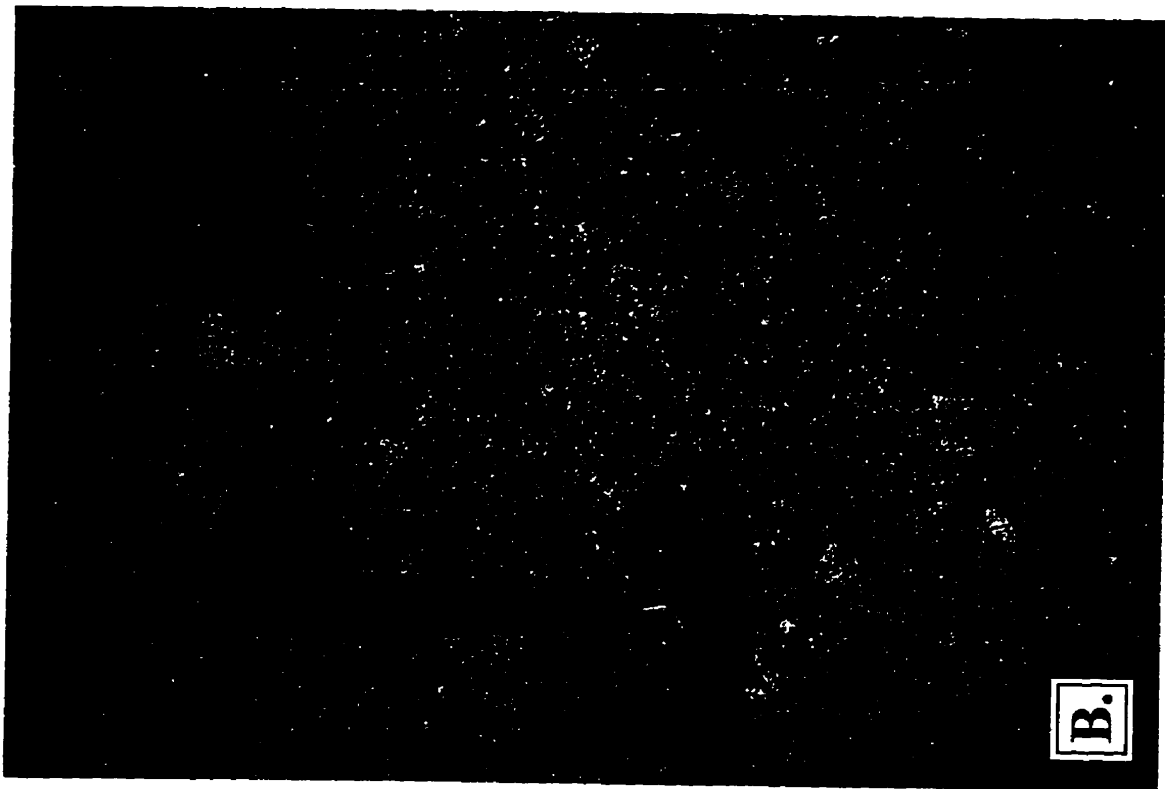
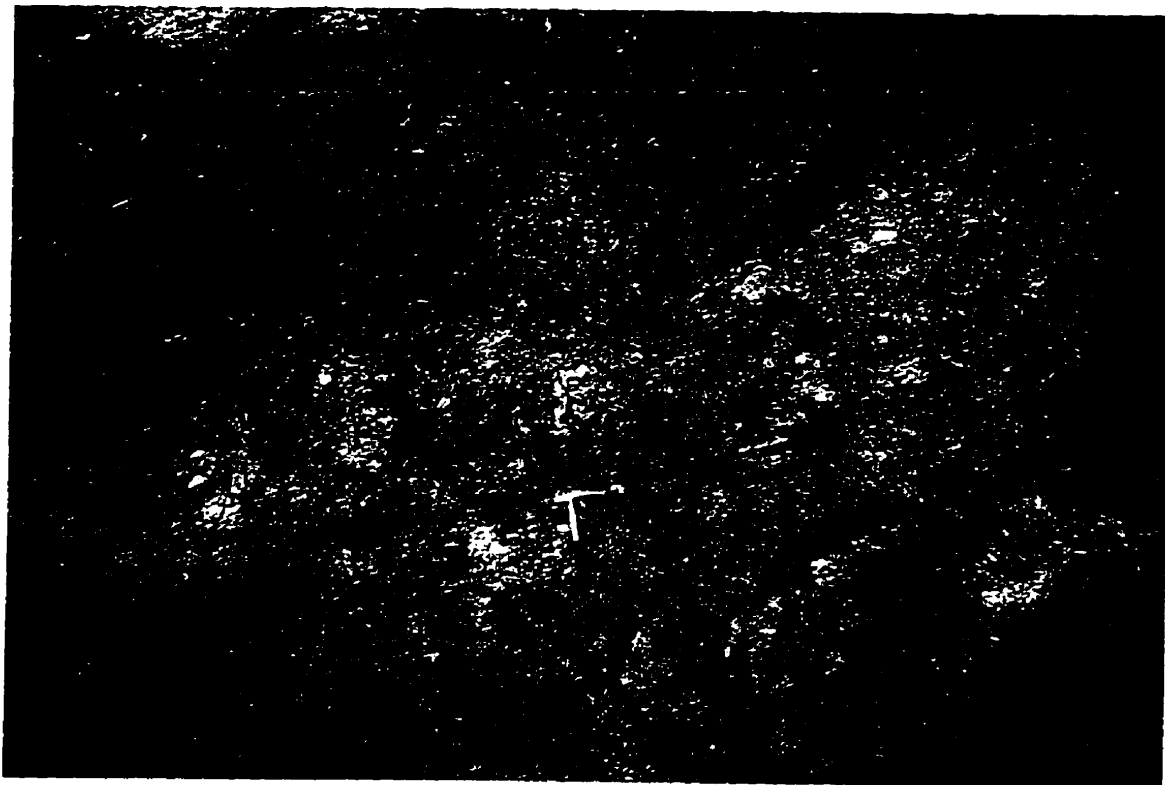


**Figure 2-19.**

*Proximal Volcaniclastic breccia flows of the central area of the Main Farallón Negro Stratovolcano.*

**A.** Typical outcrop pattern from the northern quadrant of the Main Farallón Negro Stratovolcano. Clasts are predominantly andesitic in composition, and rounded to sub-angular, constituting in a clast-supported breccia. The irregular contact with an underlying flow is seen in the lower-right corner. This outcrop is located along the northern (main) access road to Bajo de la Alumbrera, several km east of "Los Amarillos".

**B.** Lithological characteristics of an andesite breccia flow exposed in Quebrada de los Leones, south-east of the Farallón Negro mine-site. The breccia is clast-supported and the majority of clasts are of hornblende-andesite porphyry set in a matrix of similar composition. Minor clasts of non-porphyrific material are also observed, *e.g.*, small dark angular clast in lower centre of photo.



type.

Breccia flows and dykes containing basement clasts are observed at Bajo El Espanto, in the southeast quadrant of the Complex. These flows are poorly stratified and are overlain by, and interbedded with, breccias lacking basement clasts and thin basaltic-andesite flows. Breccia-dykes of identical composition and bearing basement clasts are observed intruding the overlying alloclastic breccia flows. Minor well-rounded clasts of granitic basement rocks were encountered in breccias in Quebrada de la Chilca, south of Bajo de la Chilca, and in Quebrada el Durazno, north of Bajo el Durazno.

Lava flows (Fig. 2-20) range in composition from basalt to dacite and are of high-K calc-alkaline-to-shoshonitic affinity (Chapter 4). Contacts and flow orientations are difficult to define in the central portion of the complex due to the abundance of intrusive units. Flows are particularly widespread in the western and northwestern portion of the complex.

Proffett (1995) describes a thick (approximately 150 m) andesitic ignimbrite in the section north of Alumbra. A thick flow-banded rhyolite (field term; Fig. 2-21) was also encountered south of the Farallón Negro mine-site, in the southwest quadrant of the complex, where it is overlain by breccias. The lateral contacts of the rhyolite were not mapped, but its thickness and restricted occurrence suggest that it was channelled along a valley incised in the southwest flank of the volcano. Incision and erosion are common during dormant phases of stratovolcanoes and periods of dormancy may be twice as long as periods of activity (Wadge, 1982). In tropical climates, such as in Guatemala, denudation and valley incision are extremely rapid (Vessell and Davies, 1981). The

**Figure 2-20.**

Basaltic flow (field term) in the central part of the Main Farallón Negro Stratovolcano. A massive flow is seen overlying a breccia flow of the *Proximal Volcaniclastic Facies* outcrop. Located along the southern access road to Bajo de la Alumbreira, several km west of Bajo las Pampitas.

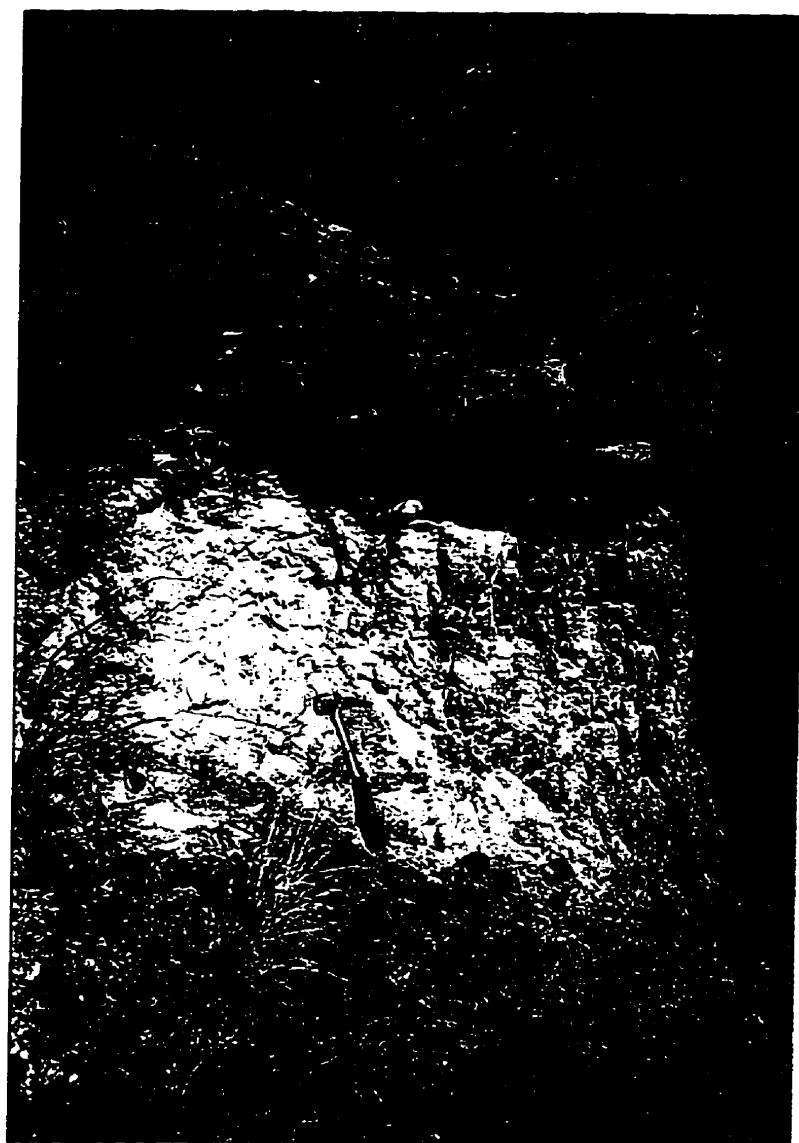
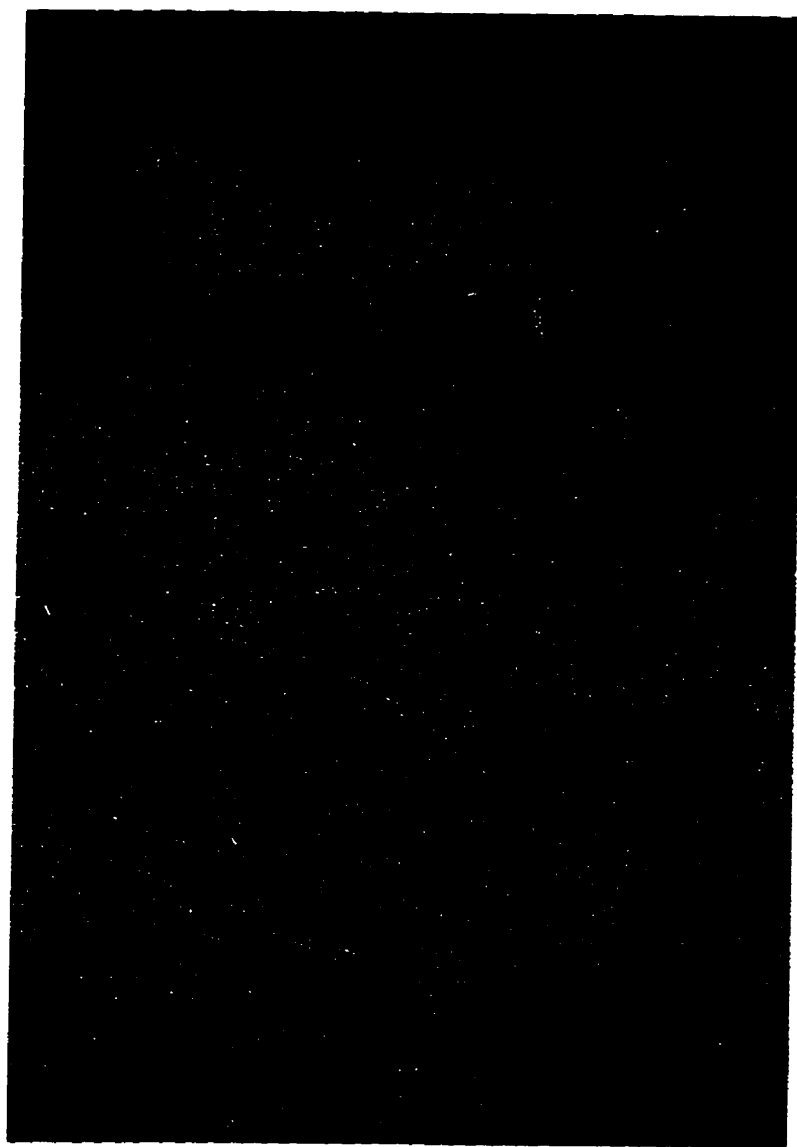


**Figure 2-21.**

Flow-banded rhyolite (field term) flow from the southwest quadrant of the complex, approximately 7 km southwest of the Farallón Negro mine-site.





Middle Miocene climate at Farallón Negro was probably arid or semi-arid, but erosion and incision of the flanks of the stratovolcano may have been relatively rapid.

A series of poorly-welded andesitic tuffs which were erupted late in the volcanic history are encountered on the west and northwest perimeter of the complex (Fig. 2-22). Tuffaceous units are also encountered as small, isolated outcrops in the central portion of its northwest quadrant. They may have infilled valleys in the volcanic topography and were preserved through rapid burial by subsequent breccia-flows. The outcrops at El Tobogán, Río Seco de la Aguada, and to the north of the Farallón Negro mine-site (Fig. 2-16) exhibit characteristics typical of pyroclastic surge deposits. These strata drape over topographic highs and thicken in depressions (as at El Tobogán), and exhibit well developed stratification and unidirectional bedforms such as dunes and cross bedding (McPhie *et al.*, 1993). The tuffs at El Tobogán, along the main access road to the Farallón Negro mine-site, are cut by basaltic dykes. Ground-surge deposits are interpreted to indicate proximity to a volcanic vent (McPhie *et al.*, *op. cit.*). The location of these outcrops in the northwest quadrant of the complex, in addition to the regional NW dips of the breccias in the area, would suggest the location of a vent to the SE, *i.e.*, in the vicinity of the Alto de la Blenda monzonite stock.

The postulated *Medial Volcaniclastic Facies* is represented by a thick sequence of unstratified breccia flows which exhibit large-scale layering through the superposition of successive flow units, which are commonly separated by partings of very fine-grained material (Fig. 2-23). These are best observed in the central portion of the complex to the south and east of Bajo de la Alumbreira, and in a series of outcrops northeast of Bola del

**Figure 2-22.**

*Field characteristics of poorly-welded andesite tuffs, Main Farallón Negro Stratovolcano.*

**A.** Regional view to the west of andesite tuffs exposed on the western perimeter of the Main Farallón Negro Stratovolcano. Uplifted basement blocks of the Sierras de Hualfin and las Cuevas form the horizon. White "glaciers" are windblown pyroclastic material transported from the *Puna*.

**B.** Detailed view of above succession. Sample FAR 206 was collected from this unit approximately 1 km to the south and yielded an age of  $7.49 \pm 0.09$  Ma. The tuffs are overlain by, and interbedded with, gravels of the *Distal Volcaniclastic Facies*.

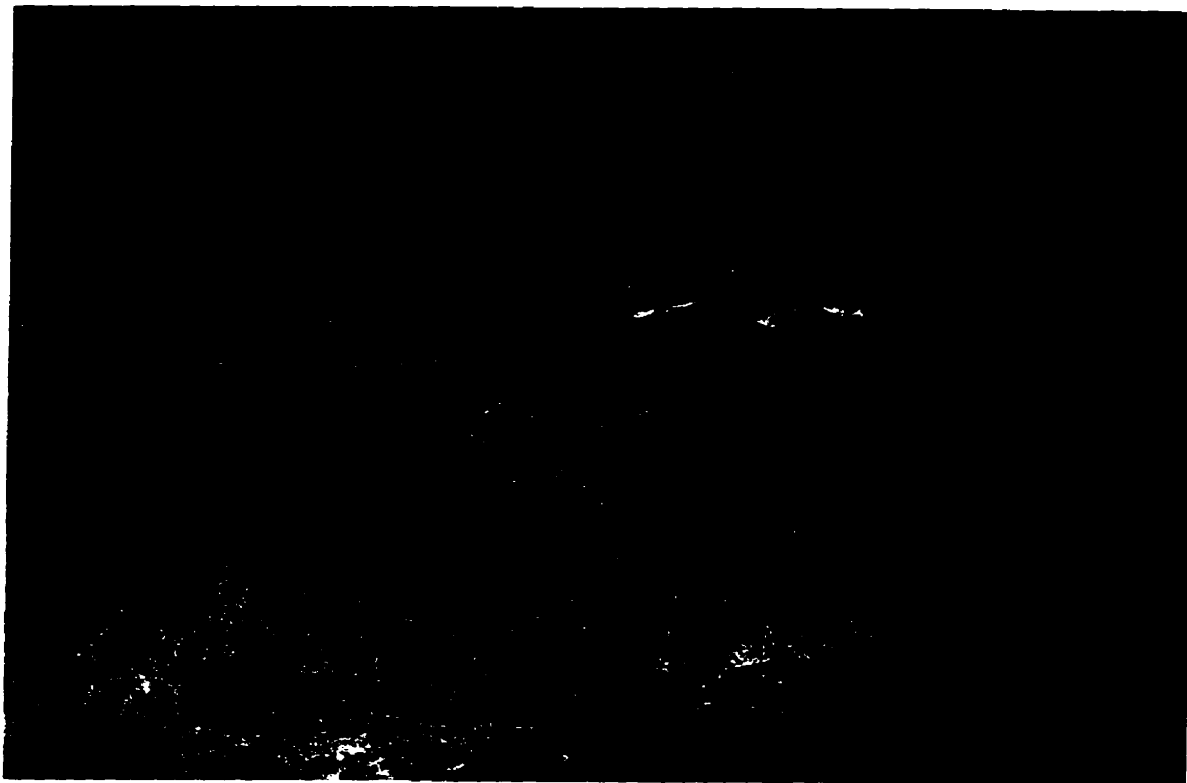
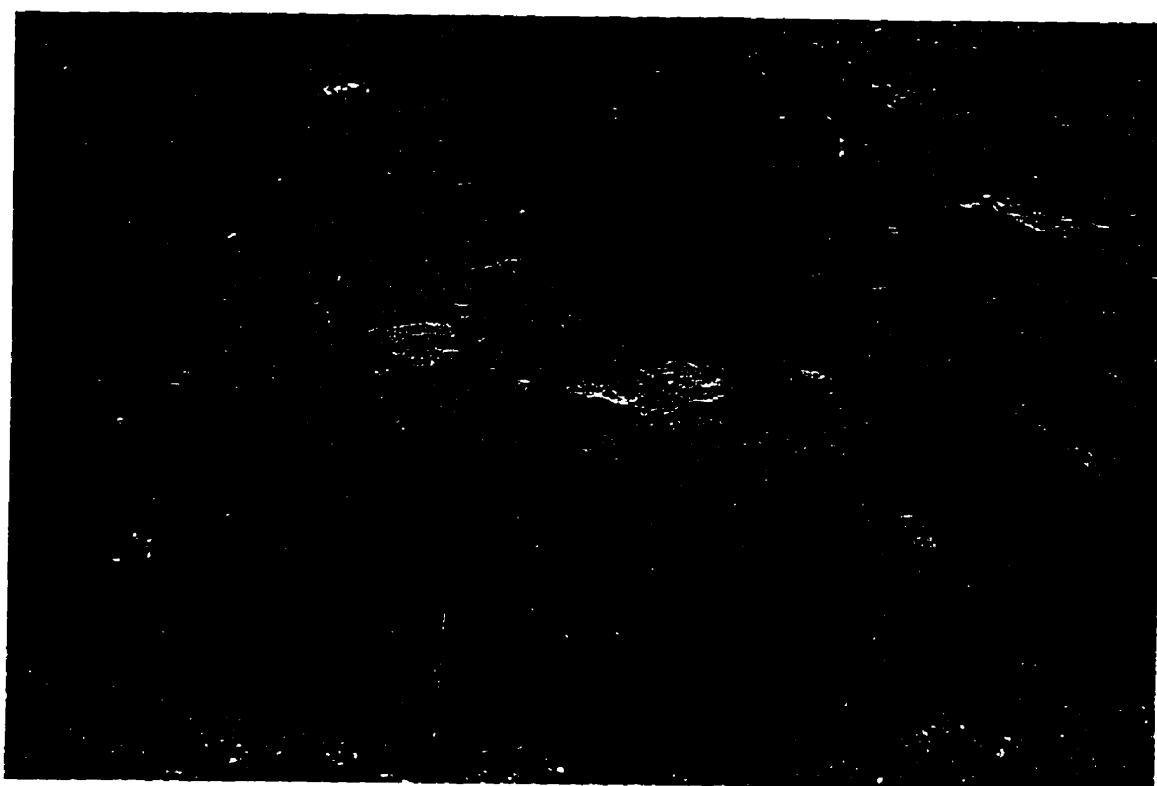
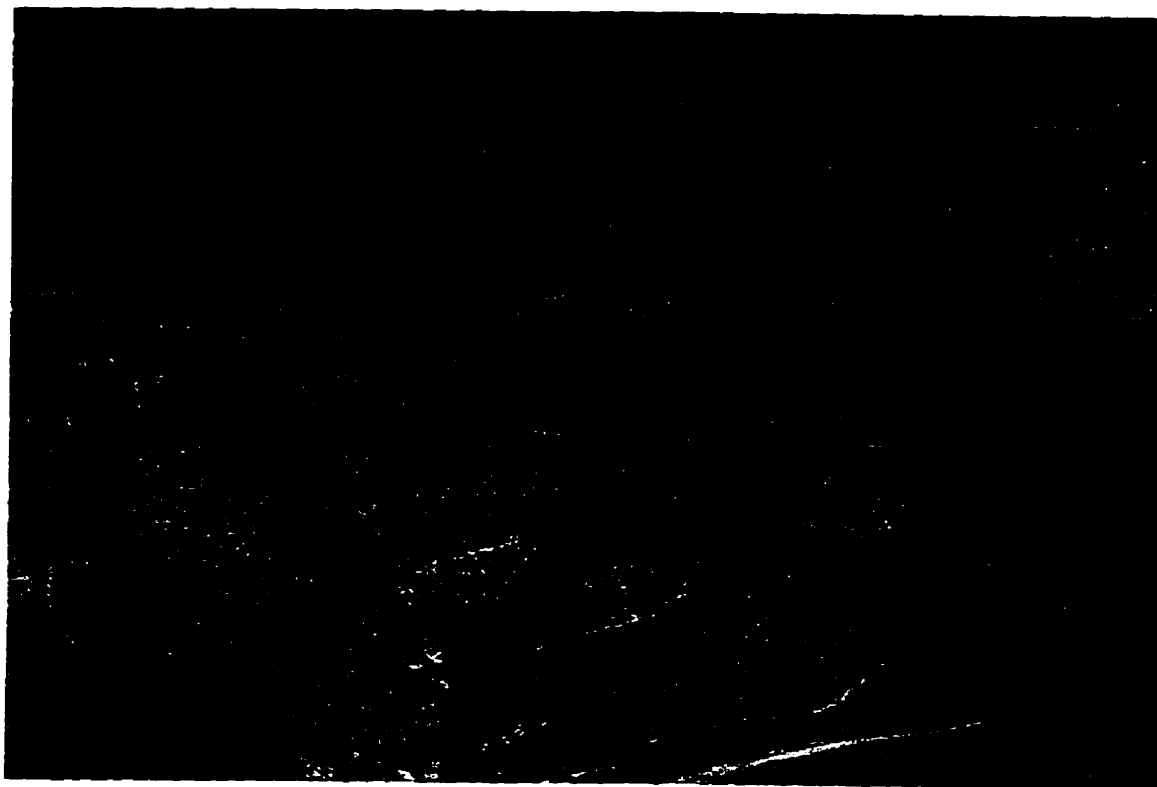


**Figure 2-23.**

*Medial Volcaniclastic Facies, Main Farallón Negro  
Stratovolcano.*

**A.** Regional characteristics of the *Medial Volcaniclastic Facies* in the south-east quadrant of the Main Farallón Negro Stratovolcano, to the east of Bajo de la Alumbraera. Large-scale layering is the result of the superposition of successive flow units which are commonly separated by very fine-grained layers, possibly representing brief erosional episodes between flow deposition. View to the south.

**B.** Lithological characteristics of the *Medial Volcaniclastic Facies* in the northern Vis Vis river valley, north of the point at which the road from Farallón Negro to Vis Vis descends into the river valley. Clasts are heterolithologic and exhibit a wide range of sizes and degree of rounding.



Atajo which are interpreted to be preserved in an ENE-trending graben (Chapter 6). Laharic and debris-flow deposits are also encountered in the west, northwest and north quadrants of the complex (Fig. 2-24). No traverses were completed in the southwest quadrant, in the region bounded by the Quebrada de la Chilca to the north and the approximate longitude of the Farallón Negro mine-site, but it is assumed from traverses to the north and east, and from TM images, that this domain is also dominated by units of this facies. Units of the *Medial Volcaniclastic Facies* increase in abundance towards the west and northwest perimeters of the complex, where they are interbedded with numerous flows and overlain by pyroclastic units (Fig. 2-25). Vessell and Davies (1981) emphasized the episodic nature of the volcanic and sedimentary events in this facies. Only eruptive phases of sufficiently large magnitude (volume) would result in the development of lahars and alluvial systems. The volcanic stratigraphy at Farallón Negro, in particular that of the northwest quadrant, appears to represent a conflation of the laterally gradational facies environments proposed by the above authors. It is therefore suggested that intervening volcanic episodes may not have been of sufficient volume to generate the sediment supply for the formation of the *Medial* and *Distal* facies, although flows generated during the "low volume" periods may have overlain lahars from a previous cycle. The repetition of these cycles resulted in the interbedding of units of the *Volcanic Core* and *Medial Volcaniclastic Facies*.

The *Distal Volcaniclastic Facies* is encountered on the periphery of the Volcanic Complex. The broad fluvial apron to the north of the Main Farallón Negro Stratovolcano (Fig. 2-26) and on the western flanks of the Sierra Durazno is characterized by well-

**Figure 2-24.**

*Lahars of the Medial Volcaniclastic Facies in the Main Farallón Negro Stratovolcano.*

**A.** Outcrops of laharic flows in the Quebrada de la Chilca, close to the western perimeter of the Main Farallón Negro Stratovolcano. The flows exhibit irregular laminations, an absence of grading and a wide variety of clast-size.

**B.** Lithological characteristics of a lahar flow. The deposits are poorly sorted, sand-to-boulder mixtures comprising rounded to angular clasts and exhibiting diffuse stratification. The overlying unit (above the hammer) is a recent gravel deposited during flash flood events in the Quebrada de la Chilca.

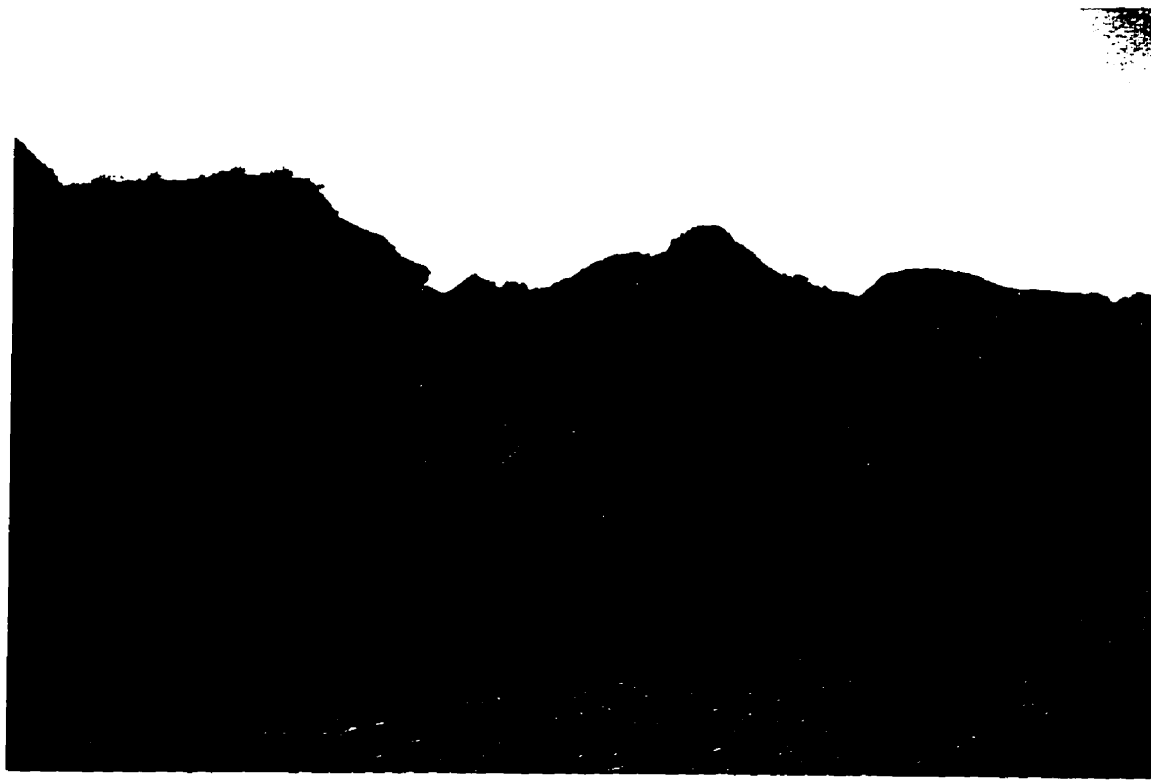




**Figure 2-25.**

*Regional field characteristics of volcanic units on the periphery of the Main Farallón Negro Stratovolcano.*

**A.** Breccias of the *Medial Volcaniclastic Facies* interbedded with tuffaceous units and massive flows in an unnamed quebrada leading to the Loma Morada dacite intrusion on the NW perimeter of the Main Farallón Negro Stratovolcano (view to the SW). The stratified units in the foreground are breccias which are interbedded with pale-grey, unstratified tuffaceous units (e.g., the small hills in middle distance at the centre of the photo), and with dark brown flows which are more resistant and form the ridges on the right and left.

**B.** Similar relationships exposed in the Quebrada de los Leones, in the southwest portion of the Main Farallón Negro Stratovolcano (view to the SW). Breccias of the *Medial Volcaniclastic Facies* appear crudely stratified. Flows are massive and dark-brown. Tuffaceous units are pale-grey and easily weathered.

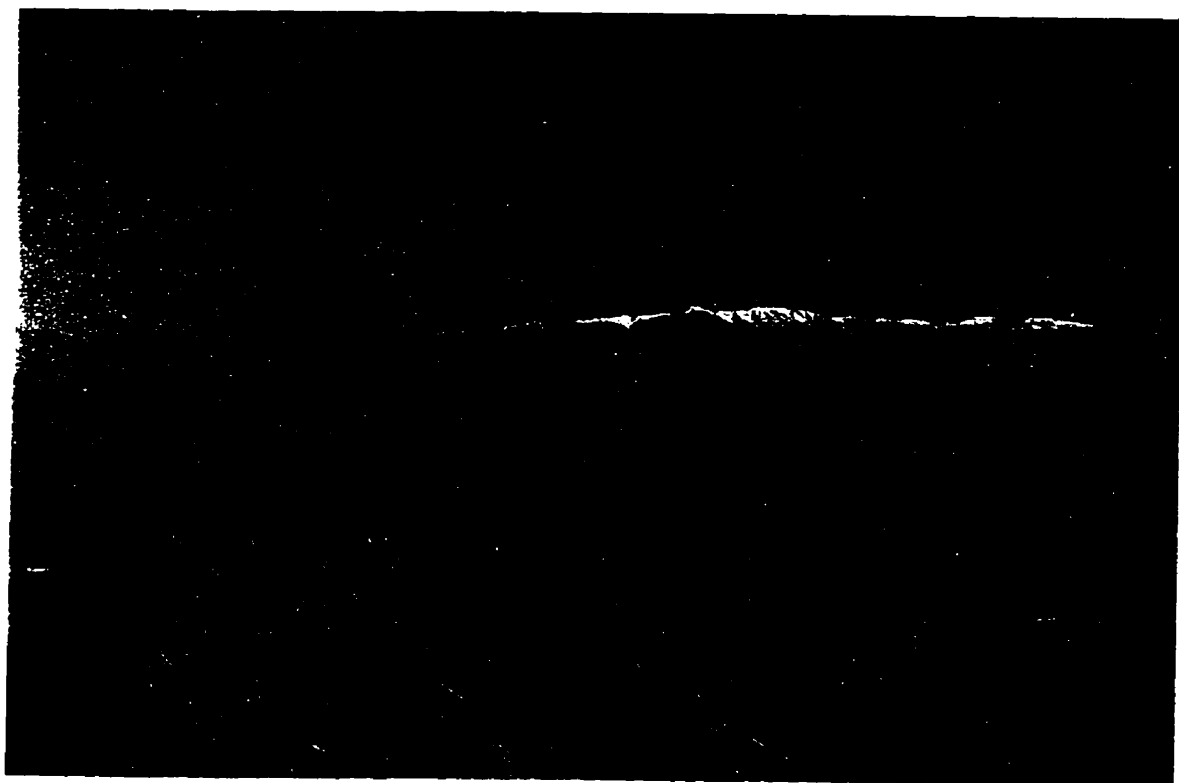
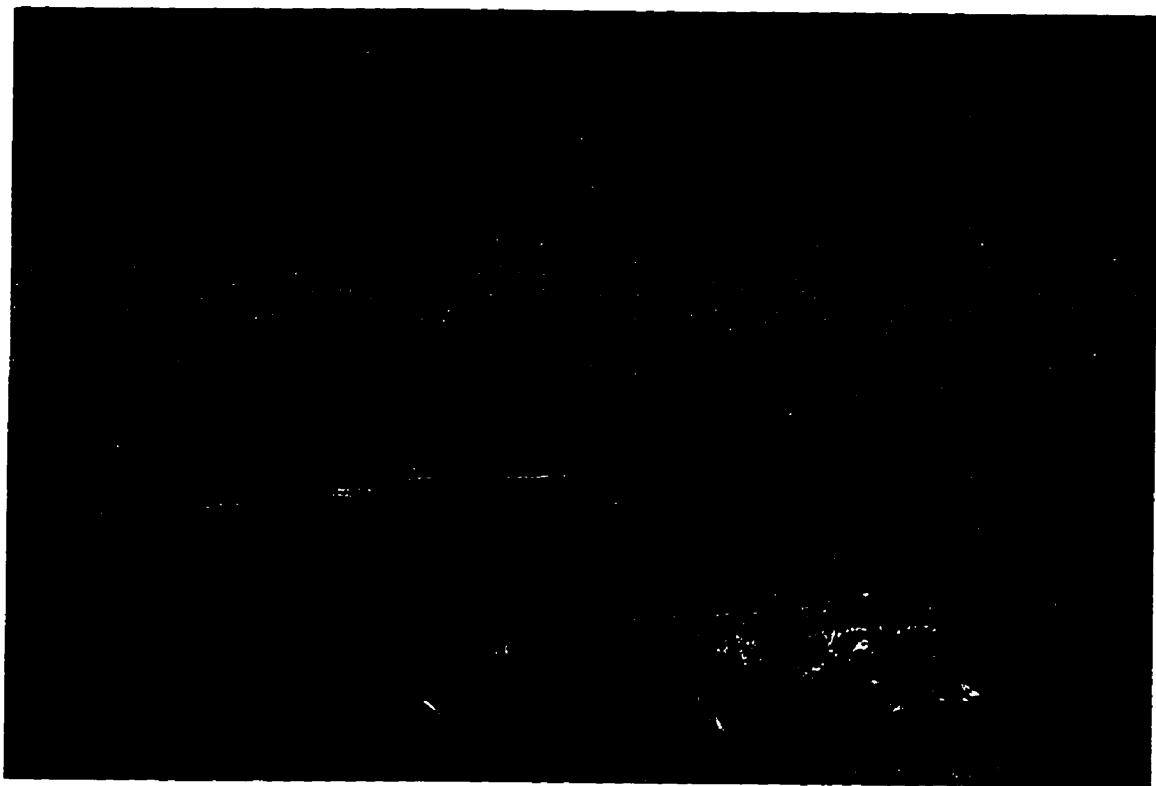


**Figure 2-26.**

*Distal Volcaniclastic Facies of the Main Farallón Negro Stratovolcano.*

**A.** View to the east of the broad fluvial apron on the northern flanks of the Main Farallón Negro Stratovolcano. The low hummocky topography in the foreground is underlain by gravels of the *Distal Volcaniclastic Facies*. The outcrops in the immediate foreground consist of gravels underlain by tuffaceous units. In the Sierra Durazno (horizon) gravels of the Distal Facies are the dominant cliff-forming units, overlying a thin basaltic flow at the base of the cliff band (not visible at this scale) and red sediments of the El Morterito Formation.

**B.** The regular series of parallel ridges in the left-central portion of the photo form a broad fluvial apron along the northern flank of Sierra Durazno and extend to the right into the Campo de Arenal (view to the northwest). They are underlain by gravels of the *Distal Volcaniclastic Facies*. In the pale-green cliffband, at the front of the ridges and extending out of the field of view to the right, an 8.75 Ma andesite tuff is interbedded with the gravels. The dark-blue ridge to the left and in front of the above band is composed of clinopyroxene-phyric basaltic flows. The red-coloured ridge and low hills in front of the pale-green cliff band (right-side of view) are eroded into a fault-cored, doubly-plunging anticline of granitic basement. Basaltic flows form the small dark-brown hills to the right and in front of the basement dome. The northern end of the Sierra de Capillitas, which is cut by numerous pegmatite bodies (linear features), is in the foreground. The ridges in the near distance are the Sierras de Hualfin (left) and Las Cuevas (right). The snow-capped peaks on the horizon mark the southern edge of the *Puna*.



bedded, coarse, braided-river gravels of volcanic provenance (*cf.* Fig. 2-15). The high cliffs forming the western scarp of the Sierra Durazno are composed of similar gravel units. A 6.72 Ma andesitic tuff was observed interbedded with these gravels in Quebrada de Pozos Verde to the north of the complex. This sequence is in the overturned limb of a footwall drag-fold related to movement along the high-angle reverse fault responsible for the uplift of the Sierra Durazno. An andesitic tuff interbedded with similar gravels on the far-eastern slopes of the Sierra Durazno yielded an age of 8.75 Ma. Abundant river gravels are observed along the northern portions of the access road to the Farallón Negro mine-site, but the age of these units is unknown. The veneer of alluvial material forming the apron mentioned above is probably of much more recent formation than those observed in Quebrada de Pozos Verde, although the sedimentary processes have remained unchanged. The occurrence of the tuffs interstratified with the gravels illustrates the importance of mass-wasting phenomena in the stratovolcanic environment and clearly indicates that erosion and extrusion were contemporaneous.

#### Intrusive Units

A generalized sequence of syn-to-post-stratovolcanic intrusion and hydrothermal mineralization has been defined by Llambías (1970, 1972) for the main volcanic centre. He proposed that the emplacement of irregular andesite stocks and endogenous domes was followed by that of numerous sub-vertical to vertical basaltic to andesitic dykes, principally along a northwest-trending belt, but also with a secondary northeast to east-northeast orientation. At the approximate centre of the complex, the Alto de la Blenda

monzonite was passively emplaced with an associated roughly radial monzonitic dyke swarm. This intrusion now underlies the highest topography (2950 m a.s.l.) within the central complex. Intrusive activity was inferred to have continued with the emplacement of numerous stocks, domes and sub-vertical dykes of andesite, andesite porphyry and dacite porphyry, followed by rhyodacite porphyry and, finally, by rhyolite and rhyolite porphyry.

This intrusive sequence is only broadly supported by the results of the geochronological study conducted herein (see Chapter 5), which suggests a more complex history. The petrochemistry and age relationships of these rocks will be discussed in detail in Chapters 4 and 5, respectively, but the field aspects and the spatial and generalized temporal relationships of the rocks are discussed here. A comparison of the sequence of intrusive events as inferred from geological relationships by Llambías (1970), and as determined by  $^{40}\text{Ar} - ^{39}\text{Ar}$  geochronology in conjunction with cross-cutting relationships observed in this study, is presented in Table 2-2. The units will be briefly discussed from oldest to youngest, as defined by the temporal sequence now defined. The names of the intrusive units used herein are proposed as a revision of the existing terms and in order to establish formal lithodemic nomenclature for the rocks of the Farallón Negro Intrusive Suite. Lithodemic names combine a geographical with a lithic, or descriptive, term. Thus, geographical qualifiers have been added to several of the original names proposed by Llambías (*op. cit.*), in conformity with the rules of the North American Stratigraphic Code (1983). Where necessary, the basis for the choice of geographical qualifier will be discussed in the appropriate sections. In addition, chemical data obtained in this study

**Table 2-2.**

Comparison of the temporal sequence of intrusive events in the Main Farallón Negro Stratovolcano as proposed by Llambías (1970), on the basis of geological relationships, and as defined by this study through a combination of  $^{40}\text{Ar} - ^{39}\text{Ar}$  geochronolgy, observed cross-cutting relationships and petrochemistry.

<b>LLAMBIAS (1970)</b>	<b>THIS STUDY</b>	<b>AGE</b>
Rhyolite dykes and dome	Los Leones Rhyolite	?
Macho Muerto Rhyodacites	Macho Muerto Dacite	5.95 to 6.14 Ma
Quartz-andesites of Bajo de Agua Tapada	Agua Tapada Dacite	6.78 to 7.39 Ma
Durazno Intrusives	Alto de la Blenda Monzonite	7.50 Ma
Alto de la Blenda Monzonite Stock	Aguila Dykes	6.30 ; 7.94 Ma
Basaltic-andesite dykes	La Chilca Andesite	7.88 Ma
Amphibole Andesites	Las Casitas Rhyolite	pre-7.94 Ma
La Chilca Andesites	Sierra Durazno Dykes	?
	Durazno Andesite	8.20 to 8.46 Ma
	Arroyo Alumbrera Andesite	12.6 Ma ?



have permitted more precise classification of several rock-types. Note that the geological map presented as figure 2-11 was completed prior to the erection of the lithodemic nomenclature and a generalized sequence of intrusive units was employed.

The majority of the intrusive units in the Main Farallón Negro Stratovolcano occupy a northwest-striking "corridor" which transects the central portion of the volcanic outcrop (Fig. 2-16). The southwest margin of the corridor is clearly delimited by the large La Chilca andesite stock which underlies Bajo la Chilca. The northeast margin is not as abrupt, the number of intrusive bodies diminishing gradually away from the margin of the Alto de la Blenda monzonite stock. The corridor transects almost the entire diameter of the stratovolcano but appears to terminate at Bajo el Espanto, short of the presently exposed southeast margin. The history of intrusive activity at Farallón Negro is dominated throughout by NW-trending dykes, NW-elongations of intrusive bodies and NW-alignments of intrusive bodies. However, a subsidiary NE-trending orientation for dykes and the intrusive bodies at Bajo de la Alumbreira, Bajo de Agua Tapada and Bajo el Durazno is also observed. Intrusive activity occurred outside of this NW-trending corridor, but was relatively minor, with the exceptions of the Bajo el Durazno centre and a predominantly N-S oriented dyke swarm in the eastern foothills of the Sierra Durazno, east and south of Bajo el Durazno.

#### *Arroyo Alumbreira Andesite*

Llambías (1970) describes a series of dark-grey to green outcrops of intrusive *Andesitas anfibólicas* in the Arroyo Alumbreira, north of Bajo de la Alumbreira. Their

occurrence, intruding *brechas moradas* which contain clasts of the *Andesitas anfibólicas*, led Llambías (*op. cit.*) to conclude that the andesites were emplaced early in the volcanic sequence. The *Arroyo Alumbreira Andesite* (new term) contains coarse hornblende and pyroxene phenocrysts and smaller plagioclase phenocrysts in a fine-grained, purple matrix (Fig. 2-27). The hornblende phenocrysts are commonly rimmed by a reddish opaque alteration assemblage ("opacite"). The unit is strongly magnetic. These outcrops were mapped by Proffett (1994, 1995) as the "Coarse Hornblende Andesite Unit" which was considered to comprise both flows and intrusions. One such flow is the oldest dated volcanic unit at Farallón Negro, yielding an age of 12.56 Ma (see Chapter 5). Proffett (*op. cit.*) does not describe the relationships between the flows and intrusions, but if the latter are broadly contemporaneous with the flows they would represent the oldest intrusive unit yet encountered in the Farallón Negro Volcanic Complex.

These bodies are assigned the name *Arroyo Alumbreira Andesite* because they crop out almost exclusively in the vicinity of Arroyo Alumbreira, less than 1 km north of Bajo de la Alumbreira. Although the presence of large amphibole phenocrysts is an important distinguishing characteristic, the name-qualifier "amphibole" has been dropped in accordance with the guidelines for naming lithodemes advocated in the North American Stratigraphic Code (1983).

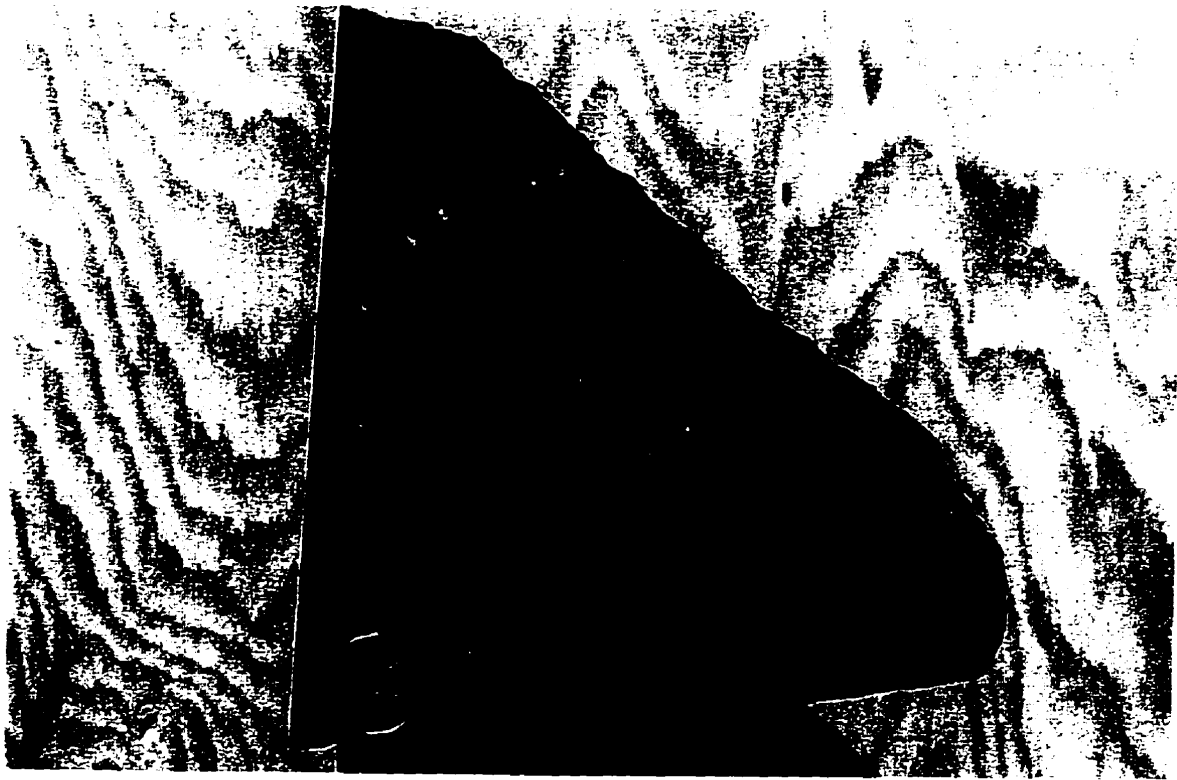
#### *Durazno Andesite*

Llambías (1970) described a series of granodiorite porphyry intrusions and andesitic-to-dacitic dykes in the area of Bajo el Durazno. The grey and greenish-grey

**Figure 2-27.**

*Arroyo Alumbraera Andesite.*

Hand sample of FAR 201 illustrating the large dark hornblende phenocrysts, rimmed by reddish 'opacite', which are typical of this unit. Hornblende from this sample yielded an age of 12.56 Ma.



rocks exhibit hornblende, plagioclase and rare biotite phenocrysts in a fine-grained matrix of similar composition. On the basis of geochemical analyses completed in this study, the rocks may be classified as andesite, and they are herein assigned to the *Durazno Andesite* lithodeme (new term). Llambías (*op. cit.*) interpreted the contact relationships of the southern borders of the Durazno Andesite bodies to be intrusive into the La Chilca Andesites (described below). However, the ages of the Durazno Andesite stocks range from 8.20 to 8.46 Ma and are statistically (at  $2\sigma$  errors) older than that of 7.88 Ma determined for the most extensive outcrop of La Chilca Andesite in the southwest quadrant of the complex. Llambías (*op. cit.*) recorded that the location of the contact between the bodies of Durazno Andesite and La Chilca Andesite in the vicinity of Bajo el Durazno is approximate due to the difficulty of distinguishing between the two lithologies, because of their inherent similarity and local hydrothermal alteration. Whereas the map pattern (see figure 2-16) would indicate an intrusive contact, it is herein suggested that the units mapped as La Chilca Andesite in the vicinity of Bajo el Durazno by Llambías (*op. cit.*) may represent phases of the Durazno Andesite. Detailed mapping may be necessary to resolve this ambiguity.

The geographical qualifier of Durazno is maintained for this lithodeme because rocks of this type occur exclusively in the vicinity of Bajo el Durazno. Chemical analyses completed during this study indicate that the various intrusive units described by Llambías (1970) are all andesitic.

### *Sierra Durazno Dykes*

A well-developed dyke swarm is observed intruding volcanic and sedimentary strata in the foothills of the Sierra Durazno, west and south of Bajo el Durazno (Fig. 2-28). The basaltic (field term) dykes exhibit well-chilled margins and crumbly, pistachio-green interiors and are characterized by abundant hornblende and pyroxene phenocrysts. Overall the dykes exhibit a consistent N-S strike orientation, although directly east of Bajo el Durazno mutually cross-cutting bodies display no preferred orientation. These dykes are located outside of the NW-trending intrusive corridor in the central portion of the Farallón Negro Complex and may represent feeders to a satellite extrusive centre (see below). The dykes were not dated in this study but their phenocryst assemblage and appearance are similar to several basaltic flows encountered in the Sierra Durazno and north of Bola del Atajo. The latter yielded an age of 8.59 Ma, and the dykes are tentatively interpreted to be of broadly similar age.

"Sierra Durazno" was chosen for the name of this lithodeme as the dykes are encountered exclusively in the foothills of this highland. The general term "dyke" is suggested until the chemical composition of the unit is confirmed.

### *Las Casitas Rhyolite*

A small stock of flow-banded rhyolite (Fig. 2-29) intrudes andesitic breccias south of Alto de la Blenda. Llambías (1970) included this stock with the young rhyolite dykes, which he interpreted as representing the last intrusive event at Farallón Negro. It is a pale-violet rock characterized by phenocrysts of quartz and plagioclase in a very fine,

**Figure 2-28.**

*Sierra Durazno Dykes.*

**A.** Two parallel basaltic (field term) dykes are seen cutting sediments of the El Morterito Formation in the structurally complex region of the SW Sierra Durazno. A steep-walled intrusion of La Chilca Andesite forms the dark ridge on the horizon, right-of-centre. Greenish-grey volcanic breccias crop out in the left-foreground and are cut by a large barren quartz vein (pale-brown outcrops). View to the SE.

**B.** Typical outcrop pattern of the Sierra Durazno dykes in the SW Sierra Durazno. Pistachio-coloured dyke with well-developed chill margins cuts sediments of the El Morterito Formation. View to the south.



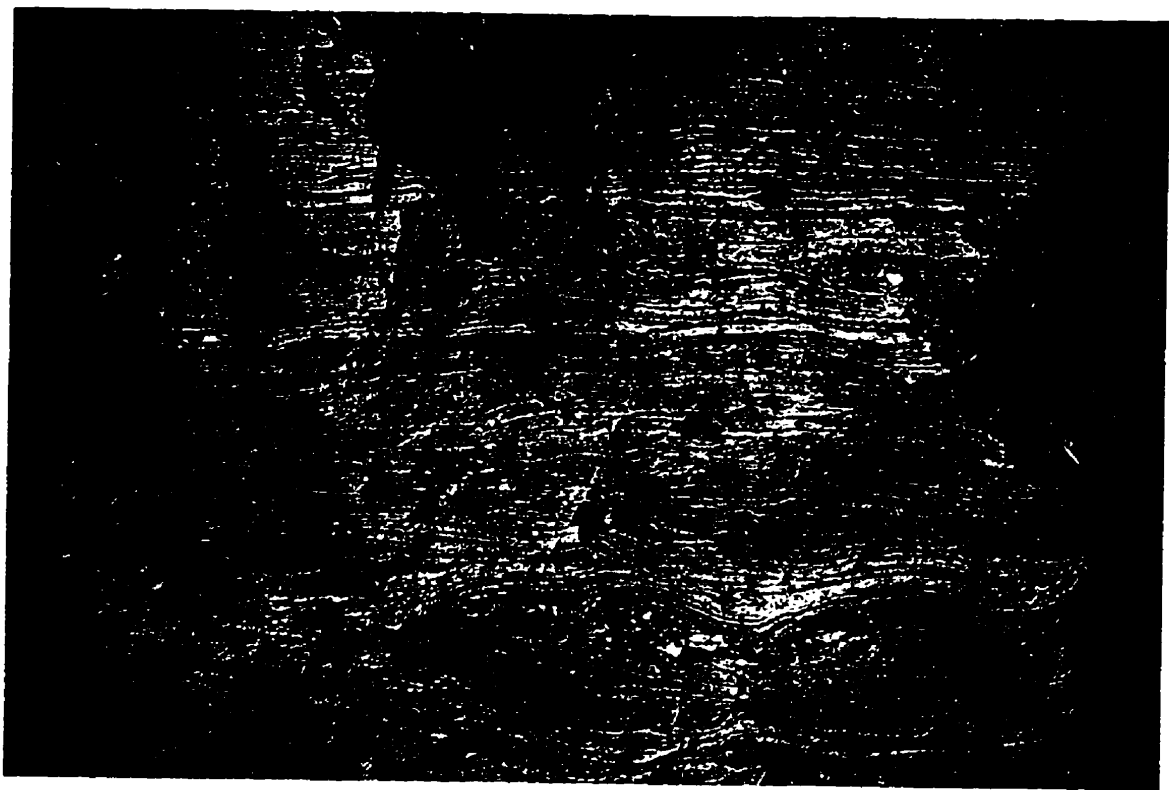


**Figure 2-29.**

*Las Casitas Rhyolite.*

**A.** View to the west of the Las Casitas rhyolite plug (pale conical hills) intruding flows and breccias of the *Proximal Volcaniclastic Facies*.

**B.** Flow-banding on the western flank of the Las Casitas Rhyolite.



cryptocrystalline, matrix. The southwest quadrant of the intrusion is cut by a basaltic dyke (Fig. 2-30). Hornblende from this dyke yielded an age of 7.94 Ma, indicating that the rhyolite was emplaced relatively early in the intrusive history at Farallón Negro.

Las Casitas is a term that was adopted in the field. Although the locality of Las Casitas indicated on Llambías' map is 2.5 km SE of the rhyolite stock, the *quebrada* that branches south off the road between the Farallón Negro mine-site and Bajo de la Alumbrera, and which is followed to arrive at the rhyolite outcrops, is marked by a weathered sign labelled "Las Casitas".

#### *La Chilca Andesite*

A series of andesitic intrusions are emplaced in an elliptical pattern peripheral to the Alto de la Blenda Monzonite (described below). The purple-to-grey rocks consist of plagioclase and hornblende phenocrysts in an aphanitic matrix and intrusions are commonly distinguished in the field by the characteristic incised weathering of the flow banding (Fig. 2-31). Variably-weathering bands on the scale of 10 - 20 cm are continuous along strike for several 10's of m. The orientation is generally conformable with that of the intrusive body, *e.g.*, elongated NW-SE in the largest body of *La Chilca Andesite*, in the southwest quadrant of the complex.. Hornblende from an outcrop of the largest La Chilca Andesite stock yielded an age of 7.88 Ma. On the basis of the similarities in the compositions of the La Chilca Andesite and the matrix of the *brecha morada* (herein *Proximal Facies* breccia flows), and the transitional contacts between the two rock units, Llambías (1970) concluded that they were genetically related and that the La Chilca

**Figure 2-30.**

View to the east of basaltic dykes cutting the southwest margin of the *Las Casitas Rhyolite* stock. Sample FAR 254 was collected from the larger of the two dykes exposed in this view and yielded an age of  $7.94 \pm 0.12$  Ma.

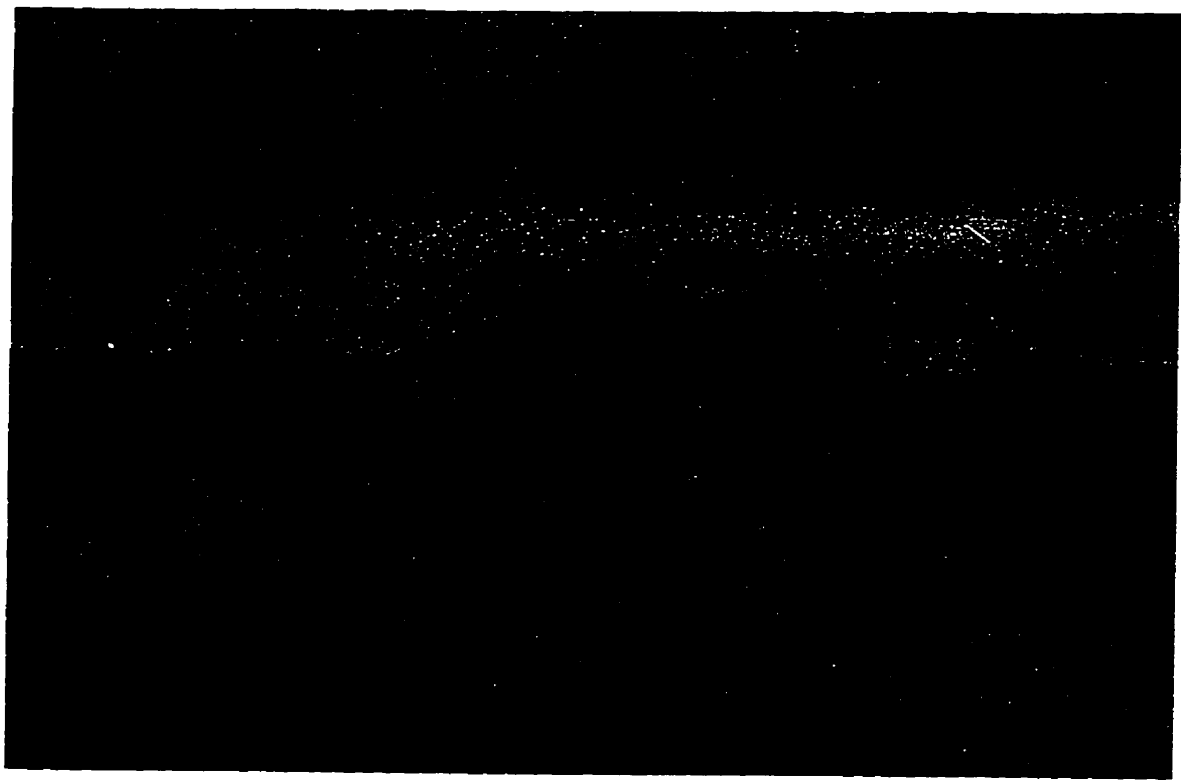
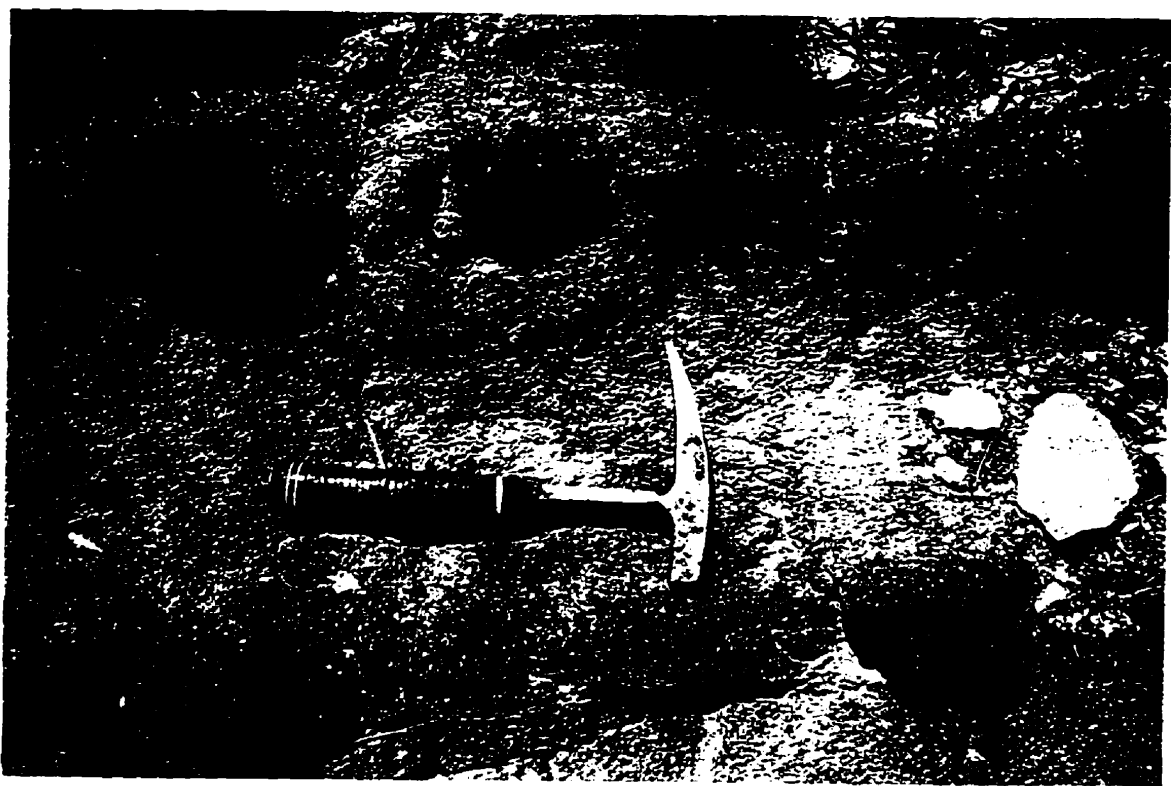


**Figure 2-31.**

*La Chilca Andesite.*

**A.** Characteristic flow-banding in the largest body of the La Chilca Andesite. View to the SW into the floor of the NW quadrant of Bajo la Chilca, taken from the ridge forming the northern margin of the *bajo*.

**B.** Detail of above. Strong differential weathering is observed between the layers, although no changes in composition are evident.



Andesite is the oldest intrusive unit in the complex and probably represents feeders to flows interbedded in the extrusive breccias. Further, the oval pattern defined overall by intrusions of this type led to the inference that their emplacement was controlled by the ring-fracture of a collapsed caldera. Llambías (*op. cit.*) emphasized that the *brechas moradas* crop out predominantly inside the limits of the proposed ring-fracture whereas *brechas polimícticas* are located peripherally. This interpretation is rejected herein. The lateral transition from the *brechas moradas* to the *brechas polimícticas* represents the transition from *Proximal* to *Medial Volcaniclastic Facies*. No annular fracture patterns were observed in the field or in TM images and given the long intrusive history recorded at Farallón Negro, it is assumed that ring fractures would have channelled successive intrusive phases rather than only one. Many of the La Chilca Andesite bodies were intruded in the NW-trending corridor described above, many exhibit NW-trending elongation and many of the bodies are aligned along a NW-trending axis. The intrusion of these bodies appears to conform to the same structural control as the majority of intrusive bodies at Farallón Negro and it is concluded that the existence of a caldera ring-fracture is not supported.

#### *Aguila Dykes*

The central portion of the Volcanic Complex is remarkable for the abundance of NW-trending dykes. These range from basalt to andesite in composition and are generally dark and aphanitic, attaining widths of up to 5 m. The highest concentration of the dykes is to the NW of Alto de la Blenda (see below). Llambías (1970) considered these units



to be older than the Alto de la Blenda Monzonite stock because they are commonly truncated by the monzonite and only rarely are dykes observed intruding the monzonite. While these field relationships are supported by this author, a sample of andesite dyke (JC-30) collected by J.C. Caelles and A.H. Clark and dated in this study, yielded an age of 6.30 Ma, postdating the age of intrusion of the monzonite by a minimum of 0.7 Ma. A basaltic dyke from south of Alto de la Blenda gave an age of 7.94 Ma (Fig. 2-30). These data suggest that mafic dyke emplacement may have persisted, albeit intermittently, through much of the intrusive history at Farallón Negro. Thus, the intrusion of basaltic and andesitic dykes overlapped with the emplacement of the La Chilca Andesite, the Alto de la Blenda Monzonite and the Agua Tapada Dacite.

The geographical term *Aguila*, from Quebrada Aguila, is suggested for this unit as this *quebrada* transects the region of greatest dyke concentration. The general term dyke is preferred as the unit ranges in composition from basalt to andesite.

#### *Alto de la Blenda Monzonite*

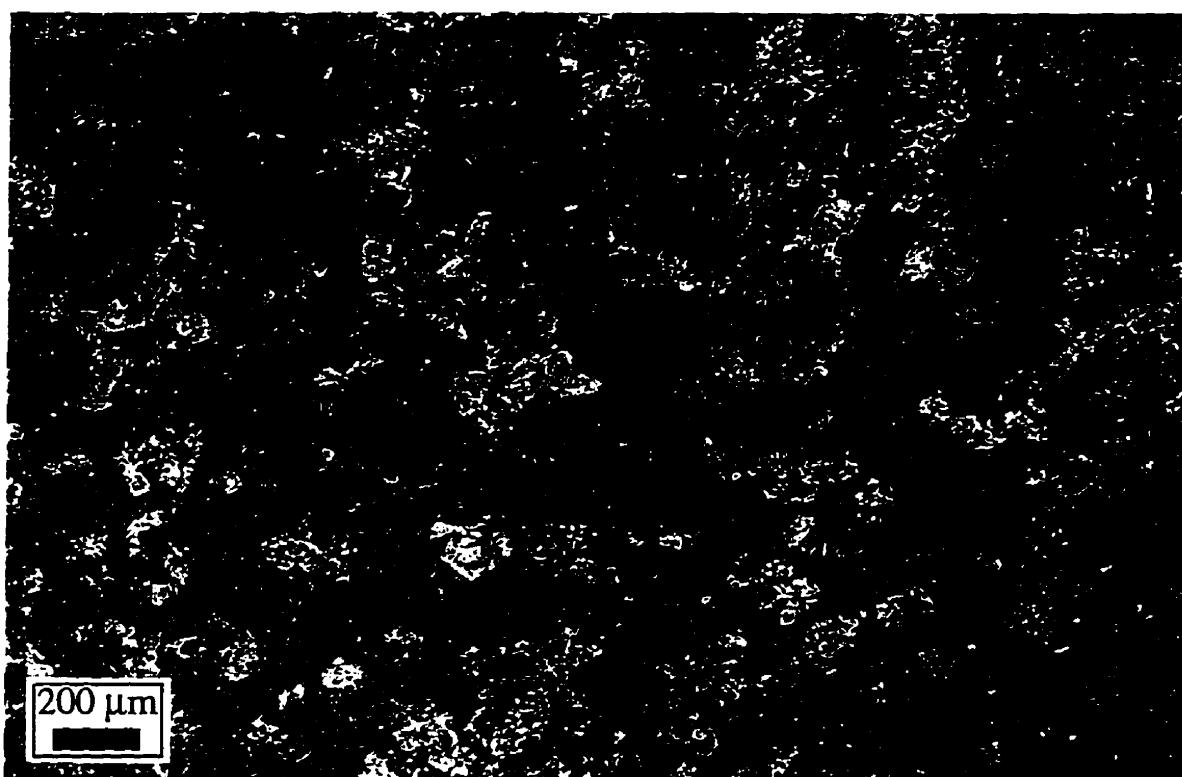
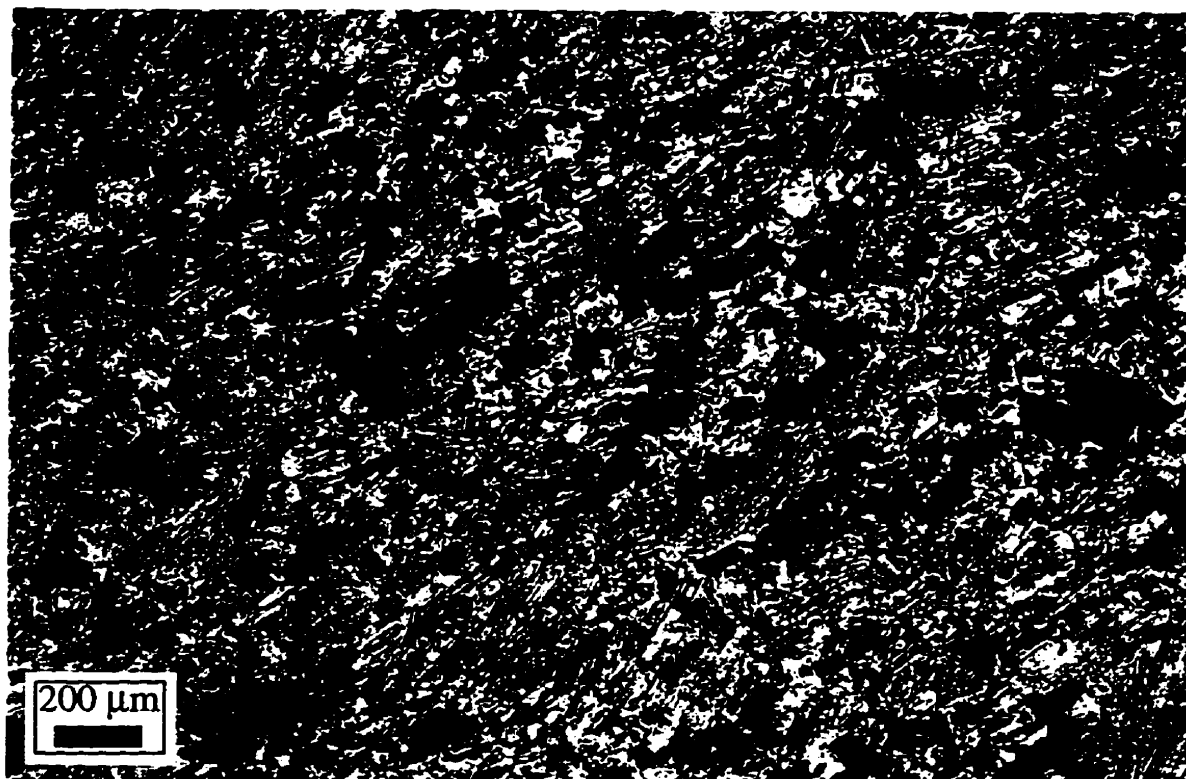
The largest intrusive body at Farallón Negro comprises the Alto de la Blenda Monzonite stock and an associated, roughly radial, monzonite dyke swarm. It differs from the other intrusions in that it is the only unit that displays plutonic textures, *i.e.*, it is coarse and equigranular rather than porphyritic (Fig 2-32). This intrusion underlies the highest topography within the central portion of the Complex (2950 m). The rocks are dark-grey or grey-green and comprise intergrown plagioclase, sanidine, quartz and pyroxene with lesser biotite and hornblende. Llambías (1970) describes a textural

**Figure 2-32.**

*Alto de la Blenda Monzonite.*

**A.** Photomicrograph in plane-polarized transmitted light to illustrate the plutonic, *i.e.*, hypidiomorphic-granular, texture of the monzonite. Equigranular intergrowths of plagioclase, sanidine and biotite with accessory oxides display trachytic texture in sample FAR 215, located along the southern access road to Bajo de la Alumbrera, approximately 3 km east of the Farallón Negro mine-site.

**B.** Cathodoluminescence (CL) photomicrograph of a second microscopic field of FAR 215 which demonstrates the abundance of primary alkali feldspar (blue,  $\text{Ti}^{4+}$  -induced CL response). Plagioclase exhibits a greenish-yellow,  $\text{Fe}^{2+}$  and/or  $\text{Mn}^{2+}$  -induced response (the intensity of the green has been enhanced during the photographic printing process). The distribution and abundance of yellow,  $\text{Mn}^{2+}$  -induced, fluorescing apatite is clearly revealed in CL. The dark patches are predominantly biotite which displays quenched luminescence resulting from the high Fe content, and Fe-Ti oxides which do not exhibit luminescence.



transition to a finer-grained, porphyritic marginal facies in the Bajo las Pampitas area. Ages of 7.02 and 7.50 Ma were determined for two samples of this unit.

Llambías (*op. cit.*) suggested that the monzonite was probably emplaced at approximately the same altitude within the stratovolcano as the other stocks in the area. He attributed the plutonic texture of the monzonite to slow cooling, reflecting its larger size. It could, however, be argued that the Alto de la Blenda stock was intruded higher into the volcanic edifice and that erosion has exposed the deeper, phaneritic portion of the stock, whereas the other intrusive units attained lower levels in the volcano.

#### *Agua Tapada Dacite*

These units were termed "Quartz-andesites of Bajo de Agua Tapada" by Llambías (1970). The pale-grey rocks are composed of plagioclase, hornblende and biotite with rare quartz phenocrysts in an aphanitic matrix (Fig. 2-33). They were emplaced in the northeast portion of the NW-trending corridor and crop out as a series of small or medium-sized bodies between Bajo de Agua Tapada in the NW and Bajo de la Alumbrera and Bajo el Espanto in the SE. These porphyries are dominantly of dacitic composition and are commonly associated with mineralization. They range in age overall from 6.78 Ma at Bajo de la Alumbrera to 7.39 Ma at Bajo de Agua Tapada. The intrusion of dacite porphyries at Bajo de Agua Tapada both predated and overlapped with that at Bajo de la Alumbrera.

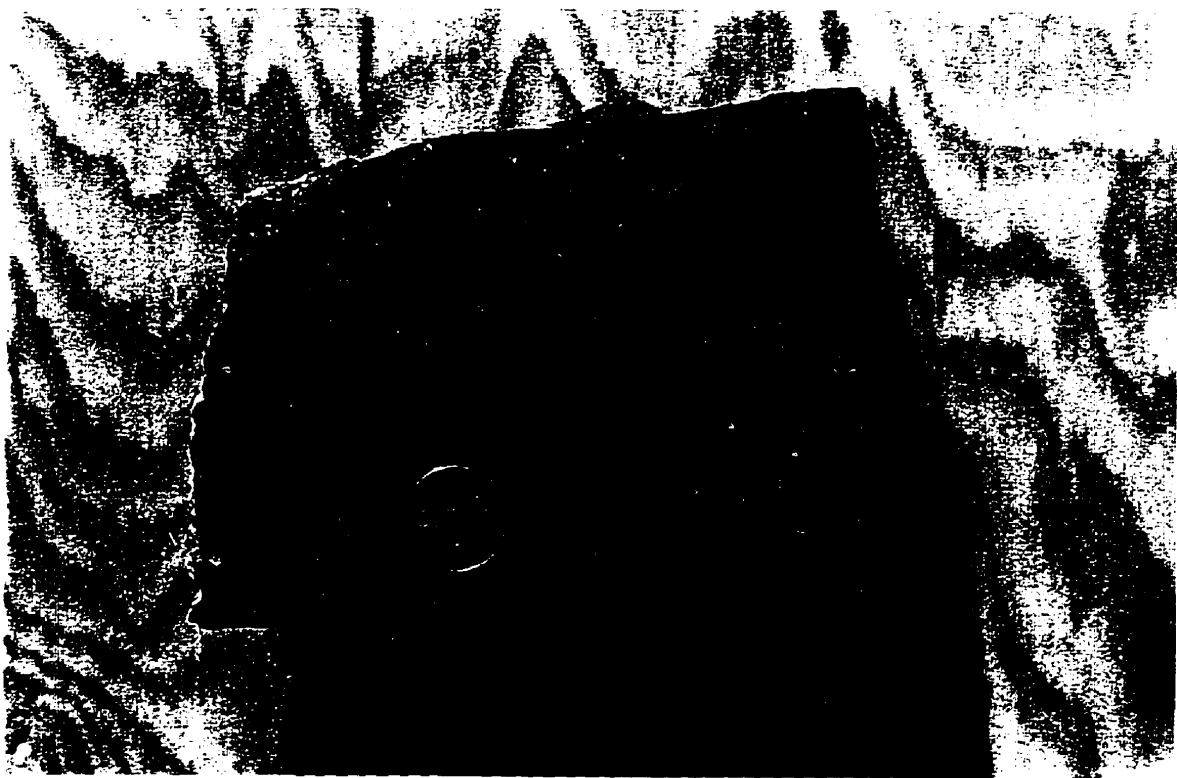
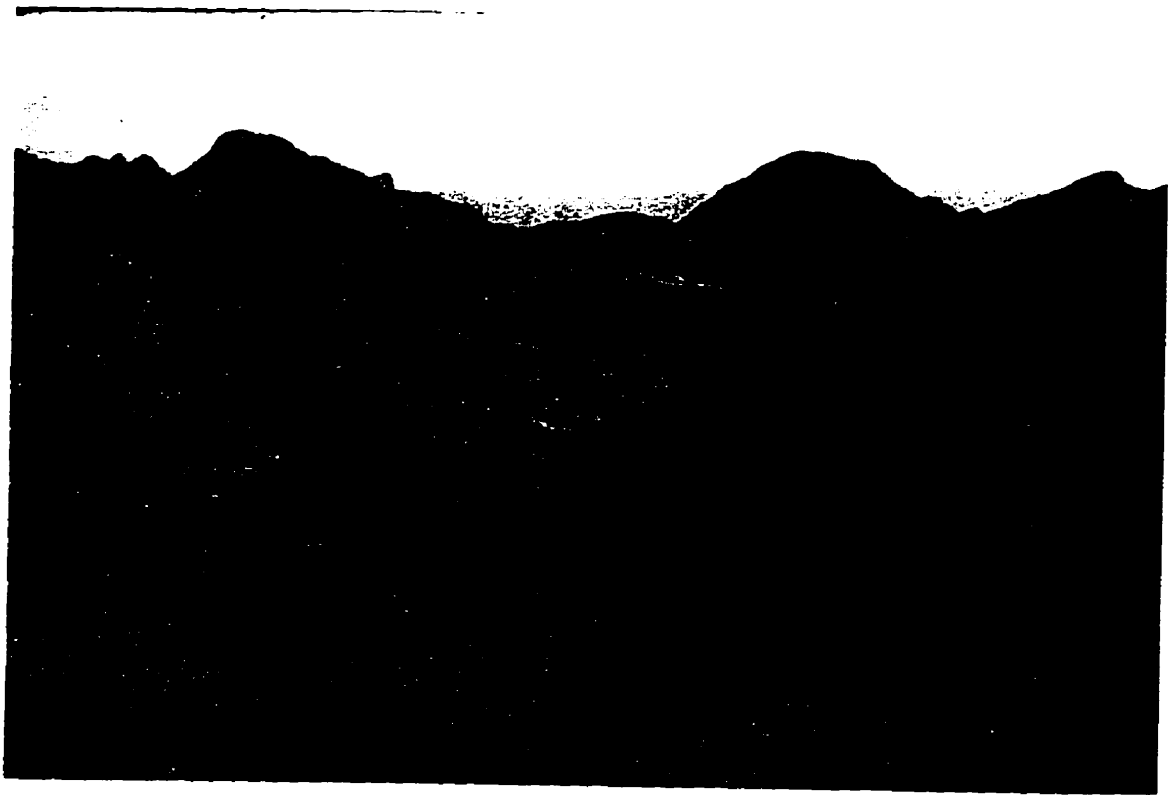
The geographic term proposed by Llambías (*op. cit.*) is maintained, but these rocks have been classified as dacites on the basis of geochemical data obtained in this study.

**Figure 2-33.**

*Agua Tapada Dacite.*

**A.** View to the NW illustrating the field characteristics of an Agua Tapada Dacite dyke (left-side of field), with chilled margins, which transects phyllically-altered breccias of the *Medial Volcaniclastic Facies* in the NW quadrant of the Bajo de Agua Tapada prospect.

**B.** Hand sample of FAR 238, from the central dacite intrusive body at Bajo de Agua Tapada, illustrating the typical porphyritic texture of this unit.



### *Macho Muerto Dacite*

A second series of dacite porphyries crops out as stocks and dykes in the NW quadrant of the Complex and as irregular, but persistent, dykes in the SE quadrant. The largest such intrusion is located at Lomo Morada on the NW periphery of the Complex. A series of similar bodies, all elongated NW-SE, are aligned in a NW direction with Loma Morada and are herein interpreted to have intruded along the trace of a normal fault. These bodies decrease progressively in size to the southeast of Lomo Morada. A large body is also located in the Río Seco de la Aguada. The units are pale-grey or buff and are characterized by phenocrysts of sanidine, attaining 10 cm in length in the Macho Muerto body, bi-pyramidal quartz, plagioclase and biotite in an aphanitic groundmass. They commonly exhibit well-developed flow-banding (Fig. 2-34) and were interpreted as endogenous domes by Llambías (1970) and Godeas (1971). Samples from this unit yielded ages of from 5.95 to 6.14 Ma.

The geographical term proposed by Llambías (*op. cit.*) is accepted. On the basis of geochemical analyses completed in this study, the rocks of this lithodeme may be classified as dacite.

### *Los Leones Rhyolite*

The youngest intrusive event observed at Farallón Negro is recorded by a restricted series of NW-trending rhyolite dykes which crop out to the south of the Farallón Negro mine-site. The rocks are pale-buff to violet with quartz, plagioclase, sanidine and rare chloritized biotite phenocrysts in an aphanitic matrix. The dykes intrude all other rock-

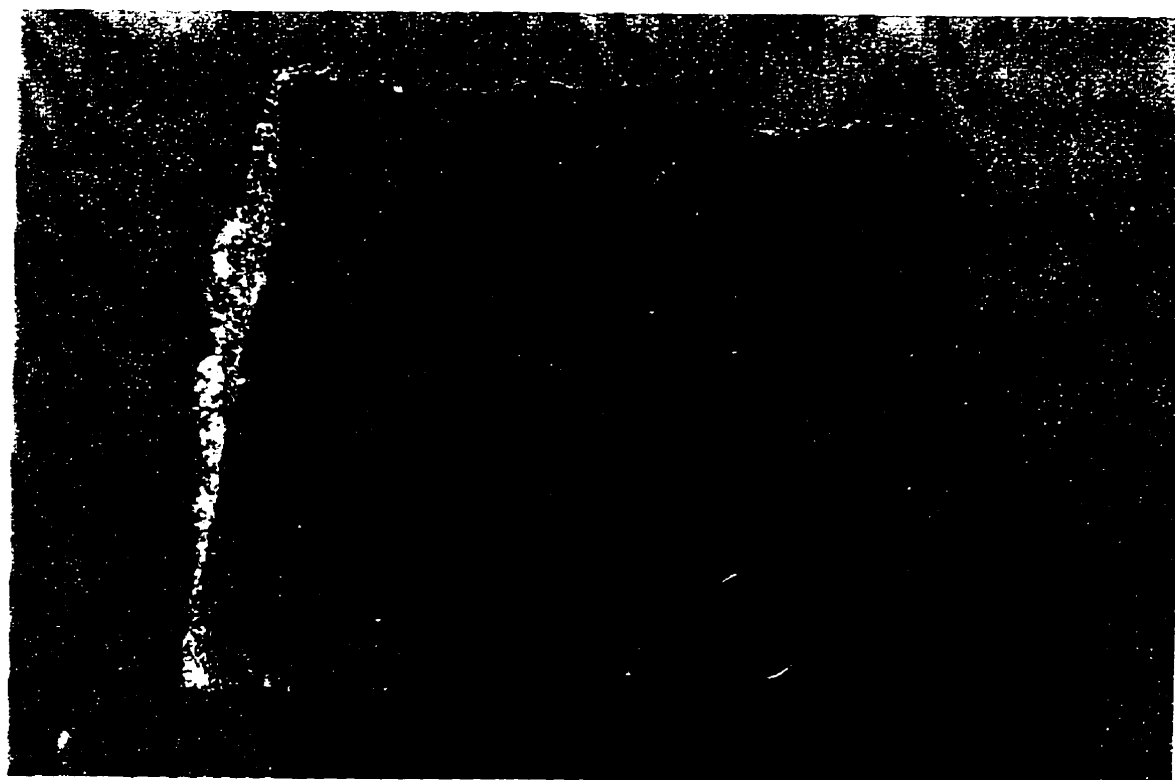
**Figure 2-34.**

*Macho Muerto Dacite.*

**A.** Field characteristics of the Macho Muerto Dacite intrusive body (pale unit in foreground). The flow banding is faintly visible as variations in the colour from pale- to purple-grey. The hills in the background are underlain by flows and breccias of the *Proximal Volcaniclastic Facies*. View to the west.

**B.** Hand-sample (FAR 288) of crowded dacite porphyry from the peak of Loma Morada, located on the NW perimeter of the Main Farallón Negro Stratovolcano. Biotite from this sample returned an age of 6.14 Ma.





types. No samples were dated in this study.

Dykes of this type are encountered in Quebrada de los Leones, south of the Farallón Negro mine-site, and Los Leones is proposed as the geographical qualifier for this lithodeme.

### *Vis Vis*

Volcanic and intrusive bodies are encountered in the vicinity of Vis Vis, south of the Main Farallón Negro Stratovolcano, and are inferred to have been separated from the main volcanic outcrop by uplift along the San Buenaventura, Vallecito and Jaci-Yaco high-angle reverse faults (Fig. 2-11). The volcanic units consist predominantly of breccias of the *Medial Volcaniclastic Facies*, identical to those exposed in the southeast portion of the Main Farallón Negro Centre. Two samples analyzed in this study are of shoshonitic composition and yielded ages of 8.37 and 8.48 Ma.

To the west of the settlement of Vis Vis these units are intruded by a series of andesitic stocks (Fig. 2-35), one of which gave an age of 8.37 Ma. They are very similar in texture, composition and age to the *Durazno Andesite* and are herein assigned to that lithodeme. Small monzonite and dacite porphyry bodies intrude basement rocks at Bajo de San Lucas and Bajo las Juntas (Fig. 2-11). Andesite dykes, with an age of 7.59 Ma, are observed at Bajo las Juntas, while the dacite porphyry at Bajo de San Lucas yielded an age of 7.35 Ma. On the basis of petrological and geochronological data these units may be included, respectively, in the *Aguila Dykes* and *Agua Tapada Dacite* lithodemes.

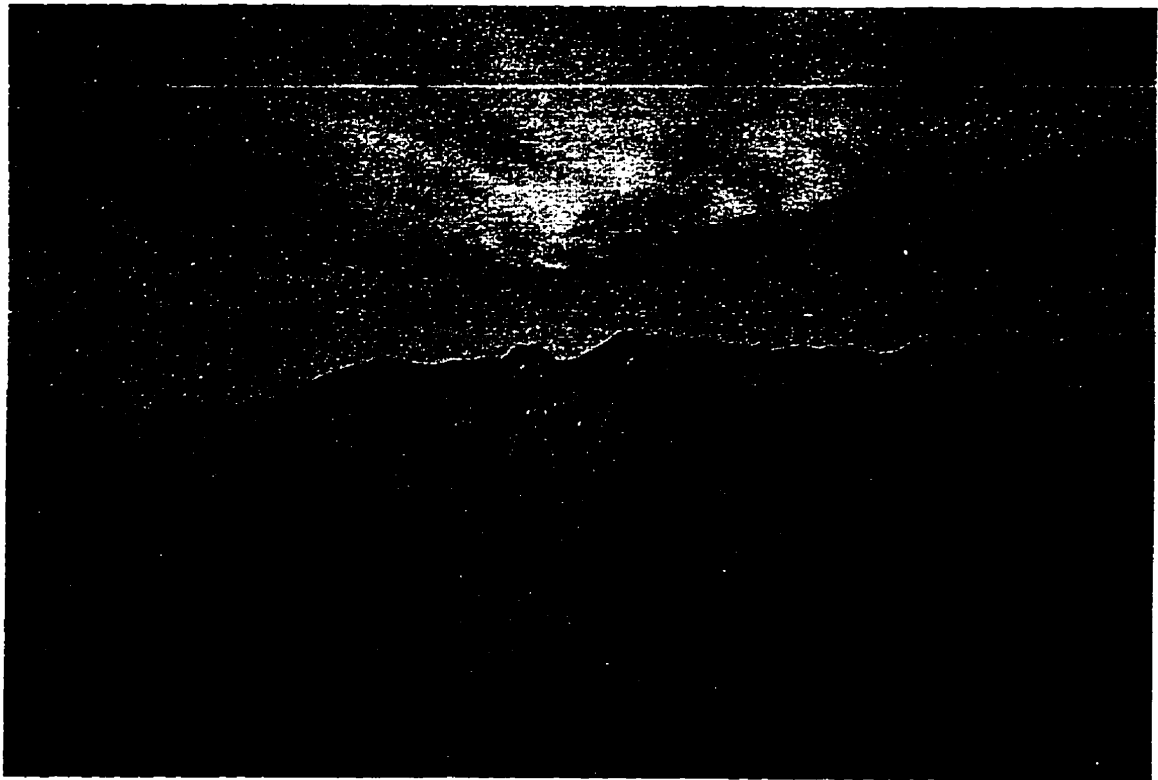
The intrusive units at Bajo de San Lucas and Bajo las Juntas are in alignment with

**Figure 2-35.**

*Durazno Andesites at Vis Vis.*

**A.** Field characteristics of an intrusion of Durazno Andesite to the west of Vis Vis. A steep-walled andesite intrusion (centre) is emplaced in breccias of shoshonitic affinity. The ridge on the horizon is the Sierra de Ovejería and is underlain by units of the Suncho Formation. View to the north.

**B.** Hand-sample of above (FAR 297) illustrating the fine-grained porphyritic texture typical of the Durazno Andesite unit. Plagioclase and hornblende are the dominant phenocryst phases that can be seen at this scale. Hornblende from this sample yielded an age of 8.37 Ma.



the SE extension of the NW-trending intrusive corridor of the Main Farallón Negro Stratovolcano. It is herein proposed that the volcanic and intrusive outcrops in the Vis Vis region do not represent a separate volcanic centre but rather the extensively dissected remnants of the southern continuation of the stratovolcano.

### ***Sierra Durazno***

#### **Western Flanks of Sierra Durazno**

The Sierra Durazno has been uplifted and separated from the Main Farallón Negro Stratovolcano by movement along an unnamed high-angle reverse fault which lies to the east of Bajo el Durazno. In the cliffs forming the western flank of the northern Sierra Durazno, red sediments of the El Morterito Formation are overlain by a pistachio-coloured basalt flow with large clinopyroxene phenocrysts in a fine-grained groundmass. The flow is itself overlain by a thick succession of volcanoclastic gravels of the *Distal Facies* (Punaschotter Formation). The southern Sierra Durazno is a structurally complex zone exposing El Morterito sediments and andesitic breccias intruded by a series of basaltic dykes (*Sierra Durazno Dykes*) and a small stock of *La Chilca Andesite*. The structure and geology of this region were not resolved in the course of this study. The southern edge of the region is marked by a series of east-striking, south-side-down, normal faults which preserve a thick sequence of *Medial Volcanoclastic Facies* breccias in a graben. This structure was recognized on TM imagery only after the completion of field work and hence was not investigated in the field.

## Eastern Flanks of Sierra Durazno

In the vicinity of the basement dome which forms the eastern flanks of the Sierra Durazno, northeast of the Cerro Atajo prospect (Fig. 2-11), the volcanic succession is relatively thin and consists of massive basalt and basaltic-andesite flows and an andesite tuff. The El Morterito Formation is overlain by a sequence of clinopyroxene-phyric basaltic flows to the southeast, and by an 8.41 Ma hornblende-phyric basaltic-andesite flow to the north of the basement dome. The stratigraphic relationship of these units is unclear. An andesitic tuff interbedded with gravels of the *Distal Volcaniclastic Facies* which crops out on an escarpment to the west of the basement dome yielded an age of 8.75 Ma. The relationships of the andesitic tuff to the above-mentioned flows were not resolved in the field. On the basis of TM image interpretation, it is suggested that a fault may trend NNE through the alluvium-filled valley at the base, and to the east, of the outcrop of andesitic tuff. Further structural mapping is required to resolve these stratigraphic relationships. No intrusive units were encountered in this region.

The ages and geochemistry of the flows exposed in the Sierra Durazno are similar to those of units of the Farallón Negro Volcanic Complex. The abundance of dykes in the southern Sierra Durazno and the similarities between the dykes and the flow cropping out in the cliffs of the north-western Sierra Durazno suggest that the dykes may represent feeders for that extrusive event. The source of the flows and tuff observed in the eastern Sierra Durazno is uncertain. However, they may be related to an extrusive source in the south-western Sierra Durazno or even in the Main Farallón Negro Stratovolcano, because the low viscosity of the melts of this composition would permit flow to considerable

distances. Alternatively, a yet unrecognized vent may have existed locally.

### ***Cerro Atajo***

An 860 m -thick section of volcanic units is observed in the immediate vicinity of the Cerro Atajo prospect. They consist predominantly of andesitic pyroclastic breccias of the *Medial Facies*, with thin volcanoclastic layers, overlain by a thick succession of breccias (possibly of the *Proximal Volcanoclastic Facies*). The Japanese International Cooperation Agency (1978) identified six stratigraphic units which comprise, from oldest to youngest: andesitic tuffaceous breccia; basalt flow; andesitic tuffaceous breccias with rare basalt and granite clasts; andesite tuffs; andesite pyroclastics; and andesite breccias. A basaltic-andesite dyke which intrudes the lower units of this sequence was dated in this study, yielding a whole-rock age of 8.15 Ma.

The volcanic succession is intruded by dacite and rhyolite stocks. A large rhyolite body was emplaced in El Morterito sediments and overlying volcanics to the west of Cerro Atajo and forms two large, white hills, Cerro Blanco (3367 m) to the south and Cerro Blanco Chico to the north (Fig. 2-36). The rock contains abundant quartz phenocrysts and minor sieve-textured plagioclase phenocrysts in a very fine-grained matrix. The age of intrusion is unknown. A body of dacite porphyry underlies the peak of Cerro Atajo. Phenocryst phases include quartz, sericitized feldspar and chloritized biotite in an altered quartzo-feldspathic matrix.

It is herein argued, on the basis of the chemical composition of the volcanic units in the area and the absence of intrusive units of similar compositions which may have

**Figure 2-36.**

Rhyolite intrusions at Cerro Atajo. Cerro Blanco Chico (centre) and Cerro Blanco (left) are surrounded by blue-grey outcrops of breccias of the Farallón Negro Volcanic Complex. Bola del Atajo, underlain by granitic basement, forms the high ridge to the right. The distant horizon is defined by basement uplifts of the Sierra de Ovejería. View to the SW from the summit of Cerro Atajo.





acted as conduits or feeders, that Cerro Atajo does not represent a major extrusive centre. The predominantly pyroclastic nature of the volcanic units suggests that these represent the *Medial Volcaniclastic* facies, albeit distal, of either the Farallón Negro Stratovolcano or some yet unrecognized extrusive centre.

### *Capillitas*

Volcanic breccias of the *Medial Volcaniclastic Facies* crop out in the Capillitas valley, south and southeast of the Capillitas Mine (Fig. 2-11). These conformably overlie the El Morterito Formation but are in fault contact with basement granites along their south-eastern margin. A series of isolated outcrops of a dacite porphyry flow with large biotite phenocrysts occur along the Agua Rica access road. The dacite porphyry is interpreted to overlie the breccias. Biotite from the dacite flow yielded an age of 9.17 Ma. The geology of the Capillitas deposit is presented in more detail in Chapter 3, but here it should be emphasized that the relationship between the volcanic units and the Capillitas diatreme is unclear: a projection of the sediment-volcanic contact, extrapolated from its exposure south of Capillitas, would lie approximately 1500 m above the present surface of the diatreme. The vertical dimensions of diatremes are inferred to be several times greater than their maximum widths and, while the full vertical extent of a pipe is nowhere observable, vertical dimensions of up to 860 m are observed (Sillitoe, 1985). It is therefore tentatively concluded that is unlikely that the Capillitas diatreme intersected the volcanic succession observed in the area. A dacite porphyry dyke which cuts the rhyolitic diatreme yielded an age of 5.16 Ma, and emplacement of the diatreme must have predated

this.

### ***Agua Rica***

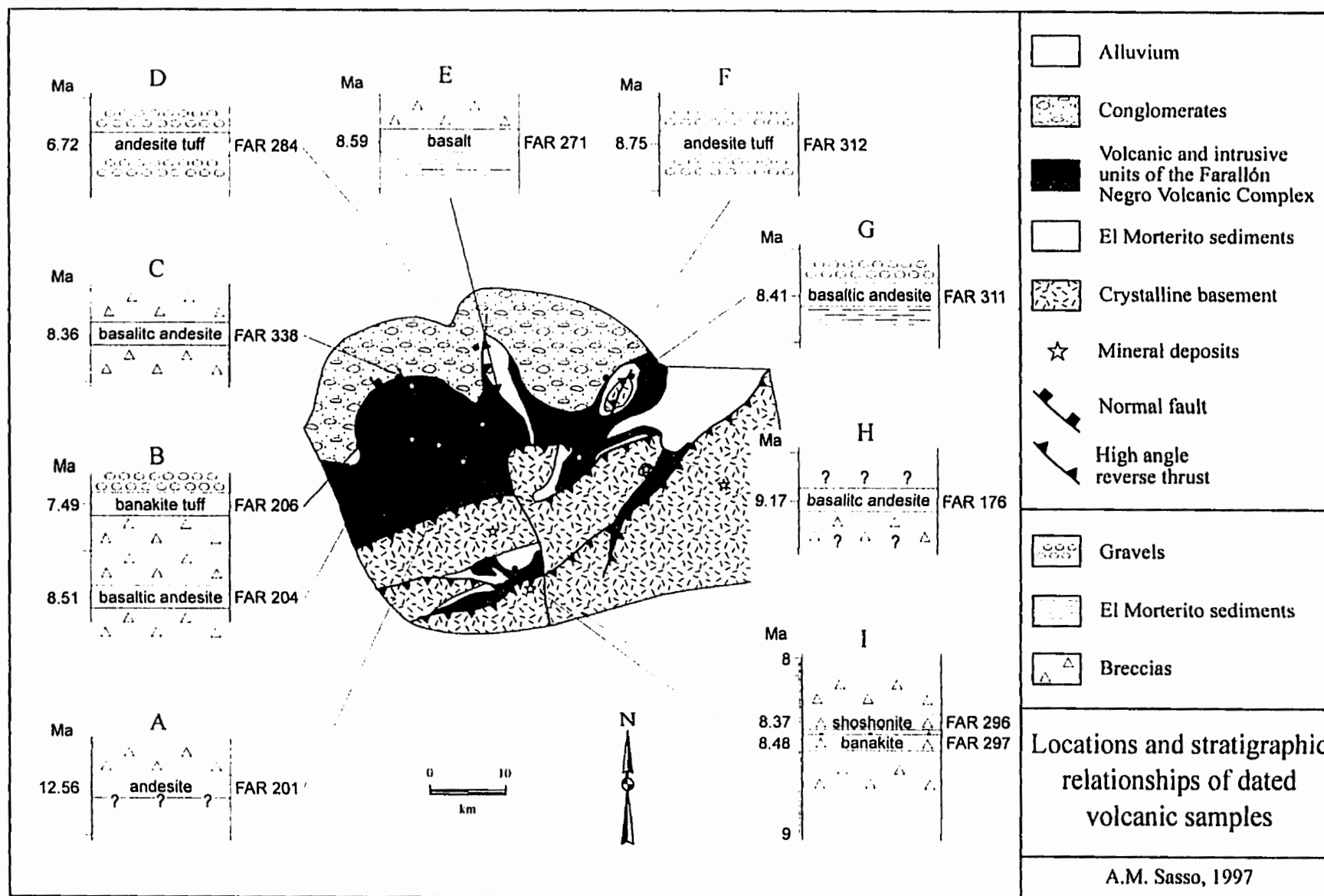
The geology of the Agua Rica deposit is described in detail in Chapter 3. No volcanic units are observed, but it is inferred that limited extrusive sequences may have overlain the prospect. Intrusive units at Agua Rica include an 8.56 Ma monzonite, a series of undated andesite porphyries associated with mineralization and a post-mineralization biotite porphyry. The ages of these units are in broad agreement with those of the Farallón Negro Volcanic Complex, but it is inferred that they represent a separate, and probably less voluminous, volcano-intrusive centre.

### ***Synthesis***

A summary diagram illustrating the locations and stratigraphic relationships of dated volcanic samples from the Main Farallón Negro Volcanic Complex is presented as figure 2-37. A large stratovolcano with a possible vent in the vicinity of Alto de la Blenda, as proposed by Llambías (1972), generated flows and breccias which encompassed the area of present exposure and probably extended south to the Vis Vis area and, possibly, east as far as Cerro Atajo and even Capillitas. That a subsidiary extrusive centre may have existed in the south-western Sierra Durazno is implied by the abundance of dykes in the area. Alternatively, the generally older ages of the flows distant from the Main Farallón Negro Stratovolcano, *e.g.*, the 9.17 Ma dacite in the Capillitas Valley, the 8.75 Ma andesite tuff and the 8.41 Ma basaltic andesite in the eastern Sierra

**Figure 2-37.**

Schematic diagram of the locations and stratigraphic relationships of volcanic rocks of the Farallón Negro Volcanic Complex dated in this study. A. Arroyo Alumbraera, B. Quebrada de los Leones, C. northern portion of the Main Farallón Negro Stratovolcano, D. Quebrada de Pozos Verde, E. north of Bola del Atajo, F. eastern Sierra Durazno, G. eastern Sierra Durazno, H. Capillitas Valley, I. west of Vis Vis.



Durazno and the 8.59 Ma basaltic flow north of Bola Del Atajo, may imply that extrusion occurred from several discrete centres early in the volcanic history of the region. This would have included eruption of the 12.56 Ma basaltic-andesitic flow in the Arroyo Alumbreira. Such possible precursor volcanic units were subsequently covered by the large stratocone construction event centred on Alto de la Blenda, involving almost continuous eruption from 8.51 to 7.49 Ma and minor extrusion of pyroclastics until as late as 6.72 Ma.

### **CHAPTER 3**

#### **MINERALIZATION ASSOCIATED WITH THE FARALLON NEGRO VOLCANIC COMPLEX**

During the past several years it has become apparent that the Farallón Negro Volcanic Complex is host to one, and possibly two, world-class deposits. The Bajo de la Alumbrera porphyry copper-gold deposit (752 Mt at 0.51% Cu and 0.65 g/t Au at 0.2% Cu cutoff: Northern Miner, June 26, 1995), scheduled to begin production in August, 1997, may be classified as a "giant" deposit in the sense of Clark (1993). The nearby Agua Rica Cu-Au-Mo prospect (802 Mt at 0.61% Cu, 0.035% Mo and 0.24 g/t Au at 0.4% Cu cutoff: J. Mortimer, pers. comm., July, 1997) may represent Argentina's first "super-giant". These deposits, along with producing mines at Capillitas (rhodochrosite, but with historical Cu production) and Farallón Negro-Alto de la Blenda (Au-Ag), and numerous porphyry Cu-Au and epithermal Au-Ag prospects, are evidence of the remarkable endowment of base- and precious-metal deposits of this restricted geographical region.

This chapter addresses aspects of the ore-genesis and metallogenesis of Cu and Au in the Central Andes and, specifically, in the 26° to 28° S transect of Chile and Argentina. The Bajo de la Alumbrera and Agua Rica deposits are described because they are the most important deposits under development in the area. The Capillitas and Farallón Negro - Alto de la Blenda epithermal deposits are also documented because they are the only deposits currently in production in the district. The salient characteristics of deposits hosted by, and associated with, the Farallón Negro Volcanic Complex are recorded to

develop a model for the porphyry Cu-Au deposits of this district. The relationship between porphyry Cu-Au and epithermal Au-Ag mineralization is also considered.

## **Review of Metallogenetic Concepts**

### ***Metallogenesis: Background***

Geologists have long been concerned with the practical and scientific question, "Why is ore where it is?". Beginning in the first half of the 19th century, this enquiry led to the evolution of the metallogenetic approach to the study of mineral deposits. Zentilli (1974) provides a comprehensive review of the historical evolution of metallogenetic thought. Significant advances have been made in recent years in the investigation of conditions governing ore deposit formation, and the recognition of the association of mineralization with specific geological environments and time intervals has generated models for the exploration for deposits. However, fundamental questions regarding the source of ore metals and the genetic controls on their concentration and distribution remain unanswered.

### ***Metallogenesis: Terminology***

The study of metallogenesis is rendered confusing by the lack, not only of precise definitions, but also of accepted usage of terms. Although metallogenetic analysis seems to be largely an exercise in geographic delimitation, it can be conducted using two governing parameters: the age of mineralization and the metal association. Table 3-1 presents a series of formal definitions for metallogenesis-related terms. A hierarchy of



**Table 3-1.**  
Definitions of metallogenesis-related terms  
(after A.G.I., 1987).

TERM	A.G.I. DEFINITION 1987
Metallogeny	The study of the genesis of mineral deposits, with emphasis on their relationship in space and time to regional petrographic and tectonic features of the Earth's crust. The term has been used for both metallic and non-metallic mineral deposits.
Metallogenic Epoch	A unit of geologic time favourable for the deposition of ores, or characterized by a particular assemblage of mineral deposits.
Metallogenic Province	An area characterized by a particular assemblage of mineral deposits, or by one or more characteristic types of mineralization. A metallogenic province may have had more than one episode of mineralization (or metallogenic epoch).
Metallotect	A term used in metallogenic studies for any geologic feature (tectonic, lithologic, geochemical, etc.) considered to have influenced the concentration of elements to form mineral deposits; an ore control but without the implication of economic value.

Note: Metallogenic = Metallogenetic; Metallogeny = Metallogenesis.

these terms may be deduced from the literature, as may be an understanding of several poorly-defined but commonly used informal terms (*e.g.*, metallogenetic *sub-province* and *belt*). Sillitoe (1976) provides the most concise outline of the practical usage of these terms. Thus, the largest areal domain is that of *metallogenetic province*. The whole Andean orogen is treated as a post-Paleozoic metallogenetic province. Each metallogenetic province results from the temporal superimposition of *metallogenetic epochs* (De Launay, 1913). In Sillitoe's hierarchy, the metallogenetic epochs appear to be divisible into *metallogenetic sub-provinces*; this would, however, contradict the spirit of De Launay's work in which the metallogenetic sub-provinces may, and commonly do, transgress metallogenetic epochs. The introduction of the term *metallogenetic episode*, after the usage of Clark *et al.* (1976), may provide a more useful temporal subdivision of a metallogenetic epoch, maintaining De Launay's (*op. cit.*) perspective. Sillitoe (1976) further introduces the concept of *metallogenetic belts* as intermediary entities between metallogenetic provinces and metallogenetic sub-provinces. A metallogenetic belt is defined (*op. cit.*), within the context of the Andean orogen, as a longitudinal zone identified on the basis of metal content. With greater knowledge of the age relationships of a belt or series of belts, they may be subdivided into smaller magmatic-metallogenic units formed during restricted episodes of magmatic activity, termed metallogenetic sub-provinces. However, this definition appears to combine the concepts of timing and metal association, thus blurring the distinction between provincial, *i.e.*, areal, and epochal parameters. The additional implication of a magmatic origin provides further potential for confusion (and mis-use). Clark and Zentilli (1972) appear to maintain this distinction by

referring to discrete longitudinal metallogenetic sub-provinces, each of which evolved within a specific metallogenetic epoch. However, this also does not allow for the transgression of epochs by sub-provinces as suggested by De Launay (1913).

Terms used in the following discussion will adhere to the definitions provided in Table 3-1. In addition, *metallogenetic episode* is used in the place of *metallogenetic epoch* to provide greater breadth in the scale of the temporal divisions. The term *metallogenetic sub-province* is redefined, within the context of Central Andean metallogenesis, to represent a definable enrichment of ore deposits within a geographic area which transgresses metallogenetic epochs. It is suggested that this hierarchy can be further extended to include *metallogenetic districts* (*metallogenetic centres* of Zentilli, 1974), which refer to a series of, possibly genetically-related, deposits of similar metal association located within a restricted geographic region (e.g., the Farallón Negro metallogenetic district).

#### ***Cu and Au Metallogenesis of the 26° to 28° S Transect of the Central Andes***

The Central Andes exhibit one of the greatest endowments of metal deposits in the world and it is generally accepted that they constitute the type-area for the study of metallogenesis along a convergent plate boundary. The broad metallogenetic relationships of the Central Andes have been well established (Stoll, 1964, 1965; Clark and Zentilli, 1972; Clark *et al.*, 1973, 1976, 1990; Sillitoe, 1976, 1981, 1988, 1991, 1992). All discussions of Andean metallogeny eventually lead to the metal tin (e.g., Clark *et al.*, 1976; Sillitoe, 1976), the Bolivian Sn belt representing a geographically clearly delimited

gross anomaly (Clark *et al.*, *opera cit.*), which must hold the key to the Andean metallogenetic puzzle. However, a discussion of Sn metallogenesis as related to the Andean orogen is beyond the scope of this thesis.

### Previous Work

In a study of the 26° - 29° S transect of northern Chile, Zentilli (1974) identified the transect as a segment of a large copper "metalliferous" province (as defined by Spurr, 1902). The adjoining region of NW Argentina was interpreted as the easterly extension of the major Cu (metallogenetic) province of Chile, with the difference that, in Argentina, it is represented by areally-discrete metallogenetic "centres". Zentilli (*op. cit.*) and Haynes (1975) remarked on the scarcity of pre-Mesozoic, *i.e.*, pre-Andean, mineralization in Chile, whereas the Mesozoic and Cenozoic rocks of the Andean orogen are rich in metallic ore deposits which are generally related spatially and genetically to shallow-seated plutonism. Thus, Andean magmatism appears to be the first-order control for copper mineralization - the regional *metallotect* (see Table 3-1). Cu mineralization formed during successive, discrete, metallogenetic episodes and becomes progressively younger from west to east, giving rise to a series of longitudinal belts or metallogenetic sub-provinces. Both Zentilli and Haynes (*opera cit.*) concluded that, in this transect, Cu had been concentrated to economic levels in all metallogenetic episodes from Early Jurassic to Neogene times, invariably in association with granitoid intrusions or associated hypabyssal units. They inferred that magmas and metals shared a similar source. The copper specialization of the transect also suggested a rather homogeneous source (see

also: Clark *et al.*, 1976; Tilton *et al.*, 1981) and a remarkable consistency in the conditions of magma generation.

This concept of the migration of the locus of base and precious metal ore deposition with plutonic and volcanic centres to yield a series of narrow and areally-discrete longitudinal metallogenetic sub-provinces had previously been advanced by Clark and Zentilli (1972) and Clark *et al.* (1973). This orderly progression terminated abruptly in the Oligocene, being replaced by the Miocene "break-out" (*opera cit.*), envisaged as an almost-instantaneous extension of magmatic activity up to 250 km to the east of the former inner boundary of the orogen, penetrating to approximately 500 km from the Peru-Chile Trench. This "break-out" (tectonic perspectives would probably favour "break-in") is of major metallogenetic significance, having given rise to intense ore formation in Argentina, including the deposits of the Farallón Negro district.

Sillitoe (1976) also recognized the spatial, temporal and genetic relationship between Andean deposits and intrusive and extrusive rocks of calc-alkaline affinity. However, he remarked on the termination or change in characteristics of the longitudinal metallogenetic belts at *transverse* tectonic boundaries. Clark *et al.* (1973) also emphasized the existence of a significant discontinuity in the now-descending plate at 27° S and suggested that it may have been initiated during the Mio-Pliocene "break-out". Zentilli (1974) moreover proposed that the conditions of magma generation north and south of 27° S may have been consistently different since the Paleozoic and Sillitoe (1976) concluded that the tectonic segmentation of the metallogenetic sub-provinces resulted from long-standing discontinuities on the underlying subduction zone. The metallogenesis of each

tectonic segment has its own peculiarities, although an overall consistency in metallogenetic zonation from segment to segment is apparent. Sillitoe (*op. cit.*) further advanced the important concept that the boundaries between metallogenetic segments may control the location of certain large ore deposits.

The specific metallogenetic relationships of gold in the Central Andes were redefined during the late-1970's and 1980's by the discovery of the Maricunga and El Indio belts in northern Chile, although Zentilli (1974) and Clark *et al.* (1976) had earlier emphasized the probability that Au mineralization may have occurred across the entire 26° - 27° S transect and in all metallogenetic episodes, in contradistinction to Sillitoe's (1972) confinement of this metal largely to a belt close to the littoral. Haynes (1975) defines a metallogenetic zonation of deposit types in the Copiapó region which are largely dominated by Cu and Au. Sillitoe (1991, 1992) identifies three preeminent Cu and Au metallogenetic epochs for the Central Andes as a whole (Fig. 3-1) viz.: Jurassic-to-Cretaceous, copper-dominated deposits, some with associated Au; Paleocene-to-early Oligocene, copper-dominated deposits; and Cu and Au deposits of Early Miocene-to-Pliocene age.

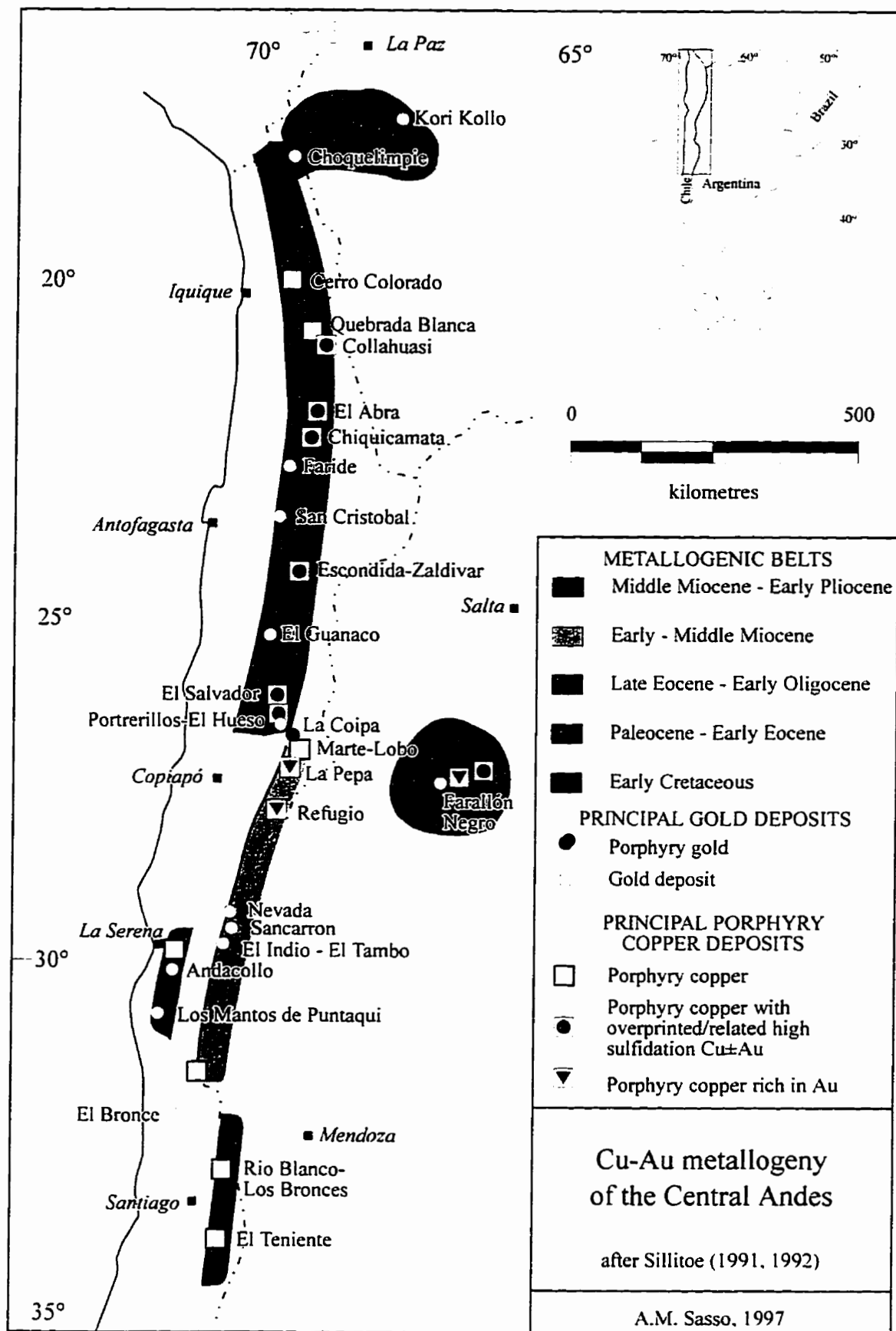
#### This Study

I concur with the above-mentioned authors that the Farallón Negro metallogenetic district was formed during the Miocene-Pliocene metallogenetic episode and forms part of the Andean metallogenetic province. I also agree that an E-W "line" at approximately 27° S represents a metallogenetic discontinuity. However, I would further argue that this

**Figure 3-1.**

Distribution of significant Cu-Au deposits of the Central Andes (after Sillitoe 1991, 1992). Illustrated are the principal Au deposits, porphyry Cu deposits in Chile and contiguous Argentina and Bolivia and the metallogenetic belts delimited by Sillitoe (*opera cit.*).



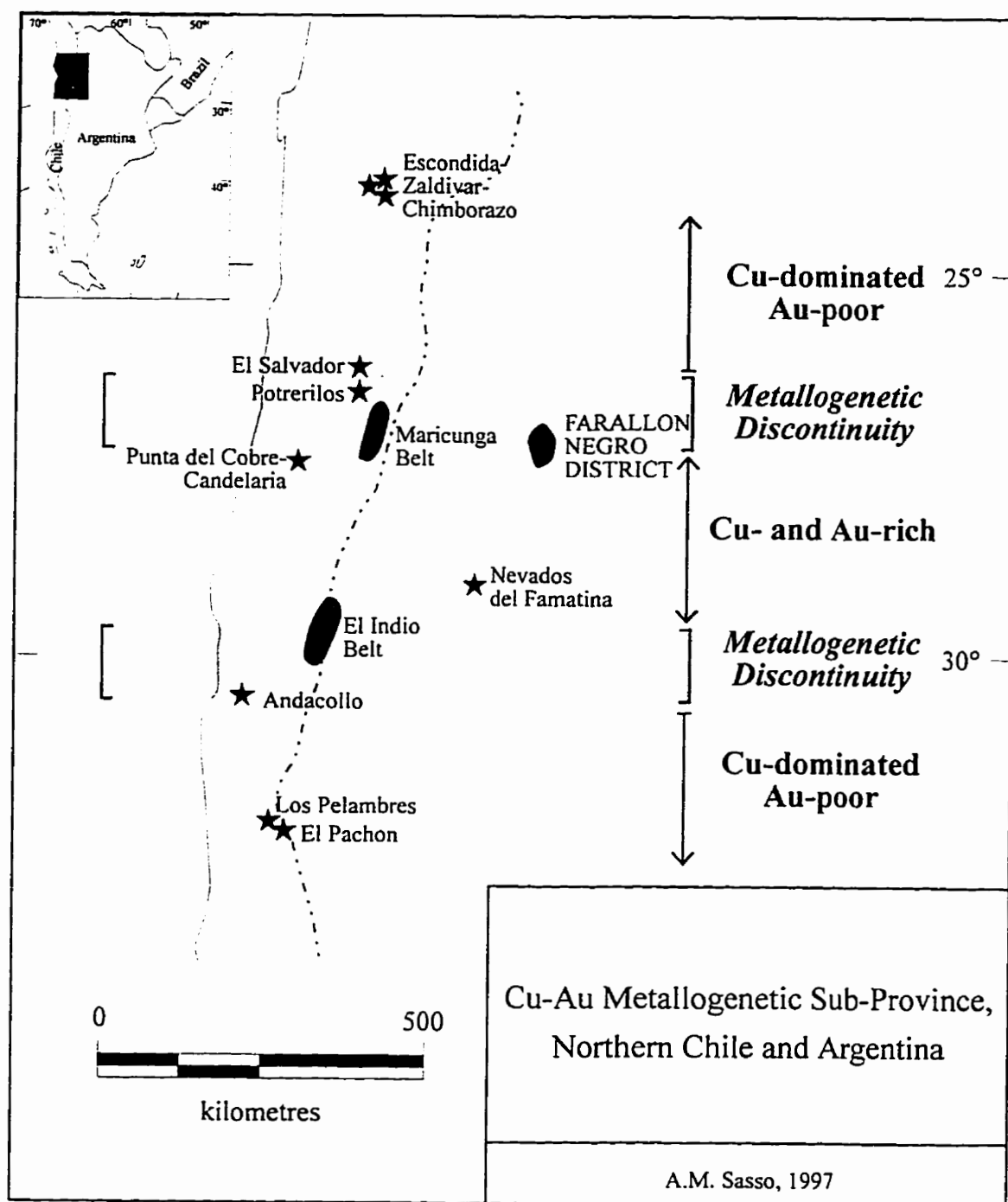


discontinuity marks the northern boundary of a significant metallogenetic sub-province (Fig. 3-2) that has experienced not only strong recurrent Cu mineralization but also that of Au since the late-Mesozoic. Sillitoe's (1976) observation that the "tectonic" discontinuities may control the location of large deposits is substantiated along this boundary by the presence of La Candelaria (Lower Cretaceous), El Salvador - Potrerillos (upper Eocene-lower Oligocene), La Coipa (upper Oligocene-Lower Miocene) and Bajo de la Alumbrera (Upper Miocene), all of which are world-class deposits or districts. Sillitoe's (1991, 1992) metallogenetic belts (defined by metallogenetic epochs) continue south of this boundary but their character changes from Cu- to Cu-Au- dominated assemblages.

The Jurassic-Cretaceous metallogenetic episode is represented by the Cu-Au deposits of La Candelaria and the contiguous Punta del Cobre district which together host approximately 650 Mt of at least 1% Cu (A.H. Clark, pers. comm., 1997). La Candelaria is a mid-Cretaceous veinlet-, disseminated- and breccia-hosted hydrothermal deposit with grades of 1.1% Cu and 0.26 g/t Au (Ryan *et al.*, 1995). The Carrizal Alto district which was a major Cu-producing centre in the latter half of the 19th century (Ruiz and Peebles, 1988) is also included in this episode. The Paleocene-early Oligocene metallogenetic episode is represented by the El Salvador and Potrerillos porphyry deposits. Whereas most Chilean porphyry Cu deposits of this episode are noticeably impoverished in Au, El Salvador (479 Mt at 0.7 - 1.12 % Cu, 0.14 - 1.07 g/t Au, 1.8 g/t Ag: Colley *et al.*, 1988) and Potrerillos (278 Mt at 1.1 - 1.2 % Cu, 0.3 - 1.25 g/t Au: Colley *et al.*, *op. cit.*) are Au-rich. Further, the El Hueso high-sulphidation epithermal deposit (16 Mt at 1.68 - 7.71

**Figure 3-2.**

Proposed Cu-Au metallogenetic sub-province in northern  
Chile and Argentina.



g/t Au: Colley *et al.*, *op. cit.*) is interpreted to be part of a cogenetic, epithermal-to-porphyry, hydrothermal system centred on the Cobre porphyry stock at Potrerillos. The Early Miocene-Pliocene metallogenetic episode is represented by the porphyry Au deposits of the Maricunga belt (Vila and Sillitoe, 1991). These deposits are remarkably Cu-poor and the district as a whole has generally been interpreted to be lacking in significant Cu mineralization. However, recent reports of 2.2 Mt of Cu and 24 million oz. of Au at the Aldebaran deposit (Bema Gold Corp., April 7, 1997, press release), place this deposit in the "very large" category (Clark, 1993), and the occurrence of massive enargite veins at depth in the La Coipa high-sulphidation epithermal Ag-Au deposit, now the second largest source of Ag globally, suggests that this region has the potential to host significant Cu mineralization. The Early Miocene-Pliocene epoch may be extended eastward to encompass the deposits of the Farallón Negro district.

I propose herein that the southern boundary of this *Cu-Au metallogenetic sub-province* lies at approximately 30° S. This boundary is marked by Andacollo, a Lower Cretaceous gold-bearing porphyry Cu-Mo deposit (440 Mt at 0.7 % Cu, 0.25 g/t Au: Reyes, 1991), with peripheral vein and stratabound, contact metasomatic gold mineralization, and the Upper Miocene gold deposits (with up to 4.5 % Cu: Sillitoe, 1991) of the El Indio belt (Fig. 3-2). The extension of this southern boundary into Argentina is tenuous because no deposits of economic significance have been discovered to date in the region. However, to the north of the boundary is located the Famatina mining district, which includes the Pliocene Nevados del Famatina porphyry Cu-Mo-Au deposit (300 Mt at 0.37 % Cu, 0.3 g/t Au, 0.06 % Mo, 0.6 g/t Ag: Losada-Calderón and McPhail, 1996)

and the La Mejicana high-sulphidation epithermal Cu-Au deposit (0.25 Mt at 6.11 g/t Au, 64.1 g/t Ag, 1.08 % Cu: *op. cit.*), together representing the most important copper mining district in Argentina in the early-20th century. Moreover, to the south, Au-skarn deposits, *i.e.*, Gualcamayo and Gualilan, of inferred Miocene age and with historic production are located in San Juan Province (Casaceli, 1993b).

No other region of the Central Andes appears to be as enriched in Au as this transect, with the possible exception of the Cajamarca-Ancash transect of northern Peru. Thus, Eocene and older porphyry Cu deposits north of the northern boundary of the proposed sub-province are remarkably poor in Au (Zweng and Clark, 1995; Clark *et al.*, 1990), as are the Miocene-Pliocene porphyry Cu deposits that lie beyond the southern border. Gold deposits are known elsewhere in Chile (see Davidson and Mpodozis, 1991), but they either represent isolated occurrences, possibly defining metallogenetic districts of insufficient geographic extent to constitute sub-provinces, or are relatively small.

It is therefore argued that Chile and Andean Argentina between roughly 27° and 30° S hosts a definable, world-class, concentration of Cu and Au deposits and constitutes a *Cu-Au metallogenetic sub-province* as defined previously. This concept was adumbrated in figure 1 of Gemuts *et al.* (1992). Although there is an apparent lack of significant Au and Cu deposits between the well-demarcated northern and southern boundaries (*e.g.*, over approximately 1° of latitude between the currently-defined limits of the Maricunga and El Indio belts), it is suggested that ongoing exploration in the *cordillera* will continue to extend the borders of the Maricunga belt southward (*e.g.*, the Caserones prospect: Davidson and Mpodozis, 1991; the Nemesis prospect: J. Piekenbrock, pers. comm., 1994),

and the El Indio belt may persist to the north (*e.g.*, the El Encierro exploration property: Barrick Gold, 1994). The eastward extension of the sub-province into Argentina is poorly constrained south of the Farallón Negro district due in part to the underexploration of that country, but it is argued that the limits of the sub-province would embrace the Nevados del Famatina Cu-Au district in La Rioja province. Increased exploration may uncover new deposits which will provide closer constraints on the locations of the eastern and southern boundaries in Argentina.

The definition of this Cu-Au sub-province posits the metallogenetic question of why this area is enriched, particularly in Au, relative to other transects of the Central Andes. In several papers, Clark (*e.g.*, 1993, 1995) stresses the difficulty of separating ore-genetic from metallogenetic observations and arguments. However, the presence of a great number of "giant" porphyry copper deposits in the Andes, with no apparent systematic anatomical differences between giant and smaller deposits, implies an inherent metallogenetic, rather than ore-genetic control. Clark (*opera cit.*) concluded that these porphyries not only had access to considerably greater volumes of metalliferous hydrothermal fluids than porphyries in other environments (*e.g.*, North America) but that the fluids were more Cu-rich. It could thus be argued that Au follows Cu, that this transect represents a fundamental enrichment in Au, and therefore that any ore-forming process operating in this region will generate deposits that will be inherently enriched in Au unless depositional environments are unsatisfactory.

## **Mineral Deposits of the Farallón Negro Volcanic Complex**

The 700 km<sup>2</sup> region encompassing the Farallón Negro Volcanic Complex and associated outlying intrusive centres represents the locus of the greatest metal endowment currently recognized in Argentina (Fig. 3-3). It is host to two world-class deposits (Bajo de la Alumbraera and Agua Rica), two producing mines (Capillitas and Farallón Negro - Alto de la Blenda), five additional porphyry Cu-Au prospects (Bajo de Agua Tapada, Bajo el Durazno, Bajo de San Lucas, Bajo las Juntas and Bajo las Pampitas) and an epithermal Au-Ag prospect (Cerro Atajo).

The most important deposits in the region, Bajo de la Alumbraera and Agua Rica, and the producing vein systems are described in this chapter. Descriptions of the other prospects mentioned above are provided in Appendix A; in addition, several minor intrusive and/or alteration centres that have been proposed in the literature as exploration targets but which exhibit little or no alteration-mineralization, are documented for the sake of completeness. The salient characteristics of the legitimate prospects are summarized, followed by the development of a model for the porphyry Cu-Au deposits of the district. New laser microprobe <sup>40</sup>Ar/<sup>39</sup>Ar ages determined during this investigation are recorded in the deposit descriptions. A detailed treatment of the laser microprobe <sup>40</sup>Ar/<sup>39</sup>Ar dating method and the age relationships of the igneous and alteration-mineralization history of the Farallón Negro Volcanic Complex is provided in Chapter 5.



### ***Bajo de la Alumbraera***

#### **Location and Access**

The Bajo de la Alumbraera deposit is centrally located within the Farallón Negro Volcanic Complex (Fig. 3-3). It may be reached by two gravel roads: a south branch off the main Farallón Negro - Nacimientos access road traverses the Alumbraera plant facilities before entering the deposit from the north, while an 8 km road from the Farallón Negro town-site leads to the SW corner of the deposit. The deposit underlies a broad, bowl-shaped depression (Fig. 3-4), approximately 1.9 km and 1.2 km in NE-SW and NW-SE dimensions respectively. The floor of the depression is at approximately 2,600 m a.s.l. and the surrounding ridges attain elevations of 2,800 to 2,900 m a.s.l. Such depressions are locally known as "*bajos*", and similar topographic features occur at several other porphyry prospects in the district.

#### **Previous Research - Discovery History**

A detailed chronicle of the discovery and history of ownership of the Bajo de la Alumbraera deposit is provided by Guilbert (1995). The deposit was discovered in 1949 during regional reconnaissance mapping by G. Cecione. Geochemical sampling in 1963 and 1968 by A.M. Mazetti and R. Sisters defined Bajo de la Alumbraera as a disseminated porphyry Cu prospect and resulted in the completion of four shallow drill-holes. J.C. Caelles and A.H. Clark in 1969 identified the association of hydrothermal biotite and magnetite at the core of the deposit (unpubl. data). The prospect was visited by R. Sillitoe in 1973 for the United Nations Development Program Plan NorOeste Argentina (UNDP

**Figure 3-3.**

Location map of deposits and prospects hosted in and associated with the Farallón Negro Volcanic Complex. Locations of the mineralized centres are plotted on an overlay on a 7,4,1 TM image (path 231, row 79, August 26, 1986) of the region.

TM Bands 14,7

Cerro Atajo

Path 231 Row 79  
25 Aug 86

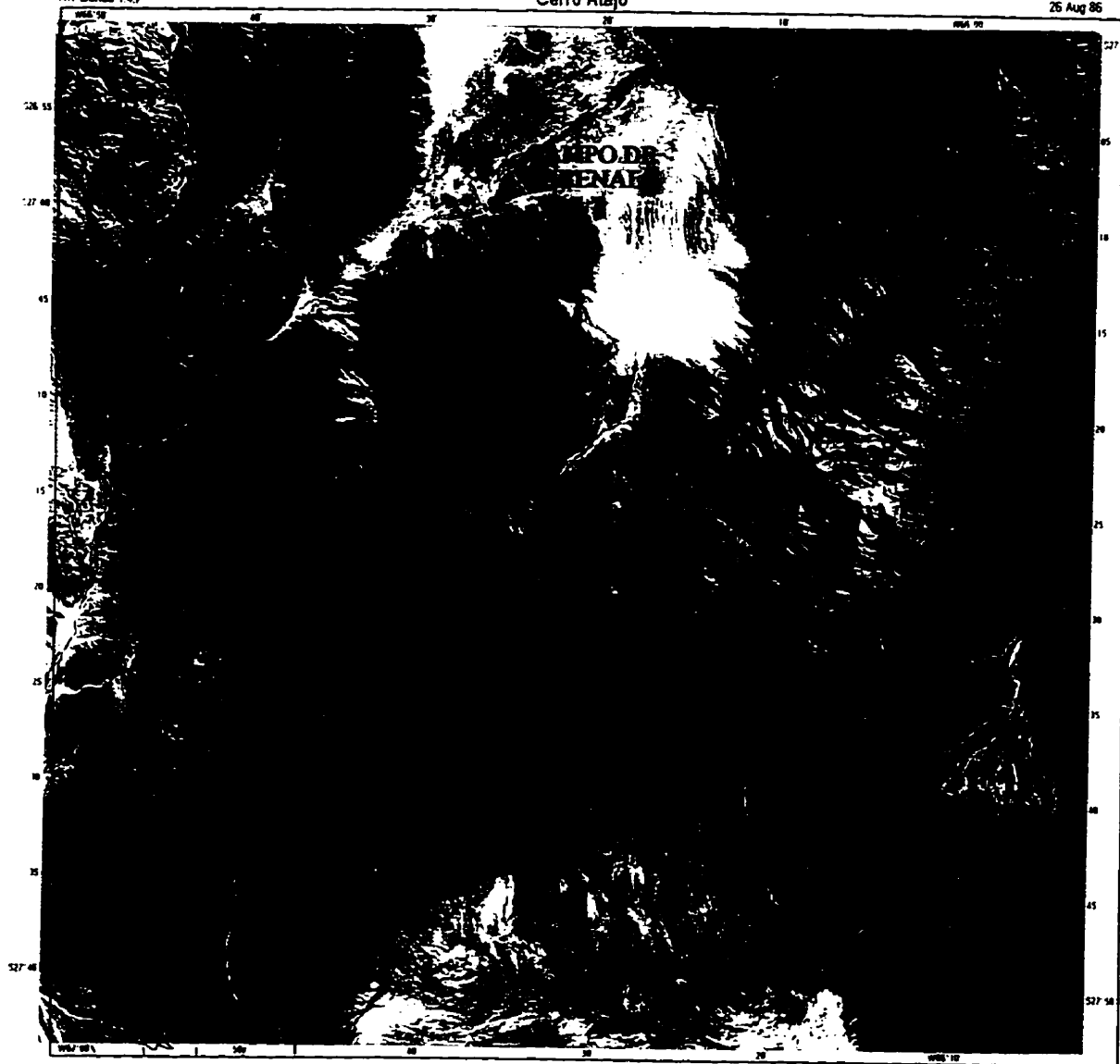


Image generated using spacecraft ephemeris  
Scene Center Latitude 27° 22'  
Scene Center Longitude 86° 20'

GEOPIC Copyright EarthSat 1982



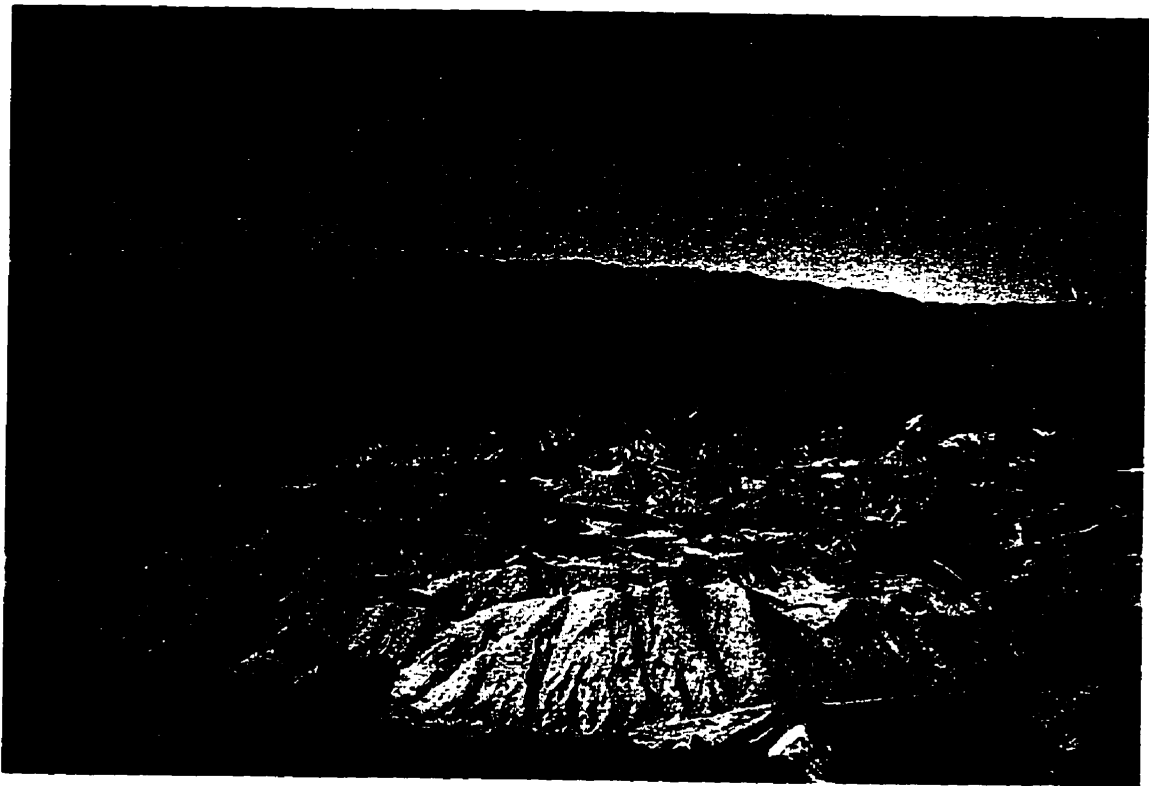
Earth Satellites Corporation  
6811 Executive Blvd., Suite 400  
Rockville MD 20852

**Figure 3-4.**

*Bajo de la Alumbreira*

**A.** View to the north of the *bajo* illustrating its bowl-shaped morphology. The two conical dark hills in the centre of the *bajo* (centre of field) are underlain by quartz - magnetite and potassic alteration zones (see figure 3-6). They are surrounded by the more subdued (pale-coloured) topography of the phyllic alteration zone. Propylitic alteration extends into the hills rimming the *bajo*. *Arroyo Alumbreira* is located in the incised valley on the far northern edge of the *bajo*. Photo taken in 1993 from one of the high ridges located between Bajo de la Alumbreira and Bajo el Espanto.

**B.** View to the east from the hills of the WSW rim. The two brown, conical hills, left of centre, middle-ground, are Cerro Colorado Norte (on the left) and Cerro Colorado Sur (to the right). They are broadly underlain by quartz-magnetite and potassic alteration zones, and represent the high grade core of the deposit which will be mined early in the production history. The arcuate ridge of bleached hills in the foreground is underlain by the Los Amarillos porphyry stock (see figure 5). Photo taken in 1993.



Plan NOA I). Sillitoe (1973) was the first to document the importance of the potassic alteration assemblage at Bajo de la Alumbrera and produced the first detailed geological and alteration maps of the prospect. Further geological mapping was conducted by O. E. González in 1975 and by Bassi and Rochefort in 1980. The first comprehensive, readily available, study of the deposit is that of Stults (1985). His maps, lithological descriptions, fluid inclusion microthermometry, quantitative alteration plots and geological observations constitute the basis for an understanding of the nature of mineralization. The results of this investigation, along with those of ongoing research under the supervision of J.M. Guilbert at the University of Arizona, form the basis of the latter's 1995 publication.

In January, 1992, International Musto Exploration Ltd., a Canadian junior company, negotiated an acquisition agreement with Yacimientos Mineros de Agua de Dionisio (Y.M.A.D., a state agency with participation by the Province of Catamarca, the National University of Tucumán and the National Government). Geologists employed by International Musto remapped the deposit (Indri and Carrizo, 1992) and proposed a classification of the hypabyssal units (Plaza, 1993) which has confused all subsequent workers (see below). In February, 1994, a 50 - 50 joint venture agreement between International Musto and Mount Isa Mines Holdings Ltd. (M.I.M.) was negotiated to develop the deposit. Minera Alumbrera Ltd. was created to oversee the operation of the joint venture. J.M. Proffett (unpublished reports) has completed the most detailed field study of the basic geological and alteration-mineralization relationships at Bajo de la Alumbrera. Detailed mapping at 1:2,000 scale during 1994 and 1995 generated a well constrained, logical nomenclature for geological units and a field-based chronology of the

intrusive units and alteration-mineralization facies, and also clarified the role of faulting in the evolution of the deposit. The results of this work are presented in two private reports to Minera Alumbrera Ltd. (Proffett, 1994, 1995). In mid-1995, International Musto Exploration Ltd. sold its 50% interest in Bajo de la Alumbrera to Rio Algom and North Ltd.

Susan Dawson Cook is completing a University of Arizona M.S. thesis on the mineralogy and distribution of gold in the ores and Thomas Ullrich, under the supervision of Christoph Heinrich, is completing a detailed study of the alteration mineralogy and chemistry at U.T.H. Zürich. I am aware of no published results from these studies.

### Geological Relationships

The broad geological relationships at Bajo de la Alumbrera are relatively uncomplicated. Alteration-mineralization was intimately associated with the intrusion of hypabyssal bodies of porphyritic dacite into the volcanic strata of the Farallón Negro Volcanic Complex. The general characteristics of the volcanic rocks have been discussed previously (Chapter 2). A comprehensive discussion of the nature of the extrusive units in the immediate vicinity of the Bajo de la Alumbrera deposit is provided by Stults (1985), while Proffett (1994, 1995) has mapped a 500 m section in the hills north and northeast of the deposit. This section incorporates the oldest-dated unit at Farallón Negro, a 12.6 Ma hornblende-phyric basaltic-andesite from the Arroyo Alumbrera Andesite (Lower Andesite Unit of Proffett, *opera cit.*).

## Nomenclature of Porphyries

The nomenclature employed to describe the intrusive units at Bajo de la Alumbrera has evolved during the course of this study. Bassi and Rochefort (1980) identified multiple stages of dacitic intrusion but did not map separate units. Stults (1985), Plaza (1993) and Proffett (1994, 1995) all recognized multiple phases of porphyritic dacite and developed systems for their classification. The terminologies presented by Stults (1985) and Proffett (1994,1995) are logically based on the abundance and composition of phenocrysts and are quite similar, with the more detailed mapping of Proffett identifying subtle differences in the units recognized by Stults. Their schemes are presented in Table 3-2.

Plaza (1993) recognized four dacite porphyry units which he termed "P1" through "P4", from oldest to youngest. However, this classification appears to have been based more on alteration assemblage rather than on igneous composition. Thus, much of his "P1" (pre-mineralization porphyry) reflects strong sericitic alteration, and volcanic units are also included. "P2" and "P3" appear to be distinguished largely on the basis of magnetite content: porphyry with abundant magnetite alteration and with K-feldspar and quartz veining was generally mapped as "P2", and that with little or no magnetite alteration as "P3". Post-mineralization porphyry dykes were mapped as "P4" and represent the only rock-type recognized in the Stults and Proffett nomenclatures. Because of the confusion generated by this classification scheme, no attempt is made to reconcile it with those of Stults or Proffett, and it is strongly suggested that its use be terminated.



**Table 3-2.**

Subdivision of intrusive bodies at Bajo de la Alumbrera  
(after Stults, (1985) and Proffett, (1995)).

<b>PROFFETT (1995)</b>	<b>STULTS (1985)</b>
Post-Mineral Porphyries	Late Dacite Porphyry Dykes
Northwest Porphyry Dykes and Late Porphyries	Main-Stage Dacite Porphyry
North Porphyry	
Main Dacite Porphyry Stock Campamiento Porphyry Quartz-Eye Porphyry Early P3 Porphyry Colorado Norte Porphyry	
Northeast Porphyry Dyke	
Los Amarillos Porphyry Stock	Pre-Main Stage Dacite Porphyry

## Intrusive Units

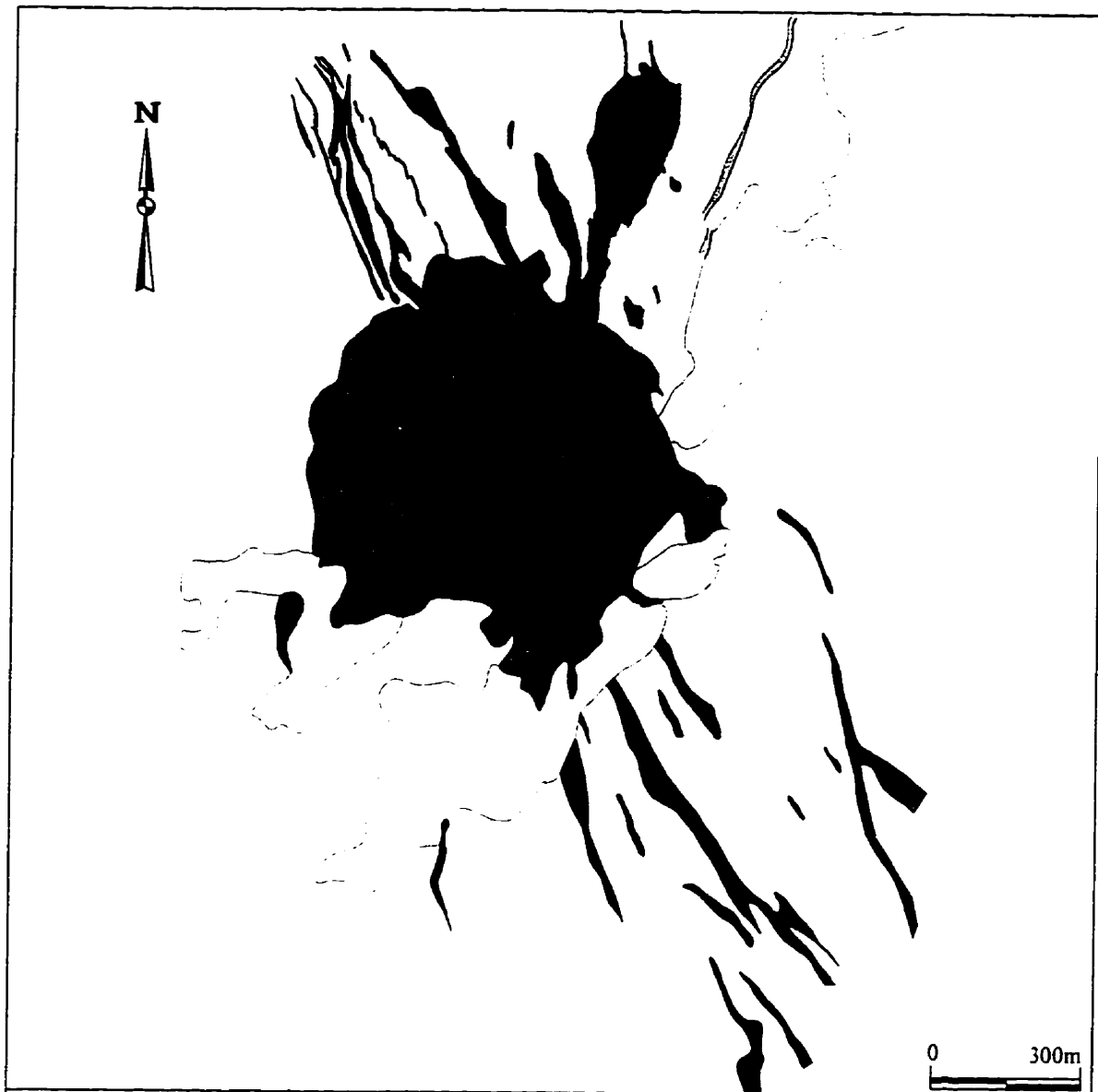
Figure 3-5 presents Stults' (1985) geological map of Bajo de la Alumbrera, reinterpreted using the updated nomenclature of Proffett (1995).

The Los Amarillos Porphyry stock underlies the bleached arcuate ridge located in the northwest and west quadrants of the *bajo* (Fig. 3-4, foreground). Phyllic alteration associated with the Main Dacite Porphyry Stock destroyed the primary mineralogy and texture of this fine-grained unit, which exhibits relict quartz phenocrysts in a quartz-sericite-chlorite groundmass. Primary feldspar and biotite phenocryst outlines are rarely observed in thin-section (Stults, 1985).

The Main Dacite Porphyry Stock underlies the central area of the *bajo* in the vicinity of Cerros Colorado Norte and Colorado Sur, and to the west and southwest of those hills (Figs. 3-4 and 3-5). It is a stock-like mass that is mineralized with weak to intense potassic alteration, quartz veinlets, and copper mineralization. It was further subdivided by Proffett (1995) into four units (Table 3-2), viz. Colorado Norte Porphyry, Early P3 Porphyry, Quartz-Eye Porphyry and Campamiento Porphyry, on the basis of cross-cutting relationships recorded primarily by truncation of alteration veinlets at contacts. Proffett (*op. cit.*) concluded that the truncation of alteration facies by later intrusive pulses which are themselves altered suggests that concomitant alteration-mineralization and intrusion occurred throughout the emplacement of the Main Dacite Porphyry. The writer's  $^{40}\text{Ar} - ^{39}\text{Ar}$  geochronological studies (Chapter 5) define the age of this intrusive unit as  $6.83 \pm 0.07$  to  $7.1 \pm 0.13$  Ma. It is medium-grey in hand-sample, with abundant plagioclase, quartz and biotite phenocrysts in a fine-grained-to-aphanitic

**Figure 3-5.**

Geological map of Bajo de la Alumbrera. Unit contacts from Stults (1985) are reinterpreted using the updated nomenclature of Proffett (1995).




## BAJO DE LA ALUMBRERA

### Geology


Reinterpretation of Stults (1983, 1985)  
geology map using terminology of  
J.M. Proffett (1994, 1995)


A.M. Sasso, 1997

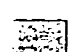
 Post-mineral  
porphyries


 Late porphyries


 Northwest porphyry  
dykes

 North porphyry

 Main dacite  
porphyry stock

 Northeast  
porphyry

 Los Amarillos  
porphyry stock

 Alluvium

matrix. Hornblende and apatite phenocrysts with minor titanite and magnetite are evident in thin-section (Stults, 1985; this study).

Stults (*op. cit.*) recognized a series of dacite porphyry dykes which extend to the N, NW and SE from the central intrusive body. Although he included them in his Main-Stage Dacite Porphyry unit, he suggested that emplacement occurred in three broadly continuous pulses over an extended period. The North Porphyry (Table 3-2) consists of a large dyke-like body with a N-to-NNE strike that crops out in the northern part of the *bajo*. It is composed of phenocrysts of plagioclase, euhedral biotite, biotitized hornblende and minor quartz in an aphanitic groundmass (Proffett, 1995). The Northwest Porphyry Dykes and Late Porphyries (Table 3-2) comprise a swarm of dacite dykes in the NW part of the *bajo*, extending from the core and continuing out of the deposit to the NW, and a series of small stocks and dykes which intrude the Main Dacite Porphyry. The dominant phenocryst phase is plagioclase, occurring with lesser biotite, hornblende and quartz in an aphanitic, pale-green matrix (Proffett, *op. cit.*). A dacite dyke on the NW rim of the *bajo*, interpreted to be of this type, yielded herein an age of  $6.78 \pm 0.15$  Ma.

The Post-Mineral Porphyries consist of discontinuous dykes which represent the youngest intrusive rocks at Bajo de la Alumbrera (Proffett, 1995). Plagioclase phenocrysts are associated with lesser biotite books, hornblende laths and prominent quartz eyes in a very fine-grained grey matrix.

#### Alteration-Mineralization

The alteration facies observed at Bajo de la Alumbrera consist of strong-to-weak

potassic alteration and peripheral epidote-chlorite (propylitic) assemblages, both overprinted by phyllic alteration (Fig. 3-6), and conforming unusually faithfully to the model porphyry copper geometry postulated by Lowell and Guilbert (1970).

Stults (1985), following earlier workers (Sillitoe, 1973; González, 1975; Bassi and Rochefort, 1980), delimited potassic (orthoclase and biotite), phyllic and propylitic zones, and emphasizes the unusual intensity of quartz veining ("flooding") at the core of the potassic alteration zone and magnetite-rich alteration (as significant groundmass replacement, veinlets and quartz-magnetite veinlets). Proffett (1995) confirmed the mineralogy and broad distribution of alteration assemblages presented by Stults (1985). He further reemphasized the strong association of Cu-Au mineralization with the potassic alteration event. Both authors propose the essential contemporaneity of potassic alteration and Main Dacite Porphyry Stock emplacement. Thus, Cu-Au mineralization is spatially and temporally associated with potassic alteration (Fig. 3-7), defined by secondary biotite - K-feldspar - magnetite - quartz  $\pm$  anhydrite - bearing assemblages, forming in "A"- and "B"-style veins (*cf.*, Gustafson and Hunt, 1975; see below) and as replacements. Potassic alteration is biotite-rich in andesites and K-feldspar - dominated in dacitic porphyries. Epidote - chlorite - albite  $\pm$  magnetite (propylitic) alteration is inferred to be similar in age to potassic alteration and forms a halo around the latter. Sericite - pyrite - quartz (feldspar- destructive), *i.e.*, phyllic, alteration dated herein at  $6.75 \pm 0.09$  Ma, overprinted both potassic and propylitic zones and forms a wide halo.

Hypogene mineralization comprises chalcopyrite + pyrite  $\pm$  magnetite veins with relatively high chalcopyrite - pyrite ratios. Veins at Alumbrera have been classified

**Figure 3-6.**

Map of alteration facies at Bajo de la Alumbrera (after  
Stults, 1985).



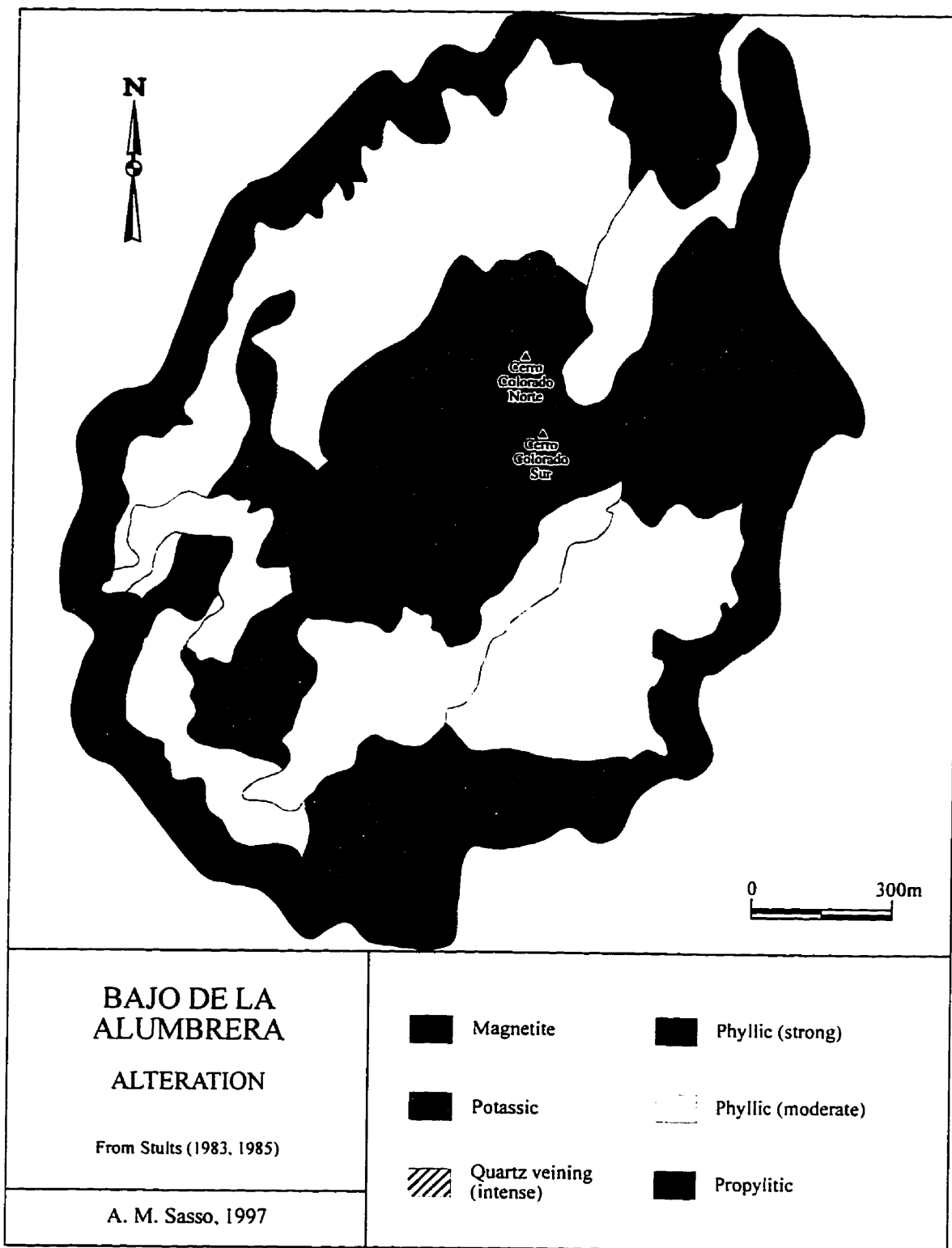
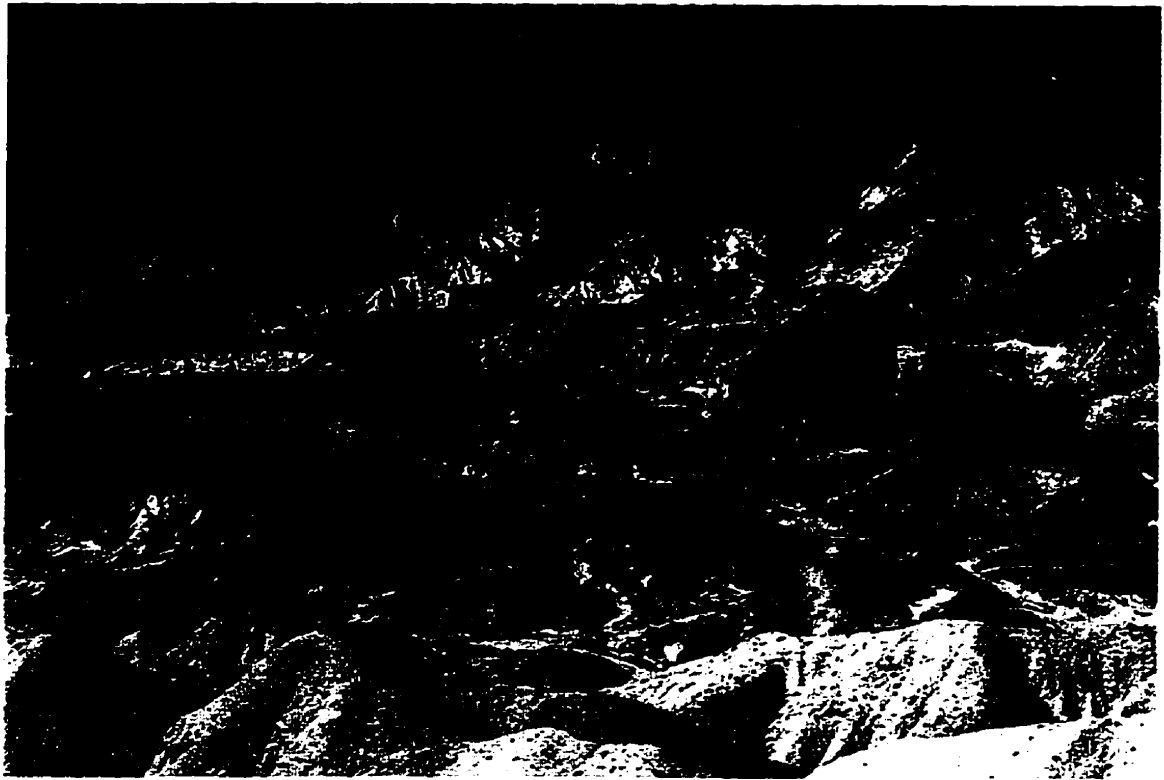


**Figure 3-7.**

*Potassic alteration zone at Bajo de la Alumbrera*

**A.** Detail of photo presented as figure 3-4B. View to the east. Cerro Colorado Norte (left), Cerro Colorado Sur (right) and the low brown hills are underlain by quartz-magnetite and potassic alteration, and high-grade Cu-Au mineralization. The change in colour of the outcrops from brown to buff is broadly coincident with the interface between the quartz-magnetite-potassic and the phyllic assemblages. Photo taken in 1993.

**B.** North face of Cerro Colorado Norte. Note the intensity of fracturing and abundance of green Cu-oxide and black Mn-oxide staining along fracture surfaces. This photo is of the scarp visible at the summit of Cerro Colorado Norte on the above photograph. Photo taken in 1993.



according to the A-B-D-vein system proposed by Gustafson and Hunt (1975) for mineralization at El Salvador, Chile. "M" veins (after Clark and Arancibia, 1995; and discussed in greater detail below), *i.e.*, early magnetite  $\pm$  quartz veins associated with groundmass replacement by magnetite (Fig. 3-8), are also recognized. Some chalcopyrite and Au deposition overlapped with this event, but mainly postdated it (V.J. Wall, written comm., 1996). Nonetheless, the highest Cu-Au grades typically occur in zones of high quartz - magnetite vein-density (M. Carrizo, pers. comm., 1994). Mineralization occurs as disseminated chalcopyrite associated with fine granular quartz and K-feldspar "A" veins which are irregular and discontinuous. Veins mapped as "B"-type at Alumbrera do not resemble the typical "B" veins as documented at El Salvador by Gustafson and Hunt (1975), which are rectilinear and characterized by the lack of alteration halos and the occurrence of coarse molybdenite and chalcopyrite in bands parallel to vein-walls and in centre-lines. Proffett (1995) refers to the presence of "B" veins but does not describe their mineralogy. Musto geologists appear to have defined "B" veins solely on the presence of sulphides along a centre-line (M. Carrizo, pers. comm., 1994), and this designation has been maintained in subsequent studies. In this study, Alumbrera "B" veins are defined as rectilinear quartz veins, lacking alteration haloes, with pyrite and rare chalcopyrite along centre-lines (Fig. 3-9). Included in this class are massive chalcopyrite veins which also lack alteration halos (Fig. 3-10). Barren, massive pyrite, "D" veins (Fig. 3-11), directly associated with phyllic alteration, exhibit radial patterns about the Main Dacite Porphyry.

Gold is intergrown with magnetite, chalcopyrite and pyrite, and also occurs free in silicates. Molybdenite is rarely observed except in a peripheral zone coinciding with

**Figure 3-8.**

*Early quartz - magnetite alteration  
at Bajo de la Alumbrera*

A. Wide quartz-magnetite vein, in the left-hand area of the sample, truncates earlier magnetite-only veinlets. The host is Main Dacite Porphyry which has undergone strong groundmass replacement by hydrothermal magnetite. Small quartz-pyrite hairline veinlets cross-cut the above veins. Chalcopyrite is disseminated in the sample, but its paragenetic relationships are unclear. Core from DDH 48.4 - 54 (note: these numbers refer to Musto grid coordinates used in the diamond drill program at Alumbrera. This coordinate system has been maintained by Minera Alumbrera.)

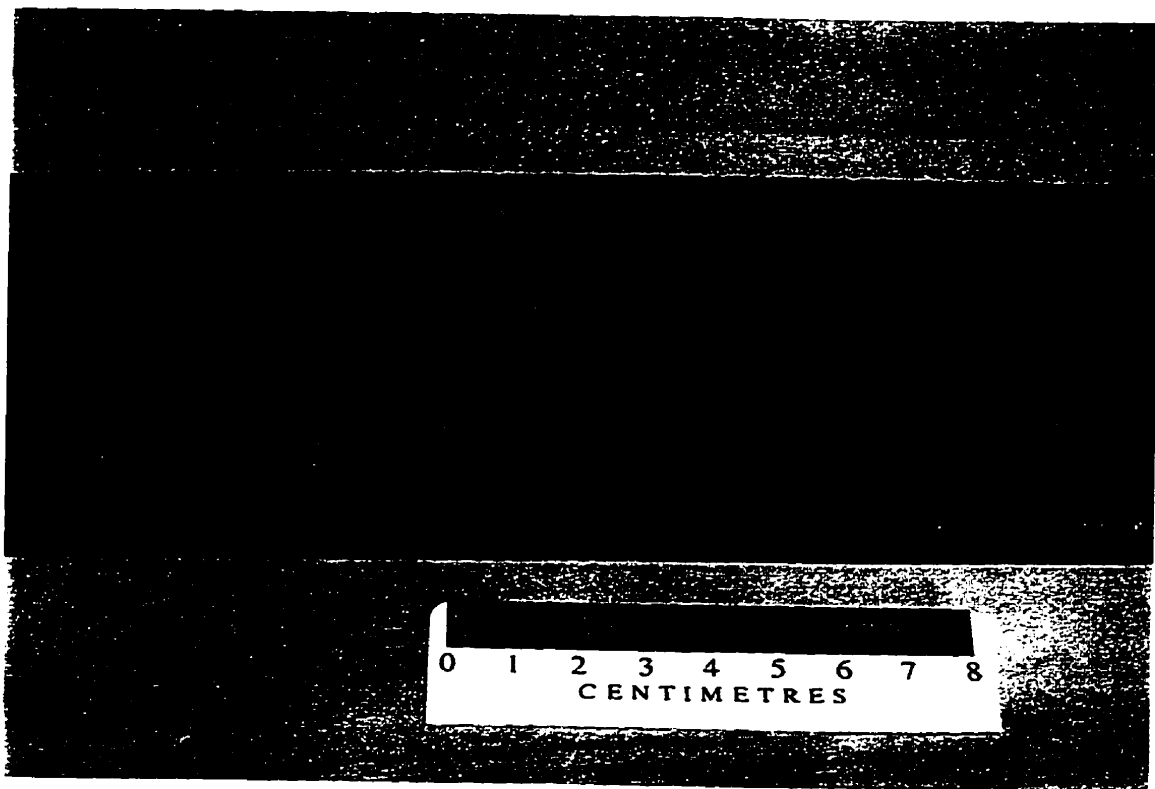


**Figure 3-9.**

*"B" Vein Characteristics  
at Bajo de la Alumbrera*

**A** A 1 cm-wide (vertical) "B" vein transects the sample. "B" veins at Bajo de la Alumbrera are characterized by the absence of alteration haloes and by sulphide development along a centre-line. A narrower "B" vein is oriented at 2 o'clock in the upper half of the sample. The host-rock is the Main Dacite Porphyry with large, white plagioclase phenocrysts. The dark colour of the matrix is a result of strong replacement by hydrothermal magnetite. A magnetite veinlet is located in the upper-right corner of the sample. Core from DDH 48.4 - 54.

**B.** Mutually cross-cutting "B" quartz veins with pyrite-chalcopyrite centre-lines and lacking alteration haloes are cut and displaced by thin pyrite "D" veinlets. The host-rock is biotitized andesite. Core from 191 m in DDH 48.4 - 54.

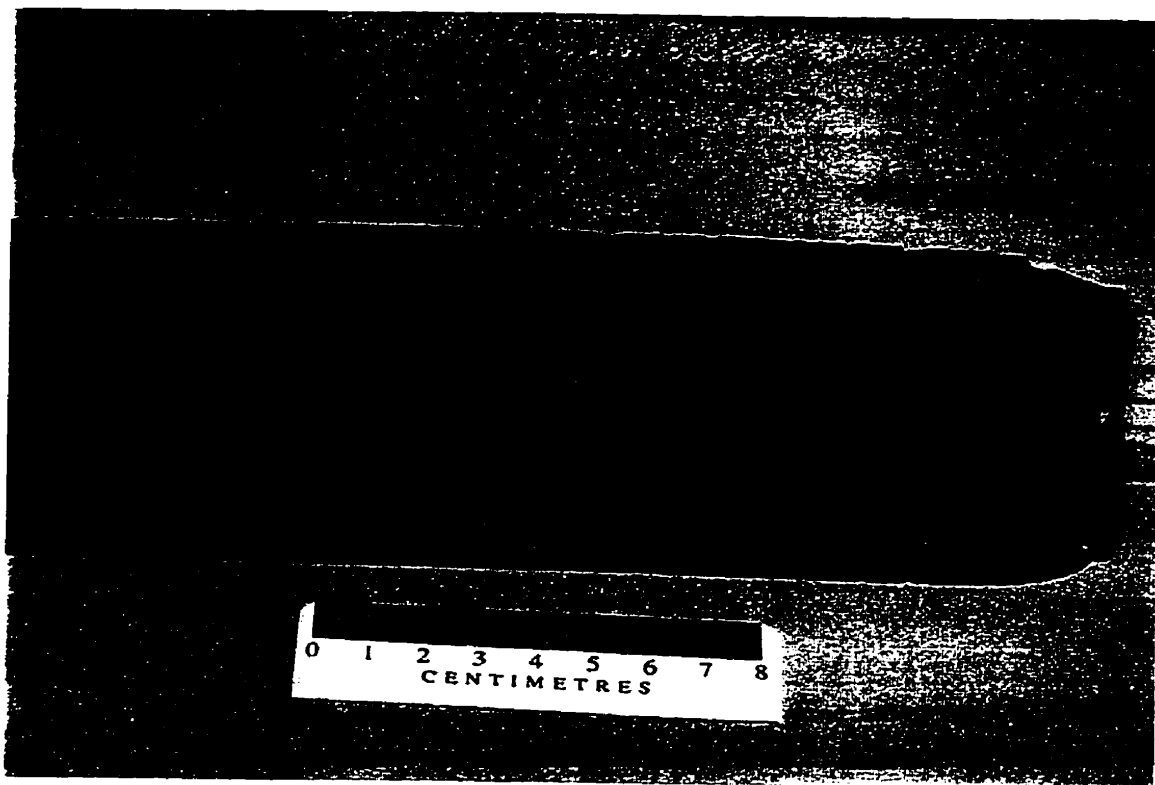
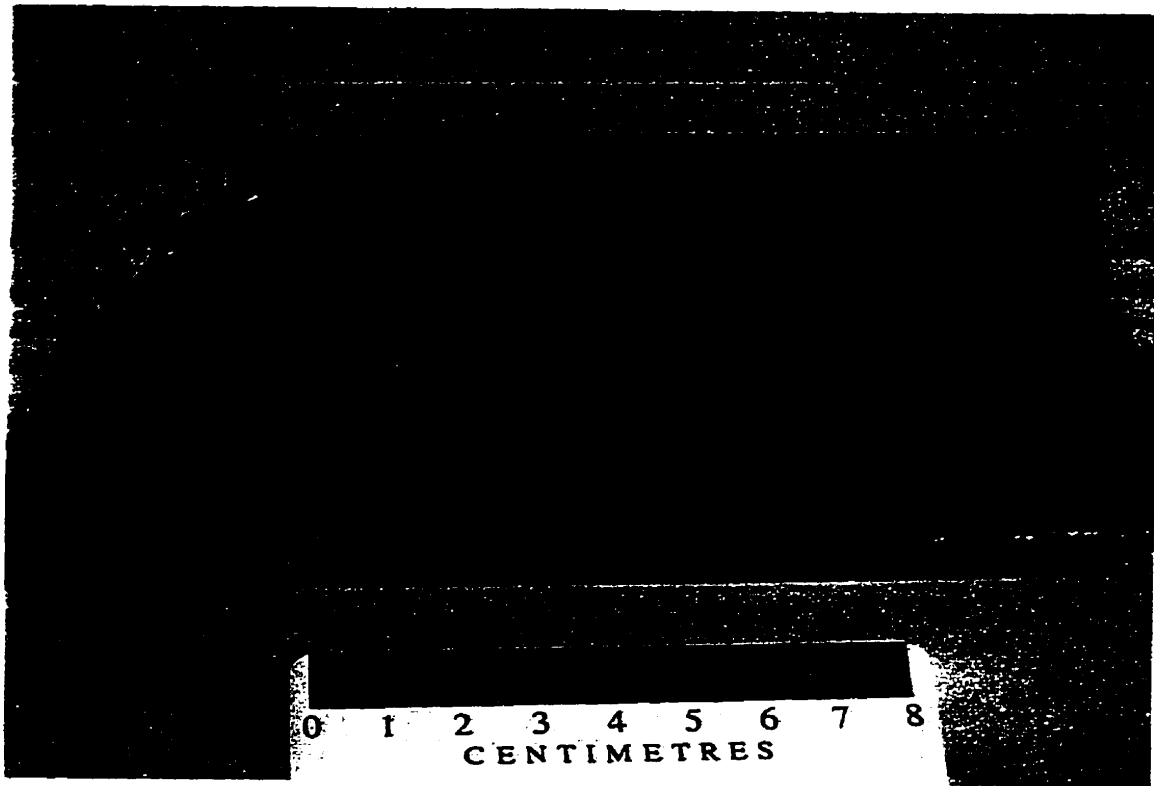




**Figure 3-10.**

*"B" Vein Characteristics  
at Bajo de la Alumbrera*

Massive chalcopyrite veins, such as that illustrated, are also included in the suite of "B"-type veins at Bajo de la Alumbrera. The host is Main Dacite Porphyry which has undergone weak-to-moderate groundmass replacement by hydrothermal magnetite.. This intersect returned grades of 0,95 % Cu and 1600 ppb Au. Core from 205.3 m in DDH 48.4 - 54.

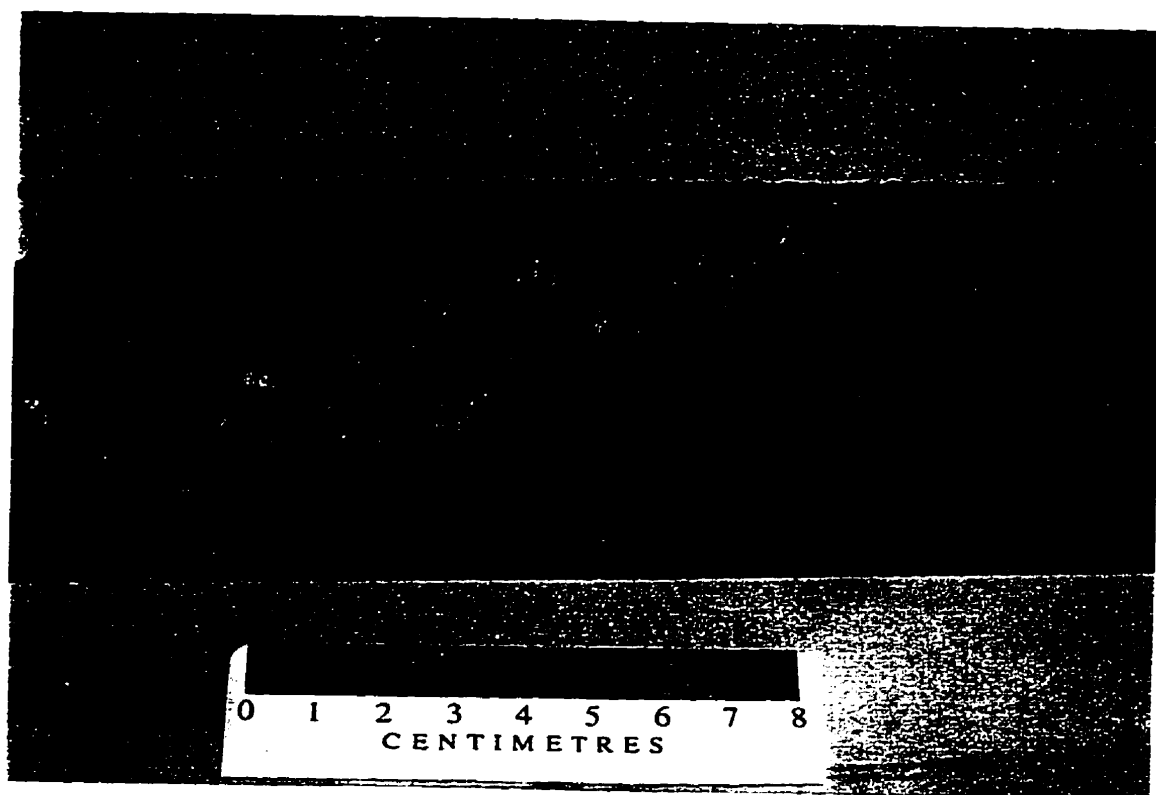
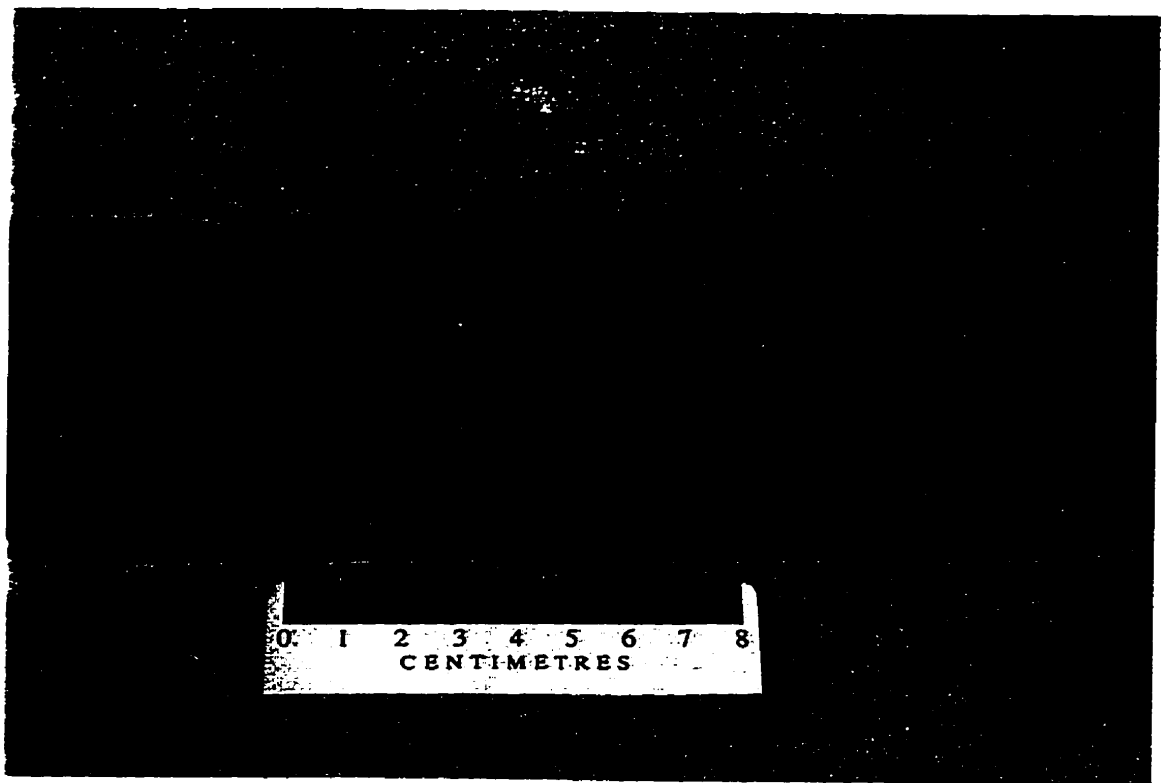
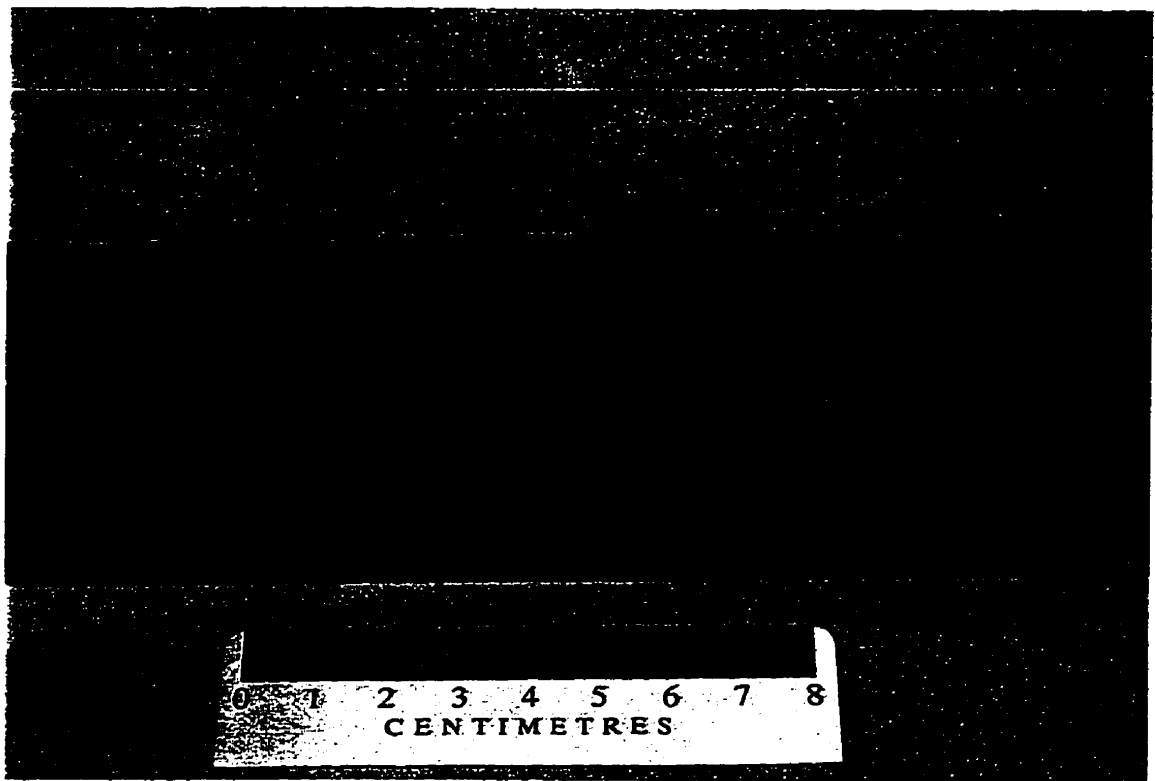


**Figure 3-11.**

*Late "D" Veins  
at Bajo de la Alumbraera*

**A.** Thin "D" vein of pyrite with 1 cm wide alteration halo consisting largely of sericite with minor chlorite (green patches). Two narrower, sub-parallel "D" veins with irregular alteration halos are located at the lower-right. All of these veins are cut by gypsum veins (*e.g.*, centre of field). The host is strongly biotitized andesite and contains disseminated pyrite. Core from 256.5 m depth in DDH 47 - 63.

**B.** Large, 1 cm-wide, "D" vein of pyrite with associated phyllic (quartz-sericite-pyrite) alteration halo. The vein truncates a 1 cm-wide "B" vein with a pyrite centre-line in the right portion of the sample. The "D" vein structure was re-used by a subsequent gypsum vein (milky white material along the upper edge of the vein). Irregular gypsum veins are evident in the bottom portion of the sample. The host unit is biotitized andesite and contains disseminated pyrite. Core from 158.8 m depth in DDH 47 - 63.



the outer edge of the copper-gold zone (Proffett, 1995). Late, epithermal-style, quartz - calcite - Mn-oxide - Au veins are encountered along the southern edge of the phyllic zone (Stults, 1985). Overall, mineralization has a shell-like distribution, enveloping a low-grade core which comprises potassically-altered porphyries with quartz - magnetite and "A" veins and late, weakly-altered porphyries (M. Carrizo, pers. comm., 1994; Proffett, 1995; V.J. Wall, written comm., 1996).

A preliminary study of fluid inclusions (Stults, 1985) reveals the involvement of at least two fluids of differing provenance. The earlier fluid, interpreted to be of magmatic origin, ranged in temperature from 300° to 700° C and contained from 40 to 62.5 weight percent NaCl equivalent, whereas the later ranged from 175° to 400° C and from 1 to 14.5 wt. % NaCl equivalent, and presumably incorporated considerable meteoric water.

## Structure

Late, steeply- to moderately-dipping normal faults displace the dacite porphyry units and early alteration by a maximum of 200 m and are accompanied by sericitic or argillic alteration. A series of NW to NNW-striking faults in the northern quadrant of the *bajo* exhibit west-side-down normal movement, whereas several faults of similar trend in the southwest part of the *bajo* experienced east-side down normal movement (Proffett, 1994, 1995). Faulting appears to have been broadly contemporaneous with the waning stages of feldspar-destructive alteration. No evidence of significant pre-intrusive or pre-alteration-mineralization faulting has been observed (Proffett, 1995).

## ***Agua Rica***

### **Location and Access**

The Agua Rica deposit is located at an average altitude of 3,300 m a.s.l. in the Sierra de Aconquija, approximately 35 km east of Bajo de la Alumbrera (Fig. 3-3). The Agua Rica access road branches from Ruta Nacional No. 63 approximately 1.5 km north of the Capillitas deposit and climbs to the east over the crest of the Aconquija Range. The deposit has also been known by the names Mi Vida and Cerro Rico.

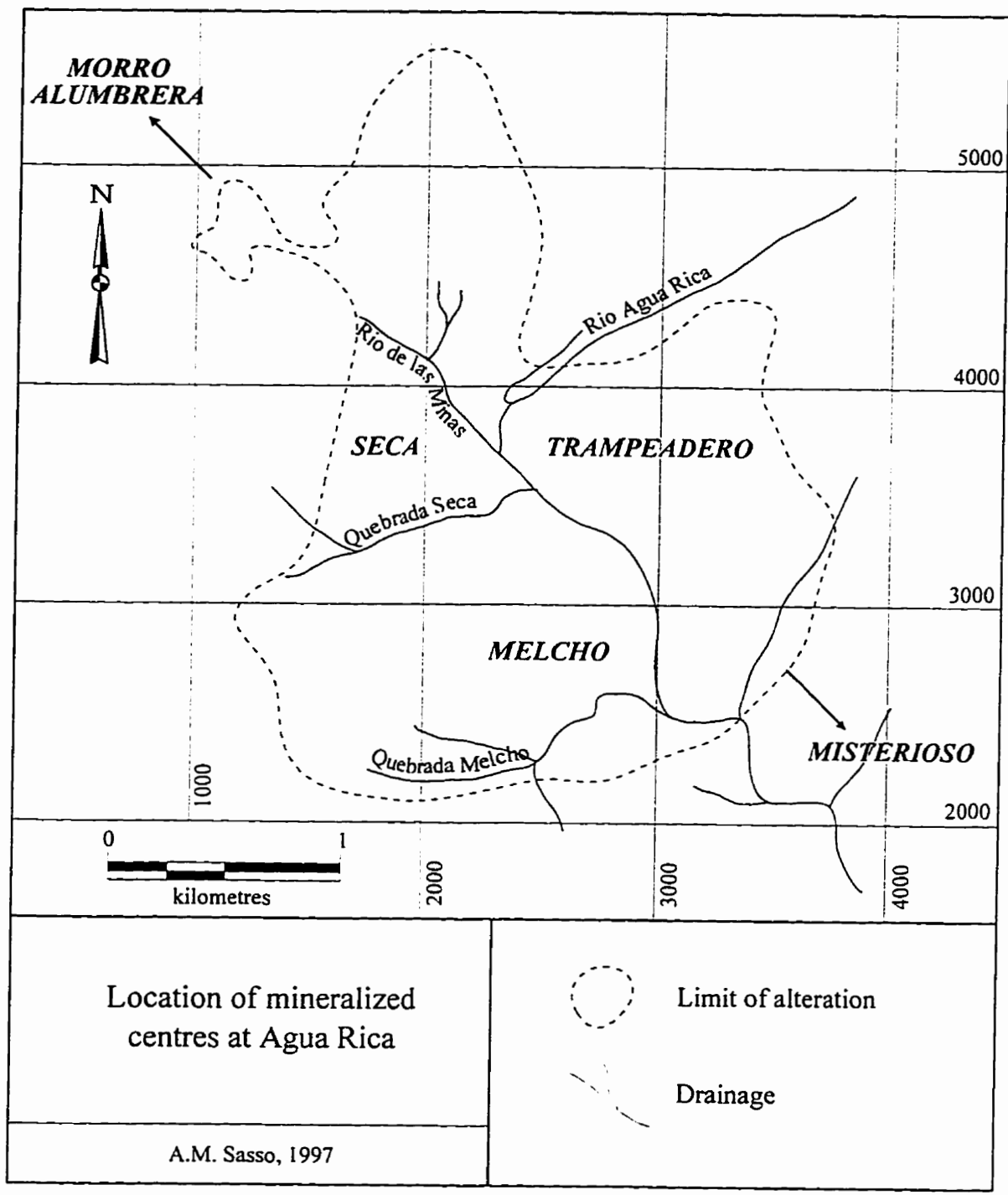
### **Previous Work - Discovery History**

Copper-stained outcrops were discovered in 1966 in Quebrada Agua Rica, immediately upstream from the present B.H.P. Agua Rica camp, and the property was staked by Sr. Hernán Navarro. The area was visited in 1969 by A.H. Clark and J.C. Caelles who observed abundant chalcopyrite veinlets and potassic (secondary biotite) alteration in a monzodioritic intrusion in the upper Quebrada Melcho (Fig. 3-12).

The property was optioned by Compañía Minera Cities Service Argentina S.A. in 1969. They conducted a two-year exploration program which included geological mapping, geochemical sampling, opening of a 162 m adit, and a diamond-drill program involving 32 surface and 6 underground holes totalling approximately 8,000 m. Core recoveries were generally poor and copper intercepts variable. A resource was delimited of 161 million tonnes with an average grade of 1.3 % Cu (Rosin, 1993), but this was located beneath a steep-sided valley and apparently overlain by barren country rocks, and the property was therefore abandoned in 1972. Koukharsky and Mirré (1976) document

**Figure 3-12.**

Location of mineralized centres and important drainages  
at the Agua Rica deposit.





the geological relationships of the deposit as exposed during this exploration program.

In 1992, American Resource Corp., through its subsidiary Recursos Americanos Argentinos S.A., negotiated an option on the Agua Rica property. They began improving access to the property in anticipation of a new drill program. Nivaldo Rojas (B.H.P. Minerals Exploration Manager for Argentina) and I visited the property in August 1993 and collected samples for lithogeochemical analysis. In early 1994, Recursos Americanos granted B.H.P. Minerals the right to earn a 70 % joint venture interest in the project. Exploration drilling began in mid-1994 to confirm resource estimates. In June, 1995, Northern Orion Explorations Ltd. acquired 100 % of Recursos Americanos and thereby gained a 30 % interest in the Agua Rica deposit. As of January 1997, a total of 40,000 m of diamond drilling had been completed by B.H.P. and a further 25,000 m is planned for 1997. Drilling, road construction, extensive metallurgical testing, resource and reserve estimation, engineering, and environmental and preliminary feasibility studies are underway (Quin and Nikic, 1997). On the basis of results from the first 39 drill-holes completed by the B.H.P. - Northern Orion joint venture, Northern Orion (Quin and Nikic, 1996) released a geological resource estimate for the deposit of 1,206 million tonnes at 0.51 % Cu, 0.22 g/t Au and 0.032 % Mo. Recent press releases (Quin and Nikic, 1997) indicate average grades of up to 6.1 g/t Ag in a supergene enrichment zone. An updated reserve estimate of 802 Mt at 0.61% Cu, 0.035% Mo and 0.24 g/t Au at a Cu cutoff grade of 0.4% has been released by B.H.P. (J. Mortimer, pers. comm., July 1997).

Published information on geological relationships at Agua Rica remains sparse (e.g., Koukharsky and Mirré, 1976; Quin and Nikic, 1996, 1997). The following

description draws on personal observations made during visits in 1993, 1994 and 1996, on discussions with B.H.P. geologists Claudio Deveau, John Mortimer, Nivaldo Rojas and Pablo Marcet, and on a written communication (July 1997) by Martin Leake.

### Geological Relationships

The Agua Rica deposit incorporates four alteration-mineralization zones, viz. Morro Alumbra, Seca (Mi Vida), Trampeadero and Melcho (Fig. 3-12), centred on intrusive units emplaced in Paleozoic metasedimentary and granitic rocks of the Aconquija Range (Figs. 3-13 and 3-14). No volcanic units have been encountered. The complicated intrusive history, involving several porphyry bodies and multiple stages of igneous and hydrothermal breccias, has yet to be completely discerned.

The large Melcho monzonite stock crops out in the Quebrada Melcho (Fig. 3-12) and was emplaced at  $8.56 \pm 0.48$  Ma (Chapter 5). It exhibits complex textural and compositional variations but is generally equigranular, consisting of a medium-grained intergrowth of orthoclase, biotite and hornblende, with minor magnetite, apatite and titanite. Brecciated zones are encountered along what is interpreted as the northern boundary of the stock exposed in the north branch of Quebrada Melcho. This breccia also contains clasts of andesite porphyry and has experienced variable hydrothermal alteration, sulphide veining and fracturing. A series of andesite porphyry bodies are exposed in the area. Coarse-grained biotite-plagioclase bearing porphyries crop out to the west of the mine camp. They occur at the boundary between the breccia pipe (see below) and basement units. Fresh samples were not available for dating. The porphyry commonly

**Figure 3-13.**

*Geology of the Agua Rica deposit.*

Note: "Breccia A" is the diatreme pipe and "Breccia B" represents undifferentiated hydrothermal and igneous breccias. This map is based on preliminary mapping by B.H.P. geologists in 1994.



## Agua Rica Project

### Geology

A.M. Sasso, 1997



Breccia A (Metamorphic  
rock fragments)



Breccia B (Porphyry  
fragments)



Andesite porphyry



Biotite porphyry



Metamorphic rocks



Structures

**Figure 3-14.**

*The Agua Rica Deposit*

View to the SE of the area of the Agua Rica deposit. The bleached scar in the foreground is the Morro Alumbra area, a zone of advanced argillic alteration which is thought to be underlain by porphyry-style mineralization. The main valley transecting the photo (right-of-centre) is Quebrada de las Minas (see figure 3-12). The B.H.P. camp is located on the north (left) bank of this *quebrada* (buildings are visible). The slopes scored by drill-roads behind and to the left of camp are referred to as the Trampeadero area. The slopes to the right of camp also scarred by drill-roads represent the Seca (Mi Vida) area. The mineralized area termed Quebrada de las Minas is located between the two. The Melcho area is located off the photo to the right, in the valley behind the ridge above (to the right) of Seca. Photo taken in 1996.



occurs as mineralized clasts in the breccia. Porphyry Cu-Mo-(Au) systems underlying the Seca (Mi Vida) and Trampeadero areas are interpreted by project geologists to be centred on intrusions of this type. Relatively fresh andesite porphyry, grey, medium-grained and with abundant plagioclase, biotite and hornblende phenocrysts, has been encountered during regional mapping of the high ridges to the west of the deposit, but its relationship to the andesite porphyries at Agua Rica is unclear. A late barren, dyke-like body of biotite porphyry crops out on a spur between the Agua Rica camp geology office and the dormitory facilities. It constitutes a large, isolated outcrop which cuts the mineralized hydrothermal breccia and is interpreted by project geologists to be the youngest intrusive event at Agua Rica (J. Mortimer, pers. comm., 1997; M. Leake, pers. comm., 1997).

A complex series of breccias interpreted to include diatreme, hydrothermal, tectonic and crackle facies (Quin and Nikic, 1996) is encountered in the central portion of the deposit (Fig. 3-15). Mapping of the different facies is difficult (P. Marcet, pers. comm., 1996); the degree of mineralization and alteration is highly variable, suggesting multiple brecciation events. The breccias contain clasts of all the rock units exposed in the area, but excluding the late biotite porphyry, in addition to "vuggy silica" and clasts of completely silicified rocks. The highest concentration of andesite porphyry clasts is encountered in the hydrothermal breccia pipe emplaced in the Seca - Trampeadero area. The breccias range from clast- to matrix-supported. In general, the matrix consists of rock flour but a rhyolitic matrix has been observed in core (C. Deveaux, pers. comm., 1994).

The contacts of the breccia pipes with the porphyries and basement are largely 60° to vertical. The breccia-basement contact is observed in a 162 m adit driven into the south

**Figure 3-15.**

*Field and lithological characteristics of breccias  
at Agua Rica*

**A.** View to the NW along Quebrada de las Minas, upstream from the confluence with Rio Agua Rica (to the SW of camp). Dark outcrops are of breccia with dominantly basement-derived clasts in a rock-flour matrix. The slopes to the left are the northern extension of the Seca (Mi Vida) area. Note that alteration is camouflaged by vegetation, surface weathering and the growth of lichen on outcrop. Photo taken in 1993.

**B.** Clast-supported diatreme breccia pipe. Clasts are of metasedimentary basement units in a rock-flour matrix. Photo taken in 1994, along the access road north of camp.





wall of Quebrada de las Minas, below the camp. Although complicated by faults, the contact is intrusive and numerous breccia dykes cut the Paleozoic rocks. The metasediments are strongly fractured and oxidized in proximity to the contact and host numerous quartz veins which are truncated by the breccia. The northern contact between breccias and basement, observed in several north-trending *quebradas* to the north of the deposit, is also marked by strong silicification of the basement rocks and abundant, wide, quartz - pyrite  $\pm$  molybdenite veins, which do not continue into the breccia.

#### Alteration - Mineralization

The Agua Rica deposit comprises at least four or, including Misterioso, five contiguous mineralized centres. The centre of the deposit is marked by a NW-trending zone of quartz - alunite alteration surrounded by an argillic zone (Fig. 3-16). Outcropping porphyries exhibit sericitic alteration but some zones of strong alunite alteration are observed. Hypogene alunite from this zone (Fig. 3-17) yields an age of  $5.35 \pm 0.14$  Ma. As mentioned above abundant quartz ( $\pm$  pyrite and molybdenite) veining is observed in the basement, close to the contact with the breccia. Quartz stockworks with pyrite and sericitic alteration (phyllic assemblages) are observed at Morro Alumbra, and quartz stockwork veining is also exposed in the slopes above Quebrada de las Minas, north of the confluence with Quebrada Melcho, as well as in road-cuts in the immediate Seca area. Abundant clasts of "vuggy silica" are observed in the breccias outcropping in Quebrada de las Minas, below the camp.

Until early-1996, project geologists did not recognize potassic alteration

**Figure 3-16.**

Alteration map of the Agua Rica deposit based on preliminary mapping by B.H.P. geologists in 1994. The view presented in figure 3-14 was taken to the NW (top-left), outside of this map area and looks down the axis of the quartz-alunite alteration zone towards the SE (bottom-right).

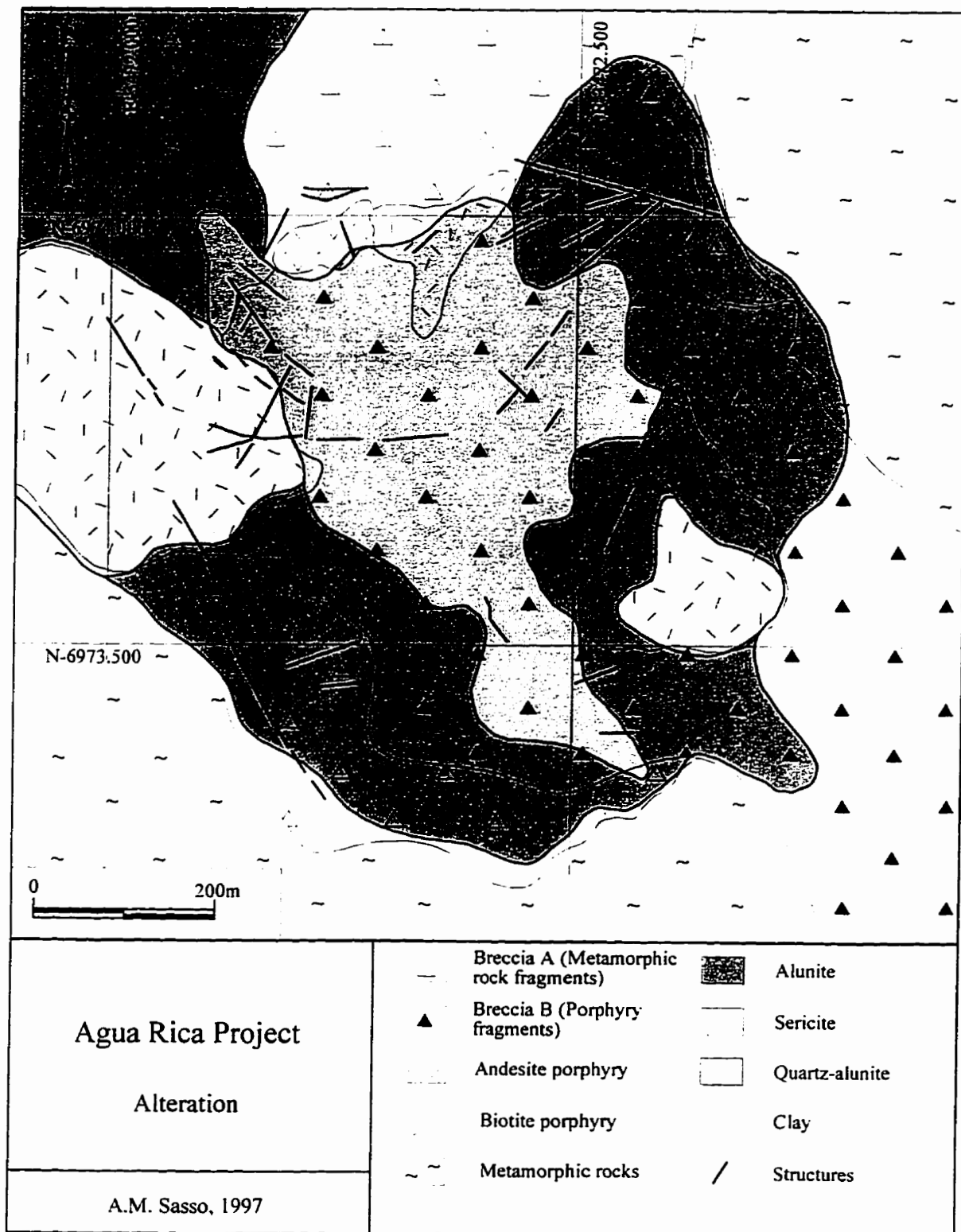
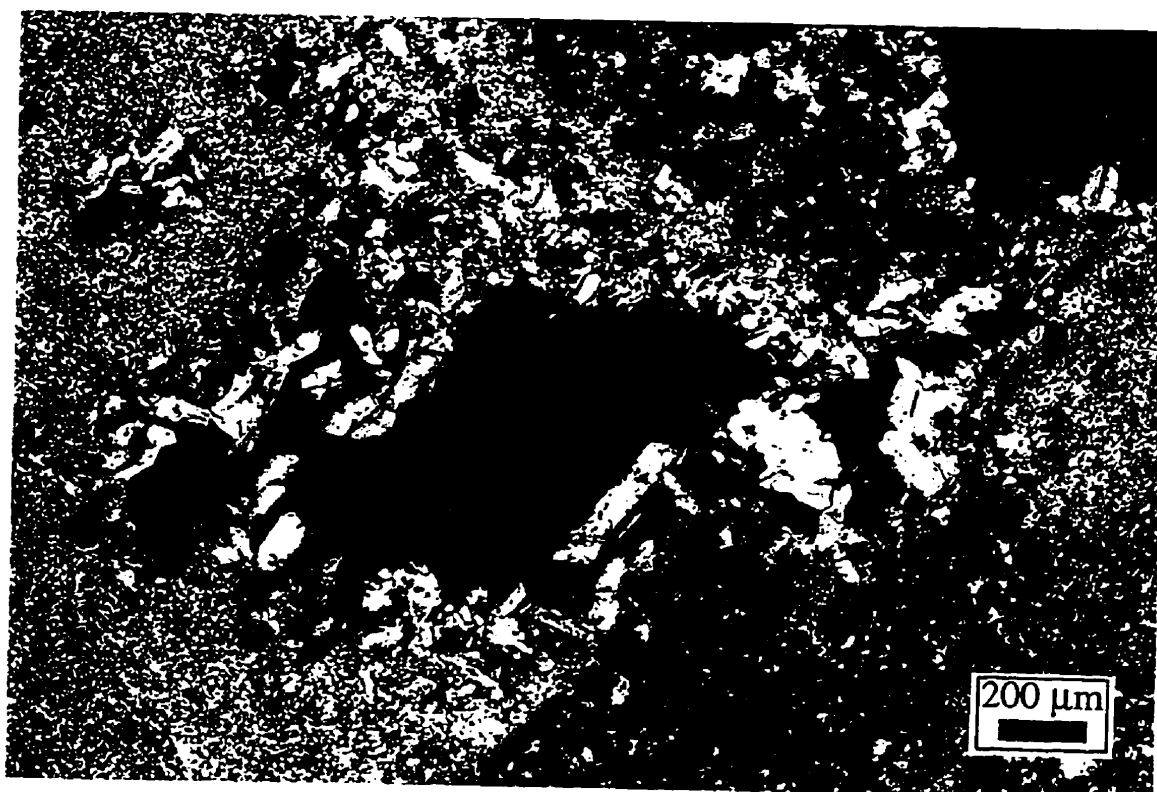
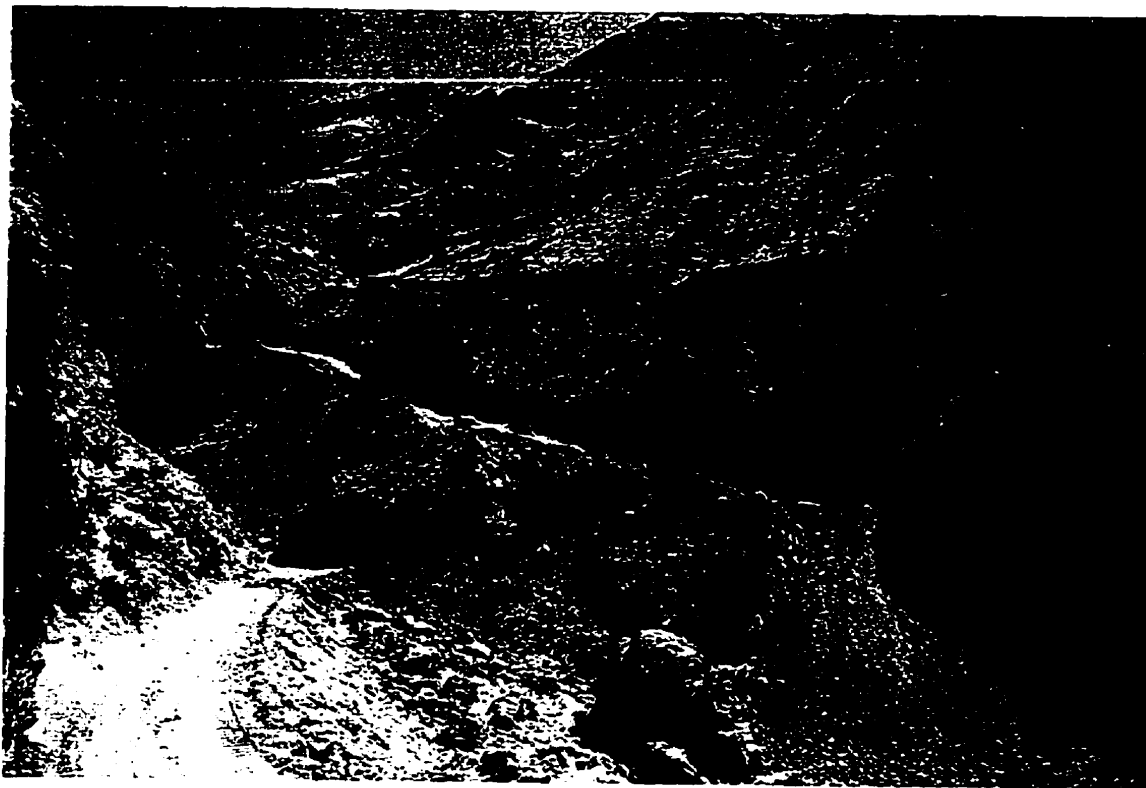


**Figure 3-17.**

*Quartz - alunite alteration  
at Agua Rica*

**A.** View to the NNW in Quebrada de las Minas, downstream from the confluence with Rio Agua Rica. Camp buildings are visible below large dark outcrops in the upper-central portion of the photo. The drill roads in the foreground expose outcrops of hydrothermal breccia with predominant andesite porphyry clasts and which has undergone strong quartz-alunite alteration related to the high-sulphidation epithermal event. The slope in the right-foreground is part of the Trampeadero area. Photo taken in 1994.

**B.** Photomicrograph, taken in crossed-polarized transmitted light, of hypogene alunite crystals (large, clear-to-pale yellow) lining cavities in hydrothermal breccia (FAR 325). This sample was collected along the uppermost drill-road visible on the slope in the right-foreground of the above photo.



assemblages at Agua Rica. However, secondary biotite, disseminated and in veinlets, and K-feldspar veining is clearly evident at the hand-sample scale in brecciated Melcho monzonite and andesite porphyry along the north branch of the Quebrada Melcho. Thin-section study reveals the complete obliteration of primary textures by K-feldspar, albite and biotite (Fig. 3-18). Secondary biotite from this area yielded an age of  $6.29 \pm 0.06$  Ma. This alteration assemblage is seen to be overprinted by later phyllic assemblages in outcrops located upstream in the same *quebrada*. A whole-rock sample of this alteration assemblage yielded an age of  $6.10 \pm 0.04$  Ma. Further, during a visit in April, 1996, abundant zones of relict secondary biotite alteration in breccia clasts were observed along newly-constructed drill-roads in the Mi Vida area. The inferred potassic core to the intact Seca porphyry system has been encountered 200m below the present topography (M. Leake, pers. comm., 1997). Drill-core from the Morro Alumbra area also revealed brownish patches of secondary biotite alteration and thin chlorite  $\pm$  quartz  $\pm$  pyrite veinlets in units mapped as meta-sediments by the B.H.P. geologists. This alteration is inferred to be associated with a discrete porphyry system underlying Morro Alumbra.

Minor quartz-magnetite veinlets were observed in the zone of potassic alteration in Quebrada Melcho. Massive, banded, secondary magnetite with quartz was encountered at depth in one deep hole in the deposit, but no Cu or Au grades are associated with it (P. Marcet, pers. comm., 1996).

A generalized cross-section through the central portion of the deposit is presented as figure 3-19. The hypogene sulphide mineralogy is complex and includes pyrite, chalcopyrite, molybdenite, covellite, chalcocite, sphalerite and galena. Late quartz-enargite

**Figure 3-18.**

*Potassic alteration in Quebrada Melcho, Agua Rica*

**A.** Photomicrograph (plane-polarized light) of sample FAR 324 from the upper Quebrada Melcho, showing secondary biotite alteration of andesite porphyry. The irregularly shaped patches of finely granular secondary biotite are recrystallized from original interstitial igneous biotite and hornblende. A biotite separate from this sample yielded an age of  $6.29 \pm 0.06$  Ma.

**B.** Cathodoluminescence (CL) photomicrograph of FAR 324 (a different field-of-view from that pictured above) which demonstrates the abundance of matrix alkali-feldspar, interpreted to be largely secondary and identified by the blue,  $\text{Ti}^{4+}$ -induced CL. A large oscillatorily-zoned plagioclase phenocryst is located in the centre of the photograph and exhibits a greenish-yellow,  $\text{Fe}^{2+}$  and/or  $\text{Mn}^{2+}$ -induced CL response. Large apatite microphenocrysts demonstrate a bright yellow,  $\text{Mn}^{2+}$ -induced response. The dark patches are predominantly biotite which displays quenched luminescence as a result of high Fe content.



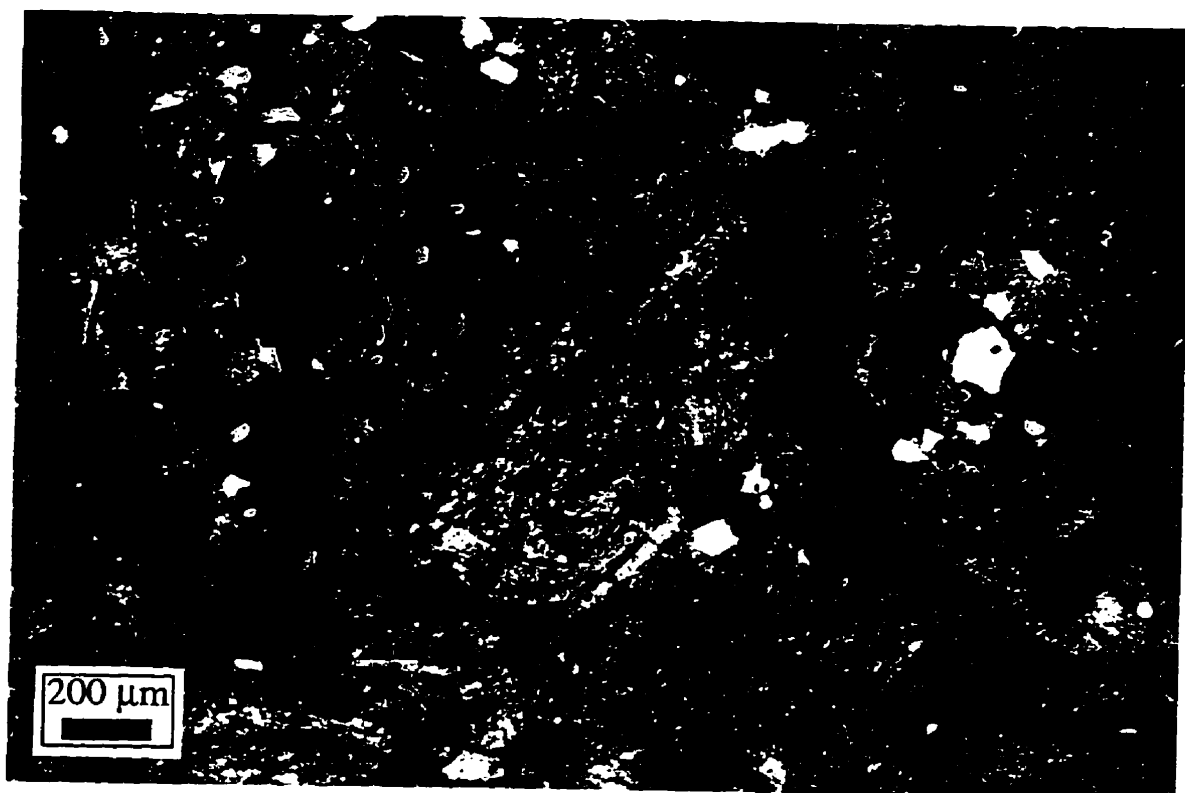
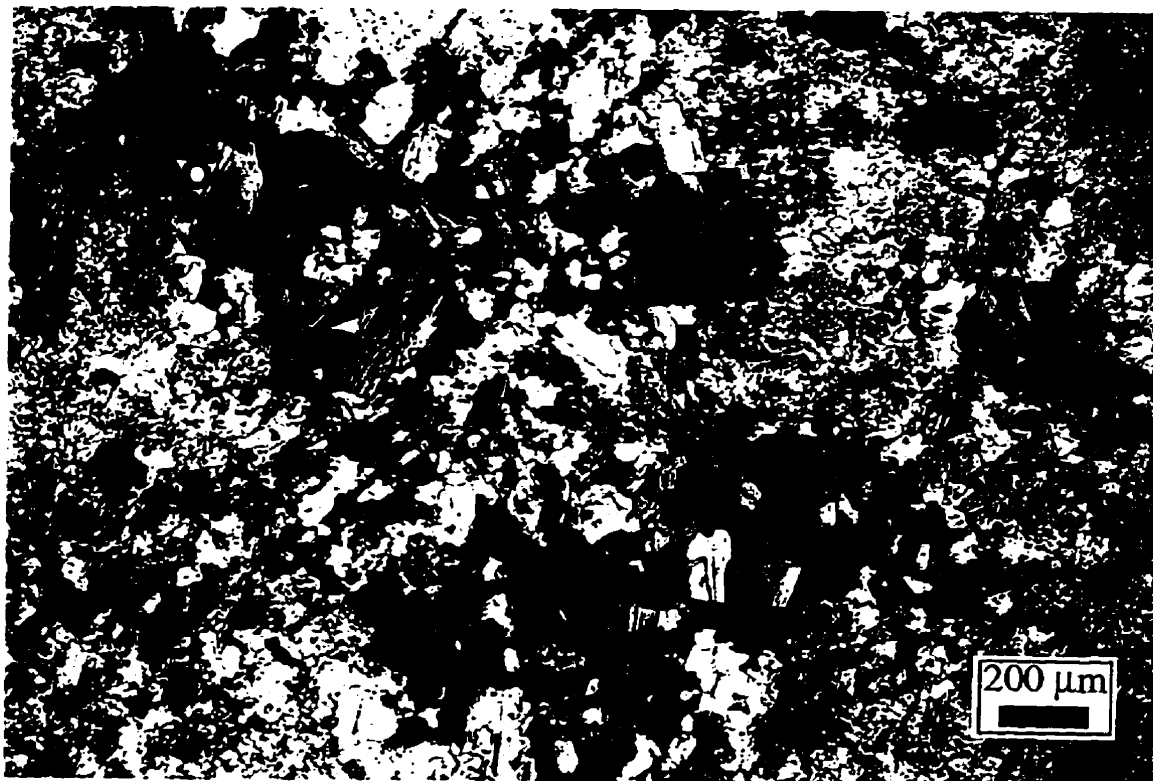
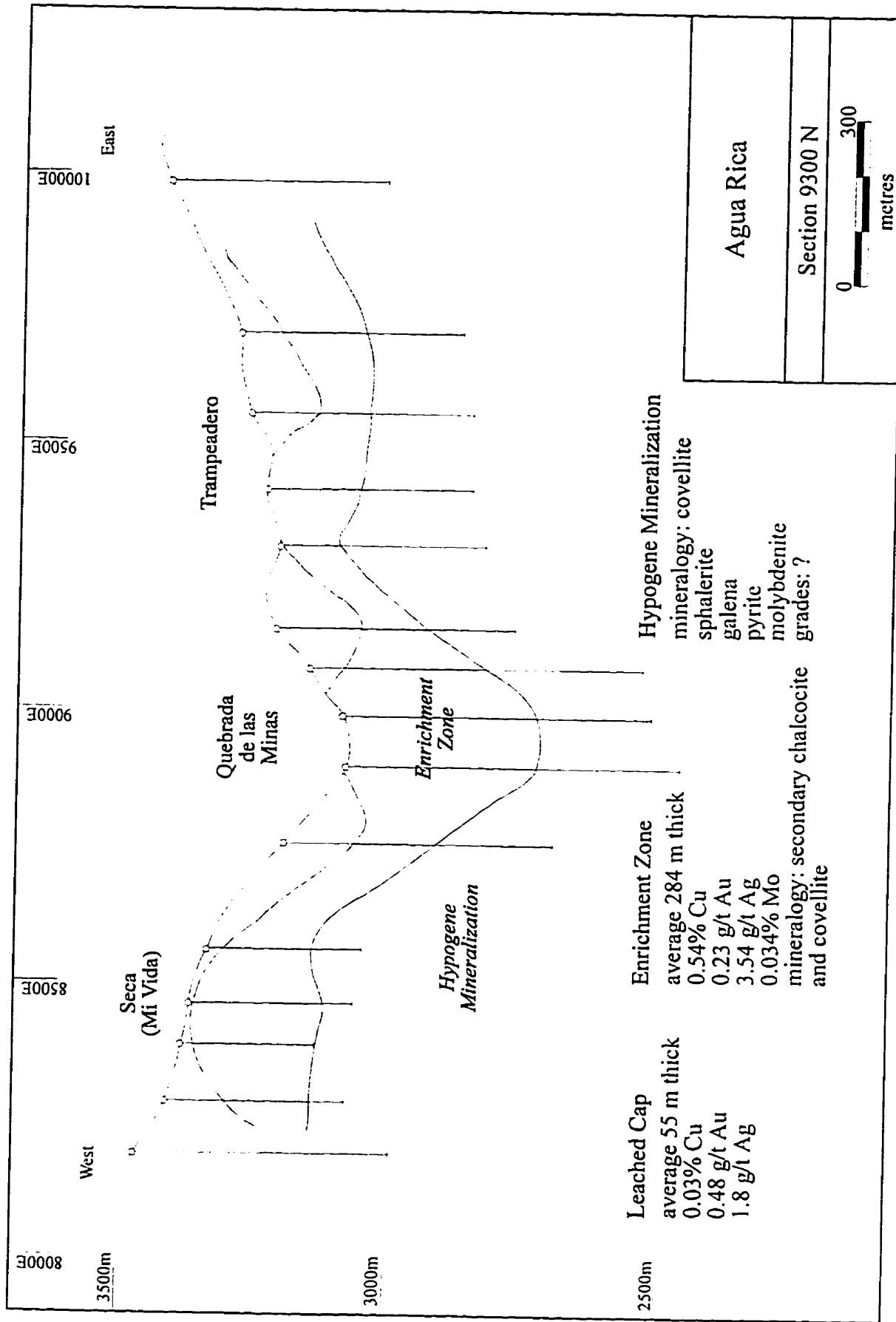


**Figure 3-19.**

Generalized E-W cross-section (view to the north) through the centre of the Agua Rica deposit (after Quin and Nikic, 1997).



veinlets are observed. Covellite is the most important hypogene copper mineral at Agua Rica, occurring as disseminations in andesite porphyry and filling open spaces in breccia. Hypogene chalcopryite is rare. The distribution of Au is poorly understood, but it is associated with clasts of "vuggy silica" and andesite porphyry in the breccia and with intense stockwork veining in the porphyries. Higher Au grades are generally associated with higher Cu grades. Molybdenite occurs disseminated and in quartz veins associated with the porphyry-style mineralization. Massive sphalerite and galena are observed filling cavities in the breccia.

Koukharsky and Mirré (1976) describe two ore mineral assemblages at Agua Rica: termed "A" and "B". Association A consists of disseminated and stockwork pyrite, chalcopryite, bornite, molybdenite and magnetite, and is associated with the potassic alteration facies. Association B is found disseminated, in veinlets, in cavities and cementing breccias, and comprises pyrite, covellite, bornite, enargite, molybdenite, galena, sphalerite, marcasite, rhodocrosite and native sulphur. It is related to sericitic alteration and is interpreted to post-date assemblage A. Breccia-type mineralization, a sub-type of assemblage B, consists of brecciated material cemented by fine-grained sulphides; vugs within the cement contain coarsely-crystalline covellite, sphalerite, galena and pyrite, with minor bornite, enargite, rhodocrosite and native sulphur. The "A"-type mineralization is associated with the porphyry event and the "B"-type assemblage with the syn- to post-breccia high-sulphidation epithermal event.

Supergene enrichment has generated a leached cap and chalcocite-covellite enrichment blanket at Agua Rica. The enrichment zone roughly mimics present

topography.

A NW-striking structural zone appears to have controlled the location of Quebrada de las Minas. E-W-trending structures are also observed, and intersections of these structures may have channelled porphyry intrusion at Agua Rica. This structural pattern is observed on TM imagery for the portion of the Aconquija Range immediately surrounding the deposit. Significant late, *i.e.*, post-epithermal, structural dissection of the deposit is observed (J. Mortimer, per. comm., 1997).

#### Geological Evolution of the Agua Rica Deposit

The following discussion of the geological evolution of the Agua Rica deposit is based largely on a sequence of diagrams of a genetic model, developed by N. Rojas, that was pinned to the wall of the Agua Rica camp geology office in April, 1996, and subsequent discussion with John Mortimer, as well as my ideas and interpretations. The ages of alteration events associated with the formation of porphyry Cu-Mo-(Au) mineralization were determined on samples from the Quebrada Melcho centre located south of the main centre of economic hydrothermal activity, *i.e.*, Seca - Trampeadero. The mineralization exposed in Quebrada Melcho is uneconomic (J. Mortimer, pers. comm., 1997). The development of the Agua Rica project was not sufficiently advanced at the time of the field investigation for this research to provide samples of alteration assemblages related to the porphyry mineralization in the Seca - Trampeadero area for geochronological study. Therefore, the ages of hydrothermal alteration events at Quebrada Melcho are inferred to be representative of the local porphyry Cu-Mo-(Au) mineralizing

event and, thus, contemporaneous with mineralization at the Seca and Trampeadero centres. As the development of the project continues, these relationships will, no doubt, be modified.

A three-stage evolution is proposed for the development of the Agua Rica deposit:

*A. Formation of Porphyry Cu-Mo-(Au) deposits*

Intrusion of the Melcho monzonite was followed by the emplacement of a series of andesite porphyry stocks in the Cambro-Ordovician basement of the Aconquija region. No extrusive units are recognized at Agua Rica, but it is assumed that volcanism occurred at this time, and that the intrusions probably represent hypabyssal bodies associated with the waning stage of eruptive activity. The 8.56 Ma Melcho monzonite stock pre-dated porphyry-style alteration-mineralization by several m. y., and is thought to be a precursor to the mineralized porphyries of Seca and Trampeadero (M. Leake, pers. comm., 1997). Hydrothermal systems, centred on the andesite porphyries, resulted in the development of potassic alteration assemblages at 6.29 Ma, attended by stockwork and disseminated Cu-Mo-(Au) mineralization. Koukharsky and Mirré (1976) document propylitic assemblages but these have been completely overprinted in the central area of the deposit within the limits of mapping by B.H.P. Phyllic alteration overprinted the potassic assemblage at 6.10 Ma.

*B. Uplift and Erosion of the Aconquija Range*

Rapid uplift of the Aconquija Range resulted in the unroofing of the porphyries, probably while they were still hot, and caused the lowering of the

water-table. The explosive interaction of magma and meteoric water resulted in the formation and emplacement of the breccia bodies, which probably intersected the paleo-surface. The superposition of near-surface conditions on a cooling porphyry environment resulted in the establishment of meteoric convection cells followed by the formation of argillic-alunitic alteration assemblages at 5.35 Ma, possibly accompanied by remobilization and concentration of Cu and Au. The breccias were probably generated by multiple explosive events. The occurrence of mineralized clasts and sulphide-cemented breccias suggest that epithermal mineralization and brecciation may have overlapped temporally, although it appears that the bulk of epithermal-style alteration-mineralization post-dated breccia pipe emplacement.

### C. Supergene Enrichment

Continued uplift of the Aconquija Range created a barrier to regional weather systems, resulting in greater precipitation on the southern and eastern slopes of the range, a situation that prevails today. Ongoing erosion and incision of river systems generated a topography which was probably very similar to that presently observed. This resulted in the exposure of the mineralized centres, permitting supergene copper leaching and enrichment.

Final uplift, erosion and river incision resulted in the present topography. The level of exposure of the deposits suggests that the supergene sulphide enrichment blanket has been partially removed at Seca and Trampeadero, but

almost completely stripped from the Melcho centre.

Thus, major uplift and erosion, probably episodic, are inferred to have played a key role during the evolution of the hydrothermal systems, causing the superimposition of different styles of alteration and mineralization, as evidenced by the overprinting of epithermal assemblages on higher- temperature porphyry-style mineralization.

### *Capillitas*

#### Location and Access

The Capillitas mine (Figs. 3-3 and 3-20) is the world's largest source of gem-quality rhodochrosite. It is situated 85 km south of Santa María and 65 km NW of Andalgala on Ruta Nacional No. 63, between 3,300 and 3,500 m a.s.l. Capillitas is approximately 15 km WNW of Agua Rica and 25 km E of Bajo de la Alumbrera.

#### Previous Work

A detailed account of the Capillitas mine is presented by Márquez Zavalía (1988). It has the longest history of any of the prospects in the district, and stone tools found in the Ortiz Vein workings are thought to date back to the Inca Empire. The veins were certainly worked by the Spanish in the 17th century. An English company, the Capillitas Copper Company, acquired the mine in 1902. After the construction of extensive infrastructure, including an unsuccessful 27.5 km long cable car from Capillitas south to the town of Muschaca for the transport of ore, the mine was abandoned due largely to the metallurgical complexity of the ore. It was thereafter worked sporadically until 1947,

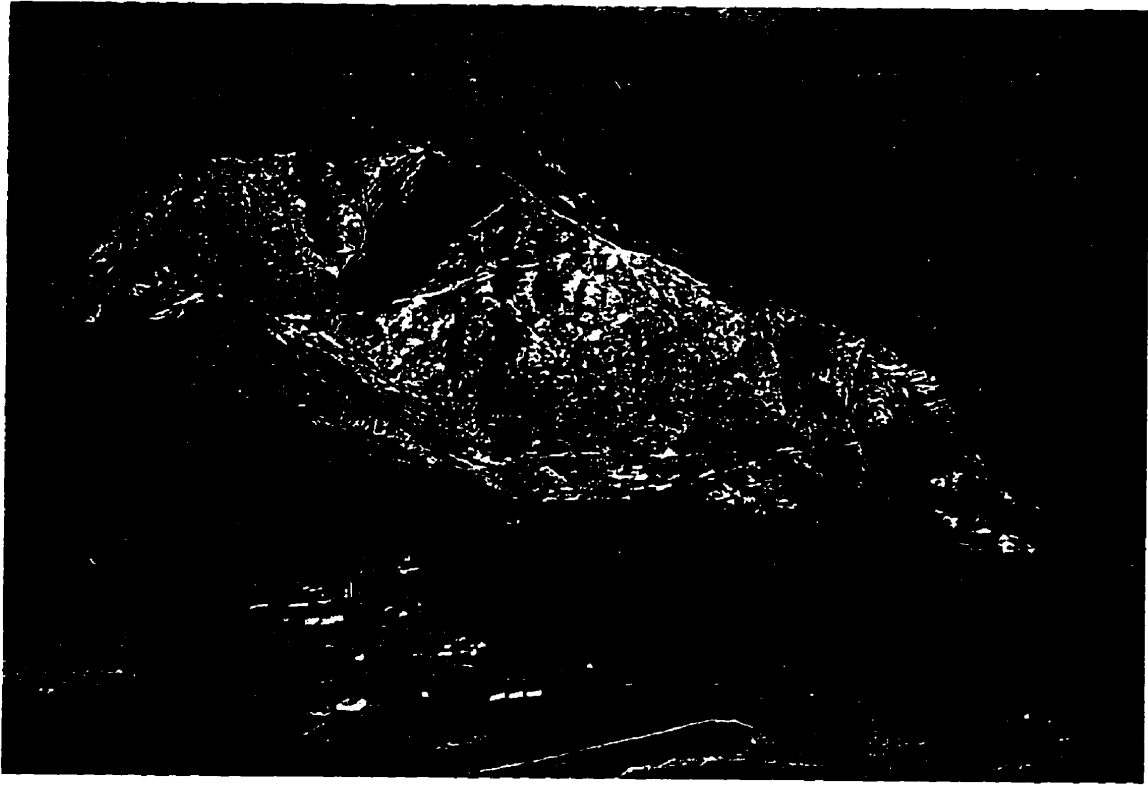


**Figure 3-20.**

*Capillitas deposit*

**A.** View, to the west, of the Capillitas rhyolite diatreme (buff-coloured outcrops) emplaced in Ordovician granites of the Capillitas Range. Cerro de la Rosario is the highest point of the diatreme, upper-left of centre. Morro Pan de Azucar, the small rounded knob of olive-coloured outcrop on the SE (left) edge of the diatreme is underlain by dacite porphyry. Sulphide veins transect the rhyolite pipe and extend into the granitic basement. Numerous abandoned workings are marked by dump piles (*e.g.*, on the north face below Cerro de la Rosario and to the right of Morro Pan de Azucar). Photo taken in 1994 from the access road to the Agua Rica deposit.

**B.** View, to the east, of mining operations on the north flank of the Capillitas diatreme. Many of the buildings were constructed in the middle of this century by Fabricaciones Militares. They are now largely abandoned. The large building, left-of-centre, houses the rhodochrosite sorting facilities and the office of the mine engineer. Dark rocks capping the flat-topped dumps in front of this building are reject rhodochrosite that oxidizes rapidly once exposed to the elements. The olive-coloured flat knob on the near horizon, right-of-centre, is Morro Pan de Azucar.



when it was taken over by Fabricaciones Militares. They worked the deposit for three years, but the complexity of the ore continued to be a major stumbling block, and eventually rhodochrosite was the only mineral that could be exploited economically. I could find no record of the historical copper production from Capillitas in the literature, but 1986 tonnes of rhodochrosite were extracted between 1951 and 1971 (Angelelli *et al.*, 1974). The mine is presently being worked by Compañía Víctor Contreras S.A. for gem-quality rhodochrosite. Reserves of 5390 tonnes rhodochrosite existed in 1979 (JICA, 1979), when production averaged 3-5 tonnes/month. The current mine engineer states that reserves are sufficient for six months of exploitation, but no systematic exploration for new reserves is planned. This has, however, been the most productive ore deposit in the region. Estimated metallic reserves (Rosin, 1993) are 0.3 Mt at 2.5% Cu, 2 g/t Au, 160 g/t Ag and *ca.* 8% Pb + Zn, with local grades of up to 25 g/t Au in the Capillitas Vein (mine staff, pers. comm. 1994).

The bibliography on the area is voluminous. Information presented herein is based on Angelelli (1950), various reports (1978 to 1981) by the Japanese International Cooperation Agency, Márquez Zavalía (1988), and personal observations.

### Geological Relationships

The deposit is located within the uplifted basement block which constitutes the Sierra de Capillitas. The host-rock is the Ordovician (McBride *et al.*, 1976) Capillitas granite. It has been intruded by a rhyolitic diatreme of the magmatic breccia type described by Sillitoe (1985). The pipe is oval in plan, 1,500 m by 800 m, and elongated

SW-NE (Fig. 3-21). It consists of a texturally-zoned body of rhyolitic tuffs. The core consists of massive rhyolite tuff which grades outwards into a flow-banded unit with elongated pumice lapilli, the flow-banding dipping steeply towards the centre of the pipe (Fig. 3-22). Several zones of brecciated, flow-banded tuff occur along the outer contact of the pipe. The breccia is matrix- to clast-supported. Blocks are angular and consist mainly of flow-banded rhyolite which range up to 2 m in diameter. Rare rounded clasts of altered granite occur. In general the contact with the granite is sharp, but some contacts are sheared. Minor argillic alteration of the host-rocks is developed within 10m of the contact, in addition to thin, fracture-controlled zones of silicification. A rhyolite plug intruded the southwest portion of the Capillitas pipe. It is flow-banded along the contact with the granite but becomes more massive towards the centre of the pipe. Late-stage dacite porphyry dykes and a larger dacite porphyry intrusive body cross-cut the pipe (Fig. 3-23). K-feldspar from one of the dykes yielded an age of  $5.16 \pm 0.05$  Ma. The J.I.C.A. reports present two K-Ar dates of  $5.0 \pm 0.5$  Ma for biotite from dacite and muscovite from rhyolite at Capillitas. No details are provided on sample location, but I assume that these represent intrusive rather than mineralization ages. A. H. Clark (pers. comm., 1995) reports outcrops of pebble breccias in the vicinity of Morro Pan de Azúcar.

The El Morterito Formation lies disconformably on top of the planated basement to the south of the deposit. Volcanic breccias and flows crop out to the south, overlying the El Morterito strata, and dacites which yield an age of  $9.17 \pm 0.08$  Ma form a NE-trending lens to the east of Capillitas.

The deposit has traditionally been interpreted as having been emplaced prior to

**Figure 3-21.**

Geology of the Capillitas deposit.

.

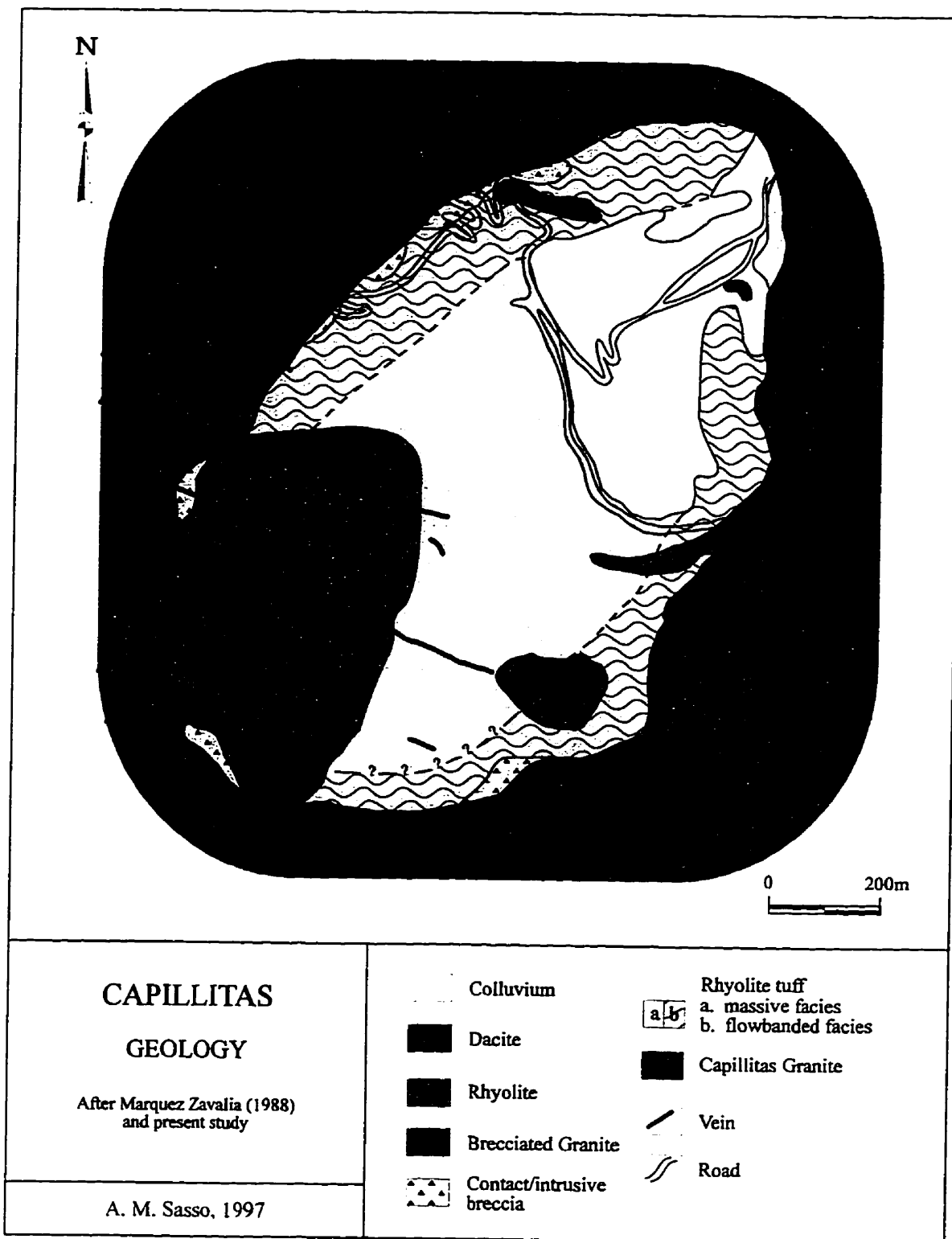


**Figure 3-22.**

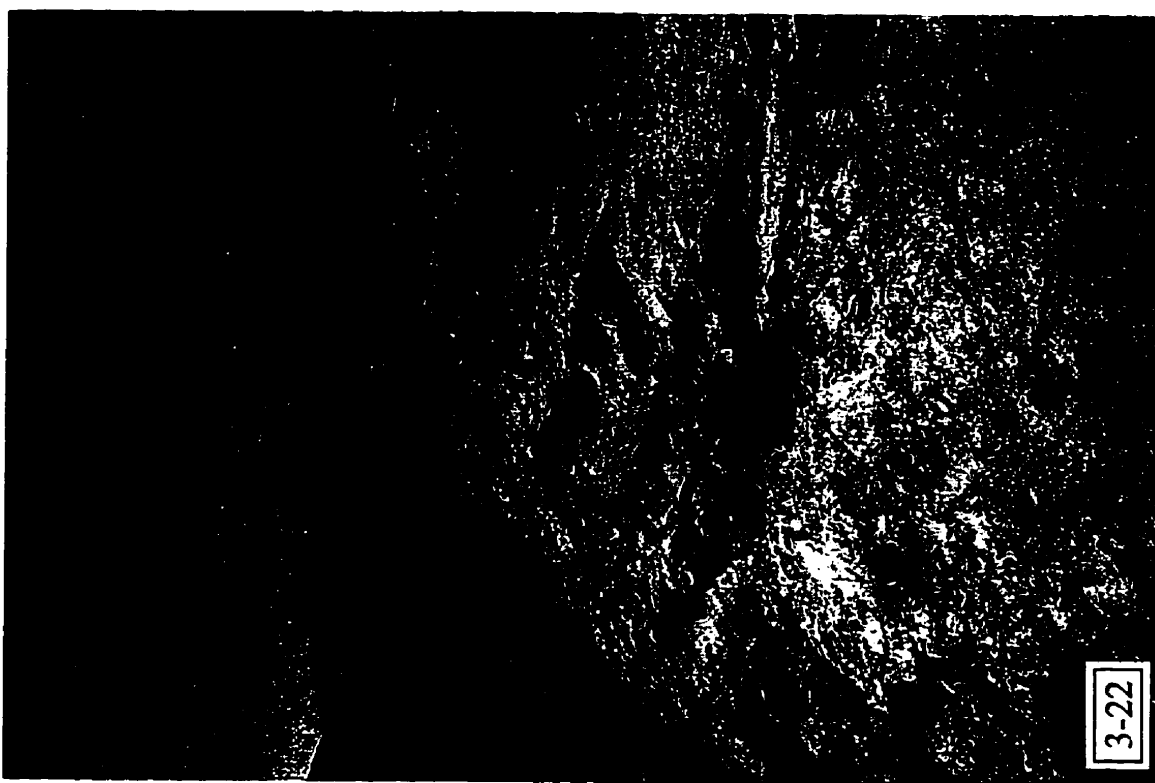
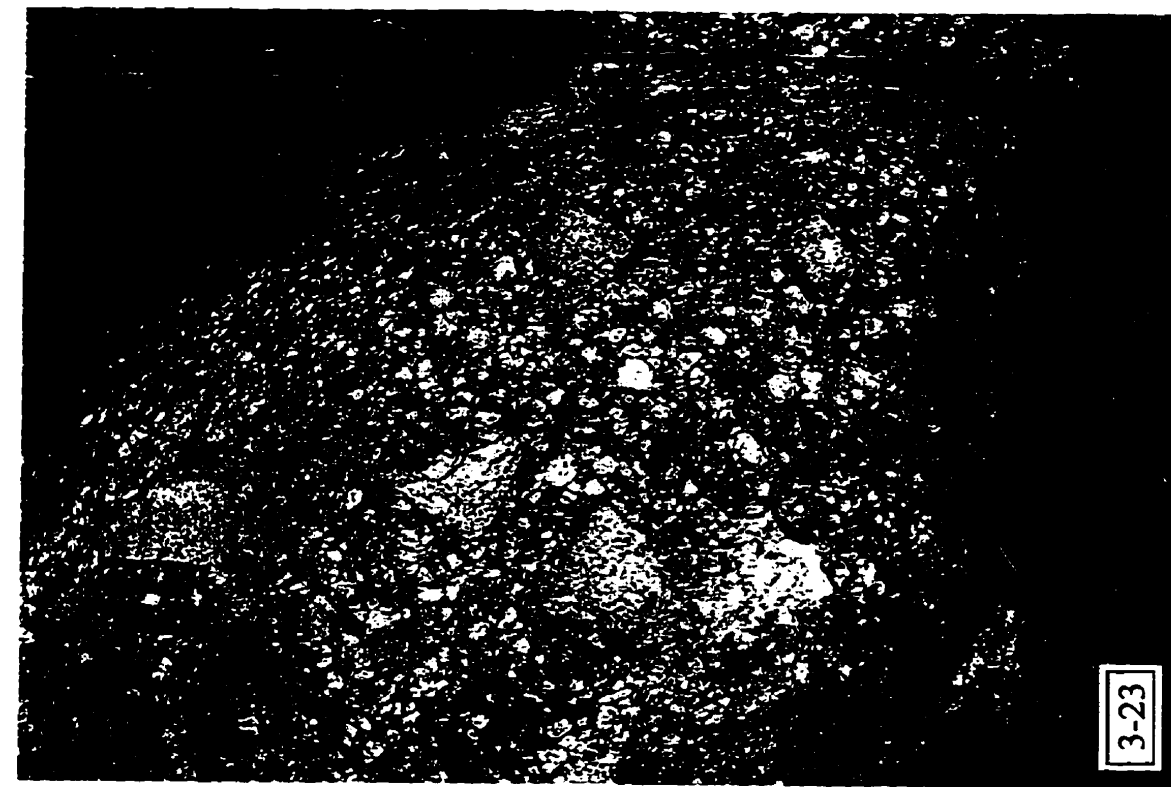
*Field characteristics of flow-banded rhyolite tuff  
at Capillitas*

View to the east of flow-banded rhyolite tuff at the summit of Cerro de la Rosario. Flow-banding is parallel to the contact with the granite and dips moderately to steeply to the east, towards the centre of the pipe. Peaks of the Aconquija Range are seen on the horizon.

**Figure 3-23.**

*Lithological characteristics of dacite porphyry dykes  
at Capillitas*

Outcrop of a dacite porphyry dyke which crops out on the north edge of the breccia pipe (see Fig. 22). The rock consists of very large K-feldspar and smaller plagioclase, biotite and chloritized hornblende phenocrysts in a fine-grained quartzo-feldspathic matrix. These dykes represent the youngest intrusive event dated in the Farallón Negro Volcanic Complex.





uplift of the Sierra de Capillitas. Márquez Zavalía (1988) provides a genetic model which involves the emplacement of a volcanic neck with associated overlying volcanic complex, multiple pulses of intrusive activity, the intrusion of a sub-volcanic stock which initiated circulation of hydrothermal fluids and provided a source for metals, the emplacement of the veins, uplift of the Sierra de Capillitas and concomitant tilting of the paleosurface ("basement peneplain") to the present attitude, and finally erosion. This interpretation is partially rejected by the writer. The contacts of the breccia pipe and the parallel flow banding dip steeply towards the centre of the pipe. The present orientation of the planated surface is  $30^{\circ}$  to the SE. Breccia pipes are generally intruded as vertical bodies, and are only rarely inclined at more than  $15^{\circ}$  to the vertical (Sillitoe, 1985). If the breccia pipe were emplaced prior to the uplift the contacts would be expected to dip as much as  $30^{\circ}$  to the NW. In Márquez Zavalía's (1988) interpretation, she neglects to incline her post-uplift schematic diagram by the full  $25\text{--}30^{\circ}$  of tilting necessary for restoration of the planated basement surface.

On the basis of geological and geochronologic relationships at Agua Rica, diatreme emplacement is postulated to have immediately post-dated uplift of the Aconquija Range. The timing of uplift is constrained by the ages of  $6.10 \pm 0.05$  Ma for pre-uplift phyllic alteration and  $5.35 \pm 0.14$  Ma on post-uplift alunite at the Agua Rica deposit. It is suggested herein that the age of uplift of the Capillitas Range is similar. Uplift had commenced, and the Capillitas diatreme pipe emplaced, prior to the intrusion of dacite dykes at  $5.16 \pm 0.05$  Ma.

## Mineralization

The Capillitas deposit appears to be transitional between the "acid-sulphate" and "adularia-sericite" types of epithermal systems (Heald *et al.*, 1987). Mineralization consists of Cu, Pb and Zn, with As, Sb, Au and Ag and trace amounts of W, Sn, Bi and Ge, in rhodochrosite-quartz-alunite gangue. It is analogous to the Anaconda vein ("D vein") system at Butte, Montana (Sales and Meyer, 1949) and the Santa Bárbara vein system, southeastern Peru (Wasteneys, 1990). Hypogene ore minerals consist of pyrite, enargite, tennantite, chalcopryrite, chalcocite, sphalerite, galena, marcasite, native gold and silver, and arsenopyrite. Supergene minerals include: chalcocite, chalcanthite, brocanthite, goslarite, anglesite, linarite, melanterite, malachite, azurite and cuprite. Alteration involved silicification and argillitization with minor sericitization in the igneous units and weak silicification in the granites. The deposit comprises 19 veins with two principal strikes, ENE and WNW. The veins average 50 - 70 cm wide and extend laterally for 100 - 800 m, cutting the Capillitas pipe and extending into the granite. There is no change in nature of mineralization or tenor of ore with change in host lithology.

Márquez Zavalía (1988) documents seven mineralization stages. The first is characterised by quartz and pyrite. The second and third stages appear to be the main sulphide mineralization events, with pyrite-pyrrhotite-arsenopyrite-galena-sphalerite-marcasite-quartz-alunite veins forming in the second stage. Chalcopryrite, enargite and tennantite formed, in addition to the above minerals, during the third stage. The fourth stage was marked predominantly by a change in gangue mineralogy to carbonates, mainly rhodochrosite, and the emplacement of minor W, Sn, Bi and Ge. The fifth stage is

characterized by the formation of quartz-pyrite-sphalerite-marcasite-wurtzite-rhodochrosite veins. Sixth-stage veins consist of chalcopyrite-rhodochrosite and the final stage is restricted to barren quartz veins. The alteration of vein envelopes is not documented. The change from alunite-dominated to carbonate-dominated gangue mineralogy indicates neutralization of the mineralizing solutions with time. A preliminary study of fluid inclusions in quartz (Márquez Zavalia, 1988) suggests formational temperatures of between 240 and 270° C.

Vein geometries tend to be lenticular with pods of mineralization separated by fine stringers of pyrite. They exhibit many features of open-space filling, suggesting the development of mineralization in extensional structures. Structural reactivation is indicated by the presence of minor slip surfaces with slickensides and zones of brecciation. Post-mineralization faulting has disrupted the continuity of the veins.

### ***Farallón Negro and Alto de la Blenda Vein System***

#### **Location and Access**

The Farallón Negro and Alto de la Blenda vein system is located 25 km south of Los Nacimientos and approximately 8 km west of Bajo de la Alumbrera (Fig. 3-3). It is the basis of the only active (1997) metallic mining operations in this region.

#### **Previous Work**

Although internal Y.M.A.D. reports are presumed to exist, no recent detailed

descriptions of the vein system have been published. Malvicini and Llambías (1963) described the mineralogy and origin of the manganese minerals at Farallón Negro, Blenda and Los Viscos. Llambías (1970) also briefly refers to the manganese vein mineralization. McBride (1972) dated supergene cryptomelane from the Farallón Negro mine (samples collected by J.C. Caelles and A.H. Clark).

### Geological Relationships

The Farallón Negro - Alto de la Blenda mine is at present the most productive hard-rock gold-silver operation in Argentina. Reserves as of early-1993 were 616,711 tonnes (proven), with an additional 180,000 tonnes (probable), with grades of 5.77 g/t Au and 104.70 g/t Ag. The deposit can be classified as an adularia-sericite type epithermal system (Heald *et al.*, 1987). The deposit is hosted by andesite breccias and the Alto de la Blenda monzonite stock of the Farallón Negro Volcanic Complex, and comprises a system of sub-parallel veins with minor cross-over splays. The main mineralized structure is the Farallón Negro Vein, which strikes NW-SE over a distance of roughly 8 km, with a width of 1 to 19 m. The parallel Alto de la Blenda Vein is located 500 m to the north and extends over a length of 3 km before it joins the Farallón Negro Vein to the SE. The most productive portions of the system, within and close to the stock, are hosted by pyrite-bearing andesite porphyry dykes which intrude the monzonite and andesite breccias. Similar veins are also encountered in Los Viscos and Macho Muerto.

Veins strike NW-SE and dips range from 60°NE to vertical. Alteration consists of argillization and sericitization and is much more extensive in the hanging-wall (up to 5

m wide) than in the footwall (avg. 80 cm). Phyllic alteration has been dated herein at  $6.55 \pm 0.14$  Ma, and was thus broadly contemporaneous with the development of phyllic alteration assemblages at Bajo de la Alumbrera.

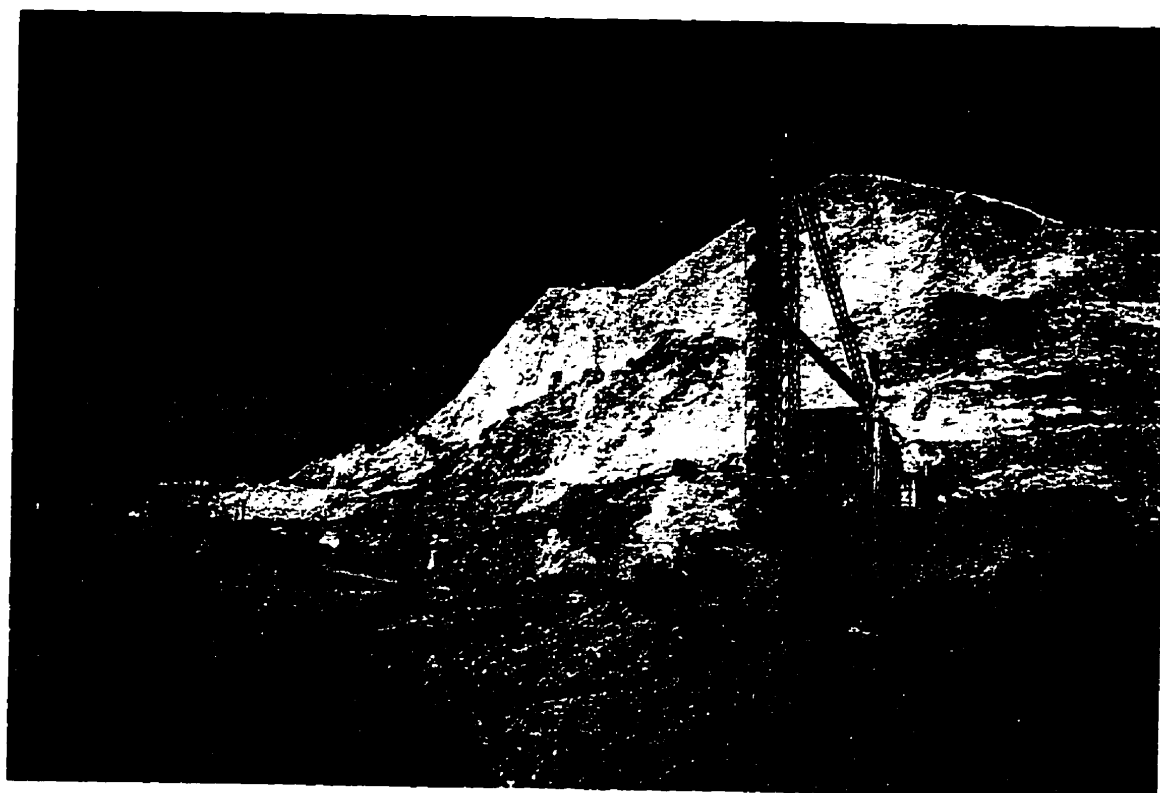
## Mineralization

Mineralization in the Farallón Negro and Alto de la Blenda vein system consists of Au, Ag and Mn with minor base metal sulphides. In the Farallón Negro Vein there is evidence for an early pulse of galena and sphalerite deposition, followed by Mn-carbonates (rhodochrosite and manganocalcite). Oxidation of the vein system resulted in the present Mn-oxide - dominated vein assemblage. Free Au occurs lining cavities and is also associated with zones of abundant pyrite. The supergene overprint appears to be variable along the length of the vein system. Quartz - manganese oxide associations grading 6 g/t Au and 90-110 g/t Ag in the SE part of the camp pass through a transitional zone into a carbonate-dominated assemblage grading 3-4 g/t Au and 40-70 g/t Ag to the NW (N. Montenegro, pers. comm., 1994). The transition zone is located at the Farallón Negro ("black cliff") that was the locus of early mining activity (Fig. 3-24).

Intense oxidation of the upper parts of the veins has resulted in enrichment of both manganese and the precious metals. Pyrolusite is the primary oxide in the Farallón Negro mine, whereas cryptomelane predominates at Alto de la Blenda. Cryptomelane, dated by the K-Ar method by McBride (1972), yielded an age of  $2.7 \pm 0.8$  Ma.

**Figure 3-24.**

View to the south of the Farallón Negro mining operation. The large, bleached rock face exposed in the right half of the photograph was the site of the original mining operations. The face once exposed black, Mn-oxide-rich vein material, presenting a black cliff (*farallón negro*), from which the mine took its name. This section of the Farallón Negro Vein is now abandoned, but the SE extension of the vein (not shown) was being mined sporadically in 1994. Current production is from the parallel Alto de la Blenda Vein located approximately 500 m to the north (left).



## **Characteristics of Porphyry Cu-Au systems at Farallón Negro**

Detailed deposit descriptions including geological and alteration facies maps of the remaining prospects in the region are presented in Appendix A. The descriptions are based on field visits undertaken in 1993 and 1994 and data collected from the literature, where available.

From these descriptions, and those in this chapter, a model for a "typical" Farallón Negro porphyry Cu-Au deposit may be deduced. The deposits are centred on hypabyssal stocks of andesitic-to- dacitic composition in which multiple intrusive pulses are commonly recorded. Alteration-mineralization, associated with the waning stages of intrusive activity, progressed from early quartz-magnetite/propylitic, through potassic/propylitic, to phyllic, with the formation of epithermal-style veins and associated alteration occurring in the final stage. Supergene oxidation and enrichment, where represented, post-dates epithermal-style mineralization. A lateral and vertical traverse from the core to the boundary of the system would encounter the following sequence of alteration assemblages: quartz-magnetite, potassium-silicate, phyllic, propylitic, unaltered (with some overlap between alteration zones). Mineralization is zoned, both laterally and vertically, from Cu-Au in the core to base metal-dominated assemblages (Pb-Zn-Ag) on the periphery. Epithermal veins are located peripherally about the top of the deposit. The characteristics of the Farallón Negro porphyry deposits conform to widely accepted models of porphyry deposits (*i.e.*, Lowell and Guilbert, 1970; Sillitoe, 1973, 1979; Gustafson and Hunt, 1975).

Evidence for the occurrence of early magnetite-rich alteration-mineralization is



preserved in a significant number of porphyry Cu, Cu-Au and Au-only deposits (Sillitoe, 1979; Cox, 1986; Clark, 1993), but it has probably been widely modified or even obliterated by superimposed K-silicate-sulphide facies (Arancibia and Clark, 1990, 1996; Clark and Arancibia, 1995). Au is commonly emplaced with the magnetite alteration, although it widely exhibits a stronger correlation with Cu and potassic alteration (*e.g.*, Island Copper, Bajo de la Alumbrera).

The alteration-mineralization assemblage appears to be host-rock dependent with quartz-magnetite  $\pm$  albite  $\pm$  Au being common in andesitic-to-more felsic lithologies (*e.g.*, porphyries of the Farallón Negro District) and more complex assemblages of magnetite - intermediate to sodic plagioclase - Ca amphibole  $\pm$  quartz in basaltic units (*e.g.*, Island Copper: Arancibia and Clark, 1996). The absence of hydrothermal feldspars and micas in zones of intense magnetite-quartz alteration in the Farallón Negro District, *e.g.*, Bajo las Pampitas, may imply that extreme Fe-metasomatism was accompanied by leaching of Na, Ca and K, and the apparent absence of albite in the quartz-magnetite assemblage of the majority of porphyry deposits of the region would suggest variability in the intensity of alkali-leaching attending magnetite alteration.

Such sulphide-deficient alteration facies are thought to represent high  $f\text{SO}_2$ :  $f\text{H}_2\text{S}$  ratios in the magma (Clark, 1993; Arancibia and Clark, 1990; Clark and Arancibia, 1995). High magmatic oxygen fugacities favour the development of early, high-temperature, highly oxidized, Fe-rich aqueous brines, which would readily precipitate chloride-complexed Au upon cooling but would permit the widespread loss of Cu and S to the overlying environment. It has been proposed (Clark, 1993; Clark and Arancibia, 1995;

Arancibia and Clark, 1996) that this early alteration assemblage and the associated veins be termed "M-veins" (for "magnetite"), by analogy with the A, B, and D veins defined at El Salvador by Gustafson and Hunt (1975). Clark and Arancibia (*op. cit.*) concluded that strong magnetite alteration associated with Au-rich porphyry systems is related to the magmatic source of the calc-alkaline lavas, possibly reflecting quenching and vesiculation of underplating basaltic melts (A.H. Clark, pers. comm., 1997) and to the mechanism of extraction of Cu, Au and S from the magmas.

Hydrothermal magnetite was first formally documented at Bajo de la Alumbrera by Sillitoe (1973). The majority of other porphyry-style deposits at Farallón Negro also demonstrate this assemblage (*e.g.*, Bajo el Durazno, Bajo de Agua Tapada, Bajo de San Lucas, and Bajo Las Pampitas). In each of these deposits, dense, commonly sheeted zones of magnetite and quartz-magnetite veinlets occupy a broadly central position (Figs. 3-25 and 3-26). In general at Farallón Negro, there appears to be a progression from early magnetite-rich to later sulphide-rich vein and disseminated mineralization assemblages, but, as at Island Copper (Arancibia and Clark, 1996), there is a temporal and spatial overlap between magnetite precipitation and the development of the potassium silicate assemblage.

At Farallón Negro, hydrothermal magnetite has commonly been assigned to the potassic alteration event even though the substantial magnetite-quartz alteration lacks K-bearing minerals and therefore records extreme potassium leaching from intermediate or felsic rocks. At Bajo de la Alumbrera, neither Stults (1985) nor Proffett (1995) recognizes a separate, early magnetite-quartz alteration event, but rather conflates the magnetite

**Figure 3-25.**

Comparison of alteration zoning of porphyry centres associated with rocks of the Farallón Negro Volcanic Complex.

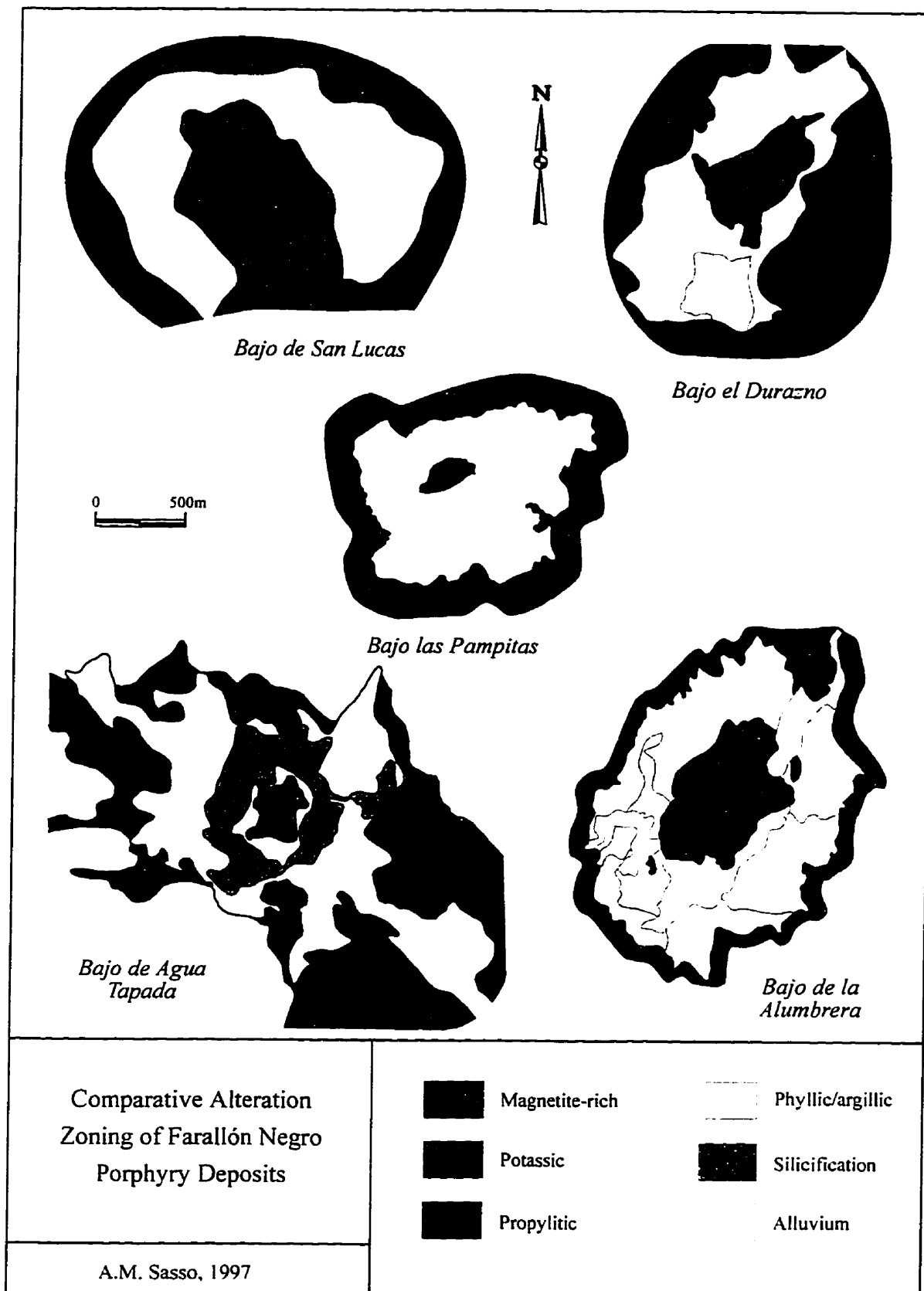
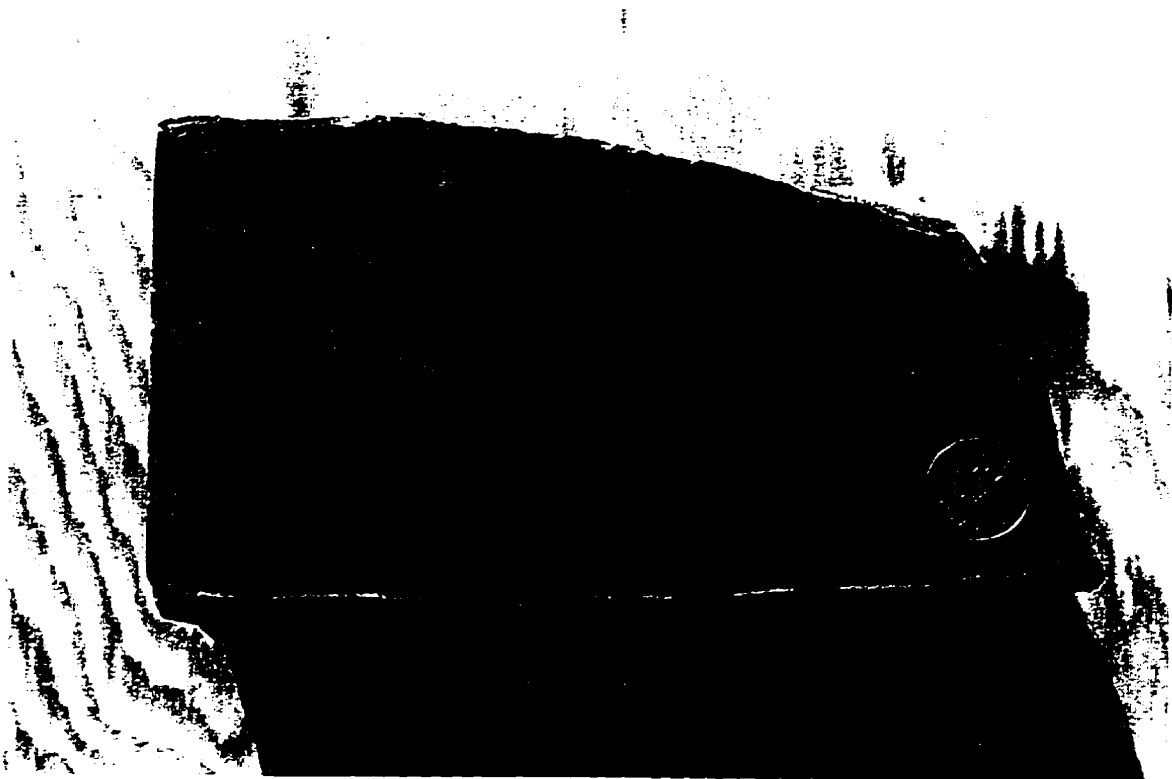
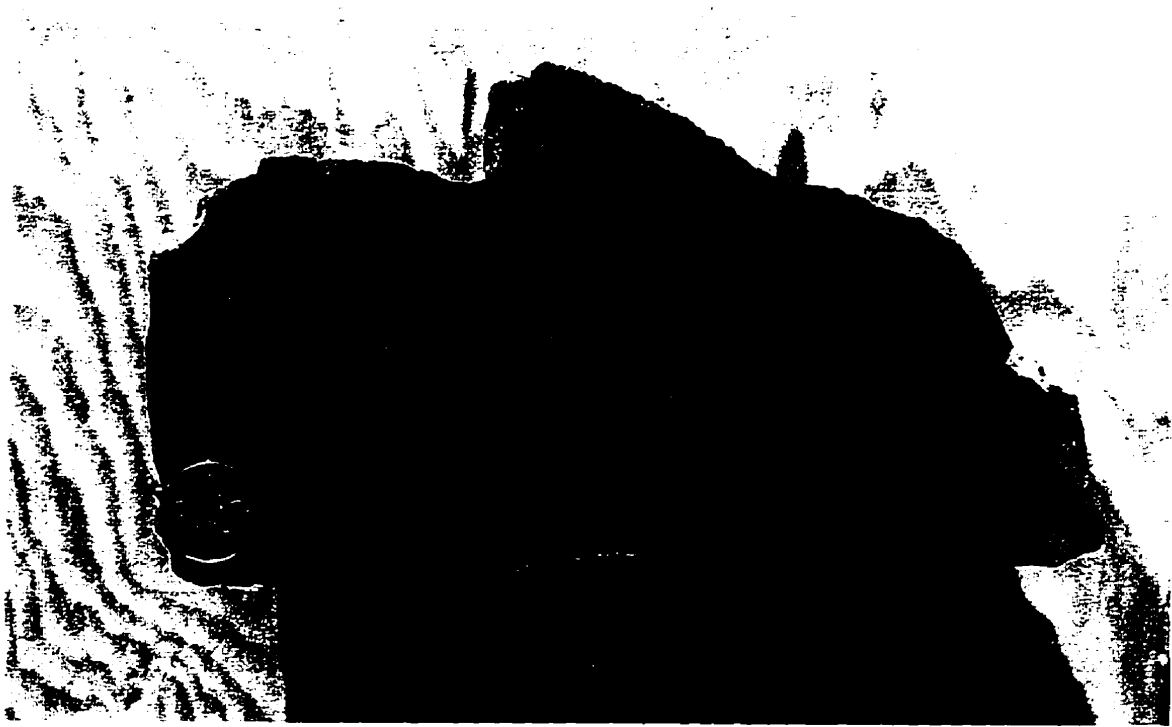


**Figure 3-26.**

*Megascopic aspects of magnetite-rich alteration-mineralization.*

**A.** Groundmass flooding of secondary magnetite and associated intense fine stockwork magnetite vein development in a sample from the adit in Cerro Colorado Norte at Bajo de la Alumbrera. The original porphyritic texture is obscured by the intense hydrothermal alteration. Later pyrite and pyrite-chalcopyrite veins cut the sample.

**B.** Strong development of sheeted quartz-magnetite veins from the core of Bajo las Pampitas. the original constituents have been completely replaced and this rock is now composed entirely of quartz and magnetite .



alteration with the potassic alteration event (*cf.* Perelló *et al.*, 1995; Arancibia and Clark, 1996). At Bajo de Agua Tapada, Suchomel (1985) also assigned hydrothermal magnetite alteration to the potassic alteration event, even though magnetite-quartz represented the bulk of the "potassic alteration". At Bajo el Durazno (Figs. 3-3 and 3-25), Allison (1986) documents magnetite alteration as an early, core, alteration assemblage that developed simultaneously with potassic and biotitic assemblages, all of which were considered to be related to Cu-Au mineralization. Elsewhere in the district, quartz-magnetite alteration is significant at Bajo de San Lucas, where potassic alteration is marked predominantly by the development of secondary biotite, and hydrothermal potassium feldspar has not been observed in thin section. At Bajo las Pampitas, strongly-developed, sheeted quartz-magnetite veins underlie the north slope of the central rhyodacitic porphyry stock. This is the most intense zone of magnetite-quartz alteration (fig. 3-26) observed in the Farallón Negro district. Secondary biotite is limited and no hydrothermal K-feldspar was observed in this study, although Sillitoe (1973) reports secondary biotite and K-feldspar as common constituents of the potassic zone at Bajo las Pampitas.

In the porphyry systems at Farallón Negro, it appears that "true" potassic alteration, normally characterized by the presence of K-feldspar (Meyer and Hemley, 1967; Lowell and Guilbert, 1970; Gustafson and Hunt, 1975; Beane, 1982), is volumetrically significant only at Bajo de la Alumbrera. Moreover, the relative volumes of magnetite-quartz *versus* K-silicate-bearing assemblages at the other porphyry centres suggest that Fe-metasomatism was overall more important than K-enrichment. The spatial and temporal relationships between Cu-Au mineralization and potassic alteration

assemblages observed at Bajo de la Alumbrera may suggest that the overprinting of an initial magnetite-quartz assemblage by a potassic assemblage is a necessary process in the formation of economic porphyry Cu-Au deposits in the Farallón Negro region.

## **Relationship between porphyry Cu-Au and epithermal Au-Ag mineralization at Farallón Negro**

### ***Background***

In Sillitoe's (1973) paper addressing the characteristic features of the "tops" and "bottoms" of porphyry Cu deposits, the relationships between porphyry Cu deposits and epithermal precious metal deposits are explored, with a strong reliance on the geology and chronology of the Farallón Negro deposits.

Porphyry deposits are considered to be related to intrusions which are normally located beneath a comagmatic pile, which is transected by a column of hydrothermal alteration representing the upper portions of the porphyry copper system. In such deposits, disseminated or stockwork Cu ( $\pm$  Au  $\pm$  Mo) mineralization is associated with an intrusive stock emplaced at depths greater than 2 km. Epithermal Cu, Pb, Zn and precious-metal mineralization is considered to represent a peripheral and late-stage co-product of porphyry Cu development. Epithermal deposits are generated at relatively shallow crustal depths, probably less than 1.5 km, typically in sub-aerial volcanic terranes.

Two broad categories of epithermal deposits are widely recognized (Bonham, 1986; Heald *et al.*, 1987; White and Hedenquist, 1990), viz.: high sulphidation / acid-sulphate; and low sulphidation / adularia-sericite. These are defined on the basis of



mineralogical relationships, which imply generation from two very different fluids, respectively strongly acid and nearly-neutral. A strong temporal and genetic connection between porphyry and epithermal deposit types is increasingly revealed by geological research (*e.g.*, Sillitoe, 1989a; Perelló, 1994; Arribas *et al.*, 1995; Losada-Calderón and McPhail, 1996; this study). High-sulphidation type gold deposits are commonly located above mineralized porphyry-hosting stocks whereas low-sulphidation type deposits tend to occur distally.

### ***Examples***

Sillitoe (1989a), elaborating on the relationships he outlined in 1973, presents a detailed description of the relationships between porphyry-style and epithermal-style mineralization in the Western Pacific island arcs. He describes a sub-class of the low-sulphidation epithermal deposit type, common amongst Philippine deposits, in which sericitic alteration of the wall-rocks is much more intense than the adularia-sericitic alteration assemblages of typical low-sulphidation deposits. Deposits of this sub-class possess a more intimate spatial relationship with intrusive rocks, commonly porphyry Cu-bearing stocks, than that exhibited by adularia-sericite type deposits elsewhere in the Pacific island arcs, possibly indicating formation at greater depths. The low-sulphidation vein system at Farallón Negro - Alto de la Blenda shares characteristics with this class of deposits.

Telescoping is common in the deposits of the Western Pacific island arcs. Rapid erosion of overlying volcanic rocks during the life of the magmatic-hydrothermal systems

resulted in the displacement of mineralized stocks much nearer the paleo-surface at the time of late-stage epithermal gold deposition than when they were emplaced. Sillitoe (*op. cit.*) documents a very narrow time interval between porphyry Cu-related K-silicate alteration assemblages and associated low-sulphidation epithermal mineralization (*e.g.*, 0.2 m.y. at Ladolam, Papua New Guinea).

Perelló (1994) documents similar, albeit more protracted, temporal relationships for the Tombulilato district, North Sulawesi, Indonesia. Porphyry Cu-Au mineralization, associated typically with magnetite-bearing K-silicate assemblages, was emplaced in the district between 2.93 and 2.36 Ma. Associated overlying high-sulphidation epithermal Cu-Au-Ag and peripheral low-sulphidation Au-Ag mineralization was emplaced within 1 - 2 m.y. of the porphyry event. Continuous syn-mineralization uplift and erosion are envisaged to have been responsible for telescoping of the systems. Arribas *et al.* (1995) argue for a genetic relation between the Far Southeast porphyry Cu-Au and the Lepanto high-sulphidation Cu-Au epithermal deposits in northern Luzon, Philippines. On the basis of the intimate spatial association between the two deposits, the identical ages on K-silicate alteration minerals and alunite associated with the epithermal system, and the abbreviated duration of hydrothermal activity, they invoke a model in which the two deposit types evolved from a single magmatic-hydrothermal system, thus implying a magmatic source for the metals in the epithermal deposit.

In Chile, Vila and Sillitoe (1991) briefly describe the overprinting of high-sulphidation epithermal mineralization on porphyry-style stockworks in deposits of the Maricunga Belt (*e.g.*, Marte and La Pepa), but the geochronological database is

insufficient to evaluate the precise temporal relationships. Preliminary results from the Ph.D. research of John Muntean at Stanford University suggests that both deposit-types were emplaced within a restricted period of time (J. Muntean, pers. comm., 1997).

Colley *et al.* (1989) suggest a cogenetic origin for the contiguous low-sulphidation Silica del Hueso (El Hueso) epithermal and Potrerillos porphyry Cu-Au deposits, northern Chile. This observation is supported by the similar ages of the deposits, the downward extension of sub-vertical, gold-bearing, silicified zones into the Potrerillos deposit and the interpreted location of the Silica del Hueso deposit topographically and structurally above the porphyry deposit after restoration along a local thrust fault. Losada-Calderón and McPhail (1996) conclude that the Nevados de Famatina Cu-Mo-Au porphyry and La Mejicana Cu-Au high-sulphidation epithermal deposits are transitional and genetically-related. The epithermal mineralization is located peripherally to the porphyry mineralization. Detailed mineralogical, fluid inclusion, stable isotope and thermodynamic modelling studies reveal almost identical conditions of formation for late-stage porphyry-related veins and the deeper-level veins of the epithermal system, suggesting a common, magmatic, fluid source. Porphyritic dacites and rhyodacites of the Mogote Formation were emplaced at 5.0 Ma during the uplift of the Famatina Ranges (McBride, 1972; Losada-Calderón *et al.*, 1994). Quartz-sericite alteration assemblages were dated at 4.0 Ma in the porphyry system, broadly contemporaneous with the emplacement of epithermal mineralization at La Mejicana at 3.6 Ma.

### ***Farallón Negro District***

The spatial relationships described between porphyry and epithermal deposits in other districts are maintained at Farallón Negro. High-sulphidation epithermal systems are clearly observed overprinting porphyry-style mineralization at Agua Rica, and possibly overlie deeper porphyry systems at Cerro Atajo and Capillitas. Low-sulphidation epithermal veins at Farallón Negro - Alto de la Blenda are located peripherally to the Bajo de la Alumbrera porphyry Cu-Au deposit. Given the lack of detailed geochemical studies on the deposits, no clear genetic relationships can be postulated, but the spatial and temporal relationships strongly suggest a genetic link between the deposit types.

The greatest geochronological detail is available for the Agua Rica deposit. Porphyry Cu-Mo-(Au)-related potassic alteration assemblages dated at 6.29 Ma are clearly seen to be overprinted by phyllic alteration assemblages dated at 6.10 Ma. Uplift and erosion of the porphyry deposit resulted in the telescoping of mineralizing environments and the superposition of high-sulphidation epithermal mineralization at 5.35 Ma. Epithermal mineralization which appears to be transitional between high- and low-sulphidation types at Capillitas is interpreted to have accompanied dacitic dyke emplacement at 5.16 Ma. Sericitic assemblages at Cerro Atajo are dated at 5.45 and 5.11 Ma. These dates suggest that epithermal mineralization, at least in the eastern mineralized centres, was a late-stage event in the evolution of the Volcanic Complex.

Porphyry Cu-Au and low-sulphidation epithermal mineralization within the main body of the Farallón Negro Volcanic Complex appears to be older than that documented for the peripheral deposits. Phyllic alteration at Bajo de la Alumbrera is dated at 6.75 Ma

and appears to have been followed very shortly by the emplacement of the Farallón Negro - Alto de la Blenda vein system at 6.55 Ma. I would argue that the Farallón Negro - Alto de la Blenda vein system may represent a member of the sub-class of low-sulphidation epithermal deposits postulated by Sillitoe (1989a), which apparently form at a greater depth than typical low-sulphidation epithermal deposits. The absence of high-sulphidation epithermal mineralization in the volcanic lithologies of the Farallón Negro Volcanic Complex proper may be due to the level of erosion of the complex: any high-sulphidation epithermal deposits which may have formed have not been preserved. Further, the apparent tectonic stability of the Main Farallón Negro Stratovolcano precluded the catastrophic uplift documented in the surrounding regions (*e.g.*, at Agua Rica in the Aconquija range) and the subsequent superposition of porphyry Cu and epithermal environments.

## CHAPTER 4

### PETROLOGY AND WHOLE-ROCK GEOCHEMISTRY OF THE FARALLON NEGRO VOLCANIC COMPLEX.

The igneous rocks of the Farallón Negro-Capillitas district exhibit compositions ranging from basalt to rhyolite and, as was tentatively proposed by Caelles (1979) and Dostal *et al.* (1977), can be divided into calc-alkaline and shoshonitic suites on the basis of geochemical data, employing the  $K_2O$  vs.  $SiO_2$  diagram of Peccerillo and Taylor (1976).

The shoshonitic suite includes volcanic units which are predominantly mafic-to-intermediate in composition and are largely indistinguishable from the calc-alkaline suites on the basis of macro- or microscopic observations. High-K calc-alkaline rocks predominate in the district, with volcanic units ranging from basaltic flows to dacitic pyroclastics, and hypabyssal intrusive bodies ranging from basaltic dykes to rhyolitic plugs. The high-K calc-alkaline units constitute the greater part of the Main Farallón Negro Stratovolcano.

In this chapter, geochemical criteria are developed for the distinction of the shoshonitic and calc-alkaline rocks. Thirty-nine representative rock samples were analyzed for 10 major elements and 21 minor or trace elements. Fifteen of these were selected for further trace element and rare-earth element (REE) analysis. Petrographic studies were performed on these samples. The igneous suite is herein compared to selected regional volcanic suites and the Farallón Negro shoshonitic suite is discussed in relation to comparable suites in other segments of the Central Andes.

Definition of the nature and petrochemical relationships of the Farallón Negro rocks is critical both to petrogenetic modelling of this step of Central Andean evolution

and to clarification of metallogenetic relationships.

### **Previous Work**

The major and minor element geochemistry of the Farallón Negro Volcanic Complex has been investigated in several previous studies (*viz.* Dostal *et al.*, 1977; Caelles, 1979; Stults, 1985; Suchomel, 1985; Allison, 1986). Dostal *et al.* (1977) observed that the rocks from the Farallón Negro area exhibit geochemical features characteristic of the shoshonite suite (*e.g.*,  $K_2O:Na_2O$  ratios close to unity). The generally high  $K_2O$  contents of the rocks were considered to represent part of a chemical zonation involving broadly increasing magmatic potassium content with increasing distance from the trench and with greater depth to the Wadati-Benioff zone. Dostal *et al.* (*op. cit.*) concluded that the Farallón Negro volcanic rocks constitute part of an evolutionary trend associated with long-lived subduction-related magmatic activity. This model was based largely on the major element chemistry, in the absence of systematic changes observed in the trace or REE patterns. However, Dostal *et al.* (*op. cit.*) noted that the limited REE data for the Farallón Negro rocks were comparable to those of shoshonites from Fiji (Gill, 1970) and New Guinea (Jakeš and Gill, 1970). Caelles (1979) reported whole-rock analyses of 10 samples from the Farallón Negro area. He concluded that the Farallón Negro Volcanic Complex consisted predominantly of high-K calc-alkaline andesites with minor high-Al basalts and dacites (after the classification of Taylor, 1969).

Suchomel (1985) presented nine partial whole-rock analyses. He noted that the high  $K_2O:Na_2O$  ratios, in combination with relatively low  $SiO_2$  contents, are suggestive

of alkalic or shoshonitic affinities. However, he emphasized the mineralogical differences with respect to "typical" shoshonites, namely greater modal hornblende, biotite and quartz, accompanied by an absence of modal sanidine and olivine. Suchomel (*op. cit.*) concluded that the Farallón Negro rocks probably represent a suite that is transitional between high-K calc-alkaline and shoshonitic.

Stults (1985) also remarked on the high K and total-alkali contents of the Farallón Negro rocks. Analyses of eight samples were presented, in partial duplication of Suchomel's (1985) data. Using the classification scheme of Joplin (1968), he concluded that, although some of the Farallón Negro rocks could be included within the shoshonite group, most of the rocks of the complex are of calc-alkaline affinity. He observed that the intrusive rocks have chemical and mineralogical parameters typical of I-type granitoids, specifically the presence of modal hornblende and titanite. The moderate or high magnetite content places the Farallón Negro rocks firmly in Ishihara's magnetite series (Ishihara, 1981). Stults (1985) emphasizes that porphyry Cu mineralization at Farallón Negro conforms with a worldwide correlation of Cu mineralization with I-type, magnetite series granitoids.

In Allison (1986), data for 16 samples (including those presented by Stults (1985 and Suchomel (1985)), as well as data from Caelles (1979), form the basis for a detailed discussion of Farallón Negro petrochemistry. She notes the high potash and relatively high total-alkali contents of the rocks, and emphasizes the chemical similarities between Farallón Negro rocks and worldwide shoshonites. While she suggests that the Farallón Negro rocks may be transitional between high-K calc-alkaline and shoshonite suites, she



concludes that the high potash contents, the  $K_2O:Na_2O$  ratios, minor element geochemistry and normative mineralogies favour a shoshonitic classification.

Two additional whole-rock analyses of samples from Farallón Negro are presented in Kay *et al.* (1988) in a discussion of regional patterns of Neogene magmatic chemistry in Chile and Argentina.

### **Analytical Techniques**

Major and trace elements for 38 samples (*i.e.*, all except FAR 201) were analyzed by inductively-coupled plasma emission spectrometry (ICP) for 35 elements, by atomic absorption (AA) for Rb and by titration for FeO (ACME Analytical Laboratories Ltd., Vancouver, B.C.), following the procedures outlined by that company. Sample FAR 201 was analyzed for major elements by X-ray fluorescence (XRF) on fused glass beads at the Department of Earth Sciences, Memorial University of Newfoundland (M.U.N.). Fifteen of the above whole-rock specimens were selected for further trace element (30 elements including REE) analysis by inductively-coupled plasma mass spectrometry (ICP-MS) at M.U.N.

The following discussion of the geochemistry of igneous rocks at Farallón Negro incorporates analyses recorded by Dostal *et al.* (1977), Caelles (1979), Allison (1986) and Kay *et al.* (1988). In the work of Dostal *et al.* (1977) major and trace elements (Rb, Sr, Ba and Zr) were analyzed by XRF. Ni, Co, Cr and V were analyzed by emission spectroscopy and REE were determined by instrumental neutron activation (INA). In Caelles (1979), major elements were analyzed by XRF and trace elements were

determined by emission spectroscopy by the author at Queen's University, Kingston, Ontario. Of the samples documented by Allison (1986), nos. AA-1, AA-2, AA-4, AA-5, AA-7, AA-8, AA-12, AA-13, AA-14, AA-15 and AA-16 were analyzed in Mendoza, Argentina, by the Dirección General de Fabricaciones Militares. SiO<sub>2</sub> was determined by gravimetry, P<sub>2</sub>O<sub>5</sub> by colorimetry and the balance of elements by atomic absorption spectroscopy. Samples AA-3, AA-6, AA-9 and AA-10 were analyzed in Tucson, Arizona by Skyline Labs Inc. using AA; FeO was determined by titration. Kay *et al.* (1988) analyzed major elements by electron microprobe on glasses fused from rock powders. Rb and Sr were determined by XRF. All remaining trace elements were analyzed by INAA. All analyses were carried out at Cornell University, Ithaca, New York.

Discrepancies among the various analytical techniques may account for scatter in some of the data.

### **Presentation of Data**

New geochemical data for 39 samples from the Farallón Negro area are presented in the appendices at the end of this thesis. Appendix B includes: a table of analyzed samples with their geographical coordinates (where available; Table B-1) and a sample location map; a table of whole-rock analyses in order of increasing sample number (Table B-2); a table of the extended trace element analyses (Table B-3); and a table of whole-rock analyses organized by rock-type for ease of group comparison (Table B-4). Appendix C includes normative data. Appendix D presents duplicate analyses for selected samples and an international standard. Previously published partial whole rock-analyses (Dostal

*et al.*, 1977; Caelles, 1979; Allison, 1986; Kay *et al.*, 1988) are presented in Tables E-1 to E-4 in Appendix E; these data have been included in the diagrams presented in this chapter. Appendix F comprises petrological descriptions of the samples, presented in a series of tables organized by rock-type. Samples were considered "fresh" if LOI (loss on ignition) was < 5 wt % (D. Müller, pers. comm., 1995; Müller and Groves, 1995). Altered samples (FAR 206, 309, 310, 312 and 337) are not included in diagrams. Because LOI was not reported in the previously published analyses, it was impossible to estimate the degree of alteration of the samples. All samples have been included in the diagrams, but alteration may account for some of the scatter observed in the trends.

### **Chemical Classification**

The  $K_2O + Na_2O$  vs.  $SiO_2$  ("TAS") plot (Irvine and Barager, 1971; Fig. 4-1) indicates that the igneous rocks at Farallón Negro are dominantly of sub-alkaline affinity. Several samples which plot within the alkaline field are those analyzed in other studies. Several of the samples presented in Dostal *et al.* (1977), Caelles (1979) and Allison (1986) exhibit anomalously high  $Na_2O$  contents (see Fig. 4-4), possibly accounting for the observed patterns. Sub-alkaline rocks may be assigned to two commonly recognized suites, calc-alkaline and tholeiitic, which can be distinguished on the basis of the degree of Fe-enrichment. A ternary diagram of  $Na_2O + K_2O$  (A) vs.  $FeO + 0.8998 \times Fe_2O_3$  (F) vs.  $MgO$  (M), the "AFM" diagram, is used to distinguish the two suites. This diagram (Fig. 4-2) indicates that the majority of the compositions of the analyzed samples fall in the calc-alkaline field and roughly conform to the calc-alkaline trend, although a

**Figure 4-1.**

Total-Alkalies vs.  $\text{SiO}_2$  diagram for rocks of the Farallón Negro Volcanic Complex (boundary between sub-alkaline and alkaline rocks after Irvine and Barager, 1971).

circles = this study

diamonds = Dostal *et al.* (1977)

triangles = Caelles (1979)

squares = Allison (1986)

asterisks = Kay *et al.* (1988)

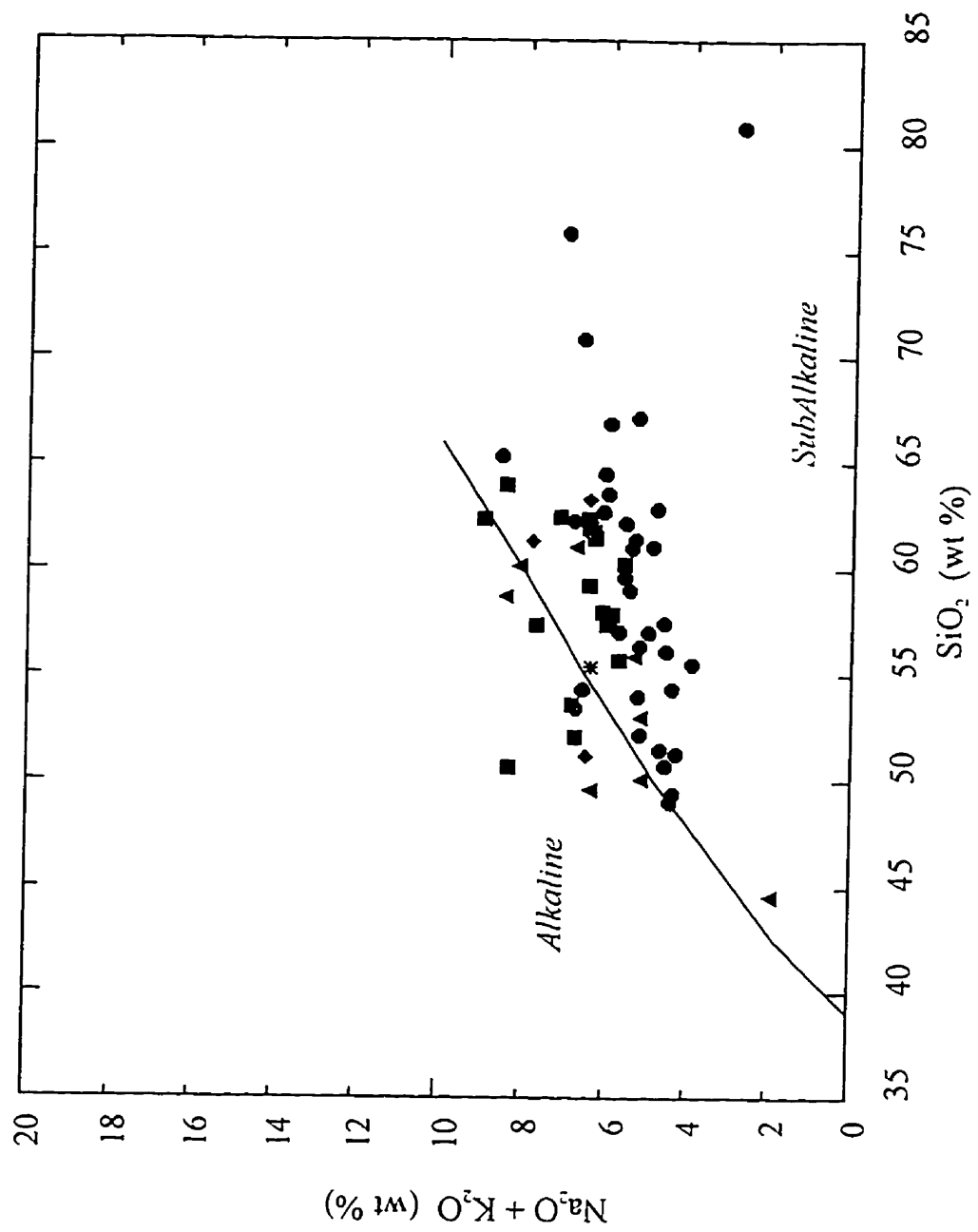


**Figure 4-2.**

AFM diagram for rocks of the Farallón Negro Volcanic Complex (boundary between tholeiitic and calc-alkaline rocks after Irvine and Barager, 1971).

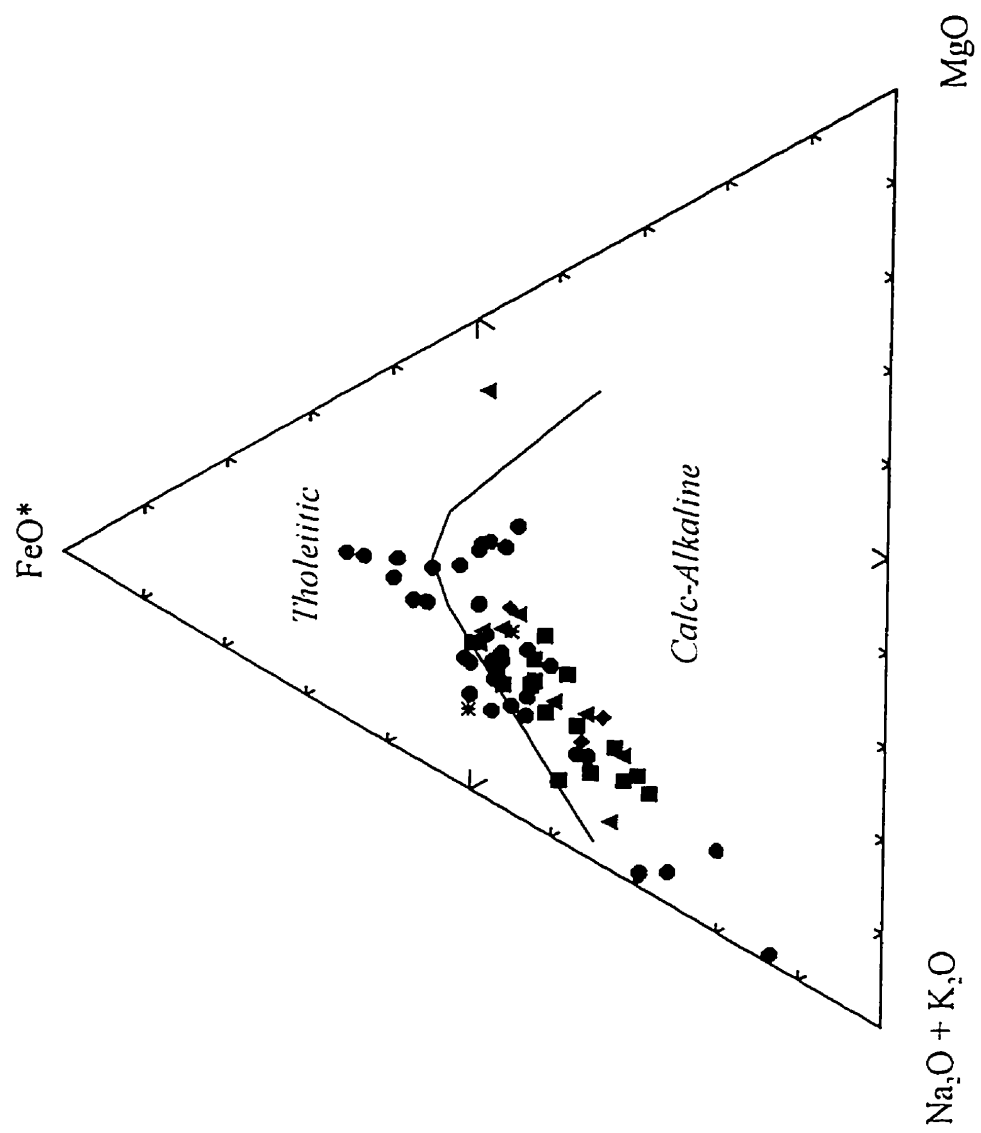
circles = this study

diamonds = Dostal *et al.* (1977)

triangles = Caelles (1979)

squares = Allison (1986)

asterisks = Kay *et al.* (1988)



significant number of samples plot in the tholeiitic field (*i.e.*, FAR 203, 207, 216, 218, 219, 222, 224, 229, 267, 302, 308 and FJ2).

## **Shoshonites**

### ***Background***

The shoshonite clan of igneous rocks was first described and defined by Iddings (1895). He observed that a series of volcanic rocks from the Absaroka Ranges of the western United States exhibits notably potassium-rich compositions in basic members and unusual mineral assemblages, including a plagioclase-alkali feldspar matrix. He proposed that these volcanic units be named the absarokite-shoshonite-banakite series, after the names of local aboriginal tribes. These concepts were further developed by Joplin (1965), who argued that such potassic volcanic rocks represent a distinct magma series which she named the *shoshonite association*. She suggested that shoshonites occur predominantly in mature (convergent margin) volcanic arcs and at greater distance from oceanic trenches than tholeiitic or calc-alkaline rocks. This relationship was documented in the Papua New Guinea Highlands by Jakeš and White (1969) and Mackenzie and Chappell (1972), in Fiji by Gill (1970) and in the Andes by Caelles *et al.* (1971) and Dostal *et al.* (1977).

Morrison (1980) defined shoshonites (*sensu stricto*) as potassic igneous rocks occurring in subduction-related tectonic settings and which can be further defined on the basis of major element chemistry. Following the formation of low-K tholeiite and calc-alkaline series, they were considered to represent a more evolved stage of arc development. They are located far inboard of the trench and at a greater height above the



Wadati-Benioff zone. Morrison (*op. cit.*) tabulated chemical criteria for the recognition of shoshonites which include: near-saturation in silica (for basalts, hypersthene and olivine in the norm); low Fe-enrichment; high total-alkalies ( $\text{Na}_2\text{O} + \text{K}_2\text{O}$ ) > 5%; high  $\text{K}_2\text{O}:\text{Na}_2\text{O}$  ratios (> 0.6 at 50 wt. %  $\text{SiO}_2$ , > 1.0 at 55 wt. %  $\text{SiO}_2$ ); low  $\text{TiO}_2$  (< 1.3 wt. %), high, but variable,  $\text{Al}_2\text{O}_3$  (14-19 wt. %); and a strong enrichment in P, Pb, LILE and LREE. Shoshonitic rocks associated with continental margins are predominantly basaltic andesites and andesites.

High-K rocks such as shoshonites have been formally incorporated in numerous classification schemes (Pecerillo and Taylor, 1976), including that recommended by the IUGS Subcommittee (LeMaitre *et al.*, 1989: used in this study).

### ***Shoshonites at Farallón Negro***

Unaltered samples from the Farallón Negro Volcanic Complex exhibit a complete range of composition from low-K calc-alkaline, through medium-K and high-K calc-alkaline, to shoshonitic (Fig. 4-3). However, the majority of the volcanic units are high-K calc-alkaline. Eighteen samples from Farallón Negro can be classified on the basis of whole-rock geochemistry as belonging to the shoshonite clan. These samples are evaluated in Table 4-1 using Morrison's (1980) criteria for shoshonite classification.

Shoshonites are considered to be distinguished petrographically by porphyritic textures with phenocrysts of plagioclase, clinopyroxene, olivine, phlogopite and/or amphiboles in a very fine-grained, commonly glassy, groundmass, consisting mainly of

**Figure 4-3.**

K<sub>2</sub>O vs. SiO<sub>2</sub> diagram for rocks of the Farallón Negro Volcanic Complex [after LeMaitre (1989) and Peccerillo and Taylor (1976)].

circles = this study

diamonds = Dostal *et al.* (1977)

triangles = Caelles (1979)

squares = Allison (1986)

asterisks = Kay *et al.* (1988)

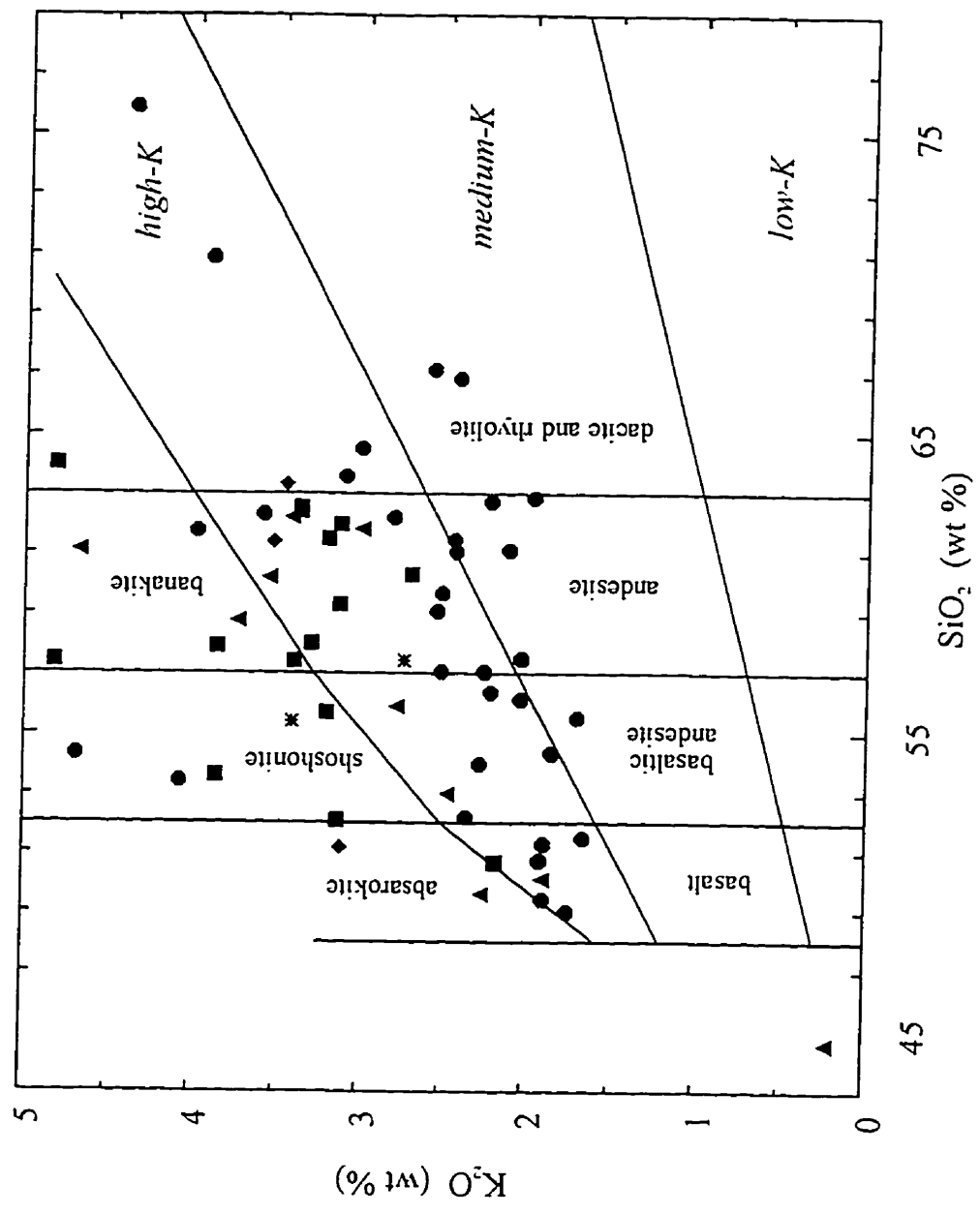


**Table 4-1.**

Classification of Farallón Negro Volcanic Complex  
Shoshonites  
(after Morrison, 1980).

\* : "enriched", indicating a concentration greater  
than the mean of the Farallón Negro  
sample population.

= : equivalent to the mean of the Farallón Negro  
sample population

plag: plagioclase; bio: biotite; hbl: hornblende

	ROCK-TYPE	Na2O + K2O	K2O/Na2O	TiO2	Al2O3	Enriched in:	K	Rb	Sr	Ba	La	Ce	P2O5	Pb
FAR 203	porphyritic plag-hbl shoshonite	6.57	2.5	1.14	16.34		*	*	=	*			*	*
FAR 205	plag-bio dacite (?)	8.57	1.59	0.39	17.07		*	*		*	*	*		*
FAR 206	plag-bio banakitic crystal tuff	5.09	1.5	0.62	14.87		*	*	*		*	*	*	
FAR 296	porphyritic plag-hbl shoshonite	6.72	1.54	0.96	17.88		*		*	*	*	*	*	*
FAR 299	porphyritic plag-bio banakite	6.38	1.66	0.61	15.89		*	*	*	*	*	*	*	*
FAR 302	glassy plag banakite	6.82	1.11	0.57	16.66		*	*	*	*		*	=	*

[illegible]

alkali feldspar (sanidine), plagioclase, and clinopyroxene (Morrison, 1980). The Farallón Negro shoshonites are generally porphyritic. Plagioclase is the dominant phenocryst phase with lesser amphibole, biotite, apatite and oxides, and rare pyroxenes, quartz and titanite in a glassy-to-trachytic-textured matrix (Appendix E). The Farallón Negro shoshonites are petrographically indistinguishable from the associated calc-alkaline units. Déruelle (1978) also noted that in the Plio-Quaternary volcanic succession of the Central Andes the shoshonitic and calc-alkaline rock associations cannot be distinguished petrographically.

The majority of the shoshonite units at Farallón Negro are extrusive. They appear to have formed early in the volcanic history of the complex: those that have been dated represent some of the oldest samples. The  $^{40}\text{Ar}/^{39}\text{Ar}$  dates cluster around 8.3 - 8.4 Ma, with the exception of sample FAR 206 which is 7.5 Ma in age. Intrusive units of shoshonitic affinity are associated with the Bajo de la Alumbraera, Bajo de Agua Tapada and Bajo el Durazno alteration-mineralization centres (Allison, 1986).

Samples FAR 203, 205 and 206 were collected along an east-west transect through the volcanic edifice along Quebrada de los Leones (Fig. 4-4). FAR 203 is stratigraphically the lowest of these, and FAR 206 the highest. These shoshonites are observed to be intercalated with high-K calc-alkaline units (*e.g.*, FAR 204 and 207). FAR 296 and 299 are samples collected south of the main volcanic complex, to the east of Vis Vis. FAR 302 was collected along the north slope of Cerro Blanco Chico near the Cerro Atajo prospect (Fig. 4-5).

Five samples of intrusive units documented by Allison (1986) belong to the shoshonite clan. Of these, AA-7 is a weakly-propylitized andesite porphyry (Suchomel,

**Figure 4-4.**

Location map for shoshonitic samples from the  
Farallón Negro Volcanic Complex.



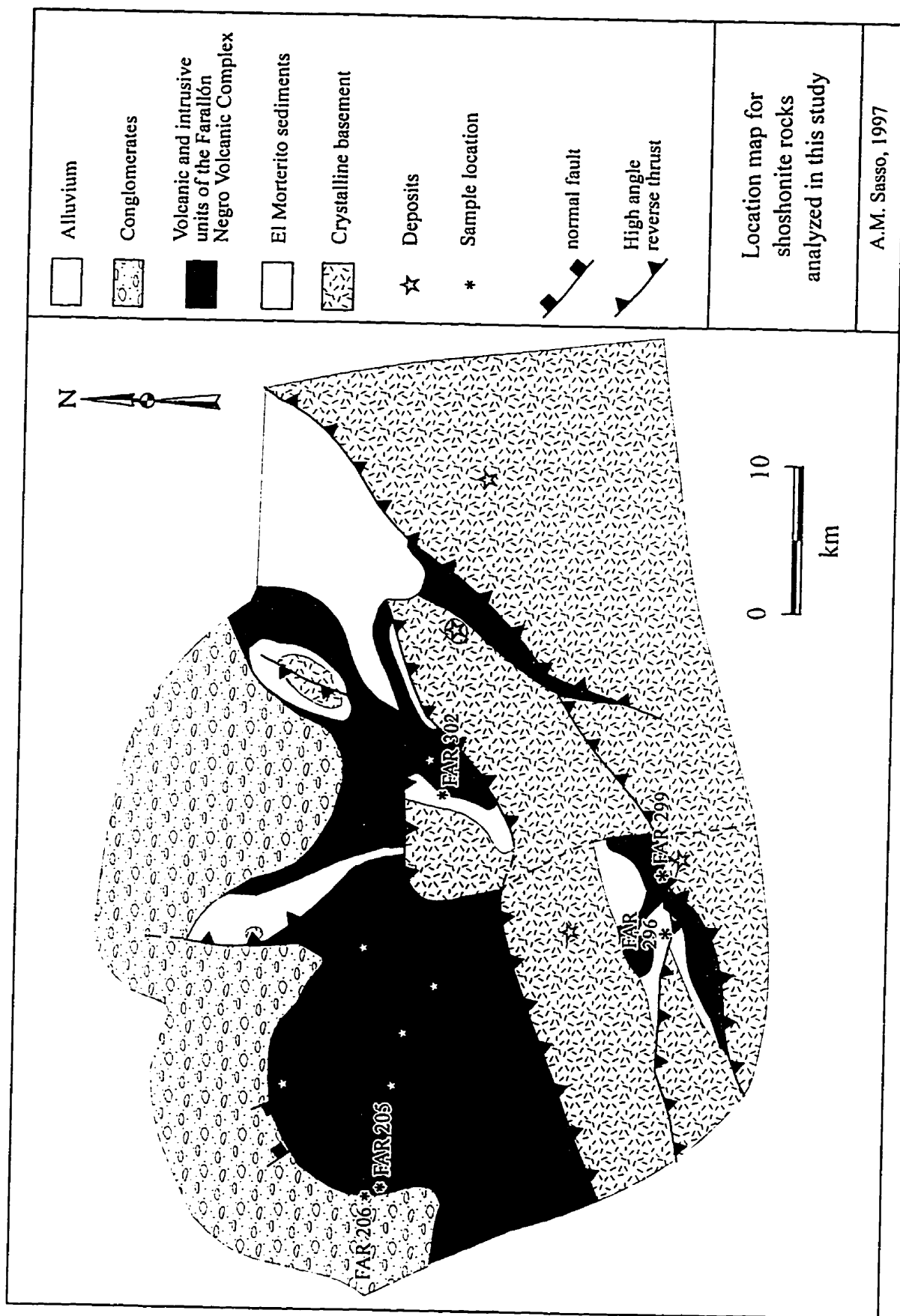


**Figure 4-5.**

Harker variation diagrams for major elements plotted  
against SiO<sub>2</sub> for Farallón Negro rocks.

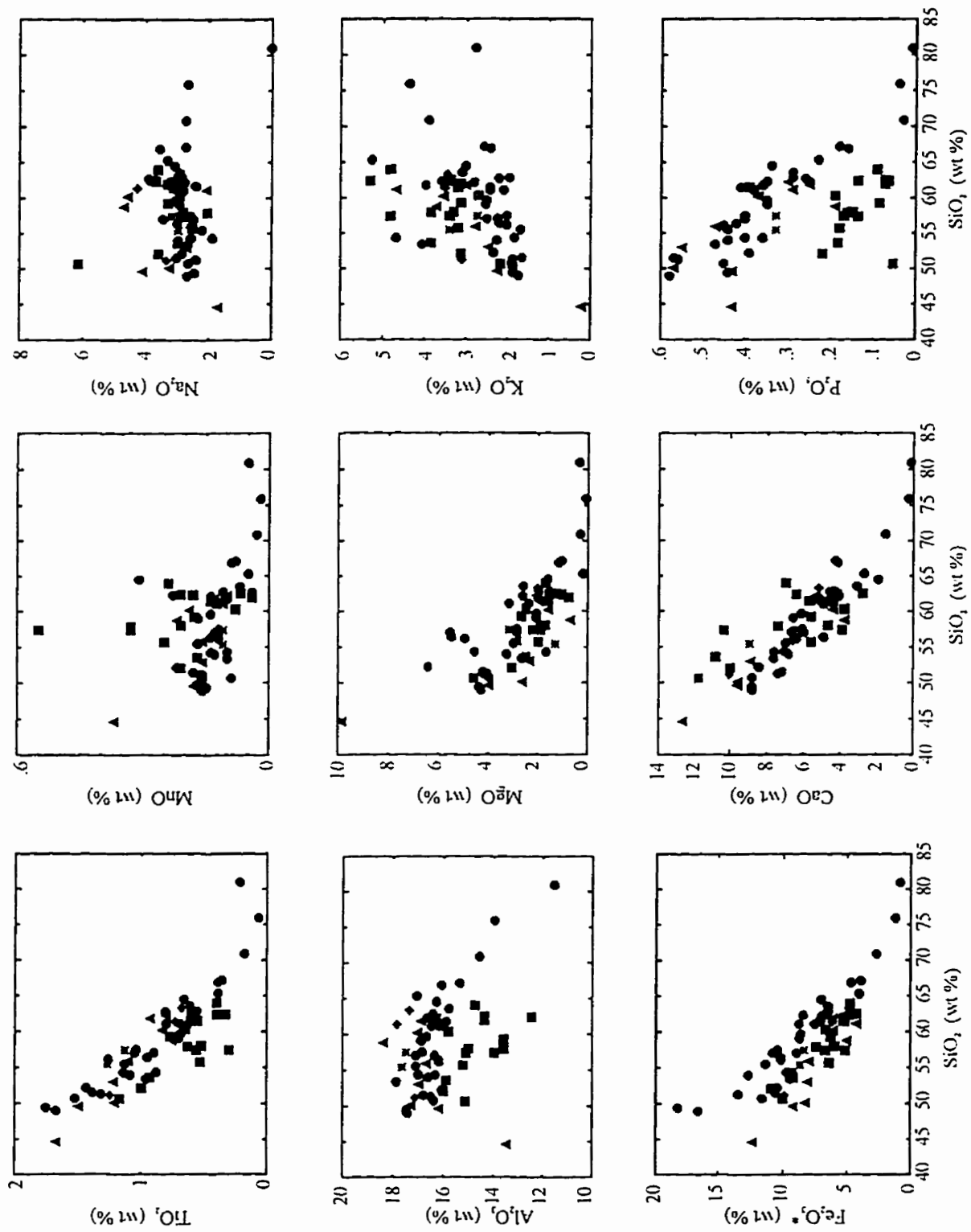
circles = this study

diamonds = Dostal *et al.* (1977)

triangles = Caelles (1979)

squares = Allison (1986)

asterisks = Kay *et al.* (1988)



1985) from Bajo de Agua Tapada, AA-15 and AA-16 are weakly-propylitized Main-Stage dacite porphyries (Stults, 1985) from Bajo de la Alumbrera and AA-9 and AA-11 are andesite porphyries from Bajo el Durazno. However the unpublished theses of Stults (1985), Suchomel (1985) and Allison (1986) do not provide detailed sample locations or descriptions, thereby rendering the structural and temporal interpretation of these samples difficult.

#### **Abundances of major and minor elements in the Farallón Negro Volcanic Complex**

As shown previously (Fig. 4-3), a plot of  $K_2O$  vs.  $SiO_2$  demonstrates that Farallón Negro suite comprise low-, medium-, and high-K calc-alkaline, as well as shoshonitic units ranging in composition from basaltic to rhyolitic.  $SiO_2$  contents vary from 44.60 to 80.94 wt. %, the highest values undoubtedly recording alteration. Covariations of major elements with  $SiO_2$  are displayed in the Harker diagrams of figure 4-5. Most elements form coherent linear trends which might indicate either magma mixing or fractional crystallization. The exceptions are  $Na_2O$  and  $K_2O$  which plot in a scattered fashion, and  $MgO$  which shows minor scatter.  $TiO_2$ ,  $Al_2O_3$ ,  $Fe_2O_3^*$ ,  $MnO$ ,  $MgO$ ,  $CaO$  and  $P_2O_5$  all decrease with increasing silica, whereas  $K_2O$  increases. This would be consistent with the fractionation of plagioclase, pyroxenes and Fe-Ti oxides with apatite. Some of the scatter in the observed trends is due to what appear to be systematic differences in element concentrations at a given  $SiO_2$  content in some of the data presented by Allison (1986).  $TiO_2$ ,  $Al_2O_3$ ,  $Fe_2O_3^*$  and  $P_2O_5$  from her database are all systematically lower than in the rest of the sample population. Some anomalously high concentrations of  $Na_2O$  are also

noted in Caelles' (1979) analyses, while his sample JC-34A demonstrates radically different MgO and CaO contents from any other Farallón Negro sample analyzed.

Harker diagrams for minor and trace elements are displayed in figure 4-6. Of the "K-group" (usage after Matthews *et al.*, 1994) elements, Rb shows a broadly increasing trend with increasing SiO<sub>2</sub> while Ba and Sr plot in a scattered fashion. The "compatible group" elements, Sc, Co, and V, show decreasing trends. V decrease is interpreted as evidence for magnetite fractionation (Garcia and Jacobson, 1979). Cr and Ni are scattered, Cr ranging from 2 to 88 ppm and Ni from 7 to 41 ppm. The chalcophile elements, Cu and Zn, demonstrate broadly decreasing trends with SiO<sub>2</sub>, although there is abundant scatter in the Cu vs. SiO<sub>2</sub> plot. The "Ti-group" elements Nb and Zr show no distinguishable trends. Of the "Th-group" elements, Th shows a weak increasing trend whereas Pb is scattered. Among the rare earths, La and Ce exhibit scattered patterns but Y decreases with SiO<sub>2</sub> content.

"Primary" magmas are those which have compositions which are considered to be in equilibrium with a mantle peridotite source. Relatively undepleted, but not primary, magmas are defined as "primitive". There are no absolute criteria for the definition of "primitive" magmas except that they represent the most likely parental compositions in a suite of mafic rocks (*i.e.*, the least depleted in compatible elements). High levels of Mg, Cr and Ni are generally interpreted to be indicative of more primitive compositions. Sample JC-34A (see above) is an alkali-olivine basalt unit which has the most primitive composition recorded at Farallón Negro. It is markedly K-poor (K<sub>2</sub>O = 0.21 wt. %). The stated sample location (27° 21' N; 66° 37' W; Caelles, 1979) is to the north of Bajo de

**Figure 4-6.**

Harker variation diagrams for minor elements plotted  
against  $\text{SiO}_2$ .

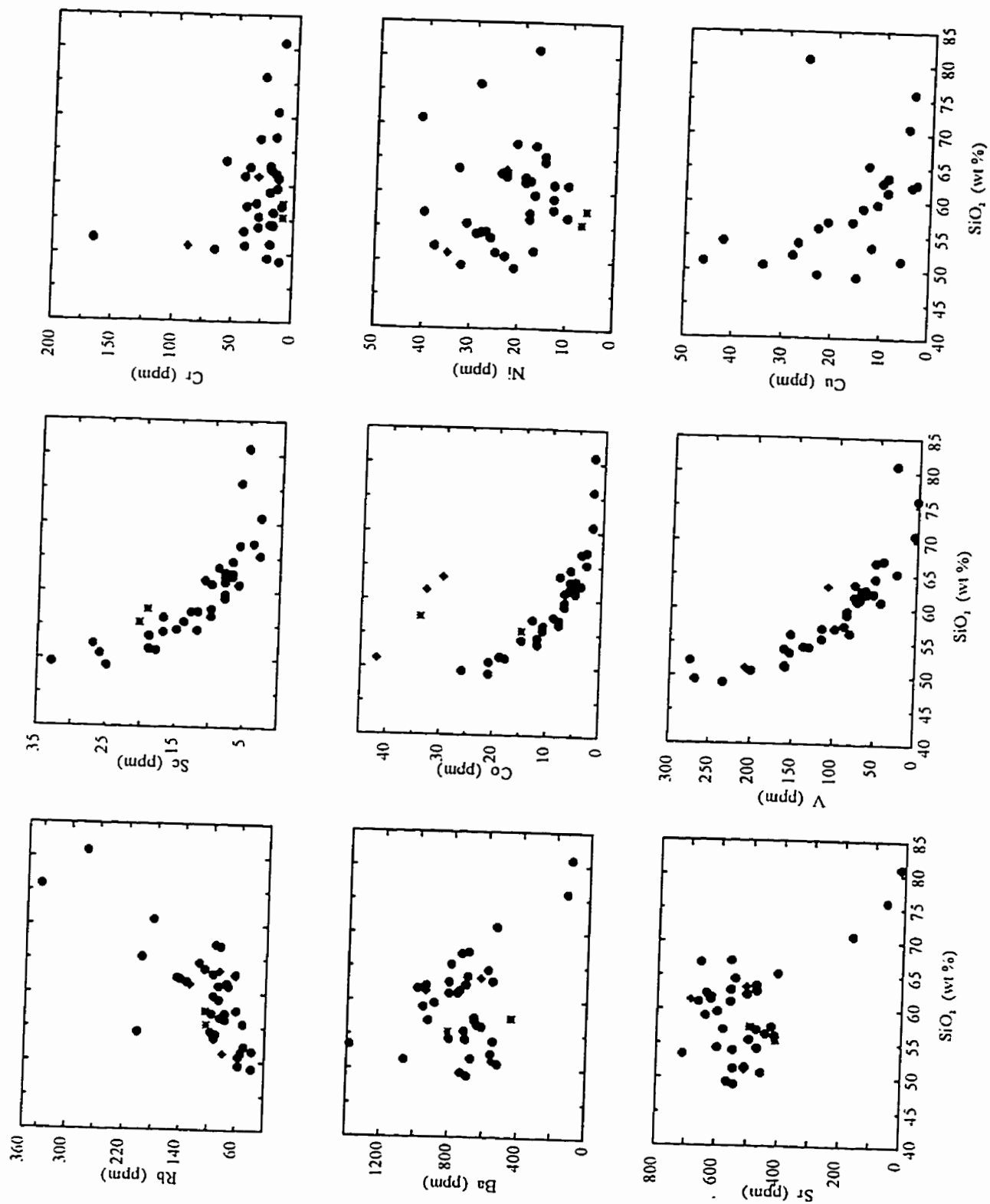
circles = this study

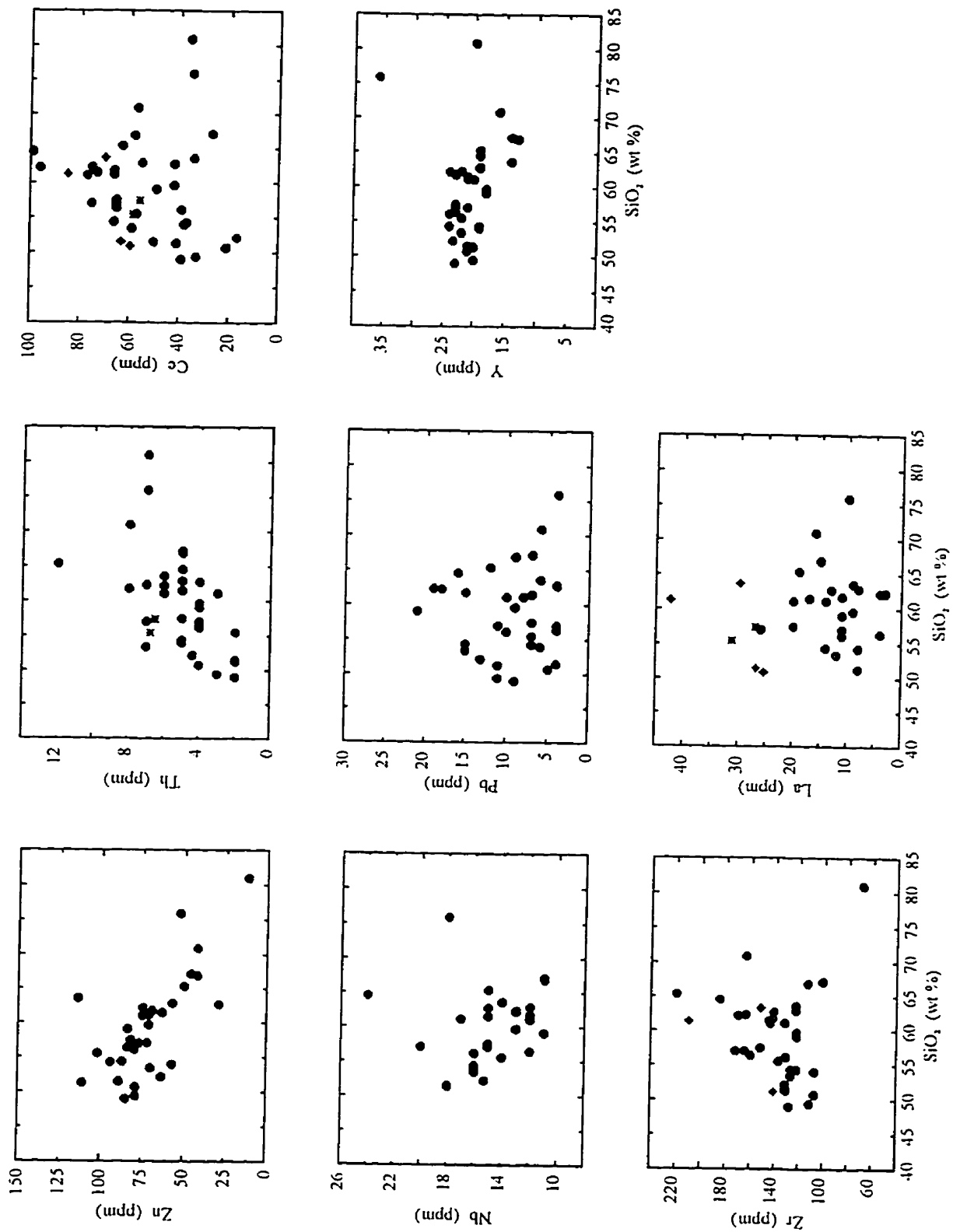
diamonds = Dostal *et al.* (1977)

triangles = Caelles (1979)

squares = Allison (1986)

asterisks = Kay *et al.* (1988)







la Alumbreira. FAR 201, a high-K basaltic andesite, represents the most primitive composition (*i.e.*, highest Cr, Ni and Mg) among those analyzed in this study. However, this composition does not approach those suggested as either primary (Swinamer, 1989) or primitive (Wasteneys, 1990). It represents the oldest mapped flow at Bajo de la Alumbreira and is the oldest dated sample at Farallón Negro. The spatial and temporal relationships between the two above samples are unknown.

CIPW norms for samples at Farallón Negro are presented in Appendix B. A uniform ratio for  $\text{Fe}_2\text{O}_3/\text{FeO}$  of 0.25 was adopted in the norm calculations because ferric and ferrous iron were not determined separately for all rocks. The norm calculation is particularly sensitive to the oxidation state of iron, but no consensus on standard procedure has been achieved. Brooks (1976) suggested standardizing the analyses of basaltic rocks at an  $\text{Fe}_2\text{O}_3/\text{FeO}$  ratio of 0.15, whereas Middlemost (1989) proposed employing a range of oxidation ratios for volcanic rocks drawn from the literature. This study implies that an average ratio of 0.35 may be appropriate for rocks of Farallón Negro composition. Cox *et al.* (1979) suggest choosing the ratio of the least oxidized sample from a suite and adjusting the rest of the database to this value. The absence of reported values for MnO and  $\text{P}_2\text{O}_5$  in the data of Dostal *et al.* (1977) skews the norm calculations of those samples.

All but 10 of the samples are hypersthene-normative, and the majority of these are silica-oversaturated, containing quartz in the norm. Déruelle (1978; Table 4-1) cited normative hypersthene as a characteristic of Andean shoshonitic lavas. Seven samples, the majority of which are absarokites, are forsterite-normative. Four of these samples (JC-30;

AA-1; AA-4; and, AA-5) are silica-undersaturated and contain both olivine and nepheline in the norm. JC-34A is the sole silica-saturated rock, with olivine and hypersthene in the norm.

#### **Incompatible element (including REE) signatures at Farallón Negro**

"Spider diagrams" (usage after Rollinson, 1993) of incompatible elements for 15 samples from Farallón Negro are presented in figures 4-7 and 4-8. Analyses were normalized to mid-ocean ridge basalt (MORB) using standard values suggested in the *Newpet* software package from the Department of Earth Sciences, Memorial University of Newfoundland (1992). Enrichment is observed in the large-ion lithophile elements (LILE: Cs, Rb, Ba, Th). Cs is highly variable. LILE are strongly partitioned into the first melt increments during small degrees of partial melting. Among the high-field-strength group of elements (HFSE: Ti, Y, Zr, Nb, Hf), strong negative anomalies are observed for Hf, Zr and Ti, and a weaker negative anomaly for Nb. Light rare earth elements (LREE: La, Ce, Nd) are enriched at Farallón Negro. These elements are mantle-incompatible and are preferentially enriched in the first melt increments during low degrees of partial melting. The middle rare earth elements (Sm, Eu, Gd, Dy) exhibit relatively flat trends, although a slight enrichment relative to the heavy rare earths (HREE; Er, Yb, Lu, Y) may reflect the involvement of hornblende as a crystallising phase. The HREE exhibit weakly-fractionated (flat) trends.

Differences in the spider diagram patterns exhibited by the high-K calc-alkaline and shoshonitic series rocks at Farallón Negro are negligible. In general, the shoshonitic

**Figure 4-7.**

"Spider diagram" for High-K Calc-Alkaline Series Units  
at Farallón Negro.

[MORB normalisation as per *Newpet* Software - MUN  
1992. Normalisation factors: Cs (0.013), Rb (1.12), Ba  
(14.3), Th (0.185), U (0.075), K (955), Nb (3.58), La  
(3.96), Ce (11.97), Sr (122), Nd (10.96), Hf (2.87), Zr  
(90), Sm (3.62), Eu (1.31), Ti (9000), Gd (4.78), Dy  
(5.98), Y (34.2), Er (3.99), Yb (3.73), Lu (0.56)]

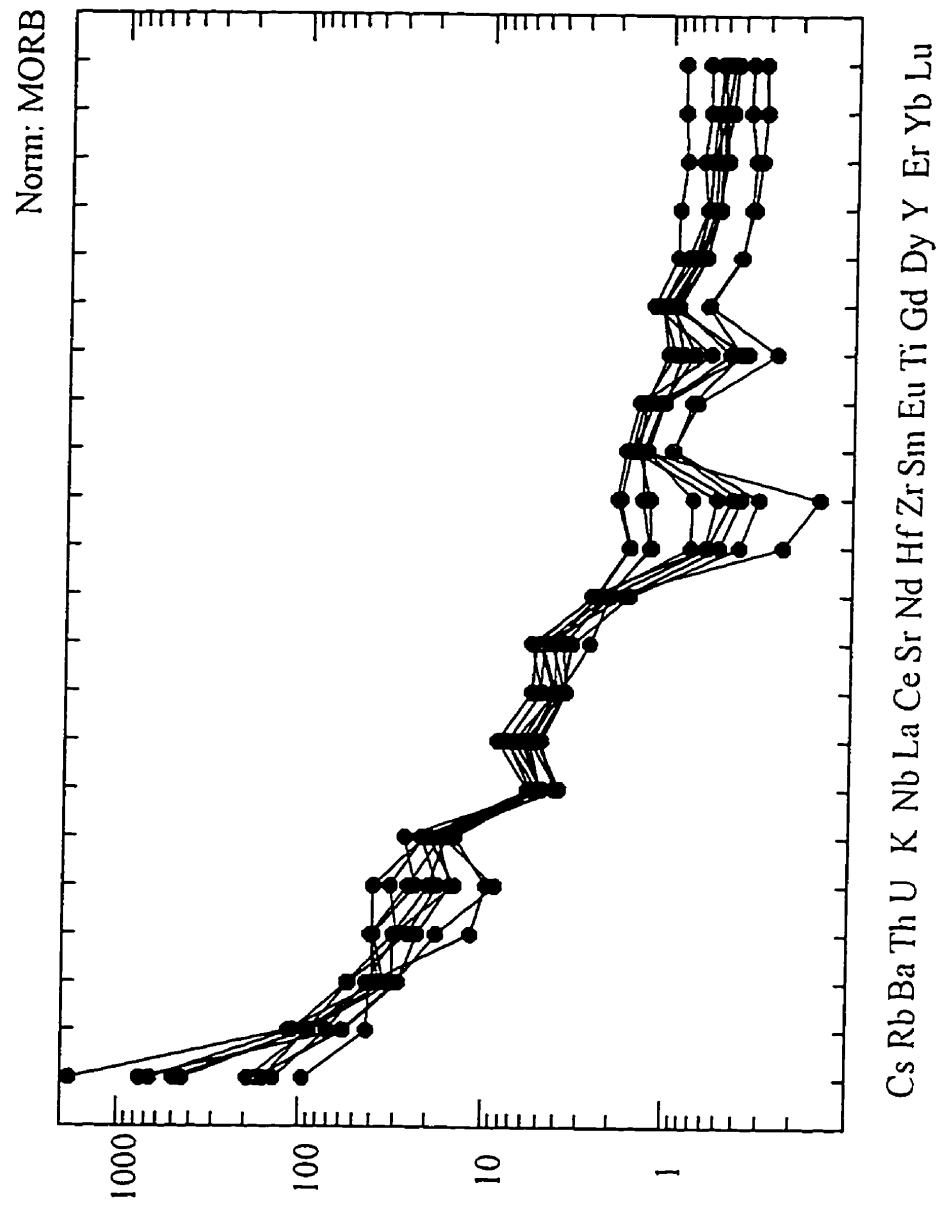
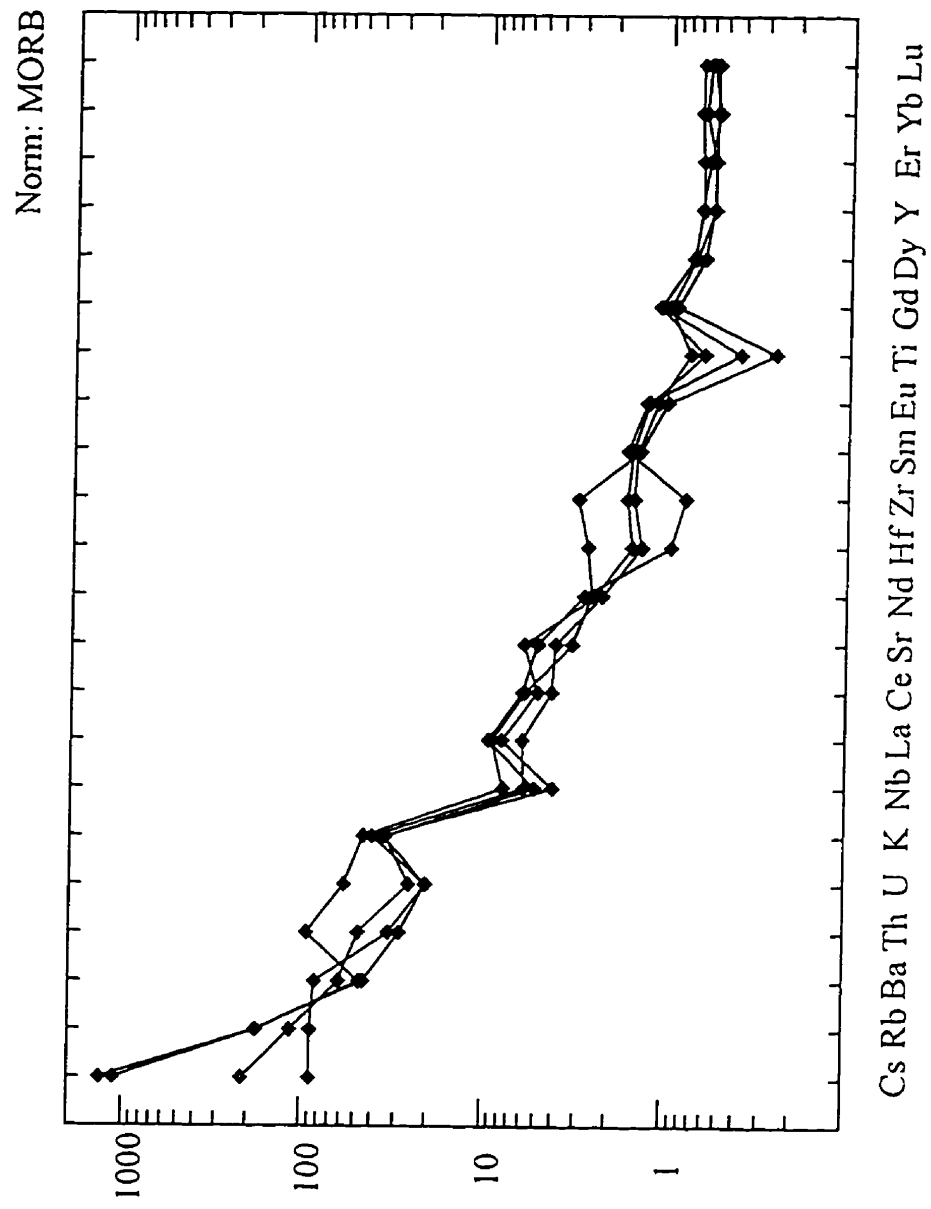


**Figure 4-8.**

"Spider diagram" for Shoshonitic Series Units  
at Farallón Negro.

[MORB normalisation as per *Newpet* Software - MUN  
1992. Normalisation factors: Cs (0.013), Rb (1.12), Ba  
(14.3), Th (0.185), U (0.075), K (955), Nb (3.58), La  
(3.96), Ce (11.97), Sr (122), Nd (10.96), Hf (2.87), Zr  
(90), Sm (3.62), Eu (1.31), Ti (9000), Gd (4.78), Dy  
(5.98), Y (34.2), Er (3.99), Yb (3.73), Lu (0.56)]



samples plot at the upper end of the range delimited by the dataset, but exhibit identical trends to those of the high-K calc-alkaline series, with the exception of less extreme negative Hf and Zr anomalies.

### **Petrography**

All of the rocks analyzed for major and minor elements, as well as those selected for  $^{40}\text{Ar}/^{39}\text{Ar}$  age determination, were examined in thin section to clarify the petrographic character of the igneous rocks of the district. These features are summarized by rock-type in Table 4-2. The mineralogy of individual samples, with brief descriptions of selected samples, are reported in Appendix E.

Because the shoshonitic suite at Farallón Negro is largely indistinguishable from the high-K calc-alkaline units on the basis of macro- or microscopic observation, they are included in the following general discussion of petrographic characteristics, rather than in a separate discussion of the shoshonitic suite. (Note: petrographic descriptions are not available for the samples analyzed by Dostal *et al.* (1977), Caelles (1979), Allison (1986) and Kay *et al.* (1988), with the exception of JC-34A.)

The dominant phenocryst phase in both volcanic and intrusive units is plagioclase. An contents range from  $\text{An}_{11}$  to  $\text{An}_{68}$ , estimated using the Michel-Levy technique. Plagioclase crystals are commonly well zoned and twinned, and some exhibit sieve textures (Fig. 4-9). Mafic minerals include clinopyroxene, orthopyroxene, hornblende and biotite. Pyroxenes (Fig. 4-10) are common phenocryst phases in volcanic and intrusive basaltic and basaltic andesitic units, but are only rarely observed in intrusive andesites.

**Table 4-2.**

Summary of the mineralogical relationships of Shoshonitic and High-K Calc-Alkaline volcanic and intrusive suites, Farallón Negro.



# Shoshonitic and High-K Calc-Alkaline Volcanic Units, Farallón Negro

	Basalt	Basaltic Andesite	Andesite	Dacite
<b>PHENOCRYSTS</b>				
Clinopyroxene	twinned zoned rarely glomerophytic	rare	not observed	not observed
Orthopyroxene	not observed	rare	not observed	not observed
Plagioclase	An17 - An62 twinned zoned	An17 - An68 twinned zoned	An11 - An60 twinned zoned minor sieve text.	An11 - An58
Hornblende	brown & green  opacite rims	brown & green euhedral opacite rims	green euhedral	not observed
Biotite	rare	minor	euhedral	euhedral
Quartz	rare	minor	rounded embayed	not observed
Apatite	microphenocrysts	microphenocrysts	microphenocrysts	microphenocrysts
Other	opaques	opaques	+/- opaques titanite	opaques
<b>MATRIX</b>				
	fine - med. grained same as phenocryst phases	glassy trachytic	glassy trachytic	glassy

## High-K Calc-Alkaline Hypabyssal Intrusive Units, Farallón Negro

	Basaltic Andesite	Andesite	Dacite	Rhyolite
<b>PHENOCRYSTS</b>				
Clinopyroxene	twinned glomerophyric	rare	rare	not observed
Orthopyroxene	not observed	rare	not observed	not observed
Plagioclase	twinned zoned	An12 - An65 twinned zoned glomerophyric	An16 - An54 twinned zoned glomerophyric	altered sieve texture
Hornblende	subhedral	brown & green euhedral opacite	minor or relict	not observed
Biotite	rare	minor irregular	euhedral	not observed
Quartz	not observed	minor rounded embayed	rounded embayed	rounded embayed
Apatite	microphenocrysts	microphenocrysts	microphenocrysts	minor
Other	opaques	opaques titanite rare alk. feld.	titanite	not observed
<b>MATRIX</b>				
	fine - med. grained feldspathic	fine grained felsic trachytic	fine grained glassy	cryptocrystalline

**Figure 4-9.**

*Petrographic characteristics of plagioclase in rocks of the Farallón Negro Volcanic Complex.*

**A.** Complex twinning and oscillatory zoning in glomerocrystic plagioclase ( $An_{63} - An_{85}$ ) in FAR 338, a massive basaltic-andesite (field term) flow from the northern portion of the Main Farallón Negro Stratovolcano.

**B.** Partially sieve-textured plagioclase in FAR 244, a porphyritic andesite dyke located on the NW rim of Bajo de la Alumbraera. The composition of the plagioclase phenocrysts ranges from  $An_{12}$  to  $An_{32}$ . Small pale-green hornblende crystals can also be seen and were separated for the geochronological study (see Chapter 5).

Note: all photomicrographs are herein presented in pairs with plane-polarized transmitted light views displayed on the left and cross-polarized transmitted light on the right.

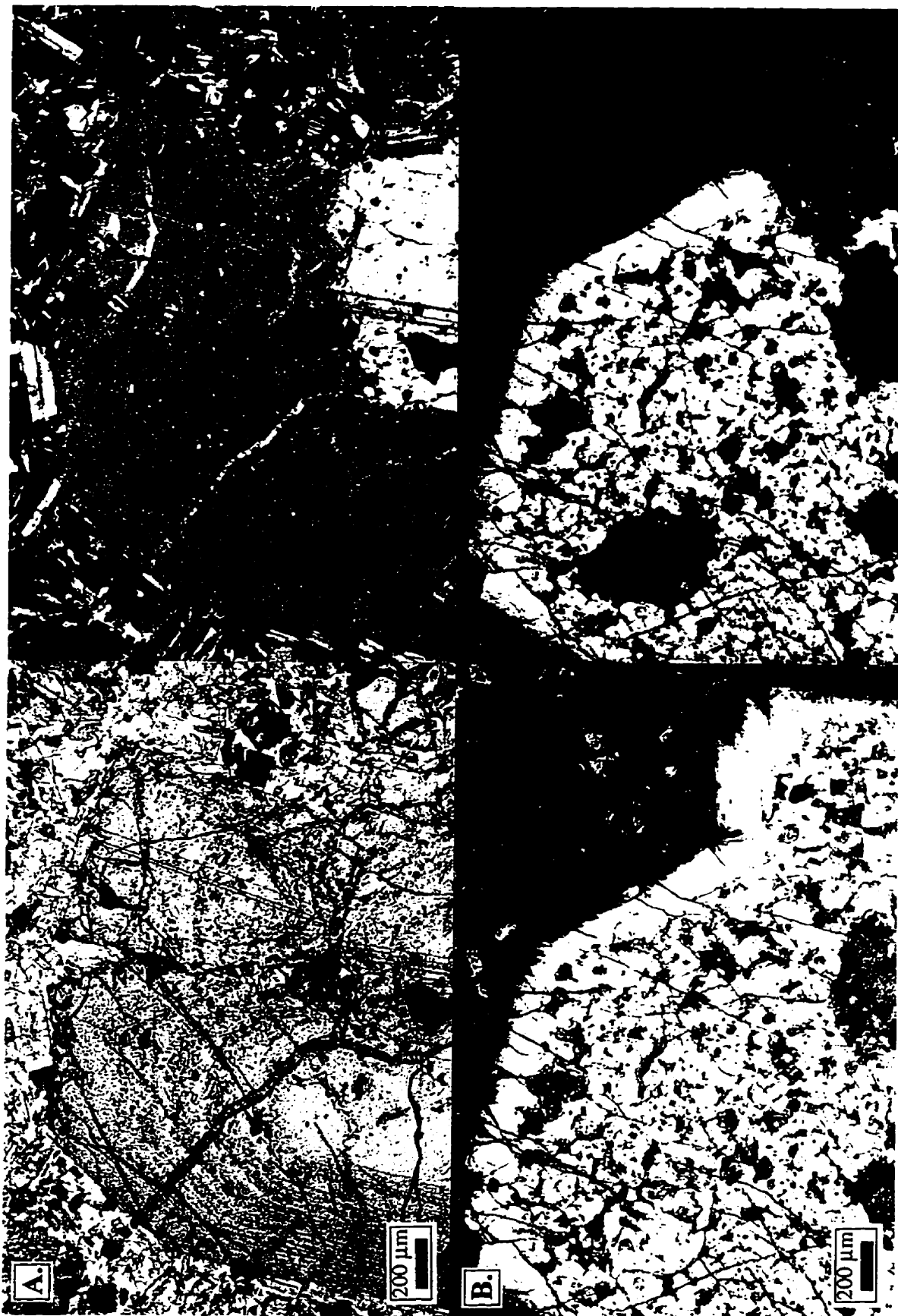


**Figure 4-10.**

*Petrographic characteristics of clinopyroxene in rocks of the Farallón Negro Volcanic Complex.*

**A.** Large, twinned and zoned clinopyroxene crystal in FAR 308, a thick, massive basalt flow overlying sediments of the El Morterito Formation on the eastern slopes of the Sierra Durazno. Small crystals of orthopyroxene are visible in the lower-right corner.

**B.** Sieve-like (possibly skeletal growth) and corroded-rim textures in clinopyroxene in JC-34a, an alkali-olivine basalt (Caelles, 1979) collected to the north of Bajo de la Alumbrera.



Hornblende is abundant in volcanic and intrusive basaltic andesites and andesites and less common in volcanic basalts and intrusive dacites. Two varieties of hornblende, green and brown, are observed (Figs. 4-11 and 4-12). The two phases do not coexist. Some hornblende crystals are corroded and many are rimmed by dark oxides ("opacite": Fig. 4-11). Biotite (Fig. 4-13) is observed in volcanic and intrusive basaltic andesites, andesites, dacites and, rarely, in volcanic basalts. Alkali-feldspar phenocrysts are rare but this mineral is locally observed in the matrix. Accessory phases include apatite, quartz, titanite and oxides (magnetite and ilmenite, commonly as intergrowths). Apatite and oxides are observed in all rock-types with the exception of the alkali-olivine basalt, which lacks apatite, and units of rhyolitic composition, in which they are both absent. Apatite generally occurs as small, euhedral, rod-shaped crystals within plagioclase and hornblende and throughout the matrix. It is abundant, attaining 1-2 modal % in some samples. Quartz phenocrysts are usually rounded and embayed (Fig. 4-13). Quartz phenocrysts are observed in volcanic and intrusive andesites, intrusive dacites, rhyolites and rarely in volcanic basaltic andesites. Titanite is a common constituent of volcanic and intrusive andesites and intrusive dacite but has not been observed in the less silicic units. Groundmass phases are identical to the phenocrystic minerals, but interstitial glass is common.

Sample JC-34A (Caelles, 1979) is the only sample of alkali-olivine basalt encountered so far at Farallón Negro and the only rock to contain relict olivine phenocrysts. Whereas Llambías (1970) reports rare olivine in volcanic flows and sills, I was unable to locate either the source of JC-34A or of Llambías' samples. Clinopyroxene

**Figure 4-11.**

*Petrographic characteristics of hornblende in rocks of the Farallón Negro Volcanic Complex (A).*

A. Euhedral, green hornblende in FAR 295, an andesite intrusive (Durazno Andesite) emplaced in shoshonitic breccias of the *Medial Volcaniclastic Facies* which crop out west of the settlement of Vis Vis.

B. Thick oxide-rich rim ("opacite") mantling a large hornblende crystal in FAR 201, an andesite flow (Arroyo Alumbra Andesite) from the Arroyo Alumbra, north of Bajo de la Alumbra. This sample is the oldest dated rock in the Main Farallón Negro Stratovolcano.





**Figure 4-12.**

*Petrographic characteristics of hornblende in rocks of the Farallón Negro Volcanic Complex (B).*

**A.** Euhedral brown hornblende with a thin oxide-rich rim ("opacite") in FAR 311, a basaltic andesite flow which overlies the El Morterito Formation approximately 12 km NNW of the Cerro Atajo deposit.

**B.** Subhedral brown hornblende laths mantled by thin oxide-rich layers ("opacite") in FAR 296, a shoshonitic breccia of the *Medial Volcaniclastic Facies* which crops out west of the settlement of Vis Vis.



**Figure 4-13.**

*Petrographic characteristics of biotite and quartz phenocrysts in rocks of the Petrographic characteristics of hornblende in rocks of the Farallón Negro Volcanic Complex.*

- A.** Euhedral biotite phenocrysts in FAR 338 (see figure 4-9).  
A sieve-textured plagioclase phenocryst is visible to the right of the central biotite crystal. Abundant high-relief, pale-green apatite microphenocrysts are seen in the matrix.
- B.** Rounded and embayed - or skeletal - quartz phenocryst in FAR 244 (see figure 4-9).



is the dominant phenocryst phase in this rock. It exhibits well-developed zoning and twinning with sieve-like and corroded-rim textures suggestive of disequilibrium. Olivine is present as large, altered phenocrysts and is commonly glomerophytic. Accessory opaques are observed. The matrix was largely glassy and is now altered.

Disequilibrium features, while not abundant, are fairly common at Farallón Negro. Mafic enclaves in more silicic units (Fig. 4-14) are interpreted to represent the commingling of two separate melt phases. Plagioclase represents a thermal record of magma chamber processes. Sieve-textured plagioclase (Fig. 4-9) has been observed in several high-K calc-alkaline samples from Farallón Negro (*e.g.*, FAR 244, 281, 311, 312 and 338). In contrast, no sieve textures have been observed in rocks of the shoshonitic suite. The sieve-textured cores represent the initial state of disequilibrium whereas the outer, clear and commonly euhedral rim of the plagioclase represent renewed equilibrium growth (Tsuchiyama, 1985; Kontak *et al.*, 1986). Thermal disturbances within plagioclase grains are indicated by numerous resorption surfaces which are visible using Nemarski differential interference contrast microscopy (Fig. 4-15). Mafic inclusions, sieve-textured plagioclase and multiple resorption surfaces are commonly cited as evidence favouring magma mixing (MacDonald and Katsura, 1965; Eichelberger, 1974; Gerlach and Grove, 1982; Singer *et al.*, 1993). It is evident that a certain degree of magma mixing took place for the calc-alkaline rocks at Farallón Negro, but the observed chemical variations suggest that it did not play a significant role in the generation or evolution of the shoshonitic units (see Wasteneys, 1990). Rather, the curving depletion array displayed by the latter rocks on the MgO vs. SiO<sub>2</sub> Harker diagram (Fig. 4-5) suggests normal fractionation processes.

**Figure 4-14.**

Mafic enclave (FAR 65) in the central andesite porphyry at Bajo el Durazno. The enclave displays a fine-grained chilled margin and the host andesite exhibits gradation in colour and composition from pale, more felsic, at the contact to dark, more mafic, with increasing distance from the enclave. Minor copper oxides (bright green) can be seen above the coin.

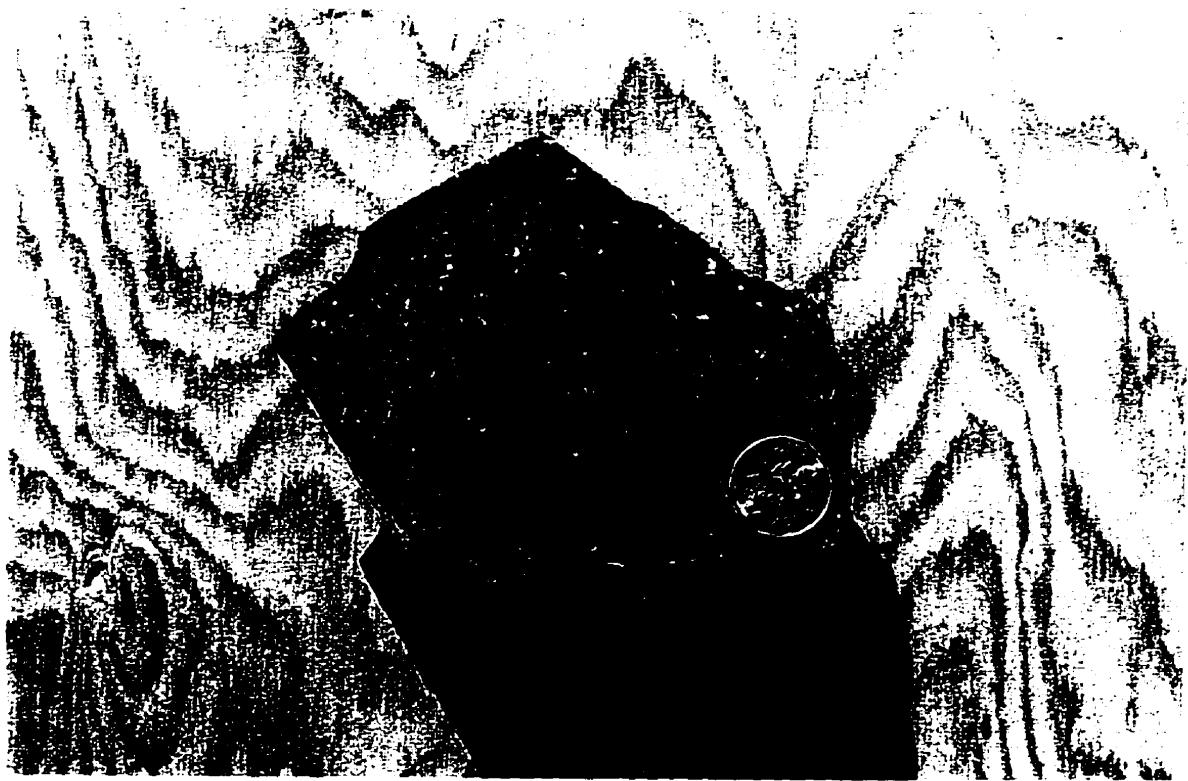


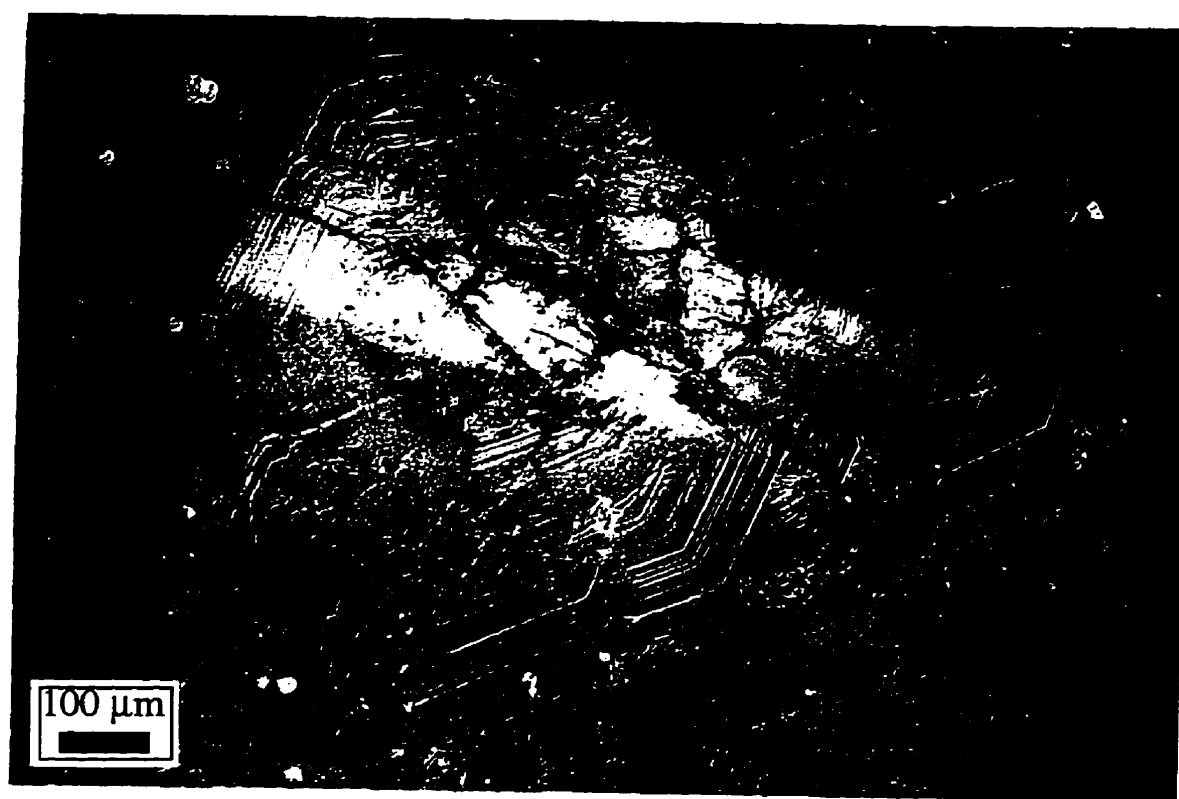


**Figure 4-15.**

*Nemarski differential interference contrast microscopy photomicrographs of resorption surfaces in plagioclase.* Etching of polished thin-sections with fluoroboric acid preferentially dissolves more calcic zones and provides a highly resolved microtopographical image of the zonal variations in An content within mineral grains. Oscillatory zoning is marked by the ordered progression of sub-parallel "high-relief" and "low-relief" layers. Resorption episodes are marked by irregular and/or rounded surfaces, which commonly appear as bright layers in the images and truncate oscillatory-zoned layers.

**A.** Large plagioclase phenocryst from FAR 338 (see figure 9). The plagioclase composition in this sample ranges overall from  $An_{63}$  to  $An_{85}$ . Rounded resorption surfaces are evident in the central portion of the grain.

**B.** Large plagioclase phenocryst from FAR 244 (see figure 9). The average plagioclase compositions range from  $An_{12}$  to  $An_{32}$ . Irregular resorption surfaces are particularly evident in the top-left quadrant of the crystal.



### **Comparison to selected regional volcanic suites**

The emplacement of Miocene volcanic units far to the east of the Peru-Chile trench in northwestern Argentina is not unique to the Farallón Negro Volcanic Complex. Several broadly contemporaneous centres (*e.g.*, Pocho and San Luis) are located in the easternmost ranges of the *Sierras Pampeanas* (Fig. 4-16). With the ongoing efforts of the federal and provincial geological surveys to remap areas of NW Argentina, additional centres of similar age are becoming better known (*e.g.*, Las Animas volcanic centre: González *et al.*, 1989; González, 1990; San Lorenzo volcanic complex: González, 1995; O. González, pers. comm., 1995; El Alisal volcanic complex: Martínez and Chipulina, 1996).

The Upper Miocene (4.5 - 7.9 Ma) potassic Pocho volcanic centre, Córdoba Province, is the best studied of these eastern complexes: detailed mapping and geochemical and petrographic investigations have been published (*e.g.*, Kay and Gordillo, 1994). The San Luis centre, San Luis Province, is less well documented. In this section, the geochemistry of the Farallón Negro Volcanic Complex will be compared with those of the Pocho (data from Kay and Gordillo, 1994) and San Luis (data from Brogioni, 1987) volcanic centres. To provide a more comprehensive regional context, general comparisons will also be made with suites from the Ojos del Salado region in Chile, west of Farallón Negro (Baker *et al.*, 1987), and from the Argentine *Puna* to the north (Kay *et al.*, 1994).

### ***Major and trace elements***

Table 4-3 highlights the enrichment or depletion of selected elements, exhibited

**Figure 4-16.**

Location map of the Farallón Negro, Pocho, San Luis, Las Animas and El Alisal volcanic centres.

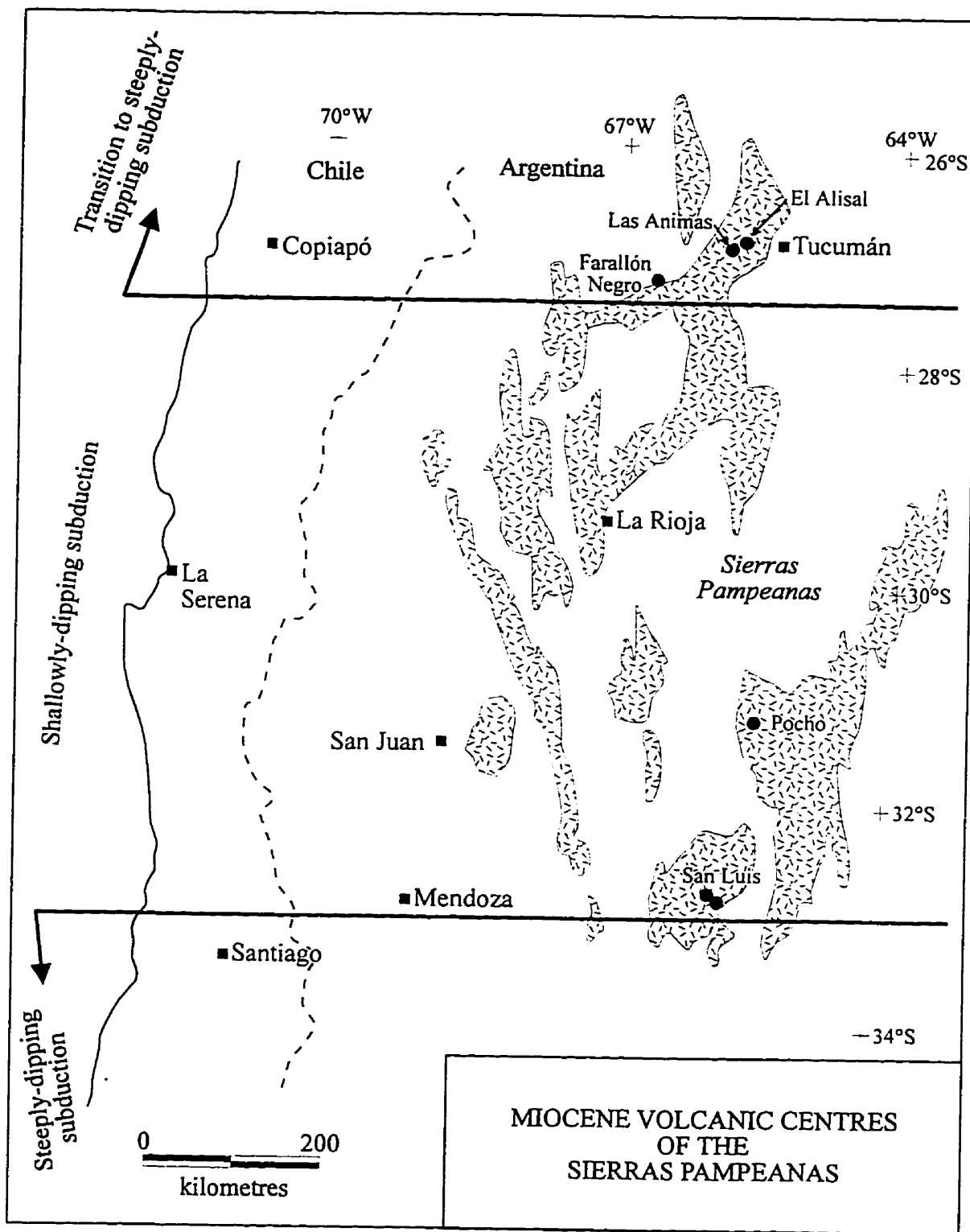


**Table 4-3.**

Comparison of selected major and trace element  
concentrations for  
the Farallón Negro and other regional suites.

(Data from: Farallón Negro: This study; Dostal *et al.*,  
1977; Caelles, 1979; Allison, 1986; Kay *et al.*, 1994;  
Pocho: Kay and Gordillo, 1994; San Luis: Brogioni, 1987;  
Ojos del Salado: Baker *et al.*, 1987; *Puna* suites: Kay *et al.*, 1994).

SUITE	POCHO	SAN LUIS	OJOS DEL SALADO	PUNA SHOSHONITE	PUNA INTRAPLATE	PUNA CALK- ALKALINE
TiO <sub>2</sub>	=	<	=	>	>	>
Al <sub>2</sub> O <sub>3</sub>	>	>	=	<	=	=
Fe <sub>2</sub> O <sub>3</sub>	< / =	<	=	=	=	=
MnO	<	> / =	=	=	=	=
MgO	< / =	<	> / =	>	>	>
CaO	=	=	=	<	=	=
Na <sub>2</sub> O	>	>	>	=	>	>
K <sub>2</sub> O	=	> / =	=	=	<	< / =
P <sub>2</sub> O <sub>5</sub>	=	<	=	>	=	=
La	>	n / a	>	>	>	>
Ce	=	n / a	> / =	>	=	> / =
Nd	=	n / a	n / a	>	> / =	>
Sm	=	n / a	n / a	>	> / =	>
Eu	=	n / a	n / a	>	< / =	=
Tb	=	n / a	n / a	>	=	=
Yb	>	n / a	n / a	<	<	<
Lu	=	n / a	n / a	<	< / =	<
Rb	=	n / a	=	>	< / =	=
Sr	>	n / a	=	>	=	> / =
Ba	=	n / a	=	>	<	<
U	=	n / a	>	>	=	>
Th	=	n / a	>	>	>	>
Zr	>	n / a	>	n / a	n / a	n / a
Nb	n / a	n / a	< / =	n / a	n / a	n / a
Hf	=	n / a	>	>	=	>
Ta	<	n / a	<	>	=	< / =
Cr	<	n / a	> / =	>	>	>
Ni	<	n / a	>	>	>	>
Co	>	n / a	>	>	>	>
Sc	=	n / a	n / a	=	>	>
<p>At a given SiO<sub>2</sub> content:</p> <p>&gt; : suite is enriched relative to FAR</p> <p>&gt; / = : suite is enriched or equivalent to FAR</p> <p>= : suite is equivalent to FAR</p> <p>&lt; / = : suite is depleted or equivalent to FAR</p> <p>&lt; : suite is depleted relative to FAR</p>						

by the other Neogene centres, with respect to the Farallón Negro samples. The major element signature at Farallón Negro is most similar to those of the suites from Ojos del Salado and the Miocene *Puna*. At a given  $\text{SiO}_2$  content, the *Puna* suites are enriched in  $\text{TiO}_2$  and  $\text{MgO}$  relative to those from Farallón Negro. They exhibit similar compositional ranges for  $\text{Fe}_2\text{O}_3$ ,  $\text{MnO}$  and, with the exception of the *Puna* shoshonites, for  $\text{CaO}$ . Variable enrichments and depletions are observed for  $\text{Al}_2\text{O}_3$ ,  $\text{Na}_2\text{O}$ ,  $\text{K}_2\text{O}$  and  $\text{P}_2\text{O}_5$ . Of interest are the  $\text{K}_2\text{O}$  contents, which are similar for all suites with the exception of the *Puna* intraplate and back-arc calc-alkaline suites, which are relatively depleted in  $\text{K}_2\text{O}$ . Overall, the Farallón Negro samples appear to be depleted in  $\text{Na}_2\text{O}$  with respect to the other suites. The Pocho and San Luis suites are enriched in  $\text{Al}_2\text{O}_3$  and  $\text{Na}_2\text{O}$  and depleted in  $\text{FeO}^\text{T}$  and  $\text{MgO}$ , but show equivalent ranges of  $\text{CaO}$  and  $\text{K}_2\text{O}$ .

The Pocho volcanic field, on the eastern side of the Sierra de Córdoba, Córdoba Province, Argentina (Figs. 4-16 and 4-17), is situated approximately 700 km from the Peru-Chile Trench in the Central Andean "flat-slab" segment at approximately  $32^\circ$  S. It lies approximately 180 km above the Wadati-Benioff Zone (Isacks, 1988). The field comprises a series of volcanic necks, small flows and pyroclastic beds of basaltic andesitic-to-dacitic composition. Two general eruptive sequences are outlined: an older ( $7.5 \pm 0.5$  Ma) high-K calc-alkaline series; and a younger ( $5.3 \pm 0.7$  Ma) shoshonitic series (Kay and Gordillo, 1994).

The San Luis volcanic centre is located along the eastern side of the Sierra de San Luis, San Luis Province, Argentina (Figs. 4-16 and 4-18), approximately 650 km from the Peru-Chile Trench at approximately  $33^\circ$  S, and approximately 160-180 km above the



**Figure 4-17.**

Geological map of the Pocho volcanic centre  
(after Kay and Gordillo, 1994).

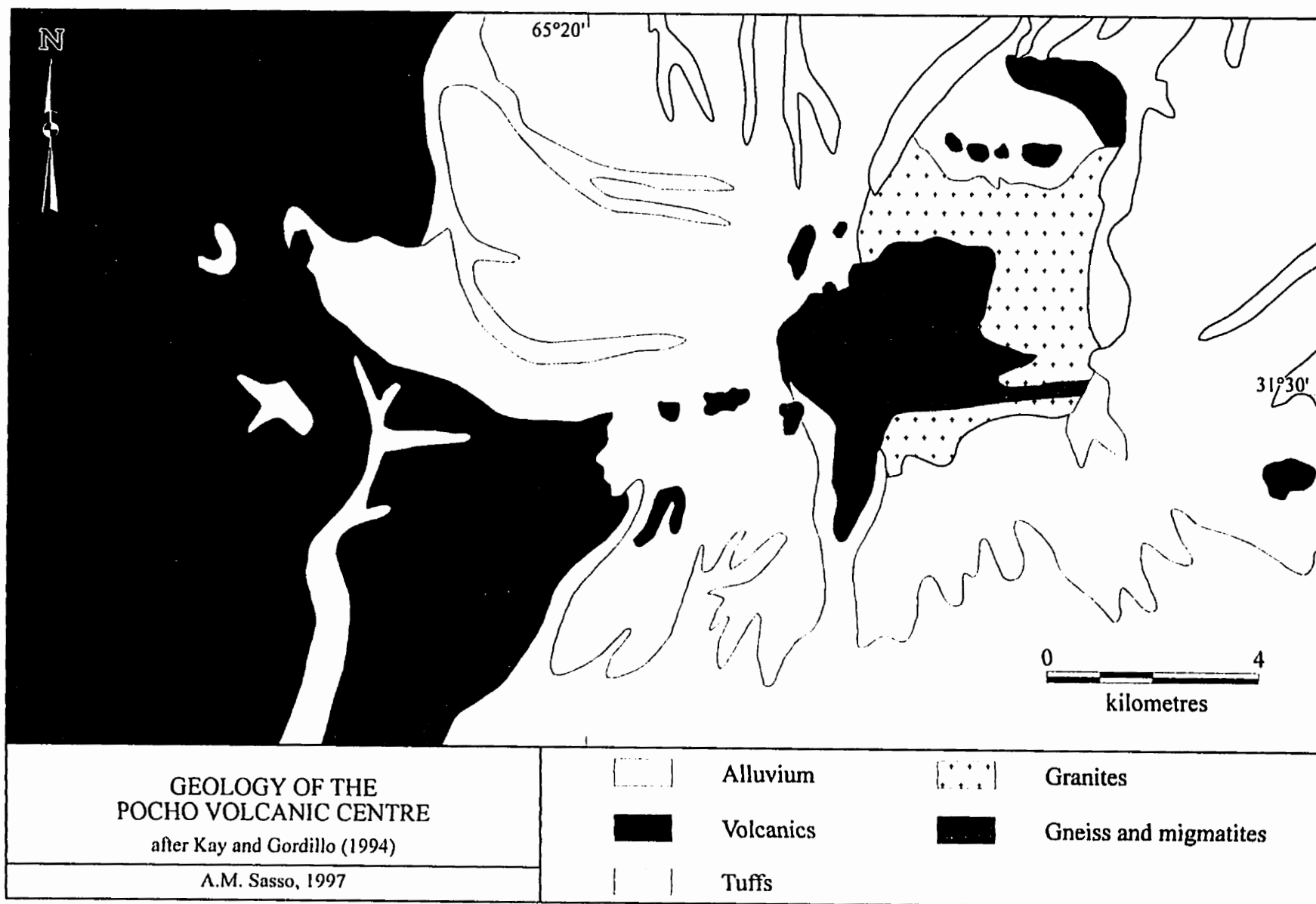
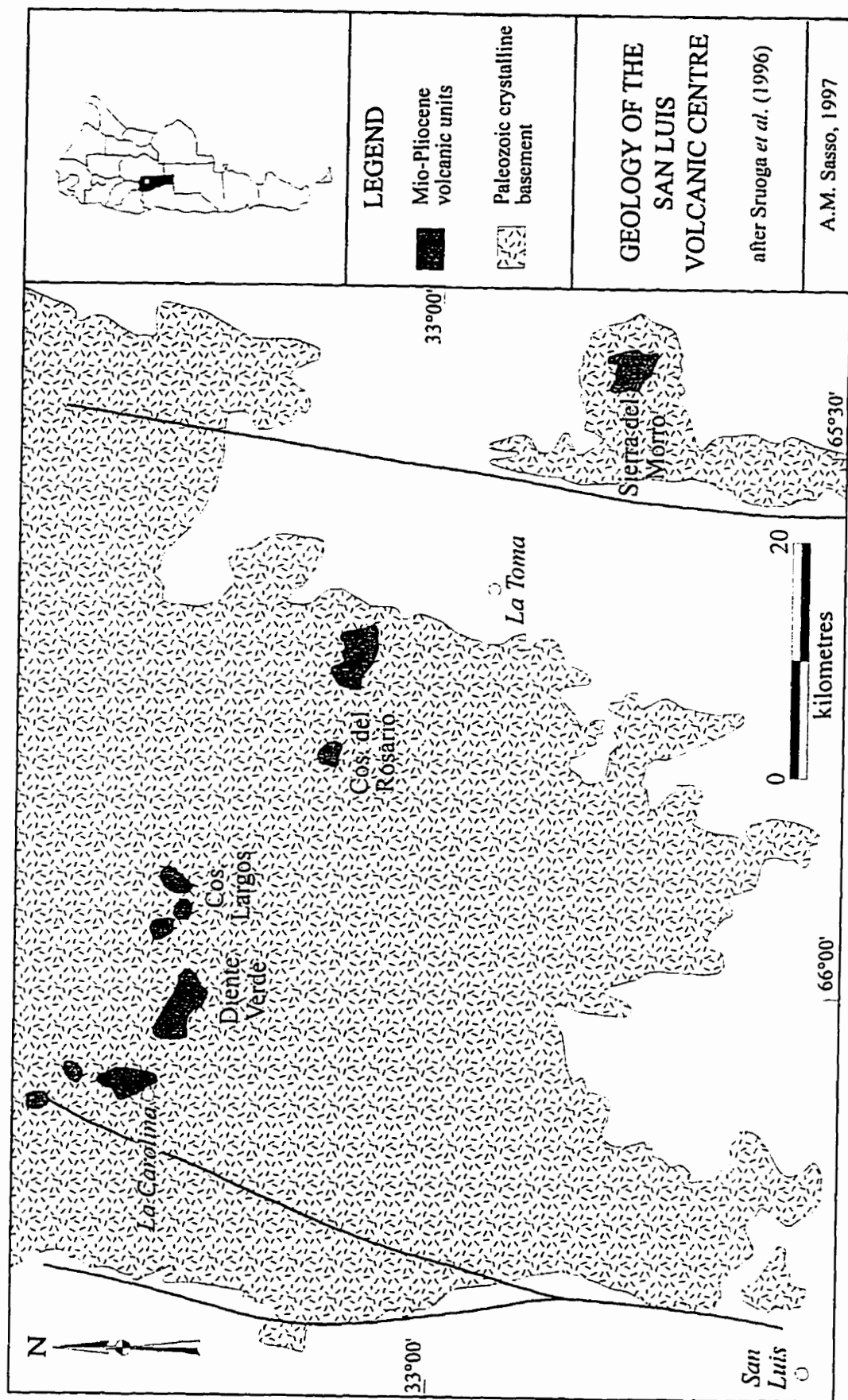


**Figure 4-18.**

Geological map of the San Luis volcanic centres  
(after Sruoga *et al.*, 1996).



Wadati-Benioff Zone (Isacks, 1988). The volcanic units crop out in an 80 km-long NW-trending belt. The field consists of a series of small volcanic cones, flows and pyroclastics which are associated with linear fracture systems in the west and calderas to the east. The rocks are predominantly alkaline, and include andesites, latites, latite-andesites and trachytes (Brogioni, 1987, 1990). Andesitic volcanism commenced as early as  $9.5 \pm 0.5$  Ma at the Diente Verde centre (Sruoga *et al.*, 1996) and was succeeded by extensive pyroclastic activity around  $2.6 \pm 0.7$  Ma in the eastern area (Ramos *et al.*, 1991). Intrusion of NW-trending dykes continued until  $1.9 \pm 0.2$  Ma (Ramos *et al.*, *op. cit.*).

A  $\text{Na}_2\text{O} + \text{K}_2\text{O}$  vs.  $\text{SiO}_2$  plot (Irvine and Baragar, 1971; Fig. 4-19) indicates that both the San Luis and Pocho suites are more alkaline than that from Farallón Negro. The majority of San Luis samples plot in the alkaline field while the Pocho samples straddle the boundary between the alkaline and sub-alkaline fields. In the AFM diagram (Fig. 4-20), the Pocho and San Luis samples plot in the calc-alkaline field and tend to cluster close to the alkali apex. Samples from San Luis range from medium-, through high-K calc-alkaline to shoshonitic (Fig. 4-21), whereas those from Pocho are dominantly shoshonitic (ranging from absarokite to highly-potassic dacites), with only minor high-K calc-alkaline compositions.

The trace element signature of the Farallón Negro rocks is most similar to that of the Pocho volcanic complex. The Farallón Negro, Pocho and *Puna* intraplate suites display the flattest REE patterns. In general, the other suites are variably enriched in the LREE, and slightly depleted in the HREE, but Eu and Tb values are similar for all suites. The *Puna* shoshonites demonstrate the greatest enrichment in LREE, although their HREE

**Figure 4-19.**

Total alkalies vs.  $\text{SiO}_2$  diagram for rocks of the Farallón Negro, Pocho and San Luis volcanic suites.  
(after Irvine and Barager, 1971)  
diamond = Farallón Negro  
circle = Pocho: Kay and Gordillo, 1994.  
square = San Luis: Brogioni, 1987.

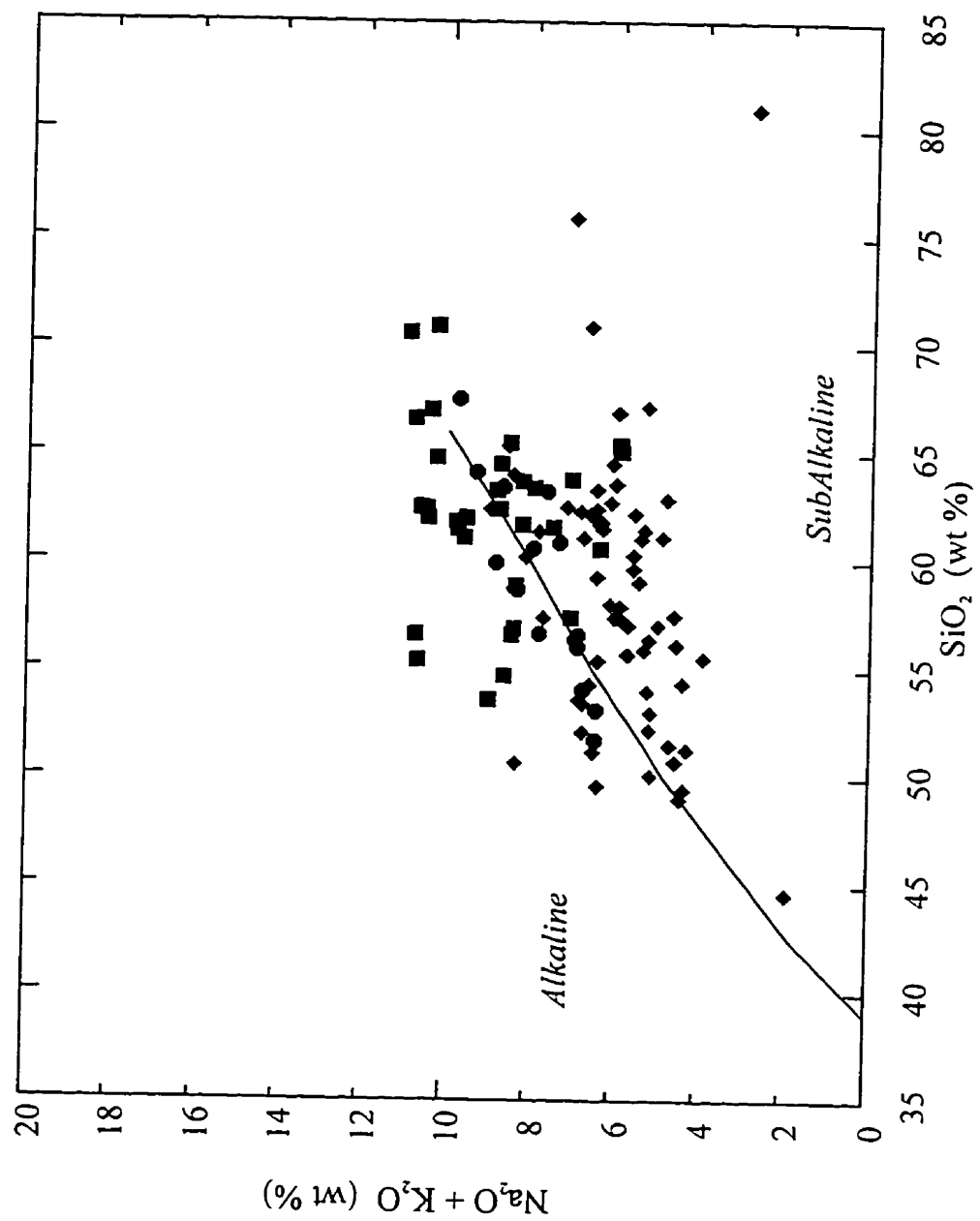


**Figure 4-20.**

AFM diagram for rocks of the Farallón Negro,  
Pocho and San Luis volcanic suites.  
(after Irvine and Barager, 1971)  
diamond = Farallón Negro  
circle = Pocho: Kay and Gordillo, 1994.  
square = San Luis: Brogioni, 1987.



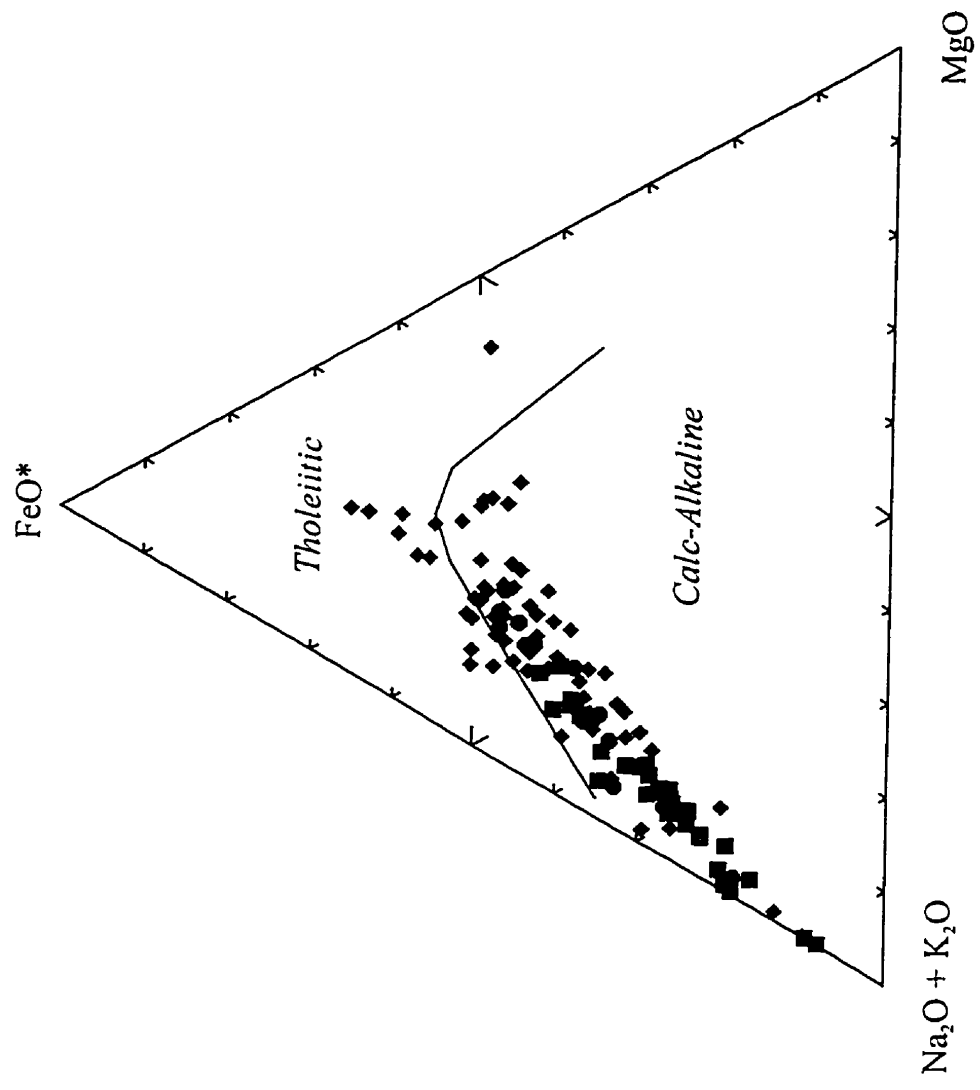
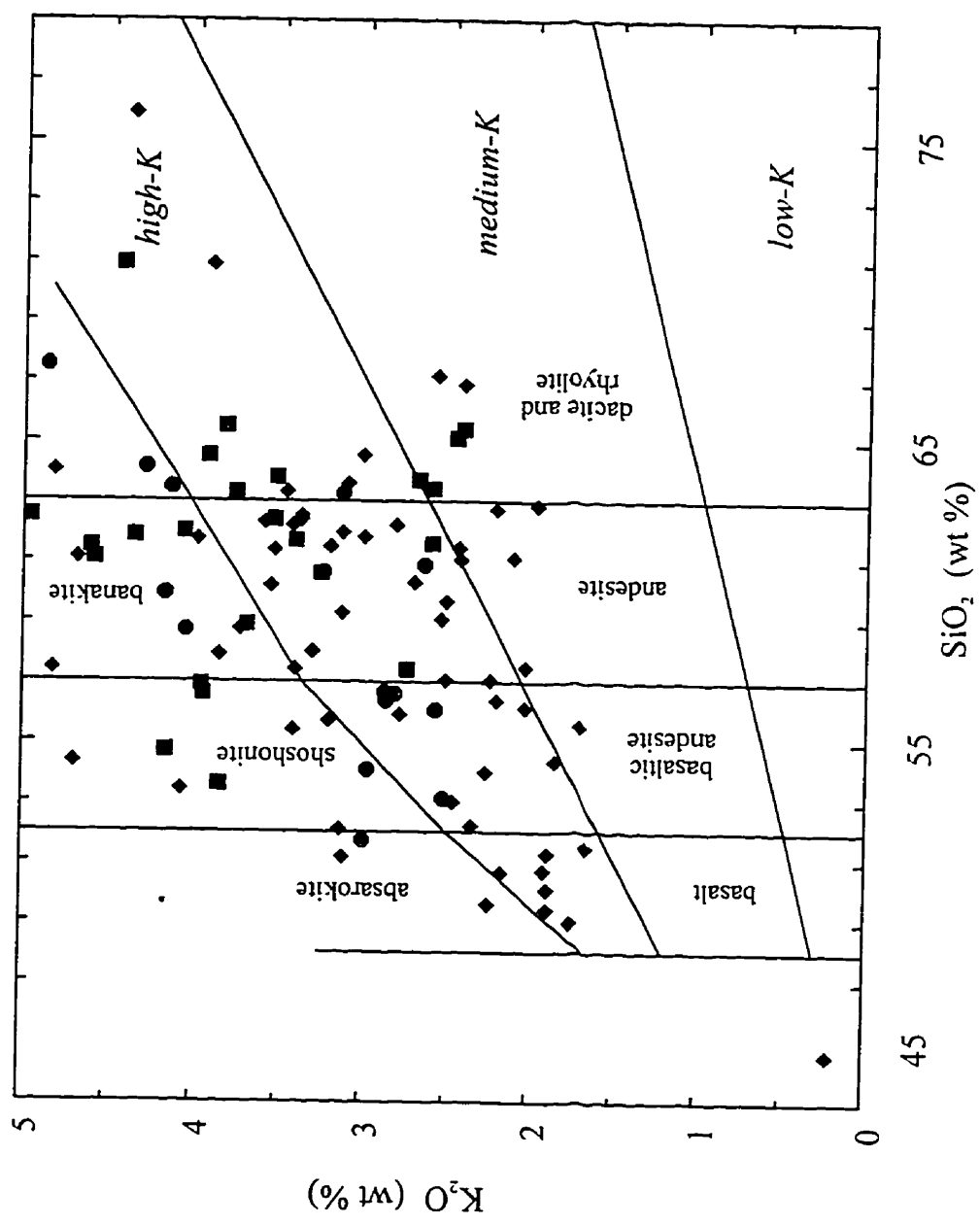


**Figure 4-21.**

K<sub>2</sub>O vs. SiO<sub>2</sub> diagram for rocks of the Farallón Negro,  
Pocho and San Luis volcanic suites.  
(after LeMaitre, 1986 and Pecerrillo and Taylor, 1976)  
diamond = Farallón Negro  
circle = Pocho: Kay and Gordillo, 1994.  
square = San Luis: Brogioni, 1987.



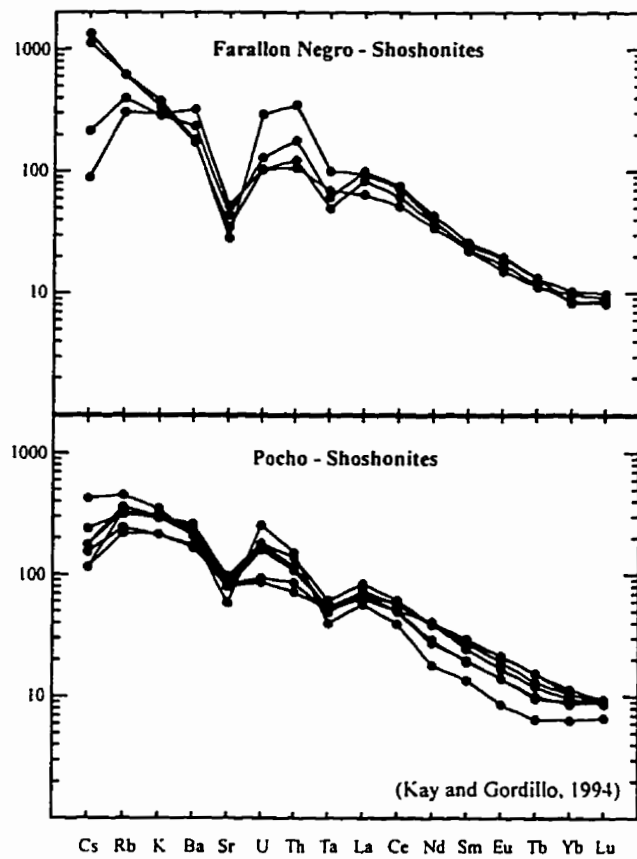
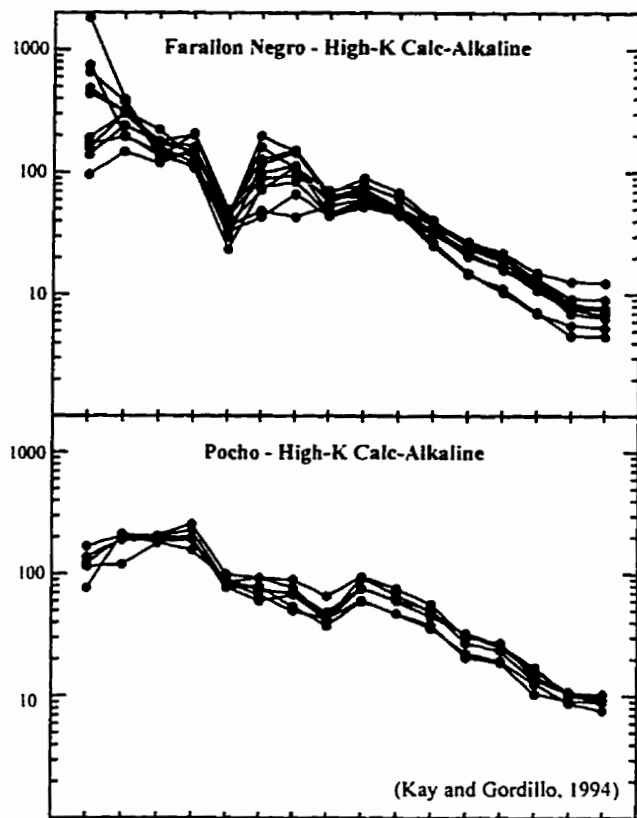
signature is similar to that of Farallón Negro. The LILE are enriched in the *Puna* shoshonites, but show both enrichment and depletion in the other suites. Th is enriched in all suites except Pocho. Rb is similar in concentration in all suites with the exception of the *Puna* shoshonites. The HFSE are enriched in the *Puna* shoshonites. In general, Cr, Ni, Co and Sc are enriched in all but the Pocho suite, where they show depletion relative to Farallón Negro rocks.

Comparative extended REE plots (using the normalization factors presented in Kay and Gordillo, 1994) for the Pocho and Farallón Negro suites are provided in figure 4-22. Both the Farallón Negro high-K calc-alkaline and shoshonite trends resemble the Pocho *shoshonite* trend. The patterns are identical, with the exception of the variable Cs and lower Sr at Farallón Negro. In contrast, the patterns displayed by the Pocho *high-K calc-alkaline* suite differ from the Farallón Negro suite in that the latter is enriched in Th, U, Rb and Cs, but significantly depleted in Sr. Similar REE patterns are reported for the Quaternary Cerro Tuzgle volcanic centre (24° S, 66.5° W: Coira and Kay, 1993).

Trace-element ratio diagrams have been employed by Kay *et al.* (1988), Coira and Kay (1993), Kay *et al.* (1994), and Kay and Gordillo (1994) to place constraints on the source of the magmas in NW Argentina. A plot of Ba/La vs. La/Yb is presented as figure 4-23. Note that Farallón Negro, Pocho and *Puna* shoshonite suites exhibit arc-like Ba/La ratios, whereas the *Puna* back-arc calc-alkaline and intraplate suites display oceanic island basalt (OIB)-like chemistry. High Ba/La ratios at Pocho were interpreted as evidence for higher alkaline-earth contents in the source region (Kay and Gordillo, 1994). The Farallón Negro and Pocho suites exhibit the lowest La/Yb ratios (flat REE patterns), consistent

**Figure 4-22.**

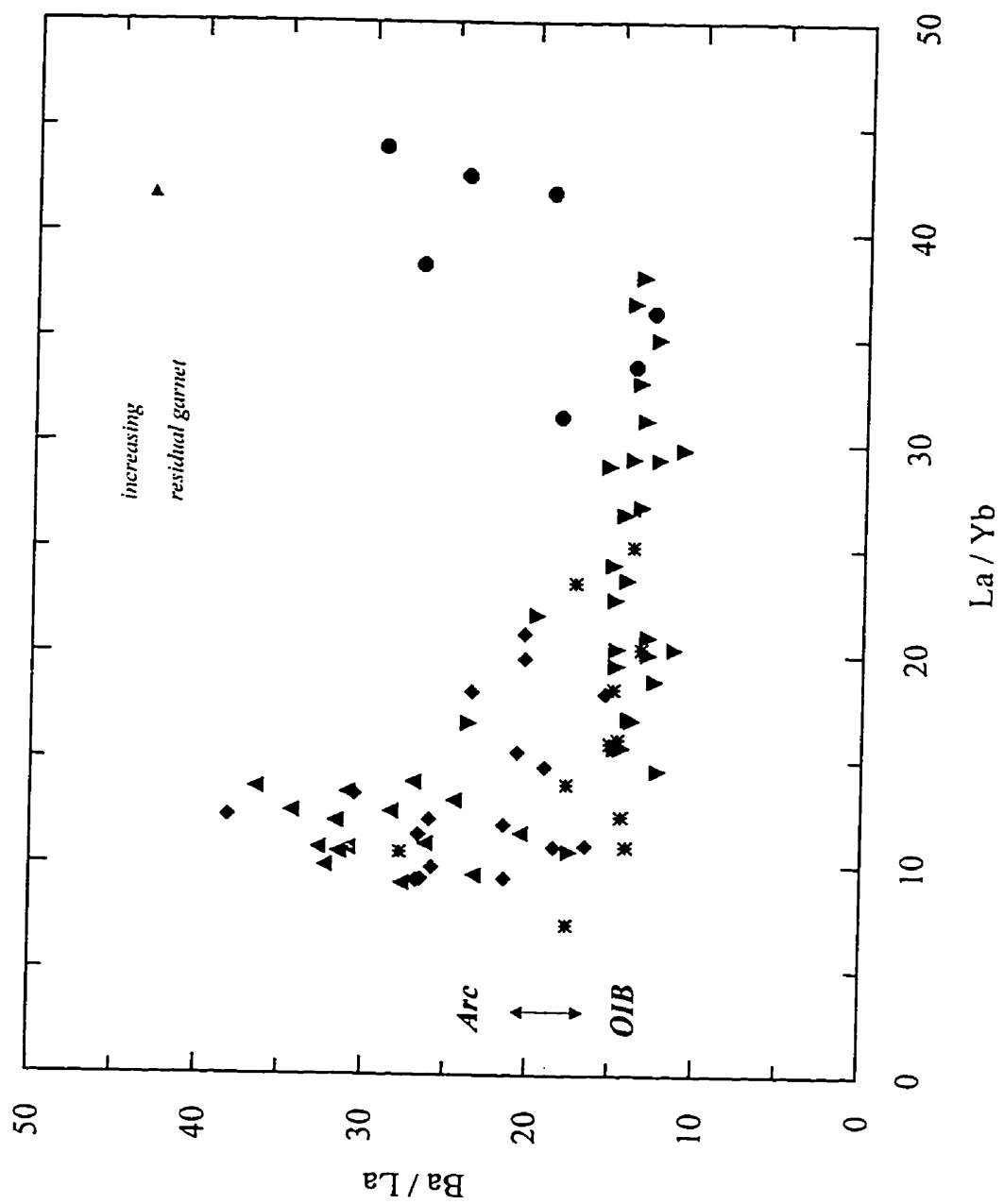
Comparative REE plots for Farallón Negro and Pocho high-K calc-alkaline and shoshonitic suites. (Normalization factors from Kay and Gordillo, 1994: normalization for Ba, Sr, U, Th, Ta and REEs with respect to Leedy chondrite. Cs, Rb and K are normalized to ocean ridge basalt KD11. Factors (ppm) are: Cs (0.013), Rb (0.325), K (116), Ba (3.77), Sr (14), U (0.015), Th (0.05), Ta (0.02), La (0.378), Ce (0.976), Nd (0.716), Sm (0.23), Eu (0.0866), Tb (0.0589), Yb (0.249), Lu (0.0387). Elements are plotted in alkali, alkaline earth, high field strength (U, Th, Ta) and REE groups to show intergroup relationships.)



Cs Rb K Ba Sr U Th Ta La Ce Nd Sm Eu Tb Yb Lu

**Figure 4-23.**

Ba/La vs. La/Yb for regional volcanic suites.  
diamond: Farallón Negro, this study;  
triangle: Pocho, Kay and Gordillo, 1994;  
inverted triangle: *Puna* back-arc calc-alkaline,  
Kay *et al.*, 1994;  
asterisk: *Puna* intraplate, Kay *et al.*, 1994;  
circle: *Puna* shoshonite, Kay *et al.*, 1994;  
square: Ojos del Salado, Baker *et al.*, 1987





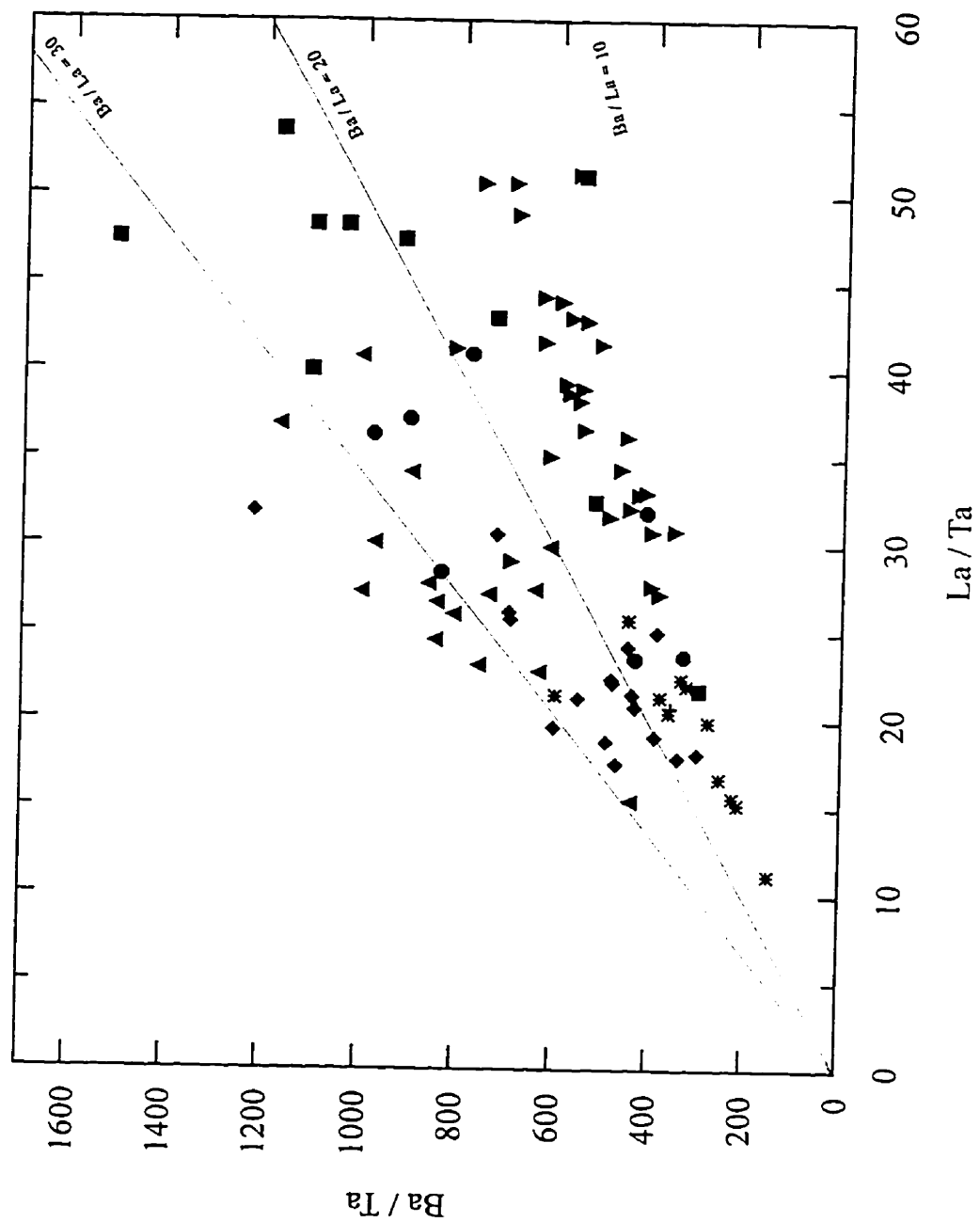
with a negligible role for garnet in the magma source regions. This is in clear contradiction to the research of Dostal *et al.* (1977), in which the Farallón Negro rocks exhibited steep La/Yb ratios, and it is suggested that their limited database was insufficient to effectively evaluate the petrochemical relationships of the Farallón Negro transect. A plot of Ba/Ta vs. La/Ta is presented as figure 4-24. High La/Ta ratios are generally interpreted to represent greater contributions by the subducted slab (Kay *et al.*, 1994), and it is inferred that the Ojos del Salado rocks incorporate considerably more slab-derived material than the Farallón Negro, Pocho and *Puna* intraplate suites, consistent with the more westerly location of the former.

#### **Comparison to Shoshonitic Suites in other regions of the Central Andes**

The distinction between the high-K calc-alkaline and shoshonite suites of this region, including those of the Farallón Negro centre, appears to be based solely on their compositions relative to a discriminant line on the K<sub>2</sub>O vs. SiO<sub>2</sub> plot of Pecerrillo and Taylor (1976; figure 4-21). Thus, in contrast to the shoshonite suites of the western United States, there are no distinguishable field or petrographic characteristics that can aid in their classification. This is also the case for the shoshonitic rocks studied by Déruelle (1978) from the Central Andes in general. The impression is that, while shoshonitic rocks abound in the Central Andes, they merely represent members of a broader compositional continuum from high-K calc-alkaline to shoshonitic. The orthodox model, *i.e.*, that shoshonitic rocks form well inboard of subduction zones and generally represent late episodes of magmatism in arc history (*e.g.*, Joplin, 1965), would suggest that rocks of this

**Figure 4-24.**

Ba/Ta vs. La/Ta plot for regional volcanic suites.  
diamond: Farallón Negro, this study;  
triangle: Pocho, Kay and Gordillo, 1994;  
inverted triangle: *Puna* back-arc calc-alkaline,  
Kay *et al.*, 1994;  
asterisk: *Puna* intraplate, Kay *et al.*, 1994;  
circle: *Puna* shoshonite, Kay *et al.*, 1994;  
square: Ojos del Salado, Baker *et al.*, 1987



petrogenetic affinity should abound in Bolivia, Peru and Argentina. However, published analyses for Bolivian and Peruvian shoshonites are scarce and, although slightly more numerous, those for Argentine shoshonites are derived from two small, isolated centres.

In this section, the most potassic units at Farallón Negro are compared to other shoshonitic rocks from the Central Andes. The latter (Fig. 4-25) are: Pocho, Argentina (Kay and Gordillo, 1994); San Gerónimo and Cerro Negro de Chorillos, Argentine *Puna* (Déruelle, 1991; Schreiber and Schwab, 1991; Kay *et al.*, 1994); La Poma, Argentine *Puna* (Kay *et al.*, 1994); Picotani Group, Peru (Sandeman, 1995); Cerro Moromoroni Formation., Peru (Kontak *et al.*, 1986); Tacaza Group, Peru (Wasteneys, 1990); two 11 Ma shoshonite samples from southern Peru documented by France (1985); Sillapaca Group, Peru (Aramaki *et al.*, 1984; France, 1985); Quaternary shoshonites, SE Peru (Carlier *et al.*, 1992; Soler *et al.*, 1992); Abaroa Formation, NW Bolivia (Jiménez *et al.*, 1993); a limited SW Bolivian suite (Kussmaul *et al.*, 1977); and a suite of Cretaceous intrusive rocks of shoshonitic affinity, *viz.* the Linga Group, of the Peruvian Coastal Batholith (LeBel *et al.*, 1985).

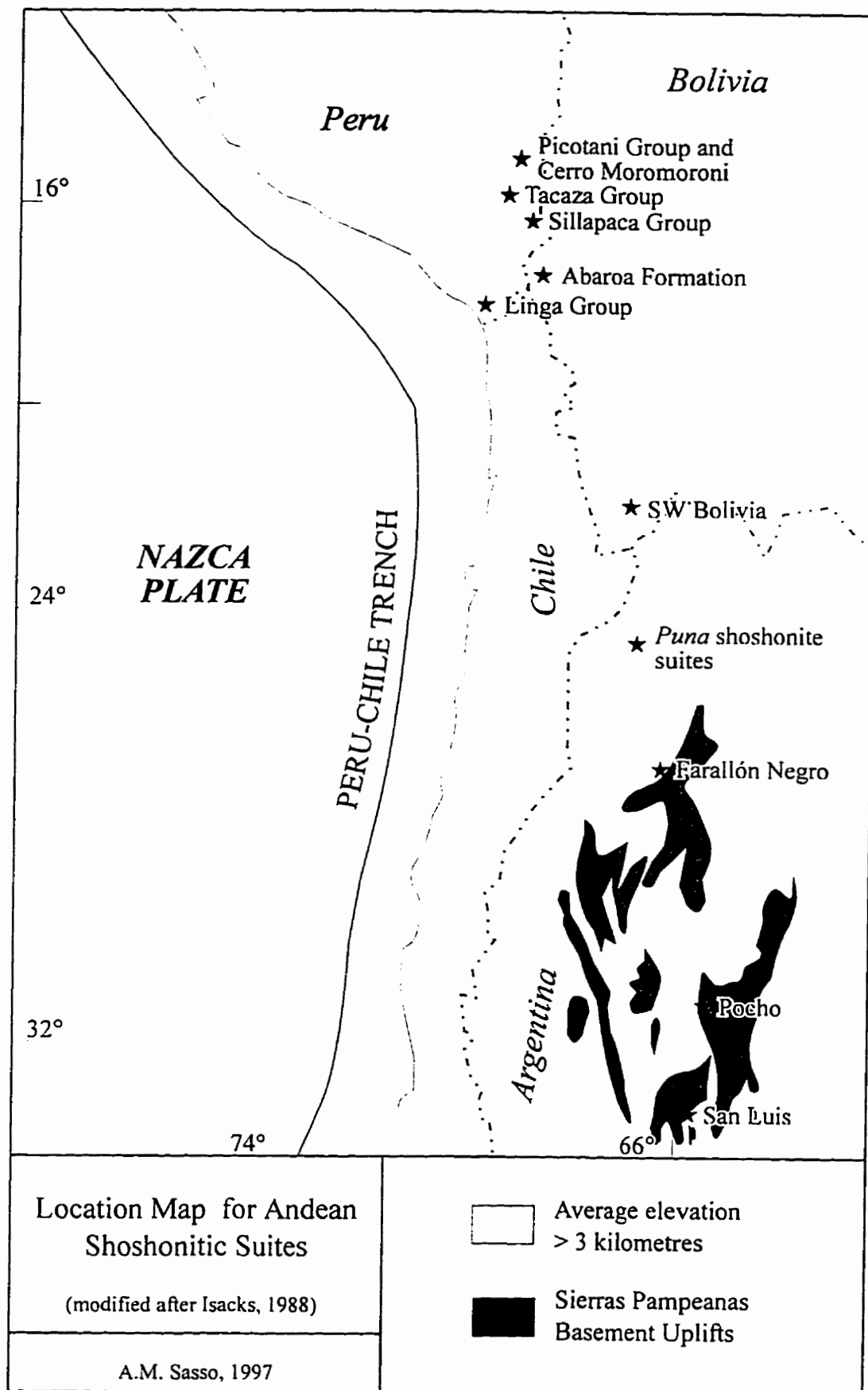
#### ***Argentine shoshonite suites:***

##### **Pocho**

Aspects of the Pocho volcanic suite have been discussed previously. The rocks are characterised by up to 30-40% of feldspar, clinopyroxene and amphibole phenocrysts in a finely-crystalline or devitrified glassy groundmass. Plagioclase is the dominant phenocryst phase. Accessories include titanomagnetite, apatite and titanite. Geochemical

**Figure 4-25.**

Location map for Andean shoshonitic suites.  
Note the location marked "*Puna* shoshonite suites"  
denotes the general location of the San Gerónimo, Cerro  
Negro de Chorillos and La Poma suites.



and petrochemical modelling indicate that the Pocho rocks can be largely explained as products of fractional crystallization of melts generated over a subduction zone. A model involving the stoping and eastward transport of blocks of basal continental lithosphere within an asthenospheric wedge is proposed to explain their distinctive, depleted-lower-crustal trace element and isotopic signatures (Kay and Gordillo, 1994).

#### San Gerónimo and Cerro Negro de Chorillos

The San Gerónimo (24° 14' S; 66° 30' W) and Chorillos (24° 16' S; 66° 24' W) centres are located on the *Puna*, over 500 km from the Peru-Chile Trench and approximately 200 km above the Wadati-Benioff zone. They are underlain by intermediate lithospheric thicknesses (Whitman *et al.*, 1992). Ages of 2 Ma for an andesite from Chorillos and 0.78 Ma for a basaltic andesite from San Gerónimo are quoted in Coira *et al.* (1993), but no details of the dating method, errors or source are provided. These units, representing low-volume flows temporally and spatially associated with extensional or strike-slip faults along or near the El Toro lineament, include absarokite, shoshonite and banakite compositions. Phenocryst assemblages, constituting approximately 10 modal % of the rocks, include olivine and clinopyroxene in the absarokites and shoshonites and orthopyroxene and hornblende in the banakites. Ti-rich phlogopite occurs in some shoshonites and banakites. Plagioclase is not recorded as a phenocryst phase, but quartz and sieve-textured feldspar xenocrysts, both rimmed by clinopyroxene, occur in all rock-types. The mineralogy and geochemistry are interpreted to indicate partial melting of a mica-bearing peridotite, storage at deep crustal levels with possible assimilation of lower

crustal material, and contamination at upper-crustal levels through the incorporation of quartz and feldspar xenocrysts (Déruelle, 1991).

The La Poma flows (24° 40' S; 66° 10' W) are located along faults near the boundary between the *Puna* and the *Cordillera Oriental*. They occupy a location with respect to the trench and the Wadati-Benioff Zone similar to that of the San Gerónimo and Chorillos suites and are inferred to be similar in age (Coira *et al.*, 1993; Kay *et al.*, 1994). Their petrology is similar to that of the other *Puna* shoshonites, with olivine and Ti-rich clinopyroxene phenocrysts, minor hornblende which is extensively resorbed, and quartz xenocrysts rimmed by clinopyroxene (Hörmann *et al.*, 1973). These units are interpreted to have been emplaced in an extensional graben setting (Hörmann *et al.*, *op. cit.*).

#### *Peruvian shoshonite suites:*

##### Linga Group

The Linga Group (LeBel *et al.*, 1985) consists of a suite of Cretaceous intrusive units which demonstrate shoshonitic chemical affinities at SiO<sub>2</sub> contents greater than 59 wt %. Units of the suite crop out in the Coastal Batholith of southern Peru. In the Arequipa segment of the batholith, this suite forms the western part of the Caldera intrusive complex. The rocks consist of diorites, granodiorites and granites. The diorites are fine-grained but are locally porphyritic. Plagioclase is the most abundant mineral, intergrown with lesser amounts of ortho- and clinopyroxene, Fe-Ti oxides and biotite, and with interstitial K-feldspar and quartz. Granodiorites exhibit a similar mineralogy, but with



green hornblende rather than orthopyroxene. Granites contain less biotite and amphibole and greater amounts of quartz. These rocks are postulated to have formed by low pressure fractional crystallization within the continental crust, yet there is little evidence for crustal assimilation. The isotopic signature of the inferred parental magmas is similar to that proposed for the "primary" magmas to the Recent Arequipa and Barroso Formation volcanic units which crop out nearby.

#### Picotani Group

The shoshonites of the upper Oligocene - Lower Miocene Picotani Group make up the Queuta Formation (Sandeman, 1995). They crop out in the northern and central areas of the Picotani Meseta (14° 30' S; 70° W) in the Inner Arc of S.E. Peru (Clark *et al.*, 1983, 1984, 1990), located approximately 550-600 km from the Peru-Chile Trench. This formation represents the lowermost unit of the Picotani Group and is dated at 24 Ma. The rocks consist of olivine-, plagioclase- and, less commonly, clinopyroxene-glomerophyric, shoshonitic to high-K calc-alkaline basalt and basaltic andesite flows. Olivine is altered. Clinopyroxene is commonly sieve-textured and resorbed. Plagioclase phenocrysts are also locally sieve-textured and exhibit thermal resorption surfaces (Sandeman, 1995). These petrological characteristics are interpreted to record mixing of basaltic magmas with the felsic products of crustal anatexis (Sandeman *et al.*, 1995). They are postulated to have been generated through an episode of anomalous asthenospheric flow caused by the foundering of a detached mass of an oceanic slab that had become coupled with the overriding crustal plate, with upwelling in its wake.

Isothermal decompression melting of the rising plume of asthenospheric mantle is inferred to have produced the high-K calc-alkaline and shoshonitic melts in the Inner Arc. Relatively thin orogenic crust and weakly extensional tectonics are postulated for this time (Sandeman *et al.*, *op.cit.*).

#### Cerro Moromoroni Formation

This shoshonitic suite crops out near the village of Antauta (14° 17' S; 70° 18' W) in the Inner Arc of southern Peru. These mafic lavas, petrologically distinctive and geographically isolated from coeval units, are assigned to the Cerro Moromoroni Formation of the Picotani Group by Sandeman (1995). The shoshonitic rocks make up a small (4.5 km<sup>2</sup>), eroded volcanic edifice. The suite has been dated (K-Ar) at  $23.7 \pm 0.6$  Ma on a whole-rock sample of unaltered absarokite. This is comparable to a <sup>40</sup>Ar/<sup>39</sup>Ar date of  $23.81 \pm 0.23$  Ma on sanidine reported in Sandeman *et al.* (submitted). The suite includes absarokites and shoshonites. The rocks consist of olivine, plagioclase and orthopyroxene phenocrysts in a fine-grained matrix of similar composition, but with opaques and glass. K-feldspar is reported in the matrix. Sieve-textured plagioclase phenocrysts are observed in the shoshonite members. Shattered quartz xenocrysts mantled by clinopyroxene coronas are observed in three-quarters of the samples studied. On the basis of chemical and textural variations, Kontak *et al.* (1986) invoke a complex history originating with partial melting of a REE- and LILE-enriched garnet peridotite source, an early period of high-pressure crystallization closely followed by a second period of relatively shallow-level fractionation, and mixing of the magma with a felsic liquid

generated by partial melting of the crust. Mixing of the two melts probably occurred in a shallow magma chamber.

#### Tacaza Group

Shoshonitic volcanics, predominantly mafic-to-intermediate in composition, comprise the bulk of the upper Oligocene - lowermost Miocene Tacaza Group in the Santa Lucía District (15° 40' S; 70° 41' W) of the Main Arc of southern Peru. The Tacaza Group ranges in age from 23.5 to 31 Ma (Wasteneys, 1990). An extensional stress regime, responsible for the development of pull-apart basins, was prevalent at this time and the orogenic crust probably did not exceed 20-25 km in thickness. The suite consists of absarokites, shoshonites and banakites. These rocks are composed of olivine-, clinopyroxene- (Ti-rich in the absarokites) and plagioclase (commonly sieve-textured in the shoshonites) phenocrysts with abundant apatite microphenocrysts and accessory Fe-Ti oxides in a trachytic, widely glassy matrix. The rocks are typically nepheline-normative but lack feldspathoid minerals. Wasteneys (1990) concluded that magma mixing was not of primary importance in the generation of the shoshonitic magmas, which are interpreted as the products of clinopyroxene- and plagioclase-dominated fractionation of mantle-derived absarokitic magmas with minimal crustal interaction. The subsequent transition from andesite-dominated shoshonitic suites to dacitic-to-rhyolitic calc-alkaline assemblages probably records a significant thickening of the continental crust (Sandeman *et al.*, 1995).

## 11 Ma shoshonites

France (1985) documents two samples of shoshonitic affinity from Cerro Contoripiña (16°18' S, 69°41' W) and Cerro Quenamichi (16°31' S, 69°39' W), approximately 25 km south of the town of Ilave, south of Lake Titicaca in the Main Arc of southern Peru. These samples returned K-Ar dates of  $11.8 \pm 0.2$  and  $11.1 \pm 0.4$  Ma, respectively. It is unclear to which stratigraphic formation these samples belong.

## Sillapaca Group

A suite of shoshonitic rocks crops out along the southern shore of Lake Titicaca, in the vicinity of the town of Puno in southern Peru (15°49' S, 70°05' W). They consist of olivine-clinopyroxene - phyrlic shoshonites, some of which also contain biotite and hornblende. They range in age from  $5.5 \pm 0.2$  Ma (France, 1985) to  $5.97 \pm 0.20$  (Kaneoka and Guevara, 1984). Also assigned to this group are the Umayo Basalts, approximately horizontal, massive and vesicular basalt (absarokite) in the area of Laguna Umayo (15°43' S, 70°08' W), 18 km northwest of Puno. Samples from this locality have been dated by K-Ar methods by McBride (unpublished data,  $4.93 \pm 0.2$ ) and France (1985,  $5.06 \pm 0.54$ ).

## Quaternary shoshonites

An array of nearly thirty small Quaternary shoshonitic centres defines a narrow W- to NW-trending belt in the Inner Arc domain of southeastern Peru (Carrier *et al.*, 1992), approximately 550-600 km from the Peru-Chile trench. In the northwestern segment of the belt they are approximately 100 km above the flat-slab segment of the Wadati-Benioff

zone whereas in the southernmost segment they lie approximately 225 km above the 30°-dipping slab. Phenocryst phases consist of olivine, clinopyroxene and phlogopite. The rocks contain xenocrysts of quartz with pyroxene coronas, sieve-textured andesine and destabilized biotites and aggregates of bronzite, augite and minor phlogopite, forsterite and plagioclase. The magmas were emplaced along normal faults. They are interpreted to have been generated by the mixing of mantle-derived mafic potassic melts with crustal felsic peraluminous melts, followed by fractional crystallization.

***Bolivian shoshonite suites:***

**Abaroa Formation**

Nepheline-normative, intermediate-to-mafic shoshonitic volcanics are the major members of the Abaroa Formation in the Berenguela Region of the northwestern *Altiplano* of Bolivia (17° 15' S; 69° 15' W). The Abaroa Formation lavas yield K-Ar ages of 20.8 ± 0.5 Ma (plagioclase separate), 14.6 Ma (augite) and 13.5 ± 0.4 Ma (whole-rock) (Jiménez *et al.*, 1993). The rocks range in composition from basalt to andesite and demonstrate shoshonitic and alkalic tendencies. They consist of clinopyroxene, olivine and plagioclase phenocrysts in a fine-grained matrix rich in plagioclase. Nepheline occurs as a trace mineral. Oxyhornblende and phlogopite are common in the more silicic units. These rocks are interpreted to have formed by small volume partial melting of a mantle source with major olivine and feldspar fractionation. The subsequent change in composition to younger "normal" high-K calc-alkaline rocks is attributed to crustal thickening and to a change in overall tectonic regime (Jiménez *et al.*, 1993).

### SW Bolivian shoshonite suite

A series of lavas from southwestern Bolivia (approximately 22° S; 68° W) can be assigned to the shoshonitic clan. They have a restricted range of SiO<sub>2</sub> content (61.57-68.29 wt. %). These dacites are highly porphyritic and contain phenocrysts of plagioclase, biotite, quartz, hypersthene and rare sanidine. The quartz is commonly rounded, embayed and rimmed by fine-grained pyroxene. This suite is interpreted to have been generated by partial melting of different crustal zones, with changes in observed composition (*e.g.*, higher K<sub>2</sub>O and SiO<sub>2</sub> contents) caused by varying composition of the source rocks. Tensional faults provided feeder channels for the eruptives (Kussmaul *et al.*, 1977 ).

### *Major and Trace Elements of Central Andean Shoshonitic Suites*

An Na<sub>2</sub>O + K<sub>2</sub>O vs. SiO<sub>2</sub> plot (Irvine and Barager, 1971; Fig. 4-26) demonstrates the alkaline tendencies of the Tacaza, Chorillos and La Poma suites. The Pocho, San Gerónimo and Sillapaca suites plot along the alkaline-subalkaline boundary. The AFM diagram (Fig. 4-27) demonstrates that all suites belong to the calc-alkaline clan *sensu lato*. The K<sub>2</sub>O vs. SiO<sub>2</sub> diagram (Fig. 4-28) demonstrates the shoshonitic character of the suites (as defined by Pecerrillo and Taylor, 1976) although it is evident that the samples assigned to the shoshonite clan by Kussmaul *et al.* (1977) in SW Bolivia would more appropriately be classified as high-K calc-alkaline.

Published whole-rock analyses for the Central Andean shoshonite suites are presented in Appendix F. Of the major and trace elements, revealing trends are demonstrated by TiO<sub>2</sub>, MgO and Cr. A plot of TiO<sub>2</sub> vs. SiO<sub>2</sub> is presented as figure 4-29.

**Figure 4-26.**

Total alkalies vs. SiO<sub>2</sub> diagram for rocks of the  
Central Andean shoshonite suites.  
(after Irvine and Barager, 1971)  
filled diamond: Farallón Negro, this study  
empty diamond: Pocho, Kay and Gordillo, 1994  
half-filled square: Cerro Negro de Chorillos,  
Déruelle, 1991; Schreiber and Schwab,  
1991; Kay *et al.*, 1994  
filled square: San Gerónimo, Déruelle, 1991;  
Schreiber and Schwab, 1991; Kay *et al.*,  
1994  
empty square: La Poma, Kay *et al.*, 1994  
empty triangle: Cerro Moromoroni, Kontak *et al.*,  
1986  
filled triangle: Picotani Group, Sandeman, 1995  
asterisk: Tacaza Group, Wasteneys, 1990  
filled inverted triangle: SW Bolivia, Kussmaul *et*  
*al.*, 1977  
empty inverted triangle: Abaroa Group, Jiménez *et*  
*al.*, 1993a  
cross: Linga Group, LeBel *et al.*, 1985  
filled circle: Sillapaca Fm, Aramaki *et al.*, 1984;  
France, 1985  
half-filled circle: 11 Ma shoshonites, France 1985

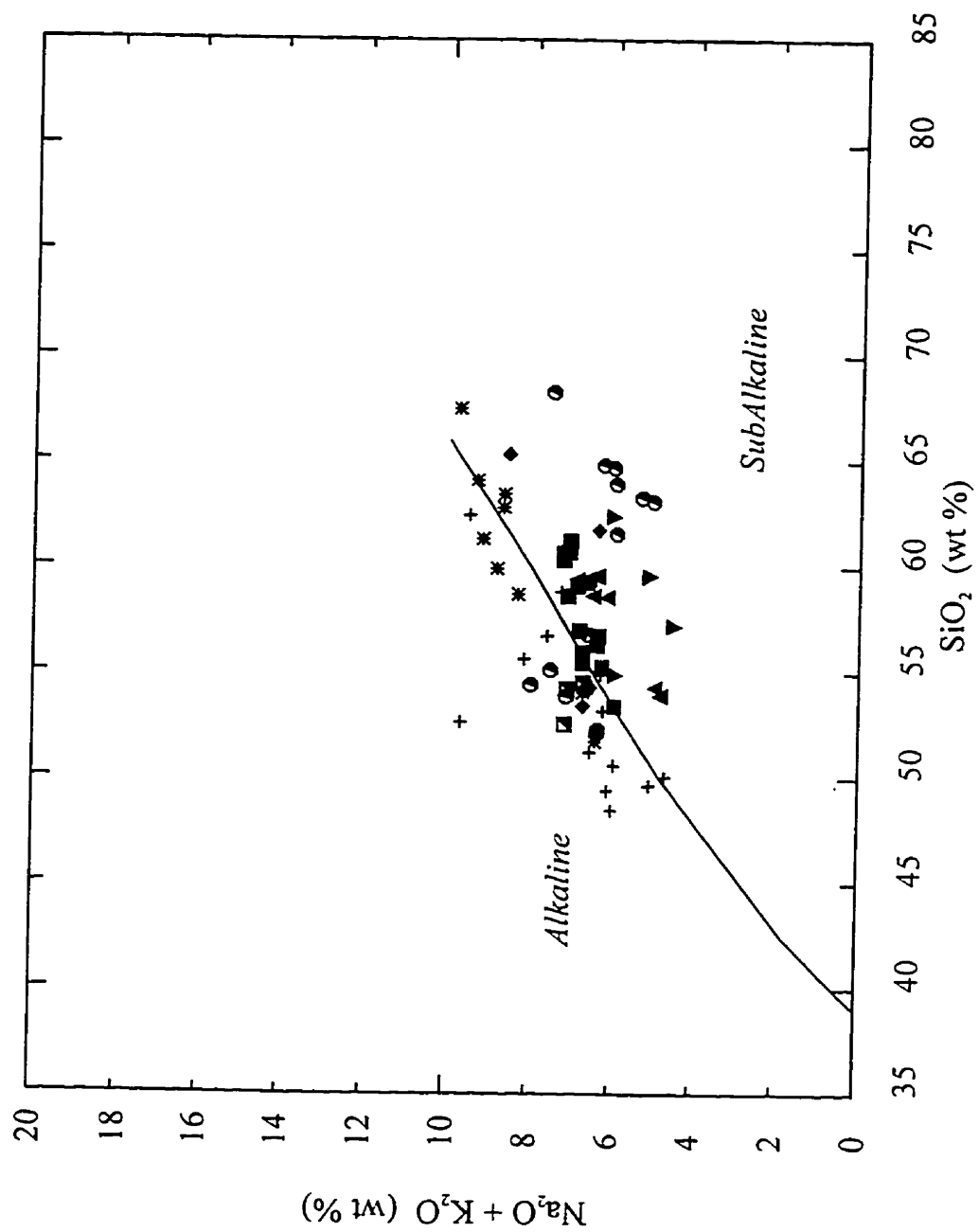




**Figure 4-27.**

AFM diagram for rocks of the Andean shoshonite suites.

(after Irvine and Barager, 1971)

filled diamond: Farallón Negro, this study

empty diamond: Pocho, Kay and Gordillo, 1994

half-filled square: Cerro Negro de Chorillos,  
Déruelle, 1991; Schreiber and Schwab,  
1991; Kay *et al.*, 1994

filled square: San Gerónimo, Déruelle, 1991;  
Schreiber and Schwab, 1991; Kay *et al.*,  
1994

empty square: La Poma, Kay *et al.*, 1994

empty triangle: Cerro Moromoroni, Kontak *et al.*,  
1986

filled triangle: Picotani Group, Sandeman, 1995

asterisk: Tacaza Group, Wasteneys, 1990

filled inverted triangle: SW Bolivia, Kussmaul *et al.*, 1977

empty inverted triangle: Abaroa Group, Jiménez *et al.*, 1993a

cross: Linga Group, LeBel *et al.*, 1985

filled circle: Sillapaca Fm, Aramaki *et al.*, 1984;  
France, 1985

half-filled circle: 11 Ma shoshonites, France 1985

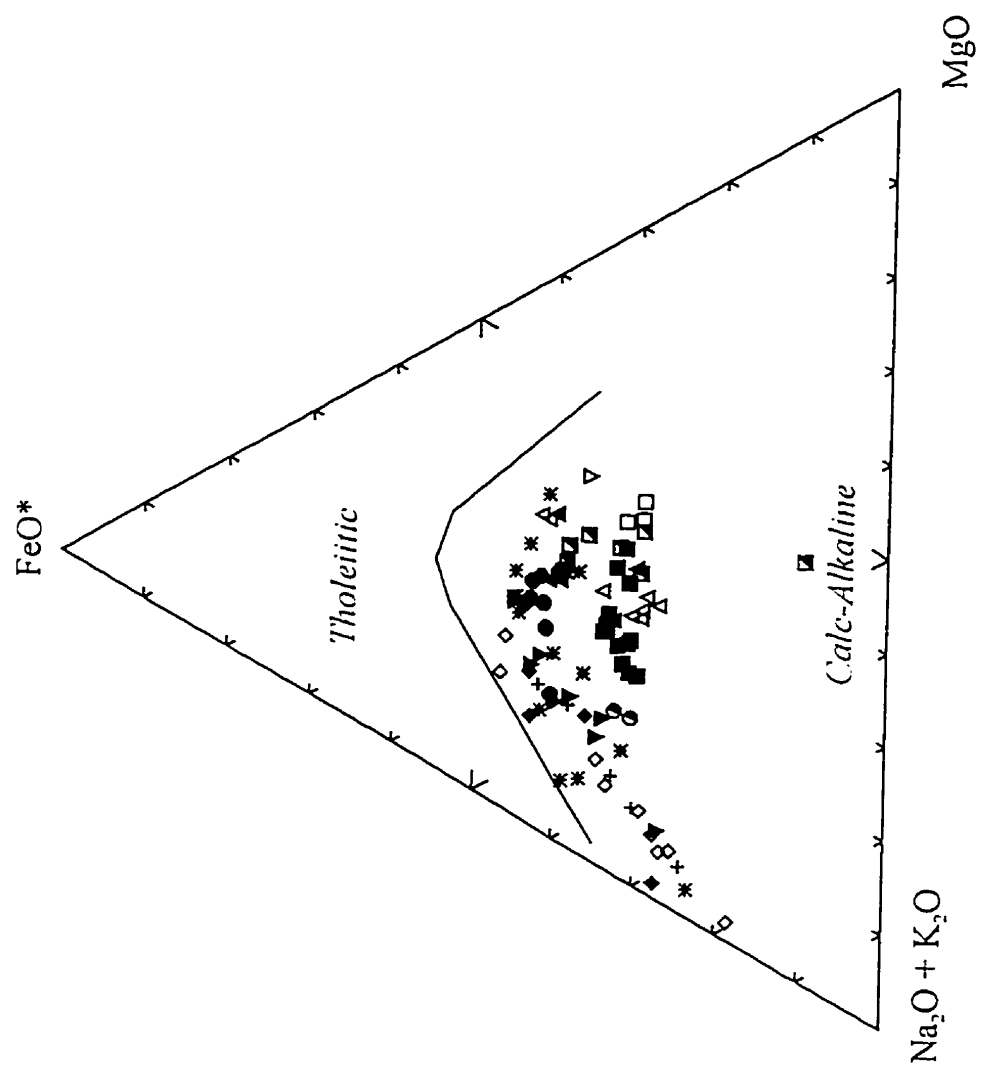


**Figure 4-28.**

K<sub>2</sub>O vs. SiO<sub>2</sub> diagram for rocks of the Central Andean shoshonite suites.

(after LeMaitre, 1986 and Pecerillo and Taylor, 1976)

filled diamond: Farallón Negro, this study

empty diamond: Pocho, Kay and Gordillo, 1994

half-filled square: Cerro Negro de Chorillos,  
Déruelle, 1991; Schreiber and Schwab,  
1991; Kay *et al.*, 1994

filled square: San Gerónimo, Déruelle, 1991;  
Schreiber and Schwab, 1991; Kay *et al.*,  
1994

empty square: La Poma, Kay *et al.*, 1994

empty triangle: Cerro Moromoroni, Kontak *et al.*,  
1986

filled triangle: Picotani Group, Sandeman, 1995

asterisk: Tacaza Group, Wasteneys, 1990

filled inverted triangle: SW Bolivia, Kussmaul *et al.*, 1977

empty inverted triangle: Abaroa Group, Jiménez *et al.*, 1993a

cross: Linga Group, LeBel *et al.*, 1985

filled circle: Sillapaca Fm, Aramaki *et al.*, 1984;  
France, 1985

half-filled circle: 11 Ma shoshonites, France 1985

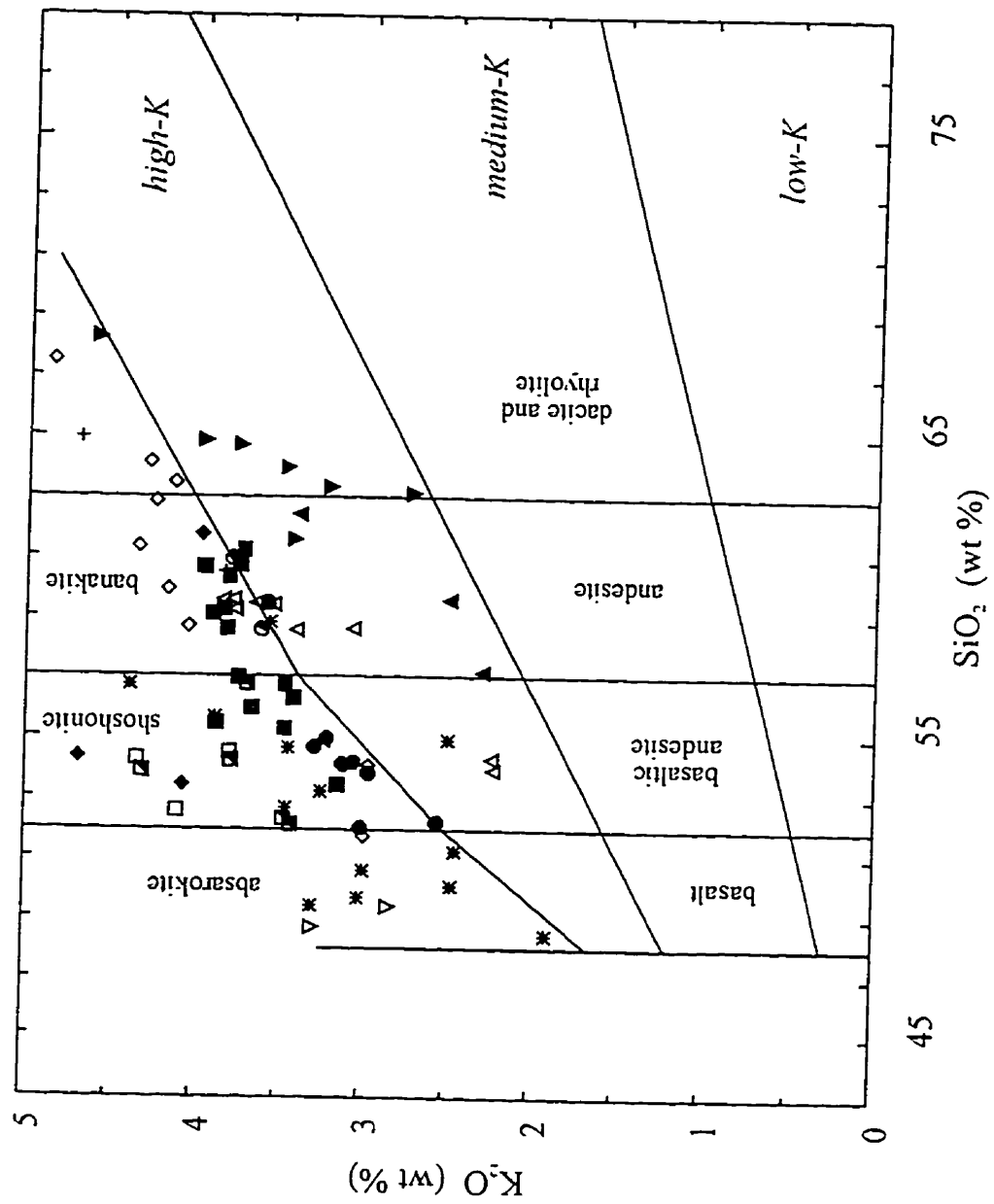
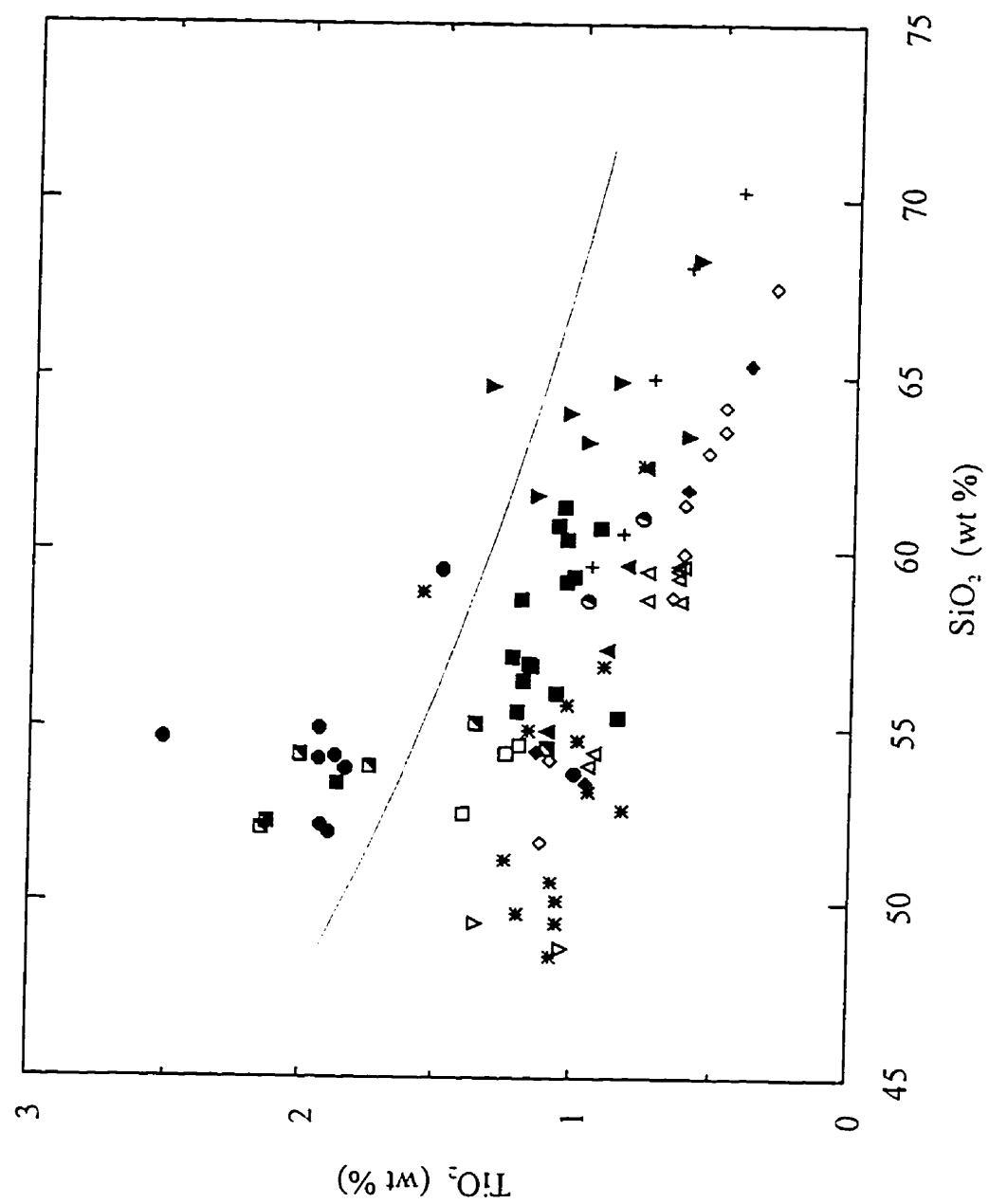


**Figure 4-29.**

TiO<sub>2</sub> vs. SiO<sub>2</sub> diagram for rocks of the Central Andean shoshonite suites.

- filled diamond: Farallón Negro, this study
- empty diamond: Pocho, Kay and Gordillo, 1994
- half-filled square: Cerro Negro de Chorillos, Déruelle, 1991; Schreiber and Schwab, 1991; Kay *et al.*, 1994
- filled square: San Gerónimo, Déruelle, 1991; Schreiber and Schwab, 1991; Kay *et al.*, 1994
- empty square: La Poma, Kay *et al.*, 1994
- empty triangle: Cerro Moromoroni, Kontak *et al.*, 1986
- filled triangle: Picotani Group, Sandeman, 1995
- asterisk: Tacaza Group, Wasteneys, 1990
- filled inverted triangle: SW Bolivia, Kussmaul *et al.*, 1977
- empty inverted triangle: Abaroa Group, Jiménez *et al.*, 1993a
- cross: Linga Group, LeBel *et al.*, 1985
- filled circle: Sillapaca Fm, Aramaki *et al.*, 1984; France, 1985
- half-filled circle: 11 Ma shoshonites, France 1985



A well-defined break in the data separates high-Ti from low-Ti shoshonites. The majority of the Chorillos lavas from the Argentine *Puna* plot in the high-Ti field. Samples from the Sillipaca Group of southern Peru plot in the high-Ti field with the exception of the Umayo basalt. A sample of the Tolaocco Fm. from the Santa Lucía District plots within the high-Ti field, as does one sample from the SW Bolivian suite. In general, the high-Ti shoshonites are confined to the younger suites (*i.e.*, younger than 5.5 Ma). In the Santa Lucía District, Wasteneys (1990) documents an enrichment of  $\text{TiO}_2$  with time which may suggest a range of parental magma compositions. The chemical differences between the Pliocene (Tolaocco Fm.) and upper Oligocene (Tacaza Group) shoshonites in that area reflect the great increase in crustal thickness in the Mio-Pliocene and imply the importance of extensional tectonism in the ascent of mafic magmas. The relative enrichment in HFSE such as Nb, Zr and Ti in the Tolaocco Fm. compared to the upper Oligocene shoshonites suggest a more ocean island basalt (OIB)-like source and, possibly, the partial melting of less metasomatized mantle peridotite. This may have developed through the less efficient transfer of fluids into the mantle wedge above a more rapidly descending Late Miocene slab. The crust was much thicker in the Late Miocene than in the Oligocene and hence a significant extensional tectonic event probably occurred to allow the mafic magmas to reach the surface. The chemistry of the SW Bolivian suite may also indicate a progression to higher  $\text{TiO}_2$  contents with time. The one high-Ti sample is from the Soniquera volcano ( $67^{\circ}15'W$ ,  $22^{\circ}02' S$ ) and appears to represent the youngest sample in this suite, although more information on the ages of the units would be required to confirm this inference.

Figure 4-30 illustrates the relationships of MgO and SiO<sub>2</sub> contents in these K-rich rocks. It is evident that, at a given SiO<sub>2</sub> content, samples from the Inner Arc and the Argentine *Puna* show higher MgO contents than the Main Arc suites. This difference is broadly duplicated in the Cr vs. SiO<sub>2</sub> plot (Fig. 4-31). These trends are interpreted herein to indicate the involvement of more primitive parental magmas in the Inner Arc and the Argentine *Puna* suites than in the Main Arc. The lowest MgO and Cr contents are observed for the Tacaza, Pocho and Farallón Negro suites, all components of the Main Arc. The Main Arc and Inner Arc (Fig. 4-32, Clark *et al.*, 1983, 1984, 1990) are delimited as magmatic domains on the basis of the overall igneous petrochemical assemblage. Main Arc volcanic and plutonic rocks are ultimately of mantle origin but display a significant range of contributions from the upper and middle continental crust and exhibit both calc-alkaline (low- to high-K) and weakly alkaline (shoshonitic) affinities. The Inner Arc is aurally restricted and also incorporates peralkaline rocks and moderately to strongly peraluminous, intermediate to acidic, volcanic and intrusive suites.

A plot of Ba/La vs. La/Yb is presented as figure 4-33. The *Puna* shoshonites demonstrate much steeper REE trends (high La/Yb ratios) than the Pocho or Farallón Negro suites, with the Picotani Group showing intermediate La/Yb ratios. With respect to Ba/La ratios, all rocks show arc-like ratios, with the exception of the San Gerónimo and several members of the Chorillos suites. A plot of Ba/Ta vs. La/Ta is presented as figure 4-34. Higher La/Ta ratios are generally interpreted to represent greater contributions by the subducted slab (Kay *et al.*, 1994). On this basis, it is inferred that the La Poma suite incorporated considerably more slab-derived material than the Pocho, Farallón



**Figure 4-30.**

MgO vs. SiO<sub>2</sub> diagram for rocks of the Central Andean shoshonite suites.

- filled diamond: Farallón Negro, this study
- empty diamond: Pocho, Kay and Gordillo, 1994
- half-filled square: Cerro Negro de Chorillos, Déruelle, 1991; Schreiber and Schwab, 1991; Kay *et al.*, 1994
- filled square: San Gerónimo, Déruelle, 1991; Schreiber and Schwab, 1991; Kay *et al.*, 1994
- empty square: La Poma, Kay *et al.*, 1994
- empty triangle: Cerro Moromoroni, Kontak *et al.*, 1986
- filled triangle: Picotani Group, Sandeman, 1995
- asterisk: Tacaza Group, Wasteneys, 1990
- filled inverted triangle: SW Bolivia, Kussmaul *et al.*, 1977
- empty inverted triangle: Abaroa Group, Jiménez *et al.*, 1993a
- cross: Linga Group, LeBel *et al.*, 1985
- filled circle: Sillapaca Fm, Aramaki *et al.*, 1984; France, 1985
- half-filled circle: 11 Ma shoshonites, France 1985

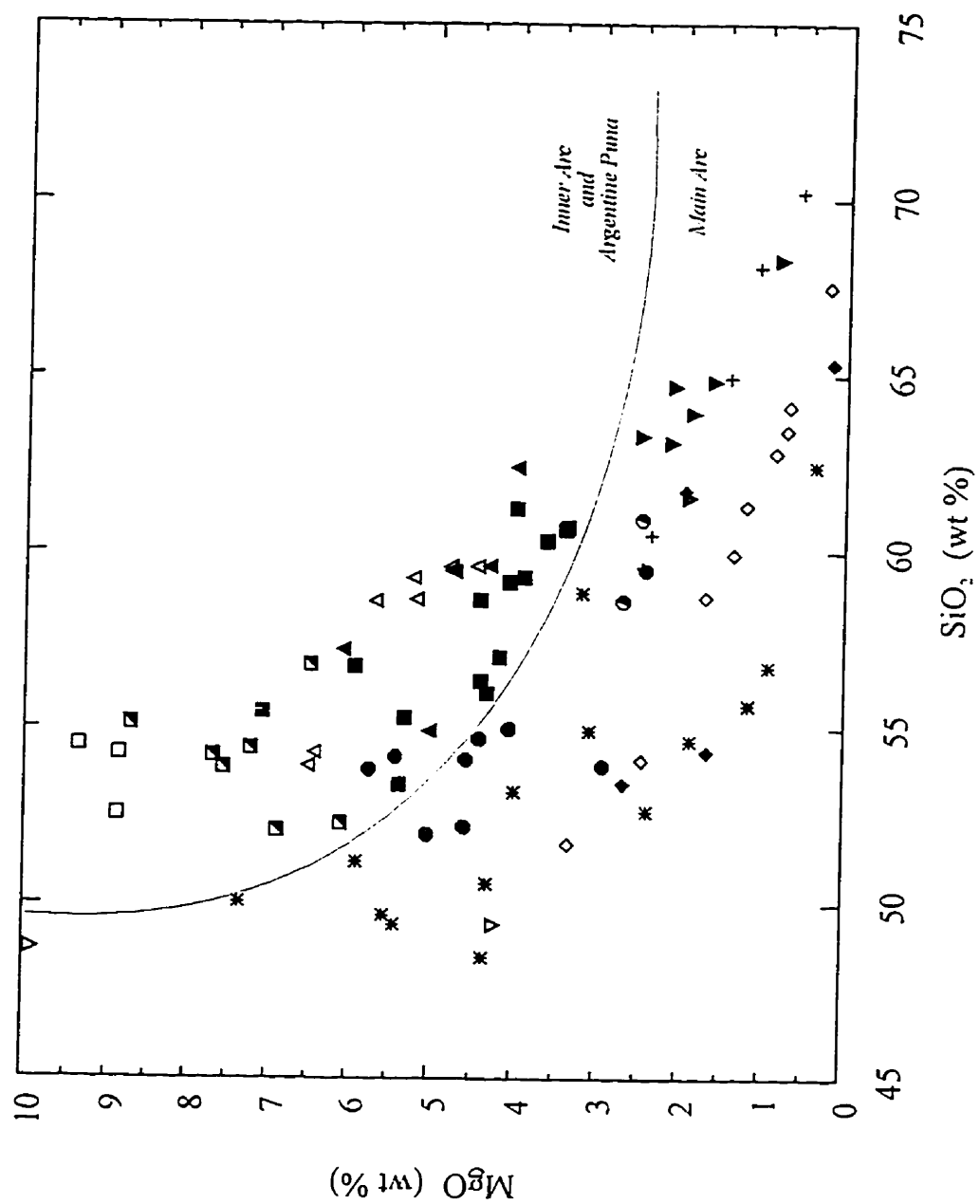


**Figure 4-31.**

Cr vs. SiO<sub>2</sub> diagram for rocks of the Central Andean shoshonite suites.

- filled diamond: Farallón Negro, this study
- empty diamond: Pocho, Kay and Gordillo, 1994
- half-filled square: Cerro Negro de Chorillos, Déruelle, 1991; Schreiber and Schwab, 1991; Kay *et al.*, 1994
- filled square: San Gerónimo, Déruelle, 1991; Schreiber and Schwab, 1991; Kay *et al.*, 1994
- empty square: La Poma, Kay *et al.*, 1994
- empty triangle: Cerro Moromoroni, Kontak *et al.*, 1986
- filled triangle: Picotani Group, Sandeman, 1995
- asterisk: Tacaza Group, Wasteneys, 1990
- filled inverted triangle: SW Bolivia, Kussmaul *et al.*, 1977
- empty inverted triangle: Abaroa Group, Jiménez *et al.*, 1993a
- cross: Linga Group, LeBel *et al.*, 1985
- filled circle: Sillapaca Fm, Aramaki *et al.*, 1984; France, 1985
- half-filled circle: 11 Ma shoshonites, France 1985

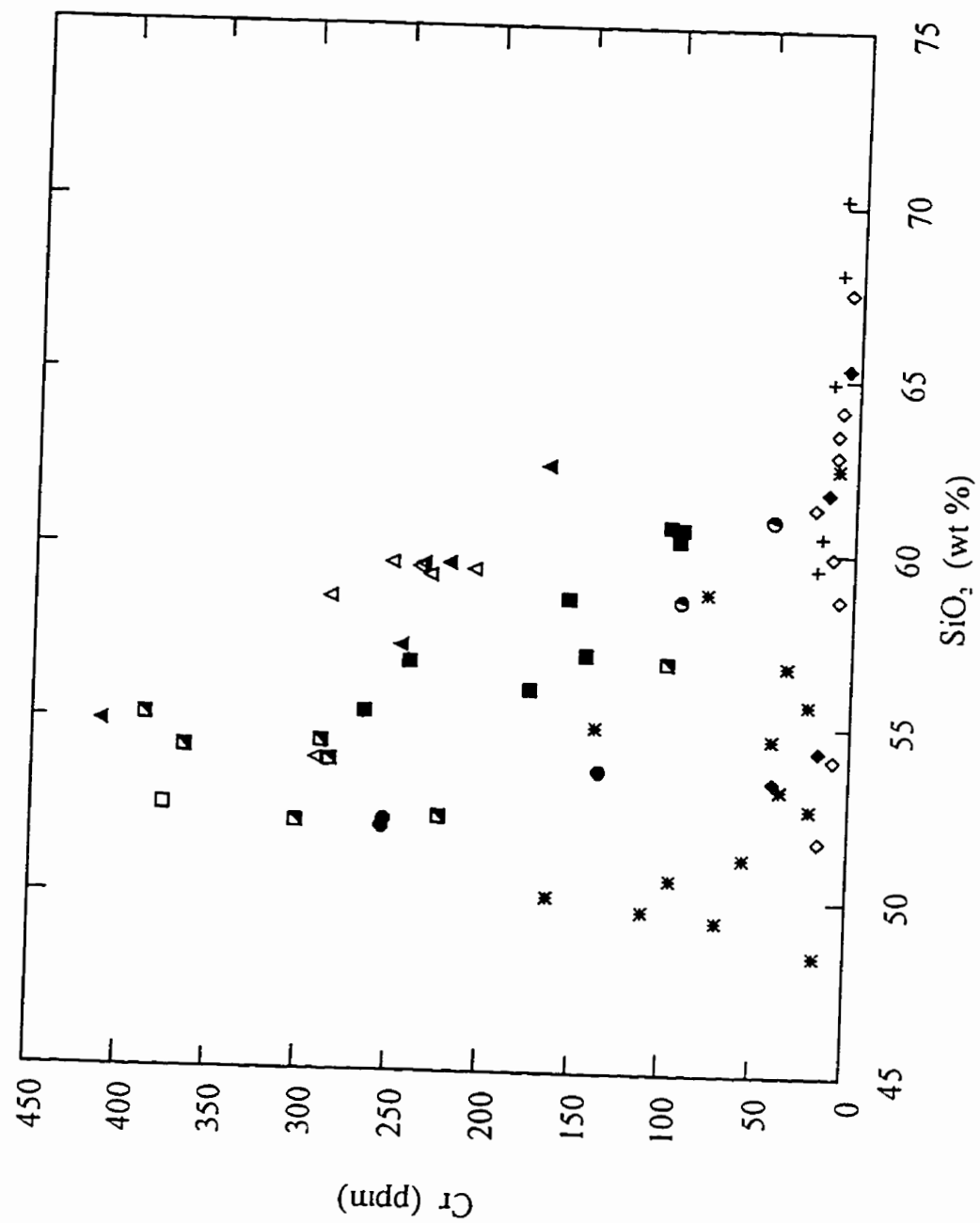


**Figure 4-32.**

Map showing the areal extent of the Central Andean  
Main and Inner Arc domains.

[Clark *et al.* (1983, 1984, 1990) and Sandeman (1995)]

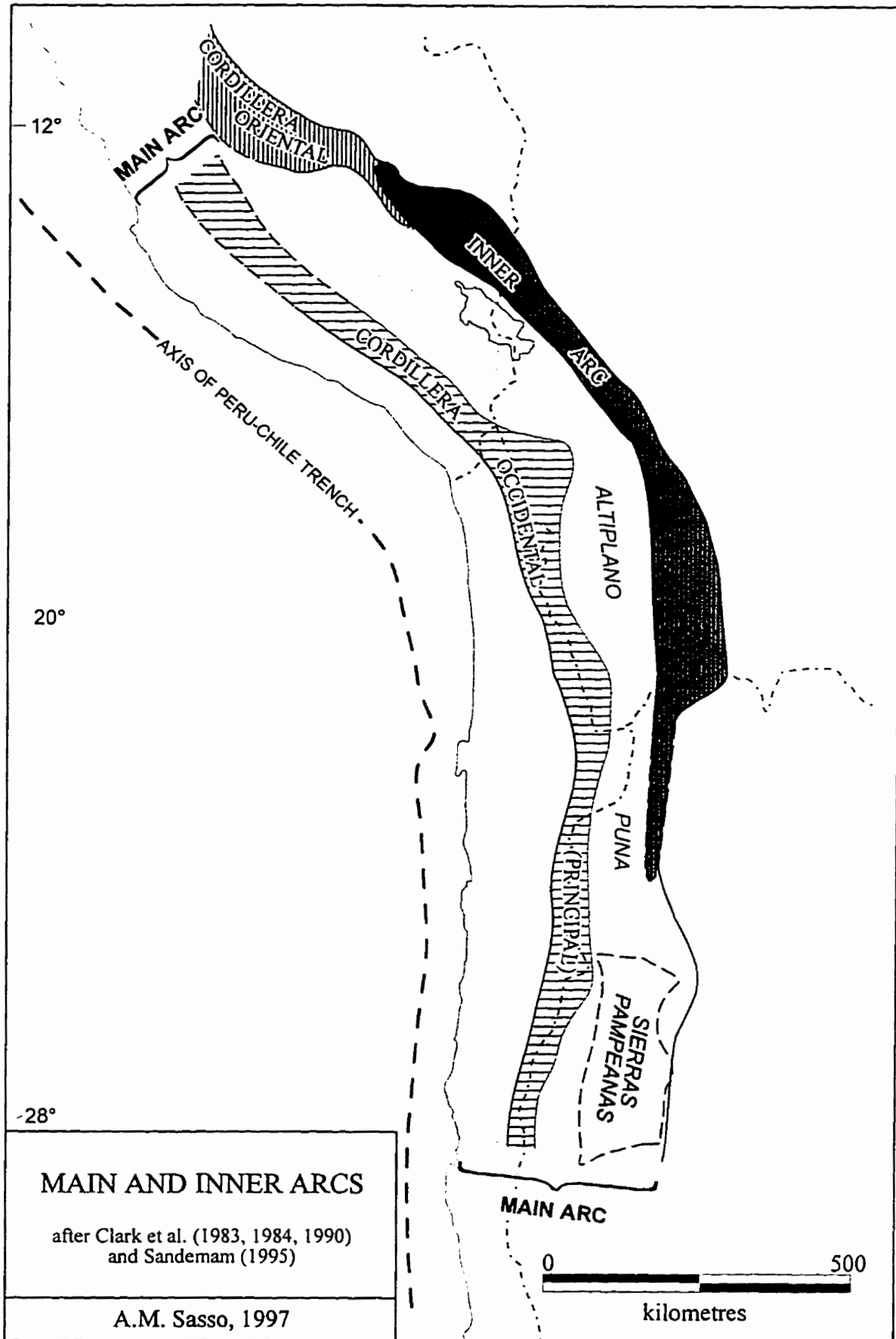


**Figure 4-33.**

Ba/La vs. La/Yb diagram for rocks of the  
Central Andean shoshonite suites.  
filled diamond: Farallón Negro, this study  
empty diamond: Pocho, Kay and Gordillo, 1994  
half-filled square: Cerro Negro de Chorillos,  
Déruelle, 1991; Schreiber and Schwab,  
1991; Kay *et al.*, 1994  
filled square: San Gerónimo, Déruelle, 1991;  
Schreiber and Schwab, 1991; Kay *et al.*,  
1994  
empty square: La Poma, Kay *et al.*, 1994  
empty triangle: Cerro Moromoroni, Kontak *et al.*,  
1986  
filled triangle: Picotani Group, Sandeman, 1995  
asterisk: Tacaza Group, Wasteneys, 1990  
filled inverted triangle: SW Bolivia, Kussmaul *et*  
*al.*, 1977  
empty inverted triangle: Abaroa Group, Jiménez *et*  
*al.*, 1993a  
cross: Linga Group, LeBel *et al.*, 1985  
filled circle: Sillapaca Fm, Aramaki *et al.*, 1984;  
France, 1985  
half-filled circle: 11 Ma shoshonites, France 1985

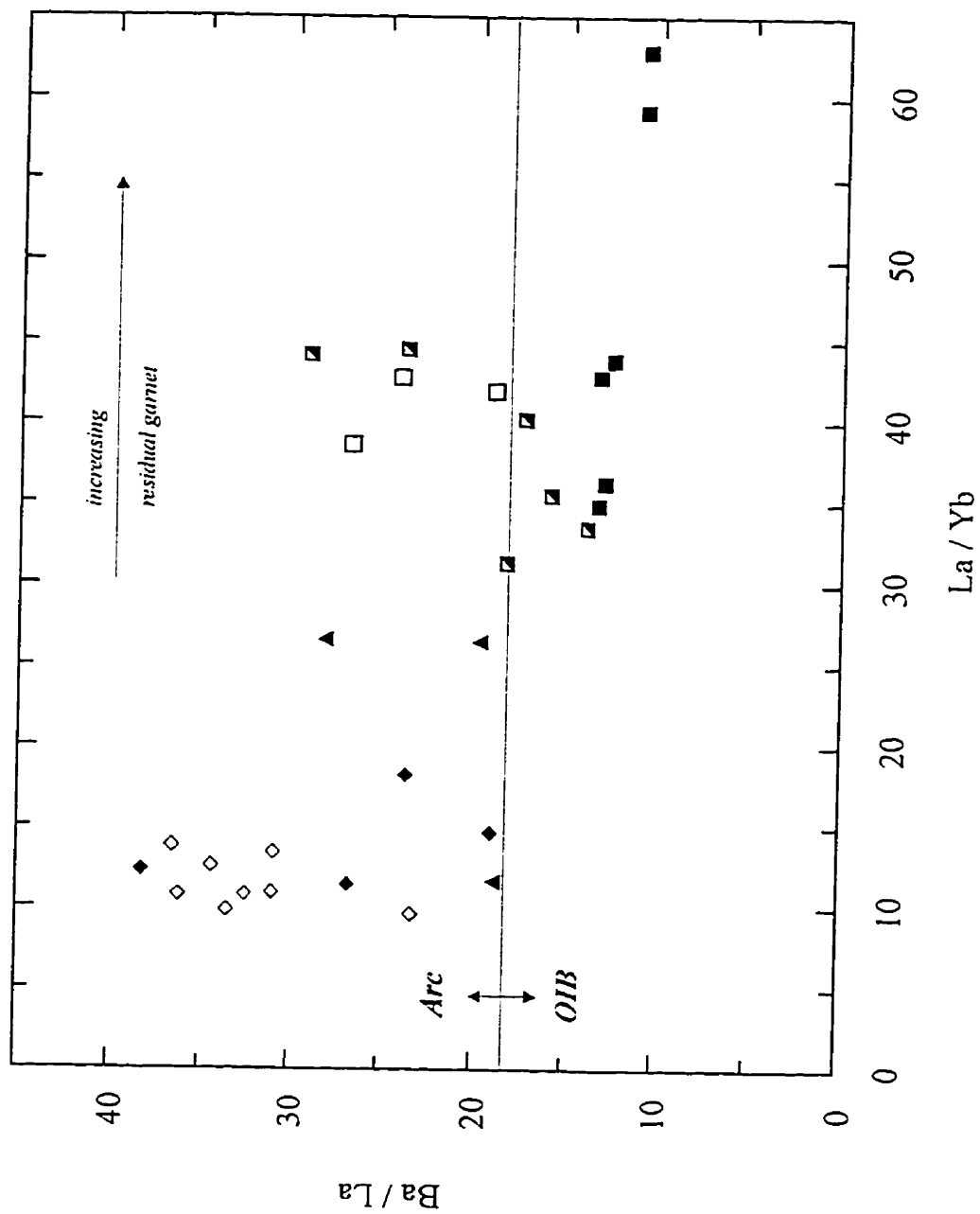
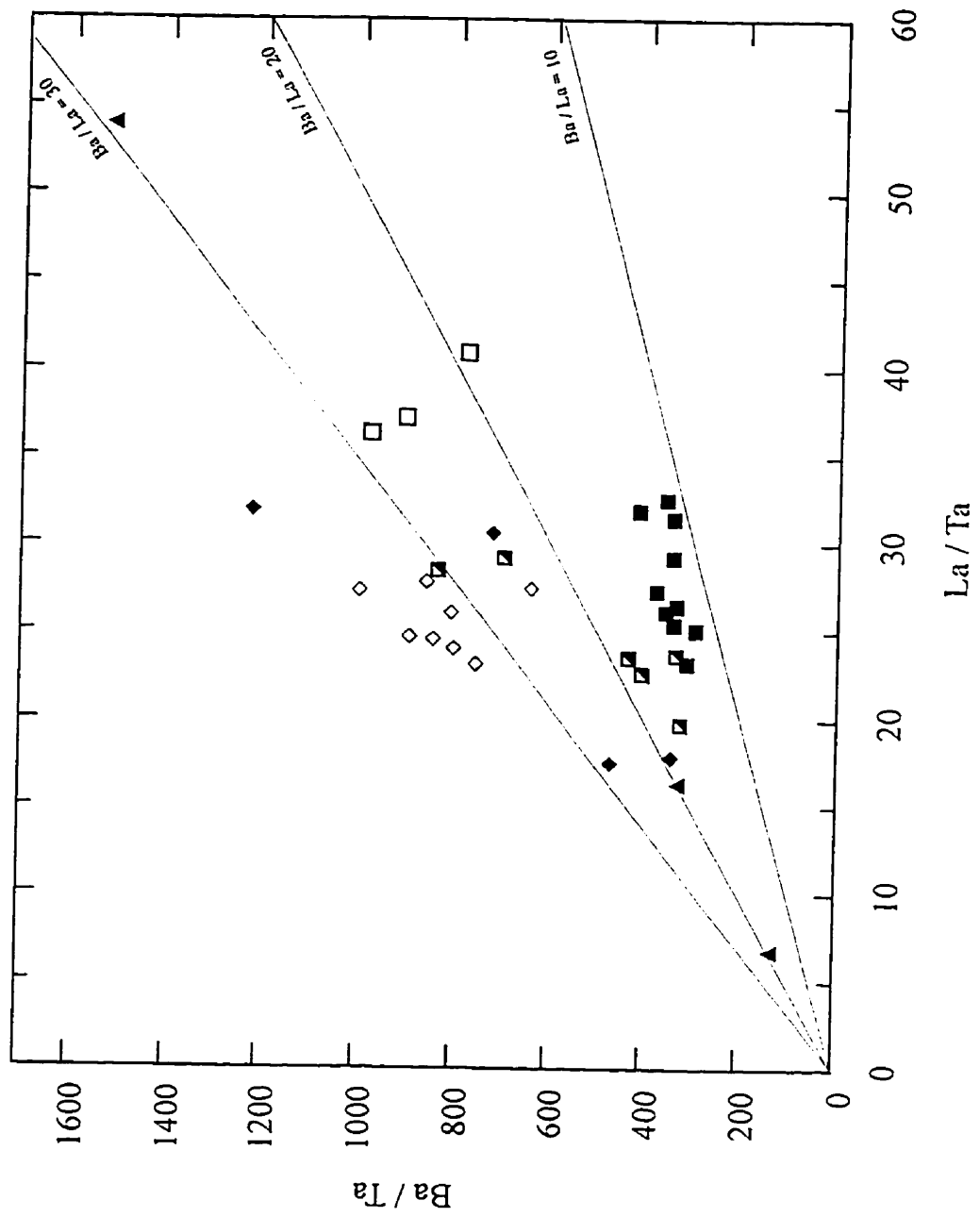




**Figure 4-34.**

Ba/Ta vs. La/Ta diagram for rocks of the  
Central Andean shoshonite suites.  
filled diamond: Farallón Negro, this study  
empty diamond: Pocho, Kay and Gordillo, 1994  
half-filled square: Cerro Negro de Chorillos,  
Déruelle, 1991; Schreiber and Schwab,  
1991; Kay *et al.*, 1994  
filled square: San Gerónimo, Déruelle, 1991;  
Schreiber and Schwab, 1991; Kay *et al.*,  
1994  
empty square: La Poma, Kay *et al.*, 1994  
empty triangle: Cerro Moromoroni, Kontak *et al.*,  
1986  
filled triangle: Picotani Group, Sandeman, 1995  
asterisk: Tacaza Group, Wasteneys, 1990  
filled inverted triangle: SW Bolivia, Kussmaul *et al.*, 1977  
empty inverted triangle: Abaroa Group, Jiménez *et al.*, 1993a  
cross: Linga Group, LeBel *et al.*, 1985  
filled circle: Sillapaca Fm, Aramaki *et al.*, 1984;  
France, 1985  
half-filled circle: 11 Ma shoshonites, France 1985



Negro, San Gerónimo and Chorillos suites.

Salient aspects of the geology, magmatic evolution and magmatic source regions of the Central Andean shoshonitic suites are summarized in Table 4-4. The majority of the studied rocks appear to have formed within a continuum of volcanic activity which includes units of high-K calc-alkaline and calc-alkaline affinities. The Peruvian, Bolivian and Farallón Negro shoshonite suites represent an early phase of magmatism in their respective regions, interpreted to be associated with thinner crust, and were followed by increasing proportions of rocks of high-K calc-alkaline and calc-alkaline compositions, suggesting changes in the petrogenetic environment in the underlying lower crust and upper mantle, possibly resulting from crustal thickening. In contrast, the young *Puna* shoshonites are late magmatic features interpreted to have formed over thickened lithospheric crust. The Pocho shoshonites formed in a magmatic continuum similar to that at Farallón Negro, but the shoshonites formed late in the sequence. They are interpreted to have formed over "normal" thickness crust. Differences in local crustal thickness are possibly reflected in the REE contents of the rocks. On the basis of the available HREE analyses, garnet appears to have been an important constituent in the source regions of the *Puna* and Cerro Moromoroni shoshonites and possibly also in the Picotani Group and Quaternary Shoshonite suites, whereas melting of a garnet-bearing source at Farallón Negro and Pocho is precluded by the flat HREE patterns. Crustal interaction is interpreted as important in the magmatic evolution of the Picotani, Moromoroni, SW Bolivian and *Puna* suites, but not in the generation of the Tacaza Group volcanics. Quartz xenocrysts rimmed by clinopyroxene have been interpreted to indicate the mixing and commingling

**Table 4-4.**

Salient aspects of the geology, magmatic evolution and  
magmatic source regions of the Central Andean  
shoshonitic suites.

(Data sources as in Figure 4-21)

SUITE	FARALLON NEGRO	POCHIO	SAN GERONIMO AND CHORILLOS	LA POMA	LINGA GROUP	PICOTANI GROUP
LOCATION	Main Arc	Main Arc	Main Arc (?)	Main Arc (?)	Main Arc	Inner Arc
GEOCHEMISTRY						
Alkalinity	along boundary	along boundary	S.G.: subalkaline Chorillos: alkaline	alkaline	subalkaline	subalkaline
Ti content	low	low	S.G.: low Chorillos: high	low	low	low
TECTONIC SETTING	extensional pull-apart basin	Caldera	extensional strike-slip faults	extensional graben	?	extensional basins
AGE (Ma)	8.3-8.4	5.3	0.78 - 2.0 Ma	Quaternary	68	24 Ma
MAGMA MIXING TEXTURES	no	sieve-textured plag.	cpx rims on quartz xenocrysts	cpx rims on quartz xenocrysts	no	cpx rims on quartz xenocrysts sieve-textured plag.
CRUSTAL INTERACTION	minimal	?	crustal assimilation	crustal assimilation	no significant contamination	yes
CRUSTAL THICKNESS	normal to slightly distended crust	"normal"	thick	thick	?	thin
SOURCE REGION (REE)	low La/Yb no garnet	low La/Yb no garnet	high La/Yb garnet	high La/Yb garnet	low La/Yb no garnet	garnet
DATA SOURCES	this study	Kay and Gordillo, 1994	Dernelle, 1991 Schreiber and Schwab, 1991 Kay et al., 1994	Kay et al. 1994	LeBel et al., 1985	Sandeman, 1995 Sandeman et al., 1995

SUITE	MOROMORONI FORMATION	TACAZA GROUP	SILLAPACA GROUP	QUATERNARY SHOSHONITE	ADAROA FORMATION	SW BOLIVIA
LOCATION	Inner Arc	Main Arc	Main Arc	Inner Arc	Main Arc	Main Arc
GEOCHEMISTRY						
Alkalinity	subalkaline	alkaline	along boundary	?	alkaline	subalkaline
Ti content	low	low	high	low?	low	low
TECTONIC SETTING	extensional basins	extensional pull-apart basin	?	normal faults	transensional	tensional faults as feeders
AGE (Ma)	23.7 Ma	23.5 - 31 Ma	5.0 - 6.0	Quaternary	25 - 20	Miocene - early Pleistocene
MAGMA MIXING TEXTURES	cpx rims on quartz xenocrysts	yes	?	cpx rims on quartz xenocrysts sieve-text. plag.	?	cpx rims on quartz xenocrysts
CRUSTAL INTERACTION	yes	no	?	crystal assimilation	no	crystal anatexis
CRUSTAL THICKNESS	thin	thin	thick	thick	thin	?
SOURCE REGION (REE)	garnet	?	?	high La/Yb garnet	?	?
DATA SOURCES	Kontak et al., 1986	Wasteneys, 1990 Sandeman et al., 1995	Aramaki et al., 1984 France, 1985	Carlier et al., 1992 Soler et al., 1992	Jimenez et al., 1993a Jimenez et al., 1993b	Kussmaul et al., 1977

of absarokitic magmas with the felsic products of crustal anatexis (Kontak *et al.*, 1986; Carlier *et al.*, 1992). Clinopyroxene coronas on quartz xenocrysts are reported in all suites with the exception of the Farallón Negro, Pocho, Tacaza and Linga suites, but insufficient petrographic information is provided for the Abaroa and Sillapaca suites to reveal the existence of these textures. Magma mixing is interpreted to have been of primary importance in the genesis of shoshonitic melts of the Picotani Group, including those from Cerro Moromoroni, but of secondary importance in the other suites. Shoshonitic volcanism occurred throughout the late Oligocene-Miocene interval and persisted into the Pleistocene in the region as a whole. The temporal association with extensional tectonics is common to all of the shoshonite suites in the Central Andes.

#### *Episodes of shoshonitic volcanism in the Central Andes*

Soler and Jiménez (1993) identify four short-lived episodes of shoshonitic volcanism along the Bolivian Orocline, at 24 - 28 Ma, 11 - 13 Ma, in the Pliocene, and in the Quaternary. The ages of the suites investigated herein corroborate the above division into four periods of shoshonitic volcanism, but the individual pulses of magmatic activity appear to have been longer-lived than as proposed by Soler and Jiménez (*op. cit.*). Extending the area of their study to include NW Argentina, it is concluded that shoshonitic volcanism was active in the Central Andes during the following periods:

20 - 31 Ma

K-rich rocks from this interval include: the Tacaza, Picotani Group and Cerro

Moromoroni suites from southern Peru, the Abaroa Formation rocks in Bolivia and a series of 22 Ma shoshonites and banakites, the Rondal lavas, related to transtensional faults in the southern *Altiplano* of Bolivia (Fornari *et al.*, 1993). This period was characterized by calc-alkaline volcanism in the Main Arc and subalkaline volcanism in the Inner Arc. Inner Arc shoshonites were generated in a garnet-bearing source region and their parental magmas were modified by crustal assimilation, a process which does not appear to have been important in the generation of Main Arc shoshonites. Insufficient information is available to evaluate the role of garnet in the source region of the K-rich Main Arc magmas. No shoshonitic volcanism of this age is reported in NW Argentina.

#### 8 - 13 Ma

Shoshonitic volcanism during this interval is documented in the northeastern *Altiplano* of Bolivia by Redwood and MacIntyre (1989). A series of *ca.* 12 Ma absarokites and shoshonites are described in a tectonic setting comparable to that of the *Puna*. The rocks are associated with minor Zn-Pb-Cu-Sb mineralization. Their distribution is tectonically controlled along the southern extension of the western margin of the Oligocene-to-Recent Puchani intermontane basin (67.25° S, 68.5° W).

Shoshonites were also emplaced during this time interval in southeastern Peru (France, 1985) and in NW Argentina at Farallón Negro.

#### 5 - 6 Ma

During this period, shoshonites of the Sillipaca and Tolaocco Formations erupted



in southern Peru and the Pocho volcanic complex was emplaced in NW Argentina.

Detailed information on the characteristics of the suites emplaced during the 8 - 13 and 5 - 6 Ma time periods is available only for the Farallón Negro and Pocho suites, and generalizations about the volcanism at this time are highly speculative. These easterly, but Main Arc magmas were emplaced into lithosphere of "normal" thickness, and were associated with extensional structures at Farallón Negro. Low La/Yb ratios indicate that garnet was not an important constituent of the source region. Both suites are of low-Ti affinity and plot along the alkaline-subalkaline field boundary.

#### Quaternary

Shoshonitic volcanism of this age is documented in the Argentine *Puna* (Déruelle, 1991; Schreiber and Schwab, 1991; Kay *et al.*, 1994) and in southeastern Peru (Carlier *et al.*, 1992; Soler *et al.*, 1992). Both areas were locally characterized by thin crust. The magmas experienced important crustal assimilation and display high La/Yb ratios indicative of the presence of garnet in the source region. All suites display magma-mixing textures and are associated with extensional tectonics.

The age relationships of the SW Bolivian shoshonite suite are not sufficiently well documented to classify them using this temporal framework, but this suite contains members that appear to belong to both the 5 - 6 Ma and Quaternary time intervals.

#### Summary

From the above synthesis, it appears that rocks of shoshonitic affinity have erupted throughout the late Oligocene-to-Recent history of the Central Andes and, moreover, extend back to the Cretaceous (*e.g.*, Linga Group). The shoshonitic magmas erupted

through both thin and thick lithosphere. Thick crustal conditions appear to have been associated with higher La/Yb ratios, implying a significant role for garnet in the magma-generating region, and with greater amounts of crustal assimilation (*e.g.*, Argentine *Puna*), although the existence of thin crust does not necessarily preclude these conditions (*e.g.*, Picotani and Moromoroni). Magma mixing appears to have played an important role in the evolution of shoshonites at several centres (*e.g.*, Picotani) but not at others (*e.g.*, Tacaza). The geochemistry of the shoshonites shows significant variation, with high-Ti and low-Ti members, variable MgO and Cr, and compositions ranging from alkaline to subalkaline. Shoshonites erupted in both the Inner and Main Arcs, and there is no apparent migration of volcanism with time. In fact, shoshonitic volcanism occurred repeatedly in restricted geographical areas (*e.g.*, Picotani area: H.A. Sandeman, pers. comm., 1997; Santa Lucía District: Wasteneys, 1990). The only feature common to all suites is their emplacement during periods of extensional tectonism.

#### **Petrogenesis of Farallón Negro rocks**

The nature of the relationship between the shoshonitic association and other igneous series, and particularly calc-alkaline magmatism, is poorly understood. In Papua New Guinea, spatial and temporal overlap of volcanic suites was observed by Jakeš and White (1969), who documented the juxtaposition of calc-alkaline and shoshonitic compositions. Dostal *et al.* (1977) suggested that the calc-alkaline volcanics in northern Chile and northwest Argentina were derived by partial melting of upper mantle above a descending slab that contributed volatiles to the melt; crustal contamination or zone

refining and high level fractionation assisted the differentiation of the magmas. They concluded that shoshonites erupted through thinner crust than high-K calc-alkaline suites.

Kontak *et al.* (1986) present evidence from upper Oligocene shoshonitic volcanic rocks in the Inner Arc of southern Peru which indicates the major involvement of magma mixing in shoshonite evolution. On the basis of chemical and textural variations, they invoke a complex history originating with partial melting of a REE- and LILE-enriched garnet peridotite source, an early period of high pressure crystallization closely followed by a second period of relatively shallow-level fractionation, and mixing of the magma with a felsic liquid generated by partial melting of the crust. Mixing of the two melts probably occurred in a shallow magma chamber. Wasteneys (1990), in a study of broadly coeval shoshonites in the Main Arc of southern Peru, determined that magma mixing was not of primary importance in the formation of shoshonitic magmas, its involvement was inferred in the generation of slightly later calc-alkaline lavas.

The geochemical continuum represented by the Farallón Negro high-K calc-alkaline and shoshonite suites strongly suggests that they originated from a common source. Whereas shoshonitic units represent some of the oldest dated units at Farallón Negro, they are interbedded with high-K calc-alkaline units. The absence of features commonly interpreted to be indicative of magma mixing (*e.g.*, sieve-textured plagioclase) in the shoshonites studied at Farallón Negro would suggest a lesser involvement of MASH processes for the shoshonites. This would imply either thinner crust at the time of eruption and/or rapid emplacement of shoshonitic melts with minimal crustal interaction. These conditions, compatible with emplacement in a tensional pull-apart basin

setting, may have predominated during a restricted time interval (*ca.* 7.5 to 8.4 Ma) The calc-alkaline melts, which do show evidence for mixing, may have experienced greater interaction with the lower crust through slower magma ascent and/or longer crustal residence time and were emplaced more or less continuously throughout the igneous history at Farallón Negro (5.2 to 12.6 Ma).

The enrichment in LILE and LREE, combined with the low abundance of HFSE, is consistent with trends observed worldwide for subduction-related potassic igneous rocks (Müller and Groves, 1995). The LILE and LREE contents also suggest that the Farallón Negro magmas may have been generated by melts formed by low degrees of partial melting. Depletion in the HFSE suggests that deep asthenospheric magma sources were probably not tapped in the generation of the Farallón Negro magmas. The relatively flat REE patterns (La/Yb ratios ranging from 9 to 20) preclude the formation of parental Farallón Negro magmas through variable partial melting of a garnet-bearing source. The relatively high Ba/La ratios are arc-like and suggest an enrichment of alkaline-earth in the source region. The low La/Ta ratios are interpreted to indicate minimal incorporation of slab-derived material.

## CHAPTER 5

### <sup>40</sup>Ar/<sup>39</sup>Ar GEOCHRONOLOGY OF THE FARALLON NEGRO VOLCANIC COMPLEX

#### **Previous Geochronological Research**

Bodenbender (1922), González Bonorino (1950), Angelelli (1950) and Turner (1971) all inferred a Neogene age for the mineralization and associated volcanic and hypabyssal rocks at Farallón Negro on the basis of stratigraphic relationships. In the course of a comprehensive analysis of geological and metallogenetic relationships in the 26° - 29° S Andean transect (Clark *et al.*, 1976, and references therein; Caelles, 1979), ten conventional K-Ar age determinations by McBride (1972) confirmed the Miocene age of the rocks of the district. Of these mineral and whole-rock dates, three were published by Caelles *et al.* (1971) and several others have been cited in regional syntheses of Andean porphyry copper mineralization by Sillitoe (1981; 1988). In Sillitoe's seminal paper (1973) addressing the characteristic features of the tops and bottoms of porphyry copper deposits, the geology and chronology of the Farallón Negro deposits were extensively drawn upon.

In addition to the above studies, four K-Ar mineral ages for rocks from the Capillitas and Cerro Atajo deposits were published by the Japanese International Cooperation Agency (J.I.C.A., 1978).

#### ***Comparison of new and published age data***

One of the secondary goals of this research was to evaluate the ages determined by McBride (1972) using modern <sup>40</sup>Ar/<sup>39</sup>Ar laser microprobe geochronologic techniques.

To this end, samples collected by J.C. Caelles and A.H. Clark, and analyzed by McBride (1972), were included in the dating study. Further, three new samples were collected during the 1993 field season in an attempt to reproduce Caelles' sample locations as described in McBride (1972; the original field records have not been accessible). Table 5-1 presents the K-Ar ages obtained by McBride (1972; recalculated with the decay constants of Steiger and Jäger, 1977), the  $^{40}\text{Ar}/^{39}\text{Ar}$  ages obtained for the same materials in this study, and the  $^{40}\text{Ar}/^{39}\text{Ar}$  ages for the new samples.

Significant discrepancies are apparent between the original and new studies. Of the ten samples analyzed by McBride (1972), material from eight was obtained and re-analyzed; samples JC-70 and JC-85 were not located. Of the eight redetermined dates, only three overlap within analytical error ( $2\sigma$ ) with the ages obtained in the original study. In general, the K-Ar ages are older than the  $^{40}\text{Ar}/^{39}\text{Ar}$  ages, and the difference in ages is significant (*i.e.*, greater than 2 m.y.) for samples JC-33 and JC-41. Sample inhomogeneity could explain some of the discrepancy observed. The larger sample size (approximately 1 g) required by the K-Ar method for young samples should minimize minor sample inhomogeneity, whereas the extremely small sample size (less than 30 mg) used in the  $^{40}\text{Ar}/^{39}\text{Ar}$  laser technique would be expected to reveal minor sample inhomogeneity. As explained in the following section on analytical technique, all samples dated by the  $^{40}\text{Ar}/^{39}\text{Ar}$  technique were analyzed at least three times, and sample inhomogeneity would be evident from disagreement among ages on different sample aliquots. This was not, however, apparent in any of the samples. The lack of agreement in the dates for some samples may be due to the fact that they were determined by entirely different techniques,

**Table 5-1.**

Comparison of conventional K-Ar dates from McBride (1972; recalculated with the decay constants of Steiger and Jäger, 1977) with new  $^{40}\text{Ar}/^{39}\text{Ar}$  laser microprobe ages obtained herein for the same materials and for new samples collected during this study from the apparent original sample locations.

Location abbreviations:

BLA: Bajo de la Alumbreira

BAT: Bajo de Agua Tapada

BAD: Bajo el Durazno

BLP: Bajo las Pampitas

MIV: Agua Rica

SAMPLE	MATERIAL DATED	McBride (1972) AGE ERROR (Ma) (2 $\sigma$ )	This study AGE ERROR (Ma) (2 $\sigma$ )	New (1993) samples SAMPLE AGE ERROR (Ma) (2 $\sigma$ )
JC-30	Whole-Rock	6.2	6.30	
JC-31a	Whole-Rock	7.8	6.91	
JC-33	Hornblende	10.9	8.09	
JC-41	Biotite	9.0	6.90	FAR 10 (bio) 6.84 0.15
JC-42a	Whole-Rock	8.1	8.95	
JC-47b	Biotite	8.9	8.46	FAR 224 (hbl) 8.33 0.18
JC-70	Cryptomelane	2.7		
JC-77a	Whole-Rock	7.9	7.02	FAR 216 (hbl) 7.50 0.20
JC-85	Biotite	7.3		
JC-191	Biotite	7.0	7.03	



*viz.* K-Ar dating using RF furnace heating in the McBride study vs.  $^{40}\text{Ar}/^{39}\text{Ar}$  dating using laser microprobe excitation in this study. Additionally, problems with sample fusion, spike calibration and/or K-analysis particularly for hornblende and whole-rock samples, which may have been encountered in McBride's research, could account for the discrepancy in ages between the two studies (D.A. Archibald, pers. comm., 1995, 1997).

The information provided by McBride (1972) is sufficient to identify only three of Caelles' (1979) sample locations with any degree of confidence. Thus, the newly-collected FAR 10 is thought to be equivalent to JC-41, FAR 216 to JC-77a and FAR 224 to JC-47b. The new  $^{40}\text{Ar}/^{39}\text{Ar}$  ages for biotite from FAR 10 and JC-41 are statistically equivalent (*i.e.*, there is overlap of the  $2\sigma$  errors), but the dates do not overlap within analytical error with the K-Ar age for JC-41. The  $^{40}\text{Ar}/^{39}\text{Ar}$  age of hornblende from FAR 224 is statistically equivalent to the  $^{40}\text{Ar}/^{39}\text{Ar}$  age on biotite from JC-47b, but not with the K-Ar age. The  $^{40}\text{Ar}/^{39}\text{Ar}$  age on hornblende from FAR 216 is mid-way between the  $^{40}\text{Ar}/^{39}\text{Ar}$  and K-Ar whole-rock ages of JC-77a and does not overlap within error with either. In light of the evolution and refinement of dating methods in the past twenty years and given the good correspondence herein between separate sample aliquots (see below) and the low errors of the laser microprobe study, these data, while limited, would suggest that the  $^{40}\text{Ar}/^{39}\text{Ar}$  determinations provide a more reliable estimate of the actual age of the samples.

Table 5-2 presents the K-Ar dates for samples from Capillitas and Cerro Atajo published by J.I.C.A. (1978) and new  $^{40}\text{Ar}/^{39}\text{Ar}$  dates determined on samples collected in this study. Detailed sample locations and descriptions were not provided by J.I.C.A.

**Table 5-2.**

Comparison of conventional K-Ar ages for Capillitas and Cerro Atajo samples dated by J.I.C.A. (1981) with  $^{40}\text{Ar}/^{39}\text{Ar}$  laser microprobe ages for samples from similar units collected during this study.

SAMPLE	JICA (1978)		This study		MATERIAL DESCRIPTION DATED	
	AGE (Ma)	ERROR (2σ)	AGE (Ma)	ERROR (2σ)		
<b>Capillitas</b>						
FAR 318			5.16	0.05	K-feldspar	Dacite dike
JICA 1	5.0	0.5			biotite	Dacite
JICA 2	5.0	0.5			muscovite	Rhyolite
<b>Cerro Atajo</b>						
FAR 304			5.11	0.04	Whole-rock	Sericitized porphyry
JICA 3	5.0	0.5			biotite	Dacite
JICA 4	5.0	1.0			biotite	Dacite

FAR 318 is a sample of a dacite dyke at Capillitas, and because there are only three outcrops of intrusive dacite at Capillitas and all exhibit similar mineral assemblages and textures, they are herein interpreted to be contemporaneous. Therefore, FAR 318 is thought to be equivalent to JICA 1. The  $^{40}\text{Ar}/^{39}\text{Ar}$  age of FAR 318 is equivalent to the K-Ar age for JICA 1 and is interpreted to represent the age of the unit. JICA 2 is a rhyolite from Capillitas, but this unit was not dated in this study.

Samples JICA 3 and 4 are biotites from a dacitic intrusive at Cerro Atajo. FAR 304 is a sericitized porphyry, possibly of dacitic composition, from the western end of the drill-road that follows the Cerro Atajo ridgeline. I encountered only one significant dacite intrusion in this area, underlying Cerro Atajo itself and represented by FAR 304. Thus, samples JICA 3 and 4 and FAR 304 probably represent the same intrusive unit. The K-Ar and  $^{40}\text{Ar}/^{39}\text{Ar}$  ages of the samples are statistically equivalent and are interpreted to represent the time of hydrothermal alteration at Cerro Atajo.

#### **$^{40}\text{Ar}/^{39}\text{Ar}$ Dating Technique**

##### ***Background***

The  $^{40}\text{Ar}/^{39}\text{Ar}$  dating method (Merrihue and Turner, 1966) is a modification of the conventional K-Ar technique, which is based upon the accumulation of radiogenic argon ( $^{40}\text{Ar}^*$ ) produced through the decay of the naturally-occurring radioactive isotope of potassium,  $^{40}\text{K}$ ; details of the K-Ar technique are given by Dalrymple and Lanphere (1969). The  $^{40}\text{Ar}/^{39}\text{Ar}$  dating method is discussed in detail by McDougall and Harrison (1988). It involves the irradiation of a sample of unknown age, together with a standard

sample of known age, in a nuclear reactor to produce  $^{39}\text{Ar}$  from  $^{39}\text{K}$  by fast neutron bombardment. After irradiation, the  $^{40}\text{Ar}/^{39}\text{Ar}$  ratios of sample and standard are measured in a mass spectrometer. By comparing these measured  $^{40}\text{Ar}/^{39}\text{Ar}$  ratios, and after applying corrections for atmospheric argon and interfering argon isotopes, an age for the sample can be calculated. An important aspect of the  $^{40}\text{Ar}/^{39}\text{Ar}$  technique is that only the isotopic composition of argon is measured. In contrast, for a conventional K-Ar date, both elemental K and  $^{40}\text{Ar}$  must be measured quantitatively. This requires two separate sample aliquots: one for the measurement of argon by isotope dilution mass spectrometry, and a second for the measurement of potassium by some other analytical method such as flame photometry or X-ray fluorescence.

The  $^{40}\text{Ar}/^{39}\text{Ar}$  method was first used in total-fusion experiments in which an irradiated sample was completely melted using a furnace and all isotopes of argon measured in a single analysis to calculate an age (Merrihue and Turner, 1966), which would be analogous to a conventional K-Ar age. However, the technique evolved rapidly to include progressive degassing by incremental heating (Turner, 1968; Lanphere and Dalrymple, 1971). In this way, an apparent age may be calculated for each increment of gas released, and the ages of all temperature increments of a sample plotted *versus* the accumulative percent of  $^{39}\text{Ar}$  released to generate an *age spectrum*. Using this technique, secondary disturbances of the K-Ar system can be recognized and geochronologically significant events may be determined.

The  $^{40}\text{Ar}/^{39}\text{Ar}$  technique possesses several advantages over the conventional K-Ar method: i) potassium and argon are measured simultaneously on the same sample aliquot,

thereby eliminating errors due to sample inhomogeneity; ii) the technique of step-wise degassing provides a record of the distribution of argon isotopes within the sample and allows the recognition of either argon loss or the presence of extraneous, "excess", argon in the sample; and, iii) "plateaux", in which the ages of several contiguous steps agree within analytical error, may be defined, providing a measure of the consistency of the Ar isotopes released and thus a more precise age (Geyh and Schleicher, 1990).

The recent development of the *laser microprobe* technique has allowed the reliable  $^{40}\text{Ar}/^{39}\text{Ar}$  dating of very small samples and even, under favourable circumstances, of individual mineral grains (York *et al.*, 1981; Maluski and Schaeffer, 1982; van den Bogaard *et al.*, 1987). Megrue (1973) first demonstrated that a pulsed laser could be used effectively for the *in situ* dating of minute volumes of lunar materials, and Maluski and Schaeffer (1980, 1982) were successful in applying this technique to terrestrial samples. Hall *et al.* (1980) subsequently presented results for terrestrial samples using a continuous, rather than pulsed, laser.

The first step-heating laser-fusion age determination was performed by varying the laser beam power (York *et al.*, 1981) in a study of an Archean slate sample. These authors also performed single-crystal laser total-fusion determinations on Proterozoic hornblende and biotite. They demonstrated good agreement within experimental error between the laser total-fusion and step-heating laser fusion ages on the one hand, and ages obtained using a conventional  $^{40}\text{Ar}/^{39}\text{Ar}$  radio-frequency (RF) fusion system, on the other. Their results demonstrated reproducible accuracy and precision for both laser and conventional methods. Van den Bogaard *et al.* (1987) applied the laser microprobe

technique to the dating of single grains of Quaternary sanidine. They found agreement between the single-grain total-fusion laser microprobe ages and  $^{40}\text{Ar}/^{39}\text{Ar}$  step-heating experiments and thereby demonstrated the precision and reproducibility of the method.

The laser microprobe technique has also been applied to the study of age variations and argon diffusion characteristics in single mineral grains (*e.g.*, Layer *et al.*, 1987; Phillips and Onstott, 1988; Lee *et al.*, 1990; Kelley and Turner, 1991). A narrowly focused laser beam is used to melt small pits, *ca.* 30  $\mu\text{m}$ , in traverses across individual mineral grains. "Spot" ages (both total-fusion and step-wise degassing) along the traverses record age gradients and hence reveal argon diffusion within the grain.

The key aspects of the laser microprobe technique are: i) the minute volume of sample material required, which reduces the time of sample preparation and the likelihood of contamination during the sample preparation stage, and moreover significantly decreases the exposure of researchers to radiation; ii) the technique is much faster than standard  $^{40}\text{Ar}/^{39}\text{Ar}$  furnace-heating experiments and allows for the rapid analysis of multiple sample aliquots, providing greater precision; iii) the blanks produced are much lower than those for  $^{40}\text{Ar}/^{39}\text{Ar}$  furnace-heating methods, thereby improving accuracy; and, iv) the laser microprobe allows for "age traverses" of single grains, providing greater insight into the thermal history of mineral formation and subsequent thermal history.

Single-grain laser microprobe step-heating experiments have traditionally used samples that are significantly older than Miocene (*e.g.*, Proterozoic hornblende and biotite: York *et al.*, 1981; Proterozoic biotite with Eocene thermal disturbance: Maluski and Schaeffer, 1982). Step-heating of minute volumes of these samples is possible due to the

relatively large amount of radiogenic  $^{40}\text{Ar}$  that has accumulated. The low radiogenic  $^{40}\text{Ar}$  contents of the very young Farallón Negro samples preclude single-grain age determinations, and moreover the volume of material necessary to provide sufficient levels of radiogenic  $^{40}\text{Ar}$  discouraged detailed multi-step heating runs using the laser microprobe.

### *Analytical Method*

$^{40}\text{Ar}/^{39}\text{Ar}$  total-fusion age determinations were herein carried out on 42 mineral separates and 14 whole-rock samples. Separates were prepared using a *Frantz* magnetic separator and heavy liquids, and by hand-shaking on coarse filter paper. Whole-rock samples collected to date phyllic alteration events were prepared using a magnetic separator to remove as much of the magnetic fraction as possible. The mineral separates and whole-rock samples were cleaned by immersion in de-ionized water in an ultrasonic bath for 10 minutes, followed by repeated washing in acetone. Mineral separates were purified by hand-picking under a binocular microscope.

Samples and neutron flux monitors (standards) were wrapped in aluminum foil and loaded into an 11.5 cm long, 2.0 cm diameter aluminum irradiation container. Unknowns and flux monitors were irradiated with fast neutrons in the region of lowest flux gradient of position 5C of the McMaster nuclear reactor (Hamilton, Ontario) for 10 hours. Flux monitors included TCR-sanidine (28.0 Ma: Baksi *et al.*, 1996) and MAC-83-biotite (24.1 Ma: Sandeman *et al.*, 1997), an intralaboratory standard dated by  $^{40}\text{Ar}/^{39}\text{Ar}$  step-heating experiments relative to standards LP-6 (128.5 Ma: Roddick, 1983), and intralaboratory standard SP-85 (18.4 Ma: R.J. Langridge, unpublished data). Groups of flux monitors (13



in can 140, 18 in can 141, and 10 in can 142) were evenly distributed throughout the irradiation container and the J-value, a unitless parameter that is the measure of neutron flux and of the efficiency of conversion of  $^{39}\text{K}$  to  $^{39}\text{Ar}$  in the nuclear reactor during irradiation, was determined for individual samples by parabolic interpolation. A typical calibration curve (can 141) is presented in figure 5-1.

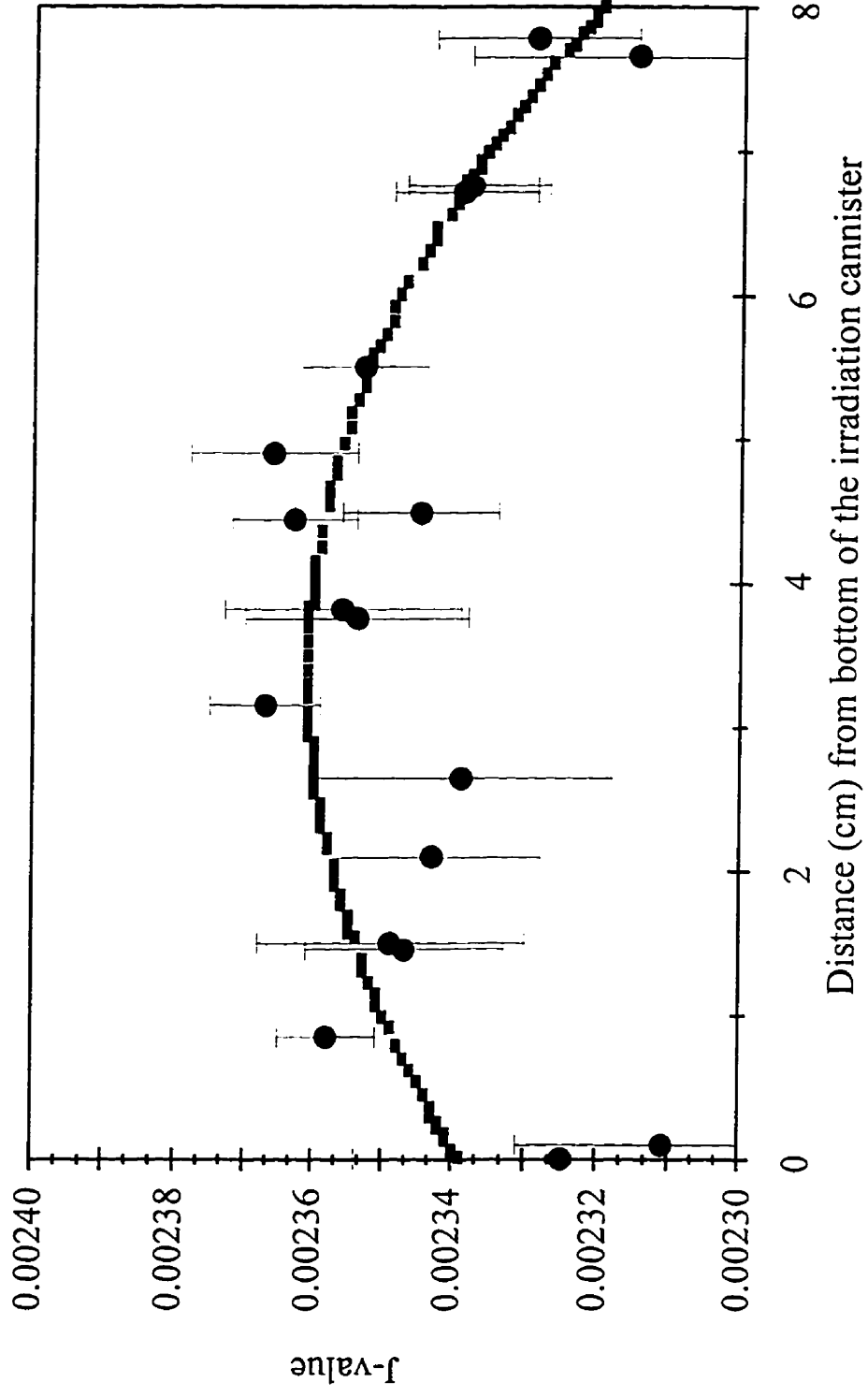
The samples were loaded in a specially-designed sample-holder which consists of an aluminum plate with over 100 pits drilled into its surface. These are approximately 2 - 3 mm in diameter and have a similar depth. The sample holder was placed beneath the sapphire view-port of a small stainless steel chamber connected to an ultra-high vacuum purification system. Samples were uniformly heated with a defocused 8W (total power) *Lexel* 3500 continuous argon-ion laser. The samples were initially excited using a low-power beam (0.3 to 0.5 W) to remove atmospheric argon contamination and other impurities. They were then heated in a total-fusion step at 7.0 W for age determination. The evolved gas, after purification using an *SAES* C50 getter, was admitted to an on-line *MAP* 216 mass spectrometer, with a *Bäur Signer* source and an electron multiplier and run in the static mode. Blanks, measured routinely every third sample run, were subtracted from the subsequent gas fractions. Each sample was analyzed in this way at least three times.

Typically, seven sets of argon-isotope peak heights were measured for each step and these were extrapolated to zero-time and normalized to the  $^{40}\text{Ar}/^{39}\text{Ar}$  atmospheric ratio (295.5). The  $^{40}\text{Ar}/^{39}\text{Ar}$  analyses were corrected for neutron-induced  $^{40}\text{Ar}$  from potassium,  $^{39}\text{Ar}$  and  $^{36}\text{Ar}$  from calcium, and  $^{36}\text{Ar}$  and  $^{38}\text{Ar}$  from chlorine. Ages and their errors were

**Figure 5-1.**

Calibration curve for canister 141 irradiated in position 5C of the McMaster nuclear reactor (Hamilton, Ontario) on August 8, 1995, illustrating the interpolation of sample J-values between calculated J-values from flux monitors of known age. Black filled circles with error bars represent flux monitors of known age (standards MAC-83 and TCR). The curve is defined by black filled squares which represent the interpolated J-values of samples.

# Can 141



calculated according to the methods of Dalrymple *et al.* (1981), using the decay constants recommended by Steiger and Jäger (1977). All errors in this thesis are quoted at  $2\sigma$ .

### *The Dating Study*

This study represents the first comprehensive investigation conducted in the new laser microprobe  $^{40}\text{Ar}/^{39}\text{Ar}$  geochronological laboratory at Queen's University. This was also the first study to date very young samples in this facility. Therefore, no standard methodology had been established and both the laboratory facility (particularly the software utilized for age calculation) and procedures evolved considerably during the course of the study. These developments are chronicled in some detail in the following sections.

The laboratory work for the dating study was conducted during three separate periods in 1995 and 1996, under the supervision of Dr. D.A. Archibald. A final round of dating was conducted in 1997 by Jerry Grant.

#### Round 1

The first stage of dating, from October 3rd to 16th and from November 13th to 23rd, 1995, resulted in the development of a two-stage fusion technique. Only igneous units were dated at this time. Three aliquots of a sample, each comprising approximately 25 to 50 grains, were loaded in the sample holder. Initially, samples were fused during 6 minute runs in a single high-powered step. Three minutes were allowed for sample fusion during which time the laser power was increased gradually so as to minimize

potentially violent degassing of samples (especially biotite) which could propel the grains into neighbouring pits. Three minutes was allowed for purification of the released gas by the getter ("gettering") before introduction into the mass spectrometer. However, it became apparent that three minutes were insufficient for the complete fusion of the samples and the sample run-time was increased to seven minutes (four minutes for sample fusion and three for purification). Sample run times were eventually increased to ten minutes to accommodate larger sample sizes and to allow five minutes for purification.

Although the least-altered samples available were chosen for the geochronological study of the igneous units, all samples have undergone some degree of deuteritic alteration. After examination of the results for the first samples analyzed, it was suggested (D.A. Archibald, pers. comm., 1995) that running an initial low-powered step with the beam defocused might drive off atmospheric argon and other low temperature impurities, *e.g.*, water vapour, hydrocarbons, CO<sub>2</sub>, CO and other volatile constituents that had not been removed during baking of the fusion system. Powers of 0.3 W for biotite and 0.5 W for hornblende were selected because they were found to release sufficient gas to lower the atmospheric <sup>40</sup>Ar content of the second step significantly, yet did not cause the minerals to become incandescent, which indicates the onset of melting and the release of argon, especially <sup>39</sup>Ar, from deeper sites within the mineral structure. The sample was then completely fused in a second step, commonly using a focused beam at maximum (7 W) power, for age determination. This two-step method reduces the atmospheric <sup>40</sup>Ar content of the second step (the age determination step) thereby reducing the error in the age and resulting in greater precision of the measurement.

A standard methodology was evolved in which the first sample aliquot was fused in a total-fusion step to determine the content of atmospheric  $^{40}\text{Ar}$ . If this was sufficiently low (arbitrarily defined as less than 40 %, *i.e.*, low enough to reduce the error-magnification effect of the atmospheric Ar correction), the two remaining aliquots were also analyzed in single total-fusion steps. If the atmospheric  $^{40}\text{Ar}$  content was greater than 40 %, the two remaining aliquots were analyzed using the two-step method outlined above.

The first round of dating employed approximately 25 to 50 grains of sample material with an average grain-size of 60 to 80 Mesh (177 to 250  $\mu\text{m}$ ), although many samples included fractions as fine as 120 Mesh (125  $\mu\text{m}$ ). It was determined that a larger volume of sample material was necessary for the majority of samples in order to provide sufficient radiogenic  $^{40}\text{Ar}$  for a precise age determination. Therefore, samples in which radiogenic  $^{40}\text{Ar}$  volumes were low (arbitrarily defined as less than 5000 counts of  $^{40}\text{Ar}$ ), or for which there was poor agreement between the ages of sample aliquots, were re-run in a second round of dating (described below). The amount of sample material necessary for the second round was determined for individual samples on the basis of the volume of radiogenic  $^{40}\text{Ar}$  obtained during the first round of dating. In general, two-to-three times the sample mass used in the first round was necessary. Hornblende, moreover, required two-to-three times more sample than biotite due to its lower K content.

It was impractical to weigh the samples run in the first round because of the very small volumes utilized. Because the replicate material for the second round of dating was obtained from previously irradiated samples, it was not weighed. However, determination

of the weight of the sample is necessary if its K and Ca contents are to be calculated. Therefore, the sample weight was roughly estimated by observing the proportion of the pit volume occupied by the sample. The estimated mass was then introduced into the spreadsheet used to calculate the sample age (and to generate the output presented in Appendix H) and was used to obtain a value for the K content of the given mineral species. Because the sample weights are poorly constrained, the potassium and calcium contents provided for the samples are similarly approximate ( $\pm 20$  %: D.A. Archibald, pers. comm., 1997).

## Round 2

At this stage, extending from December 1st to 17th, 1995, many samples from the first round were re-analyzed using larger volumes of material, and alteration minerals, including biotite, sericite and alunite, were also analyzed.

Sericite and biotite were analyzed following the two-step method with 0.3 W used for the low-power step. Prior to running the alunite samples, the system was opened and Cu tinsel was placed in the inlet tube between the sample chamber and the getter, to provide additional purification of the gas emitted from the sample. The alunite samples generally had very high atmospheric  $^{40}\text{Ar}$  contents. A nine-step run was conducted on sample FAR 24 in an attempt to drive off much of the atmospheric  $^{40}\text{Ar}$ . However, the first 8 steps were all at powers lower than 0.5 W, the atmospheric  $^{40}\text{Ar}$  content remained consistently above 97 %, and the 9th step at 7 W had 100 % atmospheric  $^{40}\text{Ar}$ . This may be due to the supergene nature of this alunite sample, because the two-step method was

effective with the hypogene alunite.

Because of the poor quality of the initial sericite dates (to be discussed in more detail in a subsequent section), it was decided to re-run the samples using whole-rock fractions, because sufficient sericite separate was not available, in order to determine if more meaningful results could be obtained.

### Round 3

This round of dating, from October 21st to 25th, 1996, involved the re-analysis of some alteration samples from the previous round as well as the completion of the dating of all alteration samples.

### *Recommendations for future dating studies involving young samples*

In this study, it was found to be necessary to fill two - to- three quarters of the pits with sample to obtain sufficient radiogenic  $^{40}\text{Ar}$  to permit calculation of a meaningful age with low error using the "two-step" method outlined above. One of the assumptions of the step-heating method is that the sample is heated evenly and the argon released in each degassing step is therefore liberated from similar sites within the mineral. With the volume of sample material necessary for the Farallón Negro age determinations and the depth of the sample holder pits used, it is assumed that uniform excitation of all grains (including those at the bottom of the pit) was achieved. Because of the young age of the samples and the low volumes of radiogenic  $^{40}\text{Ar}$ , the ages obtained in this study clearly represent total-fusion ages. However, if a greater number of heating steps were to be used,



more sample would be required, and this would probably preclude the even heating of all grains in the pit. During the two-step procedure the release of gas was often sufficiently violent to drive grains out of the pits, in some cases into neighbouring pits, resulting in contamination. This could be avoided to a certain extent by using a defocused beam and by slowly increasing the laser power to the desired range, thereby assuring the gradual release of gas from the grains, and also by loading samples of similar age and type in the same part of the sample holder. This contamination is not thought to have significantly affected the outcome of this dating study, because the volume of radiogenic  $^{40}\text{Ar}$  contributed by any errant grain would have been negligible.

One sample holder used in this study has several larger-sized pits (approximately 7 mm by 3 mm) which can accommodate a greater volume of sample material and may allow the step-wise degassing of young samples. It is suggested herein that in order to conduct effective laser fusion step-heating experiments on samples of Miocene or younger age, a new sample holder must be developed. This should have broad, shallow pits that could accommodate larger volumes of sample material which could be spread uniformly, allowing the even heating of all grains by a defocused beam. Further, some provision for minimizing pit-to-pit contamination should be investigated. Several laboratories have attempted to cover the sample holder with glass cover slips (such as are used in microscopic studies) but the degassing is nonetheless still sufficiently violent to drive grains into nearby pits (D.A. Archibald, pers. comm., 1997). However, such modifications of the sample holder would greatly increase the time necessary to run a batch of samples, because a smaller number of samples could be accommodated at one time (possibly on

the order of 20 rather than 100).

### ***Final Round of Dating***

In May, 1997, it was decided to attempt detailed stepwise degassing laser microprobe  $^{40}\text{Ar}/^{39}\text{Ar}$  dating on large volumes of a limited number of samples from Bajo de la Alumbrera, Agua Rica and the Farallón Negro - Alto de la Blenda vein system. Material from nine previously dated samples (FAR 169, 202, 322, 324, 325, 327, 333, 334 and 336) was loaded and run in a series of degassing experiments of four to six steps. Each sample was run twice. Most of the resulting age determinations do not differ significantly from those determined in earlier dating rounds by the two-step method, confirming the reliability of the ages determined in that manner in the earlier dating rounds of this study. An example of a step-wise degassing spectra is presented as figure 5-2.

Because of the time elapsed since sample irradiation (22 months for samples from can 141; 18 months for samples from cans 140 and 142),  $^{37}\text{Ar}$  (derived from Ca) had decayed below measurable limits. Therefore the volume of  $^{37}\text{Ar}$  was not measured by the mass spectrometer during the sample runs but the Ca/K ratios (ratio of Ca-derived  $^{37}\text{Ar}$  to K-derived  $^{39}\text{Ar}$  produced during irradiation) measured during earlier dating rounds were used to estimate the volume of  $^{37}\text{Ar}$  and thereby to calculate an age for the sample.

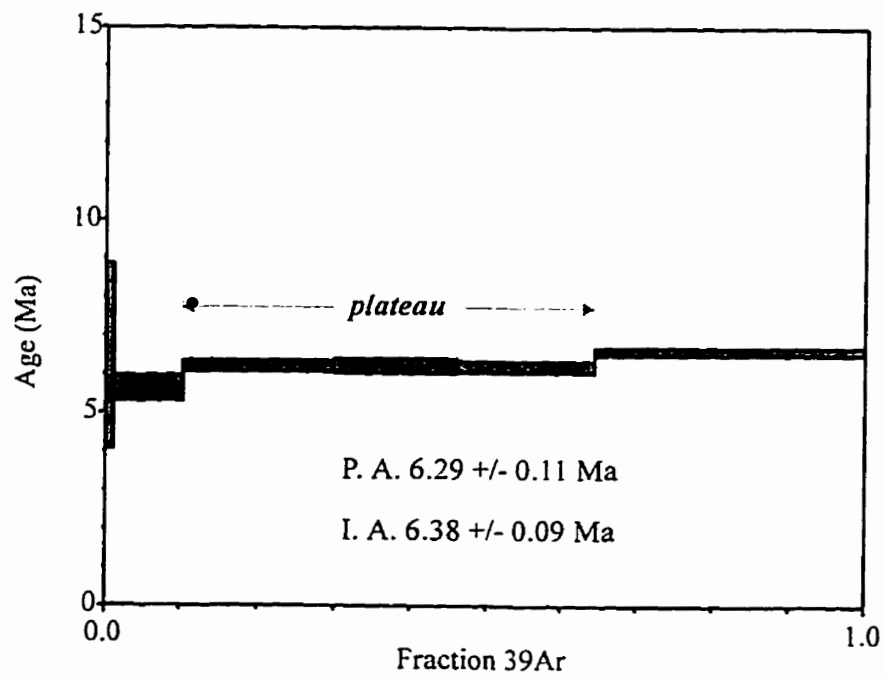
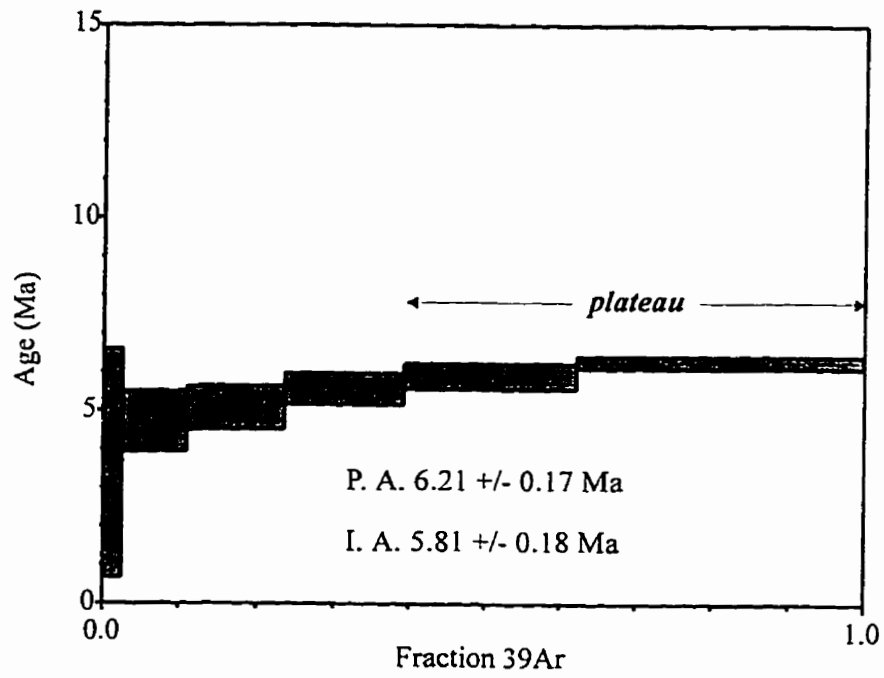
### ***The presentation of analytical data***

Detailed data for  $^{40}\text{Ar}/^{39}\text{Ar}$  age determinations for individual samples are presented

**Figure 5-2.**

Illustration of a representative step-wise degassing spectra for two aliquots of biotite from sample FAR 324. Each shaded box represents a single step-heating fraction with the vertical width of the box being a measure of analytical error. P.A. is the plateau age, calculated from the indicated steps. I.A. is the integrated age, calculated from all the steps.

## SAMPLE FAR 324 (BIOTITE)

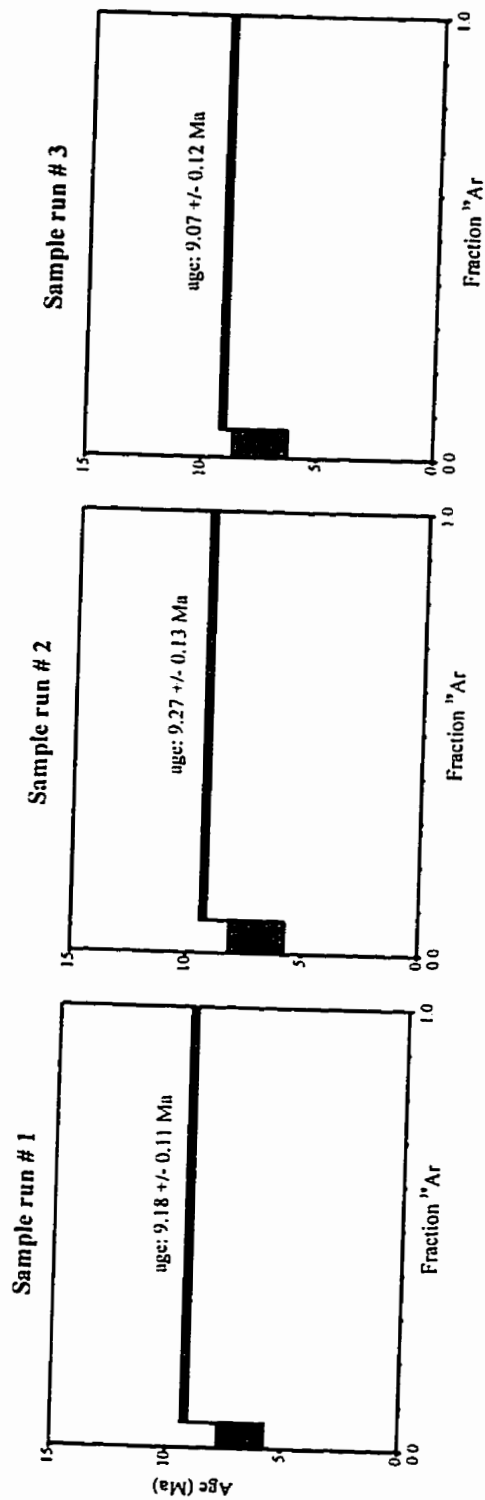


in Appendix H. The basis for most  $^{40}\text{Ar}/^{39}\text{Ar}$  age spectrum studies is that the age of a sample is indicated by a plateau age comprising a series of contiguous temperature steps whose individual ages overlap within experimental error and whose cumulative potassium-derived  $^{39}\text{Ar}$  comprises greater than 50% of the total potassium-derived  $^{39}\text{Ar}$  released. Because of the total-fusion nature of the age determinations in these three rounds of dating, information regarding either argon loss or excess argon in individual samples is not revealed. However, the method of representing degassing spectra commonly used to illustrate conventional step-heating age determinations is retained. Figures 5-3 and 5-4 present examples of degassing curves used to interpret the sample ages. The apparent  $^{40}\text{Ar}/^{39}\text{Ar}$  ages for the individual degassing steps are plotted vs. the total degassed  $^{39}\text{Ar}$  which has been recalculated and is presented as a cumulative percentage of the degassed  $^{39}\text{Ar}$ . In the case of laser  $^{40}\text{Ar}/^{39}\text{Ar}$  determinations, three or more individual runs on separate sample aliquots are plotted sequentially on a graph. This provides a visual evaluation of the reproducibility of the age determinations. The irregular "dips" on the left of the graph and between plateau segments record the initial low-power steps used to rid samples of atmospheric contamination and other gaseous impurities. Steps interpreted to be representative of sample age, the high-power second step in the two-step method, are selected, and a weighted average age is then calculated. The latter is the age quoted in the following discussion. Argon isotope correlation plots are also presented in Appendix H but, for most samples, there are insufficient steps to yield a valid isochron. However, for the biotite and hornblende samples that did yield isochron ages, the correlation age is approximately equal to the plateau age, albeit with larger errors, and with initial ratios

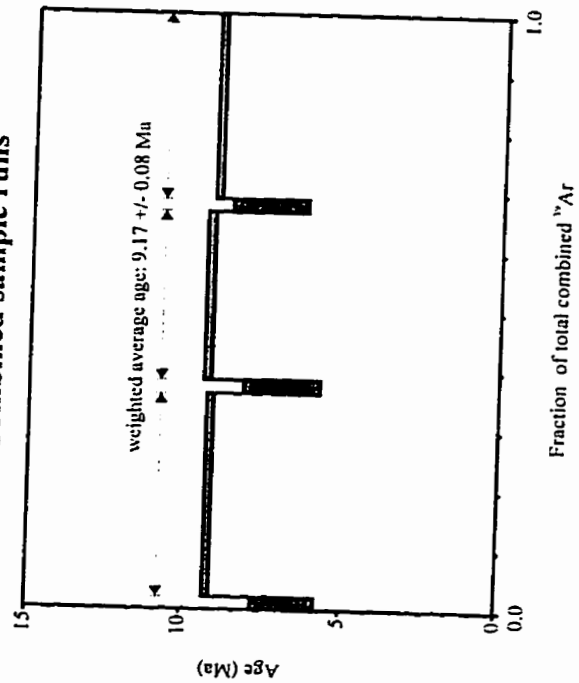
**Figure 5-3.**

Illustration of representative degassing spectra used in this study. Traditional  $^{40}\text{Ar}/^{39}\text{Ar}$  stepwise degassing spectra in which the data are plotted as apparent age against percent of  $^{39}\text{Ar}$  released are presented for three sample runs on aliquots of biotite from sample FAR 176 (upper three diagrams). The ages represent those calculated from the second high-power step of the two-step degassing runs. The amount of  $^{39}\text{Ar}$  released in the three steps is summed and the individual steps are recalculated as fractions of that sum. The three runs are then plotted sequentially on a graph of apparent age vs. percent of total  $^{39}\text{Ar}$  released (lower diagram). The high-power steps, *i.e.*, those in which the greater part of the  $^{39}\text{Ar}$  has been released, are selected and a weighted average age is then calculated. This type of diagram provides a visual evaluation of the reproducibility of the age determinations and of the errors in the individual steps. For FAR 176 there is good reproducibility among the ages of sample aliquots.

# SAMPLE FAR 176



## Combined sample runs



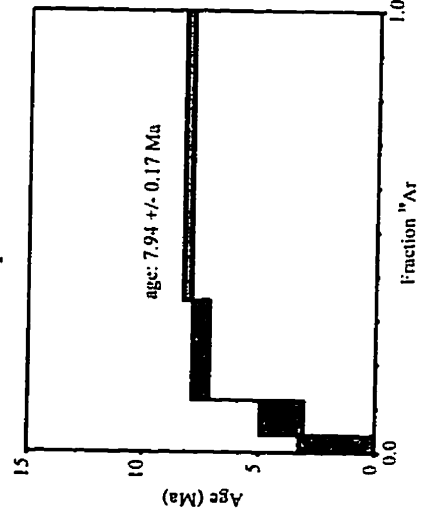
**Figure 5-4.**

Illustration of degassing spectra for biotite from sample FAR 65 (see caption from figure 5-3). Sample run #1 consists of a four-step incremental degassing experiment. The two high-power steps define a plateau, representing the greater part (approximately 88%) of the  $^{39}\text{Ar}$  released by the sample, and are used to calculate the age. The reproducibility in the ages of sample aliquots is not as good as that for FAR 176 (see figure 5-2) and the errors in the ages are larger.

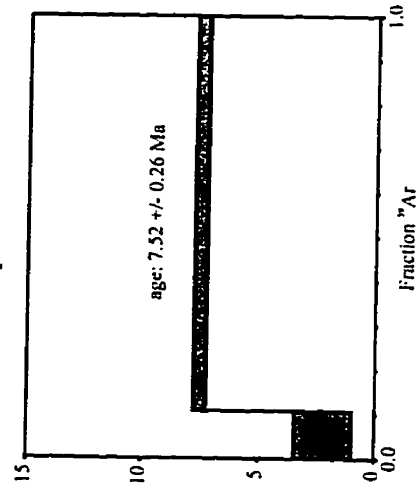


# **SAMPLE FAR 65**

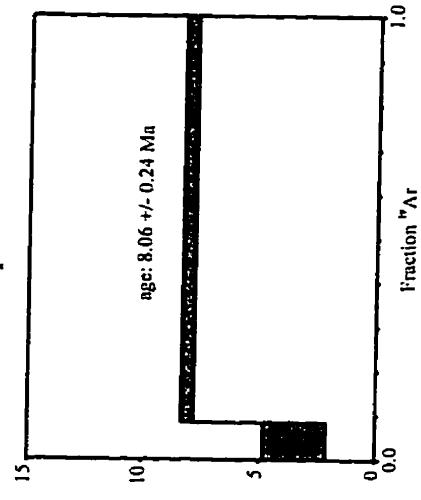
**Sample run # 1**



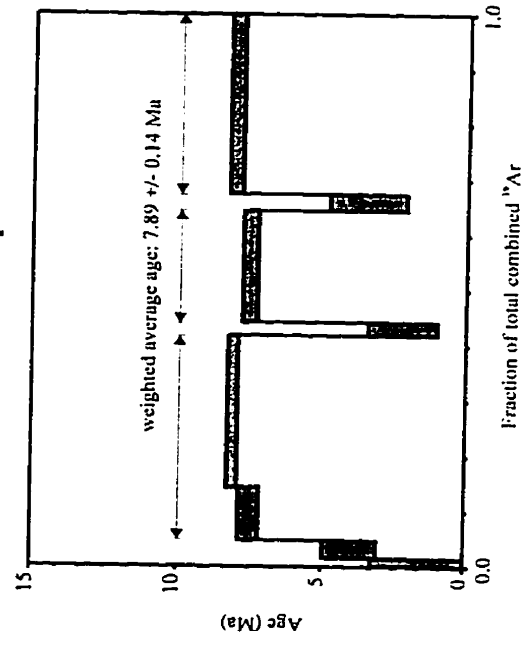
**Sample run # 2**



**Sample run # 3**



**Combined sample runs**



indistinguishable from atmospheric argon (*e.g.*, biotite: FAR 2, 228, 334, 336, JC-47B; hornblende: FAR 216, 244, 271, 296, 297, 338).

### ***Mineral pairs***

Biotite-hornblende mineral pairs were dated for five samples (Table 5-3). In only one, FAR 244, is there overlap of the mineral ages within analytical error. Thus, the hornblende ages are older than the biotite ages for samples FAR 65 and FAR 244, whereas the reverse is observed for FAR 262, 297 and 299.

Older hornblende ages for igneous rocks are normally ascribed to the higher Ar-closure temperature of this mineral relative to biotite, and hence to slow cooling. However, the extended cooling history implied by the difference in hornblende and biotite ages for FAR 65, a hypabyssal intrusion, is too long. There is, moreover, good reproducibility between the ages of sample aliquots for both biotite and hornblende. The first biotite sample aliquot was analyzed using a four-step incremental degassing run. The resulting spectrum shows a steady rise to a plateau at higher power (fig. 5-4, sample run #1). This form of release spectrum is suggestive of the loss of radiogenic  $^{40}\text{Ar}$  subsequent to crystallization (Turner, 1968). In thin-section, the biotite grains are irregularly-shaped, with minor recrystallization along grain edges. It is inferred, therefore, that the hornblende age represents the intrusion age of the sample, whereas the biotite age was partially "reset" by a later hydrothermal (alteration) event.

Hornblende from FAR 244 similarly yielded older ages than the associated biotite. Errors are low and there is good agreement between the ages for different aliquots of

Table 1

Comparison of basic and total

population on a basis

of age, sex, and

race. (Data from

U. S. Bureau of

**Table 5-3.**

Comparison of biotite and hornblende mineral-pair ages.

Location abbreviations:

BAD: Bajo el Durazno

BLA: Bajo la Alumbraera

BLC: Bajo la Chilca

SAMPLE	AGE (Ma)	ERROR (2 $\sigma$ )	MATERIAL DATED	LOCATION	DESCRIPTION
FAR 65	8.20 7.89	0.11 0.14	Hornblende Biotite	BAD	Central andesite intrusive, in main quebrada
FAR 244	6.78 6.48	0.15 0.85	Hornblende Biotite	BLA BLA	Andesite porphyry dike from northwest rim of BLA
FAR 262	7.88 9.14	0.22 0.13	Hornblende Biotite	BLC BLC	Andesite dike cross-cutting centre of BLC
FAR 297	8.37 8.91	0.11 0.07	Hornblende Biotite		Andesite intrusive from west of Vis Vis
FAR 299	8.48 9.41	0.08 0.09	Hornblende Biotite		Fragmental banakite flow in footwall of Jaci Yaco fault

hornblende. The biotite ages on separate aliquots show poor reproducibility, and have high errors and high atmospheric argon contents. In thin-section, the biotites exhibit minor chloritization, possibly contributing to recoil of  $^{39}\text{Ar}$  (Turner and Cadogan, 1974; McDougall and Harrison, 1988). The hornblende age is again interpreted to be a more reliable indicator of the primary cooling age of the rock.

In contrast, the older biotite ages for samples FAR 262, 297 and 299 may be due to excess  $^{40}\text{Ar}$ . It is relatively common for minerals to contain  $^{40}\text{Ar}$  in the first few percent of gas released. In some recorded cases, the concentration is sufficient to cause the total-fusion age to be significantly older than the plateau age (*e.g.*, Harrison, 1983). Biotite is particularly prone to excess-argon uptake and  $^{40}\text{Ar}/^{39}\text{Ar}$  biotite dates older than cogenetic hornblende dates are a good indicator of such excess (Hanes, 1991). Age discordancies between mineral species from single samples of young volcanic rocks have been previously noted (Swanson *et al.*, 1987; Lavenu *et al.*, 1989; Davies *et al.*, 1994). H.A. Sandeman (*pers. comm.*, 1997) observed similar age differences between biotite and both hornblende and feldspar in Neogene rocks from southern Peru. In step-heating experiments, apparent ages commonly decreased with increasing temperature.

Hornblende from FAR 262 exhibits good agreement in the ages determined for several sample aliquots, whereas greater discrepancies are observed in the ages of the biotite aliquots. In thin-section, three populations of biotite are observed: large euhedral crystals; smaller irregularly-shaped grains with recrystallized boundaries; and fine-grained crystal aggregates. These different populations suggest a complex crystallization history, possibly including the incorporation of biotite xenocrysts from older units. Because all

three types of biotite were inevitably included in the mineral separate and may not all represent the same intrusive event, the biotite age is rejected for this sample.

Hornblende ages on different aliquots of FAR 297 demonstrate good agreement. In thin-section, the euhedral hornblende crystals are rimmed by thin layers of oxides; the biotites are euhedral with minor recrystallization of the grain edges. The poor agreement between biotite ages on different aliquots may reflect the latter process and suggests some resetting of the biotite ages. Therefore, the hornblende age is preferred for this sample.

Both hornblende and biotite ages on aliquots of FAR 299 are statistically equivalent, but the biotite ages are almost 1 m.y. older than those for hornblende. In thin-section both minerals are euhedral, there is no evidence of recrystallization or alteration. There appears to be no reason to reject either mineral age.

Sericite mineral separates were dated in the second round of age determinations, but the spectra were found to be disturbed and several of the ages of separate sample runs do not mutually overlap within analytical error, possibly due to problems with excess argon, recoil effects or poor reactive gas clean-up (D.A. Archibald, pers. comm., 1997). In the third round, sufficient sericite separate not being available, whole-rock fractions were used to determine if more meaningful spectra could be obtained. Results for the sericite separates and whole-rocks are presented in Table 5-4. In general, the age spectra for the whole-rock samples are statistically equivalent between sample aliquots and have low errors. All of the sample ages overlap within analytical error, with the exception of those for FAR 304. The whole-rock ages of samples FAR 239 and FAR 266 overlap within error with those for unaltered intrusive units from the same centres (*i.e.*, FAR 238

**Table 5-4.**

Comparison of sericite and whole-rock pair ages for  
phyllically-altered samples.

Location Abbreviations:

BAT: Bajo de Agua Tapada

BLC: Bajo la Chilca

CAT: Cerro Atajo



SAMPLE	AGE (Ma)	ERROR (2σ)	MATERIAL DATED	LOCATION	DESCRIPTION
FAR 239	7.81 7.55	0.36 0.24	Sericite Whole-Rock	BAT BAT	Sericitized dacite porphyry
FAR 266	6.82 8.01	2.01 0.10	Sericite Whole-Rock	BLC BLC	Sericitized unit
FAR 303	5.41 5.45	0.05 0.06	Sericite Whole-Rock	CAT CAT	Sericitized rhyolite dike
FAR 304	5.73 5.11	0.08 0.04	Sericite Whole-Rock	CAT CAT	Sericitized CAT porphyry

from Bajo de Agua Tapada and FAR 262 from Bajo la Chilca, respectively), suggesting that hydrothermal alteration took place very shortly after intrusion.

Samples FAR 303 and 304 are from the Cerro Atajo prospect and yielded apparent ages for a sericitized rhyolite dyke and a sericitized dacite porphyry, respectively. In FAR 304, the slightly older sericite age may reflect either excess  $^{40}\text{Ar}$  or recoil loss of  $^{39}\text{Ar}$ , as discussed for biotite above. Due to the reproducibility of the ages between separate sample aliquots and the low errors, the whole-rock ages are herein considered to represent the ages of the alteration events. These samples will be discussed in greater detail in a subsequent section on the timing of alteration.

## Synthesis of Results

Forty-eight samples of igneous and altered units from the 1993 and 1994 field seasons were selected for geochronological study. In addition, eight samples collected by J.C. Caelles and A.H. Clark and analyzed using conventional K-Ar methods by S.L. McBride (McBride, 1972; Caelles *et al.*, 1971) were re-analyzed using laser  $^{40}\text{Ar}/^{39}\text{Ar}$  techniques. New  $^{40}\text{Ar}/^{39}\text{Ar}$  laser microprobe ages for the samples dated in this study are presented in Table 5-5. A histogram of the sample ages is presented in figure 5-5. Results from a sample of very young, windblown pyroclastic unit (FAR 228) mantling topography in the NW region of the Farallón Negro Volcanic Complex, and which yielded a biotite age of  $0.51 \pm 0.06$  Ma, and a sample of supergene alunite (FAR 24) from the Bajo de Agua Tapada prospect, which yielded an age of  $0.14 \pm 0.33$  Ma, are not included in the histogram.

**Table 5-5.**

Compilation of new laser microprobe  $^{40}\text{Ar}/^{39}\text{Ar}$  ages of samples collected during the 1993 and 1994 field seasons and by J.C. Caelles from the Farallón Negro Volcanic Complex.

Location abbreviations:

BLA: Bajo la Alumbreira  
BAT: Bajo de Agua Tapada  
BAD: Bajo el Durazno  
BSL: Bajo de San Lucas  
MIV: Agua Rica  
BLC: Bajo la Chilca  
BLJ: Bajo las Juntas  
CAT: Cerro Atajo

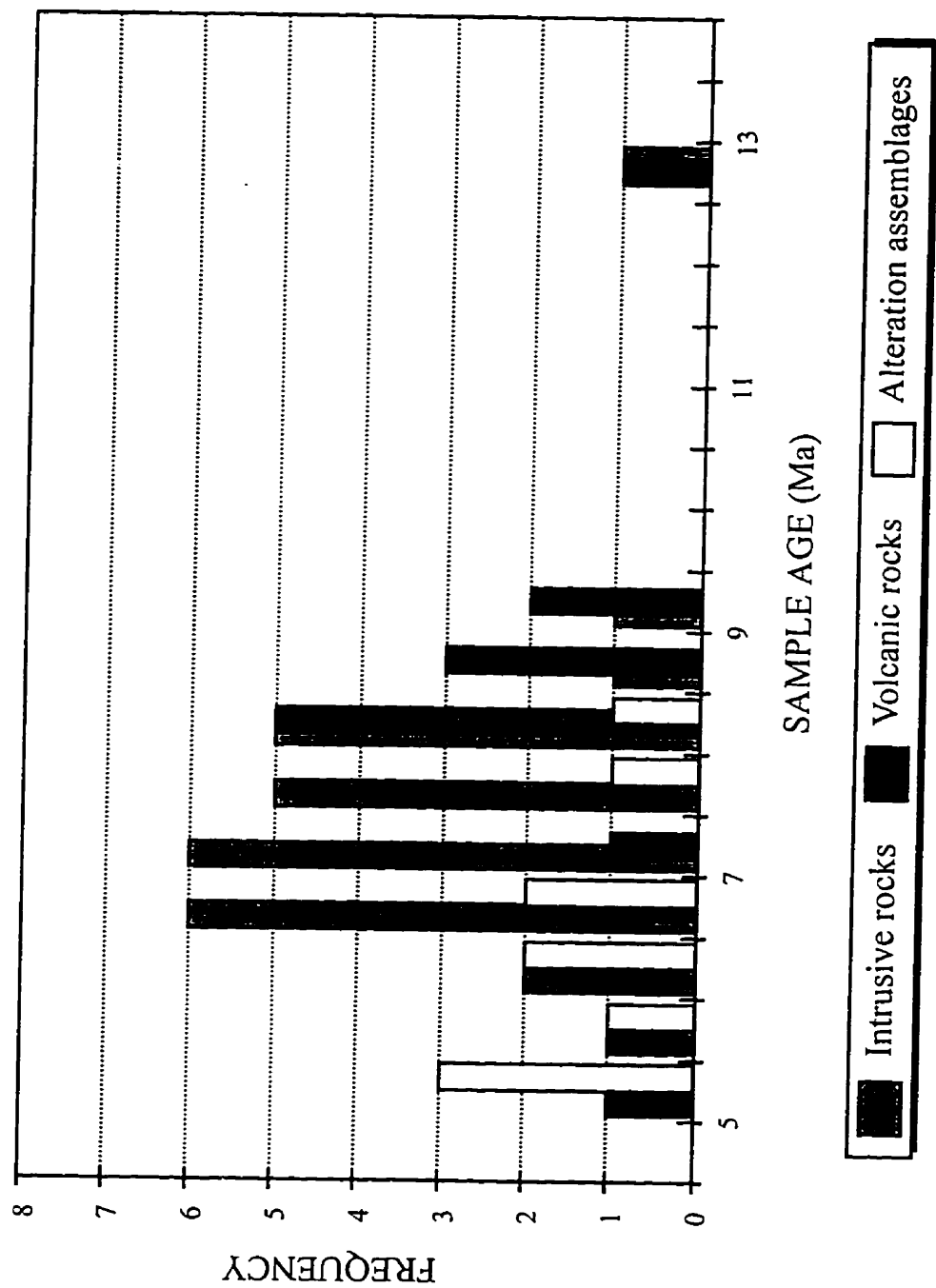
SAMPLE	AGE (Ma)	ERROR (2σ)	MATERIAL DATED	LOCATION	DESCRIPTION
FAR 2	7.10	0.13	Biotite	BLA	Colorado Norte Porphyry (P4 dike - Musto - vicinity of DDH 51-56)
FAR 10	6.84	0.15	Biotite	BAT	Fresh dacite dike north of old camp
FAR 12	5.95	0.07	Biotite		Dacite intrusive at Macho Muerto
FAR 24	0.14	0.33	Alunite	BAT	Supergene alunite
FAR 57	7.88	0.11	Hornblende		Andesite intrusive on north rim of Bajo la Chilca
FAR 65	8.20	0.11	Hornblende	BAD	Central andesite intrusive, in main quebrada
FAR 101	14.04	0.28	Whole-Rock	BAD	Secondary biotite alteration in central andesite intrusive
FAR 113	6.98	0.08	Biotite	BLA	Main Dacite Porphyry (P3 - Musto)
FAR 147	7.35	0.06	Biotite	BSL	Dacite porphyry
FAR 169	8.56	0.48	Hornblende	MIV	Melcho monzonite, relatively leucocratic phase with hornblende as the dominant mafic mineral, in Quebrada de Melcho
FAR 176	9.17	0.08	Biotite		Dacite in Capillitas valley along access road to Agua Rica
FAR 201	12.56	0.36	Hornblende		Basaltic andesite from the Arroyo Alumbreira, north of BLA (Coarse Hornblende Andesite unit of J.Proffett)
FAR 202	6.55	0.14	Whole-Rock		Sericitized wall rock to Alto de la Blenda vein system
FAR 204	8.51	0.35	Hornblende		Basaltic andesite, Quebrada de los Leones, south of Farallon Negro town
FAR 206	7.49	0.09	Biotite		Banakite tuff at northwest edge of volcanic complex
FAR 216	7.50	0.20	Hornblende		Alto de la Blenda monzonite, hornblende-phyric phase
FAR 224	8.33	0.18	Hornblende	BAD	Andesite intrusive, eastern edge of BAD
FAR 227	11.02	0.13	Whole-Rock	BAD	Sericitized fragmental andesite
FAR 228	0.51	0.06	Biotite		Windblown pyroclastic "sand" mantling topography north of BAD
FAR 229	8.24	0.10	Hornblende	BAD	Andesite intrusive, western edge of BAD
FAR 238	7.39	0.17	Biotite	BAT	Dacite porphyry from central hills of BAT prospect
FAR 239	7.55	0.24	Whole-Rock	BAT	Sericitized dacite porphyry
FAR 244	6.78	0.15	Hornblende	BLA	Andesite porphyry dike from northwest rim of BLA

SAMPLE	AGE (Ma)	ERROR (2σ)	MATERIAL DATED	LOCATION	DESCRIPTION
FAR 254	7.94	0.12	Hornblende		Basaltic dike cross-cutting Casitas rhyolite plug
FAR 262	7.88	0.22	Hornblende	BLC	Andesite dike cross-cutting centre of BLC
FAR 266	8.01	0.10	Whole-Rock	BLC	Sericitized unit
FAR 271	8.59	0.10	Hornblende		Basalt flow low in stratigraphy near Bola del Atajo
FAR 284	6.72	0.08	Hornblende		Andesite tuff in Quebrada de Pozos Verdes
FAR 285	9.14	0.09	Hornblende		Fragmental basaltic andesite flow in Villa Vil river, north of FAR
FAR 288	6.14	0.05	Biotite		Crowded dacite porphyry from Loma Morada, north edge of volcanic complex
FAR 296	8.37	0.08	Hornblende		Fragmental shoshonite flow from west of Vis Vis
FAR 297	8.37	0.11	Hornblende		Andesite intrusive from west of Vis Vis
FAR 299	8.48	0.08	Hornblende		Fragmental banakite flow in footwall of Jaci Yaco fault
FAR 301	7.59	0.08	Hornblende	BLJ	Andesite dike
FAR 303	5.45	0.06	Whole-Rock	CAT	Sericitized rhyolite dike
FAR 304	5.11	0.04	Whole-Rock	CAT	Sericitized CAT porphyry
FAR 307	8.15	0.10	Whole-Rock	CAT	Basaltic andesite dike
FAR 311	8.41	0.08	Hornblende		Basaltic andesite north of CAT
FAR 312	8.75	0.07	Biotite		Andesitic tuff north of CAT
FAR 318	5.16	0.05	K-spar	CAP	Dacite dike
FAR 322	6.10	0.04	Whole-Rock	MIV	Sericitized intrusive in Quebrada Melcho
FAR 324	6.29	0.06	Biotite	MIV	Secondary biotite in unit of brecciated Melcho
FAR 325	5.35	0.14	Alunite	MIV	Hypogene alunite
FAR 327	12.67	0.30	Biotite	MIV	Biotite porphyry
FAR 333	6.75	0.09	Whole-Rock	BLA	Sericitized Main Dacite Porphyry
FAR 334	5.78	0.44	Biotite	BLA	Chloritized biotite vein at 475.5m in DDH 51-61.1
FAR 336	6.83	0.07	Biotite	BLA	Main Dacite Porphyry (P3 - Musto) from 118.8 - 126.9m in DDH 48.4-54

SAMPLE	AGE (Ma)	ERROR (2 $\sigma$ )	MATERIAL DATED	LOCATION	DESCRIPTION
FAR 338	8.36	0.13	Hornblende		Massive basaltic andesite flow
JC-30	6.30	0.11	Whole-Rock		Andesite dike near Alto de la Blenda
JC-31a	6.91	0.25	Whole-Rock		Macho Muerto rhyolite dike
JC-33	8.09	0.22	Hornblende		Dacite flow north of BLA
JC-41	6.90	0.12	Biotite	BAT	Dacite dike
JC-42a	8.95	0.10	Whole-Rock	BAD	Hydrothermally-altered sample
JC-47b	8.46	0.10	Biotite	BAD	Granodiorite
JC-77a	7.02	0.22	Whole-Rock		Monzodiorite (Alto de la Blenda) near BLP
JC-191	7.03	0.10	Biotite	MIV	Secondary biotite in Melcho monzodiorite at MIV

**Figure 5-5.**

Histogram of new laser microprobe  $^{40}\text{Ar}/^{39}\text{Ar}$  ages for  
rocks of the Farallón Negro Volcanic Complex.





### ***Volcanic Units***

$^{40}\text{Ar}/^{39}\text{Ar}$  laser microprobe ages for volcanic rocks are presented in Table 5-6 in reverse chronological order, and in partial duplication of Table 5-5. Sample locations are recorded in figure 5-6. On the basis of the new  $^{40}\text{Ar}/^{39}\text{Ar}$  age dates, it is evident that magmatic activity resulting in the construction of the volcanic edifice was underway by 12.6 Ma. Volcanism is inferred to have peaked between 8 and 9.2 Ma, and thereafter an apparent waning stage terminated with the extrusion of andesitic tuffs at 6.7 Ma. These dates suggest a more protracted period of volcanism than that, 10.6 to 6.0 Ma, originally postulated by Caelles (1979).

FAR 201 is the oldest dated volcanic sample, yielding a hornblende age of  $12.56 \pm 0.36$  Ma. It is a coarse hornblende-phyric basaltic-andesite from the Arroyo Alumbreira Andesite (Lower Andesite Unit mapped by J.M. Proffett, 1994, 1995) which crops out in Arroyo Alumbreira, north of Bajo de la Alumbreira. This is the lowermost unit exposed at Bajo de la Alumbreira: the outcrop may now be obliterated due to construction of the haul-road at the deposit. Given the lack of detailed mapping and stratigraphy in the Complex outside of the immediate Bajo de la Alumbreira area, it is not known whether older units crop out.

In figure 5-5, an absence of ages between 9.2 and 12.6 Ma is evident. It is not clear whether this gap represents a magmatic hiatus or is an artifact of sampling or reflects exposure, but the former model is preferred.

In general, volcanic units lying in close proximity to the contact with the underlying red sediments exhibit the oldest ages. These samples are from the peripheral

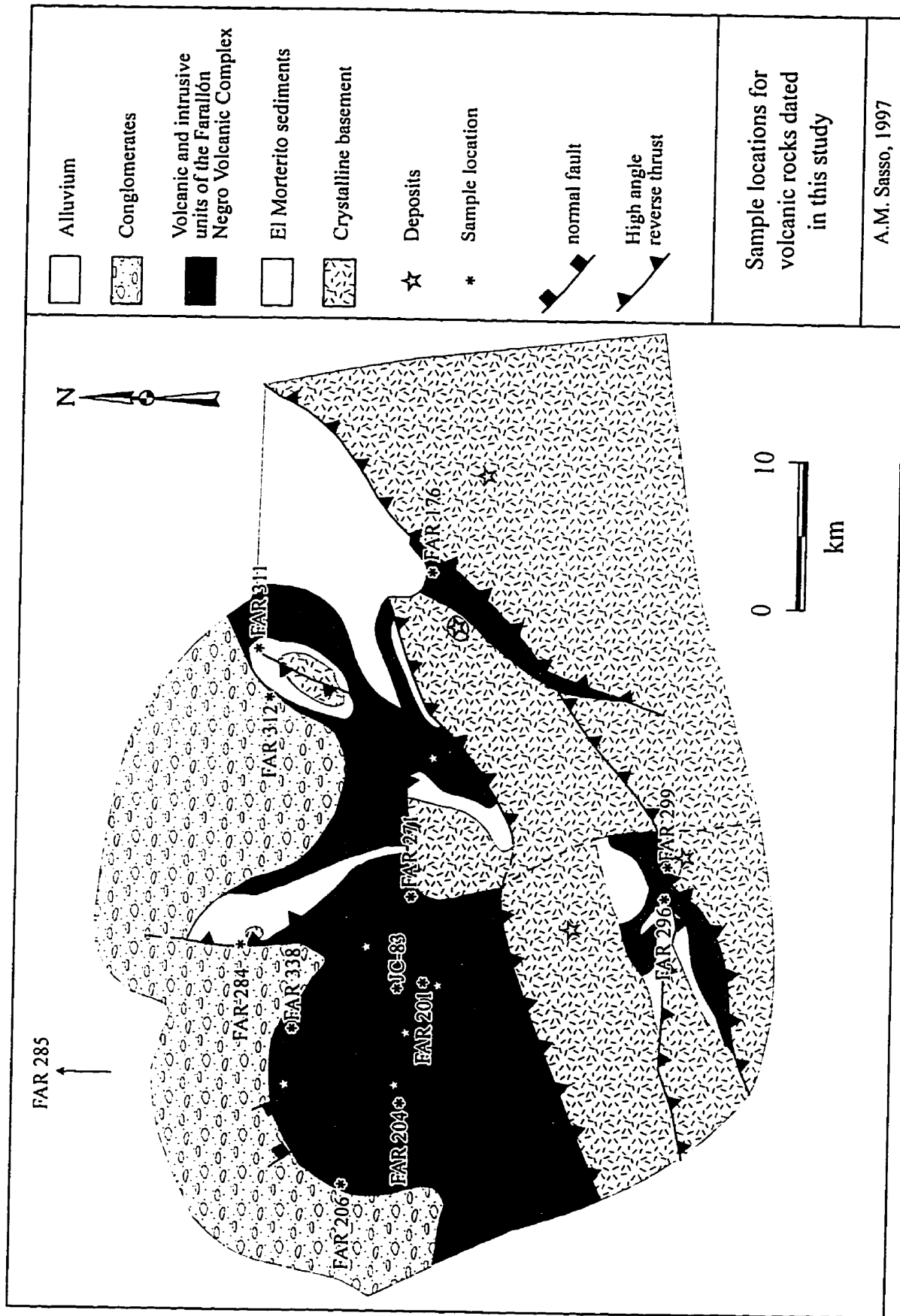
**Table 5-6.**

New laser microprobe  $^{40}\text{Ar}/^{39}\text{Ar}$  ages for volcanic rocks from the broader Farallón Negro Volcanic Complex. The data are presented in reverse chronological order, in partial duplication of those in Table 5-5. Location abbreviations as in Table 5-5.

SAMPLE	AGE (Ma)	ERROR (2 $\sigma$ )	MATERIAL DATED	DESCRIPTION
FAR 284	6.72	0.08	Hornblende	Andesite tuff in Quebrada de Pozos Verdes
FAR 206	7.49	0.09	Biotite	Banakitite tuff at northwest edge of volcanic complex
JC-33	8.09	0.22	Hornblende	Dacite flow north of BLA
FAR 338	8.36	0.13	Hornblende	Massive basaltic andesite flow
FAR 296	8.37	0.08	Hornblende	Fragmental shoshonite flow from west of Vis Vis
FAR 311	8.41	0.08	Hornblende	Basaltic andesite north of CAT
FAR 299	8.48	0.08	Hornblende	Fragmental banakitite flow in footwall of Jaci Yaco fault
FAR 204	8.51	0.35	Hornblende	Basaltic andesite, Quebrada de los Leones, south of Farallon Negro town
FAR 271	8.59	0.10	Hornblende	Basalt flow low in stratigraphy near Bola del Atajo
FAR 312	8.75	0.07	Biotite	Andesitic tuff north of CAT
FAR 285	9.14	0.09	Hornblende	Fragmental basaltic andesite flow in Villa Vil river, north of FA
FAR 176	9.17	0.08	Biotite	Dacite in Capillitas valley along access road to Agua Rica
FAR 201	12.56	0.36	Hornblende	Basaltic andesite from the Arroyo Alumbreira, north of BLA (Coarse Hornblende andesite unit of J.Proffett)

**Figure 5-6.**

Sample locations for volcanic rocks dated in this study  
from the broader Farallón Negro Volcanic Complex.



areas of the Farallón Negro Volcanic Complex, but this may be due to exposure. Biotite from FAR 176 (equivalent to FAR 310), a porphyritic biotite dacite from an outcrop along the access road to the Agua Rica project in the Capillitas valley, gave an age of  $9.17 \pm 0.08$  Ma. These are isolated outcrops in the footwall of the Aconquija range-front, high-angle reverse fault. They may represent remnants of the volcanic succession which may have overlain the Capillitas diatreme but subsequent tectonism and erosion have obliterated their stratigraphic relationship to other units of the Farallón Negro Volcanic Complex.

FAR 285, a hornblende-phyric basaltic andesite, yielded a hornblende age of  $9.14 \pm 0.09$  Ma. This sample is from an isolated sequence of fragmental flows with variable amounts of basement clasts located in the Villa Vil area, approximately 24 km north of Farallón Negro town. The sequence is approximately 100 m thick and extends for a mapped strike-length of approximately 42 km. The flows demarcate the stratigraphic boundary between the Calchaquense (red) and overlying Araucanense (buff) sediments. The age and the geochemistry of FAR 285, in addition to the lack of associated intrusive units and absence of an apparent local source for these outcrops, suggest that these rocks are temporally and genetically related to the Farallón Negro Volcanic Complex, as originally postulated by Llambías (1970). They may represent a voluminous and relatively mobile eruption sequence that was subsequently buried by sedimentary units, or a domain that has undergone greater uplift and erosion than the main Farallón Negro area, and within which only the oldest stratigraphic units are preserved.

FAR 204 (hornblende age of  $8.51 \pm 0.35$  Ma) and FAR 206 (biotite age of 7.49

$\pm 0.09$  Ma) represent respectively the bottom and top of an approximately 3000 m-thick section of flows transected by the E-W-trending Quebrada de los Leones. FAR 204 is a hornblende-plagioclase - phyrlic basaltic andesite and FAR 206 a plagioclase-biotite - phyrlic banakitite tuff.

The youngest samples, located on the north and west margins of the volcanic outcrop, represent the highest stratigraphic units exposed, and generally underlie, and/or are interbedded with, gravels formed by the erosion of the volcanic pile. FAR 206 (discussed above) is located in the easternmost exposures of volcanic units associated with the complex. FAR 284, the youngest dated volcanic unit at  $6.72 \pm 0.08$  Ma, is a hornblende-biotite andesitic tuff from the Quebrada de Pozos Verdes, located on the northern edge of the complex. It is possible that younger volcanic units may have been associated with the Farallón Negro Volcanic Complex but, due to uplift and erosion, have not been preserved, particularly in the south and east quadrants of the complex.

### ***Intrusions***

Laser microprobe  $^{40}\text{Ar}/^{39}\text{Ar}$  ages for intrusive rocks are presented in Table 5-7 in reverse chronological order. Sample locations are provided in figure 5-7. On the basis of the new age data it is suggested that intrusion may have occurred in the Agua Rica area as early as 12.7 Ma, contemporaneously with eruption of the oldest dated volcanic unit. As with the volcanic units, there was an apparent lull in intrusive activity from 8.6 to 12.7 Ma. This lends support to the identification of a general magmatic hiatus during this interval (see earlier), in that representative samples of the majority of the intrusive units

**Table 5-7.**

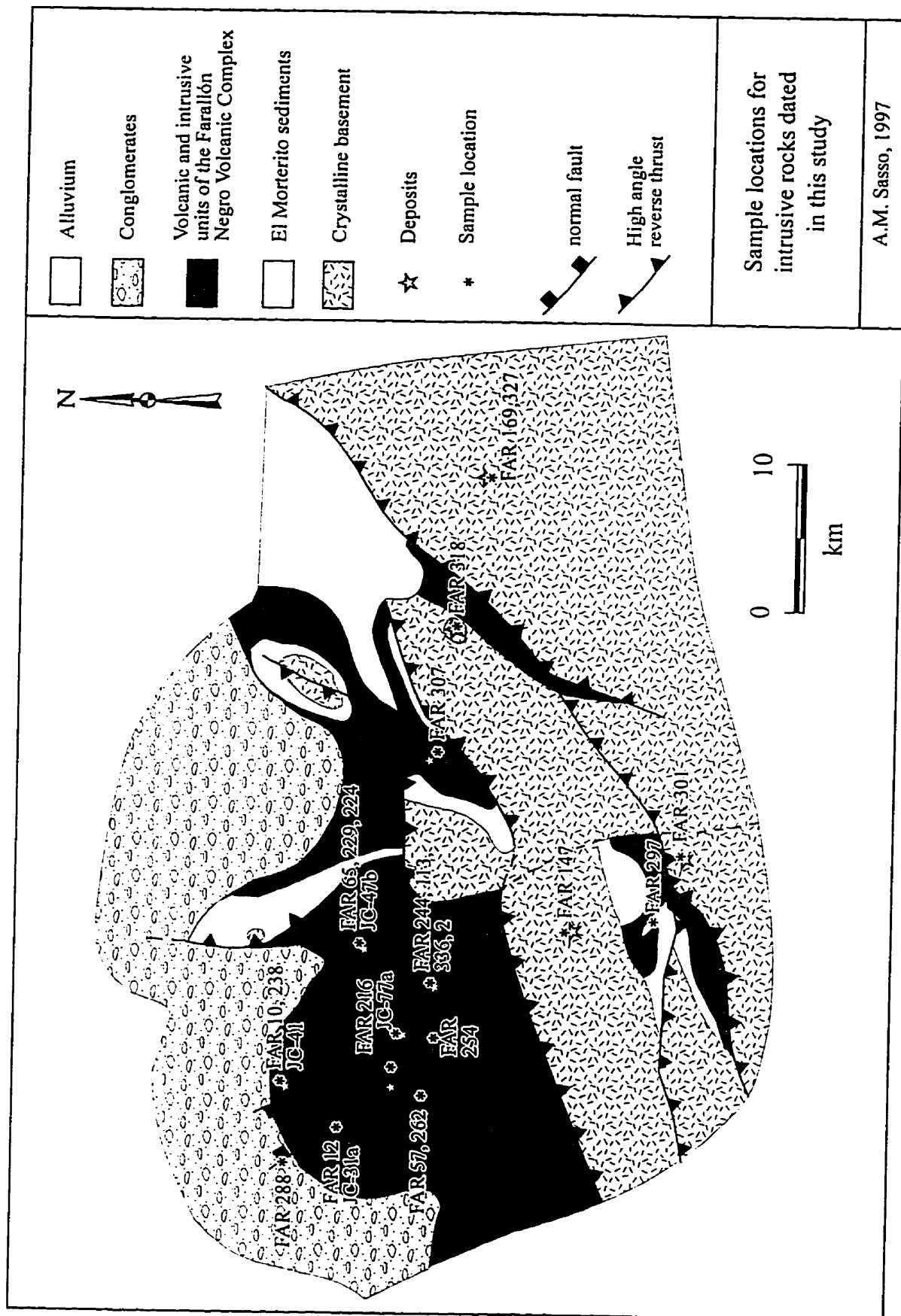
New laser microprobe  $^{40}\text{Ar}/^{39}\text{Ar}$  ages for intrusive rocks from the broader Farallón Negro Volcanic Complex. Data are presented in reverse chronological order, in partial duplication of data in Table 5-5. Location abbreviations as in Table 5-5 and CAP: Capillitas



SAMPLE	AGE (Ma)	ERROR (2 $\sigma$ )	MATERIAL DATED	LOCATION	DESCRIPTION
FAR 318	5.16	0.05	K-spar	CAP	Dacite dike
FAR 12	5.95	0.07	Biotite		Dacite intrusive at Macho Muerto
FAR 288	6.14	0.05	Biotite		Crowded dacite porphyry from Loma Morada, north edge of volcanic complex
JC-30	6.30	0.11	Whole-Rock		Andesite dike near Alto de la Blenda
FAR 244	6.78	0.15	Hornblende	BLA	Andesite porphyry dike from northwest rim of BLA
FAR 336	6.83	0.07	Biotite	BLA	Main Dacite Porphyry (P3 - Musto) from 118.8 - 126.9m in DDH 48.4-54
FAR 10	6.84	0.15	Biotite	BAT	Fresh dacite dike north of old camp
JC-41	6.90	0.12	Biotite	BAT	Dacite dike
JC-31a	6.91	0.25	Whole-Rock		Macho Muerto rhyolite dike
FAR 113	6.98	0.08	Biotite	BLA	Main Dacite Porphyry (P3 - Musto)
JC-77a	7.02	0.22	Whole-Rock		Monzodiorite (Alto de la Blenda) near BLP
FAR 2	7.10	0.13	Biotite	BLA	Colorado Norte Porphyry (P4 dike - Musto - vicinity of DDH 51-56)
FAR 147	7.35	0.06	Biotite	BSL	Dacite porphyry
FAR 238	7.39	0.17	Biotite	BAT	Dacite porphyry from central hills of BAT prospect
FAR 216	7.50	0.20	Hornblende		Alto de la Blenda monzonite, hornblende-phyric phase
FAR 301	7.59	0.08	Hornblende	BLJ	Andesite dike
FAR 57	7.88	0.11	Hornblende		Andesite intrusive on north rim of Bajo la Chilca
FAR 262	7.88	0.22	Hornblende	BLC	Andesite dike cross-cutting centre of BLC
FAR 254	7.94	0.12	Hornblende		Basaltic dike cross-cutting Casitas rhyolite plug
FAR 307	8.15	0.10	Whole-Rock	CAT	Basaltic andesite dike
FAR 65	8.20	0.11	Hornblende	BAD	Central andesite intrusive, in main quebrada
FAR 229	8.24	0.10	Hornblende	BAD	Andesite intrusive, western edge of BAD
FAR 224	8.33	0.18	Hornblende	BAD	Andesite intrusive, eastern edge of BAD
FAR 297	8.37	0.11	Hornblende		Andesite intrusive from west of Vis Vis
JC-47b	8.46	0.10	Biotite	BAD	Granodiorite
FAR 169	8.56	0.48	Hornblende	MIV	Melcho monzonite, relatively leucocratic phase with hornblende
FAR 327	12.67	0.30	Biotite	MIV	Biotite porphyry

**Figure 5-7.**

Sample locations for intrusive rocks dated in this study  
from the broader Farallón Negro Volcanic Complex.



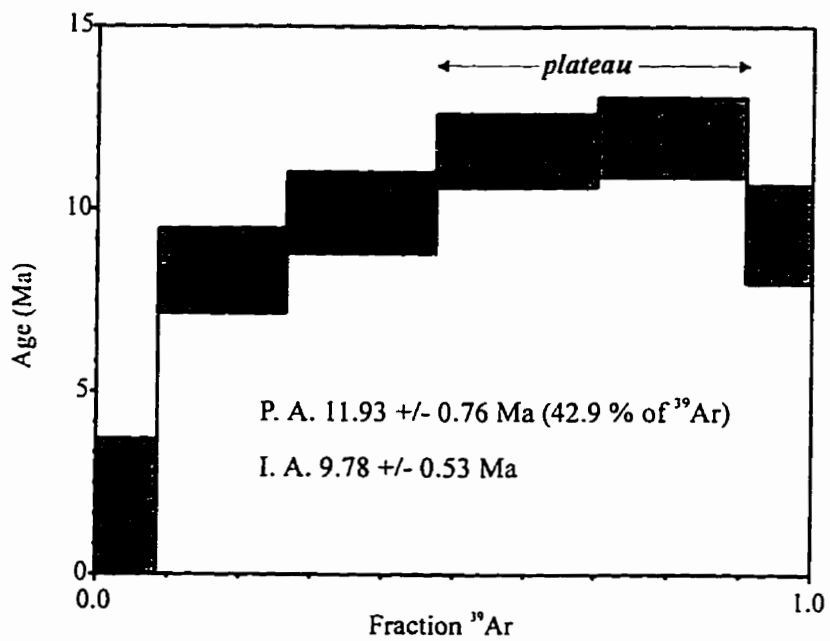
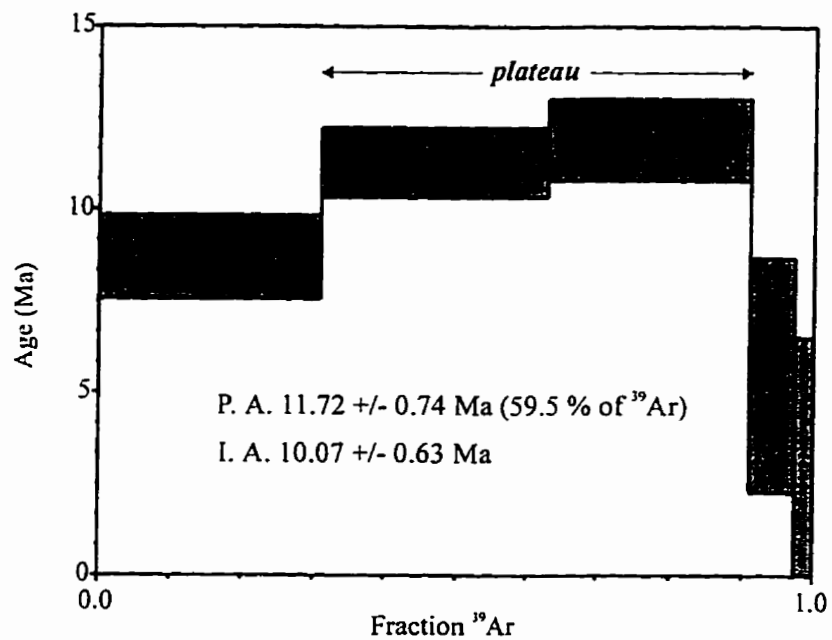
within the Farallón Negro Volcanic Complex were dated in this study. Intrusive activity, however, is inferred to have peaked between 6.5 and 8.6 Ma, overlapping with, but persisting after, the main volcanic episode. A waning stage appears to have terminated with dacitic and possibly rhyolitic dyke intrusion between 5.2 and 6.1 Ma.

The oldest intrusive unit dated (FAR 327) is an altered biotite porphyry from the Agua Rica deposit, which yields a biotite age of  $12.67 \pm 0.30$  Ma. The large biotite phenocrysts are slightly bent, but do not appear to be recrystallized and are free of chlorite and other alteration products. The step-wise degassing spectra have concave-downward configurations with the steps contributing the largest volume of radiogenic  $^{40}\text{Ar}$  yielding the oldest ages (Fig. 5-8). This pattern is typical for disturbed biotites (Hanes, 1991), the lower dates in the spectrum being interpreted to have resulted from partial argon loss (York and Lopez-Martinez, 1986). The unit crops out on a spur located between the Agua Rica camp geology office and dormitory facilities. It constitutes a large, isolated body surrounded by the hydrothermal breccia and is termed the "Camp Porphyry" by project geologists, but its relationships to the other units at Agua Rica are unclear: it has been suggested that it may represent a large block transported vertically in the breccia (N. Rojas, pers. comm., 1996) alternatively, field relationships suggest that it may be a late intrusive which post-dates the hydrothermal breccia (M. Leake, pers. comm., 1997). Although the field relationships do not support the age determined on this sample herein, the age may not be dismissed on analytical grounds. The biotite is intact and unaltered and while there is evidence for thermal overprinting possibly caused by the epithermal mineralization event, the higher-power steps reveal reproduceable plateaux which yield

**Figure 5-8.**

Step-wise degassing spectra for two sample aliquots of FAR 327, a biotite porphyry from Agua Rica. Shaded boxes represent the range in error of each step. P.A. is the plateau age. I.A. is the integrated age calculated from all the steps. The concave-downward shape of the spectra is interpreted to represent minor thermal disturbance and argon-loss, possibly reflecting the epithermal event at Agua Rica. The low ages of the high-power steps are interpreted to reflect gas release from impurities (*e.g.*, feldspar) in the sample as all the biotite-related  $^{39}\text{Ar}$  would have been completely released prior to these steps (D.A. Archibald, pers. comm., 1997).

# **SAMPLE FAR 327 (BIOTITE)**



an average age of  $12.67 \pm 0.3$  Ma. Detailed mapping and dating studies may be necessary to further resolve the temporal relationships of this unit. Thus, its origin remains problematic but the age indicates that magmatic activity took place in the Agua Rica area as early as 12.7 Ma. Intrusive activity continued with the emplacement of the Melcho monzonite stock (Fig. 5-9). A hornblende separate from a leucocratic phase collected in the Quebrada de Melcho (FAR 169) gave an age of  $8.56 \pm 0.48$  Ma.

The peak intrusive phase in the region began with the emplacement of hypabyssal andesites at Bajo el Durazno. Four separate samples of these rocks (Fig. 5-10) yielded ages of between 8.15 and 8.46 Ma (all overlapping within analytical error). These units are separate areally (Allison, 1984; this study), but their similar ages and, in the case of samples FAR 224 and 229, almost identical whole-rock geochemistry (Appendix B) would suggest that they may represent apophyses of a larger stock.

Intrusions of basaltic and basaltic-andesitic composition were also emplaced during this period. Hornblende from a basaltic dyke (FAR 254) that cuts the Casitas rhyolite plug yielded an age of  $7.94 \pm 0.12$  Ma. The field relationships (*i.e.*, basalt cutting rhyolite) and the  $^{40}\text{Ar}/^{39}\text{Ar}$  age suggest that the original sequence of events proposed by Llambías (1970) is over-simplified. Elsewhere, a basaltic andesite dyke, FAR 307, cutting the volcanic sequence that underlies the northern slope of Cerro Atajo, yielded a whole-rock age of  $8.15 \pm 0.10$  Ma.

Andesitic intrusion at Bajo de la Chilca occurred at 7.88 Ma (FAR 57 and 262). Andesitic intrusion also occurred at Bajo las Juntas where hornblende from an andesite dyke (FAR 301) yielded an age of  $7.59 \pm 0.08$  Ma. Hornblende from a hornblende-phyric

**Figure 5-9.**

Geological map of the Agua Rica deposit showing the locations of dated samples of intrusive units.



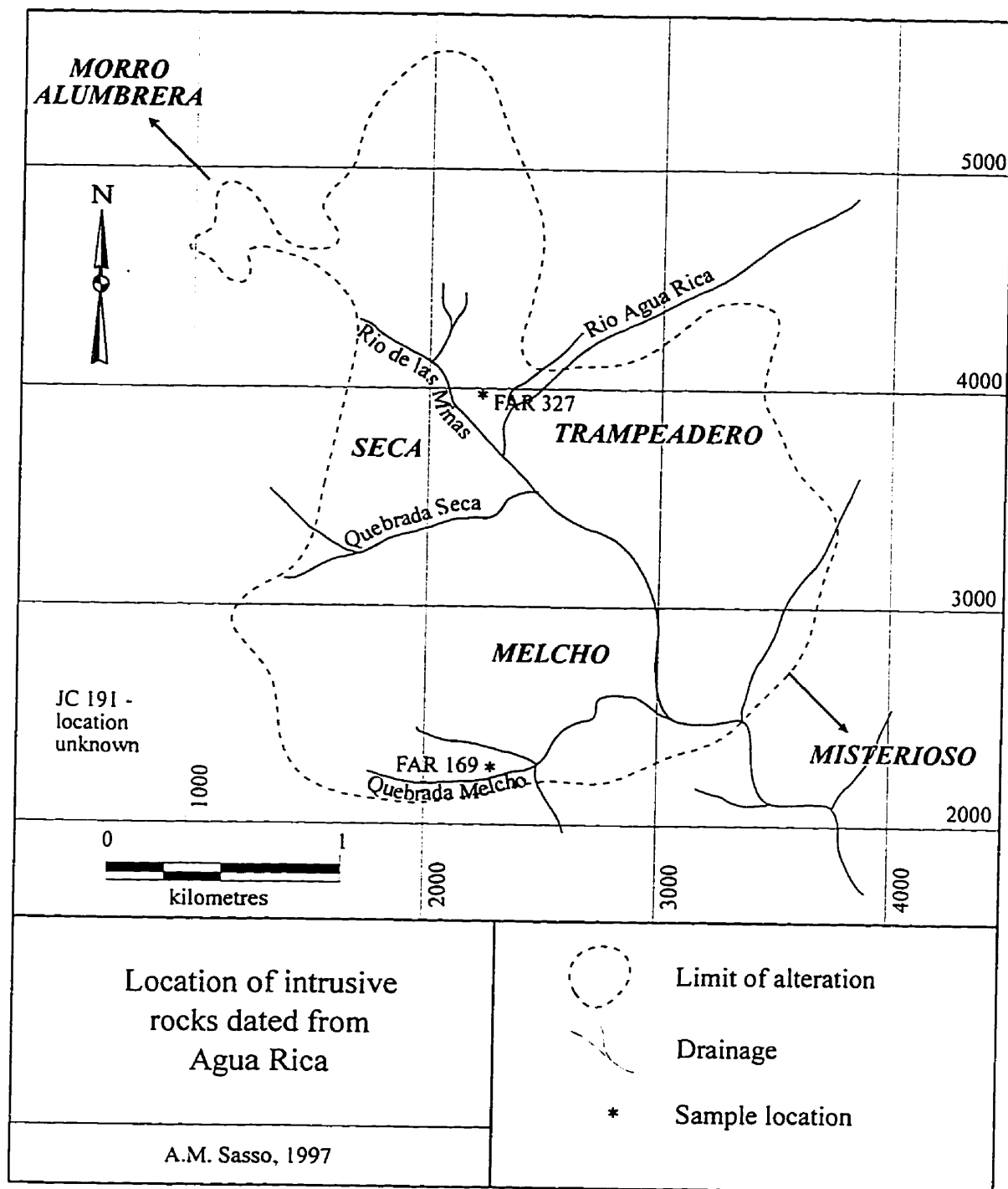
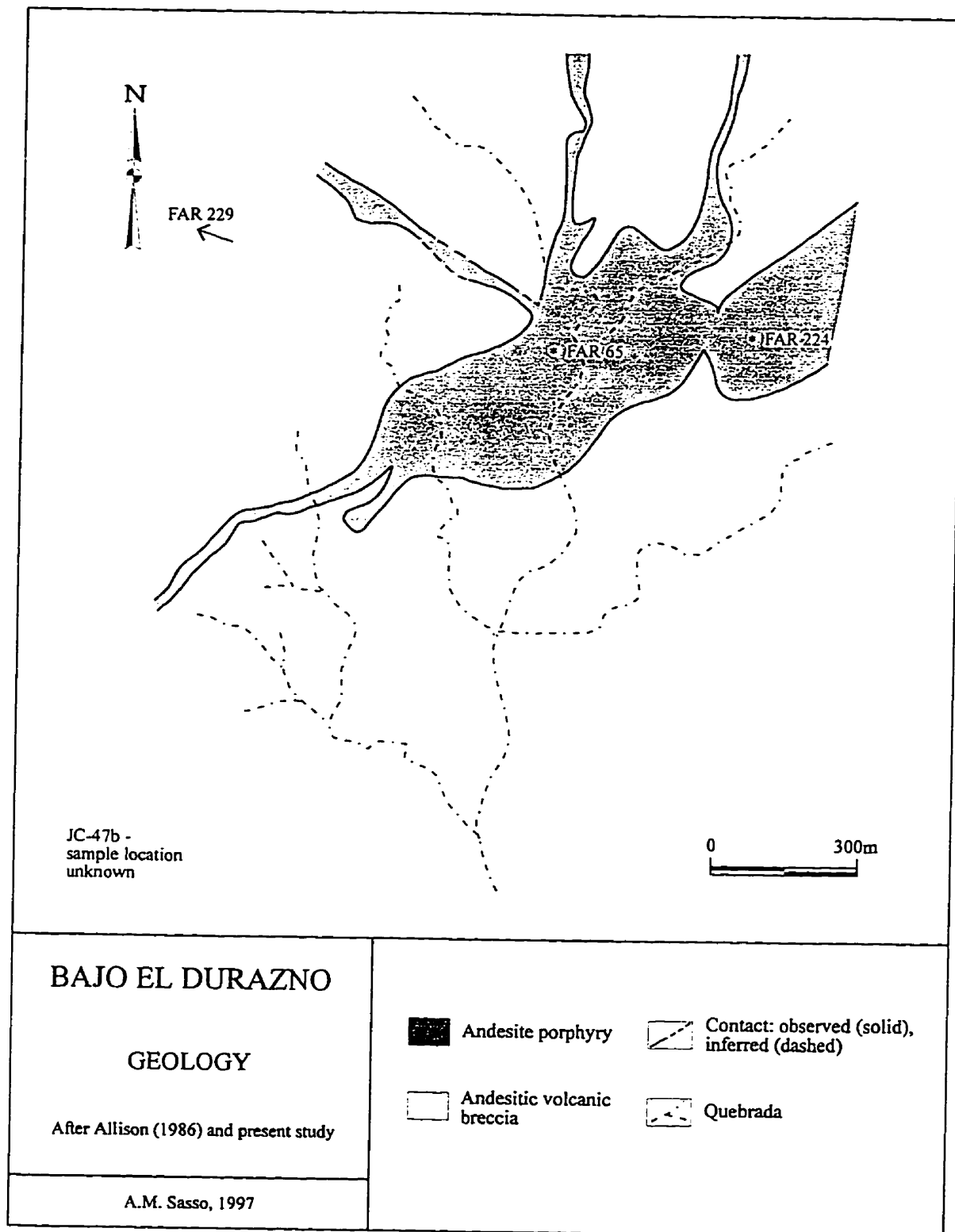


**Figure 5-10.**

Geological map of the Bajo el Durazno prospect showing  
the locations of dated intrusive samples.

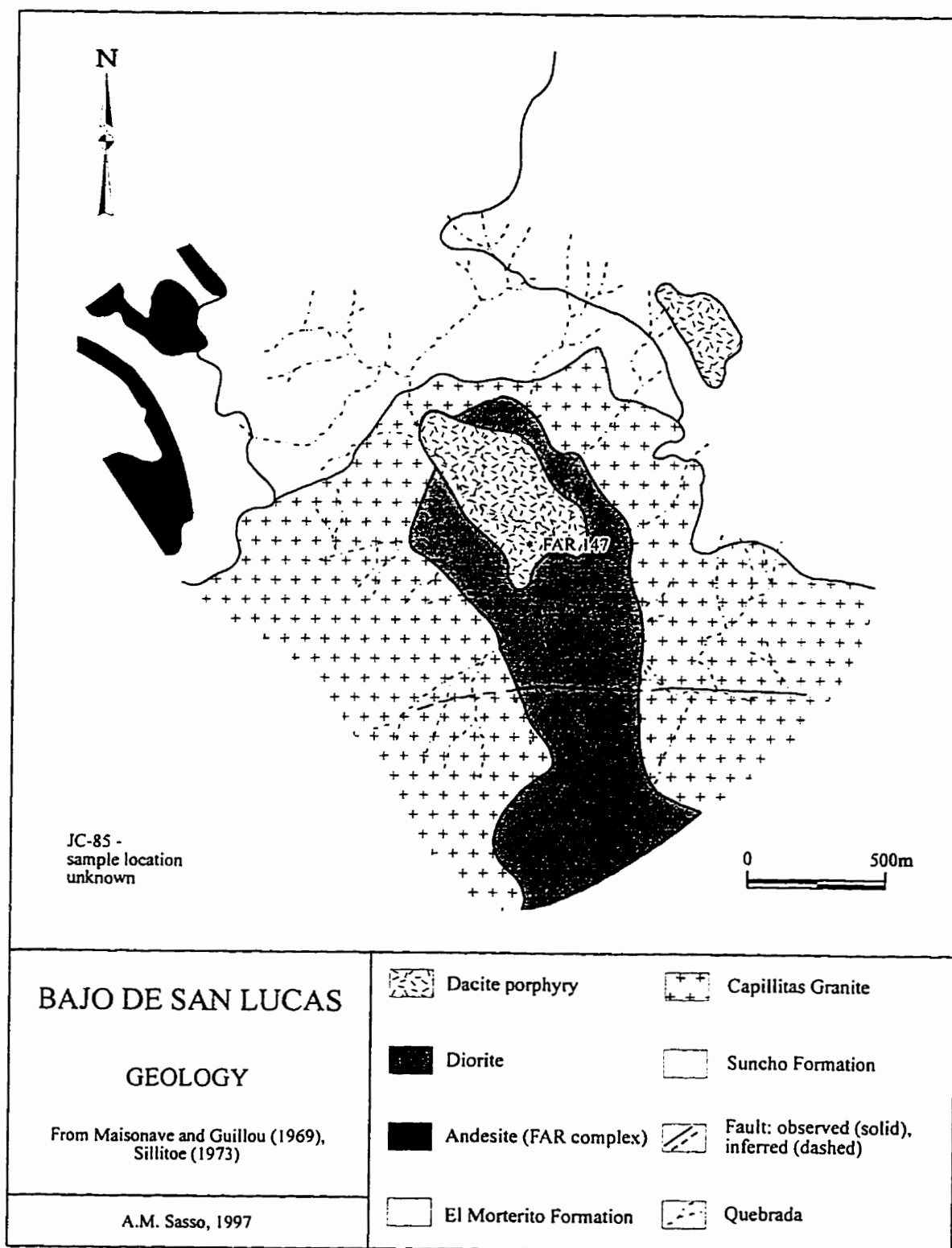


phase of the Alto de la Blenda monzonite (FAR 216) gave an age of  $7.50 \pm 0.20$  Ma. However, this age does not overlap within analytical error with that for sample JC-77a, a monzodiorite from a large intrusive body at Bajo las Pampitas, which yielded a whole-rock age of  $7.02 \pm 0.22$  Ma. JC-77a was interpreted to represent a phase of the Alto de la Blenda stock on the basis of field relationships at Bajo las Pampitas (A.H. Clark, written comm., 1993). These ages would suggest a protracted intrusive history for this unit.

By 7.4 Ma, the composition of intrusive melts in the Farallón Negro centre had become more silicic, and dacitic magmatism dominated. This episode began at  $7.39 \pm 0.17$  Ma (biotite date for FAR 238) with the intrusion of dacite porphyry in the central area of the Bajo de Agua Tapada prospect. At Bajo de San Lucas, the age of  $7.35 \pm 0.06$  Ma obtained for magmatic biotite from FAR 147 is in agreement with the K-Ar age of  $7.3 \pm 0.2$  Ma for magmatic biotite from sample JC-85 by McBride (1972). This unit is described by McBride (*op. cit.*) as a small monzonite porphyry stock which hosts the porphyry-style alteration-mineralization at Bajo de San Lucas, whereas sample FAR 147 is from the small dacite body which is mapped as the core of the alteration-mineralization zone (Fig. 5-11). Field relationships reveal an oval-shaped diorite body, with well-developed secondary biotite, similar in appearance to the Alto de la Blenda monzonite (Maisonave and Guillou, 1969; Sillitoe, 1973), which is intruded by a dacite porphyry unit, interpreted as the source of the mineralizing fluids. If sample JC-85 is a sample of the diorite body, these ages would suggest the almost synchronous intrusion of these two bodies. However, because JC-85 was not re-analyzed using laser microprobe techniques

**Figure 5-11.**

Geological map of the Bajo de San Lucas prospect  
showing the locations of the intrusive units dated in this  
study.



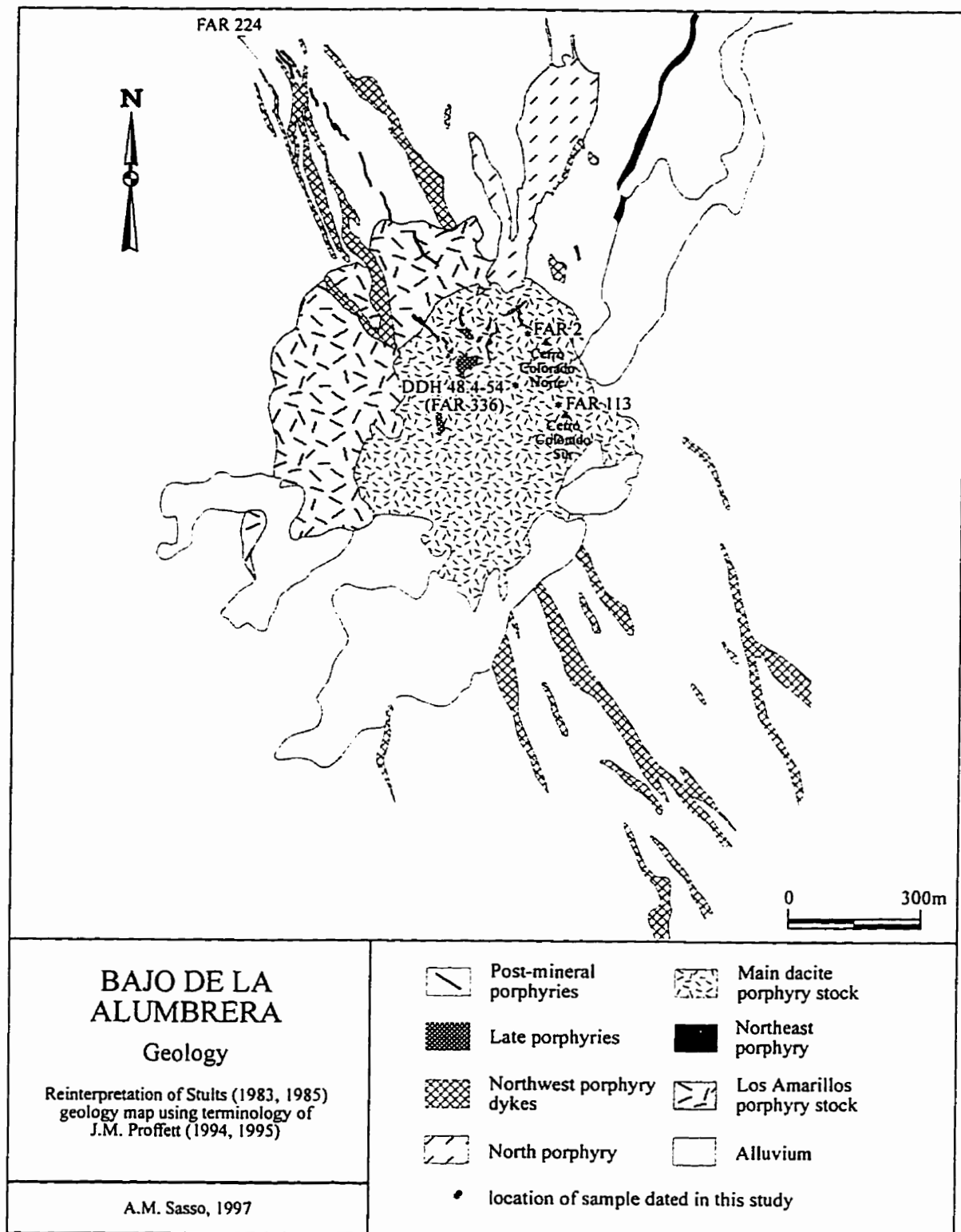
and many of the ages determined by McBride (1972) have been supplanted by ages generated by this study, the K-Ar age is better regarded as representing a minimum value for the intrusion for this unit.

Three samples of dacite porphyry were dated from Bajo de la Alumbrera (Fig. 5-12). As discussed in a previous section, the nomenclature of the intrusive units at Bajo de la Alumbrera has evolved over the course of this study. Samples FAR 2 and FAR 113 were collected during the 1993 field season when the nomenclature developed by geologists working for International Musto Ltd. was still in use. They recognized four dacite porphyry intrusives, termed P1 (pre-mineralization) - through - P4 (post-mineralization). FAR 2 was collected near the collar of drill-hole 51-56, west of Cerro Colorado Norte. The discontinuous dykes are relatively fresh and were mapped as "P4" by Musto geologists. These outcrops represent weakly-mineralized "Colorado Norte Porphyry", the oldest phase of the Main Dacite Porphyry Stock, as subsequently mapped by J.M. Proffett (1994; 1995; pers. comm., 1995). A biotite separate from FAR 2 yielded an age of  $7.10 \pm 0.13$  Ma. Biotite occurs in the sample as large euhedral-to-subhedral, relatively fresh phenocrysts and as fine-grained, shreddy aggregates, possibly replacing amphibole in the matrix. FAR 113 was collected approximately mid-way between drill-holes 51-57 and 50-56. This area was mapped as "P3" prior to its designation as "Main Dacite Porphyry" by J.M. Proffett (1994; 1995). Biotite from FAR 113 yielded an age of  $6.98 \pm 0.08$  Ma. It occurs in this sample as large, fresh, euhedral phenocrysts and as a hydrothermal alteration product of amphiboles. In neither sample is there evidence of recrystallization of the biotite phenocrysts, and the hand-picking of the mineral separates

**Figure 5-12.**

Geological map of the Bajo de la Alumbrera deposit  
showing the locations of samples dated in the present  
research.





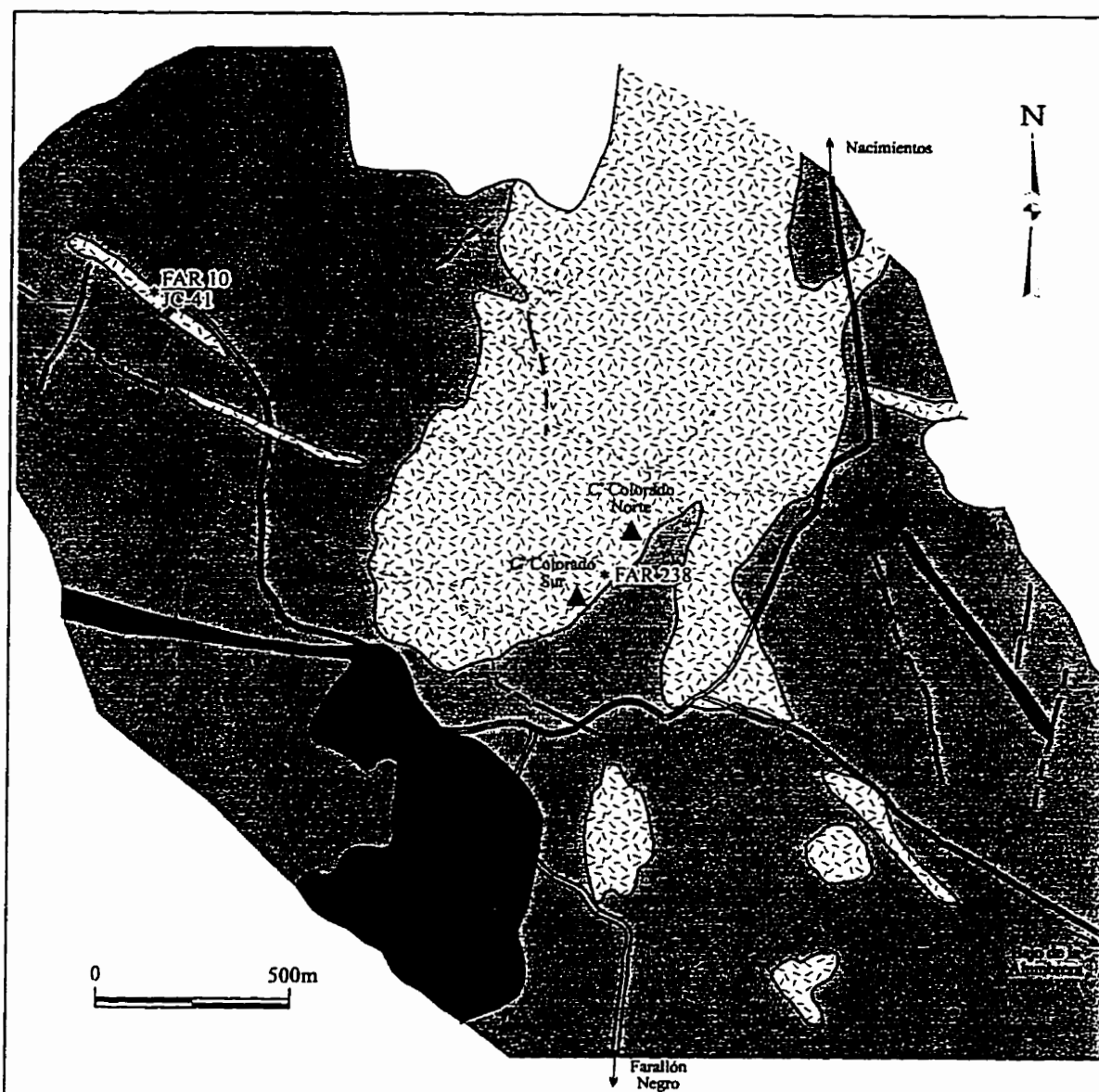
prior to dating would have ensured that the larger biotite grains were dated. These ages are therefore interpreted as minimum intrusion ages for the Main Dacite Porphyry Stock rather than alteration ages. FAR 336 is a conflated sample of core rejects from depths of 118.8 to 126.9 m in drill-hole 48.4-54. This interval was logged as "P3" porphyry by the Minera Alumbrera geologists prior to the adoption of J.M. Proffett's nomenclature. On the basis of its age,  $6.83 \pm 0.07$  Ma, *i.e.*, younger than FAR 2 but overlapping within analytical error with FAR 113, it is interpreted to be a further sample of Main Dacite Porphyry, albeit possibly of one of the younger intrusive phases of this unit.

No samples suitable for dating of the other porphyry units mapped by J.M. Proffett were found on surface and, because the drill-core had yet to be re-logged, no core samples were available for the other units. However, an andesite porphyry dyke (FAR 244) cropping out on the northwest rim of the deposit may represent an extension of the Northwest Porphyry dyke swarm mapped by Proffett (1994; 1995). Hornblende from this outcrop yielded an age of  $6.78 \pm 0.15$  Ma, *i.e.*, slightly younger than the dates for the Main Dacite Porphyry, and therefore consistent with the cross-cutting relationships documented by Proffett (*opera cit.*).

Dacite porphyry bodies were also intruded at Bajo de Agua Tapada. FAR 10 is a sample collected near the Agua Tapada shaft to the northwest of the old camp (Fig. 5-13). Magmatic biotite yielded an age of  $6.84 \pm 0.15$  Ma. This sample location corresponds to the description of the location for the Bajo de Agua Tapada dacite, JC-41, dated by McBride (1972). As discussed previously, biotite from JC-41 is dated at  $6.90 \pm 0.12$  Ma, in agreement with the above date. This dyke extends to the south-southeast into the zone

**Figure 5-13.**

Geological map of the Bajo de Agua Tapada prospect showing the locations of intrusive units dated in this study.



# BAJO DE AGUA TAPADA GEOLOGY

After Suchomel (1983)

A.M. Sasso, 1997

Alluvium

Dacite porphyry

Andesite porphyry

Andesitic volcanic  
breccias

Veins

Road

Agua Tapada Camp

of intense phyllic alteration associated with the Bajo de Agua Tapada prospect, where its contacts are obscured by the pervasive alteration.

A whole-rock sample of what is termed a quartz-phyric andesitic dyke (JC-30) by A.H. Clark (written comm., 1993), and collected by J.C. Caelles from the northwest slopes of Alto de la Blenda (Fig. 5-7), yielded an age of  $6.30 \pm 0.11$  Ma. This indicates that andesitic magmatism was active as late as 6.3 Ma.

Fresh biotite from a dacite porphyry at Loma Morada (FAR 288; Fig. 5-7) yielded an age of  $6.14 \pm 0.05$  Ma. This is a large intrusive plug located on the northwest perimeter of the volcanic complex.

FAR 12 is a sample of the Macho Muerto intrusion (Fig. 5-7), a unit classified as a rhyodacite by Llambías (1971). A biotite separate yielded an age of  $5.95 \pm 0.07$  Ma. This age is significantly younger than the whole-rock age of  $6.91 \pm 0.25$  Ma for sample JC-31a, described by A.H. Clark (written comm., 1993) as a flow-banded rhyolite forming a wide dike near Macho Muerto. Because Macho Muerto is readily accessible and only one felsic intrusive body crops out in the area, these samples are interpreted to be of the same unit. The discrepancy of almost 1 m.y. between the two ages might be interpreted to represent a protracted intrusive history for this unit. However, the Macho Muerto body is relatively small ( $0.24 \text{ km}^2$ ) and exhibits homogeneous petrographic features and mineral chemistry (Godeas, 1971), suggesting a simple, short-lived intrusive history. Given the greater coherence of the degassing spectra from FAR 12 and the relatively low error, they are interpreted to indicate the age of this unit.

The youngest intrusive event in the region is recorded by sample FAR 318 from

the Capillitas deposit. K-feldspar from a coarse-grained dacite dyke which cuts the eastern margin of the Capillitas diatreme (Fig. 5-14) yielded an age of  $5.16 \pm 0.05$  Ma. This age is in satisfactory agreement with the K-Ar dates for dacite porphyry from Capillitas published by J.I.C.A. (1981) and indicates that the emplacement of the rhyolitic diatreme occurred prior to this event.

### ***Alteration-mineralization***

$^{40}\text{Ar}/^{39}\text{Ar}$  laser microprobe ages for hydrothermally-altered samples are presented in Table 5-8 in reverse chronological order. Sample locations are indicated in figure 5-15. Separates of alteration minerals (sericite, biotite and alunite) were commonly difficult to date: of the 15 samples examined only 9 are interpreted to have yielded reliable ages of alteration events. In this section, the ages of the alteration-mineralization episodes will be discussed for individual mineralized centres. Data for Bajo de la Alumbrera and Agua Rica are discussed first, followed by those from the other deposits within the main Volcanic Complex and then the outlying deposits. Alteration age data are discussed in conjunction with the previously discussed intrusive ages for each centre.

#### **Bajo de la Alumbrera**

Two representative samples of the major alteration facies were selected (Fig. 5-16). FAR 334 is a chloritized biotite separate from a hydrothermal biotite vein intersected at a depth of 475.5 m in diamond drill-hole 51-61.1. It yielded an age of  $5.78 \pm 0.44$  Ma (Table 5-9). FAR 333, a sample of intensely sericitized Main Dacite Porphyry, yielded

**Figure 5-14.**

Geological map of the Capillitas deposit showing the location of the intrusive unit dated in this research.

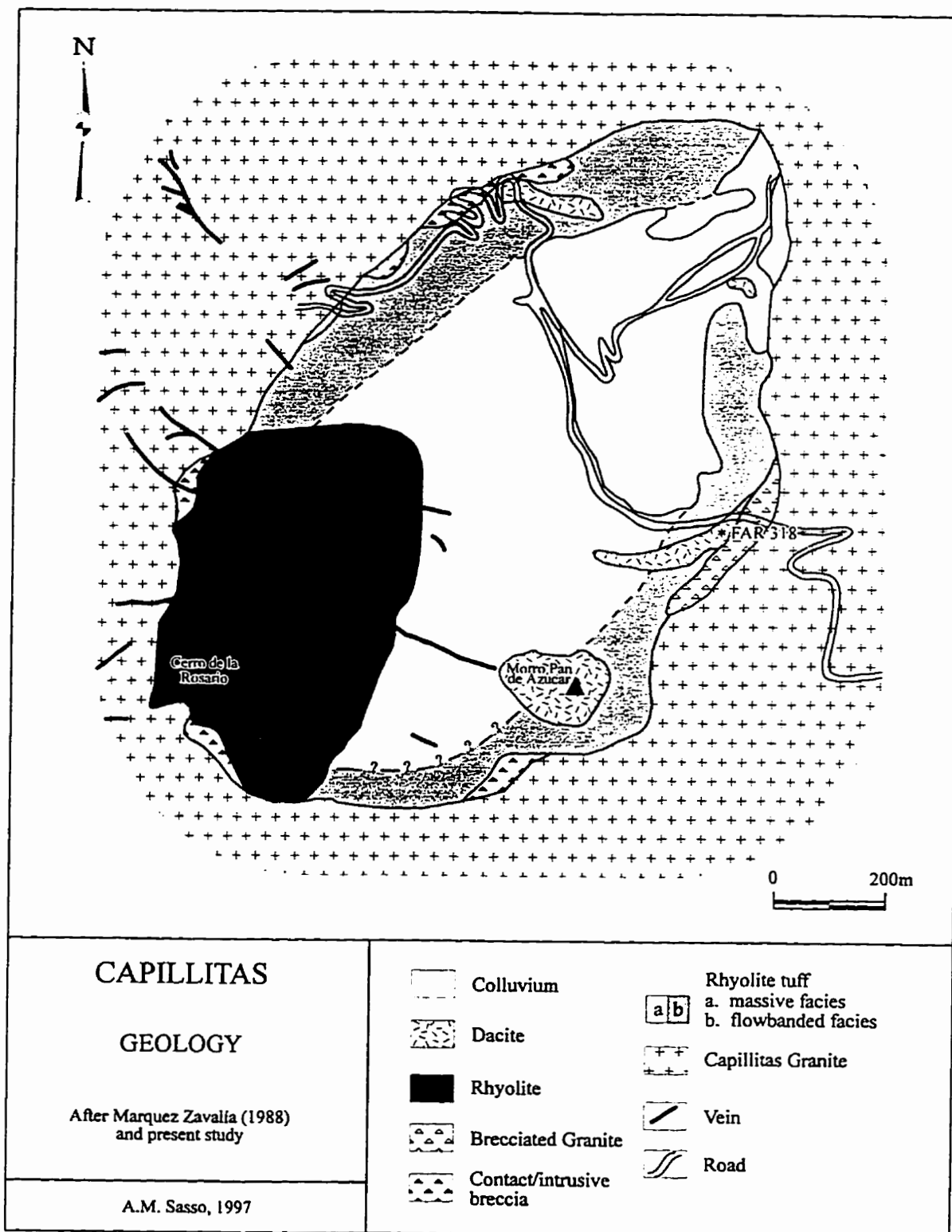




**Table 5-8.**

New laser microprobe  $^{40}\text{Ar}/^{39}\text{Ar}$  ages for alteration events  
in the broader Farallón Negro Volcanic Complex.  
Location abbreviations as in Tables 5-5 and 5-7.

SAMPLE	AGE (Ma)	ERROR (2σ)	MATERIAL	LOCATION	DATED	DESCRIPTION
FAR 24	0.14	0.33	Alunite	BAT		Supergene alunite
FAR 304	5.11	0.04	Whole-Rock	CAT		Sericitized dacite porphyry at CAT
FAR 325	5.35	0.14	Alunite	MIV		Hypogene alunite
FAR 303	5.45	0.06	Whole-Rock	CAT		Sericitized dacite dike
FAR 334	5.78	0.44	Biotite	BLA		Chloritized biotite vein at 475.5m in DDH 51-61.1
FAR 322	6.10	0.04	Whole-Rock	MIV		Sericitized intrusive in Quebrada Melcho
FAR 324	6.29	0.06	Biotite	MIV		Secondary biotite in unit of brecciated Melcho
FAR 202	6.55	0.14	Whole-Rock			Sericitized wall rock to Alto de la Blenda vein system
FAR 333	6.75	0.09	Whole-Rock	BLA		Sericitized Main Dacite Porphyry
JC-191	7.03	0.10	Biotite	MIV		Secondary biotite in Melcho monzoniorite
FAR 239	7.55	0.24	Whole-Rock	BAT		Sericitized dacite porphyry
FAR 266	8.01	0.10	Whole-Rock	BLC		Sericitized unit
JC-42a	8.95	0.10	Whole-Rock	BAD		Hydrothermally-altered sample
FAR 227	11.02	0.13	Whole-Rock	BAD		Sericitized fragmental andesite
FAR 101	14.04	0.28	Whole-Rock	BAD		Secondary biotite alteration in central andesite intrusive

**Figure 5-15.**

Sample locations for alteration minerals dated in this study from the broader Farallón Negro Volcanic Complex.

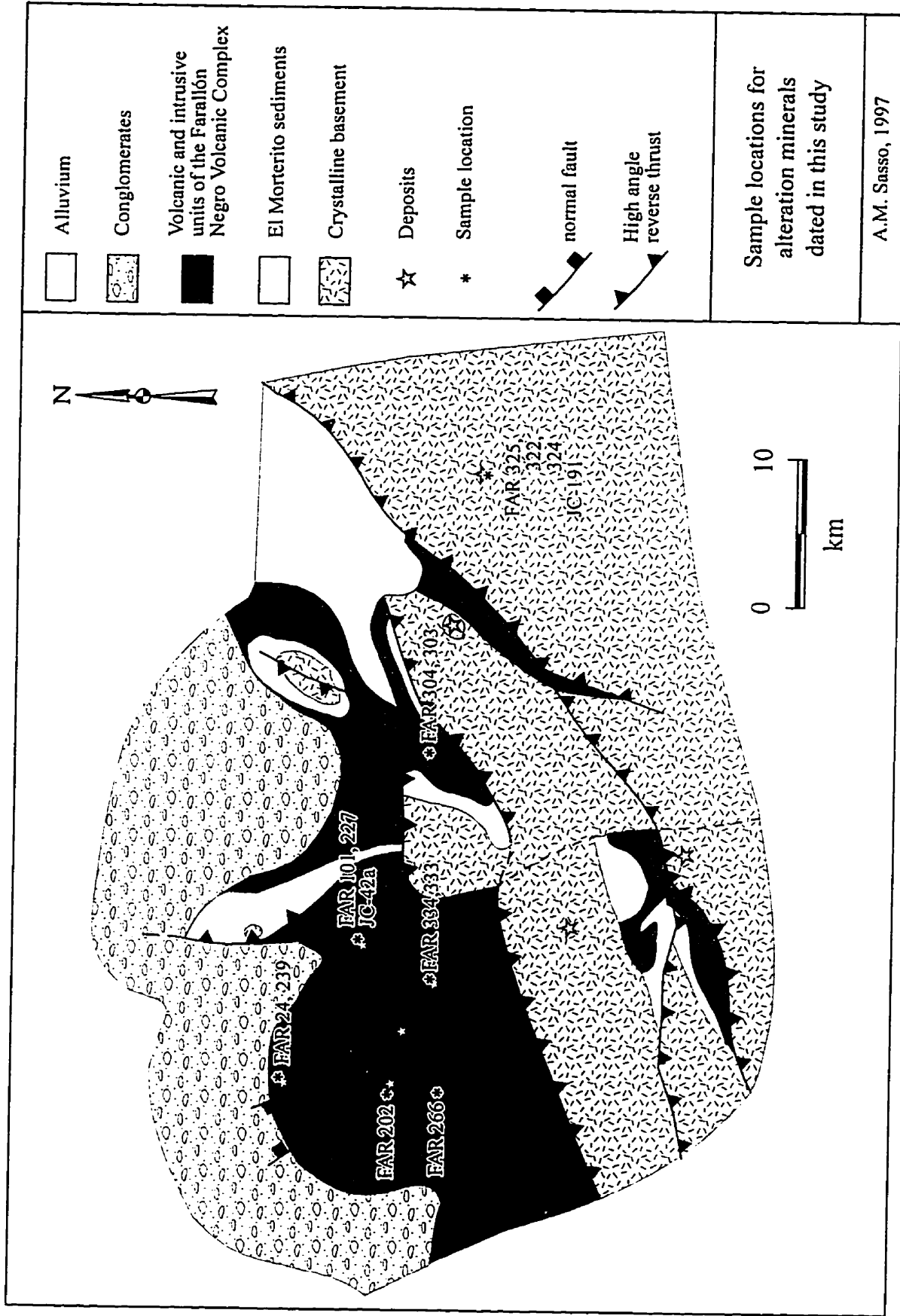


**Figure 5-16.**

Geological map of the Bajo de la Alumbrera deposit  
showing the locations of hydrothermally-altered rocks  
dated in this study.

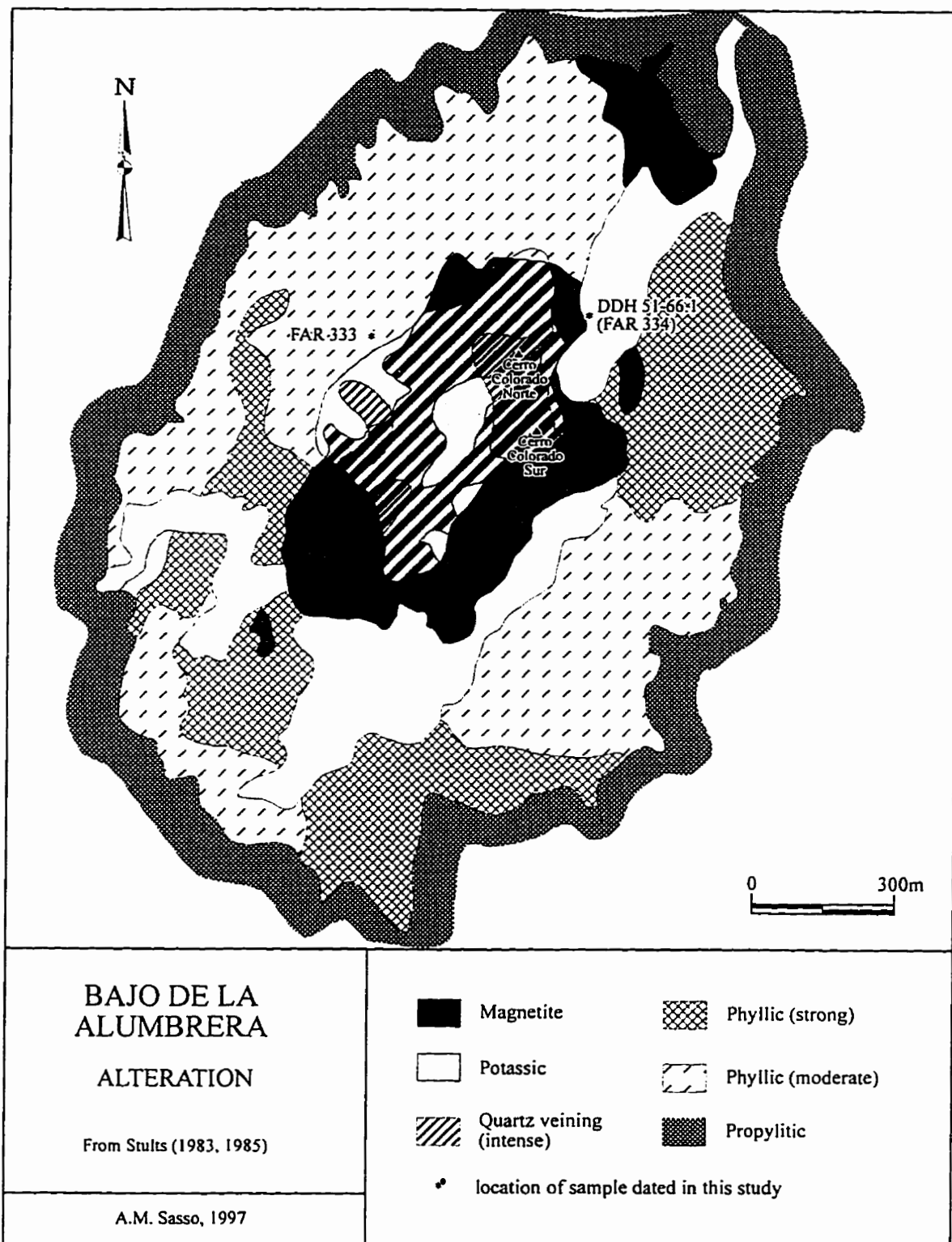


**Table 5-9.**

Summary of preferred new laser microprobe  $^{40}\text{Ar}/^{39}\text{Ar}$  ages for intrusive units and alteration facies from the Bajo de la Alumbrera deposit. (Data are in partial duplication of those from Tables 5-7 and 5-8).

<b>SAMPLE</b>	<b>AGE (Ma)</b>	<b>ERROR (2σ)</b>	<b>MATERIAL DATED</b>	<b>LOCATION</b>	<b>DESCRIPTION</b>
FAR 334	5.78	0.44	Biotite	BLA	Chloritized biotite vein at 475.5m in DDH 51-61.1
FAR 333	6.75	0.09	Whole-Rock	BLA	Sericitized Main Dacite Porphyry
FAR 244	6.78	0.15	Hornblende	BLA	Andesite porphyry dike from northwest rim of BLA
FAR 336	6.83	0.07	Biotite	BLA	Main Dacite Porphyry from 118.8-126.9m in DDH 48.4-54
FAR 113	6.98	0.08	Biotite	BLA	Main Dacite Porphyry (P3 - Musto)
FAR 2	7.10	0.13	Biotite	BLA	Colorado Norte Porphyry (P4 dike - Musto - vicinity of DDH 51-56)

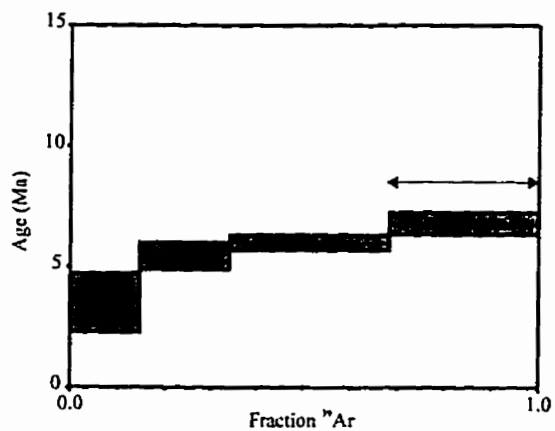


a whole-rock age of  $6.75 \pm 0.09$  Ma. The younger age for the secondary biotite does not agree with the alteration-mineralization paragenetic sequence documented by previous workers (*e.g.*, Stults, 1985; Guilbert, 1995; Proffett, 1995) at Bajo de la Alumbrera, in which the phyllic assemblage overprints secondary biotite. The degassing spectrum for FAR 333 (Fig. 5-17) defines a plateau with very low errors, but that for FAR 334 (Fig. 5-17) has higher errors and very high atmospheric argon content. It was suggested (D.A. Archibald, pers. comm., 1997) that the integrated age of  $6.09 \pm 0.66$  Ma for all runs on sample FAR 334 might give the best estimate of the age given the intense chloritization of the sample, but this age is still younger than that indicated for phyllic alteration by FAR 333, and is therefore also rejected. The younger apparent age for the hydrothermal biotite is perhaps to be attributed to loss or redistribution of  $^{39}\text{Ar}$  as a result of recoil effects during irradiation due to the intensely chloritized nature of the sample. The age of sericite alteration inferred from FAR 333 ( $6.75 \pm 0.09$  Ma) only slightly postdates the intrusion age for FAR 244 ( $6.78 \pm 0.15$  Ma), representing the interpreted NW extension of the Northwest Porphyry dyke swarm. The Northwest Porphyry dykes are observed to truncate quartz- and quartz-magnetite veinlets (classified as part of the early potassic alteration phase) in the Colorado Norte, "early P3" and Campamiento porphyries. In the northwest part of the *bajo* they are also altered to propylitic epidote-chlorite assemblages inferred to be contemporaneous with potassic alteration in the centre of the deposit. To the south, the dykes are strongly altered in the feldspar-destructive phyllic zone. These field relationships strongly suggest that the intrusion of the Northwest Porphyry body was sensibly contemporaneous with the potassic alteration-mineralization event at  $6.78 \pm 0.15$

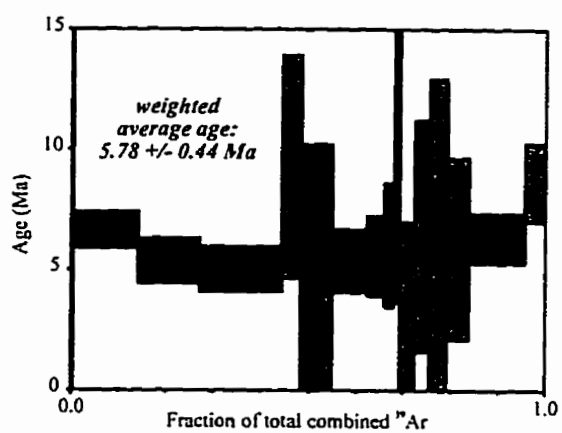
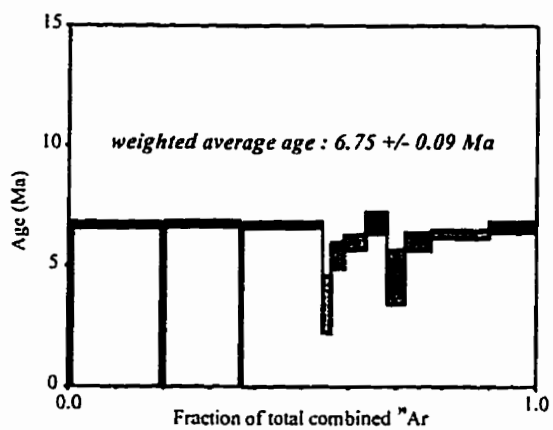
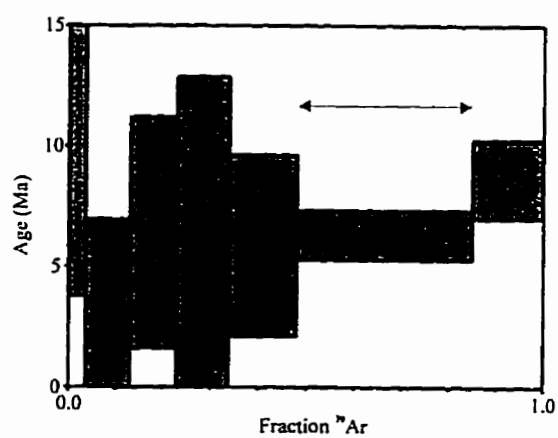
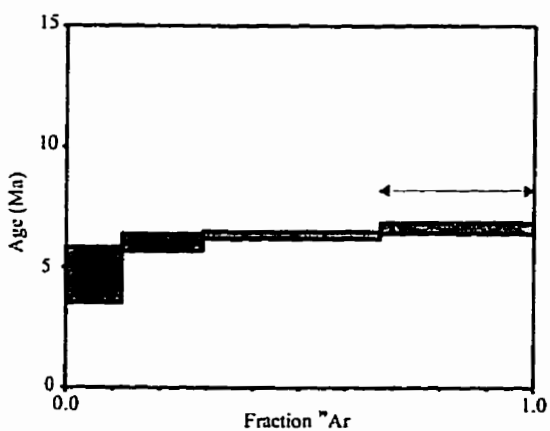
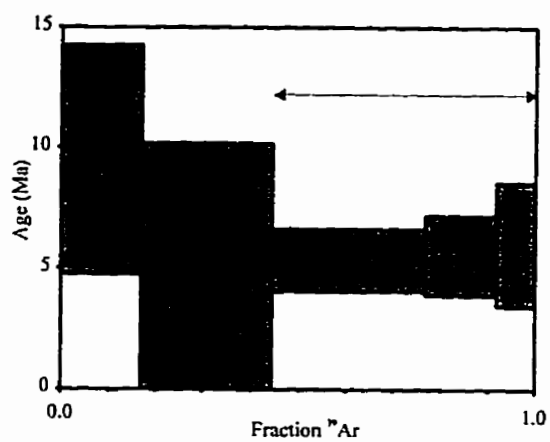
**Figure 5-17.**

Comparison of  $^{40}\text{Ar}/^{39}\text{Ar}$  degassing spectra from hydrothermally-altered samples at *Bajo de la Alumbraera*. The two upper diagrams in each column are step-wise degassing spectra, determined in the final round of dating, for aliquots of a whole-rock sample of intensely sericitized Main Dacite Porphyry, FAR 333 (on the left), and chloritized hydrothermal biotite from sample FAR 334 (right). The steps interpreted as best approximating the sample age are indicated by the arrows. The lowermost row of diagrams combines spectra from runs using the two-step method (described previously) and those illustrated immediately above to calculate a weighted average age (cf. Figs. 5-3 and 5-4). The steps used in the calculation of the weighted average age are coloured in black. The vertical width of the boxes represents the range in error for each step. Note the good reproducibility and low errors among the high-power steps for aliquots of FAR 333, whereas errors are large, possibly due to the low K content of the sample or difficulty in cleaning the released gas during the steps, and reproducibility is poor for aliquots of FAR 334.

### FAR 333 (WHOLE-ROCK)



### FAR 334 (BIOTITE)



Ma and was closely followed by hydrolytic alteration at  $6.75 \pm 0.09$  Ma.

### Agua Rica

Sample JC-191 was collected in 1969 from a monzonitic phase of the Melcho stock where exposed in the upper stretch of Quebrada Melcho at the south-east margin of the mineralized zone (A.H. Clark, written comm., 1993; Fig. 5-18). Biotite from this sample was interpreted by A.H. Clark and J.C. Caelles to be secondary, and related to potassic alteration at the Agua Rica (Mi Vida) deposit as documented subsequently by Koukharsky and Mirre (1976). The sample area displays numerous chalcopyrite-rich veinlets and the abundance of biotite, its extensive replacement of magmatic hornblende, as well as its pronounced greenish cast, strongly suggest that it is an alteration product (A.H. Clark, written comm., 1993). It yielded an  $^{40}\text{Ar}/^{39}\text{Ar}$  age of  $7.03 \pm 0.10$  Ma (Table 5-10). Sample FAR 324 is of a brecciated phase of the Melcho stock, located in the northern branch of Quebrada Melcho (near B.H.P. sample-site M5694). The secondary biotite in this sample occurs as very fine-grained groundmass clusters, possibly replacing magmatic hornblende, and as hairline veinlets. It yielded a weighted-average age of  $6.29 \pm 0.06$  Ma. FAR 322 was collected at higher altitude, and to the west, along the same *quebrada* as FAR 324 (near B.H.P. sample site M5697), where phyllic assemblages clearly overprint the potassic alteration assemblage. The whole-rock age of  $6.10 \pm 0.04$  Ma is considered to constrain the age of the phyllic alteration event. Hypogene, coarsely-crystalline, alunite (FAR 325) collected along a drill-road immediately SE of the old Agua Rica geology camp (B.H.P. sample site G6465) yielded an age of  $5.35 \pm 0.14$  Ma.

**Figure 5-18.**

Geological map of the Agua Rica deposit showing the locations of samples of alteration facies dated in this study.

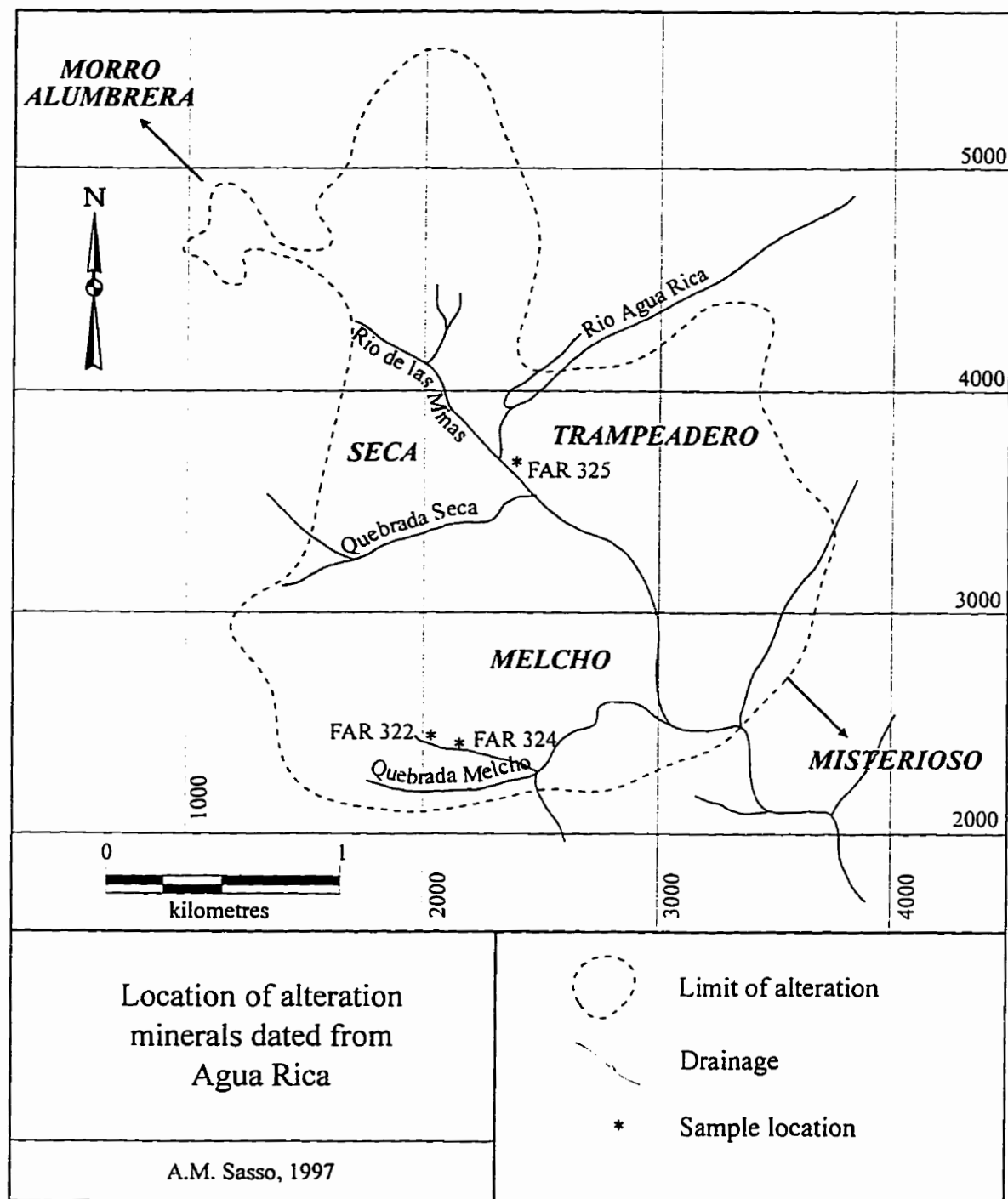


**Table 5-10.**

Summary of preferred new laser microprobe  $^{40}\text{Ar}/^{39}\text{Ar}$  ages for intrusive units and hydrothermally-altered samples from the Agua Rica deposit. (Data are in partial duplication of those from Tables 5-7 and 5-8).

SAMPLE	AGE (Ma)	ERROR (2σ)	MATERIAL DATED	LOCATION	DESCRIPTION
FAR 325	5.35	0.14	Alunite	MIV	Hypogene alunite
FAR 322	6.10	0.04	Whole-Rock	MIV	Sericitized intrusive in Quebrada Melcho
FAR 324	6.29	0.06	Biotite	MIV	Secondary biotite in unit of brecciated Melcho
JC-191	7.03	0.10	Biotite	MIV	Secondary biotite in Melcho monzodiorite
FAR 169	8.56	0.48	Hornblende	MIV	Melcho monzonite, relatively leucocratic phase with hornblende as the dominant mafic mineral, in Quebrada de Melcho
FAR 327	12.67	0.30	Biotite	MIV	Biotite porphyry



The new age data for this area imply that potassic alteration in the upper Quebrada de Melcho may have commenced as early as 7.0 Ma and persisted for a period of 0.7 m.y., and that phyllic alteration had overprinted potassic alteration at 6.1 Ma. This would suggest an extended period of at least 0.9 m.y. for the development of porphyry-style alteration-mineralization in the Melcho area. Although precise geochronological data on the durations of mineralization systems are lacking, existing geochronological studies of mineralization systems suggest formation during a very restricted time interval, *e.g.*, Arribas *et al.* (1995) postulate a lifespan of 0.2 to 0.6 m.y. for the Far Southeast Porphyry Cu-Au deposit, Philippines and Tosdal *et al.* (1997) allow 1 m.y. for the intrusion, cooling and mineralization of porphyry Cu-Mo related stocks at El Salvador. It is therefore suggested that the age of  $7.03 \pm 0.10$  Ma on biotite from JC-191 may represent the intrusive age of a phase of the Melcho monzonite and that potassic alteration ( $6.29 \pm 0.06$  Ma on FAR 324) and phyllic alteration ( $6.10 \pm 0.05$  Ma) thereafter formed rapidly over an interval of approximately 0.2 m.y. Abrupt uplift of the Aconquija Range resulted in the overprinting of porphyry-style alteration-mineralization by epithermal alunite alteration at 5.35 Ma.

#### Bajo de Agua Tapada

A sample of sericitized dacite porphyry (FAR 239) from the Bajo de Agua Tapada prospect yielded a whole-rock date of  $7.55 \pm 0.24$  Ma, which is older than all intrusive ages documented at this location (Table 5-11). If correct, this date would suggest a protracted period of phyllic-style alteration at Agua Tapada, in that samples FAR 10 and

**Table 5-11.**

New laser microprobe  $^{40}\text{Ar}/^{39}\text{Ar}$  ages for rocks from the Bajo de Agua Tapada prospect. (Data are in partial duplication of data from Tables 5-7 and 5-8).

SAMPLE	AGE (Ma)	ERROR (2σ)	MATERIAL DATED	LOCATION	DESCRIPTION
FAR 24	0.14	0.33	Alunite	BAT	Supergene alunite
FAR 10	6.84	0.15	Biotite	BAT	Fresh dacite dike north of old camp
JC-41	6.90	0.12	Biotite	BAT	Dacite dike
FAR 238	7.39	0.17	Biotite	BAT	Dacite porphyry from central hills of BAT prospect
FAR 239	7.55	0.24	Whole-Rock	BAT	Sericitized dacite porphyry

JC-41, which have experienced phyllic alteration, are approximately 0.7 m.y. younger than FAR 239. This would also imply the almost simultaneous intrusion and alteration of sample FAR 238. Supergene alunite (FAR 24), which occurs in small veinlets in the phyllic alteration halo at Agua Tapada (and is also encountered at Bajo de la Alumbrera), yielded an age of  $0.14 \pm 0.33$  Ma. The degassing spectrum is poorly constrained, with negative ages, large errors on some steps and very high (up to 100%) atmospheric argon contents, but the correlation age is in agreement with the plateau age. This suggests that this age is an acceptable indication of the time of ongoing weathering of the deposit following the exhumation and oxidation of the Volcanic Complex, as indicated by the age of cryptomelane from the Farallón Negro vein system discussed in a later section.

#### Bajo el Durazno

The three samples of alteration materials (Fig. 5-19) all give dates significantly older than the ages of intrusion for the Bajo el Durazno centre (Table 5-12). FAR 101 is a whole-rock sample which contains abundant, very fine-grained, secondary biotite. It yielded a whole-rock age of  $14.04 \pm 0.28$  Ma, but the ages for the three sample aliquots do not overlap within analytical error, and this age is not considered to be geologically meaningful. For FAR 227, a sericitized fragmental andesite, the high-temperature steps demonstrate good agreement between sample aliquots, but the whole-rock age of  $11.02 \pm 0.13$  Ma is 2.5 m.y. older than those of the intrusive units which are themselves altered to a phyllic assemblage. Several explanations are possible: i) two intrusive-alteration systems were active at Durazno, separated in age by *ca.* 2.5 m.y.; ii) the whole-rock age

**Figure 5-19.**

Geological map of the Bajo el Durazno prospect showing  
the locations of dated alteration facies samples.

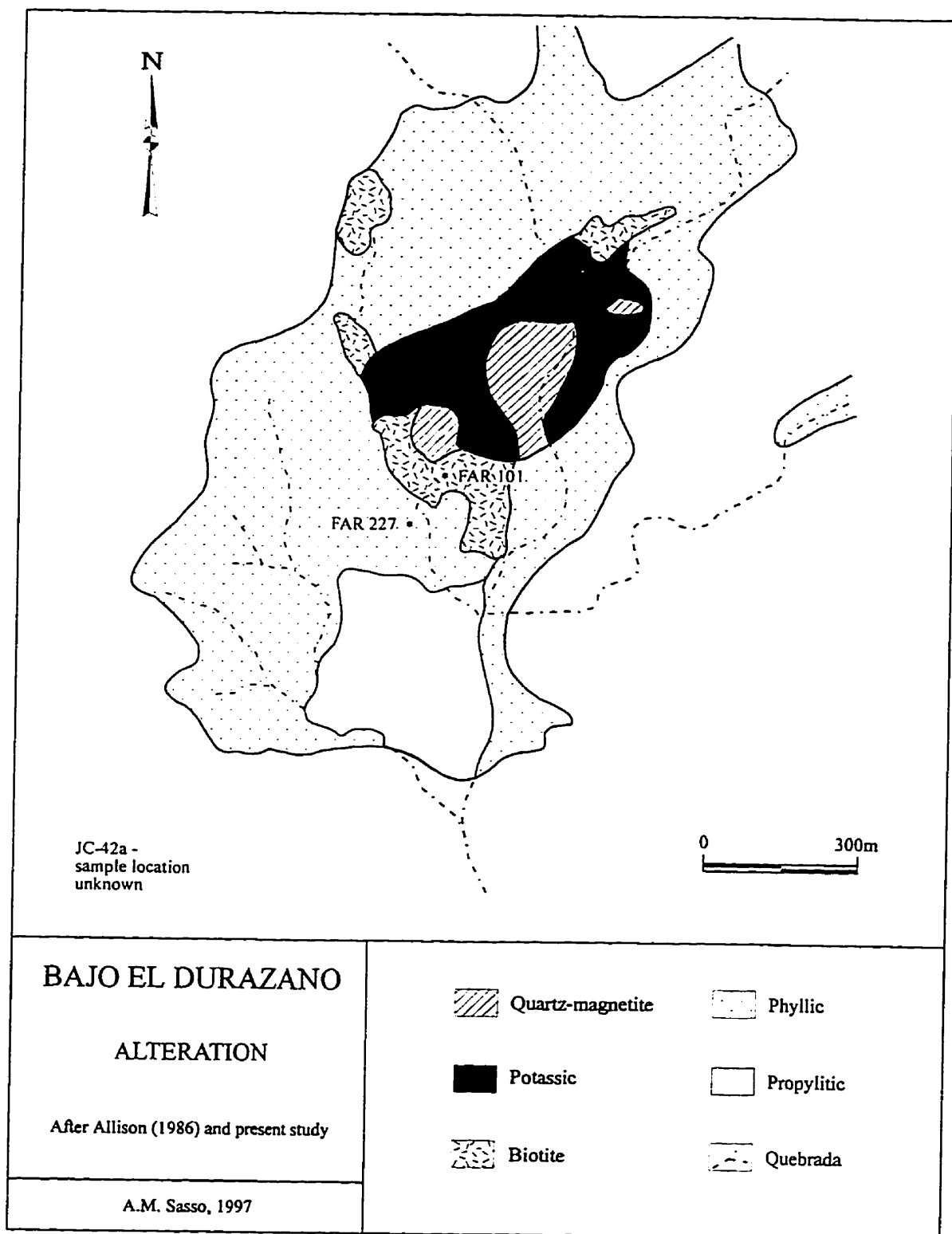


**Table 5-12.**

New laser microprobe  $^{40}\text{Ar}/^{39}\text{Ar}$  ages for rocks from the Bajo el Durazno prospect. (Data are in partial duplication of data from Tables 5-7 and 5-8).

SAMPLE	AGE (Ma)	ERROR (2 $\sigma$ )	MATERIAL DATED	LOCATION	DESCRIPTION
FAR 228	0.51	0.06	Biotite		Windblown pyroclastic "sand" mantling topography north of BAD
FAR 65	8.20	0.11	Hornblende	BAD	Central andesite intrusive, in main quebrada
FAR 229	8.24	0.10	Hornblende	BAD	Andesite intrusive, western edge of BAD
FAR 224	8.33	0.18	Hornblende	BAD	Andesite intrusive, eastern edge of BAD
JC-47b	8.46	0.10	Biotite	BAD	Granodiorite
JC-42a	8.95	0.10	Whole-Rock	BAD	Hydrothermally-altered sample
FAR 227	11.02	0.13	Whole-Rock	BAD	Sericitized fragmental andesite
FAR 101	14.04	0.28	Whole-Rock	BAD	Secondary biotite alteration in central andesite intrusive



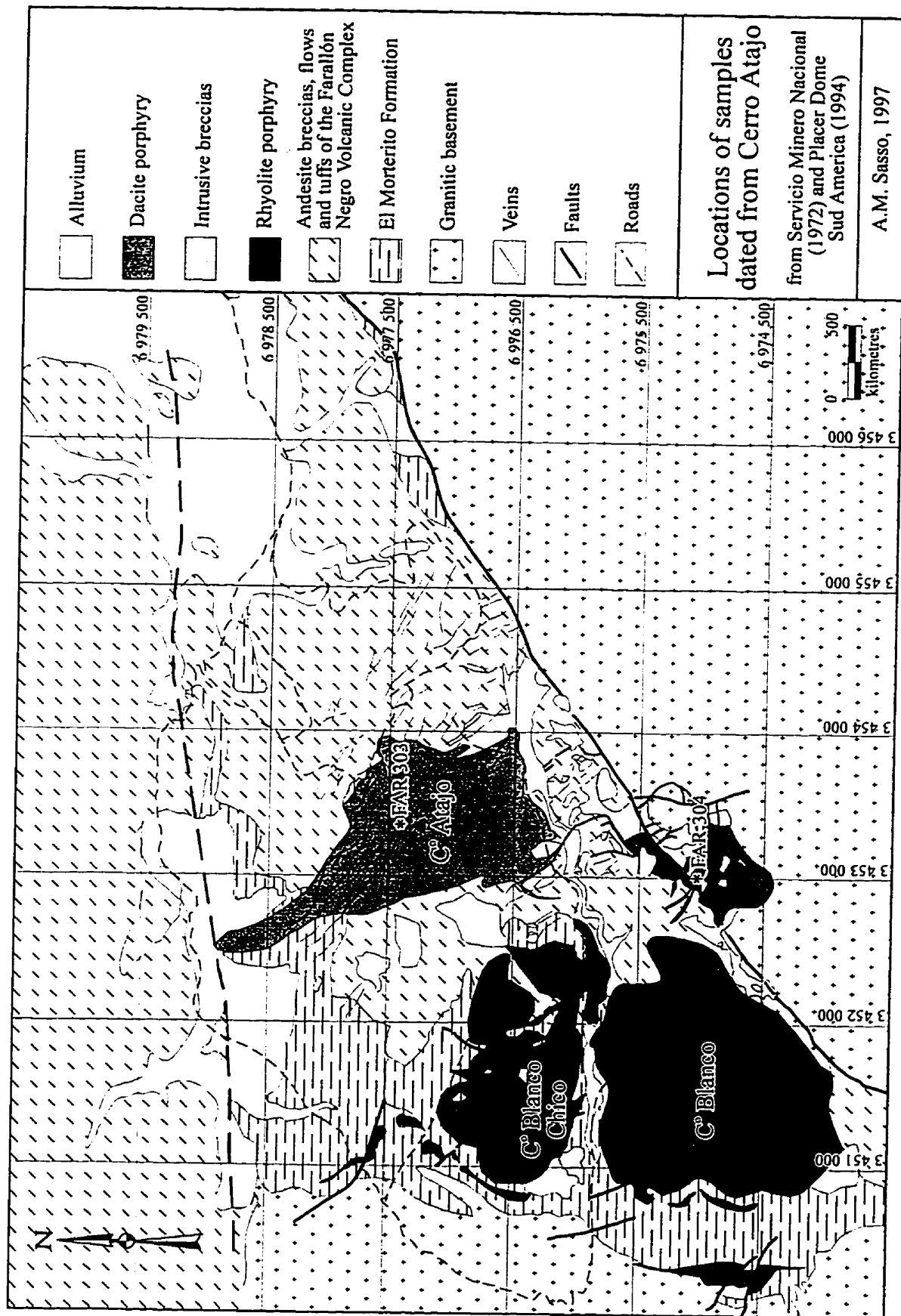
represents the time of volcanism and the alteration event was of sufficiently low temperature that complete resetting of the minerals did not occur. However, thin-section study reveals almost complete obliteration and replacement of primary volcanic textures and minerals by sericite and clays; or iii) excess  $^{40}\text{Ar}$  or recoil loss of  $^{39}\text{Ar}$  is responsible for the older age. The last is the preferred interpretation. Sample JC-42a is of hydrothermally-altered material from Bajo el Durazno (A.H. Clark, written comm., 1993). It yielded an age of  $8.95 \pm 0.10$  Ma which is 0.5 m.y. older than the oldest dated intrusive unit. Without additional information about this sample (*i.e.*, petrographic description and location), this age is difficult to interpret, but excess  $^{40}\text{Ar}$  is again suspected.

#### Cerro Atajo

FAR 303, collected on the southern edge of the Cerro Atajo prospect and to the east of Cerro Blanco (Fig. 5-20), yielded a whole-rock age of  $5.45 \pm 0.06$  Ma. The sample represents an intensely sericitized porphyry, possibly originally of dacitic composition. It crops out as a small intrusive unit in basement, bounded on the north by the high-angle reverse fault responsible for uplift of the Capillitas Range. FAR 304 is a sericitized porphyry, possibly andesitic or dacitic in composition, from the western end of the drill-road that follows the Cerro Atajo ridgeline. It yielded a whole-rock age of  $5.11 \pm 0.04$  Ma. The dates suggest a minimum age of 5.45 Ma for epithermal alteration-mineralization.

**Figure 5-20.**

Geological map of the Cerro Atajo prospect showing the locations of alteration facies samples dated in this study.



#### Other alteration centres

A sericitized unit from Bajo la Chilca (FAR 266) yielded a whole-rock age of  $8.01 \pm 0.10$  Ma. This is consistent with the magmatic hornblende age of  $7.88 \pm 0.22$  (FAR 262) from an andesite dyke which is itself unaltered and cross-cuts the weakly-developed alteration zone. The Bajo la Chilca sample represents the oldest dated alteration event at Farallón Negro.

A sample of the host-rock of the Farallón Negro - Alto de la Blenda epithermal vein system was collected in an attempt further to constrain the timing of epithermal mineralization within the context of magmatism and mineralization at Farallón Negro. FAR 202 is a strongly-sericitized andesite with abundant clay minerals, and yielded a whole-rock age of  $6.55 \pm 0.14$  Ma. This would imply that alteration-mineralization events were more or less synchronous at Alto de la Blenda and Bajo de la Alumbrera 8 km to the east. Supergene cryptomelane, formed by the intense oxidation of the upper parts of the veins, was dated by McBride (1972; sample JC-70, not duplicated in this study). McBride's pioneering work was stimulated by that of Chukrov *et al.* (1966). Vasconceles *et al.* (1993) later confirmed the reliability of  $^{40}\text{Ar}/^{39}\text{Ar}$  dating of cryptomelane in the determination of the age of weathering profiles. Although the atmospheric argon content of the Farallón Negro sample was high, the determined date of  $2.7 \pm 0.8$  Ma is in permissive agreement with our expectations for the age of supergene oxidation of the veins. If hypogene mineralization took place at *ca.* 6.8 Ma within the core of the large stratovolcano, the interval of 3-5 m.y. implied for exhumation and oxidation of the veins would not be unreasonable.

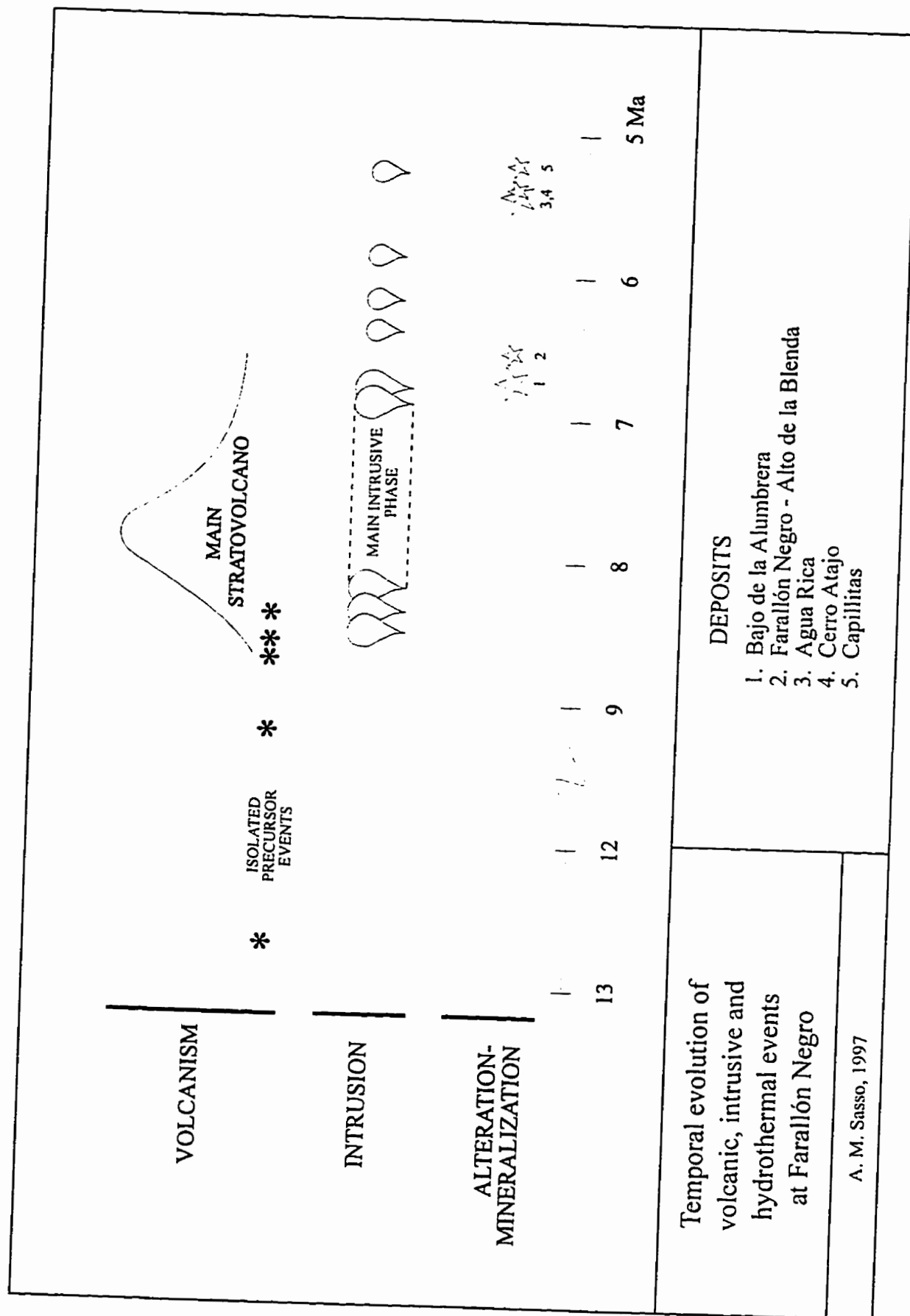
### ***Summary***

A cartoon of the temporal evolution of magmatic and hydrothermal events in the Farallón Negro region is presented as figure 5-21. An early stage of volcanism at 12.6 Ma and intrusion at 12.7 Ma is recorded in the Bajo de la Alumbrera and Agua Rica areas, respectively. An apparent magmatic hiatus ensued until approximately 9.2 Ma, as is indicated by the absence of samples which yielded ages in this interval. It has been suggested (see Chapter 2) that the older volcanic events, *i.e.*, those between 9.2 and approx 8.6, may represent extrusion from several discrete centres early in the volcanic history of the region. The construction of the Main Farallón Negro Stratovolcano was underway by 8.5 Ma and appears to have involved successive eruption events until 7.49 Ma followed by the minor, and perhaps episodic, extrusion of pyroclastics until as late as 6.72 Ma. The stratocone-building event was accompanied by hypabyssal intrusion, which peaked between 6.8 and 8.6 Ma. Intrusive activity continued until 5.2 Ma with the emplacement of dacite and rhyolite dykes which represent the terminal stages of magmatic activity in the region.

Porphyry Cu-Au and sensibly coeval epithermal Au-Ag alteration-mineralization formed early in this terminal stage. Thus, phyllic alteration occurred at Bajo de la Alumbrera at 6.75 Ma and alteration associated with the Farallón Negro - Alto de la Blenda deposit took place at 6.55 Ma. At Agua Rica, the porphyry-style mineralization, which was emplaced between 6.10 and 6.29 Ma and therefore slightly postdated that at Bajo de la Alumbrera, was overprinted by an epithermal system at 5.35 Ma. Epithermal alteration at Cerro Atajo, occurring between 5.11 and 5.35 Ma, was contemporaneous with

**Figure 5-21.**

Schematic illustration of the temporal evolution of the volcanic, intrusive and hydrothermal events associated with the Farallón Negro Volcanic Complex.



that at Agua Rica.



## CHAPTER 6

### CONCLUSIONS

In this chapter, the new observations on the geology, geochemistry and geochronology of the Farallón Negro Volcanic Complex are evaluated with regard to their implications for the geotectonics, petrogenesis and metallogenesis of the region

#### **Integrated tectono-magmatic model for the evolution of the Farallón Negro Volcanic Complex**

The location of the Farallón Negro Volcanic Complex in the transition zone between the domains of shallowly-dipping subduction to the south and more "normal" subduction to the north, and its proximity to the southern edge of the *Puna*, suggest that its formation may have been controlled by a complex interaction of: (1) subduction-related stresses, (2) compressive stress related to the uplift of the *Puna*; and (3) pre-existing crustal inhomogeneities. These potentially important factors are discussed below.

#### ***Subduction-related effects***

A major reorganization of the southeastern Pacific Ocean spreading centres occurred during the late Oligocene (Mammerickx *et al.*, 1980; Pilger, 1984), resulting in an increase in the trench-normal convergence rate and a change in the angle of convergence to one normal to the South American margin at the approximate latitude of Farallón Negro. These geodynamic events were contemporaneous with the establishment of a calc-alkaline magmatic arc in the *Cordillera Principal* at approximately 26 Ma (Kay

*et al.*, 1988). This extended north to 25°S and far to the south (37°S) of the present southern boundary of the flat subduction zone (Kay *et al.*, 1994; Chapter 2 herein), suggesting that "normal" subduction must have occurred along this extended segment of the plate margin, without first-order segmentation of the slab (Reynolds, 1987).

Flattening of the subducted slab in the 28° - 33° S segment has been inferred to have commenced by 18 Ma, with rapid shallowing, as indicated by the abrupt eastward migration of volcanism (see below), occurring after 10 Ma (Kay *et al.*, 1988, Reynolds, *op. cit.*, Kay *et al.*, 1994). This timing is in broad agreement with models in which the uplift of the *Sierras Pampeanas* is directly related to low-angle subduction. It has been suggested that higher convergence rates result in low-angle subduction, which in turn causes basement-involved foreland deformation (Jordan *et al.*, 1983). Plate reconstructions (Pilger, 1984) indicate that low-angle subduction has been occurring beneath the *Sierras Pampeanas* since approximately 13 Ma. Reynolds (1987) inferred that uplift of the Pampean Ranges occurred in a random manner, *i.e.*, that there was no apparent directional migration of uplifts with respect to time, in the period 3 - 7 Ma.

Earthquake focal mechanism solutions (Chinn and Isacks, 1983) and the kinematic analysis of minor fault arrays (Allmendinger, 1986; Urreiztieta *et al.*, 1993, 1996; Marrett *et al.*, 1994) for regions north (*e.g.*, the Santa María valley) and south (*e.g.*, south of Fiambalá) of the immediate Farallón Negro area indicate E-W horizontal shortening interpreted to be related to bulk convergence between the Nazca and South American plates (Urreiztieta *et al.*, 1996).

### ***Puna-related effects***

Assumpção and Araujo (1993) have documented a fanning of maximum horizontal stresses around the *Altiplano (Puna)* consistent with the arcuate shape of its eastern boundary. This pattern is attributed to plateau-spreading stresses. This implies an important effect of topography on Andean kinematics: the stress applied by the *Puna* is envisaged to have been sufficient locally to override the effect of the subduction-related stress.

On the basis of  $^{40}\text{Ar}$ - $^{39}\text{Ar}$  geochronology of tuffs interbedded with evaporite sequences interpreted to indicate an internally-drained depositional environment, Vandervoort *et al.* (1995) demonstrate that by approximately 15 Ma internal drainage resulting from regional uplift was established in the southern *Puna*. In contrast, Allmendinger (1986) suggested that uplift of the southern *Puna* between 24° and 26° S could have begun between 5 and 10 Ma. This proposed timing appears to be based largely on the 6 - 7 Ma northwest-trending dyke swarm documented in the Farallón Negro region by Caelles *et al.* (1971) and Llambías (1972), the emplacement of which is consistent with a NW-SE shortening direction related to the uplift of the plateau (Allmendinger, 1986). More recent studies indicate, however, that uplift began at about 13 Ma and lasted until 1 - 2 Ma (Marrett *et al.*, 1994).

Kinematic analysis of fault-slip data in the vicinity of the Farallón Negro region, *e.g.*, in the Sierras de Hualfin, Las Cuevas, Chango Real, Capillitas and Belén, and at one locality within the Main Farallón Negro Stratovolcano (El Tobogán), indicate NW-SE principal shortening directions (Allmendinger, 1986; Urreiztieta *et al.*, 1996), interpreted

to be associated with the southward attenuation of the *Puna*.

### ***Crustal inhomogeneities***

#### **Arequipa-Antofalla craton - Precordillera terrane suture zone**

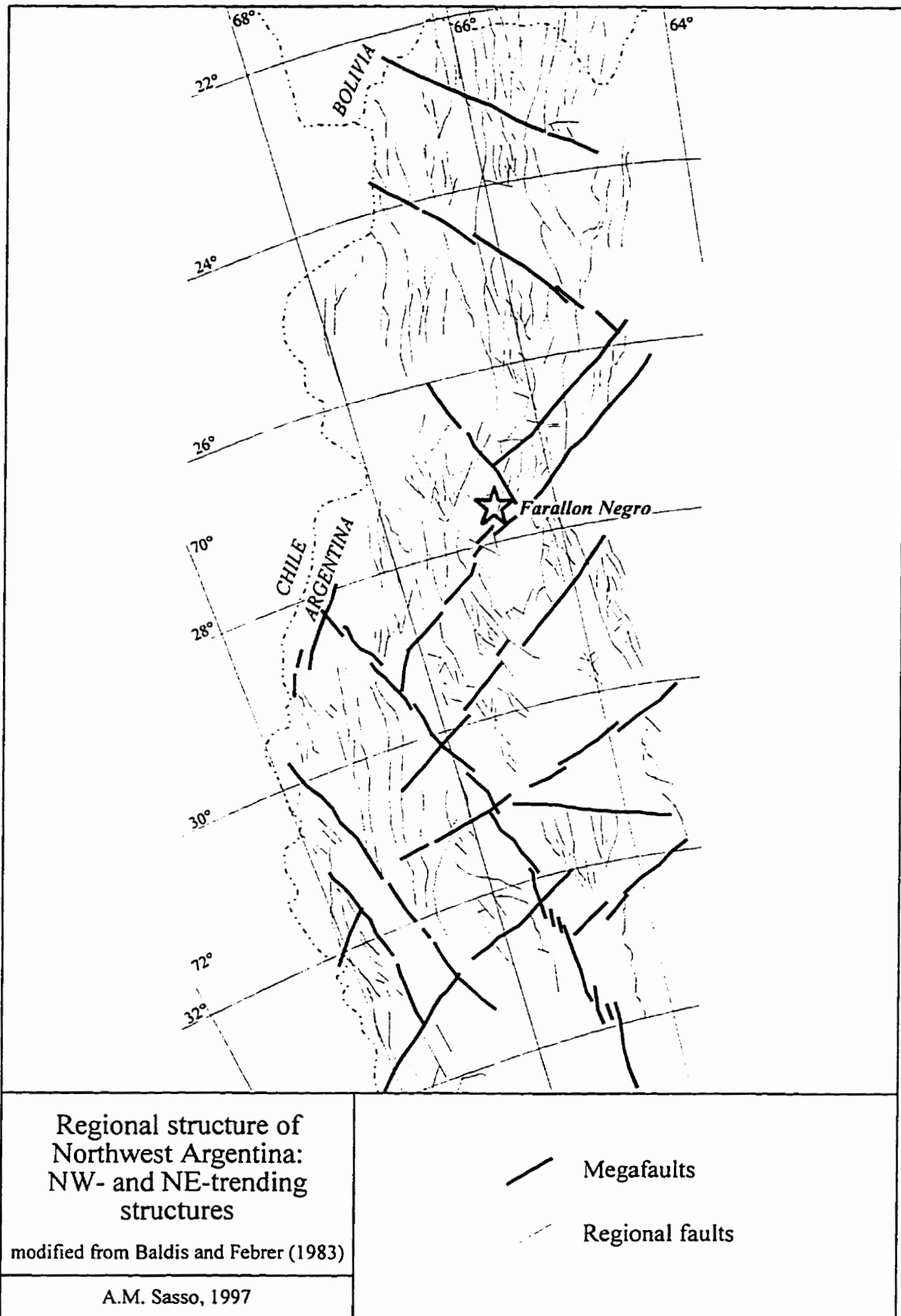
The Arequipa-Antofalla craton (Ramos *et al.*, 1986) is a coherent block of Middle Proterozoic rocks underlying the Andes in western Bolivia, western Argentina and northern Chile and Early Proterozoic rocks of the Arequipa massif in southern Peru. A fundamental north-to-south difference in Pb isotopic signature has been demonstrated (Tosdal, 1996) at approximately 27°S between the Arequipa-Antofalla craton and the Precordillera terrane to the south and is interpreted (Tosdal, *op. cit.*) to represent a crustal province boundary which might represent a suture of Grenvillian or early Proterozoic age.

#### **NW- and NE-trending orogen-oblique faults**

A major conjugate series of transcurrent NW- and NE-trending structures (Fig. 6-1) is interpreted to have developed in the southern South American crust in the late Precambrian / Early Paleozoic (Baldi and Febrer, 1983; Bassi, 1988; Casaceli, 1993a, 1993b; Coughlin, 1996). They are envisaged as crust-penetrating structures with a complex history of alternating left-lateral and right-lateral displacement. However, the displacement history along NW-trending structures is characterized predominantly by left-lateral displacement and that along the NE-trending structures by right-lateral movement (Jordan *et al.*, 1983). In general, when two conjugate fault sets are developed, one will usually dominate (Ramos, 1977). The NW-trending system appears to be the major trend in northern Argentina although, as will be demonstrated below, NE-striking structures are locally important. Transtensional stresses along some of the NW-trending megastructures have opened basins and locally controlled volcanism during the early-Middle-to-Late Jurassic (Nullo, 1991). The locations of depocentres within the Cretaceous Salta Rift Basin (Grier *et al.*, 1991) are thought to have been controlled by NE- and NW-trending

**Figure 6-1.**

Orthogonal structural fabric of the basement of northwestern Argentina interpreted from the compilation of aerial photographs, interpretation of satellite imagery and field investigations (after Baldi and Febrer, 1983).



lineaments (Salfity, 1982). Casaceli (1993b) proposes that right-lateral transtensional jogs form during restricted intervals along NW-trending structures and suggests that these periods may coincide with volcanism and precious metal hydrothermal activity, *e.g.*, at El Hueso, in the El Salvador district of northern Chile. The localized transtension is thought to have initiated magmatism and ultimately to have controlled the emplacement of Cu and Au mineralization. Left-lateral, NW-striking faults are observed controlling upper Oligocene magmatic complexes throughout the Maricunga Belt in Chile (Kay *et al.*, 1994). Late Miocene to Pliocene volcanic activity in the *Puna* is concentrated in NW-SE transverse belts (Coira *et al.*, 1993), and a complex tectonic regime involving both extensional and compressional deformation styles is documented in the southern *Puna* for the interval, 3-4 Ma (Kay *et al.*, 1994a). Casaceli (1993a and b) remarks on the similarity between the NW- and NE-trending strike-slip faults in South America and the orthogonal basement fabric in North America, where ore deposits are controlled by major lineaments such as the NW-trending Lewis and Clark Lineament, Olympic-Wichita Lineament, Carlin Trend, Battle Mountain Trend, Walker Lane, Texas Lineament, Mojave-Sonora Megashear and the Trans-Mexican Volcanic Belt, and the NE-trending Trans-Challis Trend, Mullen-Nash Fork Shear zone, Colorado Mineral belt and Jemez Lineament.

#### *Tucumán Transfer Zone*

The study-area is the locus of a sharp change in the strike of basins and ranges from a regional N-S elongation to NE-SW orientations at the boundary between the southern margin of the *Puna* and the northwestern margin of the *Sierras Pampeanas*. González Bonorino (1950) observed that this change in orientation of the regional structures appears to reflect a "push" by the large mass of the *Puna*. This zone, approximately 100 km wide, is marked by a complex series of linked NE-striking faults and isolated Tertiary basins. This feature has long been commented upon in the literature

and was termed the "Tucumán Lineament" by Mon (1976). He described it as a strike-slip lineament which is highly oblique to regional structural trends and may have been an ancient feature that was reactivated during Andean tectonism in Late Pliocene - to - Early Pleistocene time. Many workers have invoked movement along parallel sets of right-lateral lineaments, including the Tucumán Lineament, to generate tensional fractures that are inferred to have controlled the emplacement of porphyry deposits in the Farallón Negro complex (*e.g.*, Ramos, 1977; Sillitoe, 1981). Jordan *et al.* (1983) postulated that the zone was one of distributed right-lateral shear, rather than strike-slip faulting along a single fault. This has been supported by further mapping along the southern edge of the *Puna* (*e.g.*, Allmendinger, 1986; Allmendinger *et al.*, 1989; Marrett *et al.*, 1994) that reveals that a series of *en echelon* structural blocks constitutes the *Puna* margin.

Recent refinements in the structural interpretation of the area have resulted in the delimitation of the *Tucumán Transfer Zone* (Urreiztieta *et al.*, 1993, 1996; Urreiztieta *et al.*, 1994). It is now argued that the transition at about 27° S between the *Puna* and the *Sierras Pampeanas* is a major dextral transpressional transfer zone (Urreiztieta *et al.*, *opera cit.*). Wrenching along this zone has been postulated to be responsible for the development of sedimentary depocentres, with or without volcanism, located and constrained within the Tucumán Transfer Zone at Farallón Negro (Sasso, 1995; Sasso *et al.*, 1995; and herein) and at Jagüe, to the southwest in San Juan Province (Coughlin, 1996; T. Coughlin, pers. comm., 1996). This zone is interpreted to reflect a long-lived lithospheric-scale structure (Coughlin, *op. cit.*).

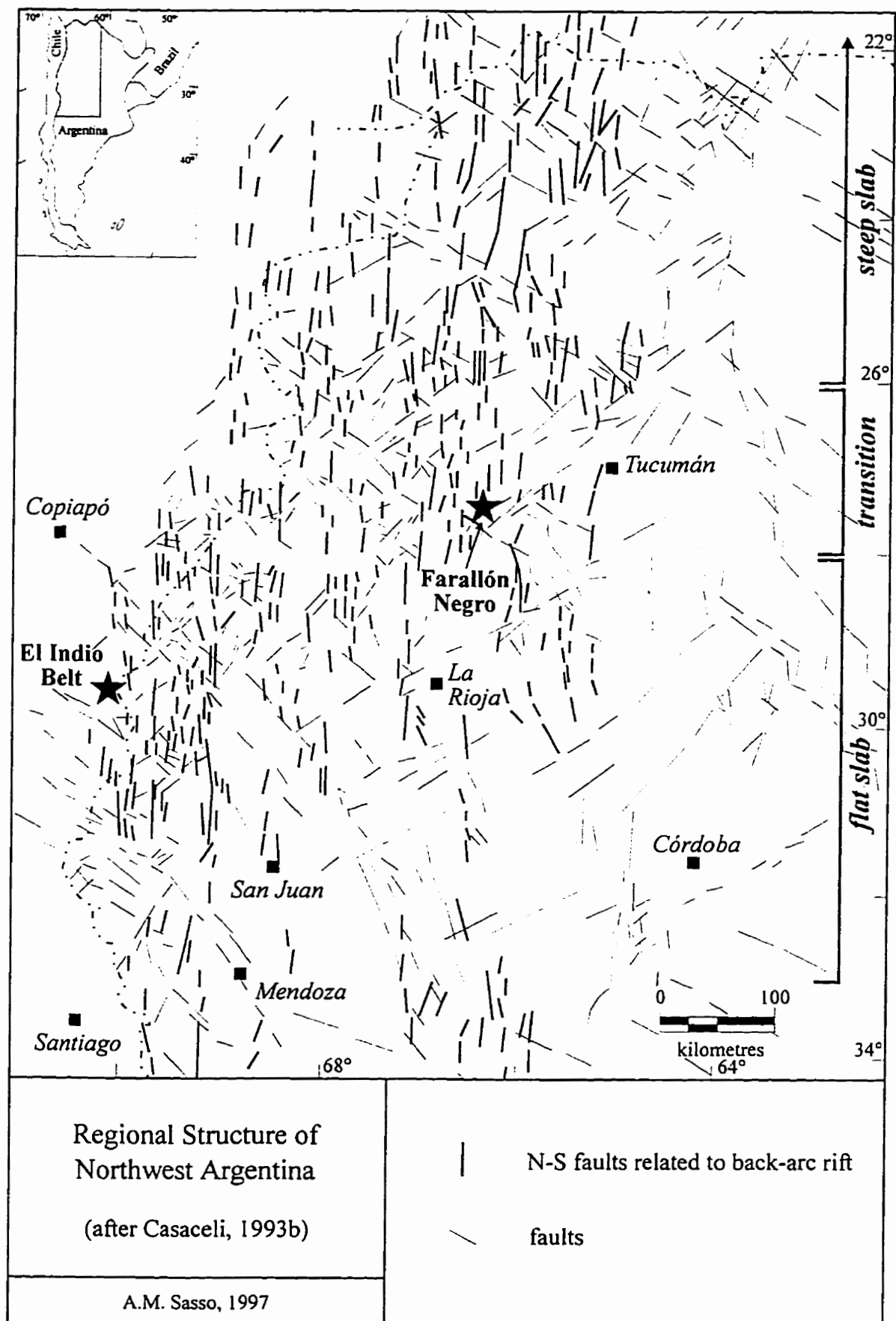


## N-S-trending faults

On the basis of the interpretation of TM imagery and geological mapping, Casaceli (1993b) has proposed that a strong N-S oriented structural grain overlaps with the transition zone and the northern portion of the flat-slab segment and is broadly coincident with the *Sierras Pampeanas* (Fig. 6-2). The structures exhibit complex histories involving normal and reverse movement. Many of the faults delimit discontinuous N-S-trending grabens which display symmetric listric faults with rotated blocks of early Tertiary sedimentary rocks as bounding structures, and exhibiting an alignment of young basaltic cinder cones and hot-spring deposits along a central axis. Casaceli (1993a, 1993b) has interpreted this structural pattern to represent a continental back-arc rift system which initially developed over a low-angle subduction zone in the Cretaceous and has continued to the present. He suggests that whereas the South American continent has been under compression since the Early Mesozoic as a result of convergence with the Nazca Plate, local magma upwelling initiated by zones of transtension associated with the NW- (and NE-) striking transcurrent faults may have created broader areas of extension that overcame the subduction-related stresses and facilitated the development of N-S-trending grabens. Froidevaux and Isacks (1984) argue that volcanism in the *Altiplano-Puna* is related to predominantly extensional or transtensional, rather than compressional tectonics. The alignment of very young basaltic cinder cones along the N-S axis of a graben north of Antofagasta de la Sierra in the *Puna* led Casaceli (1993a) to conclude that extension is ongoing. This is supported by kinematic studies in the southern *Puna* by Allmendinger *et al.* (1989), while Francis *et al.* (1978) document the emplacement of the Cerro Galán

**Figure 6-2.**

North-south oriented structural fabric of northwestern Argentina interpreted from TM imagery and regional geological mapping (after Casaceli, 1993b). The N-S faults are presented in bold tones for illustrative purposes. These structures are commonly subsidiary to reactivated transcurrent movement on the older NW- and NE-trending basement structures. The proposed rift is a broad zone within which extensional fault mechanisms have been observed. Extension is caused by the intrusion of magma into the crust above a shallow- to moderately-dipping subduction zone. The western boundary of the rift includes the region of the El Indio Belt in Chile. The eastern boundary lies approximately at the longitude of Tucumán. The rift system is best developed in the region of shallow dip but is also well expressed in the transition zone to the north. South of Mendoza, the rift loses continuity and disappears.



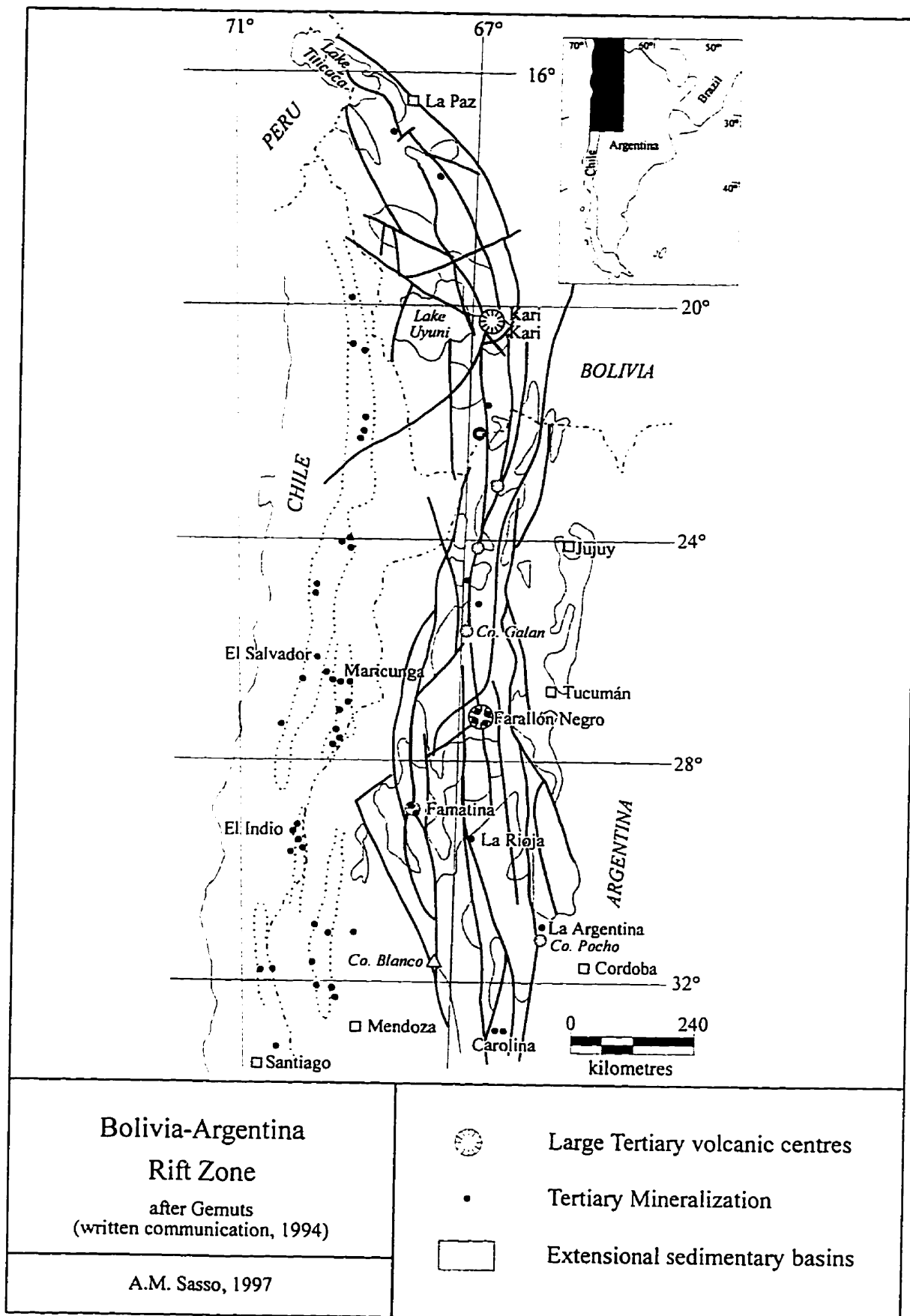
caldera in a N-S-trending graben in which normal faulting began at least 10 m.y. ago. Grier *et al.* (1991) propose that a N-S-trending failed rift, the Cretaceous Salta Rift Basin, formed in response to the opening of the South Atlantic and experienced Mio-Pliocene inversion in which the N-S rift-bounding normal faults were reactivated as thrusts. Casaceli (1993a) has suggested that, given the accretionary tectonic history of Paleozoic South America as outlined by Ramos (1988; see also Caelles, 1979), it is unlikely that the northern Argentine continental crust had the structural integrity to form foreland flexural basins in response to tectonic and sedimentary loading, as suggested by Jordan and Alonso (1987), but would be more likely to fracture and form localized grabens in an ensialic rift setting.

This model of an ensialic back-arc rift system in NW Argentina is new and controversial. It has yet to be formally published and the existing reports (*e.g.*, Casaceli, 1993a, 1993b) are not readily available to the Argentine geological community, and therefore little discussion of the model has occurred. However, aspects of the model are supported by members of the international exploration community operating in Argentina, *e.g.*, I. Gemuts, pers. comm., 1994; V.J. Wall, pers. comm., 1995; E.M. Baker, pers. comm., 1996; Gemuts *et al.*, 1996.

A broadly similar model has been proposed by I. Gemuts (pers. comm., 1994) and is outlined by Gemuts *et al.* (1996). In this model a 100 - 150 km wide rift zone which extends from Lake Titicaca in NW Bolivia to the Pocho area in Córdoba Province (Fig. 6-3) was initiated at approximately 12 Ma. The central axis of the rift is envisaged to be defined by a series of large silicic Miocene volcanic centres, *e.g.*, the 20 Ma Kari Kari

**Figure 6-3.**

Proposed Tertiary rift zone in northwestern Argentina (after  
I. Gemuts, written comm., 1994).



*Meseta* (Francis and Baker, 1978), the Upper Miocene Cerro Panizos (Ort *et al.*, 1989; de Silva and Francis, 1991), and the 2.2 - 15 Ma Cerro Galán complex (Sparks *et al.*, 1985), and analogies are made with volcanic structures in the Rio Grande Rift of the southwest U.S. (*e.g.*, the Valles Caldera in New Mexico). However, these complexes have also been interpreted to have erupted through thickened plateau crust underlain by thin continental lithosphere by Kay *et al.* (1994b). In SE Peru and NW Bolivia, Sandeman *et al.* (1995) interpret the 20-27 Ma events (*e.g.*, Kari Kari) as resulting from extrusion tectonics related to development of the Bolivian Orocline while, although the 12-13 Ma period was a time of tectonic differentiation in the *Cordillera Oriental* and *Altiplano*, it was not clearly one of rifting. Additional geological support is needed for the regional rift model, but the structures observed by Gemuts in NW Argentina may be the southward manifestation of the indentor tectonic regime proposed by Sandeman *et al.* (1995). On the basis of field observations and regional aeromagnetic surveys, Gemuts *et al.* (1996) have recognized a series of large extensional Tertiary grabens which appear to control the emplacement of Miocene (?) porphyry bodies in the Uspallata graben, in the Province of Mendoza, which are temporally and spatially associated with porphyry Cu-Au and epithermal Au-Ag deposits, and where volcanic rocks yield K-Ar ages of between 16.2 and 18.9 Ma (Kay *et al.*, 1991). The mechanism driving extension is unclear, but back-arc "movement" or incipient intracontinental rifting are suggested. I. Gemuts (written comm., 1994) speculates that the extension may be related to the generation of a hot spot by crustal fusion at the base of the subducted plate and draws analogies with the association of high heat flow and extension in Nevada.

## Local structures

The most obvious faults in the Farallón Negro region are high-angle reverse structures which juxtapose rocks of the volcanic complex against crystalline basement lithologies. These, *e.g.*, the San Buenaventura, Vallecito, Jaci-Yaco, Lavadero, El Tigre and Aconquija Faults (see figure 2-11), generally strike NE to ENE and dip steeply to the south. The displacement is uncertain, although up to 6000 m was suggested for the Aconquija Fault by González Bonorino (1950). That author also calculated displacements of 4000 m along the Lavadero Fault in the Capillitas Range and 3000 m along the San Buenaventura Fault in the Ovejería Range. Although these fault-zones are encountered in the field (Fig. 6-4), kinematic indicators are rare. Reverse movement is implied by the juxtaposition of the basement and younger units of the Farallón Negro Volcanic Complex and by the footwall synclines developed in the latter (Fig. 6-5). Synclinal fold axes defined in the field are sub-horizontal, suggesting vertical movement along the faults, and lines drawn perpendicular to the fold axes in the horizontal plane were taken by the writer to indicate the transport direction of the reverse faults responsible for the formation of the folds. Figure 6-6 illustrates the attitudes of the footwall syncline fold axes measured in the field and the calculated direction of transport for the faults. In general, this is compatible with the NW-SE directed shortening documented to the north of the study area by Allmendinger (1986) and Urreiztieta *et al.* (1996).

Two unnamed high-angle reverse faults on the eastern and western margins of Sierra Durazno have orientations distinct from the dominant trend. The western fault trends NNW and dips to the east, and exhibits reverse movement along its northern



**Figure 6-4.**

*Bola del Atajo fault zone.*

View to the east of the high-angle reverse fault along the northern margin of Bola del Atajo. Granites of the crystalline basement (right) are placed on top of volcanic breccias of the Farallón Negro Volcanic Complex. The fault zone is approximately 1 - 1.5 m wide and is marked by gouge (white and red clay-rich material). Field assistant, David Braxton, is of average North American height, approximately 1.70 m.



**Figure 6-5.**

*Footwall synclines related to high-angle reverse faults  
in the Farallón Negro region.*

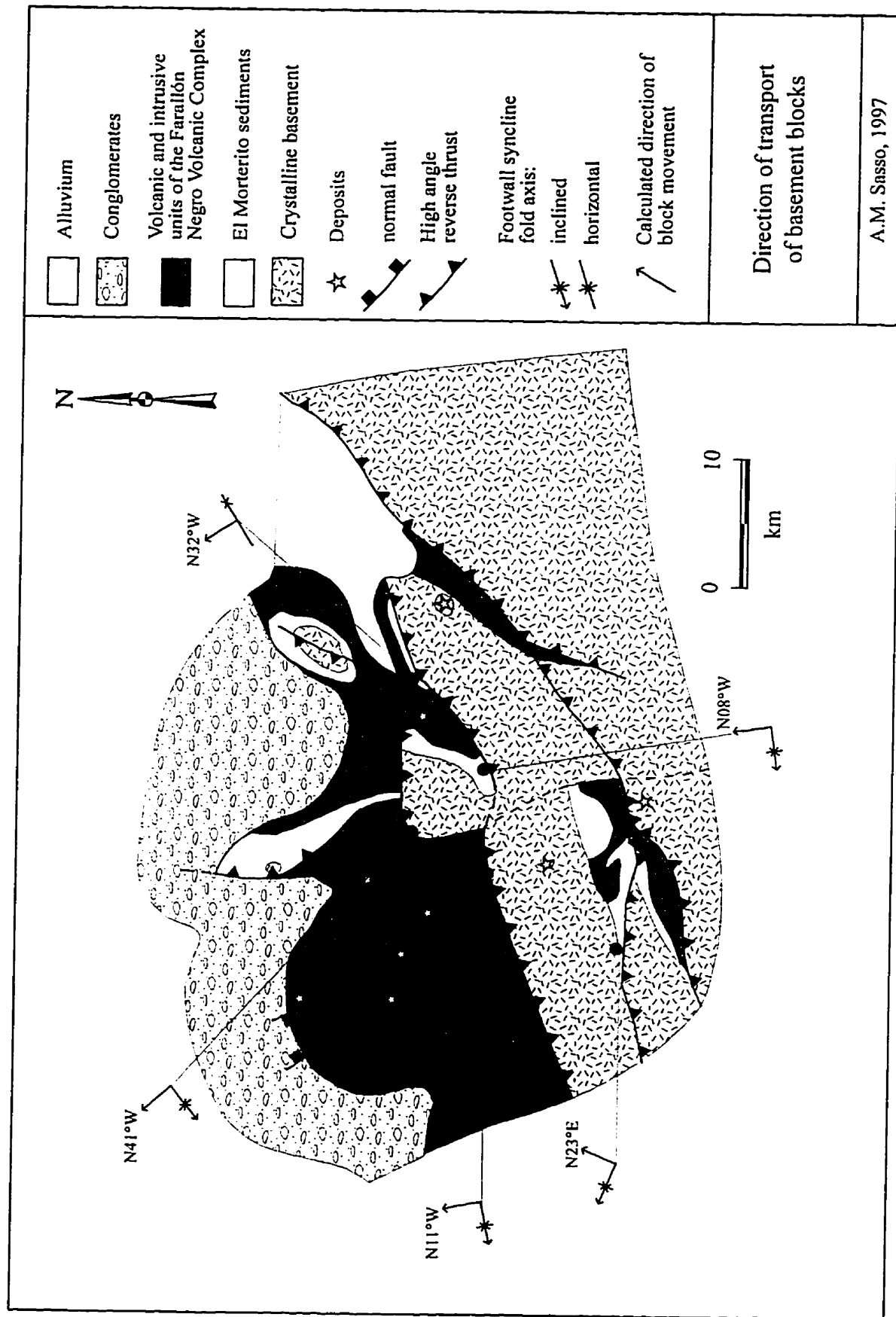
A. View to the east of the Bola del Atajo fault-zone in the region of Las Escaleras (see figures 2-11 and 2-16). Granitic basement rocks (pale units, right-foreground) have been thrust over volcanic breccias of the Farallón Negro Volcanic Complex (dark bedded units, left-foreground) along a high-angle reverse fault which is located in the small valley (middleground) which trends into the picture and is marked by a change in lithology. The volcanic strata were folded into a footwall syncline during fault movement. High peaks of the Sierra de Aconquija are seen on the horizon.

B. View to the west along the trace of the San Buenaventura fault. The Quebrada de Vis Vis (see figure 2-11) is the main drainage that cuts diagonally from right to left. The Quebrada de San Buenaventura is the large valley that drains into Quebrada de Vis Vis in the centre of the photo. The San Buenaventura fault zone lies in the former valley. Metamorphic rocks of the Suncho Formation (to the left of the *quebrada*) are displaced along a high-angle fault over volcanic breccias of the Farallón Negro Volcanic Complex (stratified units to the left of Quebrada de San Buenaventura). The volcanic strata are seen gently upturned in proximity to the fault-zone and were folded into a syncline during the faulting. The Río del Atajo is located in the left-foreground and granitic rocks underlying the southern flank of Bola del Atajo make up the right-foreground.



**Figure 6-6.**

Illustration of the transport directions of selected uplifted basement blocks as indicated by the attitude of footwall synclines. The attitudes of volcanic units were measured in the synclines developed in the footwalls of the high-angle reverse faults and fold axes were calculated. Lines drawn perpendicular to the fold axes in the horizontal plane were taken to indicate the transport direction of the reverse faults responsible for the formation of the folds.



A.M. Sasso, 1997

extension and normal displacement along its southern trace. It is responsible for uplift of the Sierra Durazno range. The eastern fault and a series of parallel minor faults strike NNE and dip to the west and core a doubly-plunging anticline developed in the granitic basement north of Cerro Atajo. Displacement along these faults is significantly less than that demonstrated by the NE-trending faults. It will be suggested (see below) that the Sierra Durazno faults are responsible for buckling of the crust and indicative of the initial stages of basement uplift (Urreiztieta *et al.*, 1996), and that the Sierra Durazno block has undergone up to 45° of clockwise rotation.

In a study of the structural evolution of the Sierra de Ovejería, Pacheco (1988) documented predominantly reverse movement related to NW-SE compression along the San Buenaventura fault (Fig. 6-5), but also reported components of normal displacement and dextral shear. The relative timing of the different displacements is unclear. Pacheco (*op. cit.*) suggested that the fault was active prior to the emplacement of the Farallón Negro Volcanic Complex but the evidence for this is not presented. The different fault solutions may indicate reactivation of a long-lived structure or, as was illustrated by Stone (1986), represent inherent complexities along faults in domains of wrenching. The latter is the preferred interpretation of the observations documented by Pacheco (1988), although it will be argued in a later section that some of the NE and ENE faults represent structures which pre-dated the emplacement of the volcanic units. The 4 km of reverse movement postulated for the San Buenaventura fault by González Bonorino (1950) would have obliterated all kinematic indicators for previous deformation events.

Because of the absence of a detailed stratigraphy of the volcanic units of the

Farallón Negro complex, the recognition of faults in the volcanic rocks is difficult. However, Proffett (1994, 1995) has documented a series of approximately NW-striking normal faults which displace alteration-mineralization facies at Bajo de la Alumbra. In general the faults in the northern portion of the *bajo* exhibit south-side-down movement, whereas those in the south display north-side-down offset. There is no evidence for significant faulting prior to the emplacement of the porphyries at Alumbra. The faults are interpreted to be associated with the waning stages of, and to post-date, phyllic alteration in the deposit (Proffett, *opera cit.*), which is dated herein at 6.75 Ma. One of the normal faults that transects the northern portion of the deposit is interpreted, on the basis of TM image and airphoto interpretation and reconnaissance mapping to extend to the northwest and southeast (see figure 2-11). A parallel normal fault with north-side-down displacement is interpreted to have controlled the emplacement of a series of intrusions of the Macho Muerto Dacite, including the Loma Morada and Macho Muerto bodies, in the northwest quadrant of the Main Farallón Negro Stratovolcano. A minor NW-trending normal fault was encountered in breccias south of Quebrada La Chilca in the SW quadrant of the complex.

#### ***Presentation of a model for the structural evolution of the Farallón Negro region***

Llambías (1972) envisaged that the emplacement of the Farallón Negro volcano occurred in a localized tectonic depression, simultaneously with gradual uplift of the surrounding basement topography. González Bonorino (1950a, 1950b) attributed the variations in the thickness of sedimentary and pyroclastic units in the *Sierras Pampeanas*



to differential movement of the basement blocks prior to the eruption of the volcanic units of the Farallón Negro Volcanic Complex.

It is proposed herein that the rocks of the Farallón Negro Volcanic Complex at the latitude of Farallón Negro were emplaced in an extensional basin which developed in a zone of transtension generated by the interaction of the NE-trending dextral Tucumán Transfer Zone (Urreiztieta *et al.*, 1993, 1996), with major N-S-trending faults, possibly related to an ensialic rift as proposed by Casaceli (1993a, 1993b), Gemuts (written comm., 1994) and Gemuts *et al.* (1996). The salient evolutionary stages of this model are presented as a series of schematic illustrations as figure 6-7. Sedimentation of the El Morterito Formation began at about 13 Ma at two main depocentres: Hualfin - Corral Quemado in the SW and Arca-Yacu (Santa María) in the NE (Bossi *et al.*, 1993). The localized crustal stretching and lithospheric thinning, coupled with a relatively low sedimentation rate, permitted high heat flow and, eventually, volcanism. Thermal softening of the crust by magmatism probably expedited extension. The intrusion and eruption of volcanic units plausibly created a new floor to the coalescing basins, and sediments of the El Morterito Formation are probably absent beneath the core of the Main Farallón Negro Stratovolcano. This helps to explain the relative thinness of the older sedimentary sequence adjacent to the volcanic edifice.

It is argued that the stress regime active at the time of the Middle Miocene initiation of the pull-apart basin was dominated by localized NE-SW-oriented extension resulting from the differential response of the northerly Arequipa-Antofalla craton and the southerly Precordillera terrane to E-W compression related to convergence of the Nazca and South American Plates. The Arequipa-Antofalla craton represents a coherent block which is interpreted to have resisted deformation while lithologies of the Precordillera underwent significant shortening, thereby creating a window of extension along the

**Figure 6-7.**

*Structural evolution model for the  
Farallón Negro region.*

**A. *Pre-12.6 Ma: Initiation of the pull-apart basin.*** Interaction of right-stepping dextral faults within the Tucumán Transfer Zone with regional N-S-trending faults resulted in the formation of an extensional basin with two main depocentres. Although the overall plate convergence vector is orthogonal, it is inferred that, at the latitude of Farallón Negro, the difference in rheidity between the Arequipa-Antofalla craton, to the north, and the more easily shortened Precordillera terrane to the south has resulted in localized NE-SW extension.

**B. *8.5 - 12.6 Ma: Development of discrete extrusive centres.*** Stretching and crustal thinning permitted high heat flow and, eventually, volcanism. The early volcanic history of the region is inferred to have been characterized by isolated, small-volume extrusive events, possibly focussed at the intersections of regional structures.

**C. *ca. 8.5 Ma: Initiation of the Main Farallón Negro stratocone construction event.*** The precursor extrusive centres are covered by flows and breccias of the Main Farallón Negro stratovolcano.

**D. *5.5 - 8.5 Ma: Peak episode of volcanic, intrusive and hydrothermal activity accompanied by a shift in the regional compression direction to NW-SE.*** The mass of the Puna, which is superimposed on the southern part of the Arequipa-Antofalla craton, imposes a NW-SE-oriented stress regime (Assumpção and Araujo, 1993). The construction of the stratovolcano from approximately 8.5 to 7.5, Ma with minor pyroclastic activity persisting until 6.7 Ma was accompanied by hypabyssal intrusion which continued until 5.95 Ma in the Main Farallón Negro edifice. The waning stages of intrusion were accompanied by hydrothermal mineralization, which included the formation of the Bajo de la Alumbrera porphyry Cu-Au deposit at *ca.* 6.75 Ma, followed shortly by the emplacement of the Farallón Negro - Alto de la Blenda Au-Ag epithermal deposit at 6.55 Ma.

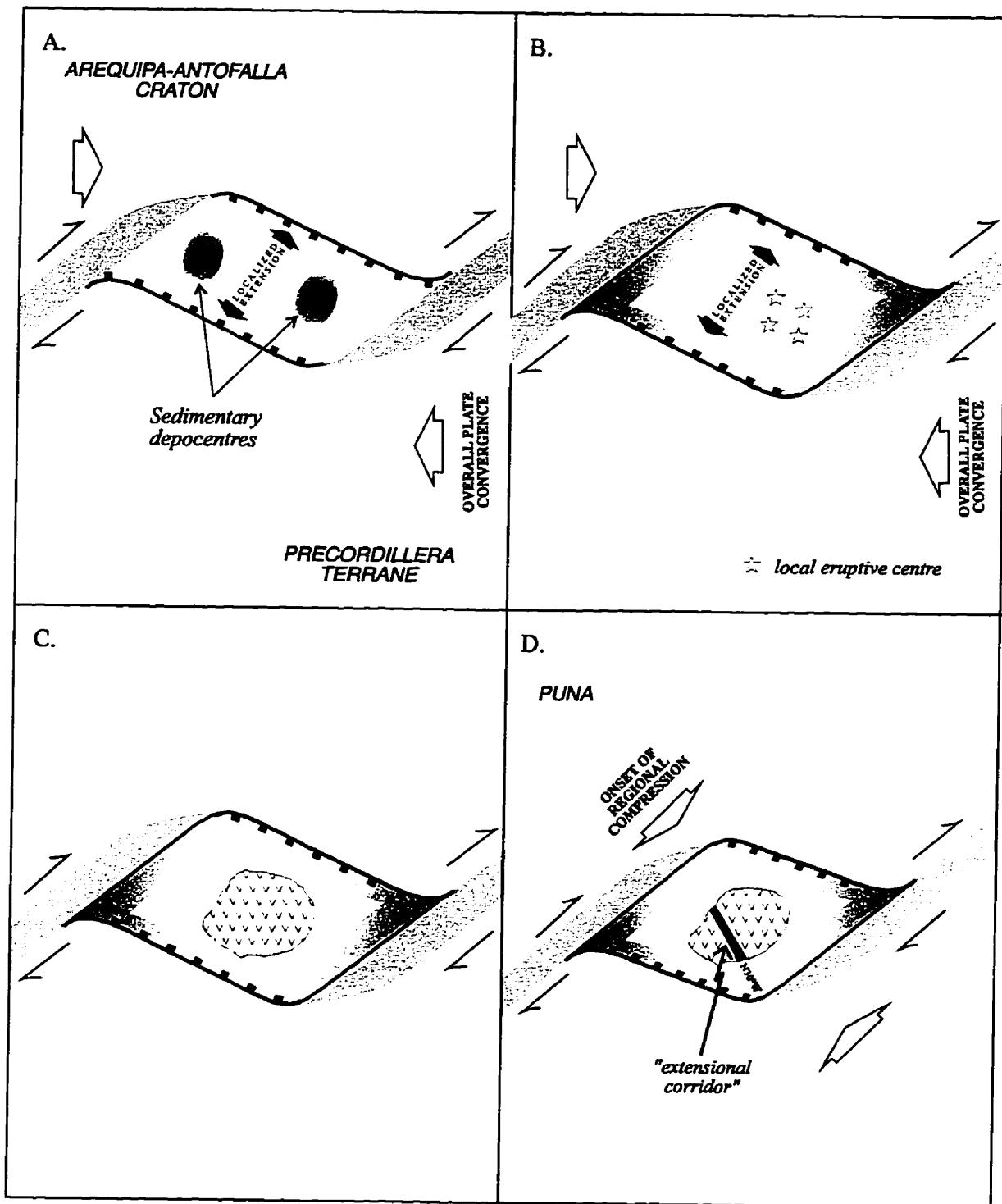
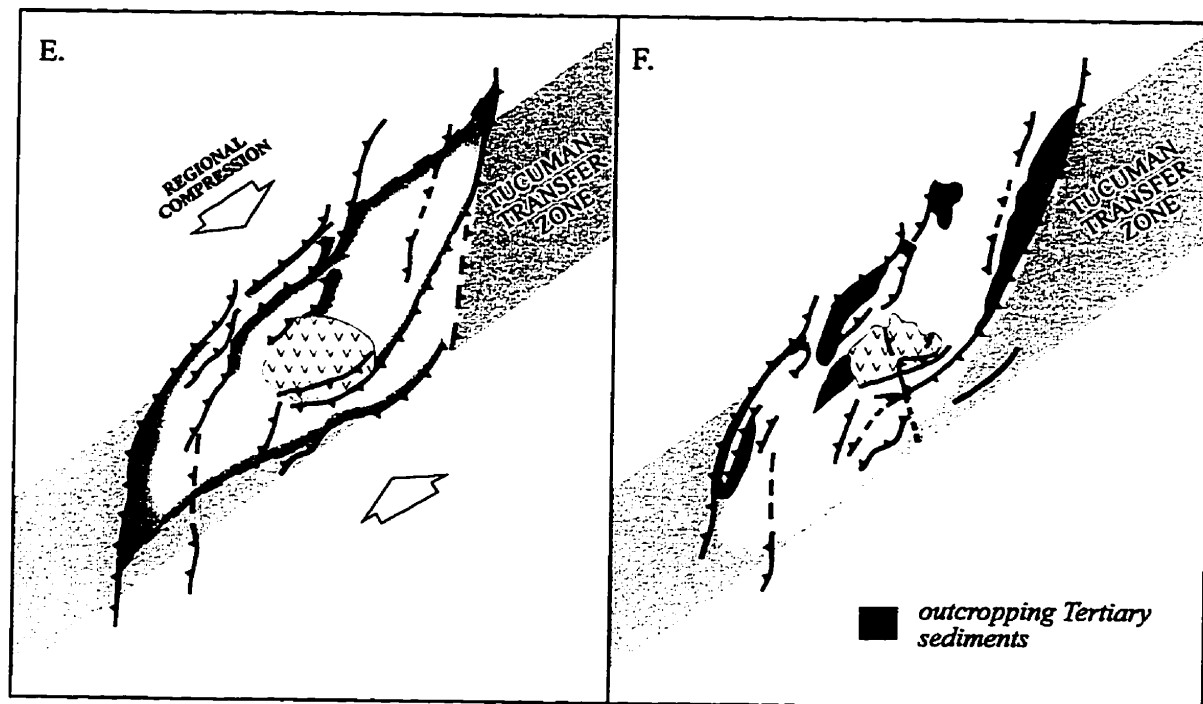


**Figure 6-7 (con't).**

*Structural evolution model for the  
Farallón Negro region.*

**E. 5.0 - 5.5 Ma: Main phase of basement uplift.** The onset of the *Sierras Pampeanas* deformation at the latitude of Farallón Negro results in the rapid uplift of the basement blocks, possibly through reactivation of faults associated with basin development. This resulted in the abrupt telescoping of the Agua Rica hydrothermal system and the formation of high-sulphidation epithermal assemblages at 5.35 Ma. Epithermal mineralization was also emplaced at Capillitas and Cerro Atajo during this interval.

**F. 5.0 - Present: Erosion.** Continued minor uplift of the basement blocks results in the formation of pediment surfaces in the Capillitas Valley.



boundary of the two domains. In the initial stages of basin formation, magma upwelling was triggered by the transtensional zone and may have been focussed at the intersections of the N-S and NE- and NW-striking structures. This is postulated to have resulted in the development of discrete extrusive centres early in the volcanic history of the region, now recorded by the 12.56 Ma basaltic andesite flow in Arroyo Alumbreira, the 9.17 Ma dacite in the Capillitas Valley, the 8.75 Ma andesite tuff and 8.41 Ma basaltic andesite in the eastern Sierra Durazno, and the 8.59 Ma basaltic flow north of Bola del Atajo.

The NW orientation of dykes at Farallón Negro, which have yielded ages as old as 7.94 Ma, is compatible with a NW-SE oriented compression (Allmendinger, 1986), implying that a shift in the dominant compressional stress regime from E-W to NW-SE may have occurred prior to initial dyke emplacement. It has been argued previously (see Chapter 2) that the older, isolated, extrusive centres were later covered by flows and breccias related to the construction of a large stratovolcano which appears to have formed from 8.51 to 7.49 Ma, with minor eruption of pyroclastic units continuing to as late as 6.72 Ma. It is herein proposed that the Main Farallón Negro Stratovolcano was emplaced into a neutral - to - compressional stress regime, which was dominated by NW-SE oriented stresses related to the uplift of the *Puna*. The influence of this stress orientation is recorded by the Aguila dykes, which were intruded as early as 7.94 Ma, and continued during the emplacement of the Agua Tapada Dacite and the Macho Muerto Dacite at least to 5.95 Ma. It is inferred that an extensional regime (extensional corridor; see Chapter 2) with a NE-SW extension direction was active throughout the formation of the stratovolcano and the associated intrusive events. The complete history of intrusive activity is dominated by NW-striking dykes and alignments of intrusive bodies and

mineralization centres, with subsidiary NE-trending structures. This dominant extensional trend may have continued to control the development of hydrothermal alteration-mineralization in the area (*e.g.*, the 6.55 Ma Farallón Negro - Alto de la Blenda and 5.11 - 5.35 Ma Cerro Atajo vein systems). Several veins in the Capillitas deposit, for which an age of emplacement of approximately 5.2 Ma is inferred (see Chapter 3), also exhibit a NW trend, but the majority are controlled by NE-oriented structures.

Parsons and Thompson (1991) describe how the intrusion of vertical dykes perpendicular to the main extension direction can change the local stress field and accommodate tectonic stresses. Rapid dyke injection may not only suppress faulting but can reorient the principal stresses to the extent that an orthogonal set of dykes may form. "Cycling" from one principal extension direction to the orthogonal direction may occur with successive pulses of magmatism. This process may have been active during the formation of the Farallón Negro complex. Rapid intrusion of basaltic-andesitic dykes parallel to the NW-trending extensional axis may have inhibited normal faulting and have been of sufficient pressure, due to density differences between solid and fluid which produced a large buoyant driving pressure, to overcome the value of the intermediate stress of the system, thereby generating a subsidiary dyke swarm with a dominant NE trend. NE-trending basaltic-andesite, andesite, monzonite and dacite dykes are observed in the Farallón Negro complex. The intrusive bodies at Bajo de la Alumbraera, Bajo de Agua Tapada, Bajo El Durazno, Capillitas and Bajo Las Pampitas all exhibit this elongation. Hydrothermal alteration zones at Bajo de la Alumbraera and Bajo el Durazno are also elongated NE - SW (see Figs. 3-5 and A-12). A related structure (trending

N78°W), possibly sub-parallel to the basin margin, may have influenced the emplacement of the Cerro Atajo, Capillitas, Agua Rica and Filo Colorado centres.

The resulting basin appears to have been Z-shaped ("lazy Z": Mann *et al.*, 1983), the development of the stratovolcano occurring in its centre. Although there appears to be no systematic pattern for the distribution of volcanism in "pull-aparts", magmatism within Z-shaped and rhomboidal basins in the Gulf of California and the Andaman Sea appears to have been along orthogonal spreading centres situated roughly in the centres of the basins (Mann *et al.*, 1983). The Main Farallón Negro Stratovolcano acted as a significant topographic high, possibly extending across almost the entire width of the basin and partially closing off the centre, thereby influencing subsequent sedimentation patterns. Paleocurrent directions indicate flow to the north in the Santa María valley and to the south in the Hualfín - Las Cuevas valley (Bossi *et al.*, 1993).

It is further argued that, although the emplacement of the Farallón Negro Volcanic Complex occurred in a broadly compressional environment which records the effect of the uplifting *Puna*, significant uplift of the bounding basement blocks (*e.g.*, Ovejería, Capillitas, Aconquija and Bola del Atajo) did not occur until late in the structural evolution of the area. Thus, major uplift of the Capillitas and Aconquija ranges is inferred to have been delayed until between 5 and 5.5 Ma (Chapter 3). Whereas Reynolds (1987) proposed that the uplift of the *Sierras Pampeanas* proceeded in a random manner, the timing of uplift advanced herein for the Farallón Negro region is in accordance with that of other Pampean ranges, *e.g.*, prior to 5.0 Ma for the Famatina Range (McBride, 1972; Losada-Calderón *et al.*, 1994) and at *ca.* 5.7 Ma for the Sierra Morada (Reynolds *et al.*,



1988; and see Reynolds, 1987). It is postulated that this was a widespread, possibly short-lived, event, as opposed to the gradual uplift suggested by Llambías (1972). This compression, very probably acting along pre-existing structures, resulted in the uplift of major basement blocks along high-angle reverse faults. This was responsible for the formation of the present topography of high mountain ranges surrounding, and serving to preserve, the Farallón Negro complex. The inherited attitude of the reactivated structures may explain the preservation of the Z-bend in the uplifted basement block pattern at this latitude. Also of interest are the bilateral orientations of the reverse fault planes, with north-dipping faults located to the north of Farallón Negro and south-dipping faults to the south, implying that the mass of the Farallón Negro complex and its underlying plumbing system acted as an "inviolable" zone, with deformation focussed around its perimeter.

On the basis of paleomagnetic (Aubry *et al.*, 1996) and structural (Urreiztieta *et al.*, 1996) data, clockwise rotation has been postulated for blocks in the Tucumán Transfer Zone. Thus, clockwise rotation of the Hualfin block (Sierra de Hualfin) with respect to the Campo de Arenal Basin is proposed by Urreiztieta *et al.* (*op. cit.*). Paleomagnetic data (Butler *et al.*, 1984) for the El Bolsón region are also consistent with clockwise block rotation. It is herein proposed that the Sierra Durazno block also experienced clockwise rotation related to dextral wrenching in the Tucumán Transfer Zone. Up to 29° of clockwise rotation was calculated for blocks in the Santa María Valley and the Sierra de Hualfin (Aubry *et al.*, 1996). It is proposed that the Sierra Durazno dyke swarm was originally emplaced along a NW-trending direction during the development of the Main Farallón Negro Stratovolcano, subsequently experiencing clockwise rotation of up to 45°

to its present N-S orientation (Fig. 6-8). More detailed structural investigation, combined with a paleomagnetic study, is needed to confirm this hypothesis, but it is inferred that the NNW-striking reverse fault along the western margin of Sierra Durazno may have been originally a NW-trending normal fault, and that rotation and continued wrenching may have resulted in compression along its northern extension, causing its reactivation as a reverse fault. The reverse movement must have post-dated the eruption of a 6.72 Ma andesite tuff which is deformed in the footwall syncline exposed in the walls of Quebrada de Pozos Verde. The southern extension of the Sierra Durazno fault is marked by a complex structural zone dominated by NW-striking, south-side-down normal faults. This may represent the border of a localized graben which formed in response to localized transtension resulting from the block rotation. On the basis of TM image interpretation, an elongate block comprising a thick succession of volcanoclastic units has been identified between the southern edge of Sierra Durazno and Bola del Atajo. It is speculated that this represents a downdropped block, possibly along an approximately E-W- to ENE-striking normal fault along the southern margin of Sierra Durazno. The structures on the eastern margin of Sierra Durazno, a doubly-plunging anticline cored by a series of NNW-striking, east-verging reverse faults, may have resulted from buckling in a region of local transpression. The fault along the northern boundary of Bola del Atajo is interpreted to post-date the rotation and to record the 5 - 5.5 Ma of major and abrupt basement uplift. Because thrusts propagate in the direction of movement, it is suggested that this fault may represent the youngest such structure in the region. The location of the "pinning point" (Treloar *et al.*, 1992) or axis of rotation for the Durazno block is not known, given the

**Figure 6-8.**

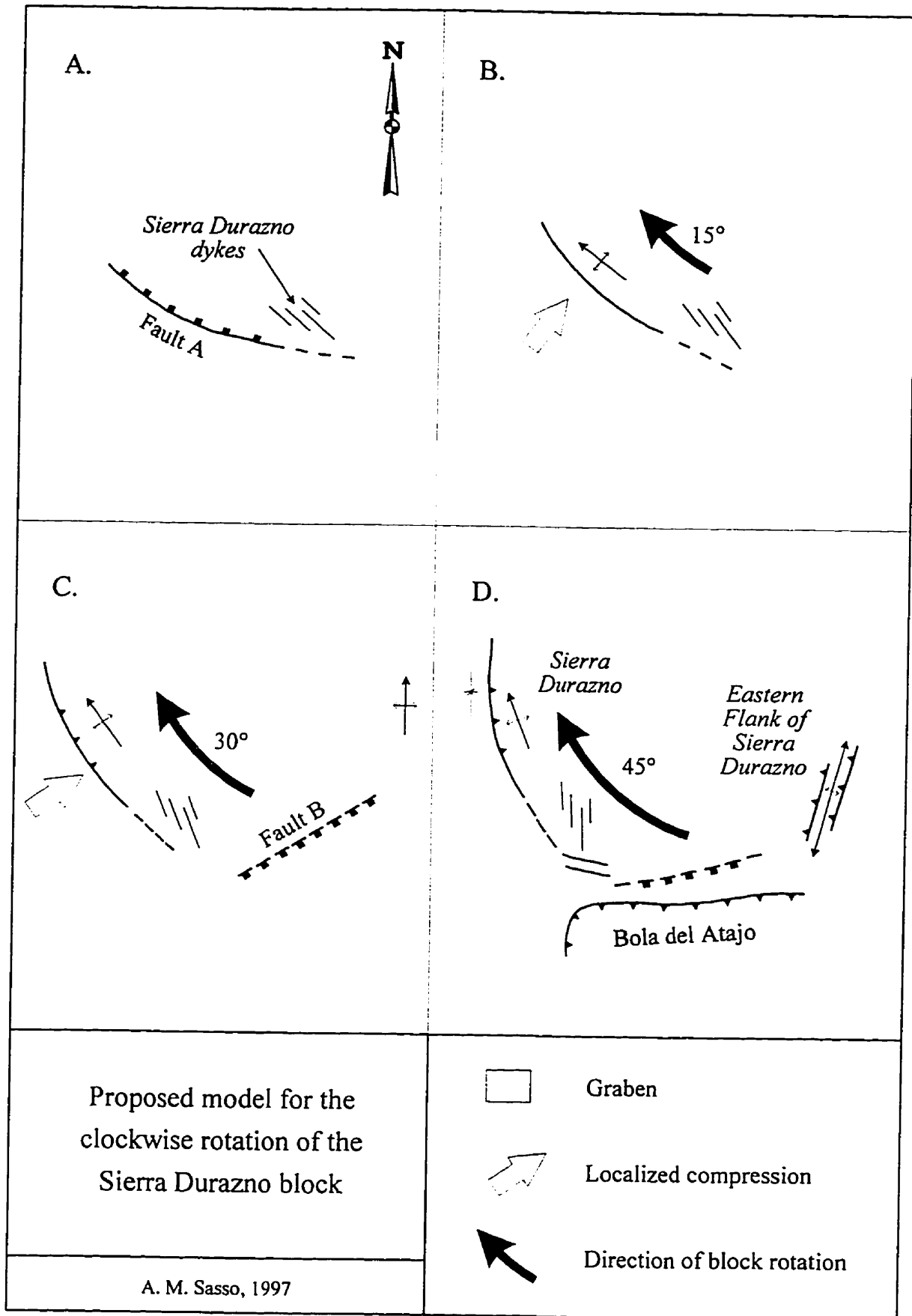
*Schematic illustration of the proposed model for the clockwise rotation of the Sierra Durazno block.*

**A. Emplacement of the Sierra Durazno Dyke swarm.** Fault 'A' is a steep normal fault dipping to the north.

**B. Initiation of rotation.** Dextral wrenching along the Tucumán Transfer Zone results in the initiation of clockwise rotation of the Sierra Durazno block. Buckling in the western Sierra Durazno results in the development of an anticline. Fault 'A' is inactive. Note: the rotational "pin-point" is not known.

**C. Continued rotation.** Thrusting begins along the northern extension of Fault 'A'. The increased rotation results in the formation of Fault 'B' and the downdropping of units on its south side (shading). Buckling begins on the eastern flank of Sierra Durazno, forming a broad, doubly-plunging anticline.

**D. Present-day relationships.** Continued rotation has resulted in the uplift of the Sierra Durazno range, with a greater degree of movement inferred for the northern extension of Fault 'A', which was also accompanied by the formation of a footwall syncline. Subsidiary normal faults developed in the zone of maximum extension along the western termination of Fault 'B'. Small high-angle reverse faults with limited displacement break the surface on the eastern flank of the Sierra Durazno. Finally, regional compression resulted in the uplift of the Bola del Atajo block to the south.



incomplete knowledge of the area.

It was originally proposed (Sasso, 1995; Sasso *et al.*, 1995) that the uplift of the Sierra Durazno and the formation of the fault-cored anticlines occurred in response to a shift in the local compressional axis to a N-S direction (E-W compression) as documented by Allmendinger (1986) to the north. However, no evidence exists in the Main Farallón Negro Stratovolcano to support this structural orientation and Urreiztieta *et al.* (1996) suggest that the clockwise rotation of blocks in the Tucumán Transfer Zone may have substantially contributed to the scatter in the observed shortening directions.

This model has important implications for the geodynamic evolution of the area, in that it provides a chronological framework which until now has been lacking (*vide* Urreiztieta *et al.*, 1996) for the compressional regimes active in the region. It implies that, by approximately 8 Ma, the elevation of the *Puna* was already of sufficient magnitude to impose a NW-SE compressional stress on the Farallón Negro region, overriding the regional South American E-W oriented subduction-related stress regime. Indeed, kinematic studies (Allmendinger, 1986; Assumpção and Araujo, 1993; Marrett *et al.*, 1994; Urreiztieta *et al.*, 1996) indicate that the NW-SE oriented stresses continue to exceed the regional stresses related to plate-related forces.

A similar tectonic history, albeit without accompanying volcanism, may have occurred along the southwestern extension of the Tucumán Transfer Zone in the Jague area of San Juan Province (T. Coughlin, pers. comm., 1996). Coughlin documents extension from 14 to 6 Ma in the lower portion of a thick sequence of continental red beds, followed by slightly higher-energy sedimentation after approximately 6 Ma, and

the deposition of syn-inversion conglomerates from 4.3 Ma. Ongoing geochronological and structural investigations by T. Coughlin at the University of Queensland, Australia, will help to clarify the temporal and spatial structural relationships recorded by this depocentre.

### **Magmatic Evolution of the Farallón Negro region**

Volcanic arcs in convergent continental margin settings are characteristically hundreds of kilometres long and only tens of km wide (Table 6-1), but they may migrate to generate a time-transgressive, wider belt of volcanic rocks (Cas and Wright, 1988). However, the existence during the Middle Miocene of strictly contemporaneous volcanism over a broadly 200 km wide area, ranging from the Maricunga Belt to the Farallón Negro region far into the continent, suggests that complex and unusual arc geometries may have existed during this interval in this Central Andean transect.

### ***Arc broadening versus arc migration***

A well-defined continent-ward younging of magmatism from the Early Jurassic to the earliest-Miocene in this region of the Andes has been well documented (*e.g.*, Farrar *et al.*, 1970; Clark and Zentilli, 1972; Clark *et al.*, 1973; Zentilli, 1974; Clark *et al.*, 1976; Dallmeyer *et al.*, 1996). The magmatic arcs - narrow, N-S-trending, volcano-plutonic sub-provinces - have been displaced systematically eastward through time. This orderly geometry was dramatically interrupted in the Miocene when the arc expanded to encompass an area up to 250 km east of the former inner boundary of the orogen. The

**Table 6-1.**

*Geographical and Geophysical data for volcanic arcs at convergent plate margins (modified from Gill, 1981).*

NB. The width of the volcanic arc was calculated from the data presented in Gill (*op. cit.*). "Height" records the elevations of the volcanoes above the earthquake foci of the dipping seismic zone; the range in height reflecting the width of the volcanic arc. The "dip" is measured from the attitude of the seismic zone at depth. Ranges in convergence rates indicate the variation in convergence rate along the portion of the plate boundary along which volcanoes occur, in a north-to-south or west-to-east direction. See Gill (*op. cit.*) for data sources.

ARC	Width (km)	Height (km)	Dip (degrees)	Rate of Convergence (cm/yr)
New Zealand	100	100-200	50	5.6
Kermadec	<50	140	65	7.3
Tonga	<50	140	53	9.4
Vanatu	<50	200	70	10.6-9.5
Solomon	<50	200	90	10
New Britain	120	90-400	70	9.2
W. Bismarck	<50	150	80	0-6
New Guinea	170	125		
Papua	<50			
Sumatra	<50	125	60	6.7-7.6
Java	150	120-360	65	7.6-7.9
Banda	200	100	40	
Halmahera	<50	150-200	45	
Sulawesi	<50	100-150	55-65	
SE Philippines	<50	125	45	
Luzon-Taiwan	<50	100	45	4.1-5.2
Ryuku-West Japan	90	100-200	45	2.7-1.8
Mariana-Izu	25	140	45-90	9.6-6.7
East Japan	150	100-200	30	9.9-9.6
Kuriles	25	90-170	45	9.2-9.9
Kamchatka	200	90-270	50	8.9-9.2
Aleutians	65	110	55	8.7-7.0
Alaska	275	100	60	7.0-6.4
Cascades	<50			2-3
Mexico	245	100-150	55	5.7-8.5
Central America	<50	105-210	60	6.9-9.2
Columbia-Ecuador	100	140-200	35	8.9-8.4
Peru-Chile	250	80-250	35	10.3-10.8
Antilles	220	100-150	45	1.4
South Sandwich	<50	120	50	9
Eolian	<50	200-250	46	0.9
Aegean	70	125	35	3.7
Turkey-NW Iran		<40		2.7
SE Iran	200	100	45	5.1



arc then retreated with similar abruptness in the Pliocene, leading to the construction of large stratovolcanoes which constitute the present *Alta Cordillera* along the Chile-Argentina border.

This Miocene *arc broadening*, or "break-out" (Clark *et al.*, 1976), is considered to have generated the Farallón Negro, Famatina, Pocho and San Luis volcanic centres, and has been attributed (Clark *et al.*, 1973; 1976) to an abrupt and perhaps considerable increase in plate convergence rate caused by a reorganization of the locus of spreading in the eastern Pacific oceanic plates as documented by Herron (1972). Zentilli (1974) and Clark *et al.* (1976) proposed that the arc broadening records a major expansion of the locus of melting and devolatilization along the hanging wall of the subducting slab, without a major change in slab inclination. This model was considered to be supported by systematic continentward changes in igneous petrochemistry, and particularly the eastward enrichment in potassium, as documented by Zentilli (*op. cit.*) and Dostal *et al.* (1977).

A more conventional model of *arc migration* was originally proposed by Kay *et al.* (1988) for the "flat slab" segment (28° - 33°S) of the Andes, a region overlapping with that investigated by Clark, Farrar and co-workers. Kay *et al.* (*op. cit.*) interpreted limited geochronological (K-Ar and fission track ages), geological and geophysical data to advance a model in which the initiation of shallowing of the subduction zone had begun by about 18 Ma and was followed by a major episode of slab "flattening" between 11 and 7 Ma. Volcanism had ceased in the "flat slab" region by approximately 4.5 Ma. In the west, this resulted from the loss of convecting asthenosphere above the subduction zone

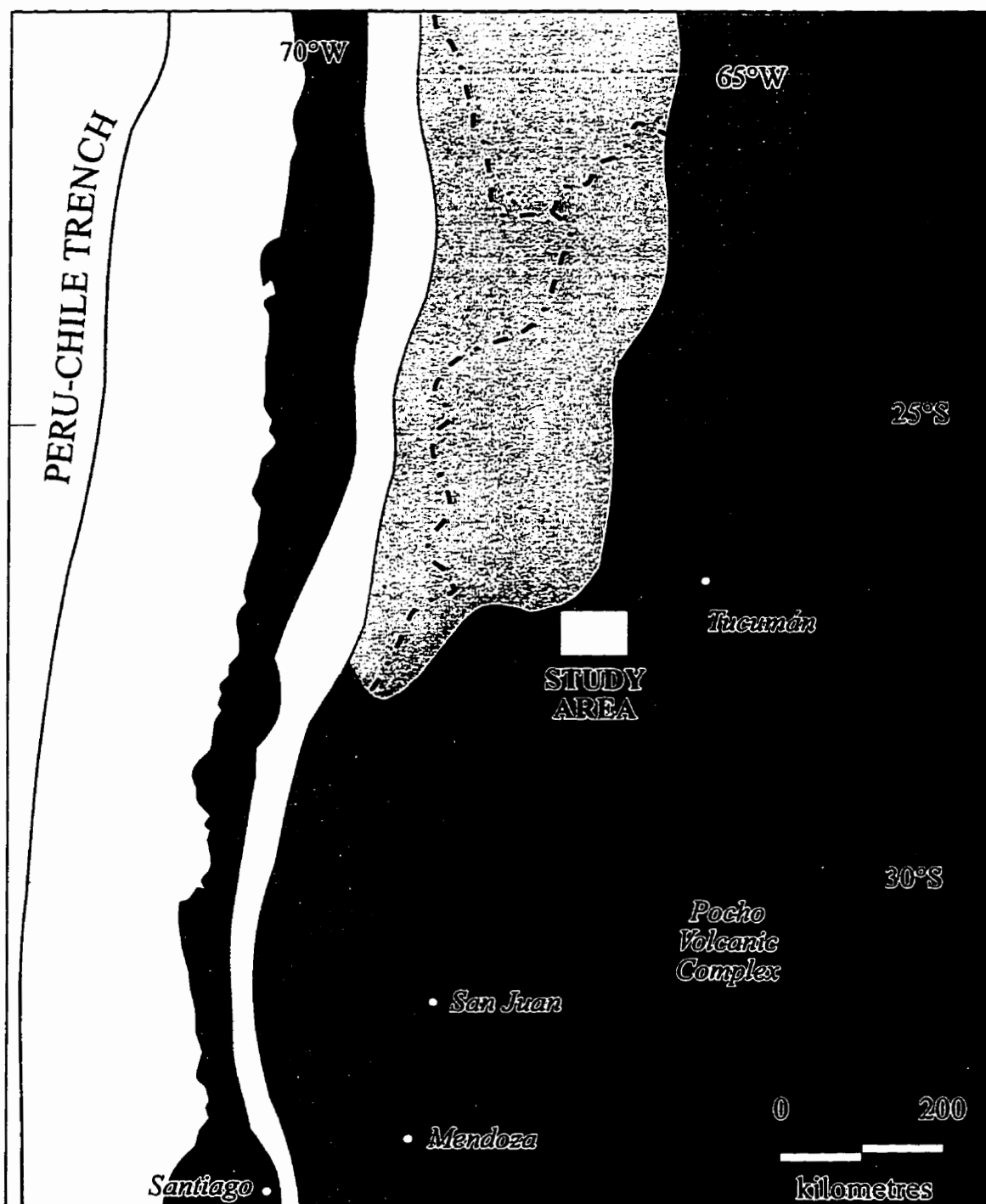
while to the east, although the asthenosphere was of sufficient volume and temperature to generate melts, the slab had previously lost the volatiles necessary to induce melting in the overlying mantle. Kay *et al.* (*op. cit.*) suggested that slab flattening is recorded by the rapid eastward migration of volcanism from the *Cordillera Principal* (Main Cordillera) to the *Sierras Pampeanas* (Fig. 6-9). However, it should be emphasized that conflicts and/or inconsistencies in the geochronological database presented by Kay *et al.* (*op. cit.*), possibly a result of the unreliability of the methods used, do not appear to support a model of clear arc migration. For example, the 6.0 Ma Cerro Blanco dacites were being emplaced in the *Precordillera* synchronously with magmatism from 7.9 to 4.5 Ma in the Pocho region of Córdoba. Moreover, K-Ar ages of 16 - 20 Ma for sub-volcanic bodies in the *Precordillera* conflict with fission-track ages of 7 - 12 Ma on ash beds in Tertiary sediments which crop out nearby. As admitted by Kay *et al.* (1988), these discrepancies could indicate either problems with the dating or a volcanic history more complex than a simple migration. The latter explanation is herein preferred.

The above-mentioned studies invoking "arc broadening", on the one hand, and "arc migration", on the other, for the southern Central Volcanic Zone suffer from a decided absence of schematic diagrams to illustrate the salient features of the models. In fact, the only clearly illustrated model specifically for arc broadening is that of Sandeman (1995) and Sandeman *et al.* (1995) for the *ca.* 29 Ma southern Peruvian Andean arc.

A revised model, better supported by the geochronological database and also embracing aspects of the arc broadening hypothesis originally proposed by Clark and Zentilli (1972), was subsequently presented by Kay *et al.* (1993). This invokes relatively

**Figure 6-9.**

Physiographic provinces of northwestern Argentina, northern Chile and southwestern Bolivia (modified from Zentilli, 1974).



Physiographic provinces  
of northwestern Argentina,  
northern Chile, and  
southwestern Bolivia  
(modified from Zentilli, 1974)

A.M. Sasso, 1997

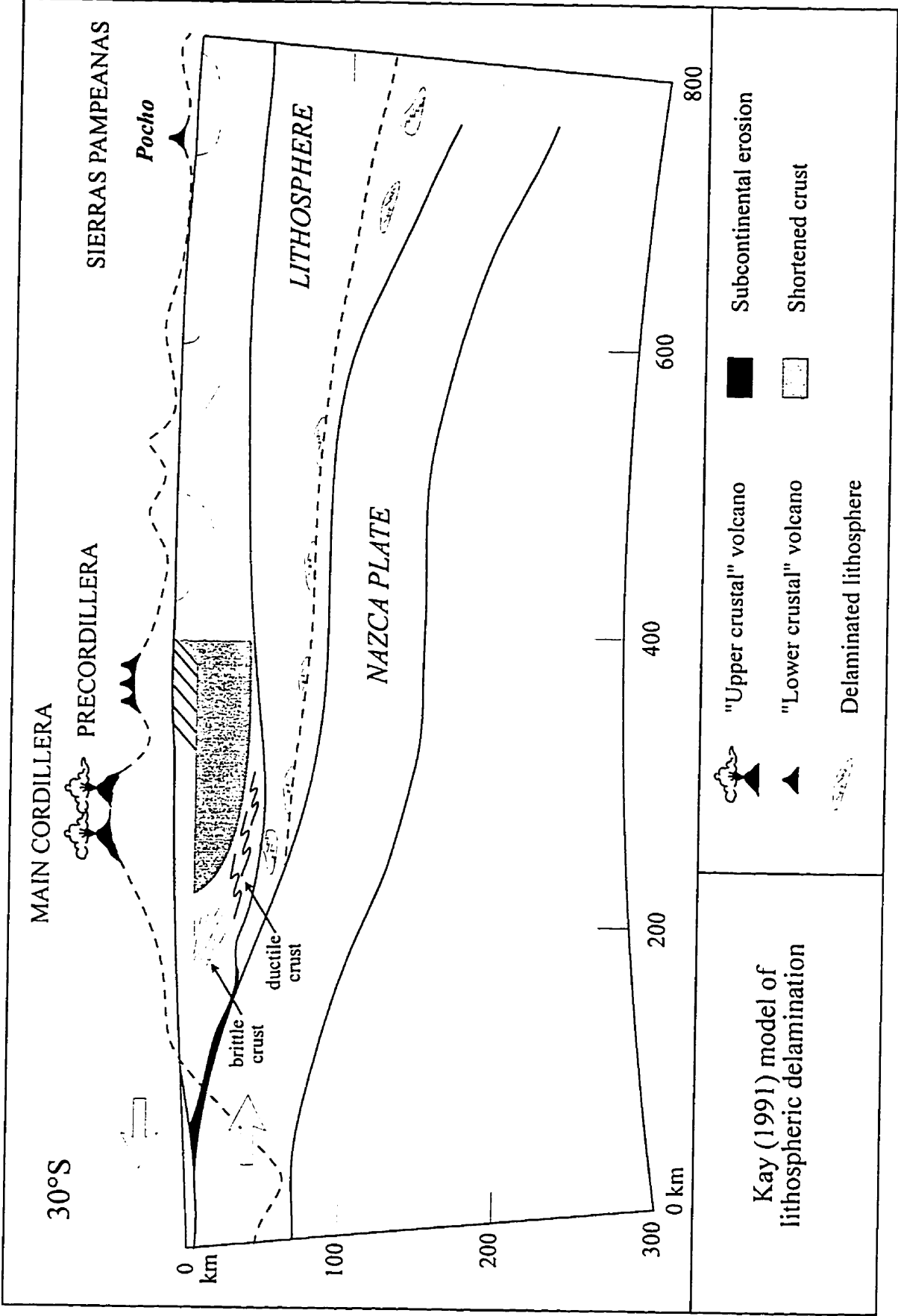
- |                         |                        |
|-------------------------|------------------------|
| Coastal Range           | Sierras Pampeanas      |
| Longitudinal Valley     | Sierras Transpampeanas |
| Chilean Precordillera   | Puna - Altiplano       |
| Main Cordillera         | Cordillera Oriental    |
| Cordillera Frontal      | Sierra Subandinas      |
| Argentine Precordillera | Chaco - Pampean Plains |

steep subduction from *ca.* 25 to 20 Ma. Initial shallowing of the subducted plate is inferred to have begun by approximately 20 to 11 Ma, as is indicated by high-angle reverse faulting in the Main Cordillera, the Early-to-Middle Miocene "broadening" of the volcanic arc into the *Precordillera*, and the initiation of thrusting and basin formation in the *Precordillera*. The "main shallowing phase" (*op. cit.*, p. 384) is considered to have occurred between 10 and 6 Ma, resulting in the termination of andesitic volcanism in the Main Cordillera (although small dacitic to rhyolitic ignimbrites and domes of the Vallecito Formation were emplaced at 5.9 Ma: Kay *et al.*, 1988), and "broadening" of the arc across the *Precordillera* into the *Sierras Pampeanas* at approximately 7 Ma. An important change in slab dip at this time is inferred from the "dramatic eastward expansion of both magmatic and deformational events" (*op. cit.*, p. 384).

This revised model better accounts for the observed variations in geochemical signatures of the volcanic rocks at these latitudes (Kay, 1991). "Upper crustal" and "lower crustal" geochemical signatures, defined by Sr and Nd isotopic ratios, Rb/Sr ratios and concentrations of Th, U, Ba, K, and REE, are recognized. Thus, "lower crustal" signatures identified in rocks located in the "back arc" (Kay, *op. cit.*) are interpreted to be derived through contamination by delaminated lithosphere from the base of the Main Cordillera which has been transported to the east by asthenospheric flow (Fig. 6-10). Kay (1991) proposed a model, modified from that of Allmendinger *et al.*, 1990, in which a décollement had formed beneath the *Precordillera* by approximately 11 Ma. Mid-to-lower crustal rocks are driven as a wedge to the west, progressively splitting the upper crust from the mid-crust beneath the arc, and pushing the latter, presumably along faults, into

**Figure 6-10.**

Schematic illustration of the proposed mechanism of lithospheric delamination beneath the Main Cordillera, near 30° - 31° S, and subsequent eastward transport of delaminated blocks (from Kay, 1991).



the lower crust. Crustal thickening associated with the shallowing of the subduction zone which was taking place at the same time, as indicated by the formation of the 9 - 12.6 Ma Atacama Pediplain on the Pacific slope of the *Cordillera Principal* further to the north (Clark *et al.*, 1967), reduced the space between the crust and the slab and, as suggested by Kay (*op. cit.*), would cause delamination of the lithosphere, possibly through mechanisms involving density increase due to phase transformations, and consequent foundering. Pieces of the foundered lithosphere would then be transported to the east by the circulating asthenosphere. The "lower crustal" signature of the Pocho rocks is interpreted to represent the presence of a fragment of delaminated lithosphere which has been transported far to the east.

A broadly similar model, although not involving wedging in the middle crust, was later proposed to explain the geochemical signature of Plio-Quaternary mafic "back arc" volcanic rocks in the *Puna* (Kay and Kay, 1993; Kay *et al.*, 1994a). In this model, the density-driven foundering of a lithospheric block (or blocks) below the *Puna* allowed the upwelling of asthenospheric mantle, which is inferred to have caused the heating of the subducting plate leading to the formation of the seismic gap documented between 24.5° and 27.5°S by Cahill and Isacks (1992). The varied geochemistry of the young volcanic units is interpreted to delimit the former location of the detached lithospheric block, with *intraplate* lavas erupted above the proposed block, rocks of *back arc calc-alkaline* affinity emplaced on its margins, and *shoshonitic* lavas to the north, overlying a zone of relatively thick, non-delaminated lithosphere.

The arc broadening model, as presented by Clark and Zentilli (1972) and Zentilli



(1974), and as variably adopted by Kay (1991) and Kay *et al.* (1993; 1994b; 1994c), implies that shallowing of the subducted slab leads to the broadening of the arc. Casaceli (1993b) has, however, suggested that arc broadening followed by the termination of arc magmatism within a subduction zone segment may indeed represent a "normal" evolutionary sequence within a shallowing slab. The low-angle slab configuration would concentrate volatiles along the nearly horizontal upper mantle - lower crust boundary, rather than in a narrow vertical zone as occurs above a steeply dipping subduction zone, causing a greater degree of partial melting of both the mantle and the crust (*vide* Zentilli, 1974). This would generate magmas over a broad zone inboard of the axis of subduction. The propagation of magmas to the surface would then be facilitated by deep crustal structures.

Casaceli (1993b) suggests that the mantle underlying northwestern Argentina is extremely heterogeneous due to the complex Paleozoic accretionary history. In a broader context, Rogers and Hawkesworth (1989) concluded that regional differences in mantle composition, independent of any recent subduction-related enrichment, were important in producing the geochemical variations observed in volcanic rocks of the Central Volcanic Zone. Mantle heterogeneity and/or enhanced MASH (melting, assimilation, storage, homogenization)-related processes (Hildreth and Moorbath, 1988, 1991), in which antithetic insertion of basement lithologies into the lower crustal keel modify the isotopic "base level" and, hence, modify ponded mantle-derived magmas, may provide alternative models to explain the differences in crustal signatures documented by Kay (1991). Large-scale heterogeneity has been observed in the sub-lithospheric mantle beneath the Brazilian

shield (VanDecar *et al.*, 1995), who, on the basis of a teleseismic travel-time study, infer the coupling of the sub-lithospheric mantle, to a depth of at least 500 km, to the South American Plate beneath the great Paraná flood basalt province since the Cretaceous. If, as these data suggest, the lithosphere and deep (sub-lithospheric) upper mantle of the South American Plate move coherently, it would follow that accreted lithosphere would entrain mantle and that the mantle below Argentina would be inevitably heterogeneous, and could therefore plausibly influence the geochemical signature of magmas generated through plate-margin processes.

*Implications for the geodynamics and petrogenesis of the Farallón Negro region*

As documented in Chapter 4, the geochemistry of the Farallón Negro volcanic rocks is very similar to that of the Pocho shoshonite suite. Thus, by analogy, they may record similar petrogenetic and geodynamic environments and evolutions. The delaminated-lithosphere model for the main *Sierras Pampeanas* transect proposed by Kay (1991) and elaborated upon by Kay and Gordillo (1994) could therefore be broadly germane to the more northerly Farallón Negro latitude. However, because the *Precordillera* does not extend to the latitude of Farallón Negro (Fig. 6-9), the "wedging" process proposed by Allmendinger *et al.* (1990), and advocated in revised form by Kay (1991) to generate delaminated lithospheric blocks, may not have been involved. Moreover, the temporal constraints imposed by the eastward transport of a delaminated block from the longitude of the *Precordillera* to that of Farallón Negro cannot be

reconciled with, on the one hand, the inferred timing of the proposed initiation of delamination of approximately 11 Ma in the *Precordillera*, as indicated by the peak crustal thickening event (Kay *et al.*, 1993), and the date of 12.6 Ma determined herein for the earliest volcanic units at Farallón Negro, on the other. Further to the north, a broadly similar delaminated-lithosphere model involving westward wedging along a mid-crustal décollement related to the Eastern Cordillera, Santa Bárbara and Subandean belts has been invoked to explain the "upper crustal" isotopic signature of Quaternary volcanism at Cerro Tuzgle (24°S, 66.5° W) in the *Puna* (Coira and Kay, 1993). The timing of initiation of this décollement is not discussed, but it might be proposed that a regime of this type may have been active at the time of initiation of magmatism at Farallón Negro. However, the Eastern Cordillera, Santa Bárbara and Subandean belts do not extend south to the latitude of Farallón Negro (see figure 6-9) and the timing constraints imposed by the present research would also preclude the invocation of this model for the study-area. Further, limited Sr isotope data for the volcanic rocks from Farallón Negro (McNutt *et al.*, 1979) fall in the field of "upper crustal" affinity as loosely defined by Kay (1991) whereas the Pocho volcanic rocks display a distinct "lower crustal" signature. Moreover, the Pb isotopic signatures of galena from the Capillitas deposit (Tilton *et al.*, 1981), assumed to reflect the composition of the parental igneous rocks rather than the Paleozoic basement (see discussion on ore genesis below, and Tosdal, 1995), fall within the ranges defined by Davidson *et al.* (1990) for the southern Central Volcanic Zone, which differ significantly from the field of Pb-isotopic compositions defined for rocks of the *Sierras Pampeanas* by Kay *et al.* (1993). The Pb signature displayed by rocks of the southern

Central Volcanic Zone, and by extension the Farallón Negro ore-lead composition, is attributed by Kay *et al.* (*op. cit.*) to the mixing of subducted upper crustal sediments with melts of the mantle wedge above the subducted slab. A more detailed isotopic study of rocks from the Farallón Negro Volcanic Complex is clearly needed. Kay and Gordillo (1994) interpret the trace element and isotopic signatures of the Pocho rocks to indicate an enriched sub-crustal component introduced through the eastward transport of blocks of the lithosphere removed from the base of the Main Cordillera, but this model is herein rejected for the igneous rocks of the Farallón Negro region.

The mid-Miocene broadening of the arc to encompass both the Maricunga belt in Chile and the Farallón Negro area in Argentina is confirmed by the precise  $^{40}\text{Ar} - ^{39}\text{Ar}$  age data presented in this thesis, as is shown by the series of compilation maps for the region between 26° and 28° S presented as figure 6-11 and the compilation of selected geochronological data for this transect in figure 6-12. However, if, as previously mentioned, arc broadening be accepted as an indication of slab-shallowing (Casaceli, 1993a), this would imply that the shallowly-subducting slab segment persisted to the north of the present "flat slab" region (28° and 33° S), at least to 26° S, during the Middle Miocene. There is no evidence for this and such a model is considered inherently improbable.

In a broader context, Isacks (1988) proposed that the subduction zone beneath the northern *Puna* could have steepened from 20° to 30° over the last 18 m.y. If the subduction zone underlying the northern *Puna* was steepening at the time when that beneath the present "flat slab" segment was shallowing, the transition zone, centred at

**Figure 6-11.**

*Geological Compilation map of Tertiary magmatism for the 26° - 28° S transect of Chile and Argentina.*

**A.** Geological map illustrating the distribution of igneous units in the 26° - 28° S transect. Data from Mpodozis *et al.* (1995), Secretaría de Minería (1994) and this study.

**B.** Series of maps illustrating the distribution of igneous units for three time periods: 26 - 17 Ma, 16 - 5 Ma and 5 Ma - Quaternary. These clearly show the location of the magmatic arc west of the international border from 26 - 17 Ma, the abrupt expansion of volcanism into Argentina during 16 - 5 Ma and the equally sudden retraction of the main locus of volcanism during 5 Ma - Quaternary to its present location along the Chile - Argentina frontier.



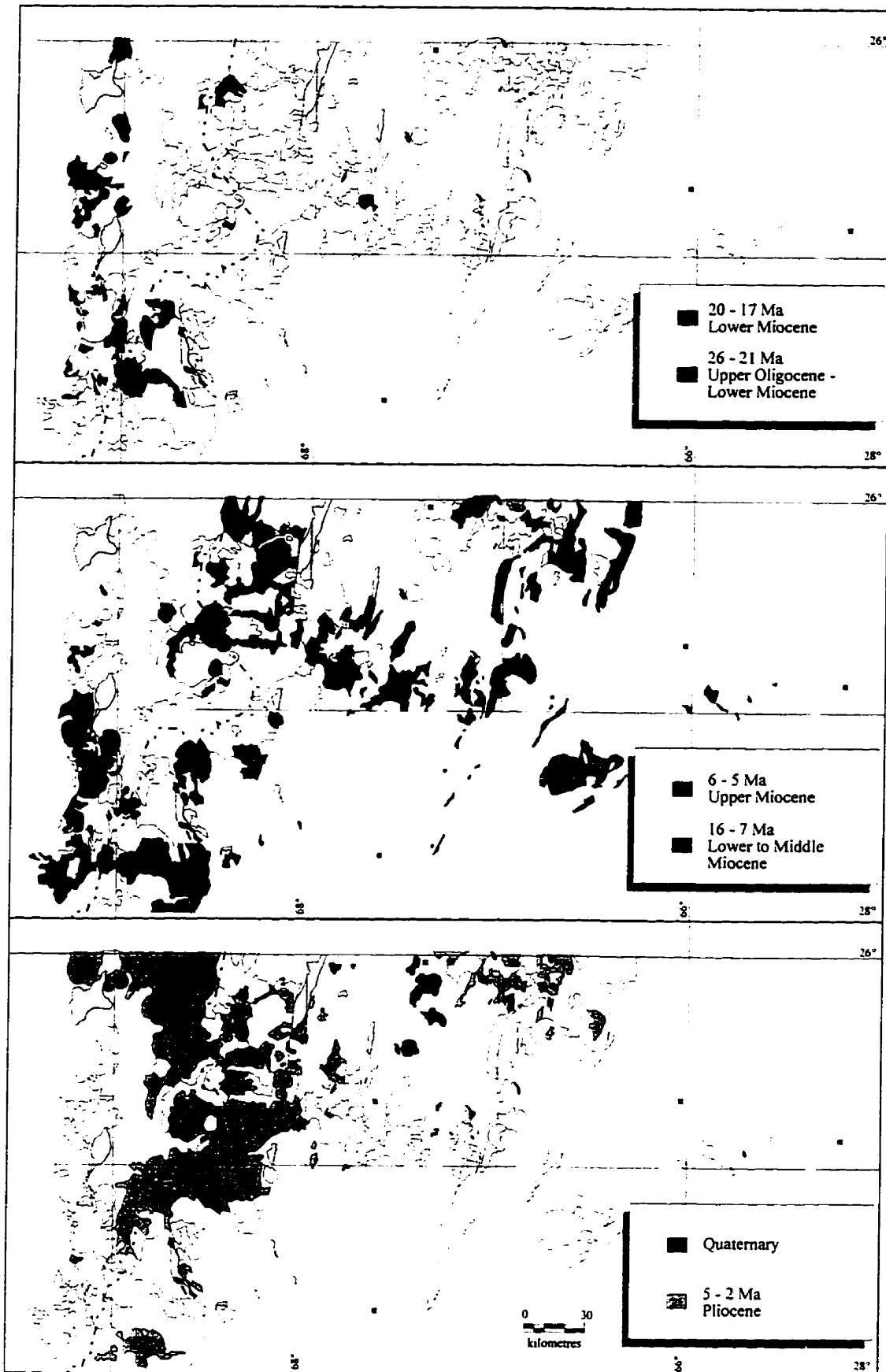
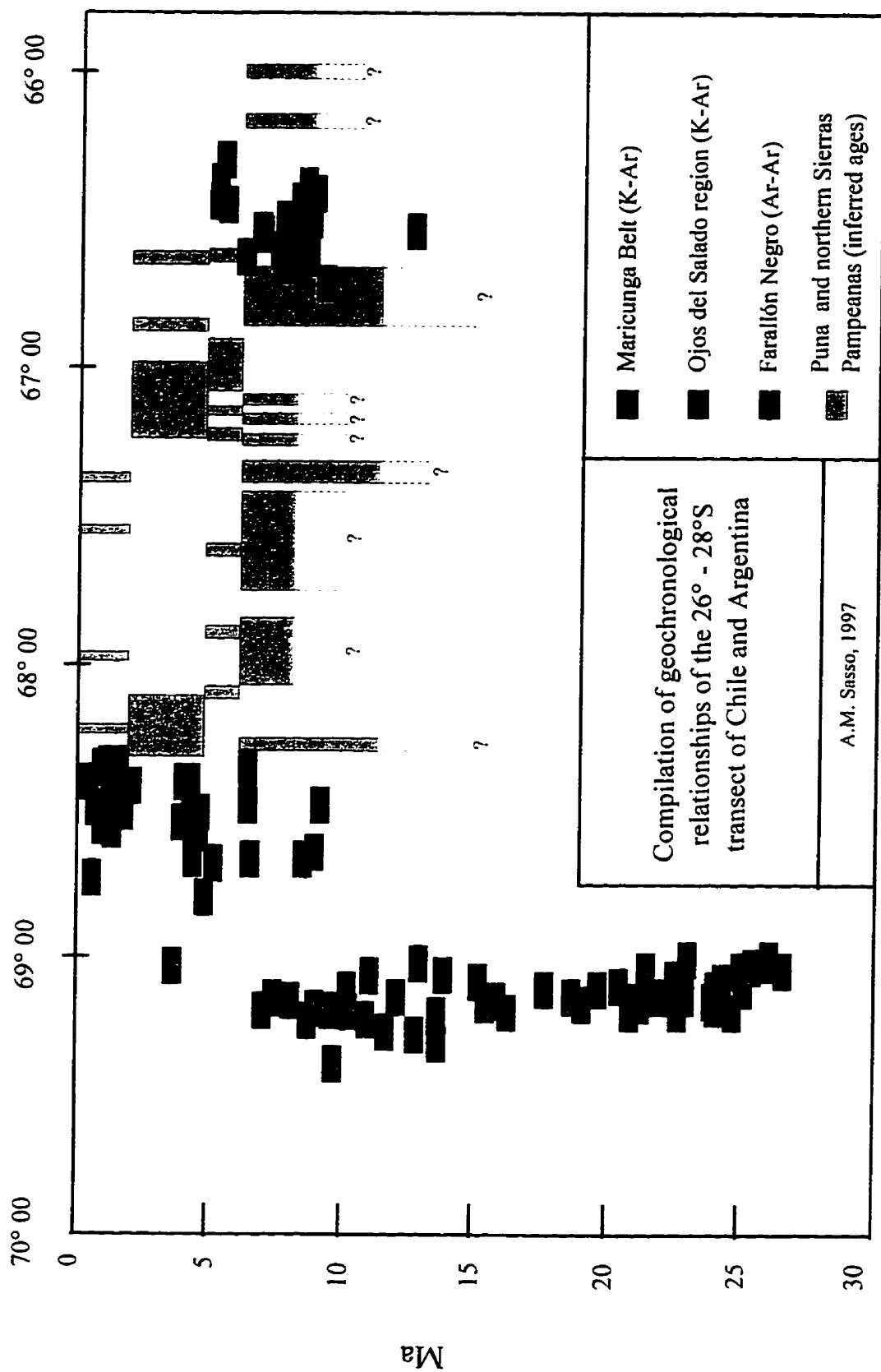


**Figure 6-12.**

Compilation of selected geochronological results for the 26° - 28° S transect of northern Chile and Argentina. Published K-Ar ages for the Maricunga Belt are from Kay *et al.* (1994c) and Mpodozis (1995), those from the Ojos del Salado region are from González-Ferrán *et al.* (1985). The Maricunga and Ojos del Salado studies do not overlap areally and the absence of data between the two regions accounts for the observed gap at this longitude in the diagram.  $^{40}\text{Ar}/^{39}\text{Ar}$  ages for the Farallón Negro region are from this study. Data for the *Puna* was interpreted from the 1995 Secretaría de Minería 1:250 000 map of Catamarca. Age intervals were assigned to the mapped units on the basis of inference from the above sources. The data have been projected onto an E-W line centred at 27° S. In the case of the undated units in the *Puna*, the approximate E-W extent of the shaded boxes on the diagram represent the E-W map extent of the volcanic units. Point sources are indicated by narrow vertical boxes. This data clearly demonstrate the abrupt broadening of the arc in the Middle Miocene and the comparably sudden arc contraction in the Pliocene.





approximately 27°S, would have acted as a hinge zone. Febrer *et al.* (1982) interpreted magnetotelluric data as indicating that the slab between 25° and 27° S has been completely detached from the continentward extension of the subducting plate, allowing the rise of asthenospheric material to within 8 - 12 km of the surface. Cahill and Isacks (1992), however, disagree with this interpretation. They suggest that slab tears may exist in the aseismic transition zone between 24.5° and 27.5° S, but that these would take the form of small gaps in the highly contorted slab rather than major segment-bounding faults with large vertical offsets. Cahill and Isacks (*op. cit.*) calculated the stress directions in the down-going slab from the focal mechanisms of Wadati-Benioff Zone earthquakes. The down-dip (*i.e.*, parallel to the movement of the plates) direction determined for the maximum compressive stress would allow for extension perpendicular to this direction, perhaps resulting in the opening of tears or gaps in the subducting plate. Humphreys (1995) has suggested that the Farallon slab beneath North America may have undergone significant stretching in the region between a flat section and one with a steeper dip. This type of stress would very probably be incurred in any segment of subducting slab that is in transition from one dip attitude to another, and would facilitate the opening of tears. Pre-existing zones of structural weakness, possibly due to inhomogeneities in the subducting plate, may further precondition the slab to failure during stretching related to flexure.

### *A model for the mid-Miocene arc broadening at the latitude of Farallón*

#### *Negro*

A model is herein proposed to explain the demonstrated broadening of the mid-Miocene arc at the general latitude of Farallón Negro. A subducting slab with pre-existing inhomogeneities, possibly concentrated at and parallel to 27° S, underwent flexure and trench-parallel extension which resulted in the opening of small tears or gaps. The latter were initiated near the trench and became progressively wider with increasing distance from the trench, as the relative difference in slab dips across the area increased (*i.e.*, the slab enters the subduction zone at a similar dip or inclination along the length of the trench, with increasing distance travelled down the trench, the difference in dips between the northern, steeper, segment and the southern, shallower, segment will inevitably increase). These tears may have provided windows to the underlying oceanic asthenosphere which either resulted in higher heat flow in the overlying slab or actually flowed through the gaps and into the overlying sub-continental asthenosphere, thereby also increasing the local heat flow. Either process would, it is inferred, markedly enhance the devolatilization of the slab, thereby increasing the extent of secondary melting in the asthenospheric wedge.

A zone of major inhomogeneities in the subducting oceanic slab may be revealed by the Easter Island volcanic chain on the Nazca Plate (Bonatti *et al.*, 1977; see Chapter 2). This is a prominent E-W topographic feature comprising an array of volcanic islands on the Nazca and Pacific Plates. It is over 6000 km long, some 200 km wide, approximately centred at lat. 27.5° S, and broadly parallel to the present direction of

motion of the Nazca Plate which has been consistent since *ca.* 26 Ma (Pilger 1981). The zone is also characterized by an abundance of seamounts relative to other areas of the sea-floor in this region. The chemistry of the Easter Island volcanic rocks is of OIB affinity, and suggests a mantle plume origin. Radiometric ages cluster around 1 Ma and 8 Ma, although one sample yielded an age of 30 Ma. The areal distribution of ages excludes the possibility that the Easter volcanic chain could have been generated by movement across a single hot-spot, and instead suggests intermittent activity at various locations along its length. Bonatti *et al.* (*op. cit.*) proposed a "mantle hot line hypothesis" in which "mantle plume type" volcanism occurs along extended crustal lineations and reflects lineations in the mantle activity itself, these are presumably crustal structures which formed as a result of underlying mantle inhomogeneity. From theoretical considerations, Richter (1973) and Richter and Parsons (1975) have suggested that two types of convection exist in the mantle: large-scale convective flow related to movement of the plates; and smaller-scale convective flow in the upper 650 km. The interaction of these two flow regimes causes the small-scale convective rolls to become aligned with their axes parallel to the direction of the large-scale rolls, *i.e.*, parallel to the direction of plate motion. This alignment may occur over short geological time spans (20 - 30 m.y.) in the case of fast-moving plates (*i.e.*, >10 cm/yr). Bonatti *et al.* (1977) propose that the "Easter Hot Line" may have developed along the rising limbs of a convective mantle roll.

In a detailed study of shear-wave splitting resulting from deformation-induced seismic anisotropy, Russo and Silver (1994) document a trench-normal flow in the mantle beneath the subducting Nazca Plate in zones coinciding with changes in slab dip.

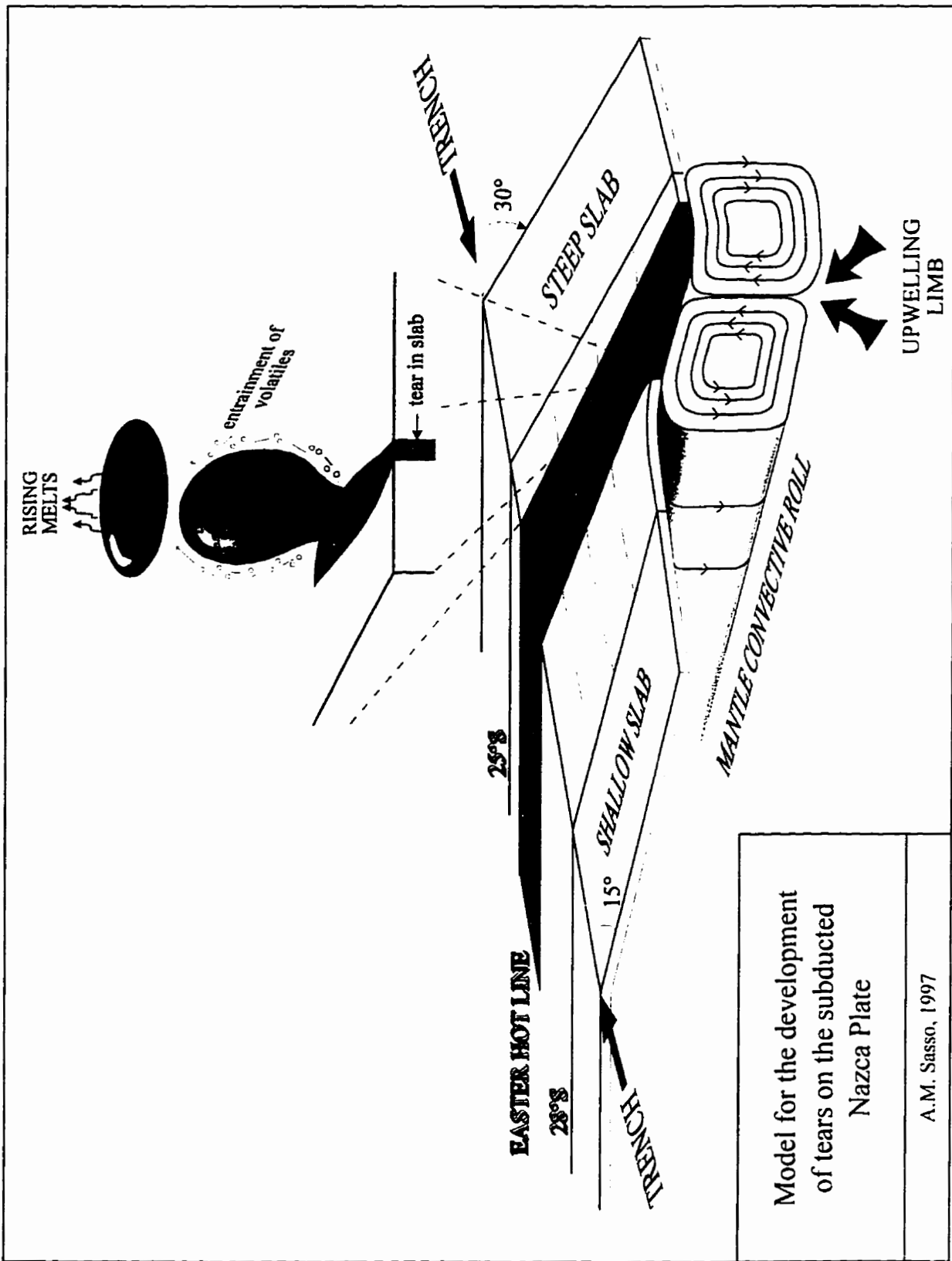
Segments of consistent slab dip are characterized by retrograde trench-parallel flow. They suggest that slab morphology, and particularly the presence of tears which would represent direct conduits for the transfer of mantle from one side of the slab to the other, may locally induce perturbations in the mantle flow field. The locus of trench-normal flow is broadly centered at approximately 25°S, but the lack of seismicity in this region renders the delimitation of this zone difficult and it may well extend further south to include the region of Farallón Negro and the Easter Hot Line.

If this hypothesis is correct, then not only does this portion of the subducted slab have an elevated concentration of inhomogeneities along which extension may have been facilitated but also entrains a higher heat flow regime imposed by the upwelling limb of a convective roll. The subduction of these features may be sufficient to influence the thermal regime in the overriding plate and the geochemistry of generated magmas. A cartoon of the proposed subduction model at approximately 27° S incorporating the effect of the "Richter" rolls, the Easter Hot Line and the generation of tears is presented as figure 6-13. This model allows the generation of melts along a subduction zone with a dip intermediate between that of the steep domain to the north and the shallow domain to the south. The increased heat flow resulting from the upwelling of asthenosphere through the tears may allow devolatilization of the subducted slab at greater than "normal" depths, possibly through the liberation of high pressure water-bearing phases such as amphibole and phlogopite, in an already extensively dewatered plate. It is also envisaged that this "rising plume" of asthenosphere, may entrain volatiles to higher levels in the overlying mantle wedge and thus, initiate melting in regions of the mantle that are not traditionally

**Figure 6-13.**

*Proposed model for the development of tears on the subducted slab at the latitude of Farallón Negro.*

The Easter Hot Line represents a zone of crustal inhomogeneities which is inferred to overlie the upwelling limb of a mantle convective roll. As this segment of slab enters the trench, inferred trench-parallel extension and warping of the plate to conform to the geometry of steep subduction to the north and shallow subduction to the south cause tears to form in the plate. Upwelling asthenosphere traverses the slab and rises into the overlying mantle wedge, increasing the temperature of the slab and resulting in enhanced devolatilization of the slab.



Model for the development  
of tears on the subducted  
Nazca Plate

A.M. Sasso, 1997

invoked for the formation of slab-related magmas. It is proposed (see previous sections) that transtension along major crustal structures, such as the Tucumán Transfer Zone at Farallón Negro, is responsible for the ascent of magmas to the surface.

This would imply that the "arc broadening" event at this latitude (and by extension in the transition zone as a whole, would be fundamentally controlled by two mechanisms: (1) the generation of melts by high heat flow and enhanced devolatilization of the subducted slab; and (2) transtension along the major crustal structures permitting the rise and emplacement of magmas into the shallow crustal environment. The latter is further supported by the significant concentration of mid-Miocene volcanic rocks along a broad, NW-trending belt between 26° and 28° S and located to the north of Farallón Negro (see figure 6-11), thus implying a strong and fundamental structural control on their emplacement. The Sr and Pb isotope signatures of the Farallón Negro rocks would be due to greater crustal involvement during ascent of the melts from an intermediate depth slab compared to those at Pocho, but the overall similarities in trace element signatures between volcanic rocks at Pocho and Farallón Negro would reflect similarities in the mechanisms of magma generation at the two regions (see Chapter 4).

#### **Ore-genetic and metallogenetic implications**

Sillitoe (1996) has recently presented a concise review of the factors influencing the formation of intrusion-related hydrothermal deposits. His observations, particularly with respect to porphyry Cu-Au-Mo deposits, are summarized below to provide a background for the following discussion of ore genesis in the Farallón Negro area.



Sillitoe (*op. cit.*) notes the apparent genetic link between little-fractionated, I-type, magnetite-series granitoid rocks (*sensu lato*) and major Cu, Mo and/or Au deposits and emphasizes the association of highly oxidized melts with increased hydrothermal Au concentration. His observations support the classical magmatic-hydrothermal theory of ore formation (*e.g.*, Lindgren 1933), in which magmas provide a direct source of metals, as is evident from the overall correlation between deposit metal ratios and the compositions of their associated granitic rocks. This view is further supported by isotopic studies of, *e.g.*, the El Salvador and Maricunga regions of northern Chile (Tosdal, 1995). On the basis of similarities in the Pb isotope ratios of ore-samples and the host and genetically-related porphyries, Tosdal (*op. cit.*), like Tilton *et al.* (1981), inferred that the ultimate source of the porphyry magmas was also the source of the ore-metals. Moreover, evidence from active hydrothermal systems and results from field and experimental studies clearly indicate that magmas contribute components such as water, metals and ligands (*e.g.*, S and Cl) to hydrothermal fluids (Burnham, 1979; Titley and Beane, 1981; Sillitoe, 1989; Cline and Bodner, 1991; Hedenquist and Lowenstern, 1994).

Candela (1989) has documented the inhibition of magmatic sulphide precipitation, and hence the deleterious sequestration of Cu and Au, in oxidized melts. This allows the partitioning of metals into the magmatic fluids, both supercritical vapour and saline liquid. The magmas are emplaced into extensional regimes or localized transtensional sites in broadly compressional settings. Sillitoe (1996) suggests that the contribution of H<sub>2</sub>O, Cl, S and ore-metals to the parental magmas through subcrustal interaction may be critical in the generation of major ore deposits. The partitioning of metals into the magmatic fluid

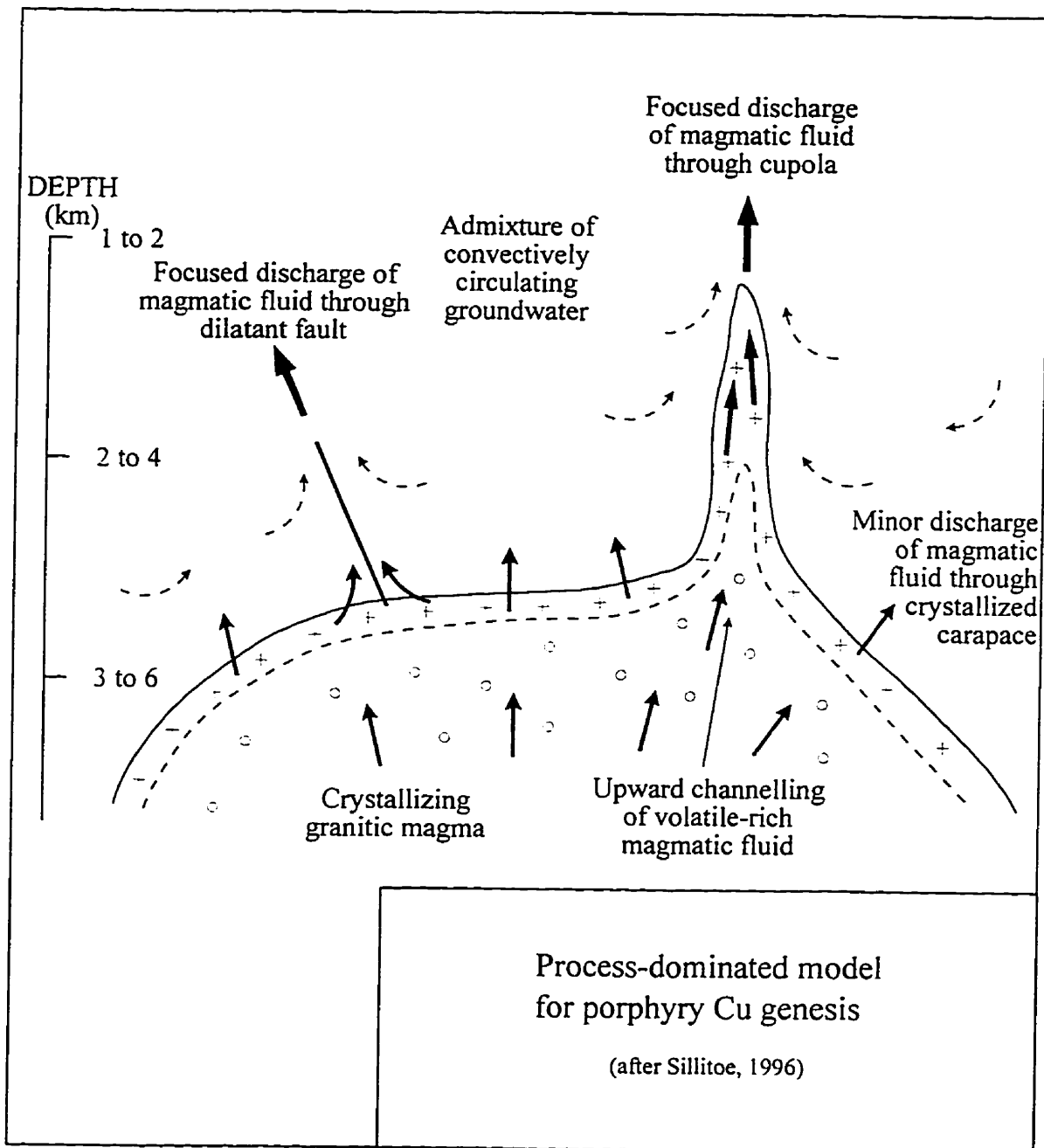
phase is most efficient at shallow crustal depths. "Wet" magmas with high Cl/H<sub>2</sub>O ratios may be emplaced at 3-4 km depth (Candela and Piccoli, 1995). Sillitoe (1996) envisages a model (Fig. 6-14) in which the parental magma chambers vent aliquots of magma and fluid through cupolas which, in porphyry Cu systems, commonly have the form of steep cylinders. Cooling, reaction with wall-rocks and, in particular, mixing with groundwater result in destabilization of the aqueous, commonly chloride, complexes, and in the deposition of metals. The characteristic porphyritic textures of the mineralized intrusions results from rapid quenching of the magma in the cupola (Burnham, 1979). Second boiling processes, *i.e.*, essentially isobaric volatile exsolution from crystallizing melts, result in the catastrophic generation of fracture networks and the formation of hydrothermal breccias which provide sites for metal deposition (Burnham, *op. cit.*; 1985).

Metal deposits, therefore are envisaged to be generated by fundamentally "normal" magmatic-hydrothermal processes, and Sillitoe contends that an initially metal-enriched melt is not a prerequisite (see also Cline and Bodnar, 1991). This would imply that the differences in quality and/or size of ore deposits (Clark, 1993) would lie fundamentally in the inherent ability of a parental magma to generate a large volume of hydrothermal fluid which has inherently greater metal contents (see A.H. Clark - preamble to the G.O.D. II short course, 1995) and to emplace this magma effectively in such a way that the metals remained concentrated, *i.e.*, were not diluted by significant crustal interaction which may have resulted in the "leaving behind" (Tosdal, 1995: p. 130) of metals. This philosophy strongly emphasizes the role of "process" over that of "provenance" and, as will be shown below, does not adequately explain the occurrence of "giant" deposits in

**Figure 6-14.**

*Aspects of process-dominated model of  
ore-genesis after Sillitoe (1996).*

Schematic diagram illustrating the formation of cupolas as an apophyse off a magma chamber. Magmatic fluids are focussed by the cupola and by a dilatant fault zone resulting in the concentration and precipitation of metals in these sites.



the Farallón Negro region.

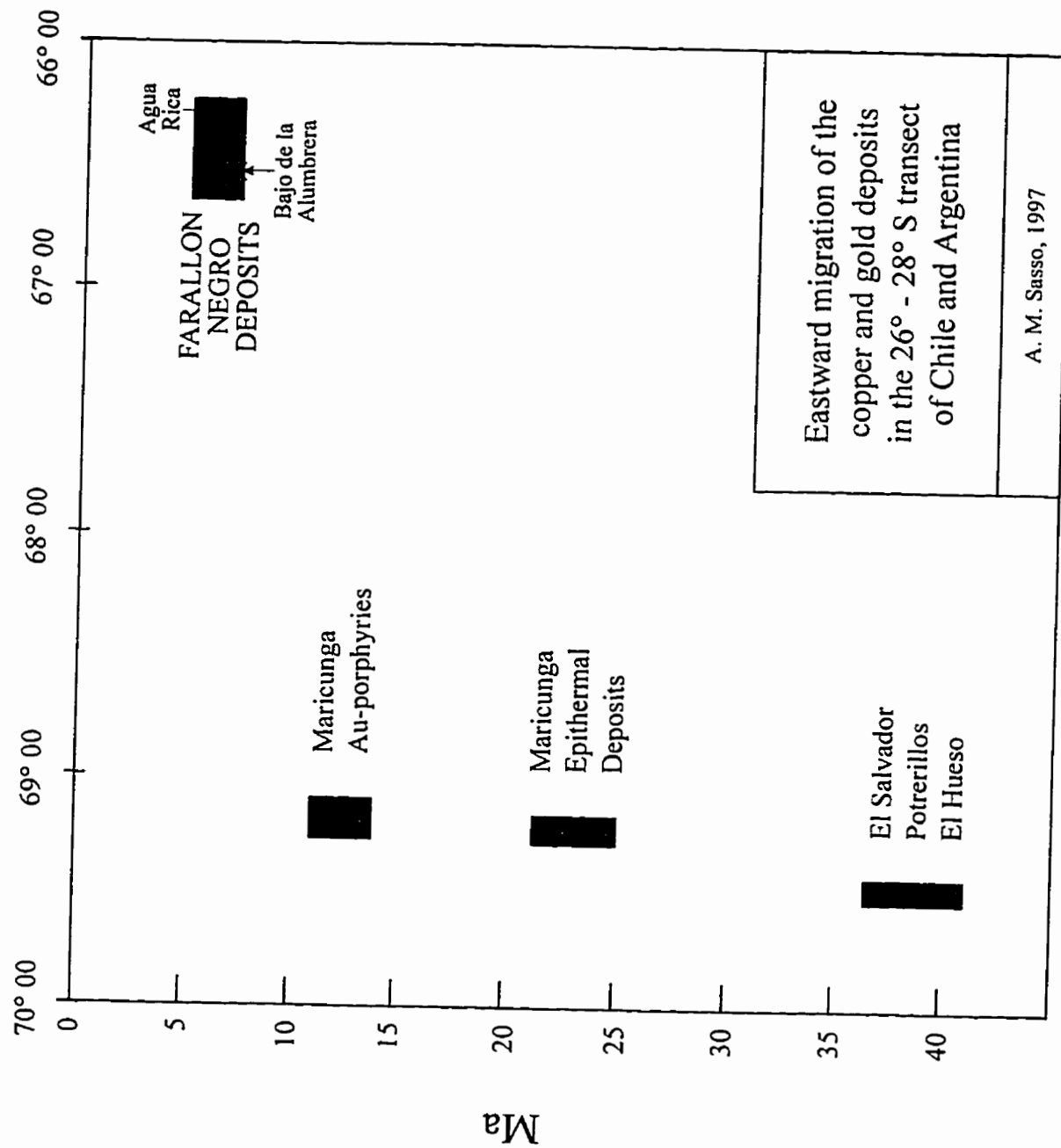
***Ore genesis and metallogenesis of the deposits of the Farallón Negro region***

As discussed in Chapter 3, this transect of the Central Andes has experienced remarkable enrichment in Cu and Au from the Cretaceous to the Neogene (Fig. 6-15), and is therefore metallogenetically anomalous. However, the petrogenetic implications of the data presented in Chapter 4 are that the rocks of the Farallón Negro Volcanic Complex are not inherently peculiar. They are ultimately slab-derived magmas, familial with those of the Ojos del Salado region, which display isotopic signatures similar to those of other Neogene suites of the southern-Central Volcanic Zone. However, although their petrochemistry may not be unusual, they are interpreted to have been emplaced in a unique environment distinct from those represented by the *Puna* and main *Sierras Pampeanas*. As outlined above, this segment of the Andean arc has been geodynamically individual since at least the Middle Miocene.

The coincidence of an unusually intense metallogenetic signature with a fundamentally peculiar geodynamic setting is not likely to be fortuitous. It implies a connection between the exceptional concentration of Cu and Au in the shallow crust and the deviance of the subduction zone, and that more is involved than the efficient extraction of fluids and metals from the magmas. This argues for a significant and fundamental role for *provenance*, *i.e.*, metallogenesis, given permissive *process* environments (ore genesis).

**Figure 6-15.**

Compilation of selected geochronological data for deposits in the 26° - 28° S transect of northern Chile and Argentina. Published K-Ar ages for the Maricunga Belt are from Kay *et al.* (1994c). K-Ar ages for the El Salvador deposit are from Gustafson and Hunt (1975) and those for the Potrerillos region are from Colley *et al.* (1989).  $^{40}\text{Ar}/^{39}\text{Ar}$  ages for the Farallón Negro region are from this study. This diagram clearly illustrates the eastward migration of Neogene mineralization with time in this transect.



### ***Process versus provenance in the Farallón Negro camp***

Bajo de la Alumbraera is a classic, textbook example of a simple porphyry Cu deposit, the only unusual features being the magnetite-dominated early hydrothermal alteration events and the markedly enriched Au content. Its evolution took place in a relatively uncomplicated manner in association with the successive emplacement of dacite porphyry bodies, at least one of which was accompanied by ore-bearing potassic alteration, followed shortly by overprinting by phyllic alteration of little economic importance but contemporaneous with the formation of low-sulphidation epithermal Au-Ag deposits elsewhere in the complex (*e.g.*, Farallón Negro - Alto de la Blenda). There is no evidence for pre- or syn-mineralization faulting, no hydrothermal breccias have been reported, and there is negligible supergene enrichment. Its emplacement in the core of the Main Farallón Negro Stratovolcano ensured an environment which was effectively sheltered from the regional tectonic processes (see Chapter 3). It therefore formed in a quiescent and persistent tectonic environment.

On the other hand, the Agua Rica deposit is unusually complex. It was initiated as a series of porphyry Cu-Mo-Au systems. Subsequent tectonic uplift, accompanied by extensive hydrothermal breccia emplacement, resulted in the telescoping of the system and the superposition of a "porphyry-scale" epithermal deposit which was further upgraded through supergene enrichment processes. It may be argued that each phase of this multifarious evolution was essential to the development of the deposit and contributed to its size and richness. The formation of Agua Rica was very unusual and tectonic modelling may be critical in the unravelling of ore paragenesis. The deposit formed in a



tectonically-active setting, experiencing a range of hydrothermal environments resulting in both porphyry- and epithermal-style alteration-mineralization and which terminated with the collapse of the local water table and the formation of a leached cap and supergene enrichment blanket.

Bajo de la Alumbraera (752 Mt at 0.51% Cu and 0.65 g/t Au at 0.2% Cu cutoff: Northern Miner, June 26, 1995) and Agua Rica (802 Mt at 0.61% Cu, 0.035% Mo and 0.24 g/t Au at a 0.4% Cu cutoff: J. Mortimer, pers. comm., July, 1997) are currently the largest deposits in the Farallón Negro camp. They are world-class, "giant" deposits which appear to reflect opposite ends of a spectrum ranging from extreme simplicity, in the case of Bajo de la Alumbraera, to extreme complexity, in the case of Agua Rica. The deposits are broadly contemporaneous, phyllic alteration at Alumbraera predating potassic assemblages at Agua Rica by only *ca.* 0.46 m.y., and are separated by approximately 32 km. They formed in broadly similar geological and geodynamic environments and by inference the associated parental magmas formed through similar petrogenetic processes, and yet their evolutions were radically different.

The enrichment of Cu and Au at Bajo de la Alumbraera is envisaged herein to be fundamental, rooted in igneous petrology, the exsolution of metal-rich magmas in the initial stages of second boiling, and, on a larger scale, the geodynamical context. The implications of the complexity of Agua Rica, on the other hand, are that *process* was critical. The hypogene grades of the large-scale precursor porphyry event were very low (J. Mortimer, pers. comm., 1997) and it is suggested that its multi-phase evolution, involving the conjuncture of several "catastrophic" tectonic and hydrothermal events, was

critical in the generation of a deposit of this size and tenor. The implication of the metal enrichment at Bajo de la Alumbraera is that the magmas generated by the subducted slab were fundamentally enriched in metals, but it is implicit that Cu and Au were not efficiently concentrated in the early stages of second boiling during the Agua Rica porphyry event. Metal dispersal was halted by massive uplift and "telescoping" of the hydrothermal system.

It must be asked whether there are more hydrothermal giants in the Farallón Negro region. The abundance of alteration-mineralization centres in the district reinforces the important role of provenance. However, Capillitas and Cerro Atajo, although emplaced in broadly similar settings to Agua Rica, *i.e.*, peripheral to the Main Farallón Negro Stratovolcano and/or hosted in uplifted basement blocks, do not record the multiplicity of mineralizing events nor the telescoping of radically differing hydrothermal environments documented at Agua Rica. An explanation for the low apparent grades of the majority of the porphyry-type deposits associated with the Main Farallón Negro Stratovolcano, *i.e.*, Bajo de Agua Tapada, Bajo el Durazno, Bajo las Pampitas, Bajo de San Lucas and Bajo las Juntas, is less evident. If, as was argued for Bajo de la Alumbraera, all that is necessary for the formation of a large deposit within the confines of the stratovolcano is metal-enriched magmas and a relatively simple, uninterrupted evolution, then why are there not more world-class deposits hosted by the stratovolcano? In the case of Bajo de San Lucas and Bajo las Juntas, it could be argued that disruptions, in the form of tectonism, may have *impeded* the ordered evolution observed at Alumbraera, but were not of sufficient magnitude to have engendered telescoping. These deposits may be analogous to the low

grade precursor porphyry events at Agua Rica.

Age determination of alteration assemblages at Bajo de Agua Tapada and Bajo el Durazno was not wholly successful (see Chapter 5), and therefore observations on the relative timing of the mineralizing systems are limited. However, the intrusive units dated at Bajo el Durazno represent some of the oldest dated intrusive bodies recorded at Farallón Negro and it may be argued that petrogenetic conditions favourable to the formation of significant hydrothermal deposits may have not yet existed at their time of emplacement. It has been suggested that magma mixing may play a significant role in the formation of ore deposits (A.H. Clark, Geol. 962 lecture, 1995). The incursion of mafic melts may both introduce metals, S and Cl, and perturb the magma chamber, initiating or enhancing hydrothermal circulation. Moreover, Clark and Arancibia (1995) ascribe the formation of magnetite-rich alteration-mineralization in a porphyry copper deposit similar in many aspects to Alumbra to mafic-melt intrusion in a dacitic magma chamber, resulting in the discharge of SO<sub>2</sub>-rich fluids which are enriched in metals such as Cu and Au through the oxidation of earlier-formed sulphides. As discussed in Chapter 4, the shoshonites at Farallón Negro, largely erupted early in the magmatic history, do not exhibit petrographical features suggestive of magma mixing processes. The high-K, calc-alkaline units, on the other hand, do show evidence for magma mixing. Moreover, the regional compressive regime, active by *ca.* 7.94 (see above), in which the Main Farallón Negro Stratovolcano was emplaced, may have impeded magma ascent and enhanced the processes of magma commingling and mixing. If the NW-SE-directed compression was necessary to drive the mafic magmas into the upper crustal environment, providing a

source of metals and initiating magma mixing and hydrothermal circulation, then it may be argued that the Bajo el Durazno magmas were intruded prior to the inception of these processes.

This argument, however, does not explain the absence of significant Cu and Au mineralization at Bajo de Agua Tapada or Bajo las Pampitas. The dacite porphyries at Bajo de Agua Tapada are broadly coeval with those at Bajo de la Alumbrera. The "rhyodacite" porphyry at Bajo las Pampitas has not been dated but on the basis of the intrusive chronology documented in Chapter 2, it may be inferred to have been emplaced synchronously with the dacites at Alumbrera and Tapada. However, the alteration-mineralization assemblages at these three deposits differ in that Bajo de la Alumbrera is the only porphyry Cu-Au deposit in the Farallón Negro region that displays a volumetrically-significant, K-feldspar-dominated, potassic alteration event superimposed on a magnetite-quartz assemblage (see Chapter 3), implying that a combination of conditions was necessary for the formation of an economic porphyry Cu-Au deposit in the Main Farallón Negro Stratovolcano. In addition, the areal coincidence of the Bajo de la Alumbrera deposit with the oldest dated volcanic unit in the region may suggest the involvement of a structure which was the locus of repeated extrusive and intrusive activity. This may have provided a favourable conduit for the focussed, rapid emplacement of magmas with minimal crustal interaction. This "preparation" of the site of mineralization, further isolating it from possibly deleterious outside influences, may have been critical for the fertility of the magmas.

The two "giant" deposits, Bajo de la Alumbrera and Agua Rica, of the Farallón

Negro district demonstrate that factors related to both *provenance* and *process* may form potentially economic deposits. However, it is suggested that without the fundamental contribution of *provenance*, the Farallón Negro district may not have become a target in the global search for the economic giants.

## REFERENCES

- Aceñolaza, F. G. and Toselli, A. J. (1978) Geocronología de las formaciones Puncoviscana y Suncho, Provincias de Salta y Catamarca: *Rev. Asoc. Geol. Arg.*, 33, 76-80.
- Aceñolaza, F. G., Toselli, A. J., Durand, F. R. and Taddei, R. D. (1982) Geología y estructura de la region norte de Andalgalá, Prov. de Catamarca: *Acta. Geol. Lilloana*, 61, 121-139.
- Allison, A. E. (1984) *A Geologic and Economic Evaluation of the Bajo el Durazno Porphyry Copper-Gold Prospect, Catamarca Province, Argentina*: Unpublished report to the United Nations Development Program, New York, 59 p.
- Allison, A. E. (1986) *The Geology of the Bajo el Durazno Porphyry Copper-Gold Prospect, Catamarca Province, Argentina*: University of Arizona, Tucson, Unpublished Masters Thesis, 167 p.
- Allmendinger, R.W. (1986) Tectonic development, southeastern border of the Puna Plateau, northwestern Argentine Andes: *Geol. Soc. Am. Bull.*, 97, 1070-1082.
- Allmendinger, R.W., Figueroa, D., Snyder, D. Beer, J, Mpodozis, M. and Isacks, B.L. (1990) Foreland shortening and crustal balancing in the Andes at 30° S latitude: *Tectonics*, 9, 789-809.
- Allmendinger, R.W., Ramos, V. A., Jordan, T. E., Palma, M. and Isacks, B. L. (1983) Paleogeography and Andean structural geometry, northwest Argentina: *Tectonics*, 2, 1-16.
- Allmendinger, R.W., Strecker, M., Eremchuck, J.E. and Francis, P. (1989) Neotectonic deformation of the southern Puna plateau, northwestern Argentina: *J. S. Am. Earth Sci.*, 2, 111-130.
- Angelelli, V. (1950) *Recursos Minerales de la República Argentina*: Inst. Nac. Investigación de las Ciencias Naturales, Buenos Aires, 542 p.
- Angelelli, V., Schalamuk, I. and Cagnoni, J. (1974) La rodocrosita del yacimiento cuprífero de Capillitas, Dpto. Andalgalá, Prov. de Catamarca, República Argentina: *Rev. Asoc. Geol. Argentina*, 29, 105-127.
- Aramaki, S., Onuma, N. and Portillo, F. (1984) Petrography and major element chemistry of the volcanic rocks of the Andes, southern Peru: *Geochemical J.*, 18, 217-232.
- Arancibia, O.N. and Clark, A.H. (1990) Early magnetite-rich alteration/mineralization in

the Island Copper porphyry copper-molybdenum-gold deposit, British Columbia [abs.]: Geol. Assoc. Canada - Mineral. Assoc. Canada, Program with Abstracts, 15, p. A4.

Arancibia, O.N. and Clark, A.H. (1996) Early magnetite-amphibole-plagioclase alteration-mineralization in the Island Copper porphyry Cu-Mo-Au deposit, British Columbia: *Econ. Geol.*, 91, 402-438.

Arribas, A., Hedenquist, J.W., Itaya, T., Okada, T., Concepción, R.A. and Garcia, J.S. (1995) Contemporaneous formation of adjacent porphyry and epithermal Cu-Au deposits over 300 ka in northern Luzon, Philippines: *Geology*, 23, 337-340.

Assumpção, M. and Araujo, M. (1993) Effect of the Altiplano-Puna plateau, South America, on the regional intraplate stresses: *Tectonophysics*, 221, 475-496.

Aubry, L., Roperch, P., de Urreiztieta, M., Rossello, E. and Chauvin, A. (1996) Paleomagnetic study along the southeastern edge of the Altiplano-Puna Plateau: Neogene tectonic rotations: *J. Geophys. Res.*, 101, 17,883-17,899.

Avila, J.C., Lazarte, J.E. and Robles Velazco, L.E. (1987) Metalogenesis del distrito minero Culampajá-Papachacra, Prov. de Catamarca, Republica Argentina: *X Congreso Geol. Argentino*, Actas II, 209-212.

Avila, J.C. and Velazco Robles, L.E. (1983) Relevamiento minero de las Sierras de Altohuasi y Culampajá, Departamento Belén, Provincia de Catamarca: *II Congreso Nac. Geol. Econ.*, Tomo I, 11-27.

Aydin, A. and Nur, A. (1982) Evolution of pull-apart basins and their scale independence: *Tectonics*, 1, 91-105.

Baker, M.C.W. (1981) The nature and distribution of Upper Cenozoic ignimbrite centres in the Central Andes: *J. Volcan. and Geothermal Res.*, 11, 293-315.

Baker, P.E., Gonzalez-Ferran, O. and Rex, D.C. (1987) Geology and geochemistry of the Ojos del Salado volcanic region, Chile: *J. Geol. Soc. London*, 144, 85-96.

Baksi, A.K., Archibald, D.A. and Farrar, E. (1996) Intercalibration of  $^{40}\text{Ar}/^{39}\text{Ar}$  Dating Standards: *Chemical Geology*, 129, 307-324.

Baldis, B.A.J. and Febrer, J. (1983) Geodynamics of the Argentine Andean arc and related features. In: R.S.J. Cabre, ed., *Geodynamics of the eastern Pacific region, Caribbean and Scotia arcs*, Geodynamics Series, 9, 127-135.

Barazangi, M. and Isacks, B.L. (1976) Spatial distribution of earthquakes and subduction of the Nazca Plate beneath South America: *Geology*, 4, 686-692.

- Barrick Gold Corporation (1994) *Annual Report*, Toronto, 72 p.
- Bassi, H.G.L. (1987) Evaluación geológica-minera del prospecto Bajo Las Pampitas, Catamarca, Argentina: *X Congreso Geol. Argentino*, Actas II, Tucumán, p.156.
- Bassi, H.G.L. (1988) Hypothesis concerning a regmagenic network controlling metallogenic and other geologic events in the South American austral cone: *Geologische Rundschau*, 77, 491-511.
- Bassi, H.G.L. (1991) Evaluación geológico-minera del distrito aurocuprífero Cerro Atajo, Catamarca, Argentina: *Congreso Geol. Chileno 1991*, 87-90.
- Bassi, H.G.L. and Rochefort, G. (1980) Estudio geológico del yacimiento cuproaurífero de la Alumbreira: *Servicio Minero Nacional*, Buenos Aires, 78 p.
- Bassi, H.G.L. and Rochefort, G. (1987) Geología y posibilidades del Nevado del Aconquija, Tucumán, Argentina: *X Congreso Geol. Argentino*, Actas II, 157-160.
- Beane, R.E. (1982) Hydrothermal alteration in silicate rocks: S.R. Titley, ed., *Advances in Geology of the Porphyry Copper Deposits: Southwestern North America*, Tucson, University of Arizona Press, 117-137.
- Bevis, M. and Isacks, B.L. (1984) Hypocentral trend surface analysis: probing the geometry of Benioff zones: *J. Geophys. Res.*, 89, 6153-6170.
- Bodenbender, G. (1922) El Nevado de Famatina: *Ann. Min. Agric., Secc. Geol., Mineral. y Min.*, XVI-1, Buenos Aires, 68 p.
- Bodenbender, G. (1924) El Cahchaqueño y los estratos de la Puna de Penck: *Bol. Acad. Nac. Cienc. Córdoba.*, 27, 405-468.
- Bonatti, E., Harrison, C. G. A., Fisher, D. E., Honnorez, J., Schilling, J. G., Stipp, J. J. and Zentilli, M. (1977) Easter volcanic chain (southeast Pacific): a mantle hot line: *J. Geophys. Res.*, 82, 2457-2478.
- Bonham, H.F. (1986) Models for volcanic-hosted epithermal precious metal deposits: A review: *Proc. Sym. 5 International Volcanological Congress*, New Zealand, 13-17.
- Bossi, G. E., Muruaga, C. M., Sanagua, J. G., Hernando, A. and Ahumada, A. L. (1993) Geología y estratigrafía de la cuenca Neogena Santa María-Hualfin (Deptos. Santa María y Belén, Provincia de Catamarca): *XII Congreso Geol. Argentino*, Actas II, 156-165.
- Bray, C.J., Spooner, T.C., Hall, C.M., York, D., Bills, T.M. and Krueger, H.W. (1987) Laser probe  $^{40}\text{Ar}/^{39}\text{Ar}$  and conventional K/Ar dating of illites associated with the McClean



unconformity-related uranium deposits, north Saskatchewan, Canada: *Can. J. Earth Sci.*, 24, 10-23.

Brogioni, N. (1987) Petrología del vulcanismo Mio-Plioceno de la provincia de San Luis: *Revista del Museo de La Plata*, Tomo X, No. 83, 71-100.

Brogioni, N. (1990) Geología y petrografía del vulcanismo Mio-Plioceno de la provincia de San Luis: *Revista del Museo de La Plata*, Tomo X, No. 90, 197-214.

Bucci, J. (1994) *Quartz-Magnetite-Rich Alteration-Mineralization of Three Porphyry Copper Deposits in Northern Argentina*, Queen's University, Unpublished B. Sc. Thesis, 39p.

Burnham, C.W. (1979) Magmas and hydrothermal fluids: In: H.L. Barnes, ed., *Geochemistry of Hydrothermal Ore Deposits*, 2nd edition, John Wiley, New York, 71-136.

Burnham, C.W. (1985) Energy release in subvolcanic environments: Implications for breccia formation: *Econ. Geol.*, 80, 1515-1522.

Butler, R. F., Marshall, L. G., Drake, R. E. and Curtis, G. H. (1984) Magnetic polarity stratigraphy and K-Ar dating of late Miocene and early Pliocene continental deposits, Catamarca Province, N.W. Argentina: *J. Geol.*, 92, 623-636.

Caelles, J. C. (1979) *The Geological Evolution of the Sierras Pampeanas Massif, La Rioja and Catamarca Provinces, Argentina*, Queen's University, Kingston, Unpublished Ph.D. thesis, 514 p.

Caelles, J. C., Clark, A. H., Farrar, E., McBride, S. L. and Quirt, S. (1971) Potassium-argon ages of porphyry copper deposits and associated rocks in the Farallón Negro-Capillitas district, Catamarca, Argentina: *Econ. Geol.*, 66, 961-964.

Cahill, T. and Isacks, B. (1985) Shape of the subducted Nazca Plate (abs): *EOS (Am. Geophys. Union Trans.)*, 66, p. 299.

Cahill, T. and Isacks, B. (1992) Seismicity and shape of the subducted Nazca Plate: *J. Geophys. Res.*, 97, 17,503-17,529.

Camínos, R. (1979) Sierras Pampeanas noroccidentales, Salta, Tucumán, Catamarca, La Rioja y San Juan: *II Simp. Geol. Reg. Arg. Acad. Nac. Ciencias*, 1, Córdoba, 225-291.

Candela, P.A. (1989) Felsic magmas, volatiles and metallogenesis: In: J.A. Whitney, and A.J. Naldrett, eds., *Ore Deposits Associated with Felsic Magmas*, Reviews in Economic Geology, 4, 223-233.

Candela, P.A. and Piccoli, P.M. (1995) Model ore-metal partitioning from melts into vapour/brine mixtures: In: J.F.H. Thompson, ed., *Magmas, Fluids and Ore Deposits*, Mineralogical Ass. of Canada Short Course Series, 23, 101-127.

Carlier, G., Soler, P. and Carlotto, V. (1992) Mineralogical, geochemical, isotopic and geotectonic constraints upon the origin of Quaternary shoshonitic lavas in the Andes of southeastern Peru (abs.): *EOS (Trans. Amer. Geophys. Union)*, 73, 341.

Cas, R.A.F. and Wright, J.V. (1988) *Volcanic Successions: Modern and Ancient*: Chapman and Hall, London, 528 p.

Casaceli, R.J. (1993a) *Argentina Trade Development Agency study - geologic section*: Unpublished report submitted to Norwest Mine Services Inc. and Direccion Nac. de Minería Argentina, 73p.

Casaceli, R.J. (1993b) The geology and mineral potential of Argentina: *Randol at Acapulco '93, Conference Proceedings*, October 25-27, 49-67.

Chinn, D.S. and Isacks, B.L. (1983) Accurate source depths and focal mechanisms of shallow earthquakes in western South America and in the New Hebrides island arc: *Tectonics*, 2, 529-564.

Chipulina, M.A. and González, R.A. (1983) Síntesis de la investigación geofísico minera en el noroeste argentino: *II Congr. Nac. de Geol. Econ.*, San Juan, 425-442.

Chukrov, F.V., Shanin, L.L. and Yermilov, L.P. (1966) Feasibility of absolute-age determination for potassium-carrying manganese minerals: *Intl. Geol. Rev.*, 8, 278-280.

Clark, A.H. (1977) Metallogenic epochs of the Central Andes: A preliminary assessment (abs.): *Econ. Geol.*, 72, 726-727.

Clark, A.H. (1993) Are outsize porphyry copper deposits either anatomically or environmentally distinctive?: In: B.H. Whiting, C.J. Hodgson and R. Mason, eds., *Giant Ore Deposits*, Queen's University, S.E.G. Special Publ. 2, 213-283.

Clark, A.H. and Arancibia, O.N. (1995) The occurrence, paragenesis and implications of magnetite-rich alteration-mineralization in calc-alkaline porphyry copper deposits: In: A.H. Clark, ed., *Giant Ore Deposits II: Controls on the Scale of Orogenic Magmatic-Hydrothermal Mineralization*, Proceedings of the Second Giant Ore Deposits Workshop, Kingston, Ontario, April, 1995, 583-640.

Clark, A.H., Farrar, E., Caelles, J.C., Haynes, S.J., Lortie, R.B., McBride, S.L., Quirt, G.S., Robertson, R.C.R., and Zentilli, M. (1976) Longitudinal variations in the metallogenetic evolution of the Central Andes: A progress report. In: D.F. Strong, ed., *Metallogeny and Plate Tectonics*, Geol. Assoc. Can. Special Paper 14, 23-58.

Clark, A.H., Farrar, E., Caelles, J.C., Haynes, S.J., Lortie, R.B., McBride, S.L., Quirt, G.S. and Zentilli, M. (1973) The magmatic, tectonic, and metallogenetic evolution of the

Central Andean mobile belt between latitudes 26° and 29° south: *Conference on Geodynamics*, Intl. Union Geodesy, Geophys., Lima, CGD-44.

Clark, A.H., Mayer, A.E.S., Mortimer, C., Sillitoe, R.H., Cooke, R.U. and Snelling, N.Y. (1967) Implications of the isotopic ages of ignimbrite flows, southern Atacama Desert: *Nature*, 215, 723-724.

Clark, A.H. and McNutt, R.H. (1982) Interrelated arc-broadening, topographic uplift and crustal contamination of magmas in two transects of the Mesozoic-Cenozoic Central Andes: *5th Intl. Conference on Geochronology, Cosmochronology and Isotope Geology*, Nikko (Tokyo), Japan, June 27- July 3, 55-56.

Clark, A.H. and Zentilli, M. (1972) The evolution of a metallogenic province at a consuming plate margin: the Andes between latitudes 26° and 29° South (extended abs.): *Can. Inst. Mining and Metall. Bull.*, 65, 37.

Cline, J.S. and Bodnar, R.J. (1991) Can economic porphyry copper mineralization be generated by a typical calc-alkaline melt?: *J. Geophys. Res.*, 96, 8113-8126.

Coira, B and Kay, S.M. (1993) Implications of Quaternary volcanism at Cerro Tuzgle for crustal and mantle evolution of the Puna Plateau, Central Andes, Argentina: *Contrib. Mineral. Petrol.*, 113, 40-58.

Coira, B., Kay, S.M. and Viramonte, J. (1993) Upper Cenozoic magmatic evolution of the Argentine Puna - a model for changing subduction geometry: *Intl. Geol. Review*, 35, 677-720.

Colley, H., Treloar, P.J. and Diaz, F. (1989) Gold-silver mineralization in the El Salvador region, northern Chile. In: R. Keays, R. Ramsey and D. Groves, eds., *The Geology of Gold Deposits: The Perspective in 1988*, Economic Geology, Monograph 6, 208-217.

Coughlin, T. (1996) High-angle accommodation zones in the Argentine Andes, abs.: A.G.U.

Cox, D.P. (1986) Descriptive model of porphyry Cu-Au. In: D.P. Cox and D.A. Singer eds., *Mineral Deposit Models*, U.S. Geol. Survey Bull. 1693, 110-114.

Crowell, J.C. (1974) Origin of Late Cenozoic basins in Southern California. In: W. R. Dickinson ed., *Tectonics and Sedimentation*, S.E.P.M. Special Publ. 22, 190-204.

Dallmeyer, R.D., Brown, M., Grocott, J., Taylor, G.K. and Treloar, P.J. (1996) Mesozoic magmatic and tectonic events within the Andean Plate boundary zone, 26° - 27°30' S, North Chile: constraints from <sup>40</sup>Ar/<sup>39</sup>Ar mineral ages: *J. Geology*, 104, 9-40.

- Dalrymple, G.B., Alexander, Jr., E.C., Lanphere, M.A., and Kraker, G.P. (1981) Irradiation of samples for  $^{40}\text{Ar}/^{39}\text{Ar}$  dating using the Geological Survey TRIGA Reactor: U.S. Geological Survey, Professional Paper 1176, 55 p.
- Dalrymple, G.B. and Lanphere, M.A. (1969), *Potassium-Argon Dating*, Freeman, San Francisco, 258 p.
- Davidson, J.P., McMillan, N., Moorbath, S., Worner, G., Harmon, R. and Lopez-Escobar, L. (1990) The Nevados de Payachata volcanic region ( $18^\circ \text{ S} / 69^\circ \text{ W}$ , N. Chile) II. Evidence for widespread crustal involvement in Andean magmatism: *Contrib. Mineral. Petrol.*, 105, 412-432.
- Davidson, J. and Mpodozis, C. (1991) Regional geologic setting of epithermal gold deposits, Chile: *Econ. Geol.*, 86, 1174-1186.
- Davies, G.R., Halliday, A.N., Mahood, G.A., and Hall, C.M. (1994) Isotopic constraints on the production rates, crystallization histories and residence times of pre-caldera silicic magmas, Long Valley, California: *Earth Plan. Sci. Lett.*, 125, 17-37.
- Davis, W.M. (1889) Topographical development of the Triassic formation of the Connecticut Valley: *Am. J. Sci.*, 37, 423-434.
- De Launay, L. (1913) *Traité de Métallogénie*, 3 vols., Beninger, Paris.
- Déruelle, B. (1978) Calc-alkaline and shoshonitic lavas from five Andean volcanoes (between latitudes  $21^\circ 45'$  and  $24^\circ 30' \text{ S}$  and the distribution of Plio-Quaternary volcanism of the south-central Andes: *J. Volcan. and Geothermal Res.*, 3, 281-298.
- Déruelle, B. (1982) Petrology of the Plio-Quaternary volcanism of the south-central and meridional Andes: *J. Volcan. and Geothermal Res.*, 14, 77-124.
- Déruelle, B. (1991) Petrology of Quaternary shoshonitic lavas of northwestern Argentina. In: R.S. Harmon and C.W. Rapela, eds., *Andean Magmatism and its Tectonic Setting*, Geol. Soc. America. Spec. Paper 265, 201-216.
- de Silva, S.L. and Francis, P.W. (1991) *Volcanoes of the Central Andes*, Springer-Verlag, Berlin, 216 p.
- Dewey, J.F. (1975) Finite plate motions: some implications for the evolution of rock masses at plate margins: *Am. J. Sci.*, 275A, 260-284.
- Dewey, J.F. and Bird, J.M. (1970) Mountain belts and the new global tectonics: *J. Geophys. Res.*, 75, 2625-2647.

- Dostal, J., Zentilli, M., Caelles, J.C., and Clark, A.H. (1977) Geochemistry and origin of volcanic rocks of the Andes (26° - 28°S): *Contrib. Mineral. Petrol.*, 63, 113-128.
- Durand, F.R. (1980) *Geología de la Sierra de la Ovejería, Provincia de Catamarca*, Universidad Nacional de Tucumán, Unpublished Ph. D. Thesis, 202 p.
- Durand, F.R. (1982) Caracteres geológicos del basamento de la Sierra de la Ovejería, Provincia de Catamarca: *Acta. Geol. Lilloana*, 61, 93-109.
- Eichelberger, J.C. (1974) Magma contamination within the volcanic pile: origin of andesite and dacite: *Geology*, 2, 29-33.
- Eremchuk, J.E., Mon, R., Suayter, L.E. and Zossi, M.M. (1981) Sismicidad y tectónica en los Andes del norte argentino: *Rev. Asoc. Geol. Arg.*, XXVI, 197-203.
- Ewart, A. (1982) The mineralogy and petrology of Tertiary-Recent orogenic volcanic rocks: with special reference to the andesitic-basaltic compositional range: In: R.S. Thorpe, ed., *Andesites: Orogenic Andesites and Related Rocks*, Wiley-Interscience Publ., John Wiley and Sons, New York, 25-95.
- Farrar, E., Clark, A.H., Haynes, S.J., Quirt, G.S., Conn, H. and Zentilli, M. (1970) K-Ar evidence for the post-Paleozoic migration of granitic intrusion foci in the Andes of northern Chile: *Earth Planet. Sci. Lett.*, 9, 17-28.
- Febrer, J.M., Baldi, B., Gasco, J.C., Mamani, M. and Pomposiello, C. (1982) La anomalía geotérmica Calchaquí en el noroeste Argentina: un nuevo proceso geodinámico asociada a la subducción de la placa de Nazca: *Quinto Cong. Latinoamericano de Geol.*, 3, 691-703.
- Figuerola, L.A. (1971) Fotolineamientos y mineralización en el Noroeste Argentino: *Primer Simposio Nac. de Geol. Econ.*, San Juan, Argentina, 1, 107-124.
- Flint, S. S., Prior, D. J., Agar, S. M. and Turner, P. (1994) Stratigraphic and structural evolution of the Tertiary Cosmelli Basin and its relationship to the Chile triple junction: *J. Geol. Soc. London*, 151, 251-268.
- Flint, S., Turner, P. and Jolley, E. J. (1991) High frequency cyclicity in Quaternary fan-delta deposits of the Andean forearc: Relative sea-level changes as a response to aseismic ridge subduction. In: D. Macdonald, ed., *Sedimentation, Tectonics and Eustasy*. Intl. Assoc. of Sedimentologists, Spec. Publ. 12, 91-102.
- Fornari, M., Pozzo, L., Soler, P., Bailly, L., Leroy, J. and Bonhomme, M.G. (1993) Miocene volcanic centres in the southern *Altiplano* of Bolivia. The Cerro Morokho and Cerro Bonete area (Sur Lipez): *Deuxième Symposium International Géodynamique Andine*,

*Colloques et Séminaires*, Oxford, Editions de l'ORSTOM, 363-366.

France, L.J. (1985) *Geochronology, Stratigraphy, and Petrochemistry of the Upper Tertiary Volcanic Arc, Southernmost Peru, Central Andes*: Queen's University, Kingston, Unpublished M. Sc. thesis, 182 p.

Francis, P.W. and Baker, M.C.W. (1978) Sources of two large-volume ignimbrites in the Central Andes: some Landsat evidence: *J. Volcanol. Geotherm. Res.*, 4, 81-87.

Francis, P.W., Hammill, M., Kretschmar, G.A. and Thorpe, R.S. (1978) The Cerro Galan caldera, northwest Argentina and its tectonic setting: *Nature*, 274, 748-751.

Froidevaux, C. and Isacks, B.L. (1984) The mechanical state of the lithosphere in the Altiplano-Puna segment of the Andes: *Earth Plan. Sci. Lett.*, 71, 305-314.

García, H.H. (1969) Consideraciones sobre algunas alineaciones de desarrollos hidrotermales tipo pórfido cuprífero en el noroeste Argentino: *Rev. Dir. Nac. Geol. Min.*, 18, 55-66.

García, H.H. (1970) Geología del yacimiento tipo pórfido cuprífero: Bajo Las Pampitas, Depto. Belén, Provincia de Catamarca, República Argentina: *Rev. Asoc. Geol. Arg.*, 26, 327-342.

García, H.H. (1971) Geología del pórfido cuprífero Bajo de San Lucas, Depto. Andalgalá, Prov. de Catamarca, República Argentina: *Rev. Asoc. Geol. Arg.*, 26, 327-342.

García, M.O., and Jacobson, S.S. (1979) Crystal clots, amphibole fractionation and the evolution of calc-alkaline magmas: *Contrib. Mineral. Petrol.*, 69, 319-327.

Gemuts, I., Little, M.L. and Giudici, J. (1996) Precious and base metal deposits in Argentina: *Soc. Econ. Geologists Newsletter*, 25, 1 and 7-15.

Gemuts, I., Lopez, G. and Jimenez, F. (1992) Gold deposits of southern Ecuador: *Soc. Econ. Geologists Newsletter*, 11, 1.

Gerlach, D.C. and Grove, T.L. (1982) Petrology of Medicine Lake Highland volcanics: characterization of end members of magma mixing: *Contrib. Mineral. Petrol.*, 80, 147-159.

Geyh, M.A. and Schleicher, H. (1990) *Absolute Age Determination*: Springer-Verlag, Berlin, 503 p.

Gill, J.B. (1970) Geochemistry of Viti Levu, Fiji, and its evolution as an island arc: *Contrib. Mineral. Petrol.*, 27, 179-203.

- Gill, J.B. (1981) *Orogenic Andesites and Plate Tectonics*, Springer-Verlag, New York, 390p.
- Godeas, M.C. (1971) El cuerpo subvolcánico riódacítico de Los Pozos, Farallón Negro, Provincia de Catamarca, República Argentina: *Rev. Asoc. Arg. Min. Pet. Sed.*, Tomo II, 19-38.
- González, O.E. (1975) Geología y alteración en el cobre porfídico "Bajo de la Alumbreira", República Argentina: *II Congr. Ibero-Americano de Geología Económica*, Tomo II, 247-270.
- González, O.E. (1978) Hallazgo de calizas cristalinas en la Sierra de Aconquija, Prov. de Catamarca, Argentina: *Actas VII Congr. Geol. Arg.*, Tomo II, 609-623.
- González, O.E. (1990) Las volcanitas del Portezuelo Las Animas, Sierra de Aconquija, Prov. de Catamarca y Tucumán: *Rev. Asoc. Geol. Arg.*, 95, 386-396.
- González, O.E. (1995) *Hoja Geológica 2766-II, San Miguel de Tucumán*, Dir. Gen. Ind. Min.,
- González, O.E., Paz, R. M. and Godeas, M. (1989) Volcanitas en El Rincón y Huertas Viejas, Sierra de Aconquija, Tucumán: *Rev. Asoc. Geol. Arg.*, 94, 169-174.
- González Bonorino, F. (1949) Diferenciación y alteración hidrotermal en Agua Tapada, Provincia de Catamarca: *Rev. Asoc. Geol. Arg.*, 4, 181-217.
- González Bonorino, F. (1950a) *Geología y petrografía de las Hojas 12d (Capillitas) y 13d (Andalgalá)*, Dir. Gen. Ind. Min. 70, 100 p.
- González Bonorino, F. (1950b) Algunos problemas geológicos de las Sierras Pampeanas: *Rev. Asoc. Geol. Arg.*, 5, 81-110.
- González Bonorino, F. (1951a) *Descripción Geológica de la Hoja 12e, Aconquija*, Dir. Gen. Ind. Min., 50 p.
- González Bonorino, F. (1951b) Granitos y migmatitas de la falda occidental de la Sierra del Aconquija: *Rev. Asoc. Geol. Arg.*, 6, 137-186.
- González Bonorino, F. (1972) *Descripción Geológica de la Hoja 13c, Fiambalá*, Dir. Gen. Ind. Min., 74 p.
- Grier, M.E., Salfity, J.A. and Allmendinger, R.W. (1991) Andean reactivation of the Cretaceous Salta rift, northwestern Argentina: *J. S. Am. Earth Sci.*, 4, 351-372.

Guerrero, M. and Lavandaio, E. (1969a) *Estudio Geológico Económico Bajo de los Jejenes*, Dir. Nac. Geol. Min., Plan Cordillera Norte.

Guerrero, M. and Lavandaio, E. (1969b) *Estudio Geológico Económico Bajo de Tampa Tampa*, Dir. Nac. Geol. Min., Plan Cordillera Norte.

Guerrero, M. and Lavandaio, E. (1969c) *Estudio Geológico Económico Bajo del Espanto*, Dir. Nac. Geol. Min., Plan Cordillera Norte.

Guilbert, J.M. (1995) Geology, alteration, mineralization, and genesis of the Bajo de la Alumbrera porphyry copper-gold deposit, Catamarca Province, Argentina: In: F. Wahl Pierce and J.G. Bolm, eds., *Porphyry Copper Deposits of the American Cordillera*. Arizona Geol. Soc., Digest 20, Tucson, 646-656.

Gustafson, L.B. and Hunt, J.R. (1975) The porphyry copper deposit at El Salvador, Chile: *Econ. Geol.*, 70, 857-912.

Hall, C.M., York, D., Yanase, Y., Kenyon, W.J., Kuybida, P., and Hanes, J.A. (1980)  $^{40}\text{Ar}/^{39}\text{Ar}$  dating with a continuous laser (abs.): *EOS, Trans. Amer. Geophys. Union*, 61, 398.

Hall, M.L. and Wood, C.A. (1985) Volcano-tectonic segmentation of the northern Andes: *Geology*, 13, 203-207.

Hanes, J.A. (1991) K-Ar and  $^{40}\text{Ar}/^{39}\text{Ar}$  geochronology: Methods and applications. In: L. Heaman and J.N. Ludden, eds., *Applications of Radiogenic Isotope Systems to Problems in Geology*, Mineral. Assoc. Canada Short Course Handbook 19, Toronto, 27-57.

Harrington, H.J. (1956) Argentina: In: W.F. Jencks, ed., *Handbook of South American Geology*, Geol. Soc. Am. Memoir 65, 131-165.

Harrison, T.M. (1983) Some observations on the interpretation of  $^{40}\text{Ar}/^{39}\text{Ar}$  age spectra: *Isotope Geoscience*, 1, 319-338.

Haynes, S.J. (1975) *Granitoid Petrochemistry, Metallogeny and Lithospheric Plate Tectonics, Atacama Province, Chile*: Queen's University, Kingston, Unpublished Ph. D. thesis, 190 p.

Heald, P., Foley, N.K. and Hayba, D.O., (1987) Comparative anatomy of volcanic-hosted epithermal deposits: Acid-sulfate and adularia-sericite types: *Econ. Geol.*, 82, 1-26.

Hedenquist, J.W. and Lowenstern, J.B. (1994) The role of magmas in the formation of hydrothermal ore deposits: *Nature*, 370, 519-527.



Herron, E.M. (1972) Sea-floor spreading and the Cenozoic history of the east-central Pacific: *Geol. Soc. Am. Bull.*, 83, 1671-1692.

Hildreth, W. and Moorbath, S. (1988) Crustal contributions to arc magmatism in the Andes of central Chile: *Contrib. Mineral. Petrol.*, 98, 455-489.

Hildreth, W. and Moorbath, S. (1991) Reply to Comment on "Crustal contributions to arc magmatism in the Andes of central Chile" by W. Hildreth and S. Moorbath: *Contrib. Mineral. Petrol.*, 108, 247-252.

Humphreys, (1995) Post-Laramide removal of the Farallon slab, western United States: *Geology*, 23, 987-990.

Iddings, J.P. (1895) Absarokite-shoshonite-banakitite series: *J. Geol.*, 3, 935-959.

Indri, D. (1979) *Geología de la Cuesta Mina Capillitas (Catamarca)*: Universidad Nacional de Tucumán, Unpublished Seminario, 58 p.

Indri, D. and Carrizo, M. (1992) Geologic Map of Bajo de la Alumbrera: 1:1000 scale map for International Musto Exploration Ltd.

Irvine, T.N., and Baragar, W.R.A. (1971) A guide to the chemical classification of the common volcanic rocks: *Can. Jour. Earth Sci.*, 8, 523-548.

Isacks, B.L. (1988) Uplift of the central Andean plateau and bending of the Bolivian orocline: *J. Geophys. Res.*, 93, 3211-3231.

Ishihara, S. (1981) The granitoid series and mineralization: *Econ. Geol. 75th Anniv. Vol.*, 458-484.

Jakeš, P. and Gill, J.B. (1970) Rare earth elements and the island arc tholeiitic series: *Earth & Plan. Sci. Letters*, 9, 17-28.

Jakeš, P., and White, A.J. (1969) Structure of the Melanesian Arcs and correlation with distribution of magma types: *Tectonophysics*, 8, 223-236.

James, D.E. (1971) Plate tectonic model for the evolution of the central Andes: *Geol. Soc. Am. Bull.*, 82, 3325-3346.

Japanese International Cooperation Agency (J. I. C. A.) (1978) *Informe de Estudios Basicos sobre la Exploración de Recursos Minerales en la Zona Norte de la República Argentina (Primer año del proyecto trienal)*, Metallic Mineral Organization of Japan, 55 p.

Japanese International Cooperation Agency (J. I. C. A.) (1979) *Informe de Estudios Basicos sobre la Exploración de Recursos Minerales en la Zona Norte de la República Argentina (segundo ano del proyecto trienal)*, Metallic Mineral Organization of Japan, 206 p.

Japanese International Cooperation Agency (J. I. C. A.) (1980) *Informe de Estudios Basicos sobre la Exploración de Recursos Minerales en la Zona Norte de la República Argentina (tercero etapa)*, Metallic Mineral Organization of Japan, 58 p.

Japanese International Cooperation Agency (J. I. C. A.) (1981) *Informe de Estudios Basicos sobre la Exploración de Recursos Minerales en la Zona Norte de la República Argentina (cuarta etapa)*, Metallic Mineral Organization of Japan, 100 p.

Jiménez, N., Barrera, L., Flores, O., Lizeca, J.L., Murillo, F., Hardyman, R.F., Tosdal, R.M., and Wallace, A.R., (1993a) Marco geológico de la región de Berenguela. In: *Investigación de metales preciosos en el complejo volcanico Neogeno-Cuaternario de los Andes Centrales*, Servicio Geológico de Bolivia, La Paz, 63-74.

Jiménez, N., Barrera, L., Flores, O., Lizeca, J.L., Murillo, F., Sanjines, O., Hardyman, R.F., Tosdal, R.M., and Wallace, A.R., (1993b) Magmatic evolution of the Berenguela - Charaña Region, Northwestern Altiplano, Bolivia: *Deuxième Symposium International Géodynamique Andine, Colloques et Séminaires*, Oxford, Editions de l'ORSTOM, 377-380.

Joplin, G.A. (1965) The problem of the potash-rich basaltic rocks: *Mineral. Mag.*, 34, 266-275.

Joplin, G.A. (1968) The shoshonite association: A review: *J. Geol. Soc. Australia*, 15, 275-294.

Jordan, T.E. and Allmendinger, R.W. (1986) The Sierras Pampeanas of Argentina: a modern analogue of Rocky Mountain foreland deformation: *Am. J. Sci.*, 286, 737-764.

Jordan, T.E. and Alonso, R.N. (1987) Cenozoic stratigraphy and basin tectonics of the Andes Mountains, 20° - 28° south latitude: *Am. Ass. Pet. Geol. Bull.*, 71, 49-64.

Jordan, T.E., Isacks, B.L., Allmendinger, R.W., Brewer, J.A., Ramos, V.A. and Ando, C.J. (1983) Andean tectonics related to geometry of subducted Nazca plate: *Geol. Soc. Am. Bull.*, 94, 341-361.

Jordan, T.E., Zeitler, P., Ramos, V. and Gleadow, A.J. (1989) Thermochronometric data on the development of the basement peneplain in the Sierras Pampeanas, Argentina: *J. S.Am. Earth Sci.*, 2, 207-222.

- Kaneoka, I. and Guevara, C. (1984) K-Ar age determinations of late Tertiary and Quaternary Andean volcanic rocks, southern Peru: *Geochemical J.*, 18, 233-239.
- Kay, S.M. (1991) Miocene "flat slab" volcanic rocks as guides to lithospheric processes in the Central Andes (25 - 33° S): *VI Congreso Geológico Chileno*, Viña del Mar, 579-583.
- Kay, S.M., Abbruzzi, J., Allmendinger, R.W. and Jordan, T.E. (1993) Isotopic constraints on Miocene to Recent evolution of the Central Andean lithosphere over the "flat slab": *Second ISAG*, Oxford, UK, October, 381-384.
- Kay, S.M., Coira, B. and Viramonte, J. (1994a) Young mafic back arc volcanic rocks as indicators of continental lithospheric delamination beneath the Argentine Puna plateau, central Andes: *Jour. Geophys. Res.*, 99, 24,323-24,339.
- Kay, S.M. and Gordillo, C.E. (1994) Pocho volcanic rocks and the melting of depleted continental lithosphere above a shallowly dipping subduction zone in the central Andes: *Contrib. Mineral. Petrol.*, 117, 25-44.
- Kay, S.M., Makshev, V., Moscoso, R., Mpodozis, C., Nasi, C., and Gordillo, C.E. (1988) Tertiary Andean magmatism in Chile and Argentina between 28° S and 33° S: correlation of magmatic chemistry with a changing Benioff zone: *J. S. Am. Earth Sci.*, 1, 21-38.
- Kay, S.M., Mpodozis, C. and Cornejo, P. (1994b) Late Cenozoic evolution of the southern CVZ (26° - 28°S): a case of progressive crustal thickening and lithospheric thinning: *7º Congreso Chileno, Actas II*, Concepcion, 1372-1377.
- Kay, S.M., Mpodozis, C., Tittler, A. and Cornejo, P. (1994c) Tertiary magmatic evolution of the Maricunga Mineral Belt in Chile: *Intl. Geol. Review*, 36, 1079-1112.
- Kelley, S.P. and Turner, G. (1991) Laser probe  $^{40}\text{Ar}/^{39}\text{Ar}$  measurements of loss profiles within individual hornblende grains from the Giants Range Granite, northern Minnesota, USA: *Earth & Planet. Sci. Letters*, 107, 634-648.
- Kontak, D.J., Clark, A.H., Farrar, E., and Pearce, T.H. (1986) Petrogenesis of a Neogene shoshonite suite, Cerro Moromoroni, Puno, southeastern Peru: *Can. Mineralogist*, 24, 117-135.
- Koukharsky, M., and Mirré, J.C. (1976) Mi Vida Prospect: A porphyry copper-type deposit in northwestern Argentina: *Econ. Geol.*, 71, 849-863.
- Kussmaul, S., Hörmann, P.K., Plonskonka, E. and Subieta, T. (1977) Volcanism and structure of southwestern Bolivia: *J. Volcan. Geothermal Res.*, 2, 73-111.

- Lallamand, S., Colotta, R. and Von Heune, R. (1989) Subduction of the Daiichi Kashima seamount in the Japan Trench: *Tectonophysics*, 160, 231-247.
- Lallamand, S. and Le Pichon, X. (1987) Coulomb wedge model applied to the subduction of seamounts in the Japan Trench: *Geology*, 15, 1065-1069.
- Lanphere, M.A. and Dalrymple, G.B. (1971) A test of the  $^{40}\text{Ar}/^{39}\text{Ar}$  age spectrum technique on some terrestrial materials: *Earth Planet. Sci. Lett.*, 12, 359-372.
- Lavenu, A., Bonhomme, M.G., Vatin-Perignon, N. and DePachter, P. (1989) Neogene magmatism in the Bolivian Andes between 16°S and 18°S: stratigraphy and K/Ar geochronology: *J. S. Am. Earth Sci.*, 2, 35-47.
- Layer, P.W., Hall, C.M. and York, D. (1987) The derivation of  $^{40}\text{Ar}/^{39}\text{Ar}$  age spectra of single grains of hornblende and biotite by laser step-heating: *Geophys. Res. Lett.*, 14, 757-760.
- Lazarte, J.E. (1990) Analisis preliminar de la alteracion de la roca de caja de las vetas auríferas de Culampajá, Catamarca: *XI Congreso Geol. Argentino*, Actas 1, 332-335.
- LeBel, L., Cocherie, A., Baubron, J.C., Fouillac, A.M. and Hawkesworth, C.J. (1985) A high-K, mantle-derived plutonic suite from "Linga", near Arequipa (Peru): *J. Petrol.*, 26, 124-148.
- Lee, J.K.W., Onstott, T.C. and Hanes, J.A. (1990) An  $^{40}\text{Ar}/^{39}\text{Ar}$  investigation of the contact effects of a dyke intrusion, Kapuskasing Structural Zone, Ontario: A comparison of laser microprobe and furnace extraction techniques: *Contrib. Mineral. Petrol.*, 105, 87-105.
- LeMaitre, R.W. (1989) *A Classification of Igneous Rocks and Glossary of Terms: Recommendations of the International Union of Geological Sciences Subcommittee on the Systematics of Igneous Rocks*, Blackwell Scientific Publications, Oxford.
- Lindgren, W. (1933) *Mineral Deposits*, McGraw-Hill, New York, 930p.
- Llambías, E.J. (1970) Geología de los Yacimientos Mineros Agua de Dionisios, Provincia de Catamarca, República Argentina: *Rev. Asoc. Min. Petrol. Sediment.*, I, 2-32.
- Llambías, E.J. (1972) Estructura del grupo volcanico Farallón Negro, Catamarca, República Argentina: *Rev. Asoc. Geol. Argentina*, 27, 161-169.
- Losada-Calderón, A.J, McBride, S.L. and Bloom, M.S. (1994) Geology and  $^{40}\text{Ar}/^{39}\text{Ar}$  geochronology of magmatic activity in the Nevados de Famatina District, Argentina: *J. S. Am. Earth Sci.*, 7, 9-24.

- Losada-Calderón, A.J and McPhail, D.C. (1996) Porphyry and high-sulfidation epithermal mineralization in the Nevados del Famatina mining district, Argentina. In: F. Camus, R. Sillitoe and R. Petersen, eds., *Andean Copper Deposits: New Discoveries, Mineralization, Styles and Metallogeny*, Soc. Econ. Geologists Sp. Publ. 5, 91-118.
- Lowell, J.D. and Guilbert, J.M. (1970) Lateral and vertical alteration/mineralization zoning in porphyry ore deposits: *Econ. Geol.*, 65, 378-408.
- MacDonald, G.A. and Katsura, T. (1965) Eruption of Lassen Peak, Cascade Range, California, in 1915: example of mixed magmas: *Geol. Soc. Amer. Bull.*, 81, 475-482.
- MacKenzie, D.E. and Chappell, B.W. (1972) Shoshonitic and calc-alkaline lavas from the Highlands of Papua New Guinea: *Contrib. Mineral. Petrol.*, 35, 50-62.
- Maisonave, H.M. (1973) Estratigrafía de los alrededores de Chaschuil, Dept. Tinogasta, Prov. de Catamarca: *Actas del Quinto Congreso Geológico Argentino*, Tomo IV, 75 p.
- Maisonave, H.M. and Guillou, J. (1969) *Los Yacimientos de Cobre Porfidico en el Area de Reserva Minera Y.M.A.D.: Bajo el Durazno, Bajo de Agua Tapada, Las Pampitas, Bajo de San Lucas.*, Dir. Nac. Geol. Min., Plan Cord. Norte.
- Maluski, H. and Schaeffer, O.A. (1980) Laser probe  $^{39}\text{Ar}$ - $^{40}\text{Ar}$  terrestrial rock ages (abs.): *EOS, Trans. Amer. Geophys. Union*, 61, 398.
- Maluski, H. and Schaeffer, O.A. (1982)  $^{40}\text{Ar}/^{39}\text{Ar}$  laser probe dating of terrestrial rocks: *Earth Planet. Sci. Lett.*, 59, 21-27.
- Malvicini, L. and Llambías, E. (1963) Mineralogía y origen de los minerales de manganeso y sus asociados en Farallón Negro, Alto de la Blenda y Los Viscos, Hualfin, Catamarca: *Rev. Asoc. Geol. Arg.*, 18, 77-202.
- Malvicini, L. and Llambías, E. (1992) El magmatismo mioceno y las manifestaciones metalíferas asociadas en Argentina: *Actas del Quinto Congreso Latinoamericano de Geología, Argentina.*, III, 547-566.
- Mammerickx, J., Herron, E. and Dorman, L. (1980) Evidence for two fossil spreading ridges in the southeast Pacific: *Geol. Soc. Am. Bull.*, 91, 263-271.
- Mann, P., Hempton, M.R., Bradley, D.C. and Burke, K. (1983) Development of pull-apart basins: *J. Geol.*, 91, 529-554.
- Marquez Zavalía, M.F. (1988) *Mineralogía y Genesis del Yacimiento Capillitas (Catamarca, República Argentina)*, Universidad Nacional de Salta, Unpublished Ph. D. Thesis, 179 p.

Marrett, R.A., Allmendinger, R.W., Alonso, R.N. and Drake, R.E. (1994) Late Cenozoic tectonic evolution of the Puna Plateau and adjacent foreland, northwestern Argentine Andes: *J. S. Am. Earth Sci.*, 7, 179-207.

Martínez, L. del V. and Chipulina, M.A. (1996) Complejo volcánico "El Alisal", Tucumán: Un nuevo prospecto de mineralización diseminada: *Serie Contribuciones Técnicas, Recursos Minerales*, 1, 1-35.

Mason, D.R. and McDonald, J.A. (1978) Intrusive rocks and porphyry copper occurrences of the Papua New Guinea - Solomon Islands region: a reconnaissance study: *Econ. Geol.*, 73, 857-877.

Matthews, S.J., Jones, A.P. and Gardeweg, M.C. (1994) Lascar Volcano, northern Chile; evidence for steady-state disequilibrium: *J. Petrology*, 35, 401-432.

McBride, S.L. (1972) *A Potassium-Argon Age Investigation of Igneous and Metamorphic Rocks from Catamarca and La Rioja Provinces, Argentina*: Queen's University, Kingston, Unpublished M.Sc.thesis, 101 p.

McBride, S., Caelles, J.C., Clark, A.H. and Farrar, E. (1975) Paleozoic radiometric age provinces in the Andean basement, Latitudes 25°-30° S: *Earth Plan. Sci. Lett.*, 29, 373-383.

McDougall, D.J. and Harrison, T.M. (1988) *Geochronology and Thermochronology by the  $^{40}\text{Ar}/^{39}\text{Ar}$  Method*: Oxford Monographs on Geology and Geophysics No. 9, Oxford University Press, Oxford, 224 p.

McNutt, R.H., Clark, A.H. and Zentilli, M. (1979) Lead isotopic compositions of Andean igneous rocks, latitudes 26° to 29° S: Petrologic and metallogenic implications: *Econ. Geol.*, 74, 827-837.

McPhie, J., Doyle, M. and Allen, R. (1993) *Volcanic Textures: a Guide to the Interpretation of Textures in Volcanic Rocks*, Centre for Ore Deposit and Exploration Studies, University of Tasmania, Hobart, 198 p.

Megrue, G.H. (1973) Spatial distribution of  $^{40}\text{Ar}/^{39}\text{Ar}$  ages in lunar breccia 14301: *J. Geophys. Research*, 78, 3216-3221.

Merrihue, C.M. and Turner, G. (1966) Potassium-argon dating by activation with fast neutrons: *J. Geophys. Research*, 71, 2852-2857.

Meyer, C. and Hemley, J.J. (1967) Wall Rock Alteration: In: H.L. Barnes, ed., *Geochemistry of Hydrothermal Ore Deposits*, First Edition, New York, Holt, Reinhart and Winston, 166-235.

Mining Secretary (1993) *Directory of Mining Investment Opportunities in the Argentine Republic*, Ministry of Economy and Public Services, Buenos Aires, 395 p.

Mirre, J.C. and Aceñolaza, F.G. (1972) El hallazgo de *Oldhamia* sp. (traza fósil) y su valor como evidencia de edad Cámbrica para el supuesto Precámbrico del borde occidental del Aconquija, Prov. de Catamarca: *Ameghiniana*, 9, 72-78.

Mon, R. (1972) Esquema estructural de la Provincia de Tucumán, República Argentina: *Rev. Asoc. Geol. Arg.*, XXVII, 223-228.

Mon, R. (1976) La tectónica del borde oriental de los Andes en las provincias de Salta, Tucumán y Catamarca, República Argentina: *Rev. Asoc. Geol. Arg.*, 31, 65-72.

Mon, R. (1976) The structure of the eastern border of the Andes in northwestern Argentina: *Geol. Rundschau*, 75, 211-222.

Morrison, G.W. (1980) Characteristics and tectonic setting of the shoshonite rock association: *Lithos*, 13, 97-108.

Mpodozis, C. (1995) *Evolución Magmática Terciaria de la Región de Transición entre la ZVC y la zona de subducción de los Andes Chilenos*: Informe Final, Proyecto Fondecyt 149/92, Servicio Nacional de Geología y Minería, 2 vols., Santiago.

Müller, D. and Groves, D.I. (1993) Direct and indirect associations between potassic igneous rocks, shoshonites and gold-copper deposits: *Ore Geol. Rev.*, 8, 383-406.

Müller, D. and Groves, D.I. (1995) *Potassic Igneous Rocks and Associated Gold-Copper Mineralization*: Lecture Notes in the Earth Sciences 56, Springer-Verlag, Berlin, 210 p.

Navarro García, L.F. (1982) *Descripción Geológica de la Hoja 10e, Cafayate*, Dir. Gen. Ind. Min.

Navarro García, L.F. (1984) Estratigrafía de la región comprendida entre los paralelos de 26° 00' a 27° 15' de latitud sur y los meridianos de 66° 30' a 67° 00' de longitud oeste, provincia de Catamarca: *IX Congreso Geol. Argentino*, Actas I, 353-383.

North American Commission on Stratigraphic Nomenclature (1983) North American Stratigraphic Code: *Am. Ass. Pet. Geologists*, 67, 841-875.

Notsu, K. and Lajo, J.A. (1984) Regional variation of  $^{87}\text{Sr}/^{86}\text{Sr}$  ratio in late Cenozoic volcanic rocks from southern Peru: *Geochemical J.*, 18, 241-250.

Nulló, F.E. (1991) Cuencas extensionales del Mesozoico inferior en el extremo sur de Sudamérica, un modelo transpresional: *Rev. Asoc. Geol. Arg.*, XLVI, 115-126.

- Onuma, N. and Montoya, M. (1984) Sr/Ca - Ba/Ca systematics of volcanic rocks from the central Andes, southern Peru, and its implication for Andean magmatism: *Geochemical J.*, 18, 251-262.
- Ort, M.H., Coira, B.L. and Mazzoni, M.M. (1989) Eruptive behaviour, vent locations, and caldera development of Cerro Panizos, Central Andes: *N.M. Bur. Mines Miner. Res. Bull.*, 131, 208.
- Pacheco, M.M. (1988) *Estructura del borde septentrional de la Sierra Overjeria (y sectores aledaños), Provincia de Catamarca*, Universidad Nacional de Tucumán, Unpublished Seminario, 41 p.
- Parsons, W.H. (1969) Criteria for the recognition of volcanic breccias: review: *Geol. Soc. Am., Memoir*, 115, 263-304.
- Parsons, T. and Thompson, G.A. (1991) The role of magma overpressure in suppressing earthquakes and topography: worldwide examples: *Science*, 253, 1399-1402.
- Peccerillo, A., and Taylor, S.R. (1976) Geochemistry of Eocene calc-alkaline volcanic rocks from the Kastamonu area, Northern Turkey: *Contrib. Mineral. Petrol.*, 58, 63-81.
- Peirano, A. (1945) *Agua de Dionisio: un centro volcánico moderno en el distrito de Hualfin, Departamento de Belén, Provincia de Catamarca*, Inst. Mineral. Geol., Univ. Nac. de Tucumán, 28-60.
- Penck, W. (1920) *Der Südrand der Puna de Atacama (NW-Argentinien)*: Leipzig, Germany, Abhandlungen Mathematisch-Physikalische Klasse der Sächsischen Akademie der Wissenschaften, 37, 420 p.
- Perelló, J.A. (1994) Geology, porphyry Cu-Au, and epithermal Cu-Au-Ag mineralization of the Tombulilato district, North Sulawesi, Indonesia: *J. Geochem. Expl.*, 50, 221-256.
- Perelló, J.A., Fleming, J.A., O'Kane, K.P., Burt, P.D., Clarke, G.A., Himes, M.D. and Reeves, A.T. (1995) Porphyry copper-gold-molybdenum mineralization in the Island Copper cluster. In: ed., *Porphyry Deposits of the Northwestern Cordillera of North America*, Can. Inst. Min. Met. Special Volume 46, Montreal, 214-238.
- Phillips, D. and Onstott, T.C. (1988) Argon isotopic zoning in mantle phlogopite: *Geology*, 16, 542-546.
- Pilger, R.H. (1981) Plate reconstructions, aseismic ridges, and low-angle subduction beneath the Andes: *Geol. Soc. Am. Bull.*, 92, 448-456.
- Pilger, R.H. (1984) Cenozoic plate kinematics, subduction and magmatism: South



American Andes: *J. Geol. Soc. London*, 141, 793-802.

Plaza, D. (1993) Bajo de la Alumbrera porphyry copper-gold project geological model: map/report for International Musto Exploration Ltd.

Prior, D.J., Murdie, R.E., Styles, P.A.D., Pearce, R., Flint, S. and Agar, S. (1994) Geophysical signatures of subducted ridges in Southern Chile: *Actas 7° Congreso Geol. Chileno*, Concepción, 1, 695-698.

Proffett, J.M. (1994) *Geology of the Bajo de la Alumbrera Porphyry Copper-Gold deposit, Catamarca Province, Argentina*, Minera Alumbrera Internal Report, Anchorage, Alaska, 27 p.

Proffett, J.M. (1995) *Geology of the Bajo de la Alumbrera Porphyry Copper-Gold Deposit, Catamarca Province, Argentina*, Minera Alumbrera Internal Report, Anchorage, Alaska, 85 p.

Quartino, B.J. (1960) Interpretación geológica del distrito volcánico de Farallón Negro (Provincia de Catamarca): *Anales de las Primeras Jornadas Geológicas Argentinas*, 2, 267-278.

Quin, S.P. and Nikic, Z.T. (1996) *Discovery and Exploration of a Giant Copper-Gold Porphyry: The Agua Rica Deposit, Catamarca Province, Argentina*: Northern Orion Ltd. handout at Cordilleran Round-up 1996, Vancouver, 6 p.

Quin, S.P. and Nikic, Z.T. (1997) *Exploration Update for The Agua Rica Copper Gold Molybdenum Deposit, Catamarca Province, Argentina*: Northern Orion Ltd. handout at Cordilleran Round-up 1997, Vancouver, 5 p.

Ramos, V.A. (1977) Basement tectonics from Landsat imagery in mining exploration: *Geol. Mijnbouw.*, 56, 243-252.

Ramos, V.A. (1988) Late Proterozoic - early Paleozoic of South America - a collisional history: *Episodes*, 11, 168-174.

Ramos, V.A., Jordan, T.E., Allmendinger, R.W., Mpodozis, C., Kay, S.M., Cortés, J.M. and Palma, M. (1986) Paleozoic terranes of the central Argentine-Chilean Andes: *Tectonics*, 5, 855-880.

Ramos, V.A., Munizaga, F and Kay, S.M. (1991) El magmatismo cenozoico a los 33° S de latitud: geocronología y relaciones tectónicas: In: *6° Congreso Geológico Chileno*, Extended Abstracts, 892-896.

Redwood, S.D. and Macintyre, R.M. (1989) K-Ar dating of Miocene magmatism and related epithermal mineralization of the northeastern Altiplano of Bolivia: *Econ. Geol.*, 84, 618-630.

Reynolds, J.H. (1987) *Chronology of Neogene Tectonics in Western Argentina (27° - 33°)*

*Based on the Magnetic Polarity Stratigraphy of Foreland Basin Sediments*, Unpublished Ph. D. Thesis, Dartmouth College, Hanover, N.H., 353 p.

Richter, F.M. (1973) Convection and large-scale circulation of the mantle *J. Geophys. Res.*, 78, 8735-8745.

Richter, F.M. and Parsons, B. (1975) The interaction of two scales of convection in the mantle: *J. Geophys. Res.*, 80, 2529-2541.

Roddick, J.C. (1983) High precision intercalibration of  $^{40}\text{Ar}/^{39}\text{Ar}$  standards: *Geochim. Cosmochim. Acta*, 47, 887-898.

Rodgers, D.A. (1980) Analysis of pull-apart basin development produced by en echelon strike-slip faults: In: P.F. Ballance and H.G. Reading, eds., *Sedimentation in Oblique-slip Mobile Zones*, Intl. Asoc. Sed. Special Pub. 4, 27-41.

Rosin, N. (1993) American Resources' growth strategy: *Mining Mag.*, March, 1993, 104-110.

Ruiz Huidobro, O.J. (1972) *Descripción Geológica de la Hoja 11e, Santa María*, Dir. Gen. Ind. Min., 65 p.

Ruiz Huidobro, O.J. (1975) *Descripción Geológica de la Hoja 12c, Laguna Helada*, Dir. Gen. Ind. Min., 55 p.

Russo, R.M. and Silver, P.G. (1994) Trench-parallel flow beneath the Nazca Plate from seismic anisotropy: *Science*, 263, 1105-1111.

Ryan, P.J., Lawrence, A.L., Jenkins, R.A., Matthews, J.P., Zamora, J.C., Marino, E. and Diaz, I.U. (1995) The Candelaria copper-gold deposit, Chile: In: F. Wahl Pierce and J.G. Bolm, eds., *Porphyry Copper Deposits of the American Cordillera*. Arizona Geol. Soc., Digest 20, Tucson, 625-645.

Sales, R.H. and Meyer, C. (1949) Results from preliminary studies of vein formation at Butte, Montana: *Econ. Geol.*, 44, 465-484.

Salfity, J.A. (1982) Evolución paleogeográfica del Grupo Salta (Cretacio-Eogenico), Argentina: *V Congr. Latinoamericano Geol.*, Actas 1, Buenos Aires, 11-26.

Salfity, J.A., Goruslovich, S.A., Moya, M.C. and Amengual, R. (1984) Marco tectónico de la sedimentación y efusidad Cenozoicas en la Puna Argentina: *IX Congreso Geol. Argentino*, Actas 1, Bariloche, 539-554.

Sandeman, H.A.I. (1995) *Lithostratigraphy, Petrology and Geochronology of the Crucero*

*Supergroup, Puno, SE Peru: Implications for the Cenozoic Geodynamic Evolution of the Southern Peruvian Andes*, Queens University, Kingston, Unpublished Ph. D. Thesis, 385 p.

Sandeman, H.A.I., Clark, A.H. and Farrar, E. (1995) An integrated tectono-magmatic model for the evolution of the Southern Peruvian Andes (13-20° S) since 55 Ma: *Intl. Geol. Rev.*, 37, 1039-1073.

Sandeman, H.A.I., Clark, A.H., Farrar, E and Pauca, G.A. (in press) The Crucero Supergroup, Puno Department, SE Peru: lithostratigraphy, petrology and  $^{40}\text{Ar}/^{39}\text{Ar}$  geochronology of the Crucero Supergroup: *J. S. Am. Earth Sci.*

Sandeman, H.A., Sasso, A.M., and Archibald, D.A. (1997) Calibration of MAC-83 biotite: A potential 24.1 Ma Laser  $^{40}\text{Ar}$ - $^{39}\text{Ar}$  geochronological standard (abs.): Ottawa '97, Geol. Ass. Canada -Mineral. Ass. Canada, Program with Abstracts, A-131.

Sasso, A.M. (1995) *Progress report: Farallón Negro and Capillitas districts research*: Unpublished report submitted to M.I.M. Exploration Pty. Ltd., Placer Dome Sud America Ltd., BHP Minerals International Exploration Inc., and Recursos Americanos Argentinos S.A., Queen's University, 94 p.

Sasso, A.M., Clark, A.H. and Farrar, E. (1995) Tectonic controls on scale of upper Miocene porphyry Cu-Au mineralization centres 250 km to the east of coeval mineralization in the Chilean Andes: preliminary results from the Farallón Negro project, Catamarca, Argentina. In: A.H. Clark, ed., *Giant Ore Deposits II*, Queen's University, Kingston, Ontario, 101-111.

Servicio Nacional Minero Geológico (1972) *Exploración Geológico - Minera del Noroeste Argentino*, Ministerio de Industria y Minería, Plan N.O.A, 117 p.

Sillitoe, R.H. (1973a) *Geology of the Farallón Negro Porphyry Copper Deposits, Northwest Argentina*, United Nations Development Project, 25 p.

Sillitoe, R.H. (1973b) The tops and bottoms of porphyry copper deposits: *Econ. Geol.*, 68, 799-815.

Sillitoe, R.H. (1976) Andean mineralization: A model for the metallogeny of convergent plate margins. In: D.F. Strong, ed., *Metallogeny and Plate Tectonics*, Geol. Assoc. Can. Special Paper 14, 58-100.

Sillitoe, R.H. (1977) Permo-Carboniferous, Upper Cretaceous and Miocene porphyry copper-type mineralization in the Argentine Andes: *Econ. Geol.*, 72, 99-109.

Sillitoe, R.H. (1979) Some thoughts on gold-rich porphyry copper deposits: *Min. Depta.*,

14, 161-174.

Sillitoe, R.H. (1981) Regional aspects of the Andean porphyry copper belt in Chile and Argentina: *Trans. Instn. Min. Metall.*, 90, (section B), B15-B36.

Sillitoe, R.H. (1985) Ore-related breccias in volcanoplutonic arcs: *Econ. Geol.*, 80, 1467-1514.

Sillitoe, R.H. (1988) Epochs of intrusion-related copper mineralization in the Andes, *J. S. Am. Earth Sci.*, 1, 89-107.

Sillitoe, R.H. (1989a) Gold deposits in Western Pacific Island Arcs: The magmatic connection: *Econ. Geol. Monograph* 6, 274-291.

Sillitoe, R.H. (1989b) Copper deposits and Andean evolution. In: G.E. Erickson, M.T. Cañas Pinochet, and J.A. Reinemund, eds., *Geology of the Andes and its Relation to Hydrocarbon and Mineral Resources*, Houston, Texas, Circum-Pacific Council for Energy and Mineral Resources Earth Science Series, 11, 285-311.

Sillitoe, R.H. (1992) Gold and copper metallogeny of the Central Andes - past, present, and future exploration objectives: *Econ. Geol.*, 87, 2205-2216.

Sillitoe, R.H. (1996) Granites and metal deposits: *Episodes*, 19, 126-133.

Sillitoe, R.H. and Bonham, H.F. (1984) Volcanic landforms and ore deposits: *Econ. Geol.*, 79, 1286-1298.

Singer, B.S., Pearce, T.H., Kolisnik, A.M. and Myers, J.D. (1993) Plagioclase zoning in mid-Pleistocene lavas from the Seguam volcanic centre, central Aleutian arc, Alaska: *Amer. Mineralogist.*, 78, 143-157.

Sister, R.G. (1963) Informe geológico-económico de Farallón Negro y zona adyacente, Distrito Hualfin, Departamento Belén, Provincia de Catamarca: *Opera Lilloana*, VIII, 164 p.

Soler, P., Carlier, G., Fornari, M. and Hérail, G. (1992) An alternative model for the origin and the tectonic significance of the Neogene and Quaternary shoshonitic volcanism of the Andes (abs.): *EOS (Trans. Amer. Geophys. Union)*, 73, 341.

Soler, P. and Jiménez, N. (1993) Magmatic constraints upon the evolution of the Bolivian Andes since Late Oligocene times (extended abs.): *Deuxième Symposium International Géodynamique Andine, Colloques et Séminaires*, Oxford, Editions de l'ORSTOM, 447-451.

Sparks, R.S.J., Francis, P.W., Hamer, R.D., Pankhurst, R.J., O'Callaghan, L.O., Thorpe, R.S. and Page, R. (1985) Ignimbrites of the Cerro Galan caldera, NW Argentina: *J. Volcan. Geothermal Res.*, 24, 205-248.

Spurr, J.E. (1902) *Trans. A.I.M.E.*, 33, 336.

Srugoa, P., Urbina, N. and Malvicini, L. (1996) El volcanismo Terciario y los depositos hidrotermales (Au, Cu) asociados en La Carolina y Diente Verde, San Luis, Argentina: *XIII Congreso Geol. Argentino y III Congreso de Exploración de Hidrocarburos*, Actas III, 89-100.

Steiger, R.H. and Jäger, E. (1977) Subcommittee on geochronology: Convention on the use of decay constants in geo- and cosmo-chronology: *Earth and Plan. Sci. Letters*, 36, 359-362.

Stoll, W.C. (1964) Metallogenetic belts, centres, and epochs in Argentina and Chile: *Econ. Geol.*, 59, 126-135.

Stone, D.S. (1986) Wrench faulting and Rocky Mountain tectonics: *The Mountain Geologist*, 6, 67-79.

Strecker, M.R. (1987) *Late Cenozoic Landscape Development, the Santa Maria Valley, Northwest Argentina*: Cornell University, Ithaca, Unpublished Ph. D. thesis, 262 p.

Strecker, M.R., Cervený, P., Bloom, A.L. and Malizia, D. (1989) Late Cenozoic tectonism and landscape development in the foreland of the Andes: northern Sierras Pampeanas (26° - 28° S), Argentina: *Tectonics*, 8, 517-534.

Stults, A. (1983) *An Economic Geologic Evaluation of the Bajo de la Alumbrera Base and Precious Metal Prospect, Catamarca Province, Argentina*, Unpublished. Report to the United Nations Development Program, New York, 36 p.

Stults, A. (1985) *Geology of the Bajo la Alumbrera Porphyry Copper and Gold Prospect, Catamarca Province, Argentina*, University of Arizona, Tucson, Unpublished M. Sc. Thesis, 75 p.

Suchomel, B.J. (1983) *An Economic Geologic Evaluation of the Bajo de Agua Tapada Base and Precious Metal Prospect, Catamarca Province, Argentina*, Unpublished Report to the United Nations Development Program, New York, 49 p.

Suchomel, B.J. (1985) *Geology of the Bajo de Agua Tapada Base and Precious Metal Prospect, Catamarca Province, Argentina*, University of Arizona, Tucson, Unpublished M. Sc. Thesis, 72 p.

Suchomel, B.J. (1988) Little-explored area of Argentina shows base and precious metal potential: *Mining Engineering*, August, 1988, 800-803.

Swanson, K.E., Noble, D.C., McKee, E.H., Sempere, T., Martinez, C. and Cirbian, M. (1987) Major revisions in the age of rock units and tectonic events in the northern Altiplano Basin of Bolivia (abs.): *Geol. Soc. Am., Abstracts with Programs*, 19, 465.

Swinamer, R.T. (1989) *The Geomorphology, Petrography, Geochemistry and Petrogenesis of the Volcanic Rocks in the Sierra del Chichinautzin, Mexico*, Queen's University, Kingston, Unpublished M. Sc. Thesis, 212 p.

Tabbutt, K., Naeser, C.W., Jordan, T.E. and Cervený, P.F. (1988) Edades nuevas por método de trazas de fisión de tobas Mio-Pliocenas en las Sierras Pampeanas y la precordillera de Argentina: *Actas del X Congreso Geol. Argentino*, Tucumán, 222-224.

Tabbutt, K., Naeser, C.W., Jordan, T.E. and Cervený, P.F. (1989) New fission-track ages of Mio-Pliocene tuffs in the Sierras Pampeanas and Precordillera of Argentina: *Rev. Asoc. Geol. Arg.*, 44, 408-419.

Titley, S.R. and Beane, R.E. (1981) Porphyry copper deposits, Part 1. Geologic settings, petrology and tectogenesis: *Economic Geology*, 75th Anniversary Volume, 214-235.

Tilton, G.R., Pollak, R.J., Clark, A.H. and Robertson, R.C.R. (1981) Isotopic composition of Pb in central Andean ore deposits: *Geol. Soc. America Mem.*, 154, 791-816.

Tosdal, R.M. (1995) Metal source differences in Cenozoic porphyry Cu-Mo-Au deposits in the central Chilean Andes between 26° and 28°: an influence on the size of porphyry deposits?: In: A.H. Clark, ed., *Giant Ore Deposits II: Controls on the Scale of Orogenic Magmatic-Hydrothermal Mineralization*, Proceedings of the Second Giant Ore Deposits Workshop, Kingston, Ontario, April, 1995, 124-137.

Tosdal, R.M. (1996) The Amazon-Laurentian connection as viewed from the Middle Proterozoic rocks in the central Andes, western Bolivia and northern Chile: *Tectonics*, 15, 827-842.

Tosdal, R.M., Cornejo, P., Mpodozis, C., Rivera, O. and Tomlinson, A.J. (1997) Geologic setting of the El Salvador (Chile) porphyry Cu deposit (abs.): *Geol. Ass. Canada / Mineral. Ass. Canada, Program with Abstracts*, A-148.

Toselli, A.J. and Durand, F.R. (1974) Geología de las áreas con alteración hidrotermal, Los Jejenes y El Espanto - Farallón Negro, Catamarca: *Bol. Asoc. Geol. Córdoba*, II, (3-4), 78-83.

Treloar, P.J., Coward, M.P., Chambers, A.F., Izatt, C.N. and Jackson, K.C. (1992) Thrust geometries, interferences and rotations in the Northwest Himalayas. In: K.R. McClay, ed., *Thrust Tectonics*, Chapman and Hall, London, 325-342.

Tsuchiyama, A. (1985) Dissolution kinetics of plagioclase in the melt of the system

diopside-albite-anorthite, and origin of dusty plagioclase in andesites: *Contrib. Mineral. Petrol.*, 89, 1-16.

Turner, G. (1968) The distribution of potassium and argon in chondrites. In: L.H. Ahrens, ed., *Origin and Distribution of the Elements*, Pergamon Press, New York, 378-398.

Turner, G. and Cadogan, P.H. (1974) Possible effects of  $^{39}\text{Ar}$  recoil in  $^{40}\text{Ar} - ^{39}\text{Ar}$  dating: *Geochim. Cosmochim. Actas.*, Supplement 5, 1601-1615.

Turner, J.C. (1962a) Las Sierras Transpampeanas como unidad estructural: *Anales de las Prim. Jorn. Geol. Argent.*, Tomo II, 387-402.

Turner, J.C. (1962b) Estratigrafía de la region al naciente de Laguna Blanca (Catamarca): *Rev. Asoc. Geol. Arg.*, 17, 11-46.

Turner, J.C. (1967) *Descripción Geológica de la Hoja 13b, Chaschuil*: Dir. Gen. Ind. Min., 78 p.

Turner, J.C. (1973) *Descripción Geológica de la Hoja 11d Laguna Blanca (Provincia de Catamarca)*: Serv. Nac. Min. Geol., 71 p.

Urreiztieta, M., Gapais, D., LeCorve, C., Cobbold, P. and Rosello, E. (1994) Développement de bassins néogènes en contexte transpressif, bordure Sud-Est de l'Altiplano-Puna (NW Argentine): *Proceedings 15th Reunion des Sciences de la Terre*, Nancy, France, 33.

Urreiztieta, M., Rosello, E.A., Gapais, D., LeCorve, C. and Cobbold, P.R. (1993) Neogene dextral transpression at the southern edge of the Altiplano-Puna (NW Argentina): Extended Abstracts, *II Intl. Sym. on Andean Tectonics*, Oxford, 267-269.

VanDecar, J.C., James, D.E. and Assumpção, M. (1995) Seismic evidence for a fossil mantle plume beneath South America and implications for plate driving forces: *Nature*, 378, 25-31.

van den Bogaard, P., Hall, C.M., Schmincke, H-U, and York, D. (1987)  $^{40}\text{Ar}/^{39}\text{Ar}$  laser dating of single grains: ages of Quaternary tephra from the East Eifel volcanic field, FRG: *Geophys Research Lett.*, 14, 1211-1214.

Vandervoort, D.S., Jordan, T.E., Zeitler, P.K. and Alonso, R.N. (1995) Chronology of internal drainage development and uplift, southern Puna plateau, Argentine central Andes: *Geology*,

Vasconceles, P.M., Renne, P.R., Brimhall, G.H. and Becker, T.A. (1993) Direct dating of weathering phenomena by  $^{40}\text{Ar}/^{39}\text{Ar}$  and K-Ar analysis of supergene K-Mn oxides:

*Geochim. Cosmochim. Acta*, 58, 1635-1665.

Vessell, R.K. and Davies, D.K. (1981) Nonmarine sedimentation in an active fore arc basin. In: F.G. Ethridge and R.M. Flores, eds., *Recent and Ancient Nonmarine Depositional Environments: Models for Exploration*, S.E.P.M. Sp. Publ. 31, 31-45.

Vila, T. and Sillitoe, R.H. (1991) Gold-rich porphyry systems in the Maricunga belt, northern Chile: *Econ. Geol.*, 86, 1238-1260.

Viruel, M.E. (1973) *Geología de la Región Comprendida entre los Ríos VisVis y Jaci Yaco, Depto. Andalgala, Prov. de Catamarca, Rep. Argentina*: Universidad Nacional de Tucumán, Unpublished Seminario, 59 p.

Wadge, G. (1982) Steady state volcanism: evidence from eruption histories of polygenetic volcanoes: *J. Geophys. Res.*, 87, 4035-4049.

Wasteneys, H.A.H.P. (1990) *Epithermal Silver Mineralization Associated with a Mid-Tertiary Diatreme: Santa Barbara, Santa Lucia District, Puno, Peru*: Queen's University, Kingston, Unpublished Ph. D. Thesis, 367 p.

White, N.C. and Hedenquist, J.W. (1990) Epithermal environments and styles of mineralization: variations and their causes, and guidelines for exploration: *J. Geochem. Expl.*, 36, 445-474.

York, D., Hall, C.M., Yanase, Y., Hanes, J.A., and Kenyon, W.J. (1981)  $^{40}\text{Ar}/^{39}\text{Ar}$  dating of terrestrial minerals with a continuous laser: *Geophys. Research Lett.*, 8, 1136-1138.

York, D. and Lopez-Martinez, M. (1986) The two-faced mica: *Geophys. Res. Lett.*, 13, 973-975.

Zentilli, M. (1974) *Geological Evolution and Metallogenic Relationships in the Andes of Northern Chile Between 26° and 29°S*: Queen's University, Kingston, Unpublished Ph.D. Thesis, 446 p.

Zentilli, M. and Dostal, J. (1977) Uranium in volcanic rocks from the Central Andes: *J. Volcan. Geotherm. Res.*, 2, 251-258.

Zweng, P.L. and Clark, A.H. (1995) Hypogene evolution of the Toquepala porphyry copper-molybdenum deposit, Moquegua, southeastern Peru: In: F.W. Pierce and J.G. Bolm, eds., *Porphyry Copper Deposits of the American Cordillera*, Arizona Geol. Soc., Digest 20, Tucson, 566-612.



## **APPENDIX A**

**Metallic Mineral Deposits of the Farallón Negro  
Volcanic Complex not documented in Chapter 3.**

## **Cerro Atajo**

### ***Location and Access***

The Cerro Atajo prospect (Figs. A-1 and A-2) is located approximately 8 km west of Capillitas at 3 000 to 3 400 m a.s.l. It is easily accessed by a road which heads west from Ruta Nacional No. 63; the turn-off is approximately 2 km north of Capillitas.

### ***Previous Work***

Old workings at Cerro Atajo are thought to date from Colonial times (Bassi, 1991). The María Eugenia vein system was explored by the Dirección General de Fabricaciones Militares in 1945. The region was subsequently explored in 1969 by the Servicio Nacional Minero Geológico, who conducted geological mapping, geochemical sampling, an I.P. survey and limited drilling. Extensive mapping, geochemical sampling, geophysical surveys and drilling were conducted during a four-year program from 1978 to 1981 by the Japanese International Cooperation Agency (J.I.C.A.). The results of this work are presented in a series of unpublished reports (J.I.C.A., 1978, 1979, 1980, 1981).

An option to explore the area was signed by American Resource Corporation in 1992. They conducted geochemical chip sampling over the property, constructed access roads and completed a reverse-circulation drill program. Placer Dome optioned the property in late-1993 and conducted the most extensive exploration to date which included detailed mapping, geochemical sampling, geophysical surveys and drilling.

The only published study of Cerro Atajo is that of Bassi (1991).

**Figure A-1.**

Location of deposits of the Farallón Negro Volcanic  
Complex.

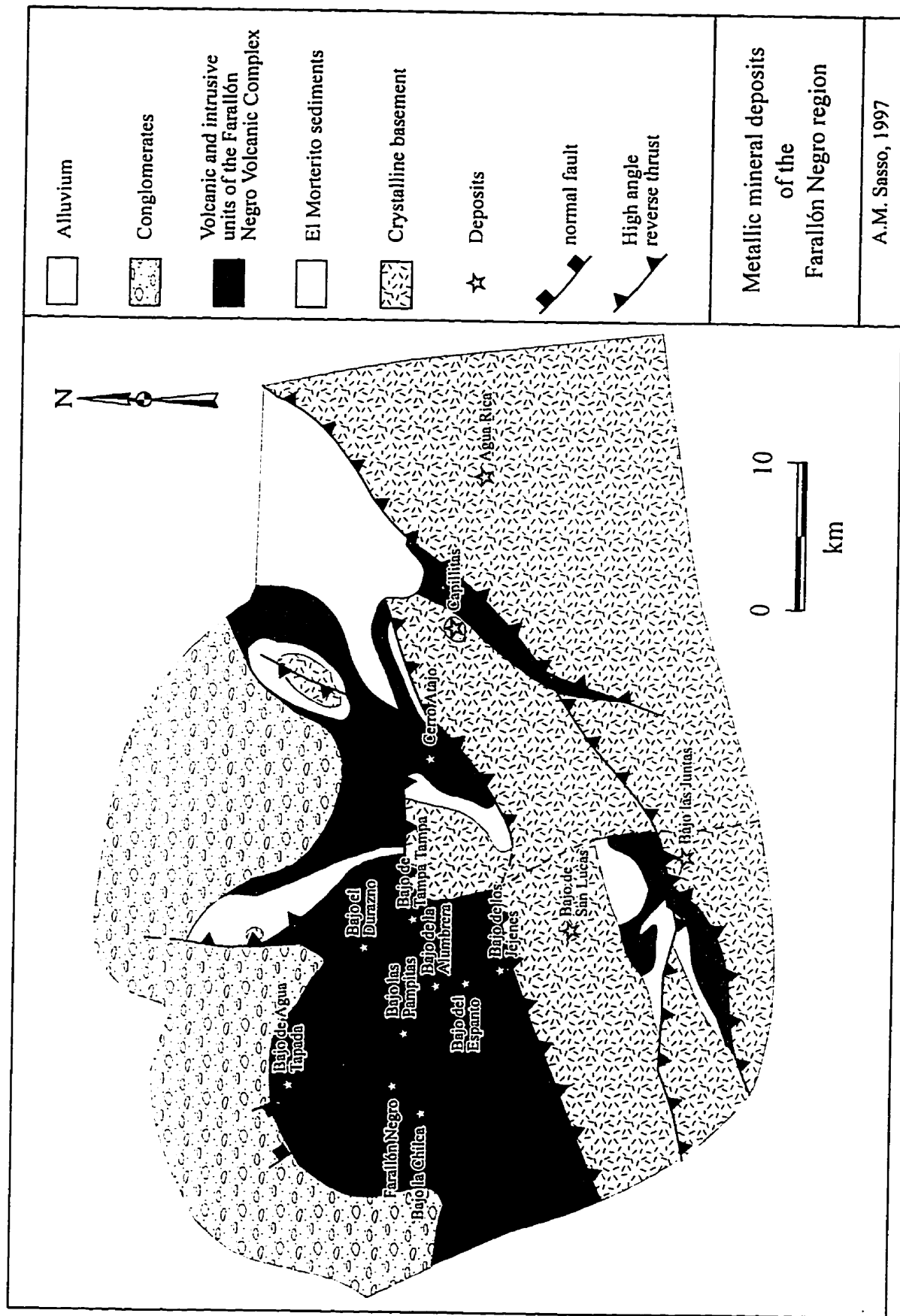
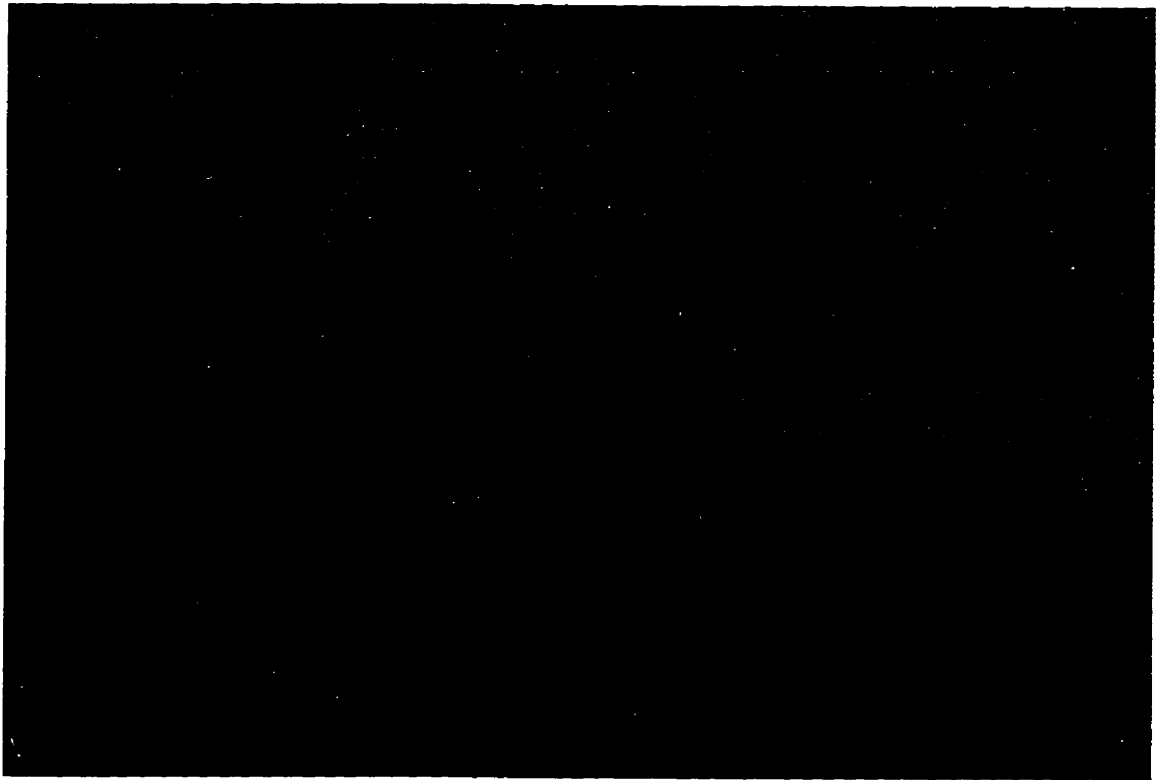


**Figure A-2.**

*Cerro Atajo*

**A.** North face of Cerro Atajo (view to the SW). The upper slopes of the peak (Cerro Atajo proper) and the ridge to the right are underlain by intrusive dacite porphyry. Well-bedded, grey-purple andesites of the Farallón Negro Volcanic Complex are exposed in the foreground. Pale-coloured areas in the centre and to the right are underlain by argillic alteration zones associated with epithermal veins. The Carmen Vein is located in the central portion of the photo but cannot be distinguished at this scale.

**B.** Southern part of the Cerro Atajo prospect (view to the NE). Dacite porphyry underlies the dark slopes in the left-foreground. The low ridge and hills in the centre expose andesites of the Farallón Negro Volcanic Complex. Outcrop in the foreground is of the rhyolite porphyry which underlies Cerro Blanco Chico. Veins and old workings are marked by brown- to buff-coloured zones in the volcanic units. The Capillitas Range forms the dominant ridge in the near-background. The Lavadero range-front, high-angle reverse fault is located at the contact between grey-blue volcanic units and vegetation-covered Ordovician granite along the lower slopes of the ridge (left-side of picture).



### ***Geological Relationships***

The Cerro Atajo deposit (Fig. A-3) is hosted by volcanic units of the Farallón Negro Volcanic Complex. The stratigraphic succession is dominated by well-bedded tuffaceous andesites and thin volcanoclastic horizons; thick autobrecciated flows are encountered near the top of the section. A basaltic-andesite dyke intruding the lower portion of the section yielded a whole-rock age of 8.15 Ma. Red beds of the El Morterito Formation crop out to the west of the deposit, where they conformably overlie the eroded basement surface forming the western flank of Cerro Bola del Atajo, and form thin lenses exposed in fault-drag folds in the footwall of the Lavadero fault, on the north side of the Capillitas Range (Fig. A-3).

The volcanic sequence is intruded by a large rhyolite porphyry stock which underlies Cerros Blanco Chico and Grande and a large dacite porphyry stock. Mineralization is thought to be associated with the latter.

### ***Structure***

The deposit is bounded to the southwest by the high-angle reverse range-front Lavadero fault (Fig. A-3) and to the north by the eastern extension of the Bola del Atajo fault, also a high-angle reverse structure. A series of parallel, NW-striking structures which cut across all lithologies observed at Cerro Atajo appear to have acted as conduits for hydrothermal fluids and host mineralized epithermal-style veins.

**Figure A-3.**

Geological map of the Cerro Atajo prospect.





### ***Mineralization***

A series of NW-trending epithermal veins carry Cu, Au, Pb, Zn and Ag mineralization. Many of the larger veins have been worked previously (Fig. A-4). J.I.C.A. (1978) documented a vertical zonation in ore mineralogy, possibly associated with changing host-rock composition, with Cu-Au in the upper andesites, Pb-Zn-(Ag) mineralization in the intermediate andesites, and pyrite  $\pm$  Au at depth, particularly in the granitic basement and Tertiary red beds.

The veins are associated with sericitic alteration of the wall rocks. The peak of Cerro Atajo is characterised by strongly-developed quartz  $\pm$  alunite veining. Tetrahedrite, chalcocite and chalcopyrite are the most important ore minerals (J.I.C.A., 1978). Wolframite and scheelite are reported from the Carmen vein system (Bassi, 1991).

The most important mineralized zones appear to be the Carmen and María Eugenia vein systems (Fig. A-4). The veins are more or less continuous over 800 m of strike length. The alteration zone surrounding the principal veins and secondary parallel veins and splays extends for up to 150 m (Bassi, *op. cit.*). Grab samples from the María Eugenia vein returned grades of 10-14 % Cu, 4.4- 5 g/t Au, 2-4 g/t Ag, 0.02 % Zn and 0.01 % Pb (Bassi, *op. cit.*).

### **Bajo de Agua Tapada**

#### ***Location and Access***

Bajo de Agua Tapada is located along the main access road to the Farallón Negro

**Figure A-4.**

*Cerro Atajo vein systems*

**A.** Old workings (small adit) in the Carmen vein system hosted by purple-grey breccias of the Farallón Negro Volcanic Complex (view to the south - detail of figure 2A). The brown-weathering veins are bordered by pale argillic alteration haloes developed in the volcanic units.

**B.** Triunfo vein system (view to the WSW). A series of coalescing veins (brown positively-weathering features) cut across the thick succession of tuffaceous breccias and flows of the Farallón Negro Volcanic Complex. Buff-coloured argillic alteration haloes are developed in the volcanic rocks. Old workings along the veins are marked by dumps, *e.g.*, middle-distant segments of the exposed vein. Drill-roads and platforms constructed by Recursos Americanos Argentinos S.A. are visible below the horizon, right-of-centre.



mine from Los Nacimientos (Fig. A-1). The road passes through the south-east edge of the Bajo de Agua Tapada phyllic alteration zone, approximately 9 km NW of Bajo de la Alumbraera.

### ***Previous Work***

The only published description of the prospect is that of Bonorino (1949). A detailed geological study and economic evaluation were undertaken by Suchomel (1983; 1985) as a Masters thesis under the supervision of John M. Guilbert at the University of Arizona and in collaboration with the United Nations. Various reports by Y.M.A.D. and Fabricaciones Militares geologists are also available. In general, the results of the surface geochemical sampling and diamond drill programs have been disappointing. However, the core, core logs and even drill hole locations have been lost.

### ***Geological Relationships***

The Bajo de Agua Tapada prospect consists of a composite dacite porphyry stock emplaced between 6.84 and 7.39 Ma into andesite breccias of the Farallón Negro Volcanic Complex (Fig. A-5). There is evidence of at least three stages of dacite intrusion: pre-, syn- and post-mineralization. The surface expression of the mineralized area is very similar to that of Bajo de la Alumbraera (Fig. A-6). A group of reddish-brown, goethite-stained hills with weakly-developed quartz-magnetite alteration is surrounded by lower-lying hills of phyllically-altered dacite and andesite breccia (Fig. A-7). The central hills are referred to as a zone of potassic alteration by Suchomel (1985) although very little

**Figure A-5.**

Geology of the Bajo de Agua Tapada deposit.



**Figure A-6.**

Bajo de Agua Tapada (view to the east). Prominent brown hills (Cerro Colorado Norte on the left and Cerro Colorado Sur) in middle-ground are underlain by dacite porphyry stocks exhibiting weak potassic and quartz-magnetite alteration. The surrounding low bleached hills are underlain by phylically-altered andesite breccias. Propylitic alteration extends into the surrounding flows and tuffs of the Farallón Negro Volcanic Complex. Its outer limit has not been mapped. The highest peak visible on the horizon is Cerro Nevado del Candado, 5450 m a.s.l., in the Sierra de Aconquija.



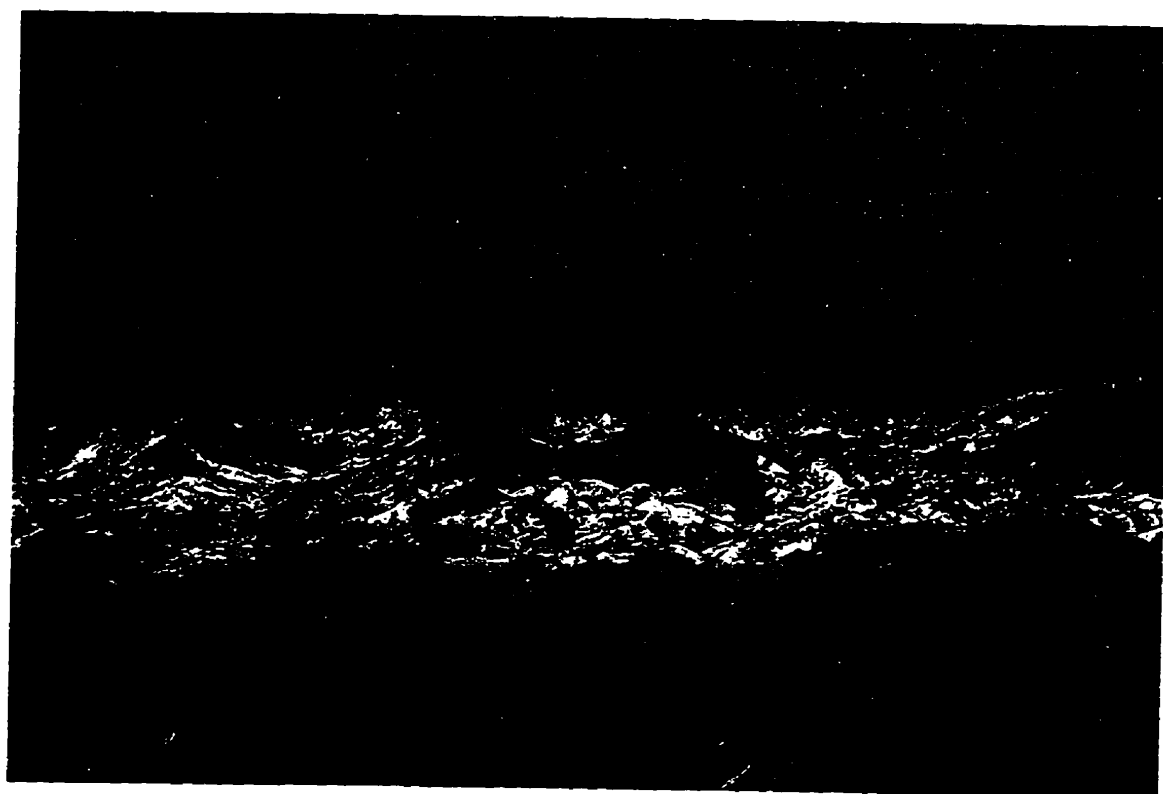


**Figure A-7.**

Alteration facies of the Bajo de Agua Tapada deposit.

# BAJO DE AGUA TAPADA

## ALTERATION

Generalized from Suhomel (1983)

A.M. Sasso, 1997

Potassic-magnetite



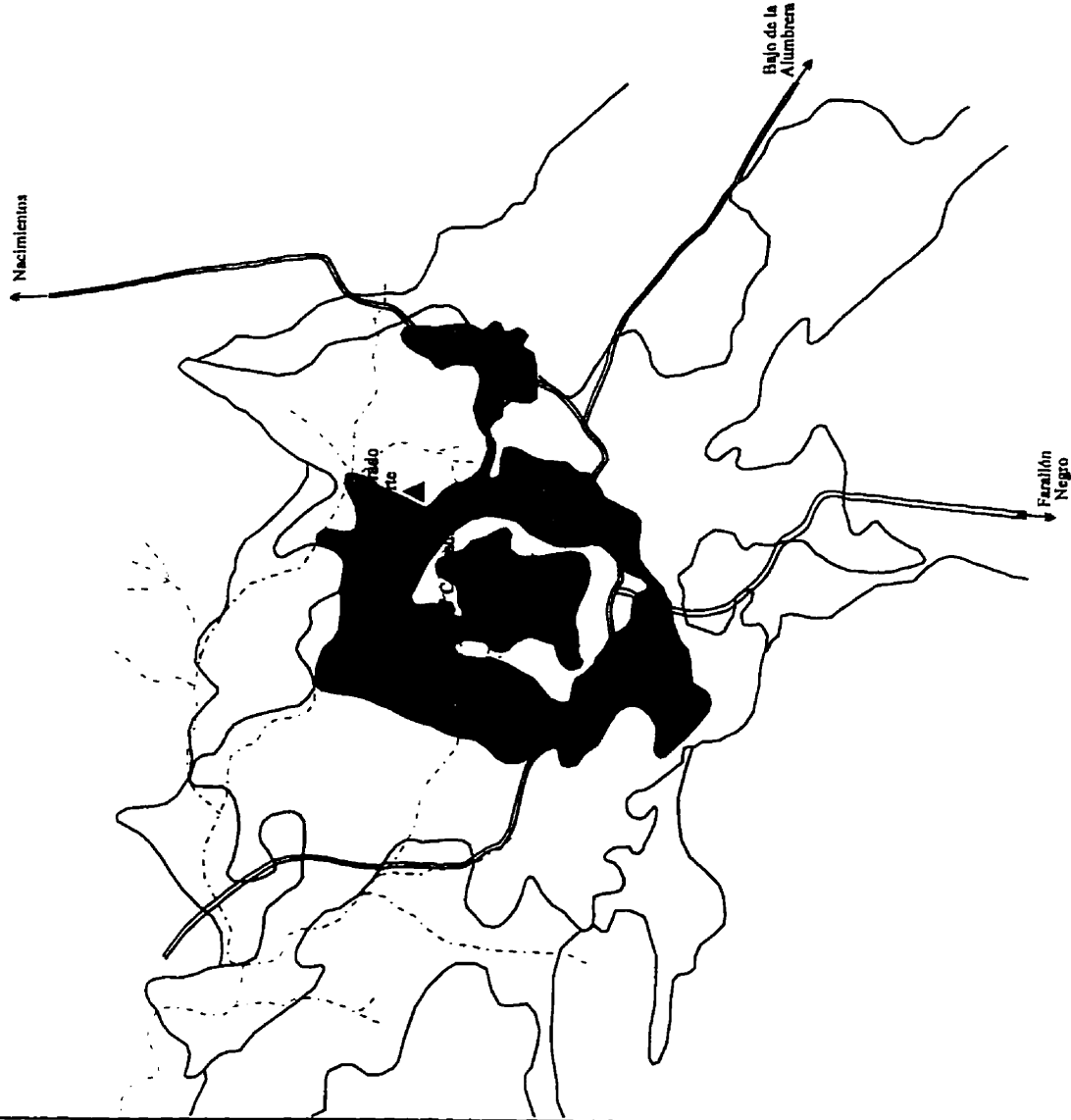
Silicic



Propylitic



Phyllic



secondary K-feldspar or biotite is documented. That Bajo de Agua Tapada may represent a higher erosional level than Bajo de la Alumbrera is suggested by the non-exposure of a true potassic alteration zone, the weaker intensity of the quartz-magnetite alteration, and the presence of radially-oriented epithermal-style jasperoid veins, best developed in the northern portion of the prospect. The latter consist of zones up to 5m-wide of intense silicification with argillic alteration envelopes (Fig. A-8). Very little sulphide or copper oxide is observed at surface.

Bajo de Agua Tapada is located on the periphery of the Farallón Negro Volcanic Complex and may therefore have been emplaced in a more superficial position within the volcanic pile than most other deposits within the stratocone. Host-rocks include tuffaceous facies, characteristic of the outer NW rim of the exposed stratocone, which are difficult to recognize through the alteration overprint.

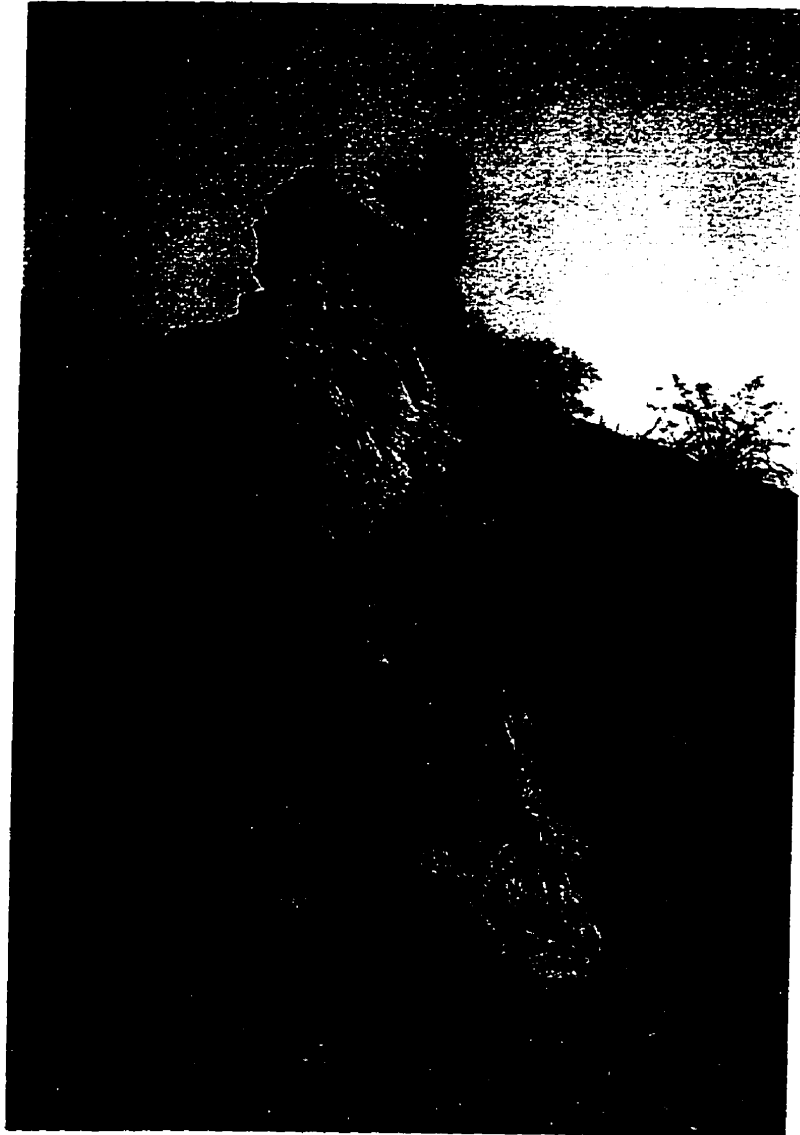
### ***Mineralization***

Mineralization at Bajo de Agua Tapada consists of disseminated and veinlet porphyry-style mineralization associated with the dacite porphyry intrusion and peripheral, fracture-controlled, late-stage veins. Supergene enrichment is not significant.

Surface lithogeochemistry (Suchomel, 1985) reveals several moderate copper, lead, zinc, cadmium and gold anomalies. Contents greater than 500 ppm Cu, Pb and Zn and greater than 0.26 ppm Au are reported within the "potassic alteration" zone. The mineralization is disseminated and in veinlets, and is zoned with respect to alteration. Minor disseminated chalcopyrite and scarce pyrite-chalcopyrite veinlets are associated

**Figure A-8.**

Jasperoid vein at Bajo de Agua Tapada. View to the NW along the axis of the vein, which is located in the south branch of an unnamed *quebrada* south of the Agua Tapada Camp (see figure A-5). Note: the geological hammer for scale in the centre of the vein.



with abundant quartz-magnetite, magnetite and magnetite-pyrite veinlets in the "potassic" zone. Quartz-magnetite and magnetite veinlets, locally abundant, contain up to 0.26 g/t Au. A 206 m drill-hole collared on the SW border of the "potassic" zone averaged 242 ppm Cu and 0.11 ppm Au, both metals increasing with depth. Several other drill-holes located peripherally to the potassic alteration zone revealed anomalous Au (up to 14 ppm) but no Cu. There appears to be a strong association of anomalous Au values with zones of silicification. In the outer extensions of the phyllic zone, a slight decrease in pyrite content coincides with abundant disseminated sphalerite and galena. In general, there is very little chalcopyrite in the system but impressive occurrences of massive galena and sphalerite were encountered on surface and in drill-core from the periphery of the phyllic zone (B.J. Suchomel, pers. comm., 1994).

Few precious metal anomalies are reported from the jasperoid veins (Suchomel, 1985), whereas Pb and Zn values are generally high (>500 ppm). Arsenic and mercury are not anomalous. The highest Au value is 2.2 g/t Au and Ag attains 174.0 g/t. The jasperoid vein system has not been tested by drilling.

Several base metal sulphide veins with high precious metal contents occur at the eastern periphery of the prospect (La Josepha sector). These veins are 10 to 50 cm in width and locally exhibit collomorphic banding and brecciation. They are hosted by andesite breccias. Alteration envelopes consist of sericite  $\pm$  quartz. The vein mineralogy comprises quartz, calcite, barite, pyrite, chalcopyrite, sphalerite and galena.

Manganese-quartz-carbonate veins with high silver contents are located in the western periphery of the prospect (La Jovita sector). These veins are similar in appearance

to those currently being exploited at Alto de la Blenda. They are characterized by black pyrolusite and banded white quartz. They are locally brecciated and contain clasts of jasperoid.

A 14,600 m dipole-dipole IP survey is recorded in a report by Chipulina and González (1983). They report a moderate geophysical response with poor definition down to 200 m depth. However, problems with many aspects of the surveys, as reported in the above paper, render the results questionable.

## **Bajo El Durazno**

### ***Location and Access***

The Bajo El Durazno prospect (Figs. A-1 and A-9) is located 10 km ENE of the Farallón Negro mine-site and 4 km north of Bajo de la Alumbreira. It may be reached by road from either the main Farallón Negro - Nacimientos access road or from Bajo de la Alumbreira.

### ***Previous Work***

This deposit was discovered in 1968 and is mentioned briefly in several reports dealing with the deposits in the region. The deposit has been described in more detail by García (1969) and Sillitoe (1973), and particularly by Allison (1984; 1986), in a Master's thesis at the University of Arizona under the supervision of John M. Guilbert and in collaboration with the United Nations. Various reports by Y.M.A.D. and Fabricaciones



**Figure A-9.**

*Bajo el Durazno.*

View to the west of the central and southern quadrants of the Bajo el Durazno prospect, taken from the highest point underlain by the eastern body of Durazno Andesite (see figure A-10). Dark hills in the right-foreground are underlain by potassic and quartz-magnetite alteration zones in the central body of Durazno Andesite. Bleached hills are eroded into phyllically-altered Durazno Andesite and breccias and flows of the Farallón Negro Volcanic Complex. The rounded ridge in the foreground is underlain by an unaltered body of Durazno Andesite. The strata exposed behind the deposit and on the horizon are breccias, flows and intrusions of the Main Farallón Negro Stratovolcano. The northwest edge of the Bajo de la Alumbrera deposit is visible to the upper-left (pale zone).



Militares geologists are also available. The prospect has been explored by an extensive surface lithogeochemical sampling program in which 653 rock-chip samples collected on a 50 m grid were analyzed for copper, gold and molybdenum. Nine drill-holes were completed from 1968 to 1976. Recursos Americanos Argentinos S.A. conducted a reverse circulation drill program in August 1993. In early-1994, Placer Dome conducted a limited surface geochemistry program, a magnetometer survey and a five-hole drill program. On this basis, they returned the mineral rights to Y.M.A.D.

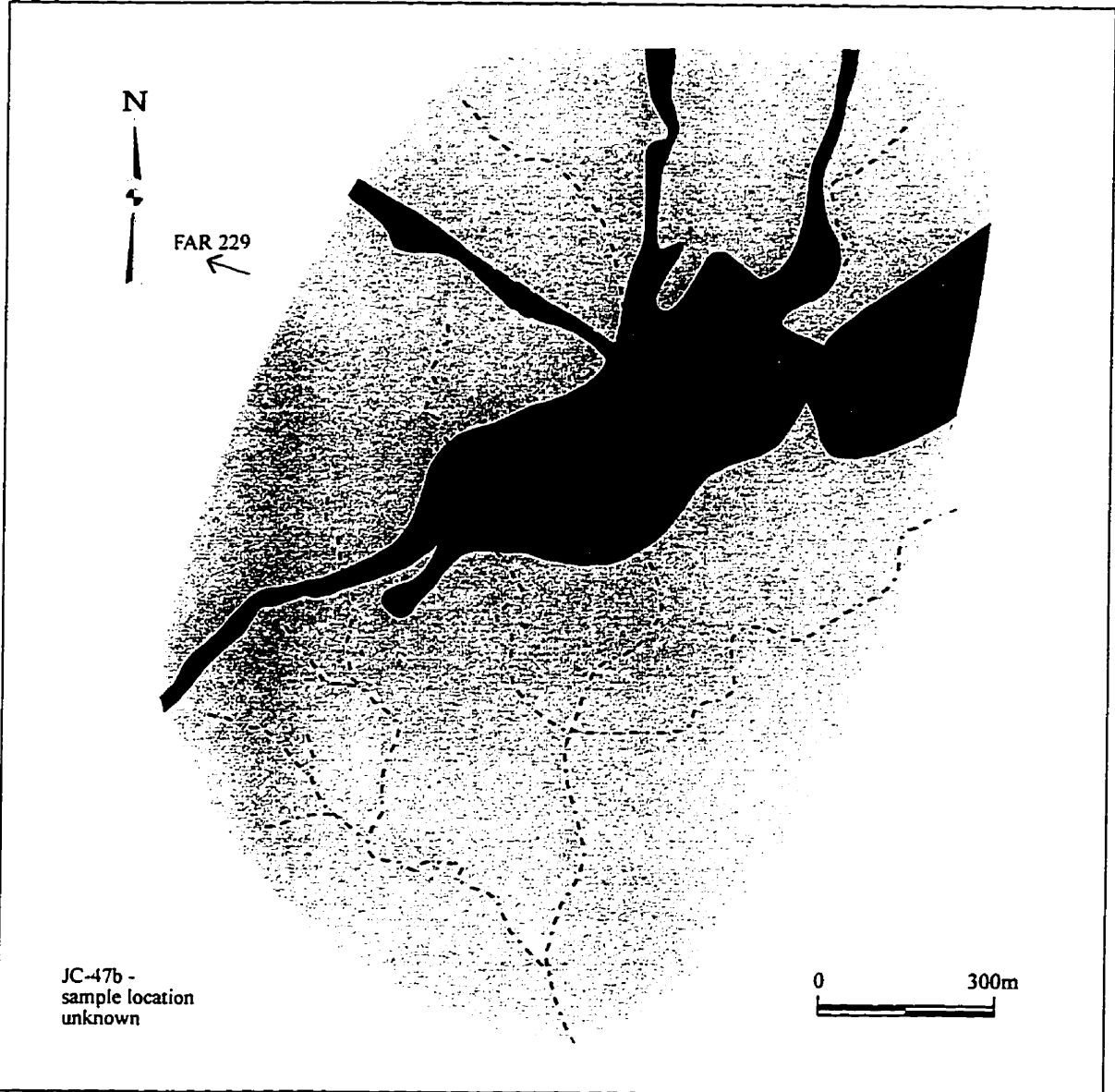
### *Geological Relationships*

The Bajo El Durazno deposit is hosted by a composite andesite porphyry stock hosted by andesite breccias and flows of the Farallón Negro Volcanic Complex (Fig. A-10). Several pulses of andesitic intrusion are inferred for the main stock, followed by the intrusion of andesite porphyry dykes that extend in a crudely radial pattern from the stock. Andesitic intrusions were also emplaced to the east, west and south of the central stock, and exhibit weak propylitic alteration. Four samples of andesitic intrusive rocks, from the main stock and the east and west intrusives, yield ages of between 8.15 and 8.46 Ma (Chapter 5). The similar ages and, in the case of the samples from the east and west andesite intrusions, almost identical whole-rock geochemistry suggest that they represent apophyses of a larger stock at depth.

The deposit consists of a central core of intense quartz-magnetite alteration (Fig. A-11) surrounded by a zone of potassic alteration which is dominated by biotite, although secondary potassium feldspar is reported by Sillitoe (1973) (Fig. A-12). Allison (1986)

**Figure A-10.**

Geology of the Bajo el Durazno prospect.



# BAJO EL DURAZNO GEOLOGY

After Allison (1986) and present study

A.M. Sasso, 1997

- Andesite porphyry
- Andesitic volcanic breccia
- Contact: observed (solid), inferred (dashed)
- Quebrada

**Figure A-11.**

*Quartz-magnetite alteration at Bajo el Durazno.*

**A.** Intense quartz-magnetite veining in the central andesite porphyry stock located in the middle branch of Quebrada el Durazno (see figure A-12).

**B.** Hand sample of the above illustrating the banded texture of the quartz-magnetite veins.

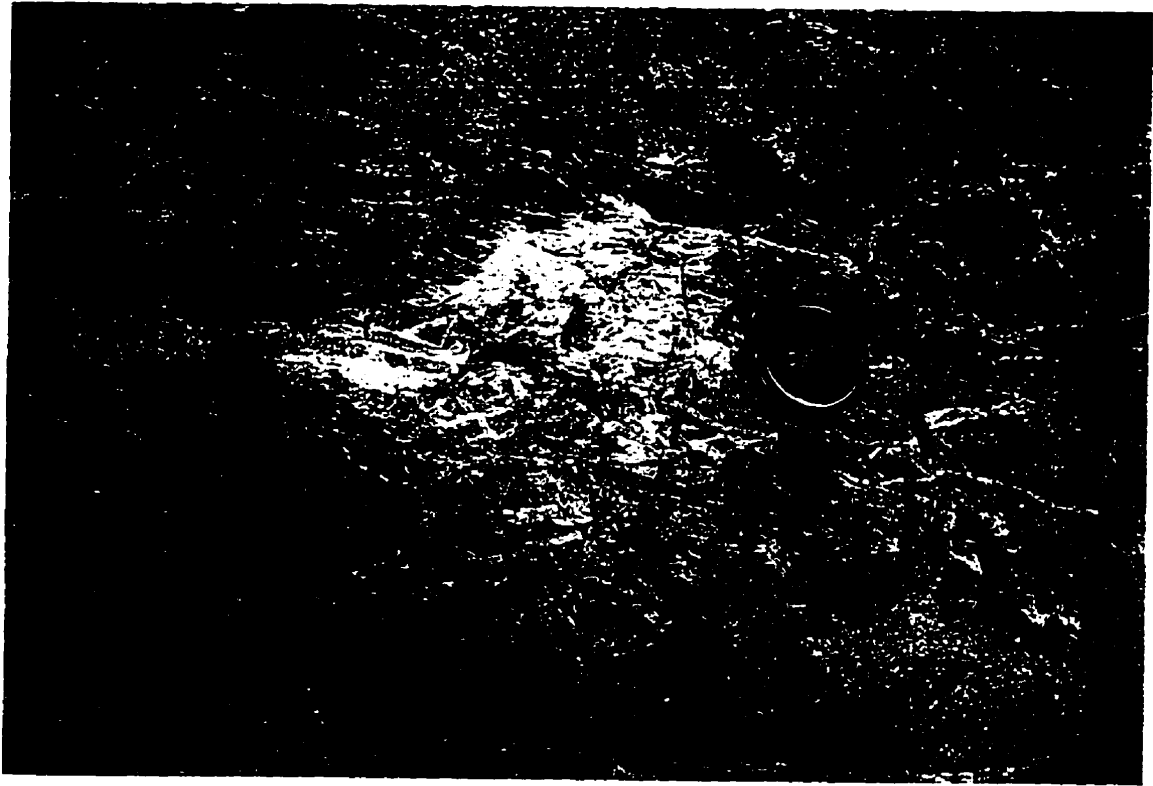
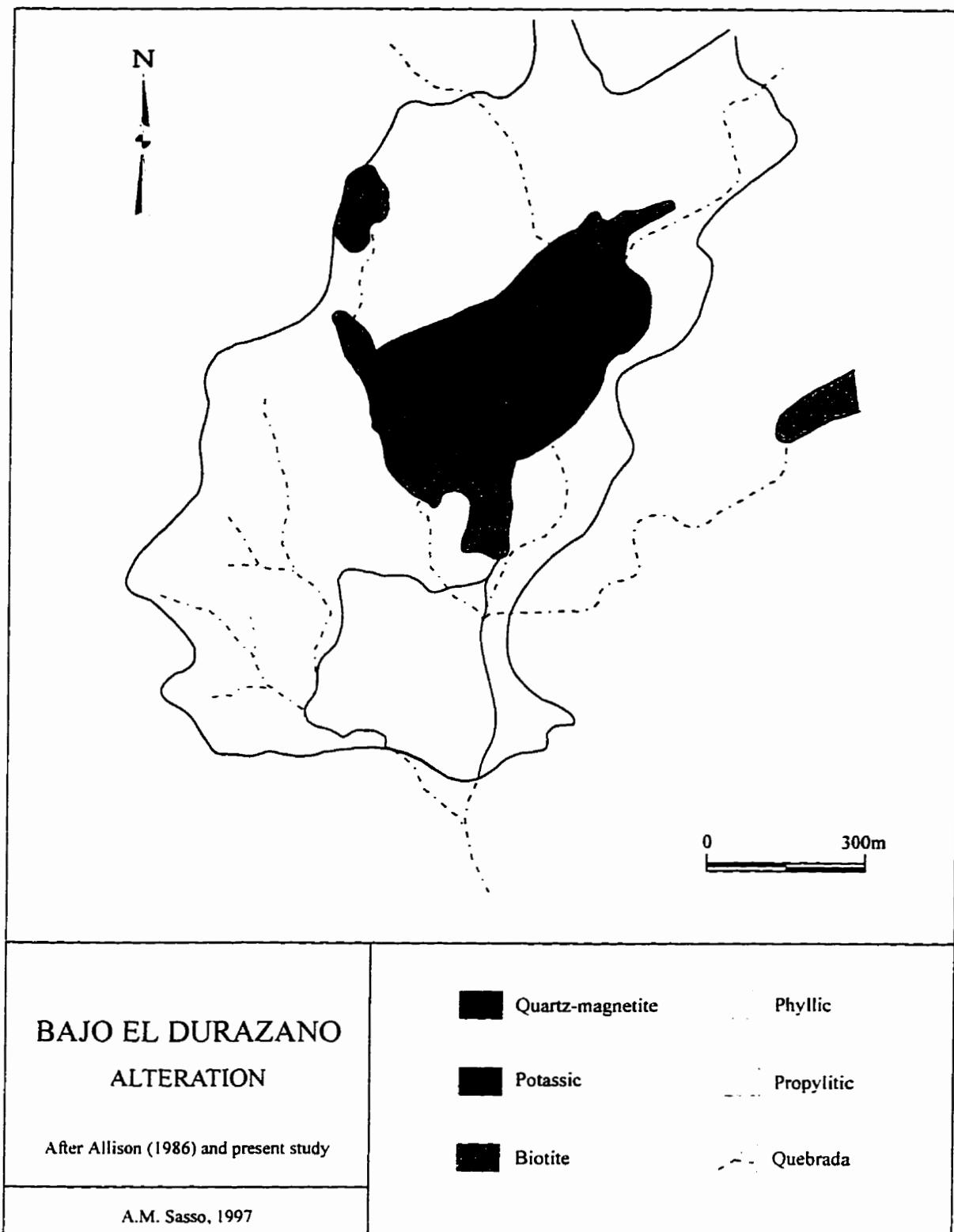


**Figure A-12.**

Alteration facies of the Bajo el Durazno prospect.





reports less than 10% secondary K-spar, discernible only in thin section after staining. A phyllic halo is developed in the central andesite stock (Fig. A-13) and is itself surrounded by a peripheral propylitic zone.

### ***Structure***

The Bajo El Durazno deposit is located to the NE, and outside, of the main NW-SE structural corridor (Chapter 2) that transects the Farallón Negro Volcanic Complex. Some dykes strike NW-SE, but this is not a dominant structural orientation. Thus, the main andesite porphyry stock and the associated alteration halo are elongated NE-SW, coinciding with the elongation direction of Bajo de la Alumbrera. The two deposits lie along a line which trends N30°E.

### ***Mineralization***

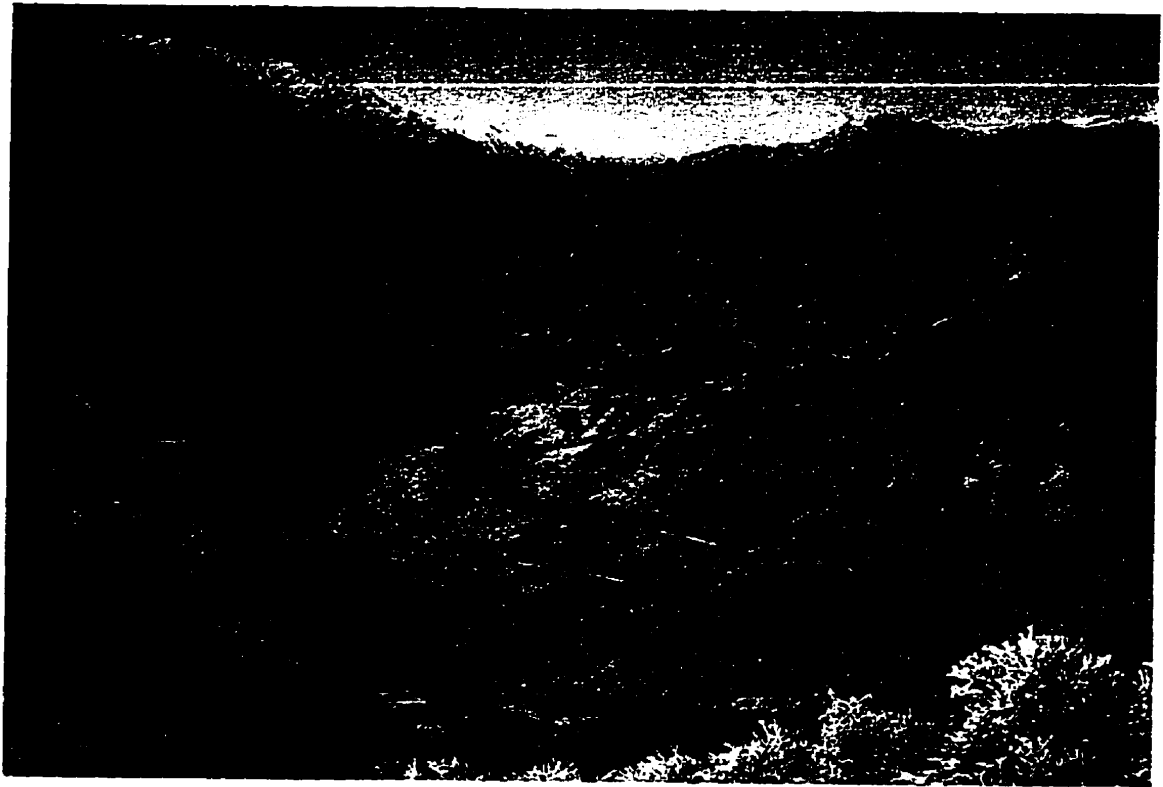
Mineralization is of Cu and Au with minor Ag and Mo. Sulphides are not abundant on surface and are largely disseminated. They are virtually absent in some marginal parts of the potassic alteration zone. The bulk of the mineralization occurs as veins within the stock and its wallrocks, containing quartz, calcite, magnetite, pyrite and chalcopryrite, with lesser sericite, chlorite, orthoclase, biotite, siderite, molybdenite, bornite, sphalerite, galena, tetrahedrite-tennantite and native gold (Allison, 1986). A limited electron microprobe study (Allison, *op. cit.*) revealed that some of the Au and Ag occurs in solid solution in sulphide minerals. A narrow zone of silicified hydrothermal breccia with interstitial chalcopryrite and bornite is located on the western edge of the

**Figure A-13.**

*Phyllic alteration at Bajo el Durazno.*

**A.** Southern extremity of phyllic alteration zone (view to the south). Areas of rusty-weathering are characterized by more intense silicification and more abundant pyrite than the bleached outcrops. Photo taken on the eastern edge of the phyllic zone. The central portion of the deposit (potassic and quartz-magnetite alteration zones) is to the left, out of the view of the photo.

**B.** Outcrop of phyllically-altered andesite. Note the intense hydrofracturing and abundance of oxidized minerals, including jarosite (yellowish patches, not easily discernable at this scale), along the fracture surfaces. Located in the northwest branch of the Quebrada el Durazno, south of the biotite alteration zone (see figure A-12).



potassic core.

Supergene enrichment appears to be absent and "limonite" is sparse, but oxidation extends to 26 m depth in drill-core (Sillitoe, 1973). Malachite and delafossite are common at surface. Sillitoe (op. cit.) concluded that the rarity of pyrite in the potassic alteration zone may account for the absence of enrichment, promoting oxidation *in situ*.

Mineralization is confined to the potassic and quartz-magnetite alteration zones. The highest surface geochemical levels are associated with the intense quartz-magnetite alteration. Surface geochemistry (Fabricaciones Militares) revealed a central anomaly of 180 to 1700 ppm Cu, 13 to 68 ppm Mo and 0.11 to 1.55 ppm Au. Resampling by both Recursos Americanos and Placer confirmed the anomalous values. Core recovery during the Fabricaciones Militares drill program was poor, and the significance of the results is uncertain. Hypogene grades in the central stock range from 0.1 to 0.3% Cu with local intersections of 0.4 to 0.5% Cu. Grades in holes drilled within the outer zone of feldspar-destructive alteration are low (0.01 to 0.02% Cu). Details of the drill programs by Recursos and Placer are not known, but the results were evidently discouraging.

## **Bajo de San Lucas**

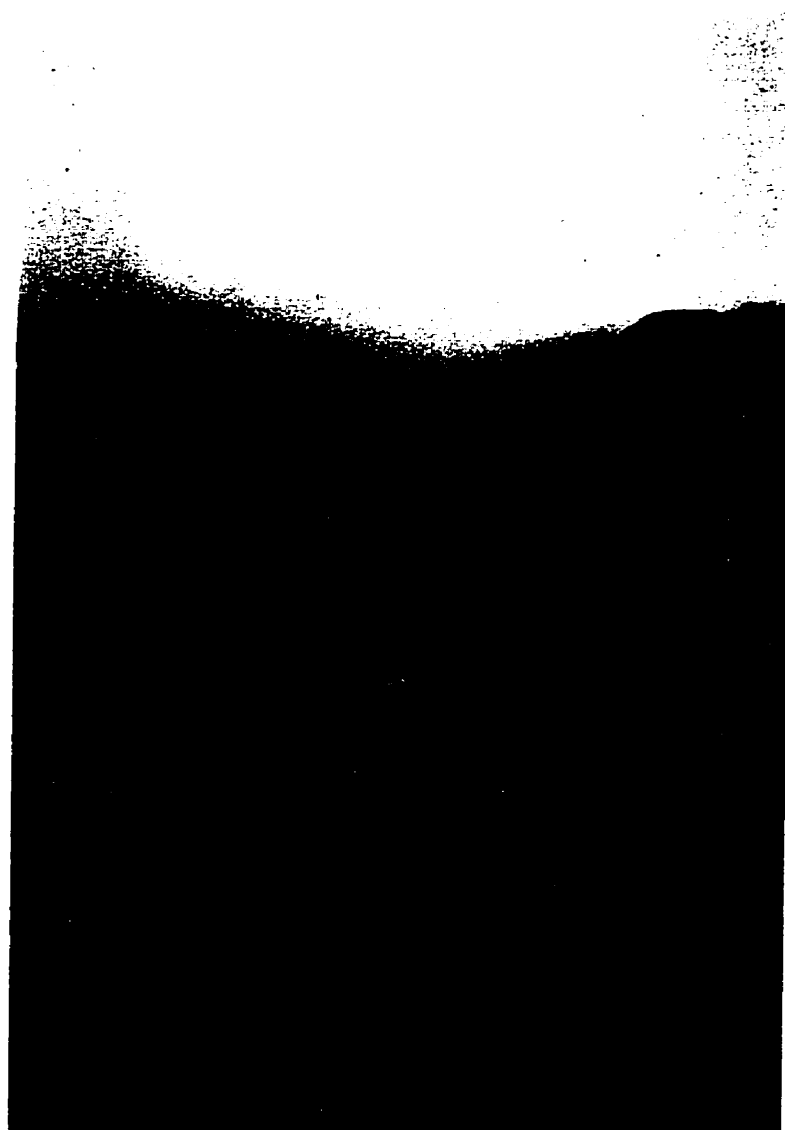
### ***Location and Access***

Bajo de San Lucas (Figs. A-1 and A-14) is located approximately 6 km SSE of Bajo de la Alumbrera. Access is by four-wheel drive vehicle along the rugged Vis Vis river valley to the small community of Vis Vis, and thereafter by foot or horseback.

**Figure A-14.**

*Bajo de San Lucas.*

View to the NW along the main unnamed *quebrada* which transects the Bajo de San Lucas prospect. The small hill in the centre of the photo capped with dark outcrop is underlain by the quartz-magnetite alteration zone developed in dacite porphyry (see figures A-15 and A-17). Lithological contacts are masked by vegetation at the scale of the photograph, but the central portion of the *quebrada*, in front of the quartz-magnetite altered hill is underlain by dacite porphyry. The vegetation-covered hills, in the foreground and extending beyond the location of the people are underlain by granitic basement.



### ***Previous Work***

Maisonave and Guillou (1969); García (1971); Sillitoe (1973) document the Bajo de San Lucas prospect. All maps in Maisonave and Guillou (1969) and Sillitoe (1973) (reproduced in Durand, 1980) have the north-arrow erroneously pointing due west. Caelles *et al.* (1971) record a K-Ar date from the prospect. Lithogeochemical assays of greater than 2000 ppm Cu and 150 ppm Mo are recorded by García (op. cit.) from the central zone of the *bajo*. Of eight shallow drill-holes completed, six holes tested the potassic alteration zone and indicated hypogene grades of 0.2 to 0.3% Cu (Sillitoe, 1973); Mo values were low (García, 1971).

### ***Geological Relationships***

The Bajo de San Lucas hydrothermal system is hosted by Paleozoic basement rocks upthrown to the south of the Farallón Negro Volcanic Complex (Fig. A-15). The deposit is located at the contact between the Ordovician Capillitas granite and the phyllites of the Suncho Formation. This contact is intruded by an oval-shaped diorite body, similar in appearance to the Alto de la Blenda monzonite, with a long axis trending NW-SE. The diorite is itself intruded by a 7.35 Ma dacite porphyry unit which is interpreted to be the source of the mineralizing fluids. The deposit consists of a small core-zone (ridge) of intense quartz-magnetite stockwork alteration surrounded by potassically-altered dacite and diorite (Figs. A-16 and A-17). The zone of potassic alteration at Bajo de San Lucas is the largest of those exposed amongst Farallón Negro porphyry prospects, including Bajo de la Alumbreira. The host granites have also



**Figure A-15.**

Geology of the Bajo de San Lucas prospect.

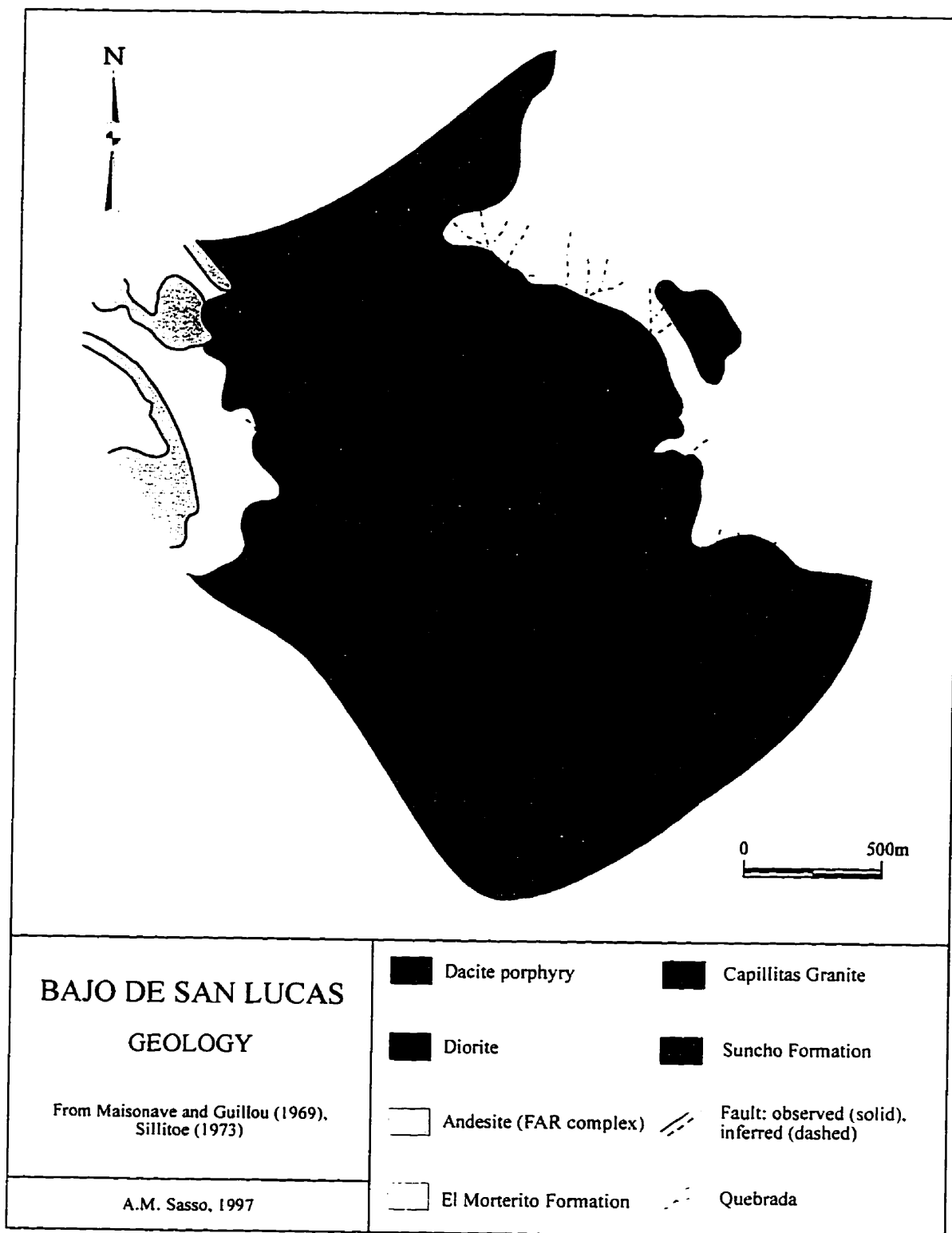


**Figure A-16.**

Quartz-magnetite veining at Bajo de San Lucas. Photo taken in the main *quebrada*, on the south edge of the quartz-magnetite alteration zone (see figures A-14 and A-17).

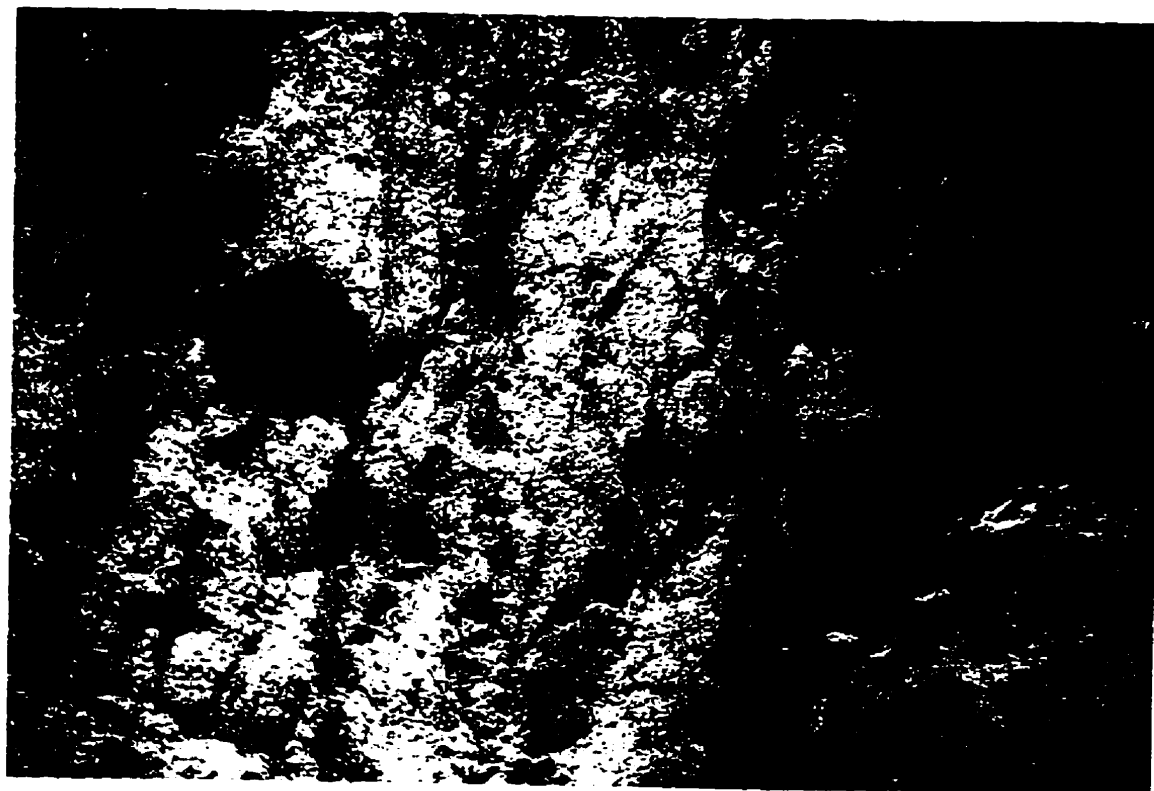
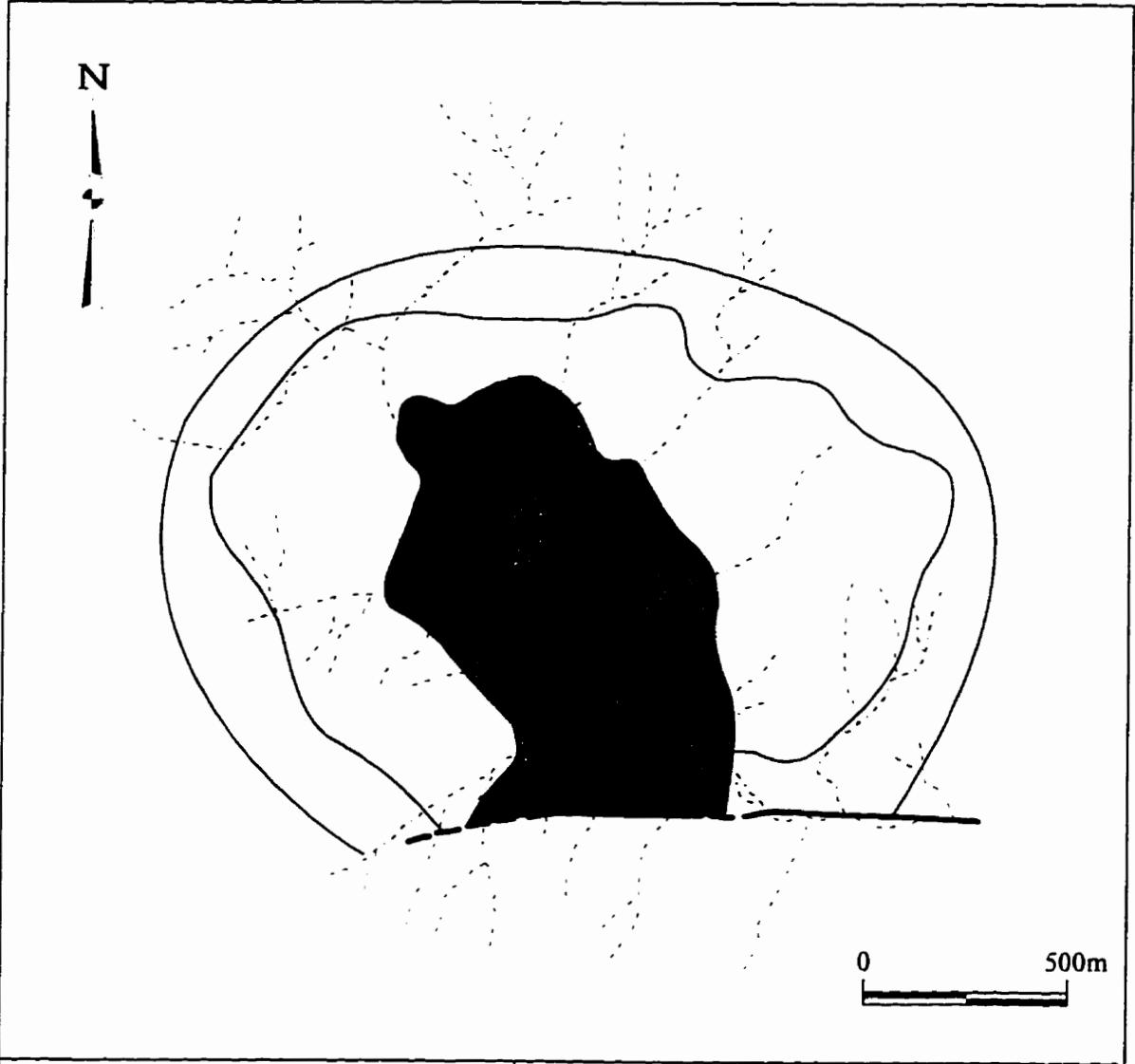


**Figure A-17.**

Alteration facies of the Bajo de San Lucas prospect.



**BAJO DE SAN LUCAS**  
**ALTERATION**

From Sillitoe (1973)

A.M. Sasso, 1997

- |                        |  |
|------------------------|--|
| Sericitic (+ argillic) | Quartz-magnetite                           |
| Propylitic             | Fault: observed (solid), inferred (dashed) |
| Potassic               | Quebrada                                   |

undergone intense phyllic alteration. Rock-type strongly influenced the nature of the alteration assemblage, with potassium-silicate alteration restricted to the diorite and dacite porphyry and sericitic alteration occurring mainly in the granite, although the latter extends peripherally into phyllites and El Morterito sandstones (Sillitoe, 1973). The valley of the Río de San Lucas displays widespread jarosite staining and small zones of intense quartz-pyrite veining within the dacite porphyry. Minor occurrences of copper oxides along fractures are encountered in some of the subsidiary *quebradas*. Vegetation is much more abundant at Bajo de San Lucas than at the prospects within the main Farallón Negro Volcanic Complex.

### ***Structure***

The Bajo de San Lucas intrusive bodies and alteration zone are elongated NW-SE, and may have been controlled by a southeast extension of the NW-trending Farallón Negro extensional corridor. Sillitoe (1973) reports a major fault to the west which due to the erroneous orientation of his map is herein interpreted to lie to the south of the zone. It transects the diorite and may offset alteration assemblages (Sillitoe, *op. cit.*).

### ***Mineralization***

Durand (1980) notes that petrographic (transmitted and reflected light) studies have been conducted on samples from the area, but no published results were encountered. Very little is known about the occurrence of the ore minerals. Sillitoe (1973) reports the presence of chalcopyrite and lesser pyrite from the potassic alteration zone.

Supergene alteration is weakly developed at Bajo de San Lucas. As reported by Sillitoe (*op. cit.*), oxidation extends to less than 13 m in six of the eight diamond-drill holes completed on the prospect. Oxidation extended to deeper levels in the remaining drill-holes and is underlain by sulphide-enriched ore, which attains grades of 0.5% Cu. The irregularity of the enrichment is attributed to local permeability differences.

Lithogeochemical sampling detected anomalies of greater than 260 ppm Cu which are restricted to the potassic and quartz-magnetite alteration zones (Sillitoe, 1973). Maisonave and Guillou (1970) document an anomalous zone exceeding 500 ppm Cu. Mo anomalies are situated marginally to the Cu anomalies. Analyses of drill-core returned high grades of 0.6 to 1.0 g/t Au in three of the drill-holes, but Sillitoe (*op. cit.*) questioned the accuracy of the assays.

A dipole-dipole I.P. survey by Plan NOA over Bajo de San Lucas is briefly mentioned in a report by Chipulina and González (1983). A 9400 m survey with 100 m line-spacings indicated the presence of mineralization up to depths of 150 m. However, problems affecting many aspects of the surveys, as reported in the above paper, render the results questionable.

## **Bajo Las Pampitas**

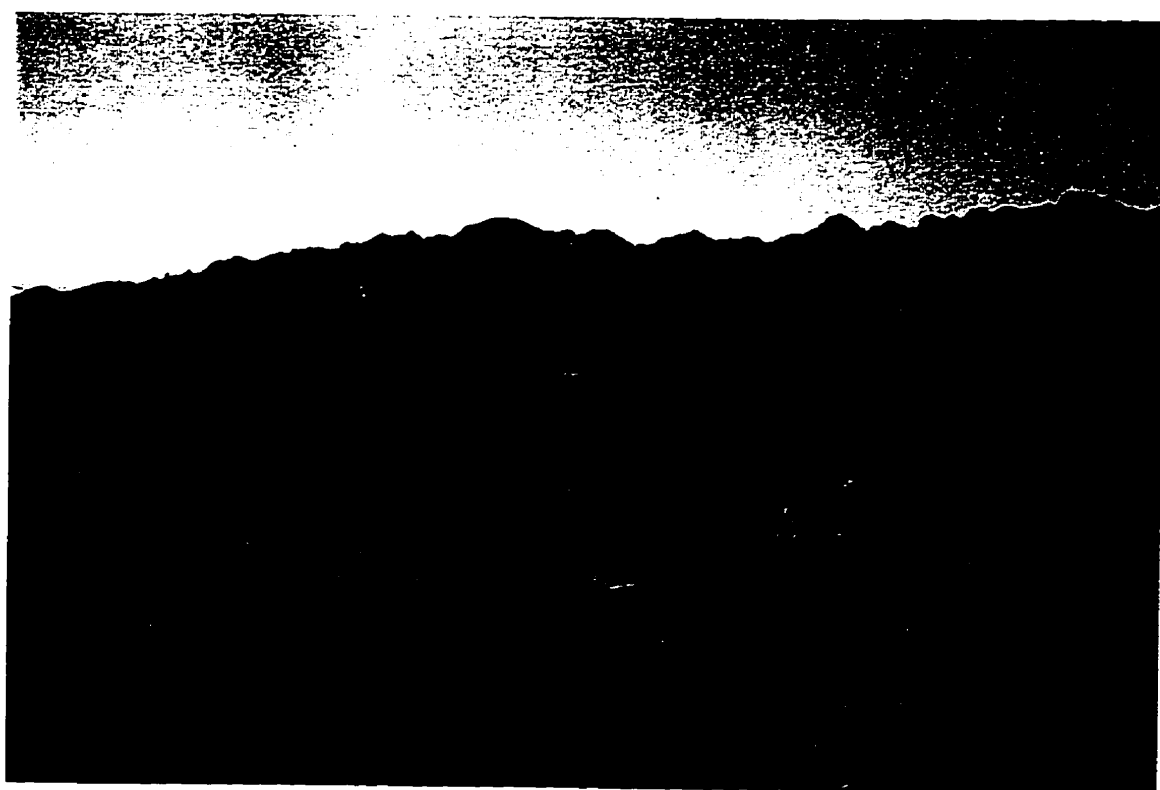
### ***Location and Access***

Bajo Las Pampitas (Figs. A-1 and A-18) is located along the southern access road to Bajo de la Alumbrera from the Farallón Negro mine-site. It is approximately 3 km NNW of Bajo de la Alumbrera.



**Figure A-18.**

Bajo Las Pampitas prospect (view to the NE). The central dark conical hill is underlain by rhyodacite porphyry with intense, sheeted quartz-magnetite veining. The low alluvium-covered *pampitas* may be underlain by phyllic alteration. The ridgeline of the Sierra Durazno is seen on the horizon.



### ***Previous Work***

Maisonave and Guillou (1969), García (1970), Sillitoe (1973), Bassi (1987) and Bucci (1994) have described Bajo Las Pampitas. Rock samples were collected by Maisonave and Guillou (1969) and analyzed for copper and molybdenum. Ten samples from the central zone of the prospect contain between 650 and 2150 ppm Cu (Sillitoe, 1973). Two shallow holes have been drilled on the prospect, but core recovery was poor. García (*op. cit.*) reports assays as high as 0.43 g/t Au from the central zone.

### ***Geological Relationships***

The Bajo las Pampitas prospect lies astride the contact between the Alto de la Blenda monzonite and an intrusion of andesite porphyry (Fig. A-19). The centre of the *bajo* is intruded by a small rhyodacite porphyry stock, the northeast quadrant of which has undergone intense quartz-magnetite stockwork veining and replacement (Fig. A-20). Sulphides are not abundant but minor copper oxides are encountered along the eastern margin of the rhyodacite stock. The central hills are surrounded by a low-lying zone, covered mainly by alluvium and colluvium. Several small dacite porphyry dykes are exposed in the *bajo* (Fig. A-21). Sillitoe (1973) reports potassic alteration of the central stock, but this is not observable in the field. Samples collected during 1993 from the central zone consisted largely of sheeted quartz-magnetite veins and veinlets, and staining studies by Bucci (1994) did not indicate the presence of potassium-feldspar.

**Figure A-19.**

Geology of the Bajo Las Pampitas prospect.

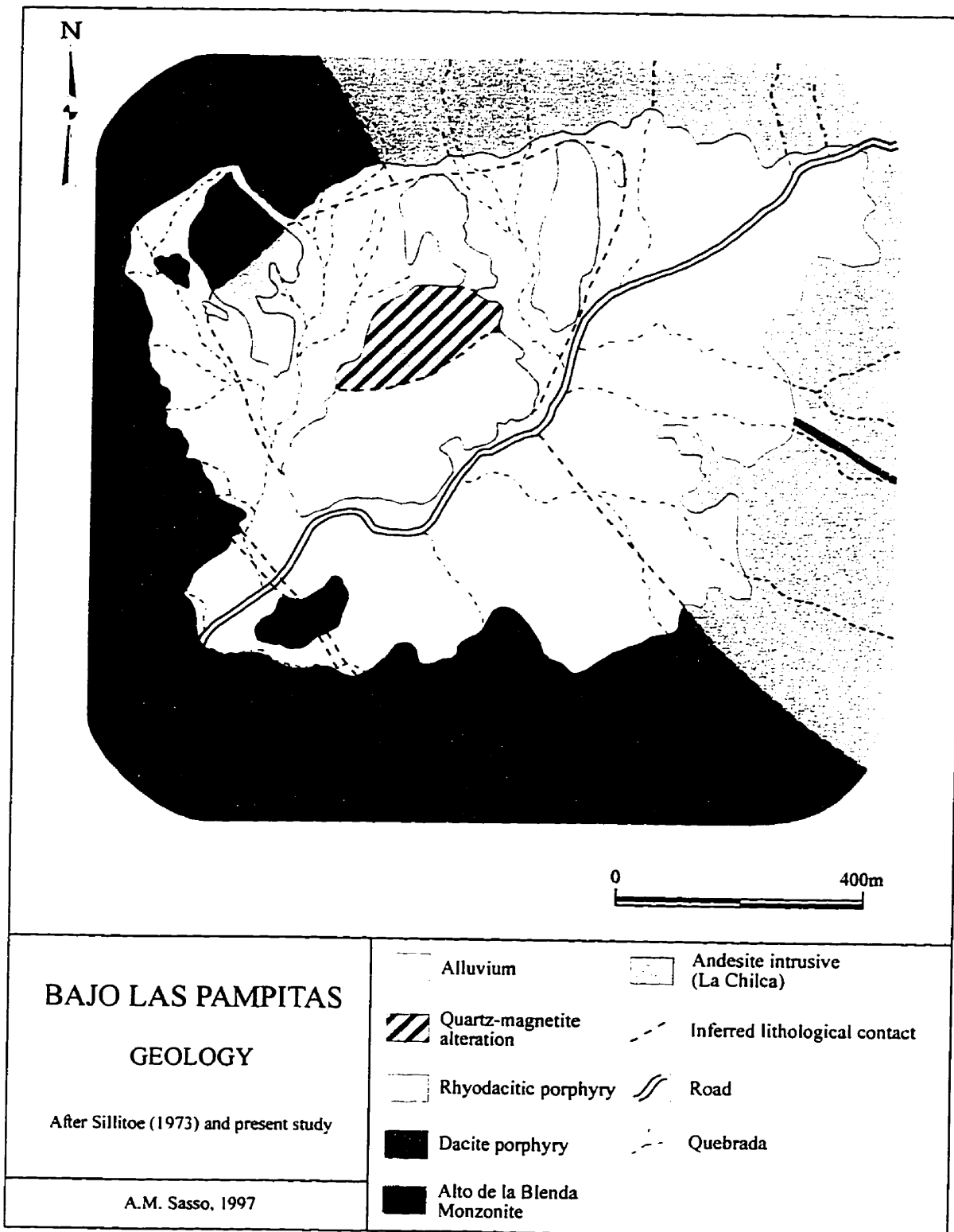


**Figure A-20.**

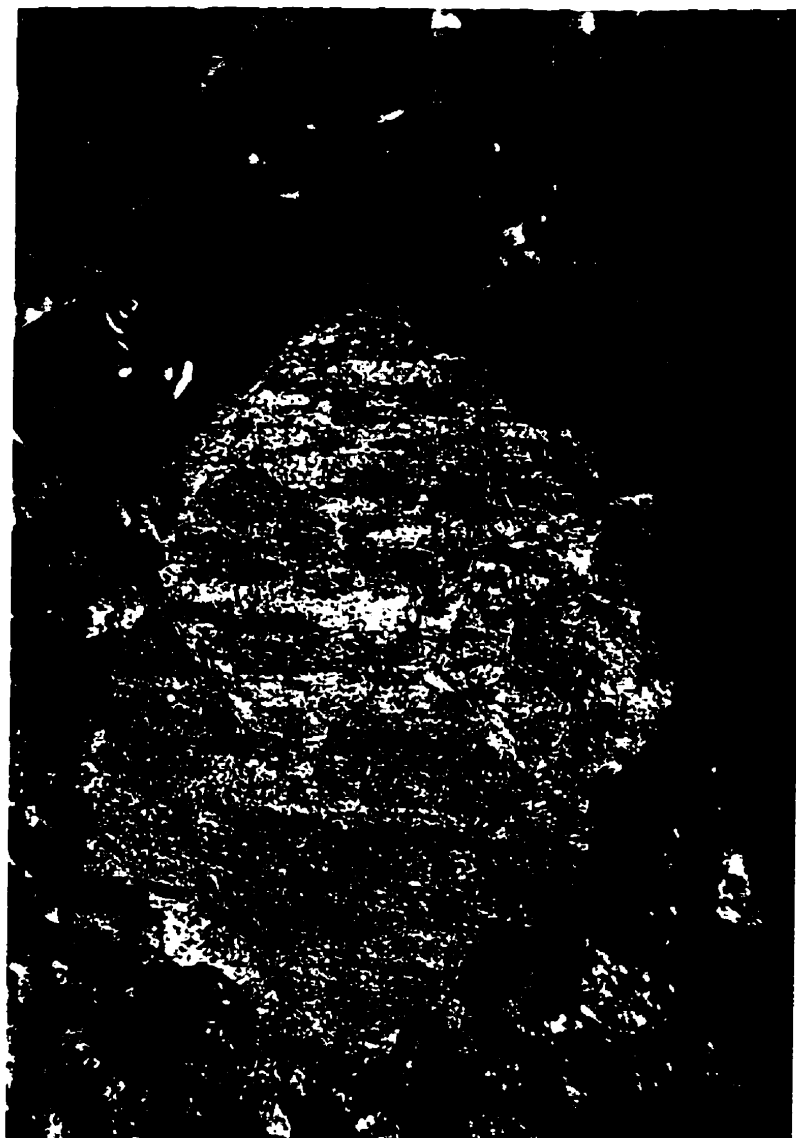
Quartz-magnetite alteration at Bajo las Pampitas. A series of banded, mutually cross-cutting quartz-magnetite veins are seen intruding the central rhyodacite porphyry. Very fine magnetite veinlets appear to pre-date the quartz-magnetite veins. Pyrite veins cut the earlier magnetite-bearing veins.



**Figure A-21.**

Flow-banded dacite porphyry from the NW quadrant of the  
Bajo las Pampitas prospect.





### ***Structure***

Bajo Las Pampitas is located within the NW-trending extensional corridor (Chapter 2) which transects the Farallón Negro Volcanic Complex. The central rhyodacitic intrusion is elongated in a NE direction, whereas the dacite dykes strike NW-SE. Mapping of phyllic alteration is impeded by colluvium, but it is assumed that the flat valley-floor represents more easily eroded material, possibly due to hydrothermal alteration. The valley is slightly elongated to the NE.

### ***Mineralization***

Bassi (1987) provides the most extensive documentation of geochemical and drill-hole results, but it is not clear if this incorporates new analyses or is simply a re-iteration of previously existing data.

Two drill-holes on the property have reported recoveries of only 15 - 20%. DDH 1 is located to the NE of the central quartz-magnetite zone within the colluvium-covered area. It is a 37 m hole that intersects 28 m of oxidized rock followed by 9 m of hypogene mineralization consisting of pyrite and chalcopyrite. Minor covellite is reported but it is not evident if this represents a hypogene or supergene phase. Average grades for the length of the hole are 0.02% Cu and 0.2 g/t Au, with restricted intervals with up to 0.5% Cu (Bassi, 1987). Sillitoe (1973) reports 0.01% Cu in argillized and some propylitically-altered andesite porphyry, and notes that oxidation extends to the bottom of the hole. DDH 2 is collared within the central silicified rhyodacite hills but to the SW of the outcropping zone of intense quartz-magnetite alteration. The 52 m hole exposed

chalcopyrite and Fe-oxides throughout. Malachite and azurite are reported from the first 25 m and native gold was encountered at 30 m. Average grades are 0.13% Cu and 0.5 g/t Au (Bassi, 1987). Sillitoe (1973) reports 0.15% Cu, largely in oxidized material with minor malachite.

Surface geochemistry over an area of roughly 1 km<sup>2</sup> delimits an anomalous zone, in the central quartz-magnetite zone, with 10 samples containing between 650 and 2150 ppm Cu. It is not clear whether other elements were analyzed. Weakly-anomalous values of 50-100 ppm Cu are encountered in the SW quadrant at the edge of the *bajo*. No regional background values are given. Any anomalies that may exist in the flat area are probably masked by the colluvium.

A geophysical survey (IP) was conducted over the central hills. Vein and veinlet mineralization is shown to continue to 250 m below the surface, with the possibility of disseminated mineralization at depth. Longer profiles were recommended to verify the extent at depth.

## **Bajo La Chilca**

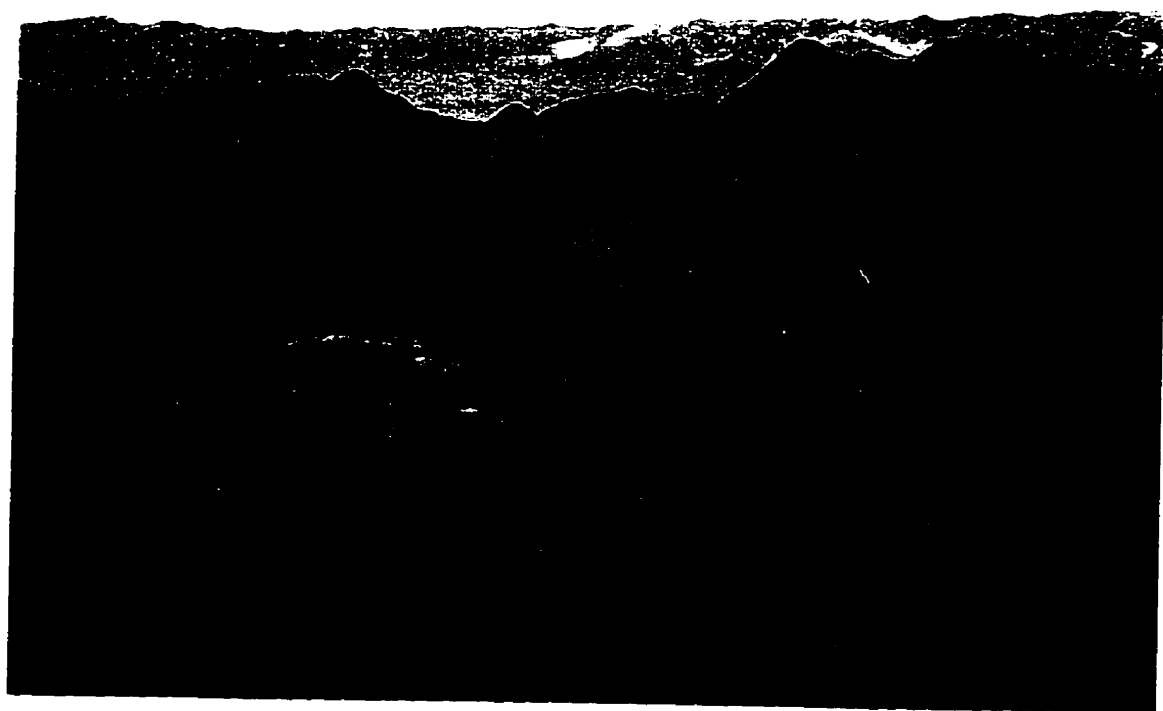
### ***Location and Access***

Bajo La Chilca (Figs. A-1 and A-22), approximately 2 km south of the Farallón Negro mine-site, is accessible by a series of animal trails from the road leading to the slaughterhouse.

**Figure A-22.**

*Bajo la Chilca.*

View to the west of the Bajo la Chilca prospect which is hosted by the largest body of La Chilca Andesite. The low, pale hills in the central valley are eroded into weakly-developed phyllic alteration in the Andesite. A young andesite dyke underlies the low ridge to the right of the central valley and cuts across the alteration zone. The hills in the background (near horizon) are underlain by breccias and flows of the Main Farallón Negro Stratovolcano. The Sierra de Hualfín forms the distant horizon.



### ***Previous Work***

No record of this prospect has been encountered in the literature. Mapping of the prospect was conducted by Mari Carrizo (mine geologist at Farallón Negro until early-1994) for a *seminario* (undergraduate thesis) at the Universidad Nacional de Tucumán in the late 70's. No assays are available.

### ***Geological Relationships***

Bajo La Chilca consists of a small porphyry centre hosted by a large andesite stock, the La Chilca Andesite, with a small central, E-W elongated, zone of potassically-altered dacite (?) bodies, interpreted to represent apophyses of a stock intruding the andesite. The zone of potassic alteration is surrounded by phyllically-altered andesites and a peripheral quartz-carbonate vein swarm (Fig. A-23). The quartz-magnetite alteration common to the other prospects in the region is absent at La Chilca. This may be due to a higher level of exposure. The area is cut by at least three different stages of andesite dykes, two of which appear to be post-mineralization. Sulphides and copper oxides are sparse.

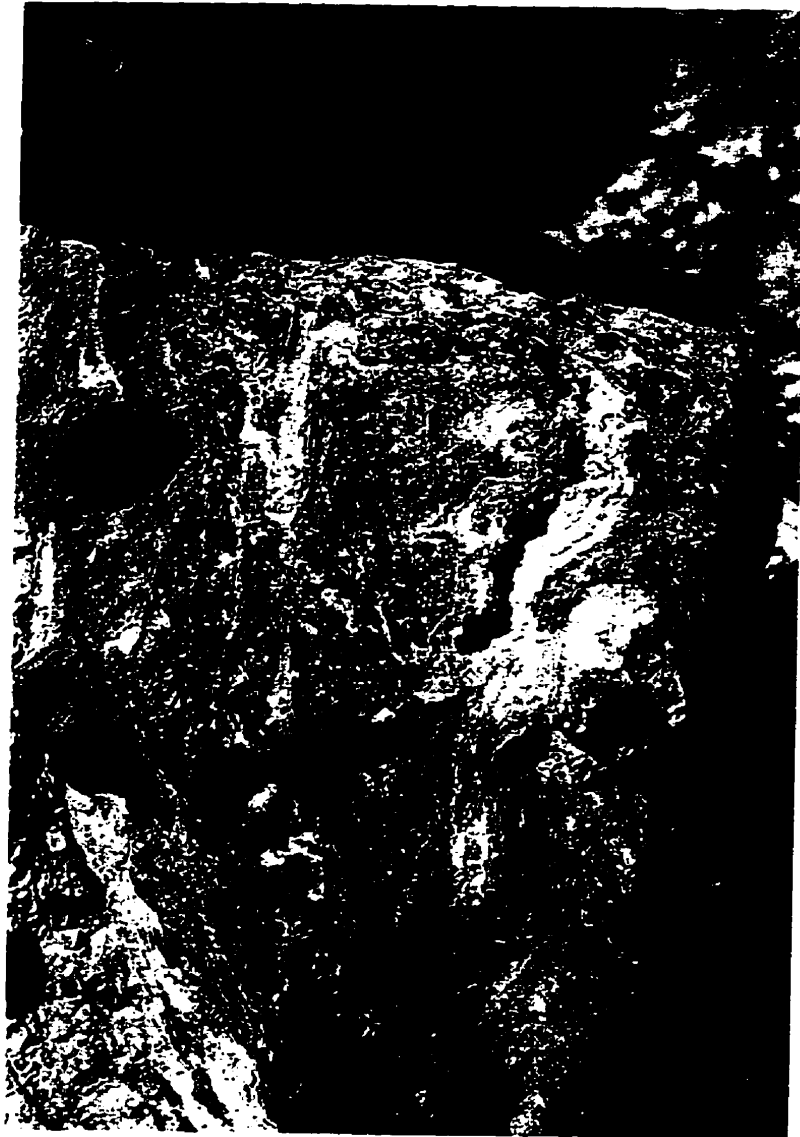
### ***Structure***

The *bajo* appears to be controlled by an E-W trending structure. The zone of potassic alteration is elongated E-W. The epithermal veins are located on the eastern and western margins of the *bajo* and also trend E-W. The northern and southern boundaries of the prospect are marked by high ridges of La Chilca andesites.

**Figure A-23.**

*Quartz-carbonate epithermal veins at Bajo la Chilca.*

A series of E-W-striking quartz-calcite epithermal veins crop out in the eastern and western quadrants of the Bajo la Chilca prospect. The veins exhibit multiple stages of fluid flow and brecciation of the host andesite, and well-developed banding; quartz crystals are commonly observed lining open spaces. No sulphides or manganese-oxides were observed.





## **Bajo Las Juntas**

### ***Location and Access***

Bajo Las Juntas is located approximately 2 km west of the confluence of the Vis Vis and Jaci Yaco rivers (Fig. A-1). Access is by four wheel-drive vehicle south along the Vis Vis river valley and west along the Jaci Yaco river valley to the mouth of Quebrada del Aguila.

### ***Previous Work***

Several unpublished Y.M.A.D. and Plan NOA reports exist on the area, but only an undergraduate thesis by Viruel (1973) and a compilation by Durand (1980) were accessible.

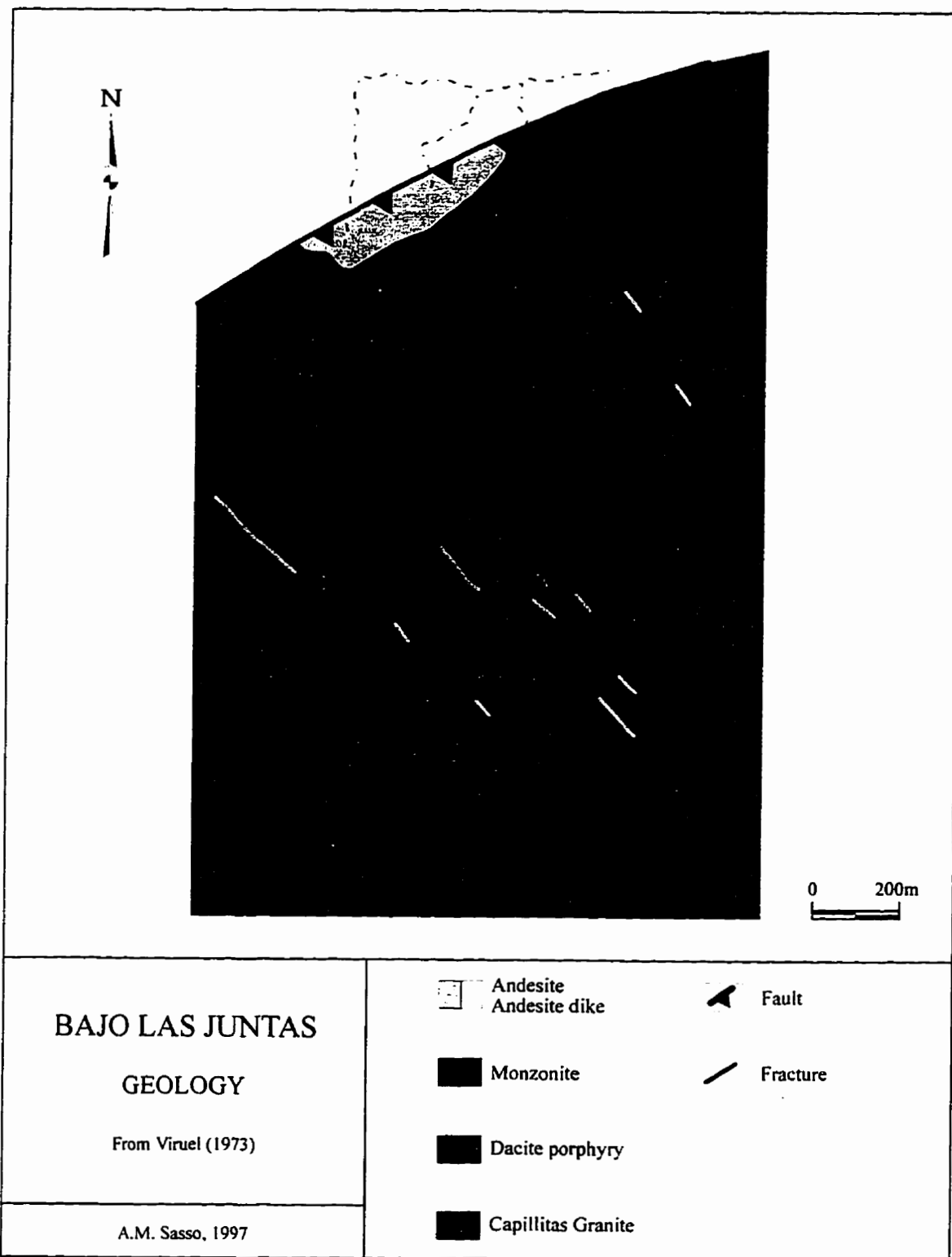
### ***Geological Relationships***

The Bajo Las Juntas prospect is largely underlain by an irregular body of andesite porphyry, hosted by the Capillitas granite (Fig. A-24). It is very similar in field appearance to the Alto de la Blenda monzonite and the Bajo de San Lucas diorite. A dacite porphyry unit also crops out in the area, and it is assumed that this represents a subsequent intrusive stage that may have been responsible for the mineralization. The nature of the dacite porphyry is not clear from the reports. Durand (1980) refers to the intrusions as a sub-volcanic body of "andesitic-dacitic porphyry". Several later andesite dykes also transect the area, one of which yielded an age of 7.59 Ma.

A sequence of andesite breccias crop out to the north of the prospect in the

**Figure A-24.**

Geology of the Bajo las Juntas prospect.



hanging-wall of the Jaci Yaco - El Tigre fault. Their exact relationship to the other units is unclear, but they are interpreted to represent erosional remnants of the southern extension of the Farallón Negro Volcanic Complex.

Alteration is largely confined to the *quebradas* and appears to be lithologically controlled (Fig. A-25). Potassic, silicic and minor quartz-magnetite alteration are developed in the andesite, whereas the Paleozoic granite is affected by phyllic and peripheral propylitic alteration.

### ***Mineralization***

Abundant quartz-pyrite veins and veinlets occur in the granite, in association with zones of silicification. Jarosite and hematite are seen on surface, but no copper minerals were encountered during a brief visit.

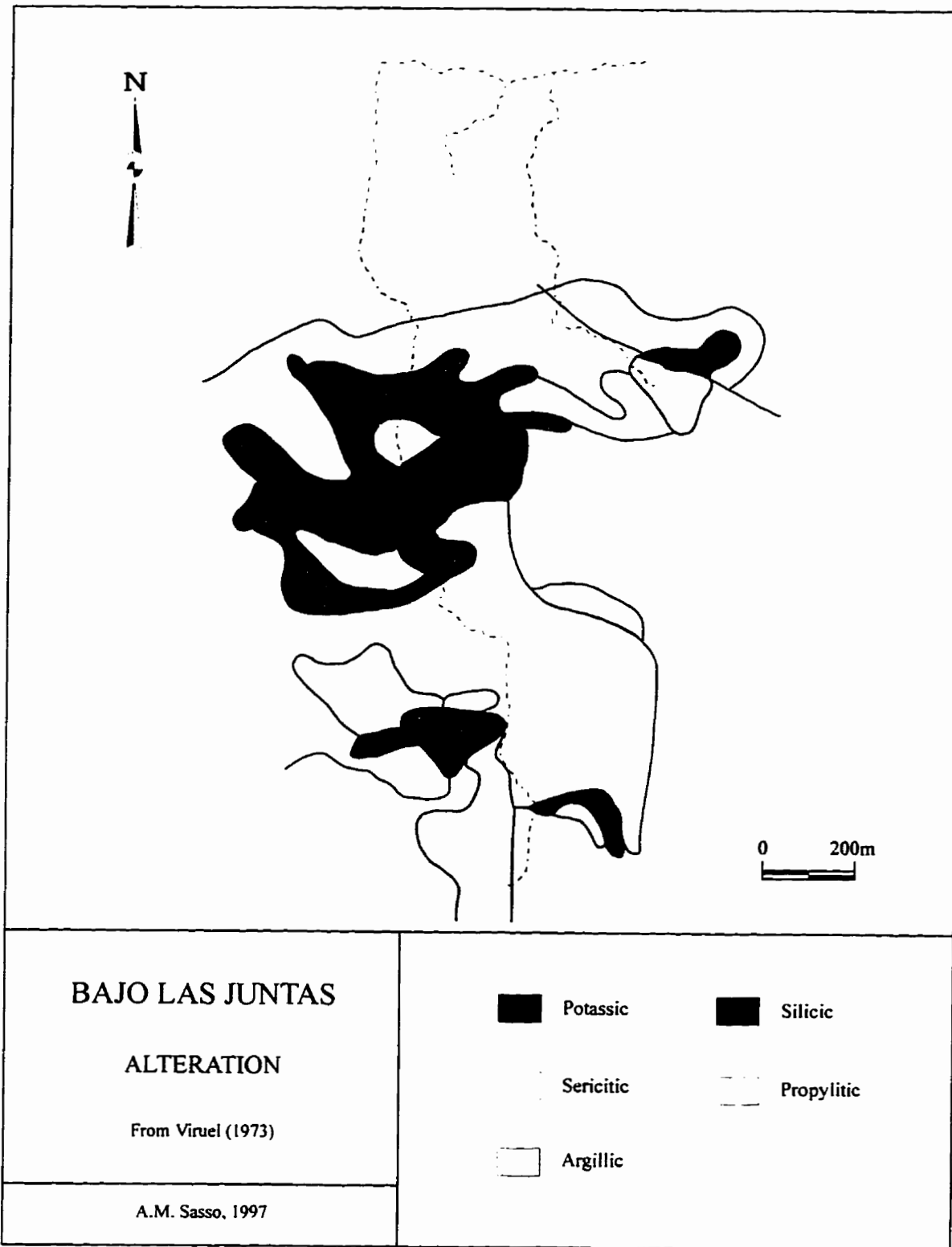
Geochemical anomalies of 100 up to 200 ppm Cu, with localized Pb and Zn, are reported for exposures in Quebrada del Aguila. Cu, Pb, Zn anomalies are also reported in Quebrada Los Amarillos. It does not appear that the samples were analyzed for gold.

A 10 400 m dipole-dipole I.P. survey with 100 m line spacing is noted by Chipulina and González (1983). They report a positive response in the central zone of alteration. On the basis of an unspecified geophysical survey, Bassi (1974; in Durand, 1980) concluded that disseminated sulphides exist at depth, but the indicated zone does not coincide with the surface geochemical anomalies.

Three exploratory drill-holes with depths of up to 200 m are recorded (Durand, 1980). The results of the drilling program were not encouraging, the core revealing

**Figure A-25.**

Alteration facies of the Bajo las Juntas prospect.



propylitic alteration with little mineralization. The locations of the drill-holes are not indicated in Durand (1980), and therefore this information is difficult to evaluate.

## **Bajo de Tampa Tampa**

### ***Location and Access***

Bajo de Tampa Tampa is located along the Quebrada del Agua Durazno, approximately 2.5-3 km south of Bajo el Durazno (Fig. A-1). It could be reached in 1993 and 1994 by driving south along the quebrada from Bajo el Durazno, or by a trunk road that bears south from the Durazno access road; construction of the Bajo de la Alumbrera mine facilities may have affected the access.

### ***Previous Work***

Guerrero and Lavandaio (1969) reported on this prospect for Y.M.A.D. Surface geochemistry conducted over the prospect was discouraging. Samples were analyzed for Cu, Pb and Mo. One shallow hole was drilled on one of the outcrops (the collar is easily located in the field). The results of drilling were also discouraging.

### ***Geological Relationships***

The Bajo de Tampa Tampa prospect consists of a small group of outcrops in Quebrada Agua del Durazno. The area lies on the western edge of a large alluvial fan draining the SW slopes of the Sierra del Durazno. The area is covered by alluvium and aeolian deposits, and exposure is poor.

The outcrops consist of bleached dacitic intrusive rocks in an andesite breccia host. The dacite is cut by scarce chalcedonic quartz veinlets and exhibits weak argillic alteration, minor gypsum veinlets and minor limonite along fracture surfaces. Dacite with similar alteration crops out 2-3 km further south along the *quebrada*.

## **Bajo del Espanto**

### ***Location and Access***

Bajo del Espanto is located approximately 2.5 km south of Bajo de la Alumbraera (Fig. A-1). Access is difficult but, the prospect may be reached by climbing the high ridges to the south of Bajo de la Alumbraera and following a narrow, steep-walled *quebrada* down into the *bajo*. This *quebrada* is characterized by numerous 5-10 m high *saltos* (cliffs). An alternative access route may be from the south, ascending from Quebrada de San Buenaventura.

### ***Previous Work***

Guerrero and Lavandaio (1969) described this prospect for Y.M.A.D. They report a large NW-trending fault in the area. Small fracture zones within the larger structure contain quartz, pyrite, abundant gypsum and limonite in a bleached host. Assays from these zones are very variable, attaining 435 ppm Cu and 630 ppm Pb, with no significant Mo.



### ***Geological Relationships***

Bajo del Espanto is nucleated by a dacite intrusive body hosted by andesite breccias and flows. The breccias contain numerous clasts of basement lithologies. The intrusive contact is locally marked by a narrow (10 cm) chilled margin. The host-rocks appear relatively unaltered. I encountered no sulphides, alteration or evidence of mineralization during a rapid traverse of the area. The fault zone described by Guerrero and Lavandaio (1969) was not observed, but it may lie to the west of the area traversed.

### ***Structure***

Bajo del Espanto lies within the NW-trending extensional corridor that transects the Farallón Negro Volcanic Complex and appears to control the location of other deposits in the area. It is a circular feature, but its classification as a *bajo* is perhaps not justified. It is bounded to the north and east by high ridges, but the south and west boundaries are less defined (Fig. A-26). It also lacks the low-lying weathering and alteration zones typical of the other *bajos* in the district.

## **Bajo de los Jejenes**

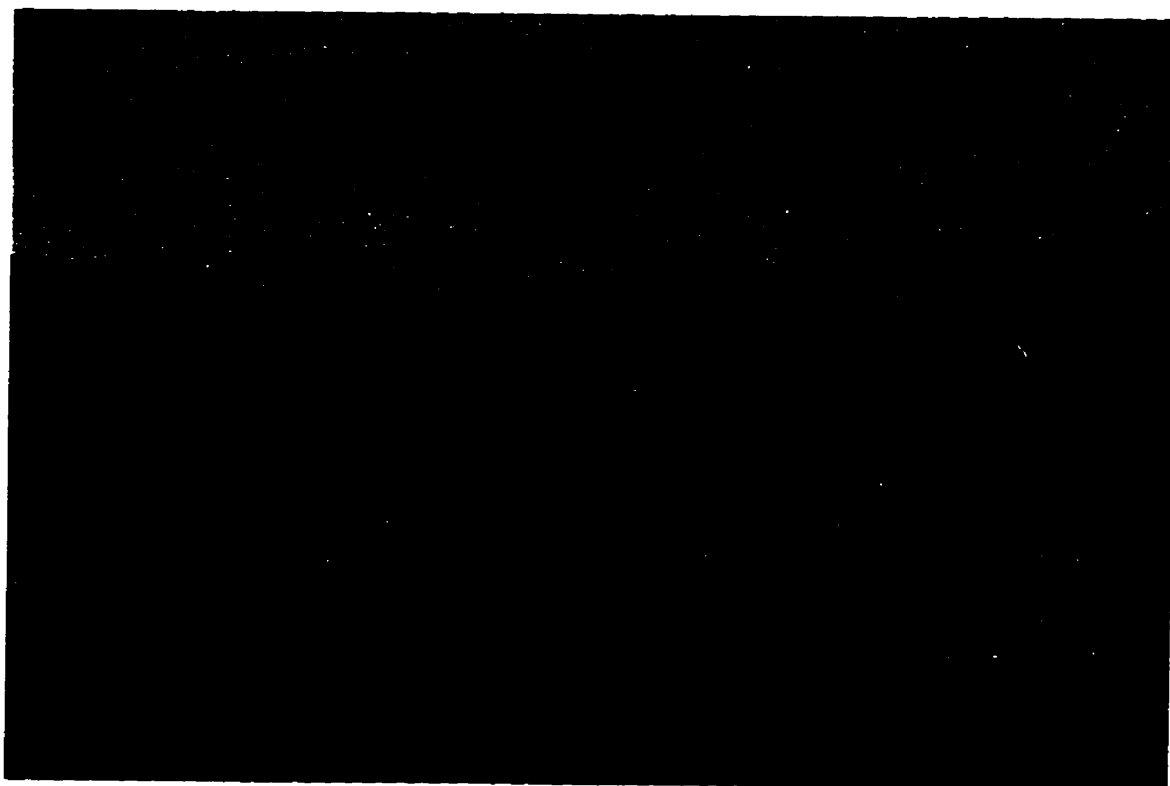
### ***Location and Access***

Bajo de los Jejenes is located approximately 6 km southwest of Bajo de la Alumbra (Fig. A-1), on the north slope of Quebrada de San Buenaventura, approximately 6.5 km west of its junction with the Vis Vis valley. It can be reached by

**Figure A-26.**

*Bajo del Espanto*

View to the southeast towards Bajo del Espanto. The area of the reported hydrothermal alteration and "*bajo*" is in the vicinity of the grey-green ridge on the left which is underlain by a body of *Agua Tapada Dacite*. A light-coloured dacite dyke, classified by Llambías as belonging to the *Macho Muerto Dacite* lithodeme, can be traced, along an irregular path, into the "*bajo*". It intrudes flows and breccias of the *Medial Volcaniclastic Facies*. The Sierra de Ovejería forms the ridge in the near distance.



driving west along Quebrada de San Buenaventura.

### ***Previous Work***

Guerrero and Lavandaio (1969) documented this prospect for Y.M.A.D. A more detailed study was undertaken by Toselli and Durand (1974), the results of which are summarized by Durand (1980).

### ***Geological Relationships***

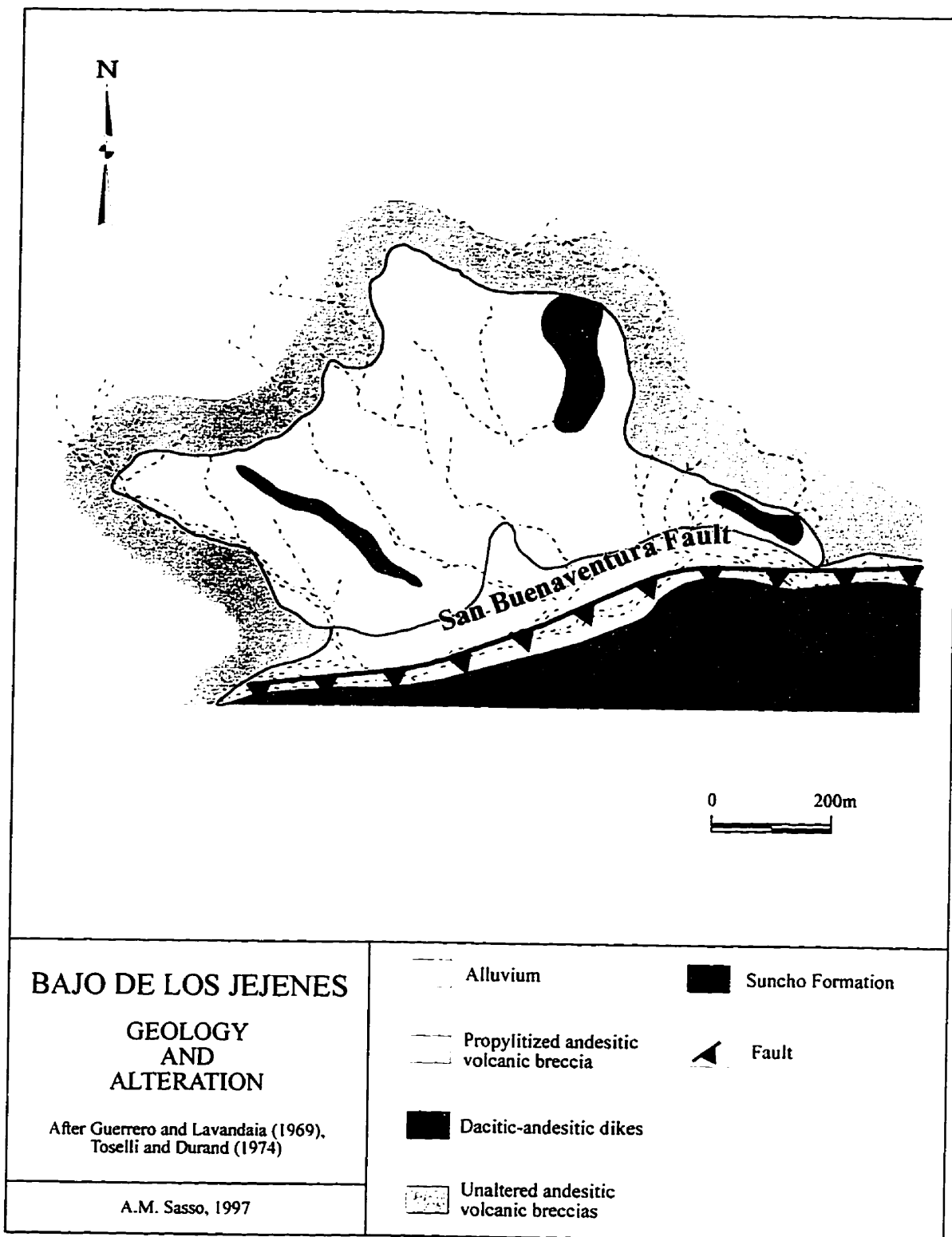
The prospect consists of a zone of propylitic alteration, in upwarped strata of andesite breccia in the footwall of the San Buenaventura Fault (Fig. A-27). Durand (1980) reports very restricted areas of phyllic and silicic alteration. No intrusive units appear to be associated with the alteration, although there are several narrow, relatively fresh, andesitic dykes in the area.

### ***Structure***

Guerrero and Lavandaio (1969) report small zones of intense fracturing with limonite staining and quartz veinlets, and minor NW-trending fault zones also hosting quartz veins. The *bajo* is located just to the west of the southern continuation of the NW-trending extensional corridor. The morphology of the prospect area does not justify classification as a *bajo*.

**Figure A-27.**

Geology of the Bajo los Jejenes prospect.



### ***Mineralization***

Rare pyrite is encountered in the area. A geochemical survey of 104 rock-samples (Toselli and Durand, 1974) revealed no significant Cu, Pb, Zn or Mo anomalies.

## **APPENDIX B.**

### **Whole-Rock Geochemical Data for Igneous Rocks of the Farallón Negro Volcanic Complex.**



**Table B-1.**

Sample locations.

SAMPLE	LOCATION			GEOCHEM	GEOCHRON	PETROLOGY
	LOCAL	LATITUDE	LONGITUDE			
FAR 2	BLA				Y	Y
FAR 10	BAT				Y	Y
FAR 12	FAR				Y	Y
FAR 57	FAR			(=FAR 267)	Y	Y
FAR 65	BAD				Y	Y
FAR 101	BAD				Y	Y
FAR 113	BLA				Y	Y
FAR 146	BSL				Y	Y
FAR 147	BSL				Y	Y
FAR 169	MIV				Y	Y
FAR 176	FAR/MIV	27 20 09.6	66 21 12.2	(=FAR 310)	Y	Y
FAR 192	FAR/CAT				Y	Y
FAR 201	BLA	27 19 10.9	66 35 56.3	Y	Y	Y
FAR 203	FAR	27 18 32.6	66 42 10.1	Y		Y
FAR 204	FAR	27 18 24.0	66 42 44.3	Y	Y	Y
FAR 205	FAR	27 17 58.7	66 44 03.6	Y		Y
FAR 206	FAR	27 17 51.0	66 44 17.4	Y	Y	Y
FAR 207	FAR	27 18 03.4	66 43 42.6	Y		Y
FAR 215	FAR	27 18 54.1	66 40 07.6			Y
FAR 216	FAR	27 18 57.3	66 40 07.1	Y	Y	Y
FAR 218	FAR	27 19 05.9	66 39 35.2	Y		Y
FAR 219	FAR	27 19 08.0	66 39 40.4	Y		Y
FAR 220	FAR	27 19 09.8	66 39 12.5	Y		Y
FAR 222	FAR	27 14 29.7	66 32 42.7	Y		Y
FAR 224	BAD	27 17 13.0	66 34 33.0	Y	Y	Y
FAR 228	BAD	27 17 11.3	66 35 05.9		Y	Y
FAR 229	BAD	27 17 03.7	66 33 15.7	Y	Y	Y
FAR 238	BAT	27 15 40.9	66 40 39.7	Y	Y	Y
FAR 239	BAT	27 15 46.6	66 40 35.9		Y	Y
FAR 244	BLA	27 19 23.5	66 36 59.9	Y	Y	Y
FAR 254	FAR	27 20 09.4	66 38 44.0	Y	Y	Y
FAR 262	BLC	27 19 29.6	66 41 05.8	Y	Y	Y
FAR 266	BLC	27 19 28.9	66 41 01.3		Y	Y
FAR 267	BLC	27 19 15.3	66 41 08.2	Y		Y
FAR 269	FAR	27 19 50.6	66 40 53.5	Y		Y
FAR 271	FAR	27 19 01.3	66 32 37.0	Y	Y	Y
FAR 281	CAT			Y		Y
FAR 284	FAR	27 13 01.2	66 35 21.8	Y	Y	Y
FAR 285	FAR/VIL	27 07 39.9	66 49 40.4	Y	Y	Y
FAR 287	FAR	27 16 38.3	66 41 18.6	Y		Y
FAR 288	FAR	27 15 18.7	66 42 25.8	Y	Y	Y
FAR 295	VISVIS	27 27 38.2	66 35 15.8	Y		Y
FAR 296	VISVIS	27 27 17.3	66 34 20.7	Y	Y	Y

SAMPLE	LOCATION			GEOCHEM	GEOCHRON	PETROLOGY
	LOCAL	LATITUDE	LONGITUDE			
FAR 297	VISVIS	27 27 11.7	66 34 26.1	Y	Y	Y
FAR 299	VISVIS	27 27 45.5	66 32 40.7	Y	Y	Y
FAR 301	BLJ	27 27 56.1	66 32 20.9		Y	Y
FAR 302	CAT	27 20 22.8	66 29 09.5	Y		Y
FAR 303	CAT	27 21 32.0	66 28 27.4		Y	Y
FAR 304	CAT	27 19 56.9	66 27 52.4		Y	Y
FAR 305	CAT	27 19 56.9	66 27 52.4		Y	Y
FAR 307	CAT	27 19 35.8	66 27 15.4		Y	Y
FAR 308	FAR/CAT	27 16 45.0	66 26 31.4	Y		Y
FAR 309	CAT	27 18 56.7	66 25 42.7	Y		Y
FAR 310	FAR/MIV	27 20 09.6	66 21 12.2	Y		Y
FAR 311	FAR/CAT	27 14 20.5	66 23 57.1	Y	Y	Y
FAR 312	FAR/CAT	27 14 22.7	66 25 20.3	Y	Y	Y
FAR 316	CAP	27 20 37.4	66 23 24.1	Y	Y	Y
FAR 318	CAP	27 20 41.0	66 22 45.9	Y	Y	Y
FAR 324	MIV				Y	Y
FAR 325	MIV	27 22 33.4	66 16 50.2		Y	Y
FAR 327	MIV	27 22 22.6	66 16 58.6		Y	Y
FAR 329	MIV	27 22 09.3	66 17 05.3		Y	Y
FAR 334	BLA				Y	Y
FAR 336	BLA				Y	Y
FAR 337	FAR	27 15 08.2	66 40 18.5	Y		Y
FAR 338	FAR	27 16 14.3	66 38 16.4		Y	Y

\* Note: FAR - Farallon Negro Regional  
 BLA - Bajo de la Alumbraera  
 BAT - Bajo de Agua Tapada  
 BLC - Bajo la Chilca  
 BSL - Bajo de San Lucas  
 BLJ - Bajo las Juntas  
 CAT - Cerro Atajo  
 CAP - Capillitas  
 MIV - Mi Vida/ Agua Rica  
 VISVIS - Vis Vis area  
 VIL - Villa Vil

**Figure 1.**  
Locations of geochemical samples analyzed  
in this study.

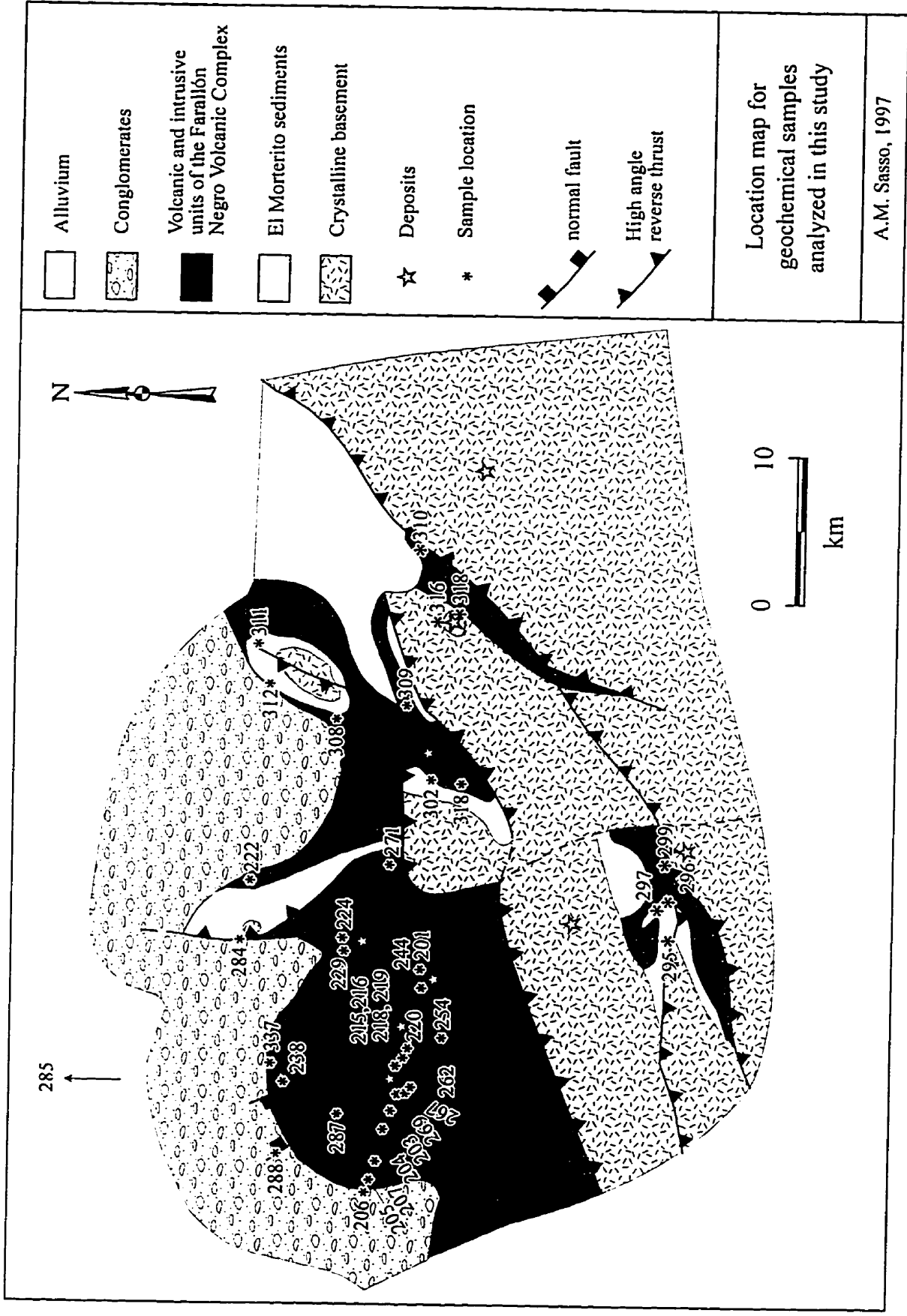


**Table B-2.**

Whole-rock geochemical analyses generated by this study  
listed in order of increasing sample number.

ELEMENT	FAR 201	FAR 203	FAR 204	FAR 205	FAR 206	FAR 207	FAR 215
SiO2	52.2	54.32	56.14	65.33	58.88	50.72	57.04
TiO2	1.44	1.14	1.26	0.39	0.62	1.53	0.9
Al2O3	16.06	16.34	16.19	17.07	14.87	16.39	17.11
Fe2O3	10.42	6.91	7.99	3.69	5.27	9.36	6.75
MnO	0.22	0.14	0.12	0.05	0.11	0.09	0.12
MgO	6.44	1.67	4.96	0.19	2.11	3.99	5.54
CaO	8.45	7.63	6.38	2.73	5.29	8.79	6.01
Na2O	2.83	1.88	2.52	3.31	2.08	2.64	2.48
K2O	2.35	4.69	2.03	5.26	3.01	1.91	2.51
P2O5	0.39	0.36	0.45	0.23	0.33	0.45	0.4
LOI		4.5	1.8	1.5	7.1	3.3	1.2
SUM		99.58	99.84	99.75	99.67	99.17	100.06
FeO	-	2.1	1.96	0.34	1.1	2.02	3.64
Cr	166	17	17	6	37	65	10
Ni	37.63	28	18	15	22	23	18
Sc	27	12	17	3	8	26	13
Co		12	11	3	7	21	8
Pb	13.1	7	10	12	7	5	11
Sn		2	2	2	2	3	2
V	275	131	154	26	75	201	100
Zn	63.21	94	80	50	58	79	77
Cu	28.1	42	23	13	33	34	21
Ba	561.77	711	619	800	544	522	659
As	6.53	4	4	50	12	5	6
Rb	108	202	78	198	152	57	97
Sr	528.61	474	417	411	692	460	478
Y	23.33	19	24	19	15	21	23
Zr	131.4	122	131	220	138	107	172
Nb	15.25	17	15	25	16	10	19
Cd		0.4	0.4	0.4	0.4	0.4	0.5
Th	4.39	5	4	12	6	4	7
U	-0.07	10	10	10	10	10	10
La		8	11	19	39	2	26
Ce	16.9	37	39	63	57	21	65

ELEMENT	FAR 216	FAR 218	FAR 219	FAR 220	FAR 222	FAR 224	FAR 229
SiO2	53.99	55.53	51.29	62.73	49.01	59.06	59.66
TiO2	1.09	1.13	1.32	0.81	1.68	0.7	0.69
Al2O3	16.62	17.11	16.51	16.42	17.45	16.91	16.69
Fe2O3	8.6	8.03	9.5	5.2	10.76	5.86	5.73
MnO	0.13	0.17	0.16	0.04	0.16	0.17	0.14
MgO	3.29	3.02	4.08	1.53	4.3	2.08	2.07
CaO	6.86	7	7.42	4.29	8.8	6.58	6.14
Na2O	2.96	2.21	2.4	3.9	2.67	2.92	3.08
K2O	2.27	1.7	1.89	2.22	1.75	2.54	2.51
P2O5	0.44	0.44	0.56	0.26	0.58	0.35	0.35
LOI	2.7	3.1	4.1	1.8	2	2.3	2.5
SUM	98.95	99.44	99.23	99.2	99.16	99.47	99.56
FeO	3.66	2.98	3.58	1.18	5.28	2.56	2.58
Cr	29	29	40	37	11	20	14
Ni	29	31	25	23	21	13	17
Sc	17	14	18	7	25	8	8
Co	15	11	18	6	21	7	7
Pb	6	7	11	4	9	21	9
Sn	2	2	2	2	2	2	2
V	162	116	160	68	234	86	86
Zn	57	102	111	29	85	84	71
Cu	27	2	46	3	15	14	11
Ba	551	720	1067	812	700	961	897
As	9	6	13	13	8	6	4
Rb	91	52	54	64	38	87	95
Sr	549	499	547	478	544	640	601
Y	19	22	20	19	23	18	18
Zr	107	137	131	141	128	122	122
Nb	11	16	14	20	16	15	15
Cd	0.5	0.4	0.4	0.5	0.5	0.7	0.4
Th	5	2	2	4	2	4	4
U	10	10	10	10	10	10	10
La	2	2	8	13	2	11	9
Ce	38	57	41	42	39	49	42



ELEMENT	FAR 238	FAR 244	FAR 254	FAR 262	FAR 267	FAR 269	FAR 271
SiO2	63.57	61.45	56.37	61.06	57.48	70.87	51.49
TiO2	0.61	0.59	0.95	0.69	1.04	0.18	1.39
Al2O3	15.78	16.03	16.19	16.49	16.87	14.57	16.81
Fe2O3	4.76	5.11	6.65	5.18	6.94	1.99	8.89
MnO	0.07	0.11	0.14	0.13	0.12	0.03	0.18
MgO	2.61	1.78	5.49	2.38	2.88	0.31	4.24
CaO	3.13	5.53	4.92	4.4	6.1	1.55	7.2
Na2O	2.9	2.9	2.99	2.98	2.57	2.72	3.02
K2O	3.1	2.44	2.21	2.43	2.03	3.91	1.66
P2O5	0.29	0.41	0.42	0.38	0.4	0.03	0.57
LOI	2.9	3.4	3	3.3	3.3	3.7	4.2
SUM	99.72	99.75	99.33	99.42	99.73	99.86	99.65
FeO	1.56	1.78	3.16	2.1	3.12	0.66	1.54
Cr	57	41	6	6	31	15	19
Ni	33	19	10	10	13	41	17
Sc	9	8	10	6	10	3	19
Co	8	6	8	5	9	2	19
Pb	6	7	4	10	7	6	4
Sn	2	2	2	2	2	2	2
V	77	70	82	45	89	5	161
Zn	114	63	84	75	82	42	89
Cu	9	9	2	2	2	5	6
Ba	704	750	644	811	663	543	679
As	4	4	4	4	4	5	4
Rb	108	76	84	74	62	183	38
Sr	479	623	448	663	428	169	511
Y	14	21	23	20	23	16	21
Zr	123	145	160	144	152	164	131
Nb	17	18	17	19	18	19	15
Cd	1	0.4	0.4	0.6	0.5	0.4	0.4
Th	6	5	4	3	5	8	2
U	10	10	10	10	10	10	10
La	9	17	4	20	20	16	2
Ce	34	73	65	77	65	57	50

ELEMENT	FAR 281	FAR 284	FAR 285	FAR 287	FAR 288	FAR 295	FAR 296
SiO2	75.91	62.87	57.05	67.16	66.88	61.12	53.42
TiO2	0.07	0.56	1.05	0.36	0.39	0.8	0.96
Al2O3	13.98	16.43	16.36	15.35	16.08	16.13	17.88
Fe2O3	0.68	4.87	7.08	3.01	3.39	5.76	7.94
MnO	0.02	0.11	0.13	0.08	0.09	0.12	0.1
MgO	0.08	1.97	2.88	1.06	1.17	3.2	2.68
CaO	0.28	4.57	6.69	4.28	4.16	4.99	7.65
Na2O	2.66	2.83	3.45	2.72	3.56	2.79	2.65
K2O	4.38	1.97	2.25	2.58	2.42	2.11	4.07
P2O5	0.04	0.29	0.4	0.18	0.16	0.38	0.47
LOI	1.8	3.2	2	3.1	1.5	2.4	1.7
SUM	99.9	99.67	99.34	99.88	99.8	99.8	99.52
FeO	0.5	1.46	1.66	0.84	1.18	2.68	1.36
Cr	26	20	39	16	29	13	41
Ni	29	24	40	21	17	13	26
Sc	6	8	12	4	6	10	19
Co	2	5	13	3	4	7	12
Pb	4	4	4	7	9	8	15
Sn	3	2	2	2	2	2	2
V	2	64	116	43	52	74	155
Zn	53	57	72	46	42	71	70
Cu	4	10	16	2	2	2	12
Ba	133	558	931	702	741	760	1385
As	4	4	4	4	4	4	4
Rb	342	96	78	93	86	88	93
Sr	60	559	582	560	658	560	712
Y	36	19	21	14	13	21	22
Zr	41	123	165	101	113	132	127
Nb	30	15	24	16	17	24	13
Cd	0.4	0.4	0.4	0.4	0.4	0.4	0.5
Th	7	5	4	5	5	6	7
U	10	10	10	10	10	10	10
La	10	8	11	2	15	14	12
Ce	35	55	75	27	58	66	59

ELEMENT	FAR 297	FAR 299	FAR 302	FAR 308	FAR 309	FAR 310	FAR 311
SiO2	62.2	61.75	62.31	49.43	57.03	66.21	54.35
TiO2	0.59	0.61	0.57	1.76	0.54	0.24	0.88
Al2O3	16.44	15.89	16.66	17.48	17.42	16.35	17.01
Fe2O3	4.88	5.25	5.46	11.27	3.89	2.22	7.42
MnO	0.14	0.1	0.23	0.15	0.09	0.03	0.1
MgO	2.64	1.96	1.54	4.39	3.14	0.6	4.57
CaO	4.1	5.15	4.26	8.8	4.34	3.92	7.07
Na2O	2.76	2.4	3.23	2.45	1.88	1.97	2.55
K2O	2.81	3.98	3.59	1.89	1.39	2.25	1.85
P2O5	0.25	0.36	0.35	0.44	0.15	0.03	0.4
LOI	3.4	3	1.6	1.9	10.7	6.1	3.3
SUM	100.21	100.45	99.8	99.96	100.57	99.92	99.5
FeO	1.87	1.63	2.67	6.3	0.55	0.59	2.06
Cr	8	15	19	21	9	2	19
Ni	19	18	23	32	19	15	27
Sc	8	11	7	33	6	3	15
Co	4	6	5	26	6	2	12
Pb	18	15	19	11	13	17	15
Sn	2	2	2	2	2	2	2
V	62	77	54	268	48	6	138
Zn	75	69	868	79	56	58	87
Cu	2	2	4	23	2	4	2
Ba	947	995	714	734	173	731	806
As	4	4	4	5	4	4	4
Rb	144	134	148	57	76	184	98
Sr	508	621	637	567	477	600	600
Y	24	23	22	20	17	22	24
Zr	170	142	164	111	138	177	127
Nb	17	16	18	13	19	19	14
Cd	0.4	0.4	0.6	0.8	0.4	0.4	0.4
Th	6	8	7	3	5	9	5
U	10	10	10	10	10	10	10
La	4	11	3	2	14	22	14
Ce	96	66	75	33	61	97	66

ELEMENT	FAR 312	FAR 316	FAR 318	FAR 337
SiO2	61.2	80.94	64.51	56.67
TiO2	0.41	0.22	0.66	0.92
Al2O3	15.92	11.54	16.29	15.95
Fe2O3	3.05	0.53	4.99	6.4
MnO	0.11	0.05	0.31	0.14
MgO	1.42	0.34	1.6	1.73
CaO	5.88	0.15	1.95	5.44
Na2O	2.32	0.03	3.07	2.86
K2O	0.83	2.79	3.01	2.18
P2O5	0.15	0.01	0.34	0.35
LOI	8.2	2.8	2.9	7.2
SUM	99.49	99.4	99.63	99.84
FeO	0.7	0.32	1.82	0.28
Cr	24	11	7	6
Ni	10	17	15	15
Sc	6	5	7	8
Co	4	2	6	7
Pb	10	160	16	17
Sn	2	2	2	2
V	37	29	52	55
Zn	44	12	722	118
Cu	2	26	2	2
Ba	330	111	585	737
As	4	26	4	10
Rb	44	278	116	94
Sr	606	17	546	309
Y	16	20	19	20
Zr	120	69	185	164
Nb	14	17	22	19
Cd	0.4	1	0.7	0.4
Th	6	7	5	5
U	10	11	10	10
La	2	2	2	7
Ce	62	36	99	64

**Table B-3.**

Trace and REE element analyses generated by this study  
listed in order of increasing sample number.

ELEMENT	LIMIT OF DETECTION	FAR201	FAR203	FAR204	FAR205	FAR207
Li	2.163	27.551	45.358	40.889	16.942	34.676
Rb	0.015	49.821	199.698	63.888	201.703	65.099
Sr	0.22	528.89	488.87	327.94	396.79	457.82
Y	0.005	22.337	19.655	19.519	19.886	21.096
Zr	0.022	109.264	136.186	124.804	276.611	113.535
Nb	0.010	14.308	21.337	14.472	28.007	15.095
Mo	0.054	2.190	1.655	1.619	2.383	1.288
Cs	0.009	2.818	14.591	2.219	17.403	9.786
Ba	0.08	510.77	645.53	410.50	679.24	421.70
Ho	0.003	0.890	0.796	0.804	0.748	0.884
Er	0.019	2.475	2.298	2.214	2.308	2.401
Tm	0.005	0.324	0.328	0.341	0.356	0.329
Yb	0.030	2.033	2.113	2.047	2.432	2.098
Lu	0.003	0.296	0.316	0.299	0.346	0.288
Hf	0.023	3.339	3.923	3.611	7.767	3.523
Ta	0.006	1.289	1.377	0.919	1.994	0.878
Tl	1.065	0.250	5.065	1.409	2.487	0.156
Pb	0.100	8.302	14.832	9.513	19.799	7.749
La	0.006	19.489	24.134	22.241	35.640	19.632
Ce	0.008	42.825	50.226	46.440	70.453	43.552
Pr	0.005	5.709	6.023	5.662	7.789	5.546
Nd	0.034	24.346	24.479	22.925	28.090	23.863
Sm	0.033	5.518	5.221	4.954	5.100	5.309
Eu	0.007	1.728	1.482	1.377	1.315	1.737
Gd	0.014	5.509	4.723	4.496	4.320	5.297
Tb	0.006	0.778	0.687	0.678	0.659	0.739
Dy	0.018	4.632	4.304	4.152	3.847	4.430
Bi	0.012	0.059	0.024	0.018	0.046	0.025
Th	0.013	3.410	5.326	4.221	17.406	3.333
U	0.011	0.938	1.542	1.136	4.374	0.651
206Pb/207Pb	NA	1.233	1.2283	1.1887	1.1714	1.1992
208Pb/207Pb	NA	2.532	2.5377	2.4322	2.4877	2.5104
147Sm/144Nd	NA	0.137	0.1272	0.1312	0.1092	0.1342
87Rb/86Sr	NA	0.273	1.1848	0.5664	1.4805	0.4118
Nb/Ta	NA	11.10	15.50	15.75	14.05	17.20
Dil(G/KG)	0.573	0.571	0.576	0.751	0.560	0.547

ELEMENT	LIMIT OF DETECTION	FAR216	FAR229	FAR238	FAR244	FAR271
Li	2.163	33.684	25.664	27.583	31.053	13.969
Rb	0.015	98.357	100.534	101.581	78.523	47.850
Sr	0.22	528.85	620.89	413.41	582.15	509.80
Y	0.005	18.377	19.071	11.942	18.522	21.598
Zr	0.022	13.524	39.862	28.548	65.453	165.339
Nb	0.010	14.023	17.575	17.592	20.273	17.977
Mo	0.054	1.609	1.082	1.423	1.917	1.063
Cs	0.009	2.505	2.059	6.365	1.813	1.250
Ba	0.08	445.55	767.83	489.97	613.61	586.30
Ho	0.003	0.765	0.752	0.478	0.755	0.950
Er	0.019	2.114	1.962	1.284	2.045	2.670
Tm	0.005	0.297	0.293	0.179	0.318	0.365
Yb	0.030	1.735	1.879	1.146	1.925	2.293
Lu	0.003	0.246	0.260	0.175	0.285	0.348
Hf	0.023	0.679	1.711	1.160	2.145	4.623
Ta	0.006	0.931	1.280	1.260	1.423	1.064
Tl	1.065	0.559	0.576	0.424	0.468	0.051
Pb	0.100	9.096	10.869	10.586	12.705	6.872
La	0.006	20.659	25.083	24.035	29.567	22.643
Ce	0.008	43.956	50.609	44.663	59.848	49.600
Pr	0.005	5.355	5.981	4.902	6.940	6.211
Nd	0.034	22.307	23.279	17.719	26.352	26.648
Sm	0.033	5.009	4.733	3.362	4.735	5.764
Eu	0.007	1.433	1.448	0.973	1.404	1.798
Gd	0.014	4.682	4.310	2.949	4.469	5.314
Tb	0.006	0.686	0.628	0.418	0.657	0.787
Dy	0.018	4.070	3.766	2.477	3.793	4.820
Bi	0.012	0.036	0.031	0.016	0.165	0.011
Th	0.013	5.669	4.745	7.308	5.417	2.157
U	0.011	1.081	1.335	1.753	2.408	0.730
206Pb/207Pb	NA	1.1583	1.1769	1.2203	1.1677	1.1469
208Pb/207Pb	NA	2.4079	2.3758	2.4637	2.4157	2.4485
147Sm/144Nd	NA	0.1336	0.1210	0.1140	0.1086	0.1314
87Rb/86Sr	NA	0.5389	0.4696	0.7103	0.3898	0.2711
Nb/Ta	NA	15.06	13.73	13.96	14.24	16.89
Dil(G/KG)	0.573	0.570	0.552	0.552	0.577	0.570

ELEMENT	LIMIT OF DETECTION	FAR284	FAR288	FAR296	FAR299	FAR311
Li	2.163	36.378	18.410	12.817	19.785	13.407
Rb	0.015	128.767	102.473	98.921	128.834	122.539
Sr	0.22	648.65	598.88	730.87	615.55	690.66
Y	0.005	21.207	12.421	22.673	23.172	30.775
Zr	0.022	48.035	35.673	147.789	71.252	173.011
Nb	0.010	20.835	17.434	14.686	18.572	18.541
Mo	0.054	1.290	1.244	2.089	3.046	1.942
Cs	0.009	23.666	5.721	1.156	2.790	8.603
Ba	0.08	524.05	559.49	1203.81	882.18	789.36
Ho	0.003	0.806	0.465	0.885	0.882	1.125
Er	0.019	2.363	1.384	2.673	2.458	3.309
Tm	0.005	0.301	0.212	0.418	0.367	0.475
Yb	0.030	1.870	1.388	2.563	2.054	3.184
Lu	0.003	0.294	0.204	0.380	0.335	0.479
Hf	0.023	1.779	1.482	4.436	2.707	4.681
Ta	0.006	1.355	1.280	0.987	1.221	1.134
Tl	1.065	0.461	0.410	0.210	0.767	0.693
Pb	0.100	13.086	12.291	20.034	19.049	17.150
La	0.006	33.918	27.482	31.518	37.372	29.710
Ce	0.008	66.824	49.647	60.100	73.401	59.050
Pr	0.005	7.445	5.358	6.913	8.176	6.959
Nd	0.034	29.044	19.125	26.762	30.815	27.783
Sm	0.033	5.665	3.442	5.568	5.945	6.211
Eu	0.007	1.589	0.901	1.662	1.714	1.903
Gd	0.014	4.799	2.863	5.370	5.280	5.902
Tb	0.006	0.706	0.407	0.768	0.782	0.886
Dy	0.018	4.212	2.422	4.479	4.407	5.492
Bi	0.012	0.131	0.094	0.016	0.099	0.011
Th	0.013	7.601	7.439	6.129	8.935	5.680
U	0.011	1.917	2.989	1.553	1.931	1.489
206Pb/207Pb	NA	1.1756	1.2499	1.2501	1.1834	1.1954
208Pb/207Pb	NA	2.4330	2.4660	2.5463	2.4924	2.4989
147Sm/144Nd	NA	0.1177	0.1081	0.1268	0.1169	0.1358
87Rb/86Sr	NA	0.5731	0.4932	0.3895	0.6063	0.5145
Nb/Ta	NA	15.38	13.62	14.88	15.21	16.34
Dil(G/KG)	0.573	0.574	0.573	0.563	0.580	0.573



**Table B-4.**

Whole-rock geochemical analyses  
listed by rock type.  
(includes data from: Dostal et al. (1977); Caelles (1979);  
Allison (1986); and, Kay et al. (1988) and this study).

# Whole-Rock Composition - Absarokites and Shoshonites

ELEMENT	JC-30	D-A	AA-5	AA-4	FAR 203	FAR 296	FJ2
SiO2	49.60	51.18	52.10	53.60	54.32	53.42	55.4
TiO2	1.50	1.25	1.00	0.93	1.14	0.96	1.27
Al2O3	16.20	17.14	16.00	15.87	16.34	17.88	17.66
Fe2O3	2.06		10.87	9.15	6.91	7.94	
MnO	0.180		0.210	0.170	0.14	0.1	0.11
MgO	4.00	4.24	3.08	2.49	1.67	2.68	1.3
CaO	9.62	10.06	10.00	10.80	7.63	7.65	8.95
Na2O	4.10	3.35	3.60	2.97	1.88	2.65	2.96
K2O	2.25	3.11	3.13	3.85	4.69	4.07	3.41
P2O5	0.430		0.220	0.183	0.36	0.47	0.33
LOI					4.5	1.7	
SUM	96.35		100.21	100.01	99.58	99.52	99.17
FeO	6.41	8.92			2.1	1.36	7.78
Cr		88			17	41	9
Ni		35			28	26	7
Sc					12	19	15
Co		42			12	12	
Pb					7	15	
Sn					2	2	
V		208			131	155	
Zn					94	70	
Cu					42	12	
Ba		556			711	1385	813.9
As					4	4	
Rb		80			202	93	104
Sr		512			474	712	414
Y					19	22	
Zr		141			122	127	
Nb					17	13	
Cd					0.4	0.5	
Th					5	7	6.77
U					10	10	1.5
La					8	12	31.2
Ce					37	59	58.3

### Whole Rock Composition - Banakites

ELEMEN	AA-9	AA-7	AA-11	AA-2	JC-193	FAR 206	JC-46
SiO2	55.70	57.40	57.40	57.90	58.75	58.88	61.10
TiO2	0.53	0.30	0.56	0.63	0.76	0.62	0.64
Al2O3	15.20	13.98	15.10	13.60	18.40	14.87	16.35
Fe2O3	4.40	5.15	4.70	7.43	1.97	5.27	1.17
MnO	0.250	0.550	0.330	0.330	0.220	0.11	0.110
MgO	2.00	1.89	2.20	1.89	0.70	2.11	1.57
CaO	5.60	10.35	3.90	7.42	3.80	5.29	4.98
Na2O	2.50	2.86	2.60	2.04	4.68	2.08	2.06
K2O	3.20	4.82	3.40	3.85	3.73	3.01	4.68
P2O5	0.180	0.137	0.170	0.160	0.190	0.33	0.290
LOI	3.90		3.60			7.1	
SUM	95.3	97.44	95.80	95.25	95.93	99.67	95.75
FeO	1.8		1.8		2.73	1.1	2.8
Cr						37	
Ni						22	
Sc						8	
Co						7	
Pb						7	
Sn						2	
V						75	
Zn						58	
Cu						33	
Ba						544	
As						12	
Rb						152	
Sr						692	
Y						15	
Zr						138	
Nb						16	
Cd						0.4	
Th						6	
U						10	
La						39	
Ce						57	

# Whole Rock Composition - Banakites and High-K Dacites

ELEMEN	FAR 299	FAR 302	AA-15	AA-16	FAR 205
SiO2	61.75	62.31	62.40	64.00	65.33
TiO2	0.61	0.57	0.33	0.40	0.39
Al2O3	15.89	16.66	14.36	14.74	17.07
Fe2O3	5.25	5.46	4.63	4.78	3.69
MnO	0.1	0.23	0.210	0.240	0.05
MgO	1.96	1.54	1.53	1.69	0.19
CaO	5.15	4.26	6.44	7.00	2.73
Na2O	2.4	3.23	3.67	3.61	3.31
K2O	3.98	3.59	5.30	4.82	5.26
P2O5	0.36	0.35	0.137	0.092	0.23
LOI	3	1.6			1.5
SUM	100.45	99.8	99.01	101.37	99.75
FeO	1.63	2.67			0.34
Cr	15	19			6
Ni	18	23			15
Sc	11	7			3
Co	6	5			3
Pb	15	19			12
Sn	2	2			2
V	77	54			26
Zn	69	868			50
Cu	2	4			13
Ba	995	714			800
As	4	4			50
Rb	134	148			198
Sr	621	637			411
Y	23	22			19
Zr	142	164			220
Nb	16	18			25
Cd	0.4	0.6			0.4
Th	8	7			12
U	10	10			10
La	11	3			19
Ce	66	75			63

# Whole Rock Composition - Alkali-Olivine Basalt

ELEMEN	JC-34A
SiO2	44.60
TiO2	1.68
Al2O3	13.50
Fe2O3	2.80
MnO	0.370
MgO	9.85
CaO	12.65
Na2O	1.70
K2O	0.21
P2O5	0.430
LOI	
SUM	96.38
FeO	8.59

# Whole-Rock Composition - Volcanic Basalts

ELEMENT	FAR 222	FAR 308	JC-34C	AA-1	FAR 207	FAR 219	FAR 271
SiO2	49.01	49.43	50.10	50.66	50.72	51.29	51.49
TiO2	1.68	1.76	1.21	1.17	1.53	1.32	1.39
Al2O3	17.45	17.48	17.30	15.12	16.39	16.51	16.81
Fe2O3	10.76	11.27	4.30	10.01	9.36	9.5	8.89
MnO	0.16	0.15	0.170	0.160	0.09	0.16	0.18
MgO	4.3	4.39	2.65	4.58	3.99	4.08	4.24
CaO	8.8	8.8	9.58	11.75	8.79	7.42	7.2
Na2O	2.67	2.45	3.24	6.15	2.64	2.4	3.02
K2O	1.75	1.89	1.89	2.17	1.91	1.89	1.66
P2O5	0.58	0.44	0.570	0.054	0.45	0.56	0.57
LOI	2	1.9			3.3	4.1	4.2
SUM	99.16	99.96	94.56	98.82	99.17	99.23	99.65
FeO	5.28	6.3	3.55		2.02	3.58	1.54
Cr	11	21			65	40	19
Ni	21	32			23	25	17
Sc	25	33			26	18	19
Co	21	26			21	18	19
Pb	9	11			5	11	4
Sn	2	2			3	2	2
V	234	268			201	160	161
Zn	85	79			79	111	89
Cu	15	23			34	46	6
Ba	700	734			522	1067	679
As	8	5			5	13	4
Rb	38	57			57	54	38
Sr	544	567			460	547	511
Y	23	20			21	20	21
Zr	128	111			107	131	131
Nb	16	13			10	14	15
Cd	0.5	0.8			0.4	0.4	0.4
Th	2	3			4	2	2
U	10	10			10	10	10
La	2	2			2	8	2
Ce	39	33			21	41	50

### Whole-Rock Composition - Volcanic Basaltic Andesites

ELEMENT	FAR 201	JC-95	FAR 311	JC-76B	FAR 204	FAR 337	FAR 309
SiO <sub>2</sub>	52.2	53.00	54.35	55.90	56.14	56.67	57.03
TiO <sub>2</sub>	1.44	1.22	0.88	1.10	1.26	0.92	0.54
Al <sub>2</sub> O <sub>3</sub>	16.06	17.00	17.01	16.70	16.19	15.95	17.42
Fe <sub>2</sub> O <sub>3</sub>	10.42	3.45	7.42	3.34	7.99	6.4	3.89
MnO	0.22	0.160	0.1	0.160	0.12	0.14	0.09
MgO	6.44	2.35	4.57	2.90	4.96	1.73	3.14
CaO	8.45	8.87	7.07	6.80	6.38	5.44	4.34
Na <sub>2</sub> O	2.83	2.69	2.55	2.55	2.52	2.86	1.88
K <sub>2</sub> O	2.35	2.46	1.85	2.78	2.03	2.18	1.39
P <sub>2</sub> O <sub>5</sub>	0.39	0.550	0.4	0.470	0.45	0.35	0.15
LOI			3.3		1.8	7.2	10.7
SUM		95.9	99.5	96.83	99.84	99.84	100.57
FeO		4.15	2.06	4.13	1.96	0.28	0.55
Cr			19		17	6	9
Ni	37.63		27		18	15	19
Sc	27		15		17	8	6
Co			12		11	7	6
Pb	13.1		15		10	17	13
Sn			2		2	2	2
V			138		154	55	48
Zn	63.21		87		80	118	56
Cu	28.1		2		23	2	2
Ba	561.77		806		619	737	173
As	6.53		4		4	10	4
Rb	49.82		98		78	94	76
Sr	528.61		600		417	309	477
Y	23.33		24		24	20	17
Zr	131.4		127		131	164	138
Nb	15.25		14		15	19	19
Cd			0.4		0.4	0.4	0.4
Th	4.39		5		4	5	5
U	-0.07		10		10	10	10
La			14		11	7	14
Ce	16.9		66		39	64	61

# Whole-Rock Composition - Volcanic Basaltic Andesites

ELEMENT	FAR 285
SiO2	57.05
TiO2	1.05
Al2O3	16.36
Fe2O3	7.08
MnO	0.13
MgO	2.88
CaO	6.69
Na2O	3.45
K2O	2.25
P2O5	0.4
LOI	2
SUM	99.34
FeO	1.66
Cr	39
Ni	40
Sc	12
Co	13
Pb	4
Sn	2
V	116
Zn	72
Cu	16
Ba	931
As	4
Rb	78
Sr	582
Y	21
Zr	165
Nb	24
Cd	0.4
Th	4
U	10
La	11
Ce	75



### Whole Rock Composition - Volcanic Andesites

ELEMENT	JC-194	AA-3	FAR 312	D-B	JC-33	JC-222	FAR 284
SiO <sub>2</sub>	60.20	60.30	61.2	61.38	61.80	62.20	62.87
TiO <sub>2</sub>	0.83	0.65	0.41	0.73	0.93	0.80	0.56
Al <sub>2</sub> O <sub>3</sub>	17.06	15.80	15.92	17.86	16.90	16.30	16.43
Fe <sub>2</sub> O <sub>3</sub>	2.97	4.20	3.05		3.12	2.95	4.87
MnO	0.190	0.080	0.11		0.130	0.100	0.11
MgO	1.57	2.50	1.42	1.81	2.02	2.05	1.97
CaO	4.40	3.80	5.88	4.39	4.70	5.38	4.57
Na <sub>2</sub> O	4.56	2.90	2.32	4.28	3.33	3.17	2.83
K <sub>2</sub> O	3.55	2.70	0.83	3.53	3.00	3.42	1.97
P <sub>2</sub> O <sub>5</sub>	0.370	0.190	0.15		0.250	0.300	0.29
LOI		1.60	8.2				3.2
SUM	98.51	96.90	99.49		98.62	98.91	99.67
FeO	2.82	2.20	0.7	5.56	2.74	2.24	1.46
Cr			24	30			20
Ni			10				24
Sc			6				8
Co			4	33			5
Pb			10				4
Sn			2				2
V			37				64
Zn			44				57
Cu			2				10
Ba			330	948			558
As			4				4
Rb			44	130			96
Sr			606	690			559
Y			16				19
Zr			120	210			123
Nb			14				15
Cd			0.4				0.4
Th			6				5
U			10				10
La			2				8
Ce			62				55

# Whole Rock Composition - Volcanic Dacite

---

---

ELEMEN FAR 310

---

---

SiO2	66.21
TiO2	0.24
Al2O3	16.35
Fe2O3	2.22
MnO	0.03
MgO	0.6
CaO	3.92
Na2O	1.97
K2O	2.25
P2O5	0.03
LOI	6.1

---

SUM	99.92
-----	-------

---

FeO	0.59
-----	------

---

Cr	2
Ni	15
Sc	3
Co	2
Pb	17
Sn	2
V	6
Zn	58
Cu	4
Ba	731
As	4
Rb	184
Sr	600
Y	22
Zr	177
Nb	19
Cd	0.4
Th	9
U	10
La	22
Ce	97

---

---

# Whole-Rock Composition - Intrusive Basalts

ELEMENT	FAR 216	FAR 218	FAR 254
SiO2	53.99	55.53	56.37
TiO2	1.09	1.13	0.95
Al2O3	16.62	17.11	16.19
Fe2O3	8.6	8.03	6.65
MnO	0.13	0.17	0.14
MgO	3.29	3.02	5.49
CaO	6.86	7	4.92
Na2O	2.96	2.21	2.99
K2O	2.27	1.7	2.21
P2O5	0.44	0.44	0.42
LOI	2.7	3.1	3
SUM	98.95	99.44	99.33
FeO	3.66	2.98	3.16
Cr	29	29	6
Ni	29	31	10
Sc	17	14	10
Co	15	11	8
Pb	6	7	4
Sn	2	2	2
V	162	116	82
Zn	57	102	84
Cu	27	2	2
Ba	551	720	644
As	9	6	4
Rb	91	52	84
Sr	549	499	448
Y	19	22	23
Zr	107	137	160
Nb	11	16	17
Cd	0.5	0.4	0.4
Th	5	2	4
U	10	10	10
La	2	2	4
Ce	38	57	65

# Whole-Rock Composition - Intrusive Andesites

ELEMENT	FAR 215	AA-11	FJ3	FAR 267	AA-10	FAR 224	AA-8
SiO2	57.04	57.40	57.42	57.48	58.00	59.06	59.28
TiO2	0.9	0.56	1.13	1.04	0.52	0.7	0.77
Al2O3	17.11	15.10	17.51	16.87	15.00	16.91	13.60
Fe2O3	6.75	4.70		6.94	4.00	5.86	6.29
MnO	0.12	0.330	0.11	0.12	0.210	0.17	0.178
MgO	5.54	2.20	3.2	2.88	1.70	2.08	2.69
CaO	6.01	3.90	6.44	6.1	4.70	6.58	5.60
Na2O	2.48	2.60	3.17	2.57	2.80	2.92	3.29
K2O	2.51	3.40	2.74	2.03	3.30	2.54	3.13
P2O5	0.4	0.170	0.33	0.4	0.150	0.35	0.087
LOI	1.2	3.60		3.3	3.50	2.3	
SUM	100.06	95.80	99.58	99.73	95.70	99.47	94.92
FeO	3.64	1.80	7.53	3.12	1.80	2.56	
Cr	10		9	31		20	
Ni	18		6	13		13	
Sc	13		19.3	10		8	
Co	8		34	9		7	
Pb	11			7		21	
Sn	2			2		2	
V	100			89		86	
Zn	77			82		84	
Cu	21			2		14	
Ba	659		446.5	663		961	
As	6			4		6	
Rb	97		106	62		87	
Sr	478		497	428		640	
Y	23			23		18	
Zr	172			152		122	
Nb	19			18		15	
Cd	0.5			0.5		0.7	
Th	7		6.5	5		4	
U	10		2	10		10	
La	26		27	20		11	
Ce	65		55.8	65		49	

### Whole-Rock Composition - Intrusive Andesites

ELEMENT	FAR 229	FAR 262	FAR 295	FAR 244	AA-6	AA-12	FAR 297
SiO <sub>2</sub>	59.66	61.06	61.12	61.45	61.50	61.96	62.2
TiO <sub>2</sub>	0.69	0.69	0.8	0.59	0.55	0.57	0.59
Al <sub>2</sub> O <sub>3</sub>	16.69	16.49	16.13	16.03	16.10	14.36	16.44
Fe <sub>2</sub> O <sub>3</sub>	5.73	5.18	5.76	5.11	5.20	5.15	4.88
MnO	0.14	0.13	0.12	0.11	0.140	0.041	0.14
MgO	2.07	2.38	3.2	1.78	1.70	0.76	2.64
CaO	6.14	4.4	4.99	5.53	5.70	4.48	4.1
Na <sub>2</sub> O	3.08	2.98	2.79	2.9	3.10	3.29	2.76
K <sub>2</sub> O	2.51	2.43	2.11	2.44	3.20	3.13	2.81
P <sub>2</sub> O <sub>5</sub>	0.35	0.38	0.38	0.41	0.390	0.073	0.25
LOI	2.5	3.3	2.4	3.4	2.70		3.4
SUM	99.56	99.42	99.8	99.75	100.30	93.81	100.21
FeO	2.58	2.1	2.68	1.78	0.05		1.87
Cr	14	6	13	41			8
Ni	17	10	13	19			19
Sc	8	6	10	8			8
Co	7	5	7	6			4
Pb	9	10	8	7			18
Sn	2	2	2	2			2
V	86	45	74	70			62
Zn	71	75	71	63			75
Cu	11	2	2	9			2
Ba	897	811	760	750			947
As	4	4	4	4			4
Rb	95	74	88	76			144
Sr	601	663	560	623			508
Y	18	20	21	21			24
Zr	122	144	132	145			170
Nb	15	19	24	18			17
Cd	0.4	0.6	0.4	0.4			0.4
Th	4	3	6	5			6
U	10	10	10	10			10
La	9	20	14	17			4
Ce	42	77	66	73			96

# Whole-Rock Composition - Intrusive Andesites

ELEMENT	AA-14	AA-13	FAR 220
SiO2	62.40	62.52	62.73
TiO2	0.40	0.60	0.81
Al2O3	12.47	14.36	16.42
Fe2O3	4.58	4.29	5.2
MnO	0.181	0.067	0.04
MgO	1.06	1.26	1.53
CaO	4.20	2.80	4.29
Na2O	3.07	3.77	3.9
K2O	3.37	3.37	2.22
P2O5	0.064	0.073	0.26
LOI			1.8
SUM	91.80	93.11	99.2
FeO			1.18
Cr			37
Ni			23
Sc			7
Co			6
Pb			4
Sn			2
V			68
Zn			29
Cu			3
Ba			812
As			13
Rb			64
Sr			478
Y			19
Zr			141
Nb			20
Cd			0.5
Th			4
U			10
La			13
Ce			42

# Whole-Rock Composition - Intrusive Dacites and Rhyolites

ELEMENT	FAR 238	FAR 318	FAR 288	FAR 287	FAR 269	FAR 281	FAR 316
SiO2	63.57	64.51	66.88	67.16	70.87	75.91	80.94
TiO2	0.61	0.66	0.39	0.36	0.18	0.07	0.22
Al2O3	15.78	16.29	16.08	15.35	14.57	13.98	11.54
Fe2O3	4.76	4.99	3.39	3.01	1.99	0.68	0.53
MnO	0.07	0.31	0.09	0.08	0.03	0.02	0.05
MgO	2.61	1.6	1.17	1.06	0.31	0.08	0.34
CaO	3.13	1.95	4.16	4.28	1.55	0.28	0.15
Na2O	2.9	3.07	3.56	2.72	2.72	2.66	0.03
K2O	3.1	3.01	2.42	2.58	3.91	4.38	2.79
P2O5	0.29	0.34	0.16	0.18	0.03	0.04	0.01
LOI	2.9	2.9	1.5	3.1	3.7	1.8	2.8
SUM	99.72	99.63	99.8	99.88	99.86	99.9	99.4
FeO	1.56	1.82	1.18	0.84	0.66	0.5	0.32
Cr	57	7	29	16	15	26	11
Ni	33	15	17	21	41	29	17
Sc	9	7	6	4	3	6	5
Co	8	6	4	3	2	2	2
Pb	6	16	9	7	6	4	160
Sn	2	2	2	2	2	3	2
V	77	52	52	43	5	2	29
Zn	114	722	42	46	42	53	12
Cu	9	2	2	2	5	4	26
Ba	704	585	741	702	543	133	111
As	4	4	4	4	5	4	26
Rb	108	116	86	93	183	342	278
Sr	479	546	658	560	169	60	17
Y	14	19	13	14	16	36	20
Zr	123	185	113	101	164	41	69
Nb	17	22	17	16	19	30	17
Cd	1	0.7	0.4	0.4	0.4	0.4	1
Th	6	5	5	5	8	7	7
U	10	10	10	10	10	10	11
La	9	2	15	2	16	10	2
Ce	34	99	58	27	57	35	36

## **APPENDIX C.**

### **CIPW Norms for Igneous Rocks of the Farallón Negro Volcanic Complex.**



**Table C-1.**

CIPW Norms for rocks from the Farallón Negro Volcanic Complex (includes data from: Dostal et al. (1977); Caelles (1979); Allison (1986); and, Kay et al. (1988) and this study). Abbreviations are: Qtz = quartz, Cor = Corundum, Zr = Zircon, Or = Orthoclase, Ab = Albite, An = Anorthite, Ne = Nepheline, Di = Diopside, WO = Wollastonite, Hy = Hypersthene, Ol = Olivine, Mt = Magnetite, Chm = Chromite, Hm = Hematite, Il = Ilmentite, Tn = Titanite, Ru = Rutile, Ap = Apatite, A/CNK = molecular  $\text{Al}_2\text{O}_3$  /  $\text{CaO} + \text{Na}_2\text{O} + \text{K}_2\text{O}$ .

MINERAL	FAR 201	FAR 203	FAR 204	FAR 205	FAR 206	FAR 207	FAR 215
Qtz	0.00	10.35	14.24	20.28	21.98	7.37	12.84
Cor	0.00	0.00	0.00	1.40	0.00	0.00	0.23
Zr	0.03	0.02	0.03	0.04	0.03	0.02	0.03
Or	13.91	27.80	12.03	31.16	17.85	11.31	14.87
Al	23.94	15.91	21.32	28.01	17.60	22.34	20.98
An	24.20	22.31	26.92	12.40	22.39	27.26	27.56
Ne	0.00	0.00	0.00	0.00	0.00	0.00	0.00
Di	12.50	8.99	1.65	0.00	1.64	10.68	0.00
Wo	0.00	0.84	0.00	0.00	0.00	0.00	0.00
Hy	15.56	0.00	11.59	0.47	4.50	4.99	13.80
Ol	3.25	0.00	0.00	0.00	0.00	0.00	0.00
Mt	3.02	3.93	3.06	0.13	2.11	2.37	9.52
Chm	0.04	0.00	0.00	0.00	0.01	0.01	0.00
Hm	0.00	4.20	5.88	3.60	3.81	7.72	0.18
Il	2.73	2.16	2.39	0.74	1.18	2.91	1.71
Tn	0.00	0.00	0.00	0.00	0.00	0.00	0.00
Ru	0.00	0.00	0.00	0.00	0.00	0.00	0.00
Ap	0.93	0.86	1.07	0.55	0.79	1.07	0.95
A/CNK	0.71	0.74	0.90	1.06	0.91	0.73	0.97

MINERAL	FAR 216	FAR 218	FAR 219	FAR 220	FAR 222	FAR 224	FAR 229
Qtz	10.89	17.85	10.55	20.65	5.10	17.07	17.61
Cor	0.00	0.00	0.00	0.31	0.00	0.00	0.00
Zr	0.02	0.03	0.03	0.03	0.03	0.02	0.02
Or	13.45	10.07	11.19	13.15	10.36	15.05	14.87
Al	25.04	18.70	20.31	33.00	22.59	24.71	26.06
An	25.40	31.81	28.77	19.98	30.51	25.60	24.37
Ne	0.00	0.00	0.00	0.00	0.00	0.00	0.00
Di	4.76	0.33	3.79	0.00	7.59	4.09	3.33
Wo	0.00	0.00	0.00	0.00	0.00	0.00	0.00
Hy	5.99	7.37	8.41	3.81	7.20	3.29	3.62
Ol	0.00	0.00	0.00	0.00	0.00	0.00	0.00
Mt	9.07	6.89	8.24	1.59	12.68	6.78	6.78
Chm	0.01	0.01	0.01	0.01	0.00	0.00	0.00
Hm	2.34	3.28	3.82	4.10	2.01	1.18	1.06
Il	2.07	2.15	2.51	1.54	3.19	1.33	1.31
Tn	0.00	0.00	0.00	0.00	0.00	0.00	0.00
Ru	0.00	0.00	0.00	0.00	0.00	0.00	0.00
Ap	1.05	1.05	1.34	0.62	1.38	0.84	0.84
A/CNK	0.84	0.94	0.85	0.99	0.78	0.87	0.88

MINERAL	FAR 238	FAR 244	FAR 254	FAR 262	FAR 267	FAR 269	FAR 271
Qtz	24.90	22.06	12.83	22.33	18.38	36.26	8.34
Cor	2.54	0.00	0.84	1.73	0.21	3.05	0.00
Zr	0.02	0.03	0.03	0.03	0.03	0.03	0.03
Or	18.36	14.45	13.09	14.39	12.02	23.18	9.83
Al	24.54	24.54	25.30	35.21	21.74	23.01	25.55
An	14.00	23.58	22.00	19.80	27.98	7.70	27.47
Ne	0.00	0.00	0.00	0.00	0.00	0.00	0.00
Di	0.00	1.25	0.00	0.00	0.00	0.00	3.82
Wo	0.00	0.00	0.00	0.00	0.00	0.00	0.00
Hy	6.50	3.86	13.67	5.93	7.17	0.77	8.80
Ol	0.00	0.00	0.00	0.00	0.00	0.00	0.00
Mt	3.49	4.39	7.89	5.20	7.43	1.72	1.53
Chm	0.01	0.01	0.00	0.00	0.01	0.00	0.00
Hm	2.35	2.08	1.21	1.60	1.81	0.81	7.83
Il	1.16	1.12	1.80	1.31	1.97	0.34	2.64
Tn	0.00	0.00	0.00	0.00	0.00	0.00	0.00
Ru	0.00	0.00	0.00	0.00	0.00	0.00	0.00
Ap	0.70	0.98	1.00	0.91	0.95	0.07	1.36
A/CNK	1.14	0.92	1.00	1.06	0.96	1.26	0.85

MINERAL	FAR 281	FAR 284	FAR 285	FAR 287	FAR 288	FAR 295	FAR 296
Qtz	42.84	26.80	12.51	31.05	26.52	22.25	5.39
Cor	4.41	1.92	0.00	0.61	0.29	0.97	0.00
Zr	0.01	0.02	0.03	0.02	0.02	0.03	0.03
Or	26.02	11.68	13.33	15.28	14.34	12.50	24.09
Al	22.51	23.94	29.19	23.01	30.12	23.61	22.42
An	1.18	21.13	22.57	20.45	20.04	22.68	24.95
Ne	0.00	0.00	0.00	0.00	0.00	0.00	0.00
Di	0.00	0.00	6.60	0.00	0.00	0.00	8.23
Wo	0.00	0.00	0.00	0.00	0.00	0.00	0.00
Hy	0.48	4.91	4.12	2.64	2.91	7.97	2.87
Ol	0.00	0.00	0.00	0.00	0.00	0.00	0.00
Mt	0.99	3.45	2.74	1.93	2.97	6.71	1.93
Chm	0.01	0.00	0.01	0.00	0.01	0.00	0.01
Hm	0.00	2.49	5.19	1.68	1.34	1.13	6.61
Il	0.13	1.06	1.99	0.68	0.74	1.52	1.82
Tn	0.00	0.00	0.00	0.00	0.00	0.00	0.00
Ru	0.00	0.00	0.00	0.00	0.00	0.00	0.00
Ap	0.10	0.69	0.96	0.43	0.38	0.91	1.12
A/CNK	1.45	1.09	0.81	1.02	1.00	1.01	0.79

MINERAL	FAR 297	FAR 299	FAR 302	FAR 308	FAR 309	FAR 310	FAR 311
Qtz	23.18	20.00	19.15	5.78	27.11	36.73	12.14
Cor	1.87	0.00	0.42	0.00	5.22	3.48	0.00
Zr	0.03	0.03	0.03	0.02	0.03	0.04	0.03
Or	16.66	23.57	21.27	11.19	8.24	13.37	10.97
Al	23.35	20.31	27.33	20.73	15.91	16.67	21.58
An	19.15	20.89	19.27	31.17	20.77	19.67	29.57
Ne	0.00	0.00	0.00	0.00	0.00	0.00	0.00
Di	0.00	2.18	0.00	7.80	0.00	0.00	2.60
Wo	0.00	0.00	0.00	0.00	0.00	0.00	0.00
Hy	6.57	3.88	3.84	7.32	7.82	1.49	10.18
Ol	0.00	0.00	0.00	0.00	0.00	0.00	0.00
Mt	4.78	3.82	7.71	15.71	0.51	1.31	4.43
Chm	0.00	0.00	0.00	0.00	0.00	0.00	0.00
Hm	1.58	2.62	0.14	0.43	3.54	1.32	4.37
Il	1.12	1.16	1.08	3.34	1.02	0.46	1.67
Tn	0.00	0.00	0.00	0.00	0.00	0.00	0.00
Ru	0.00	0.00	0.00	0.00	0.00	0.00	0.00
Ap	0.60	0.86	0.84	1.05	0.36	0.07	0.95
A/CNK	1.09	0.90	0.98	0.79	1.39	1.28	0.89

MINERAL	FAR 312	FAR 316	FAR 318	FAR 337	D-A	D-B	D-C
Qtz	30.10	69.21	29.36	18.46	0.00	8.61	16.82
Cor	0.78	8.19	5.14	0.00	0.00	0.00	0.00
Zr	0.02	0.01	0.04	0.03	0.03	0.04	0.03
Or	4.92	16.60	17.83	12.92	18.41	20.91	20.48
Al	19.63	0.25	25.97	24.20	19.11	36.21	25.21
An	28.51	0.71	7.80	24.30	22.57	19.17	23.91
Ne	0.00	0.00	0.00	0.00	0.00	0.00	0.00
Di	0.00	0.00	0.00	0.00	22.83	2.61	1.90
Wo	0.00	0.00	0.00	0.00	0.00	0.00	0.00
Hy	3.54	0.85	3.98	4.31	0.00	9.15	8.65
Ol	0.00	0.00	0.00	0.00	6.41	0.00	0.00
Mt	1.43	0.56	4.97	0.00	2.87	1.79	1.41
Chm	0.01	0.00	0.00	0.00	0.02	0.01	0.00
Hm	2.07	0.14	1.56	6.40	0.00	0.00	0.00
Il	0.78	0.42	1.25	0.89	2.37	1.39	1.29
Tn	0.00	0.00	0.00	0.51	0.00	0.00	0.00
Ru	0.00	0.00	0.00	0.24	0.00	0.00	0.00
Ap	0.36	0.02	0.82	0.83	0.00	0.00	0.00
A/CNK	1.03	3.45	1.37	0.94	0.63	0.95	0.96

MINERAL	JC-30	JC-33	JC-34A	JC-34C	JC-46	JC-76B	JC-95
Qtz	0.00	18.04	0.00	4.17	17.77	12.38	8.47
Cor	0.00	0.23	0.00	0.00	0.00	0.00	0.00
Zr	0.00	0.00	0.00	0.00	0.00	0.00	0.00
Or	13.30	17.73	1.24	11.17	27.66	16.43	14.54
Al	25.38	28.17	14.38	27.41	17.43	21.58	22.76
An	19.16	21.68	28.59	27.08	21.55	25.92	27.05
Ne	5.04	0.00	0.00	0.00	0.00	0.00	0.00
Di	21.15	0.00	25.34	13.26	1.04	3.84	10.83
Wo	0.00	0.00	0.00	0.00	0.00	0.00	0.00
Hy	0.00	6.19	5.30	1.61	6.72	8.67	3.65
Ol	5.49	0.00	13.28	0.00	0.00	0.00	0.00
Mt	2.99	4.52	4.06	6.23	1.70	4.84	5.00
Chm	0.00	0.00	0.00	0.00	0.00	0.00	0.00
Hm	0.00	0.00	0.00	0.00	0.00	0.00	0.00
Il	2.85	1.77	3.19	2.30	1.22	2.09	2.32
Tn	0.00	0.00	0.00	0.00	0.00	0.00	0.00
Ru	0.00	0.00	0.00	0.00	0.00	0.00	0.00
Ap	1.02	0.59	1.02	1.35	0.69	1.11	1.30
A/CNK	0.61	0.98	0.52	0.70	0.93	0.85	0.73

MINERAL	JC-193	JC-194	JC-222	AA-1	AA-2	AA-3	AA-4
Qtz	7.44	9.41	17.67	0.00	13.45	21.76	0.00
Cor	0.21	0.00	0.00	0.00	0.00	1.65	0.00
Zr	0.00	0.00	0.00	0.00	0.00	0.00	0.00
Or	22.05	20.98	20.21	12.83	22.76	15.96	22.76
Al	39.60	38.58	26.82	11.34	17.26	24.54	22.11
An	17.61	15.60	20.15	7.25	16.58	17.61	18.60
Ne	0.00	0.00	0.00	22.04	0.00	0.00	1.63
Di	0.00	3.07	3.61	41.75	16.17	0.00	28.34
Wo	0.00	0.00	0.00	0.00	0.00	0.00	0.00
Hy	4.28	4.13	3.95	0.00	4.71	6.23	0.00
Ol	0.00	0.00	0.00	0.56	0.00	0.00	0.99
Mt	2.86	4.31	4.28	2.90	2.15	5.47	2.65
Chm	0.00	0.00	0.00	0.00	0.00	0.00	0.00
Hm	0.00	0.00	0.00	0.00	0.00	0.43	0.00
Il	1.44	1.58	1.52	2.22	1.20	1.23	1.77
Tn	0.00	0.00	0.00	0.00	0.00	0.00	0.00
Ru	0.00	0.00	0.00	0.00	0.00	0.00	0.00
Ap	0.45	0.88	0.71	0.13	0.38	0.45	1.43
A/CNK	0.99	0.88	0.87	0.45	0.65	1.08	0.55

MINERAL	AA-5	AA-6	AA-7	AA-8	AA-9	AA-10	AA-11
Qtz	0.00	18.69	3.25	12.56	15.69	17.70	18.10
Cor	0.00	0.00	0.00	0.00	0.00	0.00	0.46
Zr	0.00	0.00	0.00	0.00	0.00	0.00	0.00
Or	18.50	18.91	28.49	18.50	18.91	19.50	20.10
Al	23.32	26.23	24.20	27.84	21.15	23.69	22.00
An	18.26	20.57	11.08	13.10	20.81	18.62	18.24
Ne	3.87	0.00	0.00	0.00	0.00	0.00	0.00
Di	25.08	3.11	22.34	11.66	4.52	2.90	0.00
Wo	0.00	0.00	5.29	0.00	0.00	0.00	0.00
Hy	0.00	2.79	0.00	7.27	2.89	2.89	5.48
Ol	4.75	0.00	0.00	0.00	0.00	0.00	0.00
Mt	3.15	0.00	1.49	1.82	5.08	4.98	5.25
Chm	0.00	0.00	0.00	0.00	0.00	0.00	0.00
Hm	0.00	5.20	0.00	0.00	0.90	0.57	1.08
Il	1.90	0.40	0.57	1.46	1.01	0.99	1.06
Tn	0.00	0.83	0.00	0.00	0.00	0.00	0.00
Ru	0.00	0.00	0.00	0.00	0.00	0.00	0.00
Ap	0.52	0.92	0.32	0.21	0.43	0.36	0.40
A/CNK	0.58	0.85	0.49	0.72	0.86	0.90	1.00

MINERAL	AA-12	AA-13	AA-14	AA-15	AA-16	FJ2	FJ3
Qtz	19.42	18.39	21.16	7.88	10.13	4.93	8.06
Cor	0.00	0.00	0.00	0.00	0.00	0.00	0.00
Zr	0.00	0.00	0.00	0.00	0.00	0.00	0.00
Or	18.50	19.92	19.92	31.33	28.49	20.19	16.24
Al	27.84	31.90	25.97	31.05	30.54	25.04	26.82
An	15.17	12.31	10.30	7.06	9.78	24.86	25.49
Ne	0.00	0.00	0.00	0.00	0.00	0.00	0.00
Di	5.62	0.92	8.56	18.00	19.07	15.15	3.81
Wo	0.00	0.00	0.00	1.03	0.62	0.00	0.00
Hy	4.11	6.77	3.28	0.00	0.00	3.63	14.11
Ol	0.00	0.00	0.00	0.00	0.00	0.00	0.00
Mt	1.49	1.24	1.33	1.34	1.39	2.51	2.43
Chm	0.00	0.00	0.00	0.00	0.00	0.00	0.00
Hm	0.00	0.00	0.00	0.00	0.00	0.00	0.00
Il	1.08	1.14	0.76	0.63	0.76	2.41	2.15
Tn	0.00	0.00	0.00	0.00	0.00	0.00	0.00
Ru	0.00	0.00	0.00	0.00	0.00	0.00	0.00
Ap	0.17	0.17	0.15	0.32	0.22	0.79	0.79
A/CNK	0.85	0.96	0.76	0.61	0.62	0.71	0.88

**APPENDIX D.**  
**Duplicate Whole-Rock Analyses.**

**Table D-1.**

Duplicate sample analyses for Farallón Negro samples.



ELEMENT	FAR 220	FAR 220	MEAN	STD DEV
SiO2	62.73	63.04	62.885	0.155
TiO2	0.81	0.78	0.795	0.015
Al2O3	16.42	16.49	16.455	0.035
Fe2O3	5.2	5.21	5.205	0.005
MnO	0.04	0.04	0.04	0
MgO	1.53	1.54	1.535	0.005
CaO	4.29	4.32	4.305	0.015
Na2O	3.9	3.95	3.925	0.025
K2O	2.22	2.2	2.21	0.01
P2O5	0.26	0.25	0.255	0.005
LOI	1.8	1.8	1.8	0
SUM	99.2	99.62	99.41	0.27
FeO	1.18	1.26	1.22	0.04
Cr	37	33	35	2
Ni	23	41	32	9
Sc	7	7	7	0
Co	6	6	6	0
Pb	4	5	4.5	0.5
Sn	2	2	2	0
V	68	67	67.5	0.5
Zn	29	29	29	0
Cu	3	2	2.5	0.5
Ba	812	819	815.5	3.5
As	13	10	11.5	1.5
Rb	64	68	66	2
Sr	478	479	478.5	0.5
Y	19	19	19	0
Zr	141	137	139	2
Nb	20	21	20.5	0.5
Cd	0.5	0.4	0.45	0.05
Th	4	3	3.5	0.5
U	10	10	10	0
La	13	28	20.5	7.5
Ce	42	52	47	5

ELEMENT	FAR 302	FAR 302	MEAN	STD DEV
SiO2	62.31	62.63	62.47	0.16
TiO2	0.57	0.58	0.575	0.005
Al2O3	16.66	16.9	16.78	0.12
Fe2O3	5.46	5.45	5.455	0.005
MnO	0.23	0.23	0.23	0
MgO	1.54	1.54	1.54	0
CaO	4.26	4.27	4.265	0.005
Na2O	3.23	3.27	3.25	0.02
K2O	3.59	3.42	3.505	0.085
P2O5	0.35	0.32	0.335	0.015
LOI	1.6	1.5	1.55	0.05
SUM	99.8	100.11	99.955	0.465
FeO	2.67	2.67	2.67	0
Cr	19	20	19.5	0.5
Ni	23	21	22	1
Sc	7	7	7	0
Co	5	6	5.5	0.5
Pb	19	20	19.5	0.5
Sn	2	2	2	0
V	54	55	54.5	0.5
Zn	868	890	879	11
Cu	4	7	5.5	1.5
Ba	714	727	720.5	6.5
As	4	4	4	0
Rb	148	146	147	1
Sr	637	647	642	5
Y	22	23	22.5	0.5
Zr	164	180	172	8
Nb	18	21	19.5	1.5
Cd	0.6	0.6	0.6	0
Th	7	7	7	0
U	10	10	10	0
La	3	5	4	1
Ce	75	68	71.5	3.5

ELEMENT	FAR 337	FAR 337	MEAN	STD DEV
SiO2	56.67	56.33	56.5	0.17
TiO2	0.92	0.92	0.92	0
Al2O3	15.95	15.92	15.935	0.015
Fe2O3	6.4	6.4	6.4	0
MnO	0.14	0.14	0.14	0
MgO	1.73	1.71	1.72	0.01
CaO	5.44	5.49	5.465	0.025
Na2O	2.86	2.85	2.855	0.005
K2O	2.18	1.98	2.08	0.1
P2O5	0.35	0.36	0.355	0.005
LOI	7.2	7.3	7.25	0.05
SUM	99.84	99.4	99.62	0.38
FeO	0.28	0.3	0.29	0.01
Cr	6	3	4.5	1.5
Ni	15	37	26	11
Sc	8	8	8	0
Co	7	6	6.5	0.5
Pb	17	16	16.5	0.5
Sn	2	2	2	0
V	55	53	54	1
Zn	118	123	120.5	2.5
Cu	2	2	2	0
Ba	737	723	730	7
As	10	9	9.5	0.5
Rb	94	93	93.5	0.5
Sr	309	306	307.5	1.5
Y	20	20	20	0
Zr	164	159	161.5	2.5
Nb	19	19	19	0
Cd	0.4	0.7	0.55	0.15
Th	5	4	4.5	0.5
U	10	10	10	0
La	7	2	4.5	2.5
Ce	64	53	58.5	5.5

ELEMENT	FAR201	FAR201	MEAN	STD DEV
Li	27.551	26.665	27.108	0.443
Rb	49.821	50.479	50.15	0.329
Sr	528.89	527.36	528.125	0.765
Y	22.337	22.766	22.5515	0.2145
Zr	109.264	111.090	110.177	0.913
Nb	14.308	14.370	14.339	0.031
Mo	2.190	2.227	2.2085	0.0185
Cs	2.818	2.860	2.839	0.021
Ba	510.77	526.07	518.42	7.65
Ho	0.890	0.930	0.91	0.02
Er	2.475	2.480	2.4775	0.0025
Tm	0.324	0.349	0.3365	0.0125
Yb	2.033	1.989	2.011	0.022
Lu	0.296	0.319	0.3075	0.0115
Hf	3.339	3.366	3.3525	0.0135
Ta	1.289	1.365	1.327	0.038
Tl	0.250	0.284	0.267	0.017
Pb	8.302	8.353	8.3275	0.0255
La	19.489	20.235	19.862	0.373
Ce	42.825	43.841	43.333	0.508
Pr	5.709	5.749	5.729	0.02
Nd	24.346	24.493	24.4195	0.0735
Sm	5.518	5.604	5.561	0.043
Eu	1.728	1.768	1.748	0.02
Gd	5.509	5.266	5.3875	0.1215
Tb	0.778	0.843	0.8105	0.0325
Dy	4.632	4.749	4.6905	0.0585
Bi	0.059	0.062	0.0605	0.0015
Th	3.410	3.512	3.461	0.051
U	0.938	0.967	0.9525	0.0145

**Table D-2.**

Duplicate sample analyses for standards.

ELEMENT	STANDARD SO-4	STANDARD SO-4	MEAN	STD DEV
SiO2	68.2	68.48	68.34	0.14
TiO2	0.58	0.55	0.565	0.015
Al2O3	10.54	10.5	10.52	0.02
Fe2O3	3.45	3.47	3.46	0.01
MnO	0.07	0.08	0.075	0.005
MgO	0.95	0.97	0.96	0.01
CaO	1.61	1.59	1.6	0.01
Na2O	1.31	1.28	1.295	0.015
K2O	2.1	2.1	2.1	0
P2O5	0.22	0.22	0.22	0
LOI	10.8	10.8	10.8	0
SUM	99.83	100.04	99.935	0.105
FeO	0	0	0	0
Cr	95	96	95.5	0.5
Ni	34	30	32	2
Sc	8	8	8	0
Co	30	31	30.5	0.5
Pb	35	37	36	1
Sn	16	15	15.5	0.5
V	107	111	109	2
Zn	126	128	127	1
Cu	50	52	51	1
Ba	851	846	848.5	2.5
As	37	35	36	1
Rb	0	0	0	0
Sr	173	187	180	7
Y	24	22	23	1
Zr	288	291	289.5	1.5
Nb	10	9	9.5	0.5
Cd	17.2	17.9	17.55	0.35
Th	37	37	37	0
U	10	10	10	0
La	25	28	26.5	1.5
Ce	55	49	52	3

## **APPENDIX E.**

**Published Whole-Rock Geochemistry for rocks of  
the Farallón Negro Volcanic Complex.**

**Table E-1.**

Whole-rock geochemical data from Dostal et al. (1977)



ELEMENT	D-A	D-B	D-C	DZ-14	DZ-15	DZ-16	DZ-17
SiO <sub>2</sub>	51.18	61.38	63.31	50.87	51.48	61.24	63.63
TiO <sub>2</sub>	1.25	0.73	0.68				
Al <sub>2</sub> O <sub>3</sub>	17.14	17.86	17.39				
FeO	8.92	5.56	4.39				
MgO	4.24	1.81	2.03				
CaO	10.06	4.39	5.21				
Na <sub>2</sub> O	3.35	4.28	2.98				
K <sub>2</sub> O	3.11	3.53	3.46				
Rb	80	130	87				
Sr	512	690	510				
Ba	556	948	628				
Zr	141	210	152				
Cr	88	30	6				
Ni	35		23				
Co	42	33	30				
V	208		110				
La				25.4	26.8	42.4	29.9
Ce				59.6	63.2	84.9	69.9
Sm				6.04	5.77	7.02	6.46
Eu				1.73	1.67	1.86	1.63
Tb				0.816	0.806	0.86	0.804
Yb				2.35	2.17	2.08	2.51
Lu				0.366	0.341	0.317	0.419

**Table E-2.**

Whole-rock geochemical data from Caelles (1979).

ELEMENT	JC-30	JC-33	JC-34A	JC-34C	JC-46	JC-76B	JC-95	JC-193
SiO2	49.60	61.80	44.60	50.10	61.10	55.90	53.00	58.75
TiO2	1.50	0.93	1.68	1.21	0.64	1.10	1.22	0.76
Al2O3	16.20	16.90	13.50	17.30	16.35	16.70	17.00	18.40
Fe2O3	2.06	3.12	2.80	4.30	1.17	3.34	3.45	1.97
MnO	0.180	0.130	0.370	0.170	0.110	0.160	0.160	0.220
MgO	4.00	2.02	9.85	2.65	1.57	2.90	2.35	0.70
CaO	9.62	4.70	12.65	9.58	4.98	6.80	8.87	3.80
Na2O	4.10	3.33	1.70	3.24	2.06	2.55	2.69	4.68
K2O	2.25	3.00	0.21	1.89	4.68	2.78	2.46	3.73
P2O5	0.430	0.250	0.430	0.570	0.290	0.470	0.550	0.190
LOI								
SUM	96.35	98.62	96.38	94.56	95.75	96.83	95.90	95.93
FeO	6.41	2.74	8.59	3.55	2.80	4.13	4.15	2.73

ELEMENT	JC-194	JC-222
SiO2	60.20	62.20
TiO2	0.83	0.80
Al2O3	17.06	16.30
Fe2O3	2.97	2.95
MnO	0.190	0.100
MgO	1.57	2.05
CaO	4.40	5.38
Na2O	4.56	3.17
K2O	3.55	3.42
P2O5	0.370	0.300
LOI		
SUM	98.51	98.91
FeO	2.82	2.24

**Table E-3.**

Whole-rock geochemical data from Allison (1986).

ELEMENT	1	2	3	4	5	6	7	8
SiO2	50.66	57.90	60.30	53.60	52.10	61.50	57.40	59.28
TiO2	1.17	0.63	0.65	0.93	1.00	0.55	0.30	0.77
Al2O3	15.12	13.60	15.80	15.87	16.00	16.10	13.98	13.60
Fe2O3	10.01	7.43	4.20	9.15	10.87	5.20	5.15	6.29
MnO	0.160	0.330	0.080	0.170	0.210	0.140	0.550	0.178
MgO	4.58	1.89	2.50	2.49	3.08	1.70	1.89	2.69
CaO	11.75	7.42	3.80	10.80	10.00	5.70	10.35	5.60
Na2O	6.15	2.04	2.90	2.97	3.60	3.10	2.86	3.29
K2O	2.17	3.85	2.70	3.85	3.13	3.20	4.82	3.13
P2O5	0.054	0.160	0.190	0.183	0.220	0.390	0.137	0.087
LOI			1.60			2.70		
SUM	98.82	95.25	96.90	100.01	100.21	100.30	97.44	94.92
FeO			2.20			0.05		

ELEMENT	9	10	11	12	13	14	15	16
SiO2	55.70	58.00	57.40	61.96	62.52	62.40	62.40	64.00
TiO2	0.53	0.52	0.56	0.57	0.60	0.40	0.33	0.40
Al2O3	15.20	15.00	15.10	14.36	14.36	12.47	14.36	14.74
Fe2O3	4.40	4.00	4.70	5.15	4.29	4.58	4.63	4.78
MnO	0.250	0.210	0.330	0.041	0.067	0.181	0.210	0.240
MgO	2.00	1.70	2.20	0.76	1.26	1.06	1.53	1.69
CaO	5.60	4.70	3.90	4.48	2.80	4.20	6.44	7.00
Na2O	2.50	2.80	2.60	3.29	3.77	3.07	3.67	3.61
K2O	3.20	3.30	3.40	3.13	3.37	3.37	5.30	4.82
P2O5	0.180	0.150	0.170	0.073	0.073	0.064	0.137	0.092
LOI	3.90	3.50	3.60					
SUM	95.30	95.70	95.80	93.81	93.11	91.80	99.01	101.37
FeO	1.80	1.80	1.80					

**Table E-4.**

Whole-rock geochemical data from Kay et al. (1988).

ELEMENT	FJ2	FJ3
SiO2	55.4	57.42
TiO2	1.27	1.13
Al2O3	17.66	17.51
FeO	7.78	7.53
MnO	0.11	0.11
MgO	1.3	3.2
CaO	8.95	6.44
Na2O	2.96	3.17
K2O	3.41	2.74
P2O5	0.33	0.33
SUM	99.17	99.58
La	31.2	27
Ce	58.3	55.8
Nd	31.1	30.5
Sm	6.15	6.13
Eu	1.6	1.52
Tb	0.824	0.88
Yb	2.57	2.47
Lu	0.406	0.377
Rb	104	106
Sr	414	497
Ba	813.9	446.5
Cs	1.6	2.6
U	1.5	2
Th	6.77	6.5
Hf	4.6	4.3
Ta	1.66	1.49
Sc	20.4	19.3
Cr	9	9
Ni	7	6
Co	15	34

## **APPENDIX F.**

**Petrography of Selected Samples from the  
Farallón Negro Volcanic Complex  
listed by rock type.**



# Mineralogy - Volcanic units - Shoshonitic Series

	FAR 203	FAR 296	FAR 206	FAR 299	FAR 302
<b>PHENOCRYSTS</b>					
Clinopyroxene	not observed	colorless irregular	not observed	not observed	not observed
Orthopyroxene	green, altered	not observed	not observed	not observed	not observed
Plagioclase	abundant twinned, zoned An17-An32	twinned zoned An32-An65	twinned zoned An17-An55	twinned zoned An31-An60	euهدral twinned, zoned An11-An40
Hornblende	rimmed by opacite	brown pleic. euهدral	not observed	green, hollow euهدral	green euهدral
Biotite	rare	not observed	euهدral	euهدral fresh	rare, euهدral alt. to chl.
Quartz	not observed	not observed	broken crystals and rounded grains	not observed	rounded resorbed
Apatite	brown phenos and green rod- shaped incl. in plag and opx	micro- phenocrysts	present	present	rare
Oxides	magnetite	present	not observed	present	magnetite
Other			pumice		rare titanite
<b>MATRIX</b>					
	glassy	devitrified glass	devitrified glass	trachytic feld-bio	trachytic glassy
<b>ROCK-TYPE</b>					
	porphyritic plag-hbl shoshonite	porphyritic plag-hbl shoshonite	plag-bio banakitite tuff	porphyritic plag-bio banakite	plag-hbl banakite

## Mineralogy - Volcanic units - Shoshonitic Series

---

FAR 205	
<hr/> <b>PHENOCRYSTS</b> <hr/>	
Clinopyroxene	not observed
Orthopyroxene	not observed
Plagioclase	euhedral twinned, zoned An17-An40
Hornblende	not observed
Biotite	euhedral not abundant
Quartz	not observed
Apatite	rare
Oxides	in matrix
Other	
<hr/> <b>MATRIX</b> <hr/>	
	weakly trachytic feld-oxide
<hr/> <b>ROCK-TYPE</b> <hr/>	
	plag-bio very high-K dacite

---

## Mineralogy - Volcanic Units - Basalts

	FAR 207	FAR 219	FAR 222	FAR 271
<b>PHENOCRYSTS</b>				
Clinopyroxene	twinned hourglass	?	twinned zoned	present
Orthopyroxene	not observed	not observed	not observed	not observed
Plagioclase	twinned, zoned An22-An56	altered to sericite	twinned, zoned An17-An62	in groundmass
Hornblende	green euh. twinned	?	not observed	brown, euh. opacite rims
Biotite	rare. rims alt. to oxides	altered	not observed	not observed
Quartz	not observed	not observed	not observed	minor rounded
Apatite	micro- phenocrysts	not observed	micro- phenocrysts	micro- phenocrysts
Oxides	present	abundant v.f. grained	present	fine grained in matrix
<b>MATRIX</b>				
	med. grained feld-mafics	altered feld-mt-chl	microcrystalline feld-pyx-oxides	altered
<b>ROCK-TYPE</b>				
	plag-pyx basalt	altered plag-bio basalt	plag-pyx basalt	mod. altered hbl basalt

## Mineralogy - Volcanic Units - Basalts

---

FAR 308

---

### PHENOCRYSTS

Clinopyroxene	zoned glomeropheres
Orthopyroxene	irr. shaped
Plagioclase	in groundmass
Hornblende	not observed
Biotite	in groundmass
Quartz	not observed
Apatite	abundant
Oxides	present

---

### MATRIX

coarse  
pheno. phases  
poss. alk. feld.

---

### ROCK-TYPE

two pyroxene  
basalt

---

## Mineralogy - Volcanic Units - Basaltic Andesites

	FAR 201	FAR 204	FAR 285	FAR 309
<b>PHENOCRYSTS</b>				
Clinopyroxene	zoned	rare	rare	not observed
Plagioclase	altered large phenos microphenos	twinned, zoned An17-An66	fresh xtal frag. alt. euh. xtals An18-An50	twinned, zoned
Hornblende	altered opacite	green opacite rims	brown, euh. opacite rims	not observed
Biotite	not observed	not observed	minor rxn. rims	fresh euhedral
Quartz	not observed	not observed	minor	rounded resorbed
Apatite	present	abundant	abundant	not observed
Oxides	in matrix	present	present	present
Other			alk. feld. phenos	pumice
<b>MATRIX</b>				
	trachytic	glassy feld	fine grained wk. trachytic feld-ox-ap	glassy devitrified
<b>ROCK-TYPE</b>				
	hbl-cpx bas-andesite	hbl-plag bas-andesite	plag-hbl bas-andesite	bio bas-andesitic tuff

## Mineralogy - Volcanic Units - Basaltic Andesites

	FAR 311	FAR 337
<b>PHENOCRYSTS</b>		
Clinopyroxene	subangular	not observed
Plagioclase	twinned, zoned glomeropheric An36-An68	altered
Hornblende	brown, euh. opacite rims	relict altered
Biotite	not observed	not observed
Quartz	not observed	not observed
Apatite	present	present
Oxides	present	present
Other		
<b>MATRIX</b>		
	glassy feld	altered
<b>ROCK-TYPE</b>		
	plag-hbl bas-andesite	altered plag-hbl bas-andesite

## Mineralogy - Volcanic Units - Andesites and Dacite

	FAR 284	FAR 312	FAR 310
<b>PHENOCRYSTS</b>			
Plagioclase	fragments twinned, zoned An17-An46	anh. and broken twinned, zoned sieve text. An17-An40	anhedral twinned, zoned glomerophoric An11-An58
Hornblende	green anhedral	not observed	not observed
Biotite	fresh anhedral	fresh anhedral	fresh anhedral
Quartz	sub-rounded	rounded resorbed	not observed
Apatite	not observed	present	present
Oxides	present	not observed	present
Other	pumice lithic frag.	pumice titanite	
<b>MATRIX</b>			
	glassy	glassy devitrified	glassy feld-bio-ap
<b>ROCK-TYPE</b>			
	hbl-bio andesitic tuff	bio andesitic tuff	porphyritic plag-bio dacite

### Mineralogy - Hypabyssal Intrusives - Basaltic Andesites

	FAR 216	FAR 218	FAR 254
<b>PHENOCRYSTS</b>			
Clinopyroxene	twinned glomeropheric	not observed	twinned
Orthopyroxene	not observed	not observed	not observed
Plagioclase	in groundmass	twinned, zoned alt. to sericite	altered
Hornblende	subhedral	? alt. to chl and oxides	euhedral
Biotite	minor	not observed	not observed
Quartz	not observed	not observed	not observed
Apatite	abundant	not observed	present
Oxides	magnetite	present	present
<b>MATRIX</b>			
	med. grained plag-alk. feld	fine grained altered	med. grained altered feld.
<b>ROCK-TYPE</b>			
	hbl bas-andesite	altered porphyritic bas-andesite	feld-hbl bas-andesite dike



## Mineralogy - Hypabyssal Intrusives - Andesites

	FAR 215	FAR 220	FAR 224	FAR 229	FAR 244
<b>PHENOCRYSTS</b>					
Clinopyroxene	not observed	not observed	altered	not observed	not observed
Orthopyroxene	not observed	not observed	not observed	not observed	not observed
Plagioclase	An-35-An65	altered	twinned, zoned An13-An53	twinned, zoned An17-An61	twinned, zoned glomeropheric An12-An32
Hornblende	not observed	brown relict	irregular	euhedral wk. altered	euhedral wk. altered
Biotite	irregular	relict	relict?	rare altered	small
Quartz	not observed	sub-rounded	not observed	not observed	resorbed large
Apatite	abundant	not observed	present	present	abundant
Oxides	magnetite	present	present	present	present
Other	alk. feld.			titanite	
<b>MATRIX</b>					
	equigranular trachytic	altered feld	altered feld-qtz	very fine grained	fine grained var. altered
<b>ROCK-TYPE</b>					
	equigranular bio andesite	altered plag-hbl-bio andesite porphyry	mod. altered plag-bio andesite porphyry	plag-hbl andesite porphyry	plag-qtz andesite porphyry

## Mineralogy - Hypabyssal Intrusives - Andesites

	FAR 262	FAR 267	FAR 295	FAR 297
<b>PHENOCRYSTS</b>				
Clinopyroxene	not observed	minor	not observed	not observed
Orthopyroxene	green twinned, zoned	not observed	one grain	not observed
Plagioclase	twinned, zoned glomeropheric An28-An55	twinned, zoned euhedral An22-An40	twinned, zoned glomeropheric An32-An45	altered
Hornblende	green	green euhedral	green euhedral	green rxn. rims
Biotite	fresh	minor	poss. recrystallized	fresh
Quartz	resorbed	rounded resorbed	rounded resorbed	not observed
Apatite	present	present	present	present
Oxides	present	present	present	present
Other	titanite		titanite	
<b>MATRIX</b>				
	v. fine grained feld	fine grained feld-qtz	fine grained feld-ox-ap	fine grained feld
<b>ROCK-TYPE</b>				
	plag-bio andesite porphyry	plag-hbl andesite porphyry	plag-qtz andesite porphyry	plag-bio andesite porphyry

## Mineralogy - Hypabyssal Intrusives - Dacites

	FAR 238	FAR 287	FAR 288	FAR 318
<b>PHENOCRYSTS</b>				
Clinopyroxene	not observed	not observed	minor	not observed
Plagioclase	twinned, zoned euhedral An25-An54	twinned, zoned glomeropheric	twinned, zoned glomeropheric An16-An36	var. altered An16-An38
Hornblende	relict	minor	brown euhedral	relict
Biotite	euhedral	euhedral	fresh euhedral	altered
Quartz	rounded resorbed	rounded resorbed	rounded minor resob.	rounded resorbed
Apatite	present	present	abundant	present
Oxides	present	minor	present	present
Other	minor titanite		titanite	titanite
<b>MATRIX</b>				
	v. fine grained feld-qtz	devitrified	glassy feld-ap	fine grained altered
<b>ROCK-TYPE</b>				
	plag-hbl dacite porphyry	plag-qtz dacite porphyry	plag-qtz dacite porphyry	altered plag-bio dacite porphyry

## Mineralogy - Rhyolites

	FAR 269	FAR 281	FAR 316
<b>PHENOCRYSTS</b>			
Plagioclase	altered	sieve texture	altered
Quartz	minor	rounded resorbed	rounded resorbed
Apatite			minor
<b>MATRIX</b>			
	crypto- crystalline	crypto- crystalline	fine-to-med. grained qtz-feld
<b>ROCK-TYPE</b>			
	altered rhyolite porphyry	rhyolite porphyry	altered rhyolite porphyry

## **APPENDIX G.**

### **Published Whole-Rock Geochemistry from the Andean Shoshonite Suites.**

**Table G-1.**

Whole-rock geochemical data for Pocho  
from Kay and Gordillo, 1994.

ELEMENT	L2B	CC2B	VE1	CB6	CC2C	V2	V5
SiO2	51.73	54.08	58.7	59.93	61.33	62.82	63.45
TiO2	1.12	1.09	0.66	0.62	0.62	0.54	0.48
Al2O3	16.37	18.12	18.22	18.75	18.3	18	18.02
FeO	8.39	8.09	5.32	5.12	4.3	3.66	3.24
MnO	0.14	0.14	0.08	0.08	0.08	0.06	0.06
MgO	3.34	2.46	1.7	1.37	1.22	0.88	0.75
CaO	9.33	7.95	5.77	5.37	4.91	4.94	5.12
Na2O	3.43	3.76	4.26	4.65	4.81	4.43	4.53
K2O	2.99	2.97	4.05	4.17	4.35	4.25	4.14
P2O5	0.47	0.45	0.2	0.19	0.19	0.1	0.14
TOTAL	97.31	99.11	98.96	100.25	100.11	99.68	99.93
La	23.7	26.9	27.8	31.8	28.1	24.9	24.3
Ce	49.3	54.8	56.1	59.6	52.5	48.9	48.5
Nd	29.2	28.7	27.7	28.3	14.2	25.3	20.8
Sm	6.41	6.82	6.29	5.65	5.17	4.51	4.4
Eu	1.87	1.85	1.67	1.46	1.33	1.24	1.23
Tb	0.904	0.901	0.773	0.708	0.63	0.555	0.562
Yb	2.6	2.83	2.58	2.37	2.86	2.29	2.25
Lu	0.34	0.364	0.364	0.333	0.294	0.38	0.357
Rb	71	79	102	117			107
Sr	1111	1164	1245	1352			1111
Ba	656	628	860	985	940	901	794
Cs	1.5	2	3.1	2.3	3.6	1.8	1.5
U	1.3	1.4	2.5	2.7	2.9	2.3	2.4
Th	3.6	4.3	5.7	6.9	6.7	5.3	5.4
Zr	171	177	176	220			214
Hf	4.4	4.8	4.5	5	4.3	4.9	4.9
Ta	1.04	0.98	1	1.22	1.17	1.01	1.05
Sc	21	14.7	8.2	8.1	9.3	5	4.8
Cr	16	9	8	12	22	11	11
Ni	8	12	3	7	4	4	6
Co	26	19	10	11	10	7	8

ELEMENT	CB3	CC3
SiO2	64.13	67.5
TiO2	0.48	0.3
Al2O3	17.64	17.59
FeO	3.68	2.28
MnO	0.06	0.04
MgO	0.72	0.24
CaO	3.77	2.22
Na2O	5.02	4.88
K2O	4.29	4.87
P2O5	0.13	0.04
TOTAL	99.92	99.96
La	26.8	21.6
Ce	48.2	38.1
Nd	19.5	12.9
Sm	4.58	3.13
Eu	1.21	0.74
Tb	0.592	0.38
Yb	2.14	1.58
Lu	0.354	0.255
Rb	106	146
Sr	1220	822
Ba	920	788
Cs	2.3	5.5
U	2.7	3.8
Th	5.8	7.6
Zr	178	164
Hf	5.1	4.7
Ta	1.09	0.79
Sc	5.2	3.5
Cr	9	6
Ni	3	3
Co	14	16



**Table G-2.**

Whole-rock geochemical data for San Gerónimo  
from Deruelle, 1991 (sample numbers beginning with N),  
Schreiber and Schwab, 1991 (sample numbers beginning with SS),  
and Kay *et al.*, 1994 (sample SJ25).

ELEMENT	SJ25	SS2	SS3	SS4	SS5	SS6	SS7
SiO2	58.63	59.27	59.13	61.24	55.46	56.32	53.41
TiO2	1.2	1.01	1.04	1.05	1.21	1.19	1.87
Al2O3	15.9	16	16.06	14.05	15.01	15.72	16.71
Fe2O3		4.24	4.4	1.28	1.73	5.27	5.32
FeO	5.82	0.96	0.89	4.1	4.75	0.66	2.46
MnO	0.08	0.1	0.1	0.1	0.12	0.11	0.14
MgO	4.43	3.9	4.08	4	7.08	4.42	5.38
CaO	5.76	5.91	5.46	5.9	6.58	8.3	7.3
Na2O	3.29	2.89	2.96	3.33	2.86	2.95	2.78
K2O	3.82	3.84	3.91	3.73	3.88	3.42	3.15
P2O5	0.49	0.51	0.53	0.53	0.57	0.58	0.55
LOI		1.25	1.27	0.07	0.22	0.99	0.68
TOTAL	99.42	99.88	99.83	99.38	99.47	99.93	99.75
La	63.8	62.9		65.1			
Ce	122	103.2		108.8			
Nd	50.3	48.4		50.7			
Sm	9.22	7.9		8.2			
Eu	1.9	1.8		1.87			
Gd							
Tb	0.806	0.8		0.82			
Dy							
Er							
Yb	1.76	1		1.1			
Lu	0.24	0.22		0.24			
Rb		156	161	149	126	129	103
Sr	673	624	620	665	716	607	662
Ba	823	679	658	709	996	691	702
Cs	6.4	11.4		8.1			
U	5.9	6	7	6	4	5	20
Th	18.8	17	17	17	12	15	12
Hf	8.3						
Ta	2	2	3	2	3		3
Sc	15.9	10	12	12	13	13	19
Cr	156						
Ni	12	9	9	10	132	13	19
Co	19	13	15	15	25	17	17
Zr		213	211	226	223	231	196
Nb		24	24	25	19	23	23
V		97	96	101	139	99	165
Cu		5	8	6	21	10	11

ELEMENT	N17A	N17B	N16Z	N17C	N16T	N16V	N16U
SiO2	55.28	55.97	56.75	56.99	60.33	60.66	60.73
TiO2	0.85	1.07	1.16	1.23	1.04	0.92	1.07
Al2O3	15.21	16.35	15.22	16.64	16.44	16.28	16.46
Fe2O3	5.75	6.25	6.55	6.31	5.57	5	5.17
FeO							
MnO	0.09	0.08	0.1	0.06	0.09	0.08	0.09
MgO	5.32	4.34	5.93	4.19	3.63	3.4	3.38
CaO	5.66	6.37	6.22	5.94	5.6	5.15	5.3
Na2O	2.79	3.08	2.88	3.08	3.4	3.25	3.34
K2O	3.47	3.67	3.47	3.75	3.81	3.96	3.75
P2O5							
LOI	4.5	1.65	0.77	0.71	0.15	1.12	0.31
TOTAL	98.92	98.83	99.05	98.9	100.06	99.82	99.6
La	51.2	47.08	53	53	64	56.91	57.44
Ce		86.46				107.61	106.33
Nd		34.19	42.83			43.19	41.48
Sm		6.83	7.55			8.23	7.89
Eu	1.96	1.57	1.73	1.89	1.95	1.74	1.7
Gd		4.9				5.69	5.78
Tb	0.66	0.72	0.67	0.68	0.69	0.68	0.7
Dy		3.25				3.43	3.38
Er		1.57				1.6	1.58
Yb		1.35				1.33	1.31
Lu		0.24				0.17	0.18
Rb	142	147	149	153	166	177	164
Sr	654	648	678	617	747	687	732
Ba	695	624	724	613	742	753	718
Cs	9.9	7.5	7.7	7.1	7	13.2	7.8
U	6.3	4.9	4.6	5.1	6.2	6.1	6.8
Th	13.9	14.9	13.8	15.1	18	17.9	18
Hf	6.3	5.6	6.2	5.9	7.3	7.1	7.1
Ta	1.96	2.03	1.94	2.11	2.19	2.24	2.17
Sc	17	17	17	17	15	14	14
Cr	266	176	242	146	95	93	100
Ni	86	23	95	23	8	7	7
Co	25	20	25	20	17	15	16
Zr	230	197	255	227	278	251	297
Nb							
V	150	158	152	140	122	122	137
Cu							

**Table G-3.**

Whole-rock geochemical data for Chorillos  
from Deruelle, 1991 (sample numbers beginning with N),  
Schreiber and Schwab, 1991 (sample numbers beginning with SS),  
and Kay *et al.*, 1994 (samples P24-4, T143, and T20).

ELEMENT	P24-4	T143	T20	SS1	N16X	N16W	N16Y
SiO2	52.12	54.21	55.12	53.89	52.3	54.43	56.8
TiO2	2.15	2.01	1.36	1.75	2.13	1.1	1.17
Al2O3	14.66	14.72	13.07	15.03	14.86	14.63	14.82
Fe2O3				2.15	8.69	7.09	1.59
FeO	8.23	8.05	6.68	5			
MnO	0.13	0.13	0.11	0.14	0.12	0.08	0.09
MgO	6.88	7.69	8.72	7.55	6.09	7.22	6.48
CaO	7.61	6.45	5.51	6.35	7.59	5.76	6.12
Na2O	2.94	2.86	2.24	2.82	2.88	2.63	2.9
K2O	3.43	3.79	5.27	4.31	3.47	5.35	3.7
P2O5			0.7	0.89			0.54
LOI				0.29	1.12	1.21	0.27
TOTAL	98.15	99.9	98.78	100.14	99.25	99.5	99.25
La	68.7	58.8	79.7	68	60.18	72.44	
Ce	131.6	125	156.8	144	111.38	143.59	
Nd	51.8	55.7	81.5	61.9	47.83	65.98	
Sm	10.4	10.5	13.8	11.6	9.59	12.94	
Eu	2.5	2.31	2.98	2.76	2.35	2.94	
Gd					6.93	8.67	
Tb	1.04	1.01	1.17	0.97	0.9	0.99	
Dy					4.42	4.79	
Er					2.09	2.04	
Yb	2.04	1.88	1.81	1.7	1.7	1.63	
Lu	0.263	0.248	0.264	0.28	0.26	0.25	
Rb	119	139	216	139	116	166	125
Sr	954	728	969	727	860	857	546
Ba	960	1079	2337	1205	970	1726	895
Cs	3.8	5	7.3	4	11.8	5.7	
U	3.7	3.7	4.4	6	3.5	4.7	
Th	13.7	13	19.1	15	12.7	15.9	
Hf	8.1	8.2	14.6		7.7	13.2	
Ta	2.9	2.5	2.8	3	3.04	2.48	
Sc	20.4	18.7	17.9	13	22	18	
Cr	302	365	387	284	224	289	100
Ni	87	145	257	139	87	202	89
Co	34	35	48	25	32	30	19
Y				21	27.25	27.16	
Zr				343	315	519	131
Nb				35			12
V				156	198	106	143
Cu				33	28	27	20

**Table G-4.**

Whole-rock geochemical data for La Poma  
from Kay *et al.*, 1994.

ELEMENT	LP199	LP36	PU16
SiO2	52.55	54.26	54.5
TiO2	1.4	1.25	1.2
Al2O3	14.19	13.86	13.68
FeO	7.32	6.62	6.62
MnO	0.11	0.1	0.12
MgO	8.88	8.86	9.35
CaO	6.85	6.24	6.48
Na2O	3.06	2.77	2.91
K2O	4.1	4.34	3.8
P2O5			0.64
TOTAL	98.46	98.3	99.3
La	85.9	67	65.4
Ce	162.8	136.6	135.8
Nd	67.4	60.3	69
Sm	12.5	11.1	11.3
Eu	2.86	2.53	2.62
Tb	1.076	0.938	1.05
Yb	2.05	1.57	1.7
Lu	0.271	0.206	0.216
Rb		145	
Sr		901	891
Ba	1633	1627	1760
Cs	1.8	3.5	4.1
U	2.8	2.2	2.5
Th	14.9	12.7	12.4
Hf	9.2	9.1	8.9
Ta	2.1	1.8	1.8
Sc	18.3	19.5	20.2
Cr	376	369	588
Ni	188	244	245
Co	38	42	34

**Table G-5.**

Whole-rock geochemical data for Picotani  
from Sandeman, 1995.



ELEMENT	MAC-19	MAC-20	MAC-21	MAC-135
SiO2	59.6	62.4	57.2	54.9
TiO2	0.82	0.76	0.89	1.1
Al2O3	16.4	16.2	16.2	15.46
Fe2O3	7.21	5.42	7.82	0.74
FeO				6.46
MnO	0.15	0.14	0.16	0.11
MgO	4.32	4	6.08	5.02
CaO	5.61	4.2	6.29	6.06
Na2O	2.6	2.6	2.2	2.69
K2O	2.5	3.4	2.3	3.24
P2O5	0.19	0.28	0.18	0.42
LOI	2.36	1.72	1.93	3.32
TOTAL	101.76	101.12	101.25	99.52
Cr	222	169	247	412
Ni	23	28	30	41
Sc				22
Cs		34	26	84
Co				29
Pb		43	27	19
Sn				
V	141	116	144	97
Ga	24	34	31	29
Cu				10
Ba	813	900	446	1673
Rb	167	228	137	224
Sr	278	422	255	448
Y	23	28	17	17
Zr	138	197	145	311
Nb	25	22	10	10
Th		18.9	9.9	30.9
U		9.2	6.3	5.6
Ta		2.8	3.5	1.1
Hf		4	3.4	10
La		45.78	23.71	59.3
Ce		94.64	51.16	117.3
Pr		10.8	6.06	
Nd		40.13	23.89	54.6
Sm		6.96	4.81	8.9
Eu		1.48	1.2	1.97
Gd		5.5	4.8	
Tb		0.62	0.61	0.87
Dy		3.58	3.94	
Ho		0.66	0.77	
Er		1.86	2.2	
Tm		0.26	0.33	
Yb		1.73	2.05	2.25
Lu		0.24	0.32	0.38

**Table G-6.**

Whole-rock geochemical data for Cerro Moromoroni  
from Kontak *et al.*, 1986.

ELEMENT	MOR22	MOR35	MOR32	MOR33	MOR34	MOR38	MOR39A
SiO2	54.3	53.91	59.58	59.25	59.59	59.47	58.58
TiO2	0.93	0.95	0.62	0.64	0.64	0.64	0.63
Al2O3	16.28	16.21	16.78	16.6	16.5	16.54	16.49
Fe2O3	1.7	3.47	1.74	3.72	3.96	2.31	1.23
FeO	6.32	5	2.62	1.45	1.24	2.64	3.97
MnO	0.13	0.12	0.07	0.07	0.06	0.07	0.09
MgO	6.43	6.5	4.79	5.23	4.47	4.78	5.69
CaO	6.45	6.33	4.81	4.4	4.3	4.68	5.04
Na2O	2.69	2.57	2.58	2.87	2.58	2.95	2.72
K2O	2.24	2.23	3.79	3.78	3.85	3.65	3.41
P2O5	0.23	0.21	0.25	0.23	0.25	0.25	0.33
Total	97.7	97.5	97.63	98.24	97.44	97.98	98.18
Nb	14	10	7	10	10	13	21
Ba	663	720	878	765	807	823	885
V	124	132	89	92	93	94	97
Cr		292	236	232	253	238	286
Rb	125	111	259	247	252	116	254
Sr	401	380	355	329	341	372	362
Zr	129	133	165	158	162	160	160
Y	23	24	16	17			
Ni	40	36	57	61	6	65	
Cu	42	16	18	14	15	17	
Pb	26	21	69	50	57	53	
Zn	109		90	79	75	78	

ELEMENT	MOR40	MOR41
SiO2	59.43	58.64
TiO2	0.75	0.75
Al2O3	16.08	16.24
Fe2O3	2.65	4.18
FeO	2.48	2.31
MnO	0.07	0.09
MgO	4.74	5.2
CaO	4.23	4.4
Na2O	3.35	3.42
K2O	3.55	3.07
P2O5	0.28	0.21
Total	97.61	98.51
Nb	13	9
Ba	920	625
V	96	103
Cr	208	
Rb	219	210
Sr	370	262
Zr	166	150
Y	21	
Ni	24	13
Cu	12	17
Pb	44	44
Zn	81	92

**Table G-7.**

Whole-rock geochemical data for Tacaza  
from Wasteneys, 1990.

ELEMENT	BARB195	BARB382	BARB417	BARB446	BARB198	BARB221	BARB313
SiO2	48.46	49.41	49.67	50.06	50.59	51.22	52.65
TiO2	1.08	1.06	1.2	1.06	1.08	1.25	0.83
Al2O3	17.03	15.39	15.98	15.21	16.05	14.97	18.4
Fe2O3	9.55	10.52	9	9.25	9.29	8.16	6.19
MnO	0.14	0.21	0.14	0.17	0.1	0.11	0.13
MgO	4.36	5.43	5.56	7.35	4.32	5.89	2.39
CaO	8.84	8.64	9.21	10.09	9.41	7.44	4.81
Na2O	4.08	2.8	2.05	2.21	2.94	4.09	6.2
K2O	1.91	3.3	3.02	2.47	2.99	2.45	3.46
P2O5	0.35	0.51	0.53	0.45	0.47	0.59	0.7
LOI	2.25	2.42	2.64	1.92	2.19	2	2.88
Total	98.05	99.69	99	100.27	99.43	98.17	98.64
Zr	114	119	143	138	124	168	158
Sr	1173	937	678	830	750	738	1648
Rb	46	50	122	119	113	88	116
Ba	647	1215	864	777	861	880	1820
Cr	17	70	111	164	96	56	21
Ni	5	16	62	100	77	39	11
V	202	290	224	206	220	94	170
Nb	5	7	5	4	5	6	14
Y	21	18	23	11	23	16	15

ELEMENT	BARB324	BARB326	BARB380	BARB419	BARB117	BARB393	BARB386
SiO2	53.19	54.63	54.92	55.65	56.73	58.83	62.45
TiO2	0.95	0.99	1.17	1.03	0.9	1.56	0.77
Al2O3	16.63	17.91	16.24	19.39	18.41	15.04	18.3
Fe2O3	9.14	6.78	7	6.04	6.06	6.67	3.36
MnO	0.12	0.06	0.11	0.06	0.04	0.09	0.03
MgO	4	1.87	3.09	1.18	0.94	3.2	0.38
CaO	7.38	6.7	7.31	6.04	5.18	5.28	2.48
Na2O	2.98	3.2	3.8	4.26	3.22	3.7	4
K2O	3.25	3.45	2.5	3.89	4.39	3.57	5.49
P2O5	0.44	0.5	0.41	0.59	0.46	0.7	0.22
LOI	2.5	3.87	2.63	2.88	2	0.5	1.66
Total	100.58	99.96	99.18	101.01	98.33	99.14	99.14
Zr	134	168	197	168	202	329	285
Sr	655	799	981	904	767	1096	590
Rb	110	114	56	161	189	86	229
Ba	866	870	1019	988	987	1589	976
Cr	37	42	140	23	35	79	10
Ni	29	52	82	26	48	59	19
V	211	201	151	175	146	124	83
Nb	7	9	13	10	10	16	17
Y	21	22	13	17	21	20	17

**Table G-8.**

Whole-rock geochemical data for SW Bolivia  
from Kussmaul *et al.*, 1977.



ELEMENT	SWB-L4	SWB-L5	SWB-L6	SWB-L7	SWB-L8	SWB-L9	SWB-L10
SiO2	63.12	64.84	64.7	68.29	63.95	61.57	63.31
TiO2	0.97	0.86	1.32	0.58	1.04	1.15	0.61
Al2O3	16.99	16.28	15.75	15.01	16.4	16.22	16.08
Fe2O3	4.3	2.6	1.43	0.92	0.9	3.69	1.67
FeO	1.51	1.86	3.68	2.28	3.2	1.86	4.09
MnO	0.08	0.05	0.08	0.05	0.06	0.08	0.09
MgO	2.14	1.63	2.11	0.84	1.88	1.91	2.5
CaO	5.05	3.86	4.19	2.78	4.47	5.05	4.99
Na2O	2.29	2.29	2.23	2.91	2.45	2.48	2.08
K2O	2.73	3.97	3.76	4.61	3.48	3.43	3.22
P2O5		0.22	0.2	0.14	0.16	0.26	0.19
CO2	0.14	0.12	0.05	0.13	0.08	0.43	0.1
H2O	0.34	1.42	0.29	1.2	1.86	1.51	1.09
Total	99.66	100	99.79	99.74	99.93	99.64	100.02
Rb	168	113	279	173			
Sr	278	272	553	259			
Zr	221	171	235	197			
Cu	26		4	25			
Co	13	7	9	7			
Ni	7	12	5	7			
Zn	99	75	126	88			

**Table G-9.**

Whole-rock geochemical data for the Abaroa Fm., Bolivia  
from Jiménez *et al.*, 1993a.

ELEMENT	NJ-35	NJ-311
SiO2	49.4	48.7
TiO2	1.35	1.04
Al2O3	18.5	12.9
Fe2O3	9.31	9.74
MnO	0.15	0.19
MgO	4.23	9.9
CaO	7.25	8.42
Na2O	3.15	2.45
K2O	2.84	3.29
P2O5	0.79	0.81
LOI	2.16	
TOTAL	99.13	98.98
Cu	206	100
Zn	95	237
Sr	880	1010
Ba	1000	1260

**Table G-10.**

Whole-rock geochemical data for the Sillapaca Group, southern Peru from Aramaki *et al.*, 1984 (sample numbers prefixed by PUNO) and France, 1985 (sample numbers prefixed by S).

ELEMENT	S50	S51	S60	PUNO44	PUNO45	PUNO46	PUNO47
SiO2	52.00	52.20	53.70	59.48	54.10	54.97	53.83
TiO2	1.90	1.93	1.65	1.49	1.94	1.94	1.84
Al2O3	16.00	15.47	17.42	16.88	16.45	16.11	15.51
FeO	0.02	1.48	1.66				
Fe2O3	9.23	7.06	5.96	7.21	9.18	8.53	8.81
MnO	0.15	0.11	0.11	0.11	0.08	0.12	0.12
MgO	5.04	4.60	2.96	2.43	4.58	4.07	5.75
CaO	7.67	6.70	5.47	4.74	6.65	6.36	7.05
Na2O	3.06	3.92	3.68	3.55	3.17	3.68	3.41
K2O	3.01	2.56	3.26	3.58	3.12	3.22	2.97
P2O5	0.86	0.81	0.79	0.53	0.74	0.79	0.71
LOI	1.29	1.49	2.59				
TOTAL	100.23	98.33	99.25				
Cr	255	254	135				
Ni	127	145	66				
Ba	1264	1223	1792				
Rb	61	36	49				
Sr	1000	979	1338				
Zr	292	290	322				
V	237	180	200				
U		2	1.4				
Li	10	9	13				

ELEMENT	PUNO48	PUNO49
SiO2	54.18	54.69
TiO2	1.88	2.52
Al2O3	15.55	14.82
FeO		
Fe2O3	9.35	9.41
MnO	0.13	0.11
MgO	5.43	4.43
CaO	6.60	6.60
Na2O	3.23	3.08
K2O	3.06	3.29
P2O5	0.59	0.97
LOI		
TOTAL		
Cr		
Ni		
Ba		
Rb		
Sr		
Zr		
V		
U		
Li		

**Table G-11.**

Whole-rock geochemical data for the 11 Ma shoshonites  
from France, 1985.

ELEMEN	S53	S59
SiO2	60.95	58.6
TiO2	0.77	0.96
Al2O3	16.73	16.73
FeO	1.36	0.35
Fe2O3	3.27	5.2
MnO	0.07	0.07
MgO	2.48	2.7
CaO	4.16	4.76
Na2O	3.49	4.13
K2O	3.8	3.62
P2O5	0.38	0.48
LOI	3.02	1.3
TOTAL	100.48	98.9
Cr	44	93
Ni	33	40
Ba	1261	1472
Rb	142	79
Sr	1123	1395
Zr	200	179
V	130	120
U	3.2	
Li	10	12



**Table G-12.**

Whole-rock geochemical data for the Linga Group, Peruvian coastal batholith, from LeBel *et al.*, 1985.

ELEMENT	BLB80	BLB48	BLB37	BLB47	BLB45
SiO2	59.57	60.50	64.94	68.08	70.22
TiO2	0.95	0.84	0.74	0.61	0.43
Al2O3	16.37	16.51	14.91	14.54	13.75
Fe2O3	7.45	6.64	5.06	4.48	3.30
MnO	0.10	0.11	0.10	0.07	0.05
MgO	2.47	2.37	1.43	1.10	0.59
CaO	5.53	4.79	3.48	2.58	1.79
Na2O	3.36	3.45	3.20	2.91	2.93
K2O	3.45	3.84	4.70	5.32	5.67
P2O5	0.30	0.16	0.20	0.19	0.10
F.L.	0.67	0.54	0.43	0.36	0.34
TOTAL	100.22	99.75	99.19	100.24	99.17
La	31.9	25.5	30.8	30.8	36.5
Ce	61.1	50.7	58.2	59.4	70.5
Nd	30.9	26.4	28.3	26.7	31.4
Sm	6.82	5.57	6.53	7.22	6.9
Eu	1.17	1.06	0.99	0.8	0.77
Gd	5.72	4.9	4.26	4.81	4.48
Tb	0.9	0.7	0.7	0.75	0.79
Tm	0.44	0.39	0.33	0.37	0.44
Yb	2.63	2.32	2.2	2.39	2.88
Lu	0.46	0.38	0.38	0.41	0.5
Rb	163	163	217	292	284
Sr	365	375	308	209	152
Ba	693	724	831	740	872
Cs	23.8	16.7	14.8	24.9	26.8
U	4.3	5.3	7.8	12.7	11.3
Th	22.7	18.6	25.6	44.1	39.5
Hf	6.5	7.4	9.5	10.4	9.4
Ta	0.69	0.66	0.77	0.81	0.86
Sc	19.2	15.9	11.5	9.8	6.3
Cr	20	18	14	11	10
Ni	24	17	14	10	7.8
Co	18	16	11	8.5	6.3
Zr	243	289	333	376	316
V	150	148	102	72	43
Cu	143	58	45	159	12
Zn	72	59	49	55	41

## **APPENDIX H.**

**$^{40}\text{Ar}/^{39}\text{Ar}$  laser microprobe geochronological data.**

# **FAR-2 Biotite (45-120 mesh)**

Run date: 1995/11/13  
Run: AS-46

Can/Pos: 141/54  
Mass: 5.1 mg

J Value: 0.002351  
± 0.000010

Volume 39Ar: 69.34 x 1E-10 cm<sup>3</sup> NTP  
Integrated Age: 6.80 ± 0.17 Ma

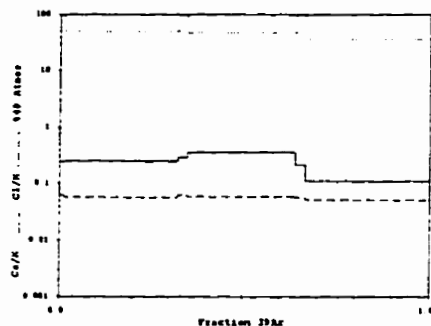
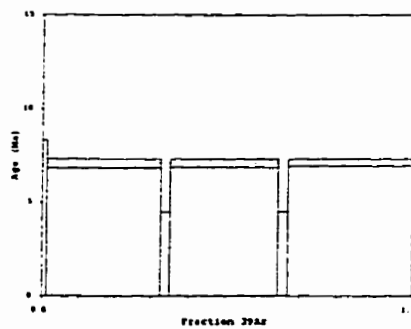
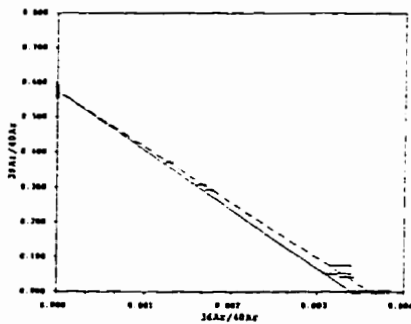
Approx. 9.15% K  
1.95% Ca

Initial 40/36: 277.33 ± 16.56 (MSWD = 1.33, isochron between 0.29 and 2.41)  
Correlation Age: 7.36 ± 0.21 Ma (100.0% of 39Ar, steps marked by >)

Plateau Age: 7.10 ± 0.13 Ma ( 93.5% of 39Ar, steps marked by <)

Power	36Ar/40Ar	39Ar/40Ar	z	Ca/K	%40Ar	%39Ar	40Ar*/39K	Age
7000	0.00321638±0.00017391	0.051903±0.000256	0.001	0.25	94.76	1.26	0.971±0.992	4.11±4.20
<7000	0.00173882 0.00000000	0.293203 0.000000	0.002	0.25	50.34	30.99	1.673 0.054	7.08 0.23
300	0.00313039 0.00000000	0.042360 0.000000	0.001	0.30	98.17	2.52	0.391 0.671	1.66 2.84
<7000	0.00165235 0.00002811	0.308551 0.000671	0.002	0.37	47.75	28.82	1.674 0.055	7.08 0.23
300	0.00325296 0.00000000	0.075472 0.000000	0.001	0.21	95.71	2.72	0.528 0.534	2.24 2.26
<7000	0.00128332 0.00000001	0.371077 0.000000	0.002	0.11	36.86	33.68	1.686 0.044	7.14 0.19

Power	40Ar	39Ar	38Ar	37Ar	36Ar	Blank 40Ar	Atmos 40/36
7000	16.32±0.00	0.89±0.00	0.27±0.00	0.027±0.00	0.040±0.00	0.087±0.00	287.67±1.00
<7000	74.25 0.10	21.63 0.09	5.73 0.05	0.444±0.01	0.135±0.00	0.066±0.00	287.67±1.00
300	41.41 0.00	1.76 0.01	0.55 0.01	0.348±0.00	0.144±0.00	0.065±0.00	287.67±1.00
<7000	65.65 0.00	20.11 0.09	5.56 0.05	0.405±0.01	0.114±0.00	0.064±0.00	287.67±1.00
300	25.17 0.00	1.91 0.01	0.52 0.01	0.038±0.00	0.087±0.00	0.065±0.00	287.67±1.00
<7000	63.98 0.00	23.50 0.10	5.77 0.05	0.215±0.00	0.087±0.00	0.065±0.00	287.67±1.00



Measured volumes are x 1E-10 cm<sup>3</sup> NTP. All errors are 2 x standard error.

# FAR-10 Biotite (45-60 mesh)

Run date: 1995/11/17  
Run: AS-59

Can/Pos: 141/70  
Mass: 1.4 mg

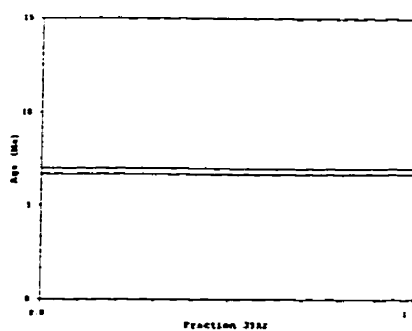
J Value: 0.002334  
± 0.000014

Volume 39Ar: 18.73 x 1E-10 cm3 NTP  
Integrated Age: 6.84 ± 0.15 Ma

Approx. 9.05% K  
0.51% Ca

Power	36Ar/40Ar	39Ar/40Ar	F	Ca/K	%40Ar	%39Ar	40Ar*/39K	Age
7000	0.00114562±0.00004721	0.409297±0.001783	0.302	0.06	32.80	100.00	1.628±0.035	6.84±0.15

Power	40Ar	39Ar	38Ar	37Ar	36Ar	Blank 40Ar	Atmos 40/36
7000	46.63±0.00	18.26±0.08	4.11±0.04	0.101±0.00	0.062±0.00	0.097±0.00	137.67±1.00



Measured volumes are x 1E-10 cm3 NTP. All errors are 2 x standard error.

# **FAR-12 Biotite (45-120 mesh)**

Run date: 1995/11/13  
Run: AS-47

Can/Pos: 141/55  
Mass: 9.0 mg

J Value: 0.002350  
± 0.000010

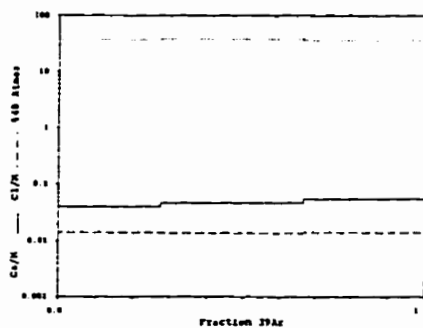
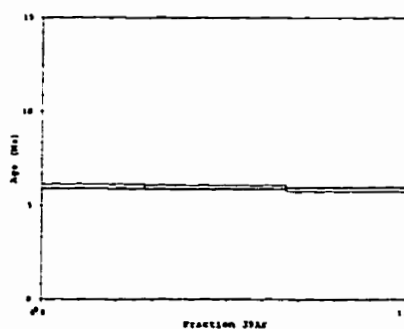
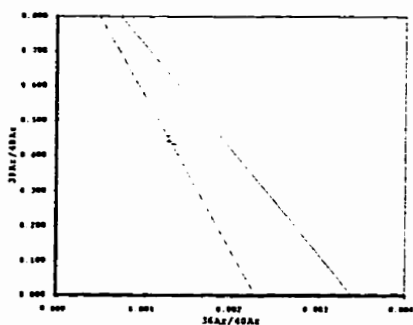
Volume 39Ar: 120.02 x 1E-10 cm3 NTP  
Integrated Age: 5.95 ± 0.07 Ma

Approx. 8.00% K  
0.38% Ca

Correlation Age: 4.19 ± 89.93 Ma (100.0% of 39Ar, steps marked by >)

Power	36Ar/40Ar	39Ar/40Ar	r	Ca/K	%40Atm	%39Ar	40Ar*/39K	Age
7000	0.00125913±0.00004062	0.441707±0.001931	0.002	0.04	36.38	27.54	1.425±0.029	6.03±0.12
7000	0.00131477 0.00000000	0.434503 0.000000	0.003	0.05	38.01	38.62	1.411 0.024	5.97 0.10
7000	0.00124343 0.00000000	0.458124 0.000000	0.003	0.06	35.90	33.84	1.384 0.025	5.86 0.10

Power	40Ar	39Ar	38Ar	37Ar	36Ar	Blank 40Ar	Atmos 40/36
7000	76.29±0.00	33.27±0.14	2.51±0.02	0.115±0.00	0.103±0.00	0.065±0.00	297.67±1.00
7000	108.67 0.00	46.66 0.20	3.47 0.03	0.194±0.00	0.150±0.00	0.065±0.00	297.67±1.00
7000	90.41 0.00	40.88 0.17	3.08 0.03	0.190±0.00	0.119±0.00	0.065±0.00	297.67±1.00



Measured volumes are x 1E-10 cm3 NTP. All errors are 2 x standard error.

# **FAR-24 Alunite (18-25 mesh)**

Run date: 1995/12/15  
Run: AS-144

Can/Pos: 141/56  
Mass: 20.0 mg

J Value: 0.002349  
± 0.000010

Volume 39Ar: 43.66 x 1E-10 cm<sup>3</sup> NTP  
Integrated Age: -0.03 ± 2.81 Ma

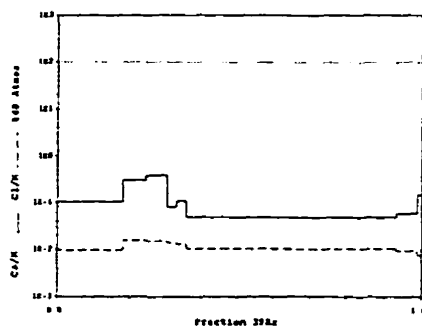
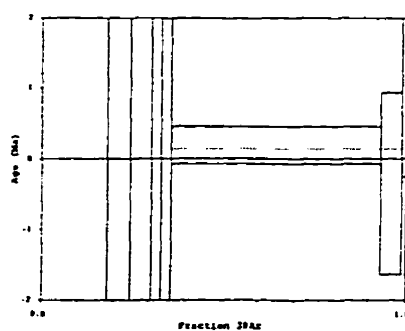
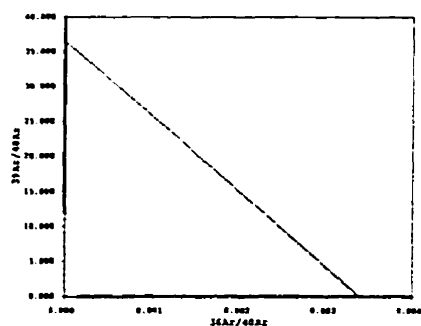
Approx. 1.31% K  
0.13% Ca

Initial 40/36: 296.91 ± 282.18 (MSWD = 1.68, isochron between 0.50 and 2.00)  
Correlation Age: 0.12 ± 0.08 Ma (100.0% of 39Ar, steps marked by >)

Plateau Age: 0.14 ± 0.33 Ma ( 64.2% of 39Ar, steps marked by <)

Power	36Ar/40Ar	39Ar/40Ar	r	Ca/K	40Ar <sub>atm</sub>	439Ar	40Ar*/39K	Age
7000	0.00339563±0.00005987	0.012026±0.000053	0.016	0.10	100.29	18.22	-0.280± 1.495	-1.19± 6.34
100	0.00340818 0.00000000	0.002683 0.000000	0.307	0.31	100.70	6.31	-2.647 6.721	-11.25 28.66
100	0.00336976 0.00000000	0.002854 0.000000	0.221	0.38	99.56	5.90	1.489 6.250	4.30 26.39
100	0.00328712 0.00003001	0.008009 0.000021	0.055	0.08	97.10	2.67	3.583 2.239	15.12 9.41
100	0.00335646 0.00000000	0.017639 0.000000	0.015	0.11	99.10	2.56	0.467 1.121	1.98 4.74
< 200	0.00333978 0.00000002	0.303592 0.000000	0.003	0.05	97.35	56.92	0.047 0.063	0.20 0.27
< 200	0.00340858 0.00000000	0.084598 0.000000	0.001	0.06	100.34	5.62	-0.082 0.304	-0.35 1.29
< 300	0.00331002 0.00000000	0.021730 0.000000	0.038	0.15	97.72	1.74	1.010 1.071	4.27 4.53
< 500	0.00344598 0.00000000	0.000674 0.000000	0.973	0.59	101.83	0.06	-27.113 33.204	-118.72 150.29
7000	0.00341591 0.00023633	0.001297 0.000574	0.936	0.41	100.93	0.10	-7.237 18.578	-30.93 90.09

Power	40Ar	39Ar	38Ar	37Ar	36Ar	Blank 40Ar	Atmos 40/36
7000	662.14±0.00	9.01±0.03	0.29±0.01	0.042±0.01	2.312±0.04	0.497±0.00	287.67±1.00
100	1026.84 0.00	2.78 0.01	0.90 0.01	0.046±0.02	3.600±0.06	0.526±0.00	287.67±1.00
100	902.69 0.00	2.60 0.01	0.79 0.01	0.052±0.01	3.129±0.05	0.531±0.00	287.67±1.00
100	146.30 0.00	1.19 0.01	0.19 0.00	0.013±0.00	0.499±0.01	0.550±0.00	287.67±1.00
100	64.05 0.00	1.14 0.01	0.13 0.00	0.014±0.00	0.226±0.00	0.541±0.00	287.67±1.00
< 200	83.30 0.00	24.97 0.11	1.57 0.01	0.062±0.00	0.288±0.01	0.557±0.00	287.67±1.00
< 200	29.68 0.00	2.48 0.01	0.16 0.00	0.015±0.00	0.109±0.00	0.545±0.00	287.67±1.00
< 300	35.49 0.00	0.78 0.00	0.06 0.00	0.014±0.00	0.126±0.00	0.539±0.00	287.67±1.00
< 500	42.52 0.00	0.04 0.00	0.04 0.00	0.010±0.00	0.156±0.00	0.540±0.00	287.67±1.00
7000	33.77 0.00	0.06 0.00	0.03 0.00	0.010±0.00	0.123±0.00	0.538±0.00	287.67±1.00



Measured volumes are x 1E-10 cm<sup>3</sup> NTP. All errors are 2 x standard error.

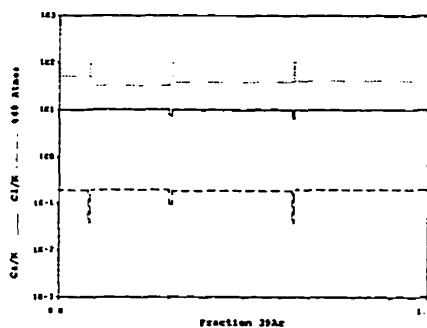
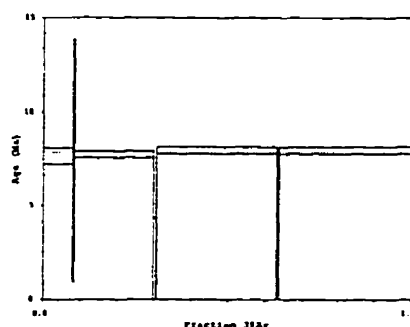
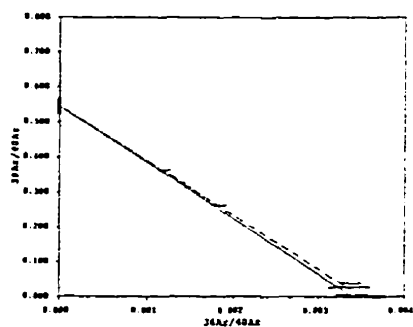
# **FAR-57 Hornblende (60-120 mesh)**

Run date: 1995/11/13 Can/Pos: 141/57 J Value: 0.002349  
Run: AS-48 & AS-120 Mass: 50.0 mg ± 0.000010

Volume 39Ar: 85.86 x 1E-10 cm<sup>3</sup> NTP  
Integrated Age: 7.72 ± 0.13 Ma Approx. 1.03% K  
Initial 40/36: 286.24 ± 22.44 (MSWD = 3.24, isochron between 0.37 and 2.26)  
Correlation Age: 7.76 ± 0.28 Ma (100.0% of 39Ar, steps marked by >)  
Plateau Age: 7.88 ± 0.11 Ma ( 97.8% of 39Ar, steps marked by <)

Power	36Ar/40Ar	39Ar/40Ar	r	Ca/K	%40Atm	%39Ar	40Ar*/39K	Age
<7000	0.00182004±0.00009247	0.262756±0.001149	0.009	9.83	51.95	7.86	1.807±0.103	7.64±0.43
500	0.00323223 0.00000000	0.025746 0.000000	0.049	10.26	95.19	0.52	1.753 1.533	7.41 6.47
<7000	0.00120693 0.00000000	0.361814 0.000000	0.012	10.36	33.34	21.14	1.828 0.044	7.73 0.18
400	0.00337558 0.00005829	0.037259 0.000035	0.029	7.55	99.48	1.02	0.098 0.923	0.41 3.91
<7000	0.00137354 0.00000000	0.326459 0.000000	0.013	9.81	38.14	32.07	1.879 0.044	7.94 0.19
400	0.00347527 0.00000003	0.025470 0.000000	0.038	6.29	102.55	0.63	-1.046 1.405	-4.44 5.97
<7000	0.00146216 0.00000000	0.312052 0.000000	0.015	9.94	40.76	36.77	1.892 0.044	7.96 0.18

Power	40Ar	39Ar	38Ar	37Ar	36Ar	Blank 40Ar	Atmos 40/36
<7000	25.95±0.00	4.80±0.03	5.75±0.05	5.32±0.07	0.063±0.00	0.093±0.00	287.67±1.00
500	17.25 0.00	0.46 0.00	0.10 0.00	0.37±0.00	0.064±0.00	0.093±0.00	287.67±1.00
<7000	50.83 0.00	18.28 0.08	16.09 0.14	15.08±0.19	0.095±0.00	0.093±0.00	287.67±1.00
400	23.44 0.00	0.89 0.00	0.40 0.00	0.340±0.00	0.088±0.00	0.070±0.00	287.67±1.00
<7000	95.29 0.00	27.72 0.12	23.01 0.20	13.55±0.17	0.165±0.00	0.093±0.00	287.67±1.00
400	21.17 0.00	0.56 0.00	0.12 0.00	0.179±0.00	0.082±0.00	0.070±0.00	287.67±1.00
<7000	102.23 0.00	31.78 0.14	27.50 0.23	15.73±0.20	0.204±0.00	0.093±0.00	287.67±1.00



Measured volumes are x 1E-10 cm<sup>3</sup> NTP. All errors are 2 x standard error.



# **FAR-65 Biotite (80-120 mesh)**

Run date: 1995/11/13  
Run: AS-50 & AS-134

Can/Pos: 141/59  
Mass: 11.0 mg

J Value: 0.002347  
= 0.000010

Volume 39Ar: 144.60 x 1E-10 cm<sup>3</sup> NTP  
Integrated Age: 7.40 ± 0.15 Ma

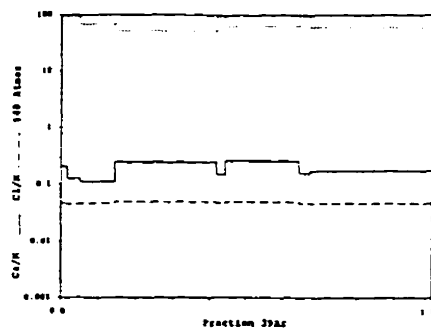
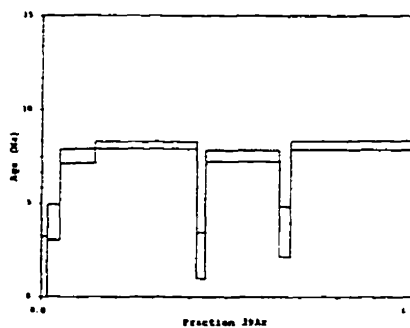
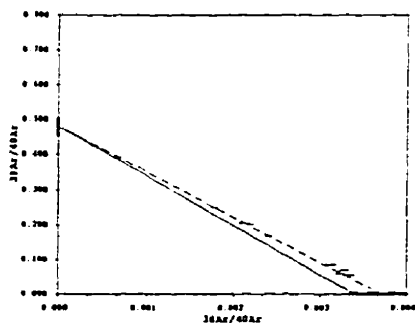
Approx. 7.90% K  
1.61% Ca

Initial 40/36: 270.61 ± 24.32 (MSWD = 4.15, isochron between 0.42 and 2.15)  
Correlation Age: 8.80 ± 0.42 Ma (100.0% of 39Ar, steps marked by >)

Plateau Age: 7.89 ± 0.14 Ma ( 89.8% of 39Ar, steps marked by <)

Power	36Ar/40Ar	39Ar/40Ar	r	Ca/K	%40Atm	%39Ar	40Ar*/39K	Age
300	0.00331946±0.00007055	0.052816±0.000231	0.001	0.21	97.81	1.62	0.374±0.460	1.58±1.69
500	0.00311387 0.00000000	0.085161 0.000000	0.001	0.13	91.59	3.24	0.950 0.223	4.02 0.94
<1000	0.00238920 0.00000000	0.166549 0.000000	0.002	0.11	69.91	9.29	1.777 0.086	7.51 0.36
<7000	0.00178184 0.00001680	0.248900 0.000540	0.002	0.25	51.80	27.46	1.915 0.042	8.09 0.18
500	0.00324401 0.00000000	0.068924 0.000000	0.001	0.15	96.09	2.38	0.527 0.291	2.23 1.23
<7000	0.00219225 0.00000001	0.200991 0.000000	0.002	0.26	63.69	19.99	1.780 0.062	7.52 0.26
300	0.00322175 0.00000000	0.058957 0.000000	0.001	0.16	94.88	3.00	0.829 0.317	3.50 1.34
<7000	0.00207373 0.00000000	0.204675 0.000000	0.002	0.18	60.45	33.02	1.907 0.057	8.06 0.24

Power	40Ar	39Ar	38Ar	37Ar	36Ar	Blank 40Ar	Atmos 40/36
300	44.42±0.00	2.37±0.01	0.54±0.01	0.049±0.00	0.159±0.00	0.092±0.00	287.67±1.00
500	55.35 0.00	4.73 0.02	1.06 0.01	0.057±0.00	0.194±0.00	0.091±0.00	287.67±1.00
<1000	81.34 0.00	13.54 0.06	3.05 0.03	0.130±0.00	0.206±0.00	0.093±0.00	287.67±1.00
<7000	161.24 0.00	32.36 0.17	9.33 0.08	0.787±0.01	0.301±0.01	0.093±0.00	287.67±1.00
500	50.19 0.00	3.48 0.01	0.79 0.01	0.051±0.00	0.175±0.00	0.092±0.00	287.67±1.00
<7000	145.09 0.00	29.10 0.12	6.82 0.06	0.598±0.01	0.331±0.01	0.093±0.00	287.67±1.00
300	73.89 0.00	4.40 0.02	1.02 0.01	0.051±0.00	0.259±0.00	0.152±0.00	287.67±1.00
<7000	235.43 0.00	48.07 0.21	10.56 0.09	0.407±0.01	0.513±0.01	0.152±0.00	287.67±1.00



Measured volumes are x 1E-10 cm<sup>3</sup> NTP. All errors are 2 x standard error.

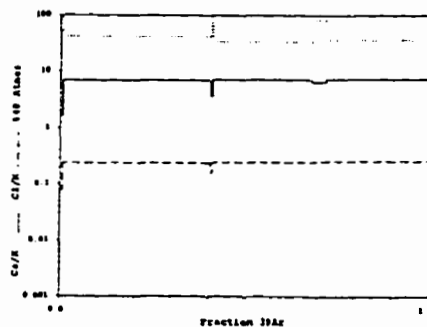
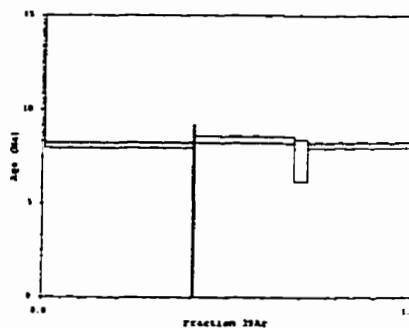
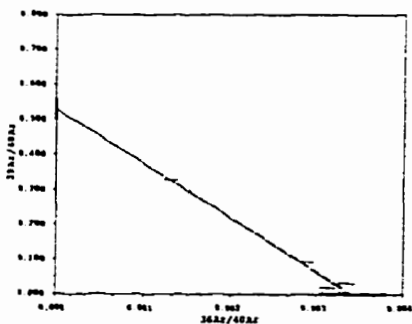
# **FAR-65 Hornblende (80-120 mesh)**

Run date: 1995/11/13 Can/Pos: 141/58 J Value: 0.002348  
Run: AS-49 & AS-121 Mass: 42.0 mg = 0.000010

Volume  $^{39}\text{Ar}$ : 67.54 x 1E-10 cm<sup>3</sup> NTP  
Integrated Age: 8.21 ± 0.13 Ma Approx. 0.971 K  
Initial 40/36: 291.87 ± 31.67 (MSWD = 5.55, isochron between 0.29 and 2.41)  
Correlation Age: 7.98 ± 0.40 Ma (100.0% of  $^{39}\text{Ar}$ , steps marked by >)  
Plateau Age: 8.20 ± 0.11 Ma ( 94.9% of  $^{39}\text{Ar}$ , steps marked by <)

Power	$^{36}\text{Ar}/^{40}\text{Ar}$	$^{39}\text{Ar}/^{40}\text{Ar}$	$\epsilon$	Ca/K	% $^{40}\text{Ar}$	% $^{39}\text{Ar}$	$^{40}\text{Ar}^*/^{39}\text{K}$	Age
500	0.00311908±0.00009764	0.019046±0.000139	0.031	1.64	92.06	0.68	4.132±1.512	17.42±6.34
<7000	0.00151111 0.00000000	0.297601 0.000000	0.010	7.03	42.28	39.51	1.922 0.040	8.12 0.17
500	0.00329960 0.00000000	0.030852 0.000000	0.011	3.61	97.22	0.59	0.860 1.317	3.64 5.57
<7000	0.00125895 0.00002255	0.328778 0.000719	0.009	7.28	34.15	26.97	1.985 0.040	8.40 0.17
500	0.00287495 0.00000000	0.091546 0.000000	0.012	6.48	83.90	3.81	1.724 0.263	7.29 1.11
<7000	0.00134556 0.00000001	0.327067 0.000000	0.010	7.33	36.59	28.44	1.923 0.038	8.13 0.16

Power	$^{40}\text{Ar}$	$^{39}\text{Ar}$	$^{38}\text{Ar}$	$^{37}\text{Ar}$	$^{36}\text{Ar}$	Blank $^{40}\text{Ar}$	Atmos $^{40}/^{36}$
500	24.05±0.00	0.47±0.00	0.19±0.00	0.066±0.00	0.082±0.00	0.068±0.00	287.67±1.00
<7000	90.64 0.00	26.86 0.11	28.72 0.25	14.346±0.19	0.171±0.00	0.070±0.00	287.67±1.00
500	13.11 0.00	0.42 0.00	0.31 0.00	0.085±0.00	0.052±0.00	0.107±0.00	287.67±1.00
<7000	56.14 0.00	18.35 0.08	20.17 0.17	6.450±0.09	0.099±0.00	0.126±0.00	287.67±1.00
500	28.23 0.00	2.61 0.01	2.95 0.03	0.846±0.01	0.093±0.00	0.108±0.00	287.67±1.00
<7000	59.48 0.00	19.34 0.08	22.12 0.19	7.061±0.09	0.109±0.00	0.109±0.00	287.67±1.00



Measured volumes are x 1E-10 cm<sup>3</sup> NTP. All errors are 2 x standard error.

# **FAR-101 Whole Rock (60-80 mesh)**

Run date: 1995/11/19 Can/Pos: 141/60 J Value: 0.002345  
 Run: AS-64 Mass: 5.0 mg ± 0.002010

Volume 39Ar: 64.55 x 1E-10 cm3 NTP  
 Integrated Age: 14.21 ± 0.28 Ma Approx. 7.76% K  
 25.02% Ca

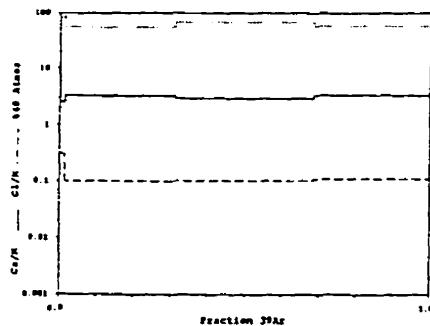
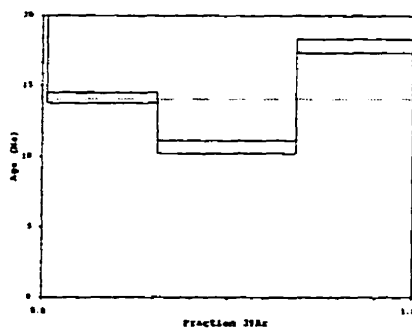
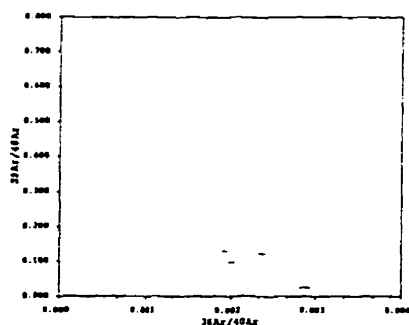
Initial 40/36: Linear regression has positive slope.

Correlation Age:

Plateau Age: 14.04 ± 0.28 Ma ( 98.7% of 39Ar, steps marked by < )

Power	36Ar/40Ar	39Ar/40Ar	$\epsilon$	Ca/K	%40Ar	%39Ar	40Ar*/39K	Age
300	0.00286041±0.00006606	0.0239831±0.000112	0.013	2.54	84.24	1.26	6.537±0.821	27.45±3.42
<7000	0.00192128 0.00000000	0.129755 0.000000	0.006	3.32	56.12	29.39	3.358 0.089	14.15 0.37
<7000	0.00235497 0.00000000	0.121510 0.000000	0.004	2.99	68.91	37.28	2.530 0.110	10.67 0.46
<7000	0.00199900 0.00001389	0.097296 0.000210	0.007	3.45	58.54	32.07	4.237 0.117	17.83 0.49

Power	40Ar	39Ar	38Ar	37Ar	36Ar	Blank 40Ar	Atmos 40/36
300	33.91±0.00	0.87±0.00	1.18±0.01	0.170±0.00	0.117±0.00	0.140±0.00	297.67±1.00
<7000	147.01 0.00	13.15 0.04	8.67 0.07	4.601±0.06	0.317±0.01	0.156±0.00	297.67±1.00
<7000	198.87 0.00	24.23 0.10	11.30 0.10	5.166±0.07	0.496±0.01	0.069±0.00	297.67±1.00
<7000	213.46 0.00	20.84 0.09	10.54 0.09	5.124±0.07	0.453±0.01	0.060±0.00	297.67±1.00



Measured volumes are x 1E-10 cm3 NTP. All errors are 1 x standard error.

# **FAR-113 Biotite (60-120 mesh)**

Run date: 1995/11/13  
Run: AS-51

Can/Pos: 141/51  
Mass: 7.2 mg

J Value: 0.002344  
± 0.000010

Volume 39Ar: 96.39 x 1E-10 cm<sup>3</sup> NTP  
Integrated Age: 6.69 ± 0.08 Ma

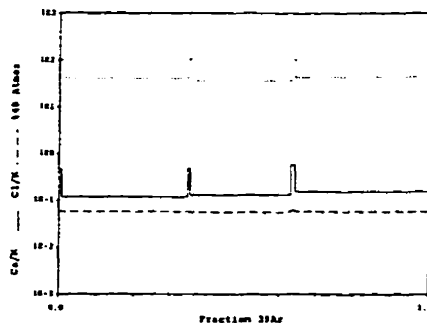
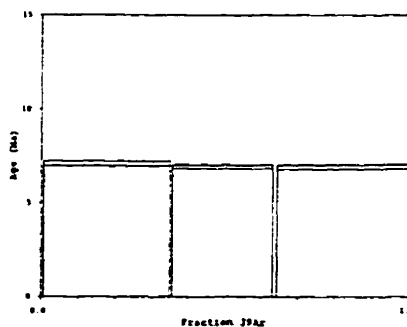
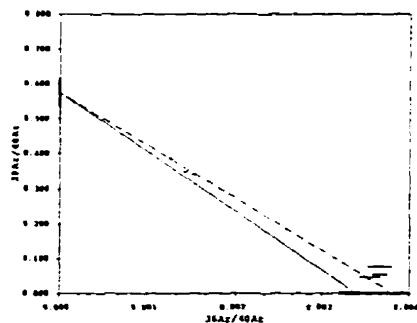
Approx. 8.05% K  
1.16% Ca

Initial 40/36: 262.41 ± 41.15 (MSWD = 17.12, isochron between 0.29 and 2.41)  
Correlation Age: 7.34 ± 0.47 Ma (100.0% of 39Ar, steps marked by >)

Plateau Age: 6.98 ± 0.08 Ma ( 97.6% of 39Ar, steps marked by <)

Power	36Ar/40Ar	39Ar/40Ar	r	Ca/K	%40Ar	%39Ar	40Ar=39K	Age
300	0.00353701±0.00012934	0.046064±0.000231	0.002	0.46	104.25	0.58	-0.966±0.833	-4.09±3.51
<7000	0.00142109 0.00000000	0.348621 0.000000	0.003	0.12	40.89	34.03	1.679 0.028	7.08 0.12
300	0.00364745 0.00000000	0.076745 0.000000	0.001	0.47	107.33	0.73	-0.999 0.579	-4.23 2.45
<7000	0.00124957 0.00001587	0.386993 0.000845	0.003	0.13	35.78	27.32	1.644 0.026	6.94 0.11
300	0.00364441 0.00000000	0.053927 0.000000	0.001	0.57	107.36	1.09	-1.410 0.523	-5.97 2.22
<7000	0.00151706 0.00000001	0.339749 0.000000	0.003	0.15	43.71	36.25	1.639 0.028	6.92 0.12

Power	40Ar	39Ar	38Ar	37Ar	36Ar	Blank 40Ar	Atmos 40/36
300	12.32±0.00	0.60±0.00	0.17±0.00	0.033±0.00	0.055±0.00	0.077±0.00	287.67±1.00
<7000	45.54 0.00	11.04 0.14	8.73 0.07	0.324±0.00	0.151±0.00	0.093±0.00	287.67±1.00
300	9.31 0.00	0.74 0.00	0.21 0.00	0.039±0.00	0.045±0.00	0.076±0.00	287.67±1.00
<7000	69.23 0.00	16.53 0.11	6.96 0.06	0.282±0.00	0.100±0.00	0.086±0.00	287.67±1.00
300	19.55 0.00	1.09 0.00	0.33 0.00	0.060±0.00	0.083±0.00	0.074±0.00	287.67±1.00
<7000	104.36 0.00	35.18 0.15	9.30 0.08	0.435±0.01	0.172±0.00	0.082±0.00	287.67±1.00



Measured volumes are x 1E-10 cm<sup>3</sup> NTP. All errors are 2 x standard error.

# **FAR-147 Biotite (60-120 mesh)**

Run date: 1995/11/15  
Run: AS-53 & AS-135

Can/For: 141/63  
Mass: 12.7 mg

J Value: 0.002343  
± 0.000010

Volume 39Ar: 170.19 x 1E-10 cm3 NTP  
Integrated Age: 7.23 ± 0.06 Ma

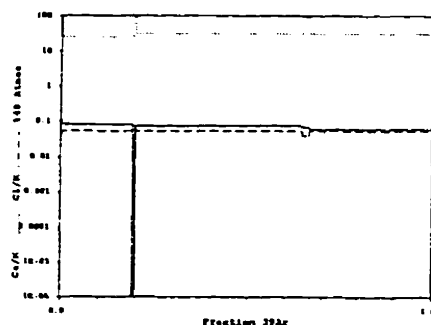
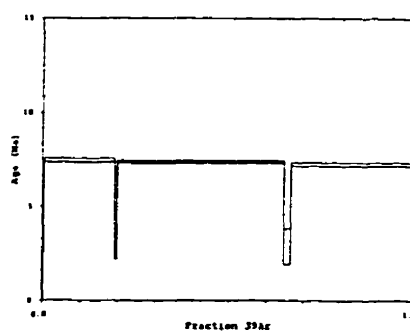
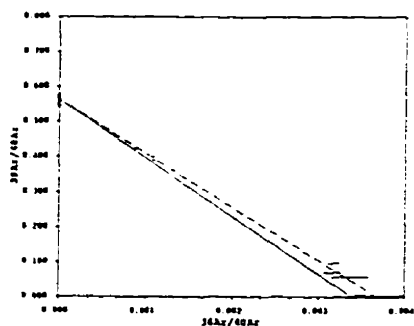
Approx. 8.06% K  
0.57% Ca

Initial 40/36: 271.55 ± 21.78 (MSWD = 6.54, isochron between 0.29 and 2.41)  
Correlation Age: 7.52 ± 0.21 Ma (100.01 of 39Ar, steps marked by >)

Plateau Age: 7.35 ± 0.06 Ma ( 97.28 of 39Ar, steps marked by <)

Power	36Ar/40Ar	39Ar/40Ar	z	Ca/K	%40Ar	%39Ar	40Ar*/39K	Age
300	0.00336294±0.00022215	0.057697±0.000342	0.002	0.11	99.07	0.22	0.119±1.139	0.50±4.81
<7000	0.00087305 0.00000000	0.422912 0.000000	0.003	0.08	24.78	18.73	1.768 0.020	7.46 0.08
300	0.00315609 0.00000000	0.070378 0.000000	0.002	0.00	92.95	0.63	0.964 0.435	4.07 1.84
<7000	0.00109249 0.00001118	0.389933 0.000852	0.003	0.08	31.25	44.25	1.750 0.019	7.38 0.08
300	0.00316527 0.00000000	0.095972 0.000000	0.001	0.07	93.04	1.91	0.687 0.226	2.90 0.95
<7000	0.00107967 0.00000001	0.399796 0.000000	0.003	0.06	30.70	34.26	1.721 0.019	7.26 0.08

Power	40Ar	39Ar	38Ar	37Ar	36Ar	Blank 40Ar	Atmos 40/36
300	6.72±0.00	0.50±0.00	0.12±0.00	0.040±0.00	0.048±0.00	0.128±0.00	287.67±1.00
<7000	76.82 0.00	32.19 0.14	3.05 0.07	0.240±0.00	0.094±0.00	0.131±0.00	287.67±1.00
300	15.31 0.00	1.19 0.01	0.18 0.00	0.035±0.00	0.075±0.00	0.128±0.00	287.67±1.00
<7000	196.44 0.00	75.92 0.32	18.50 0.16	0.490±0.01	0.249±0.00	0.154±0.00	287.67±1.00
300	34.20 0.00	3.31 0.01	0.65 0.01	0.029±0.00	0.125±0.00	0.151±0.00	287.67±1.00
<7000	148.42 0.00	58.69 0.25	14.50 0.12	0.183±0.00	0.178±0.00	0.154±0.00	287.67±1.00



Measured volumes are x 1E-10 cm3 NTP. All errors are 2 x standard error.

# **FAR-157M Muscovite (60-80 mesh)**

Run date: 1995/12/12  
Run: AS-137

Can/Pos: 143/S7  
Mass: 0.5 mg

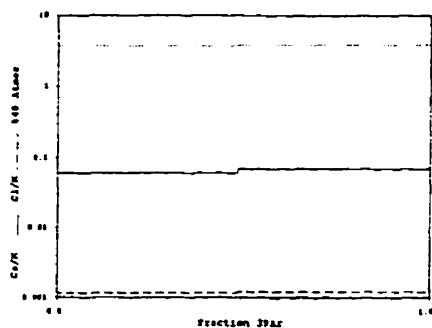
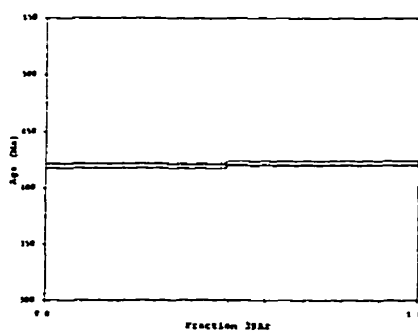
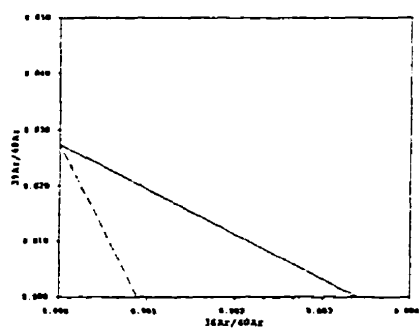
J Value: 0.006436  
± 0.000080

Volume 39Ar: 15.16 x 1E-10 cm3 NTP  
Integrated Age: 421.24 ± 4.90 Ma

Approx. 6.544 K  
0.434 Ca

Power	36Ar/40Ar	39Ar/40Ar	r	Ca/K	%40Ar	%39Ar	40Ar-39K	Age
7000	0.00012479±0.00001090	0.023644±0.000094	0.001	0.06	3.68	48.72	40.734±0.216	420.05±1.99
1500	0.00013094 0.00000000	0.023453 0.000000	0.001	0.07	3.86	51.28	40.999 0.227	422.28 2.09

Power	40Ar	39Ar	38Ar	37Ar	36Ar	Blank 40Ar	Atmos 40/36
7000	312.80±0.00	7.46±0.03	0.15±0.00	0.044±0.00	0.044±0.00	0.053±0.00	294.57±1.00
1500	331.93 0.00	7.85 0.03	0.16 0.00	0.056±0.00	0.048±0.00	0.057±0.00	294.57±1.00



Measured volumes are x 1E-10 cm3 NTP. All errors are 2 x standard error.

# **FAR-157B Biotite (60-80 mesh)**

Run date: 1995/12/12  
Run: AS-138

Can/Pos: 143/S5  
Mass: 0.3 mg

J Value: 0.006409  
± 0.000064

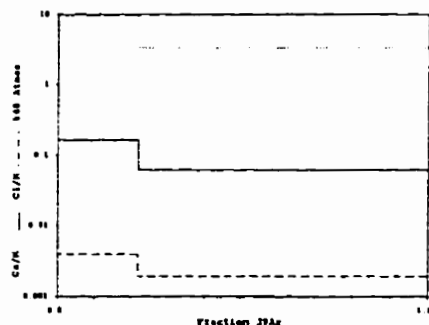
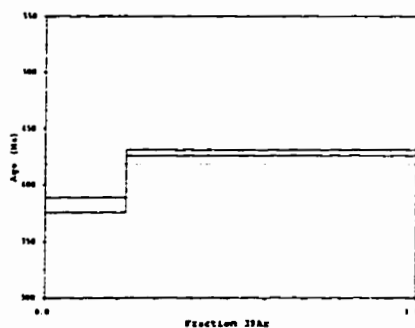
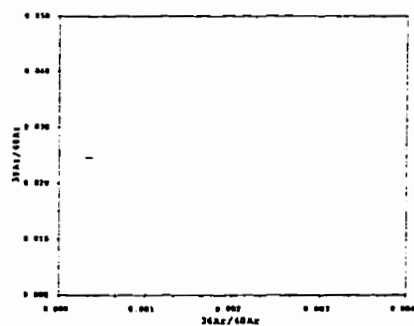
Volume 39Ar: 6.01 x 1E-10 cm<sup>3</sup> NTP  
Integrated Age: 418.57 ± 5.43 Ma

Approx. 7.03% K  
0.59% Ca

Initial 40/36: Linear regression has positive slope.  
Correlation Age:

Power	36Ar/40Ar	39Ar/40Ar	r	Ca/K	%40Ar	%39Ar	40Ar*/39K	Age
2500	0.00033452±0.00005663	0.024551±0.000106	0.003	0.16	9.87	21.89	36.706±0.701	382.22±6.57
2500	0.00011307 ± 0.00000000	0.023172 ± 0.000000	0.001	0.06	3.34	78.11	41.714 ± 0.266	428.62 ± 2.44

Power	40Ar	39Ar	38Ar	37Ar	36Ar	Blank 40Ar	Atmos 40/36
2500	71.56±0.00	1.73±0.01	0.04±0.00	0.033±0.00	0.022±0.00	0.075±0.00	294.57±1.00
2500	270.31 ± 0.00	6.32 ± 0.03	0.15 ± 0.00	0.042±0.00	0.036±0.00	0.072±0.00	294.57±1.00



Measured volumes are x 1E-10 cm<sup>3</sup> NTP. All errors are 2 x standard error.

# **FAR-169 Hornblende (80-120 mesh)**

Run date: 1995/11/15  
Run: AS-54

Can/Pos: 141/64  
Mass: 7.0 mg

J Value: 0.002341  
± 0.000012

Volume 39Ar: 11.13 x 1E-10 cm<sup>3</sup> NTP  
Integrated Age: 9.94 ± 0.62 Ma

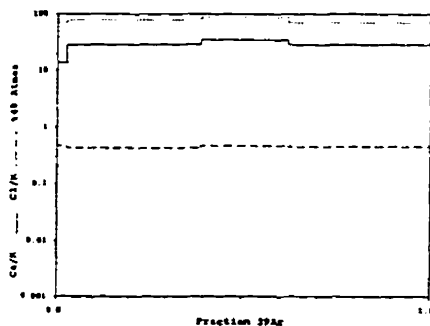
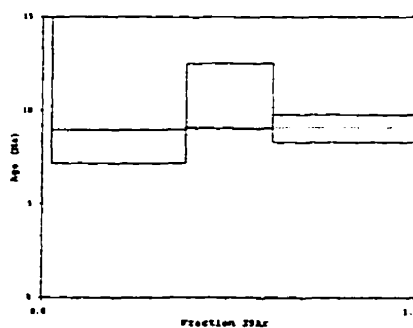
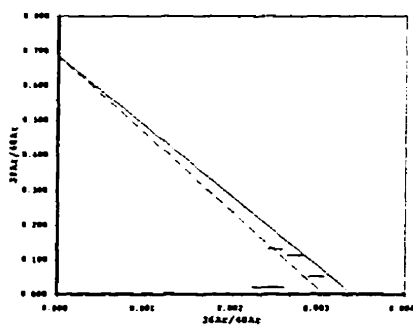
Approx. 0.96% K  
28.49% Ca

Initial 40/36: 327.69 ± 558.39 (MSWD = 25.36, isochron between 0.00 and 3.00)  
Correlation Age: 6.16 ± 6.93 Ma (100.0% of 39Ar, steps marked by >)

Plateau Age: 9.08 ± 0.60 Ma ( 98.38 of 39Ar, steps marked by <)

Power	36Ar/40Ar	39Ar/40Ar	r	Ca/K	%40Atm	%39Ar	40Ar*/39K	Age
500	0.00240636±0.00019372	0.020470±0.000179	0.069	14.02	70.80	1.68	14.234±2.767	59.13±11.31
<7000	0.00269864 0.00000000	0.112277 0.000000	0.146	29.20	78.13	35.39	1.915 0.210	8.07 0.88
<7000	0.00295935 0.00000000	0.051172 0.000000	0.373	34.56	86.65	21.80	2.562 0.415	10.79 1.74
<7000	0.00248022 0.00004668	0.131297 0.000301	0.128	29.11	71.39	41.13	2.149 0.176	9.05 0.74

Power	40Ar	39Ar	38Ar	37Ar	36Ar	Blank 40Ar	Atmos 40/36
500	9.22±0.00	0.12±0.00	0.43±0.00	0.238±0.00	0.048±0.00	0.121±0.00	287.67±1.00
<7000	35.00 0.00	4.07 0.02	7.55 0.06	5.977±0.11	0.138±0.00	0.123±0.00	287.67±1.00
<7000	46.88 0.00	2.55 0.01	4.96 0.04	6.540±0.08	0.179±0.00	0.121±0.00	287.67±1.00
<7000	34.82 0.00	4.71 0.02	9.04 0.08	10.392±0.13	0.133±0.00	0.122±0.00	287.67±1.00



Measured volumes are x 1E-10 cm<sup>3</sup> NTP. All errors are 2 x standard error.



# **FAR-169 Hornblende (80-120 mesh)**

Run date: 1997/05/06  
Run: JG-073 & JG-074

Can/Pos: 141/64  
Mass: 30.0 mg

J Value: 0.000041  
± 0.000016

Volume 39Ar: 48.04 x 1E-10 cm<sup>3</sup> NTP  
Integrated Age: 9.78 ± 0.56 Ma

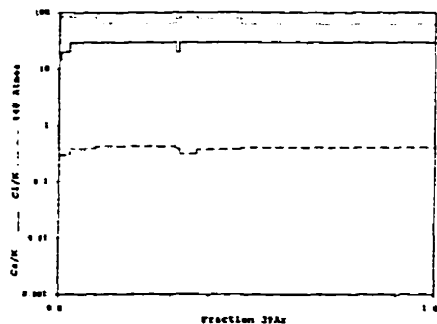
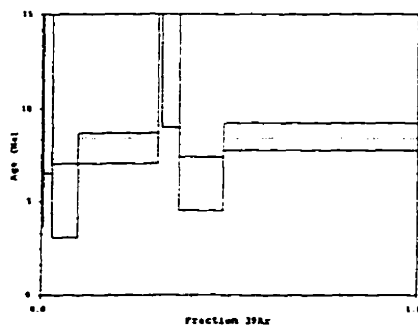
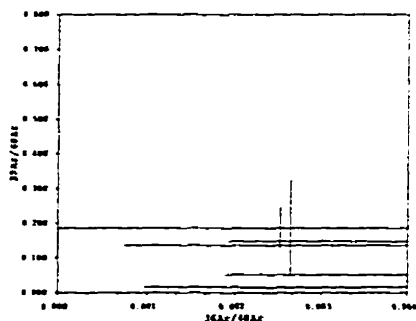
Approx. 0.964 K  
28.264 Ca

Initial 40/36: Linear regression has positive slope.  
Correlation Age:

Plateau Age: 8.40 ± 0.59 Ma ( 73.5% of 39Ar, steps marked by < )

Power	36Ar/40Ar	39Ar/40Ar	r	Ca/K	40Ar <sub>atm</sub>	39Ar	40Ar*/39K	Age
1000	0.00285394±0.00189865	0.016754±0.005222	0.867	15.00	83.45	0.42	9.844±9.058	41.10±77.39
3000	0.00297355 0.00000000	0.051535 0.000000	0.904	19.93	85.12	2.30	2.852 1.289	11.87 5.35
5000	0.00311831 0.00000000	0.136332 0.000000	0.967	30.00	82.92	6.81	1.218 0.473	5.08 1.97
<8000	0.00264505 0.02721223	0.186569 0.070271	1.000	30.00	64.29	20.92	1.887 0.201	7.86 0.82
2000	0.00273579 0.00000000	0.014656 0.000000	0.935	20.00	79.85	0.93	13.713 2.507	56.36 10.15
4000	0.00295116 0.00000020	0.052048 0.000001	0.902	30.00	84.35	4.58	2.971 0.816	12.37 3.33
6000	0.00298358 0.00000000	0.147272 0.000000	0.899	30.00	78.39	11.51	1.435 0.345	5.98 1.44
<7200	0.00252172 0.00000000	0.186503 0.000000	1.000	30.00	61.53	52.55	2.037 0.178	8.49 0.74

Power	40Ar	39Ar	38Ar	37Ar	36Ar	Blank 40Ar	Atmos 40/36
1000	12.35±0.11	0.14±0.03	0.23±0.02	0.017±0.00	0.060±0.01	0.413±0.02	284.57±11.00
3000	21.72 0.07	1.15 0.02	1.51 0.02	0.017±0.00	0.095±0.00	0.415±0.02	284.57±11.00
5000	24.30 0.09	3.33 0.03	5.64 0.06	0.019±0.00	0.119±0.01	0.422±0.02	284.57±11.00
<8000	54.15 0.14	10.15 0.07	19.25 0.17	0.021±0.01	0.222±0.01	0.441±0.02	284.57±11.00
2000	30.43 0.08	0.46 0.02	0.79 0.01	0.010±0.00	0.100±0.00	0.272±0.01	284.57±11.00
4000	42.18 0.14	2.23 0.04	3.05 0.04	0.014±0.00	0.156±0.01	0.303±0.02	284.57±11.00
6000	37.70 0.11	5.58 0.04	9.14 0.10	0.016±0.00	0.162±0.01	0.329±0.02	284.57±11.00
<7200	135.38 0.36	25.40 0.19	45.13 0.40	0.020±0.01	0.468±0.01	0.427±0.04	284.57±11.00



Measured volumes are x 1E-10 cm<sup>3</sup> NTP. All errors are 2 x standard error.

# **FAR-169 Hornblende (80-120 mesh)**

Run date: 1997/05/06 Can/Pos: 141/64 J Value: 0.002341  
Run: AS-54, JG-073 & JG-074 Mass: 20.0 mg = 0.000012

Volume 39Ar: 59.17 x 1E-10 cm3 NTP Approx. 1.78% K  
Integrated Age: 9.00 ± 0.48 Ma 52.36% Ca

Initial 40/36: 306.63 ± 120.34 (MSWD = 0.85, isochron between 0.53 and 1.94)  
Correlation Age: 7.65 ± 1.92 Ma ( 99.7% of 39Ar, steps marked by > )

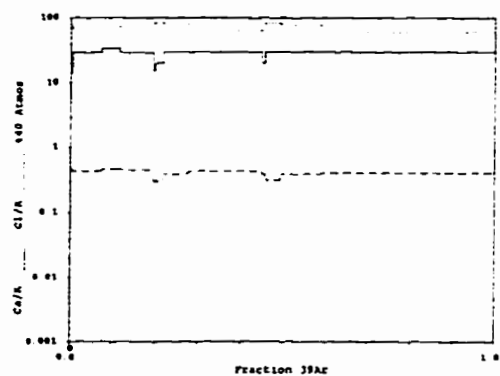
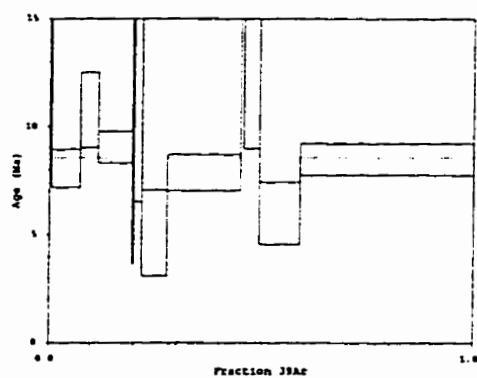
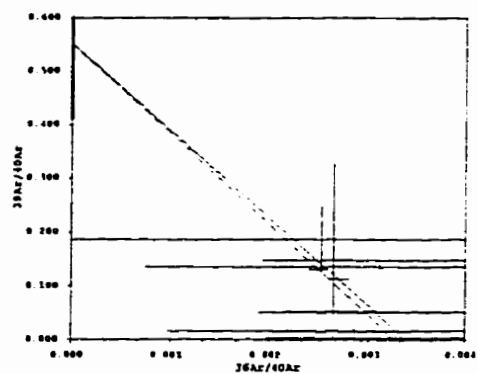
Plateau Age: 8.56 ± 0.48 Ma ( 78.1% of 39Ar, steps marked by < )

Power	36Ar/40Ar	39Ar/40Ar	r	Ca/K	%40Atm	%39Ar	40Ar*/39K	Age
500	0.00240636±0.00019372	0.020470±0.000179	0.069	14.02	70.80	0.32	14.234±2.767	59.13±11.3
<7000>	0.00269864 0.00000000	0.112277 0.000000	0.146	29.20	78.13	6.66	1.915 0.210	8.07 0.8
<7000>	0.00295935 0.00000000	0.051372 0.000000	0.373	34.56	86.65	4.10	2.562 0.415	10.79 1.7
<7000>	0.00248022 0.00004668	0.131297 0.000301	0.128	29.11	71.39	7.74	2.149 0.176	9.05 0.7
1000>	0.00285394 0.00000000	0.016754 0.000000	0.867	15.00	83.45	0.34	9.944 9.058	40.65 36.9
3000>	0.00297355 0.00000027	0.051535 0.000001	0.906	19.93	85.12	1.86	2.852 1.289	11.87 5.3
5000>	0.00311831 0.00000000	0.136332 0.000000	0.967	30.00	82.92	5.53	1.218 0.473	5.08 1.9
<8000>	0.00264505 0.00000000	0.186569 0.000000	1.000	30.00	64.29	16.98	1.887 0.201	7.86 0.8
2000>	0.00273579 0.00000000	0.014656 0.000000	0.935	20.00	79.85	0.75	13.713 2.507	56.38 10.1
4000>	0.00295116 0.00003487	0.052048 0.000096	0.902	30.00	84.35	3.71	2.971 0.816	12.37 3.3
6000>	0.00298358 0.00007330	0.147272 0.000205	0.899	30.00	78.39	9.34	1.435 0.345	5.93 1.4
<7200>	0.00252172 0.000203392	0.166503 0.005254	1.000	30.00	61.53	42.66	2.037 0.178	8.49 0.7

Power	40Ar	39Ar	38Ar	37Ar	36Ar	Blank 40Ar	Atmos 40/3
500	9.22±0.00	5.23±0.00	0.43±0.00	0.238±0.00	0.048±0.00	0.121±0.00	287.67±1.0
<7000>	35.00 0.00	4.07 0.02	7.55 0.06	8.977±0.11	0.138±0.00	0.123±0.00	287.67±1.0
<7000>	46.88 0.00	2.55 0.01	4.96 0.04	6.540±0.08	0.179±0.00	0.121±0.00	287.67±1.0
<7000>	34.82 0.00	4.71 0.02	9.04 0.09	10.392±0.13	0.133±0.00	0.122±0.00	287.67±1.0
1000>	12.35 0.11	0.24 0.03	0.29 0.02	0.017±0.00	0.060±0.01	0.419±0.02	284.57±1.0
3000>	21.72 0.07	1.15 0.02	1.51 0.02	0.017±0.00	0.095±0.00	0.415±0.02	284.57±1.0
5000>	24.30 0.09	1.33 0.03	5.64 0.06	0.019±0.00	0.119±0.01	0.422±0.02	284.57±1.0
<8000>	54.15 0.14	10.15 0.07	19.25 0.17	0.021±0.01	0.222±0.01	0.441±0.02	284.57±1.0
2000>	30.43 0.09	0.46 0.02	0.79 0.01	0.010±0.00	0.100±0.00	0.272±0.01	284.57±1.0
4000>	42.18 0.14	2.23 0.04	3.05 0.04	0.014±0.00	0.156±0.01	0.309±0.02	284.57±1.0
6000>	37.70 0.11	5.58 0.04	9.34 0.10	0.016±0.00	0.162±0.01	0.329±0.02	284.57±1.0
<7200>	135.38 0.36	25.40 0.19	45.13 0.40	0.020±0.01	0.488±0.01	0.427±0.04	284.57±1.0

Measured volumes are x 1E-10 cm3 NTP. All errors are 2 x standard error.

# FAR-169 Hornblende (80-120 mesh)



Measured volumes are x 1E-10 cm<sup>3</sup> NTP. All errors are 2 x standard error.

# **FAR-175M Muscovite (60-80 mesh)**

Run date: 1995/12/12  
Run: AS-139

Can/Pos: 143/S3  
Mass: 0.5 mg

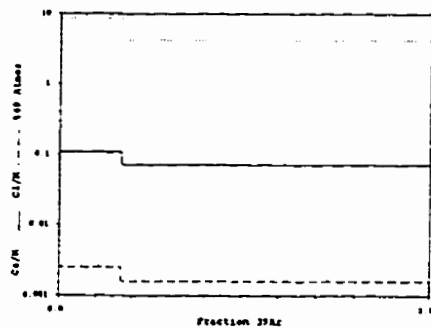
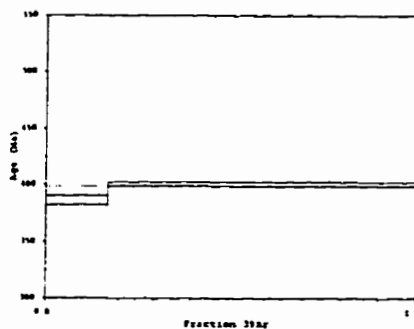
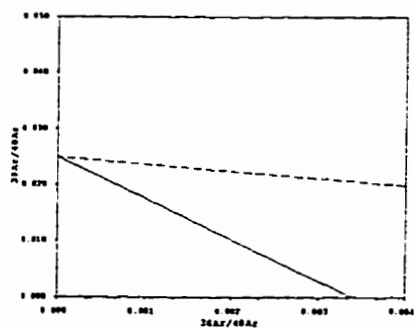
J Value: 0.006421  
± 0.000038

Volume 39Ar: 14.25 x 1E-10 cm<sup>3</sup> NTP  
Integrated Age: 398.42 ± 5.18 Ma

Approx. 6.261 K  
0.45% Ca

Power	36Ar/40Ar	39Ar/40Ar	z	Ca/K	40Ar <sub>atm</sub>	439Ar	40Ar*/39K	Age
3000	0.00029360±0.00003417	0.024539±0.000191	0.002	0.11	8.67	16.85	17.217±0.441	396.53±4.12
3000	0.00014182	0.00000000	0.001	0.07	4.19	33.15	18.745 0.199	400.81 1.84

Power	40Ar	39Ar	38Ar	37Ar	36Ar	Blank 40Ar	Atmos 40/36
3000	98.03±0.00	0.43±0.01	0.07±0.00	0.023±0.00	0.033±0.00	0.060±0.00	284.57±1.00
3000	479.71 0.00	11.36 0.05	0.27 0.00	0.084±0.00	0.074±0.00	0.072±0.00	284.57±1.00



Measured volumes are x 1E-10 cm<sup>3</sup> NTP. All errors are 2 x standard error.

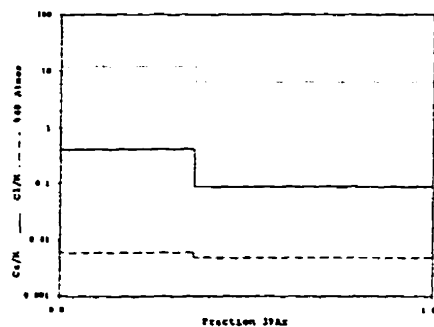
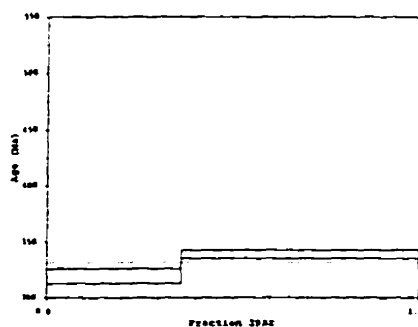
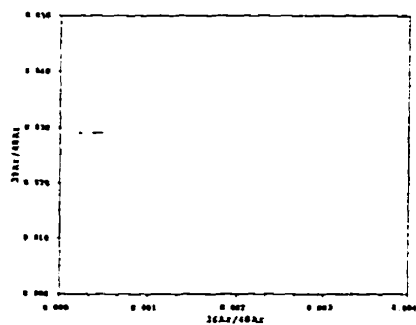
# **FAR-175B Biotite (60-80 mesh)**

Run date: 1995/12/12 Can/Pos: 143/S1 J Value: 0.006413  
 Run: AS-140 Mass: 0.3 mg = 0.000092

Volume 39Ar: 4.83 x 1E-10 cm3 NTP  
 Integrated Age: 331.80 ± 5.45 Ma Approx. 4.25% K  
 Initial 40/36: Linear regression has positive slope. 0.88% Ca  
 Correlation Age:

Power	36Ar/40Ar	39Ar/40Ar	r	Ca/K	%40Atm	%39Ar	40Ar*/39K	Age
2000	0.00041344±0.00004699	0.029093±0.000125	0.002	0.42	12.20	35.65	30.185±0.694	319.25±6.72
2000	0.00021764 0.00000000	0.029054 0.000000	0.001	0.09	6.42	64.35	32.206 0.363	338.72 3.48

Power	40Ar	39Ar	38Ar	37Ar	36Ar	Blank 40Ar	Atmos 40/36
2000	53.11±0.00	1.74±0.01	0.08±0.00	1.973±0.00	0.029±0.00	0.072±0.00	284.57±1.00
2000	107.11 0.00	3.14 0.01	0.12 0.00	0.031±0.00	0.027±0.00	0.040±0.00	284.57±1.00



Measured volumes are x 1E-10 cm3 NTP. All errors are 2 x standard errors.

# **FAR-176 Biotite (60-120 mesh)**

Run date: 1995/11/16  
Run: AS-55

Can/Pos: 141/65  
Mass: 9.8 mg

J Value: 0.002340  
± 0.000012

Volume  $^{39}\text{Ar}$ : 129.93 x 1E-10 cm<sup>3</sup> NTP  
Integrated Age: 9.03 ± 0.09 Ma

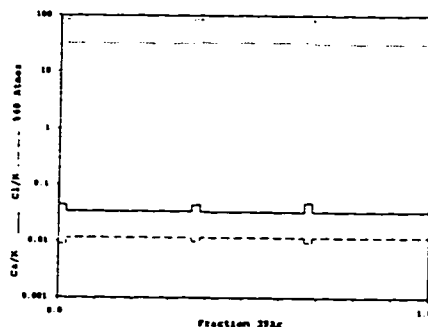
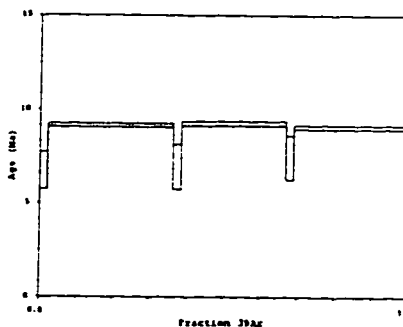
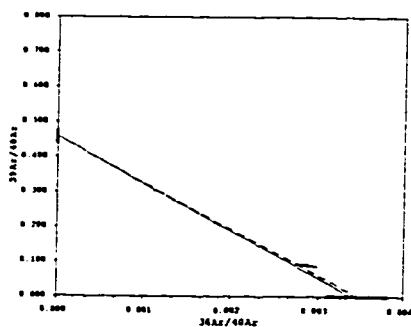
Approx. 7.99% K  
0.28% Ca

Initial 40/36: 289.16 ± 29.83 (MSWD = 7.19, isochron between 0.29 and 2.41)  
Correlation Age: 9.20 ± 0.35 Ma (100.0% of  $^{39}\text{Ar}$ , steps marked by >)

Plateau Age: 9.17 ± 0.08 Ma ( 93.6% of  $^{39}\text{Ar}$ , steps marked by <)

Power	$^{36}\text{Ar}/^{40}\text{Ar}$	$^{39}\text{Ar}/^{40}\text{Ar}$	$\epsilon$	Ca/K	%40Atm	% $^{39}\text{Ar}$	$^{40}\text{Ar}^*/^{39}\text{K}$	Age
300	0.00292525±0.00006628	0.084624±0.000372	0.001	0.04	86.12	2.06	1.605±0.234	6.76±0.99
<7000	0.00110434 0.00000000	0.109472 0.000000	0.003	0.03	32.13	33.98	2.180 0.024	9.18 0.10
300	0.00289224 0.00000000	0.088437 0.000000	0.001	0.04	85.13	2.20	1.646 0.284	6.94 1.19
<7000	0.00112514 0.00001332	0.103720 0.000660	0.002	0.03	32.74	28.08	2.201 0.028	9.27 0.12
300	0.00282463 0.00000000	0.093723 0.000000	0.001	0.05	83.12	2.11	1.766 0.278	7.44 1.17
<7000	0.00107313 0.00000001	0.117595 0.000000	0.002	0.03	31.20	31.57	2.153 0.026	9.07 0.11

Power	$^{40}\text{Ar}$	$^{39}\text{Ar}$	$^{38}\text{Ar}$	$^{37}\text{Ar}$	$^{36}\text{Ar}$	Blank $^{40}\text{Ar}$	Atmos $^{40}/^{36}$
300	31.87±0.00	2.72±0.01	0.17±0.00	0.020±0.00	0.104±0.00	0.065±0.00	287.67±1.00
<7000	144.58 0.00	44.44 0.19	2.94 0.03	0.129±0.00	0.171±0.00	0.065±0.00	287.67±1.00
300	32.44 0.00	2.89 0.01	0.19 0.00	0.022±0.00	0.104±0.00	0.073±0.00	287.67±1.00
<7000	121.71 0.00	36.72 0.16	2.44 0.02	0.106±0.00	0.147±0.00	0.073±0.00	287.67±1.00
300	29.42 0.00	2.77 0.01	0.19 0.00	0.022±0.00	0.093±0.00	0.073±0.00	287.67±1.00
<7000	130.96 0.00	41.29 0.18	2.71 0.02	0.117±0.00	0.151±0.00	0.074±0.00	287.67±1.00



Measured volumes are x 1E-10 cm<sup>3</sup> NTP. All errors are 2 x standard error.

# **FAR-201 Hornblende (45-100 mesh)**

Run date: 1995/10/03  
Run: AS-9 & AS-77

Can/Pos: 141/1  
Mass: 30.0 mg

J Value: 0.000343  
± 0.000019

Volume 39Ar: 49.42 x 1E-10 cm3 NTP  
Integrated Age: 12.39 ± 0.25 Ma

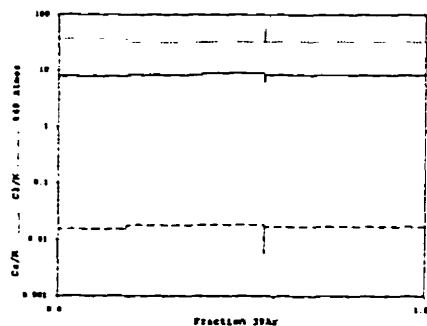
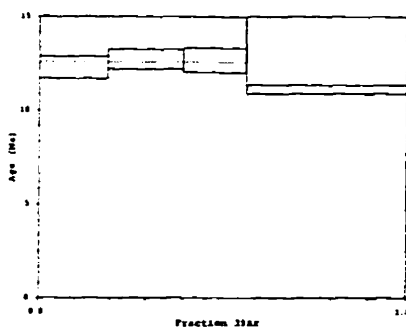
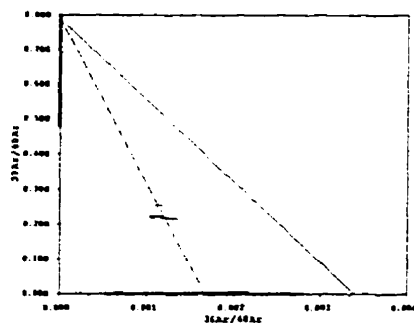
Approx. 0.55% K  
8.21% Ca

Initial 40/36: 601.00 ± 407.37 (MSWD = 3.07, isochron between 0.18 and 2.63)  
Correlation Age: 5.38 ± 2.08 Ma (100.0% of 39Ar, steps marked by >)

Plateau Age: 12.56 ± 0.36 Ma ( 56.78 of 39Ar, steps marked by <)

Power	36Ar/40Ar	39Ar/40Ar	r	Ca/K	40Ar <sub>atm</sub>	439Ar	40Ar*/39K	Age
<7000	0.00125527±0.00010510	0.215858±0.000941	0.006	7.97	36.71	19.02	2.917± 0.143	12.23± 0.60
<7000	0.00111295 0.00000000	0.222686 0.000000	0.007	8.33	32.53	20.79	3.016 0.127	12.71 0.53
<7000	0.00114533 0.00000000	0.220013 0.000000	0.007	9.07	33.48	16.94	3.009 0.155	12.62 0.65
300	0.00192395 0.00012458	0.007035 0.000180	0.222	6.38	56.83	0.19	61.332 10.109	242.24 37.36
7000	0.00112521 0.00000000	0.253609 0.000000	0.013	8.38	32.77	43.07	2.637 0.053	11.11 0.22

Power	40Ar	39Ar	38Ar	37Ar	36Ar	Blank 40Ar	Atmos 40/36
<7000	43.93±0.00	3.47±0.04	0.73±0.01	13.78±0.16	0.070±0.00	0.113±0.00	287.67±1.00
<7000	46.54 0.00	10.35 0.04	0.99 0.01	15.73±0.20	0.068±0.00	0.110±0.00	287.67±1.00
<7000	38.38 0.00	8.43 0.04	0.83 0.01	13.947±0.18	0.059±0.00	0.109±0.00	287.67±1.00
300	13.25 0.00	0.10 0.00	0.01 0.01	0.038±0.00	0.029±0.00	0.114±0.00	287.67±1.00
7000	94.68 0.00	21.42 0.09	1.96 0.02	10.263±0.13	0.125±0.00	0.118±0.00	287.67±1.00



Measured volumes are x 1E-10 cm3 NTP. All errors are 1 x standard error.

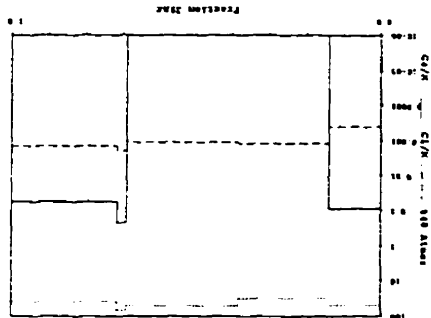
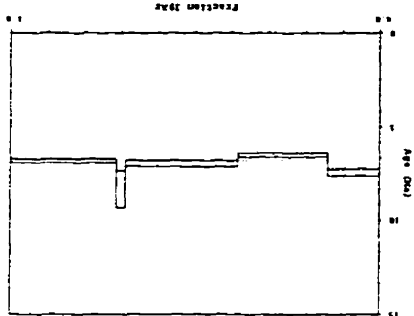
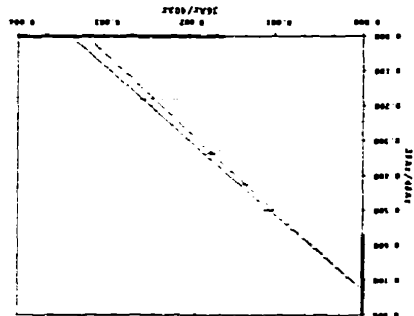
FAR-202 Whole Rock (45-80 mesh)

Run date: 1995/10/23  
Run: AS-200  
Can/Box: 140/2  
Mass: 100.0 mg  
J Value: 0.002647  
= 0.000014

Volume 39Ac: 73.73 x 1E-10 cm3 NTP  
Integrated Age: 6.90 ± 0.08 Ma  
Approx. 0.39% K  
Initial 40/36: 312.11 ± 156.57 (MSWD = 6.43, Isochron between -0.41 and 3.83)  
Correlation Age: 6.55 ± 1.39 Ma ( 83.5% of 39Ac, steps marked by > )  
Plateau Age: 6.77 ± 0.08 Ma ( 83.5% of 39Ac, steps marked by < )

Power	36Ar/40Ar	39Ar/40Ar	z	Ca/K	%40Ca	%39Ar	40Ar-/39Ar	Age
300	0.001644339±0.00007981	0.329232±0.001356	0.110	0.09	47.89	13.91	1.563±0.040	7.45±0.19
<7000>	0.00107706 0.00000000	0.500799 0.00000000	0.043	0.00	31.13	24.22	1.362 0.025	6.49 0.12
<7000>	0.00172799 0.00000000	0.335385 0.00000000	0.071	0.00	50.33	30.27	1.460 0.030	6.96 0.14
500	0.00231751 0.00013920	0.180218 0.000553	0.512	0.22	67.95	2.59	1.750 0.211	8.34 1.00
<7000>	0.00131013 0.00000000	0.425796 0.00000000	0.040	0.06	38.57	29.01	1.427 0.021	6.80 0.10

Power	40Ar	39Ar	38Ar	37Ar	36Ar	Blank 40Ar	Atmos 40/36
300	31.65±0.00	10.33±0.04	0.19±0.01	0.90±0.01	0.055±0.00	0.076±0.00	284.57±1.00
<7000>	16.50 0.00	17.99 0.07	0.36 0.02	0.003±0.01	0.042±0.00	0.105±0.00	284.57±1.00
<7000>	67.59 0.00	22.49 0.09	0.45 0.02	0.004±0.01	0.122±0.00	0.122±0.00	284.57±1.00
500	11.02 0.00	1.93 0.01	0.05 0.01	0.003±0.00	0.028±0.00	0.339±0.00	284.57±1.00
<7000>	51.45 0.00	21.55 0.09	0.45 0.01	0.004±0.01	0.072±0.00	0.332±0.00	284.57±1.00



Measured volumes are x 1E-10 cm3 NTP. All errors are 2 x standard error.



# **FAR-202 Whole Rock (45-80 mesh)**

Run date: 1997/05/06  
Run: AS-200 & JG-076

Can/Pcs: 140/2  
Mass: 100.0 mg

J Value: 0.002647  
= 0.000014

Volume 39Ar: 131.74 x 1E-10 cm3 NTP  
Integrated Age: 6.64 ± 0.13 Ma

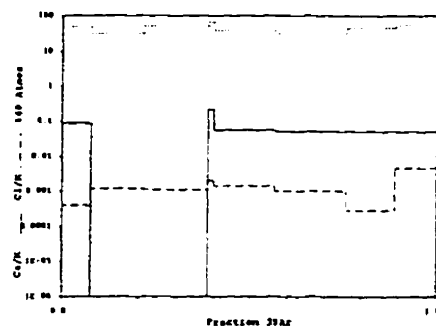
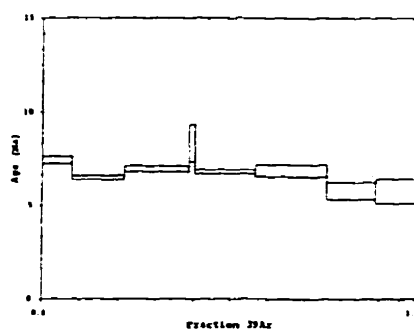
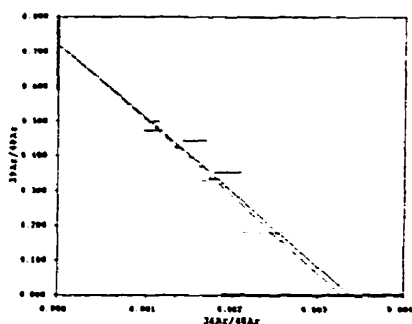
Approx. 0.701 K  
0.033 Ca

Initial 40/36: 304.22 ± 130.08 (MSWD = 8.05, isochron between 0.29 and 2.41)  
Correlation Age: 6.62 ± 1.16 Ma ( 90.8% of 39Ar, steps marked by >)

Plateau Age: 6.55 ± 0.14 Ma ( 90.8% of 39Ar, steps marked by <)

Power	36Ar/40Ar	39Ar/40Ar	ε	Ca/K	%40Atm	%39Ar	40Ar*/39K	Age
300	0.00164339±0.00007981	0.329232±0.001356	0.110	0.09	47.89	7.78	1.563±0.040	7.45±0.19
<7000>	0.00107706 0.00000000	0.500799 0.000000	0.043	0.00	31.13	13.55	1.362 0.025	6.49 0.12
<7000>	0.00172799 0.00000000	0.335385 0.000000	0.071	0.00	50.33	16.94	1.460 0.030	6.96 0.14
500	0.00231761 0.00013920	0.180218 0.000553	0.512	0.22	67.95	1.45	1.750 0.211	8.34 1.00
<7000>	0.00133013 0.00000000	0.425796 0.000000	0.040	0.06	38.57	16.24	1.427 0.021	6.80 0.10
<2000>	0.00105084 0.00000003	0.475237 0.000001	0.011	0.05	30.46	19.24	1.450 0.069	6.84 0.32
<5000>	0.00153370 0.00000000	0.446040 0.000000	0.017	0.05	44.48	12.32	1.226 0.099	5.79 0.47
<7000>	0.00192613 0.00000000	0.353516 0.000000	0.026	0.05	55.98	11.86	1.225 0.140	5.78 0.66

Power	40Ar	39Ar	38Ar	37Ar	36Ar	Blank 40Ar	Atmos 40/36
300	31.65±0.00	10.33±0.04	0.18±0.01	0.304±0.01	0.055±0.00	0.076±0.00	134.57±1.00
<7000>	36.50 0.00	17.39 0.07	0.36 0.02	0.003±0.01	0.042±0.00	0.105±0.00	134.57±1.00
<7000>	67.59 0.00	22.49 0.09	0.45 0.02	0.004±0.01	0.122±0.00	0.122±0.00	134.57±1.00
500	11.02 0.00	1.93 0.01	0.05 0.01	0.003±0.00	0.028±0.00	0.329±0.00	134.57±1.00
<7000>	51.45 0.00	21.55 0.09	0.45 0.01	0.004±0.01	0.072±0.00	0.329±0.00	134.57±1.00
<2000>	55.59 0.15	25.58 0.11	0.38 0.01	0.024±0.00	0.100±0.01	1.207±0.06	133.60±1.00
<5000>	40.09 0.14	17.21 0.09	0.31 0.01	0.025±0.00	0.105±0.01	1.213±0.06	133.20±1.00
<7000>	46.37 0.19	15.84 0.09	0.40 0.02	0.027±0.00	0.138±0.01	1.449±0.07	133.50±1.00



Measured volumes are x 1E-10 cm3 NTP. All errors are 2 x standard error.

# **FAR-202 Whole Rock (45-80 mesh)**

Run date: 1997/05/06  
Run: JG-076

Can/Pos: 140/2  
Mass: 150.0 mg

J Value: 0.000647  
± 0.000009

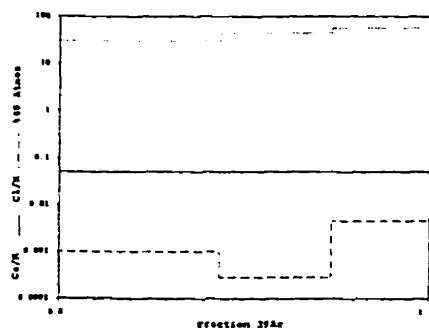
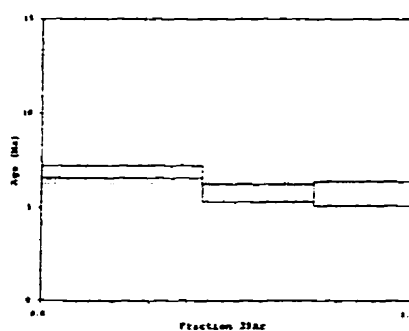
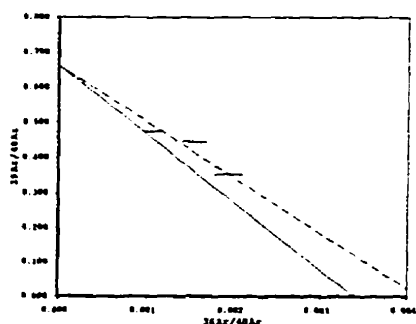
Volume 39Ar: 58.01 x 1E-10 cm<sup>3</sup> NTP  
Integrated Age: 6.31 ± 0.27 Ma

Approx. 0.21% K  
0.01% Ca

Initial 40/36: 241.81 ± 2313.04 (MSWD = 10.31, isochron between -0.41 and 3.83)  
Correlation Age: 7.20 ± 29.98 Ma (100.0% of 39Ar, steps marked by >)

Power	36Ar/40Ar	39Ar/40Ar	r	Ca/K	%40Atm	%39Ar	40Ar*/39K	Age
2000	0.00105084±0.00011019	0.475237±0.002513	0.911	0.05	30.46	43.68	1.450±0.069	6.31±0.33
5000	0.00153376 0.00000000	0.446040 0.000000	0.017	0.05	44.48	29.34	1.226 0.099	5.79 0.47
7000	0.00192613 0.00000000	0.353536 0.000000	0.026	0.05	55.88	26.98	1.225 0.140	5.79 0.66

Power	40Ar	39Ar	38Ar	37Ar	36Ar	Blank 40Ar	Atmos 40/36
2000	55.59±0.15	25.58±0.11	0.39±0.01	0.024±0.00	0.100±0.01	1.207±0.06	283.82±1.00
5000	40.09 0.14	17.21 0.09	0.31 0.01	0.025±0.00	0.105±0.01	1.219±0.06	283.82±1.00
7000	46.37 0.15	15.94 0.09	0.60 0.02	0.027±0.00	0.138±0.01	1.443±0.07	283.82±1.00



Measured volumes are x 1E-10 cm<sup>3</sup> NTP. All errors are 2 x standard error.

# **FAR-204 Hornblende (80-100 mesh)**

Run date: 1995-10-03  
Run: AS-10 & AS-104

Can/Pos: 141/3  
Mass: 20.0 mg

J Value: 0.002345  
± 0.000016

Volume 39Ar: 36.14 x 1E-10 cm3 NTP  
Integrated Age: 9.56 ± 0.38 Ma

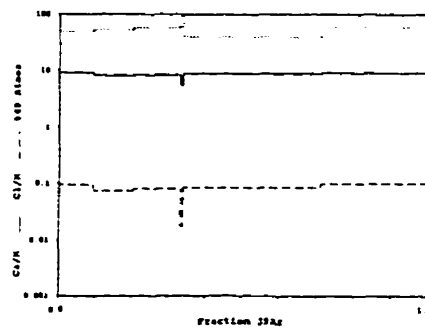
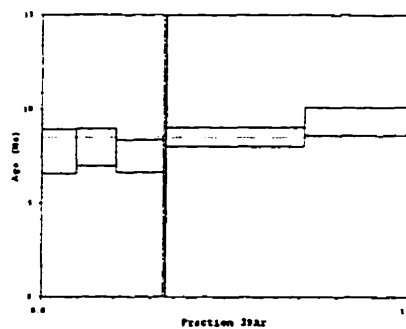
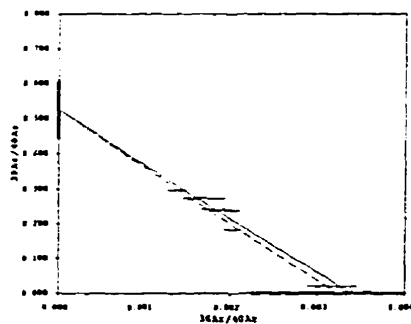
Approx. 1.0% K  
9.57% Ca

Initial 40/36: 310.30 ± 92.13 (MSWD = 2.53, isochron between 0.29 and 2.41)  
Correlation Age: 8.02 ± 1.20 Ma (100.0% of 39Ar, steps marked by >)

Plateau Age: 8.51 ± 0.35 Ma ( 99.28 of 39Ar, steps marked by <)

Power	36Ar/40Ar	39Ar/40Ar	ε	Ca/K	%40Ar	%39Ar	40Ar*/39K	Age
<7000	0.00169312±0.00025530	0.274024±0.001210	0.003	9.05	49.08	9.32	1.838±0.275	7.76± 1.16
<7000	0.00184485 0.00000000	0.241978 0.000000	0.003	8.17	53.71	10.88	1.891 0.230	7.98 0.97
<7000	0.00195508 0.00000000	0.238487 0.000000	0.004	8.48	56.92	12.78	1.783 0.205	7.53 0.86
300	0.0015717 0.00014840	0.020577 0.000082	0.076	5.44	93.20	0.84	3.264 4.230	13.76 17.76
<7000	0.00137472 0.00000000	0.297349 0.000000	0.005	8.87	39.35	36.84	2.023 0.116	8.54 0.49
<7000	0.00202541 0.00000003	0.183738 0.000000	0.009	9.23	58.83	29.34	2.216 0.175	9.35 0.74

Power	40Ar	39Ar	38Ar	37Ar	36Ar	Blank 40Ar	Atmos 40/36
<7000	12.51±0.00	3.40±0.01	1.48±0.01	5.40±0.07	0.029±0.00	0.121±0.00	287.67±1.00
<7000	16.43 0.00	3.97 0.02	1.36 0.01	5.907±0.08	0.038±0.00	0.121±0.00	287.67±1.00
<7000	19.62 0.00	4.66 0.02	1.75 0.02	7.192±0.09	0.047±0.00	0.121±0.00	287.67±1.00
300	14.84 0.00	0.31 0.00	0.04 0.01	0.093±0.00	0.051±0.00	0.084±0.00	287.67±1.00
<7000	45.29 0.00	13.40 0.06	5.23 0.05	4.263±0.08	0.083±0.01	0.102±0.00	287.67±1.00
<7000	56.05 0.00	10.68 0.05	4.81 0.04	5.190±0.07	0.137±0.01	0.118±0.00	287.67±1.00



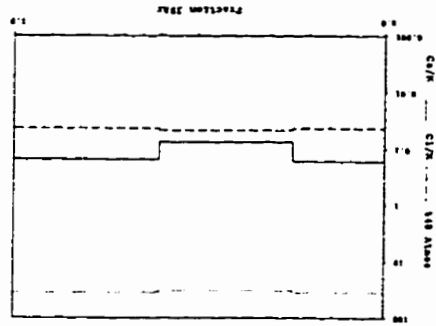
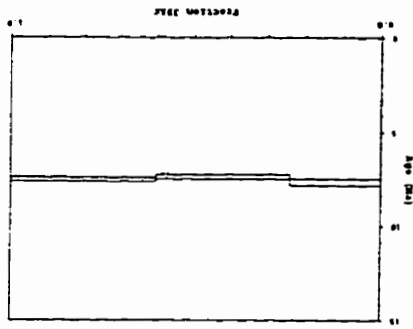
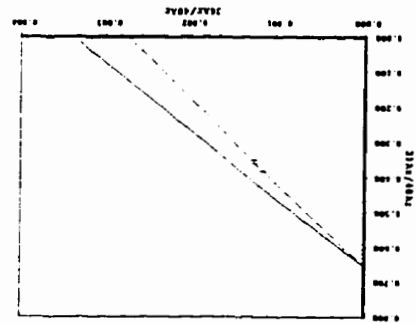
Measured volumes are x 1E-10 cm3 NTP. All errors are 2 x standard error.

# FAR-206 Biotite (45-80 mesh)

Run date: 1995/10/04  
 Can/Pcs: 141/4  
 Mass: 8.0 mg  
 J value: 0.002346  
 ± 0.000016  
 Approx. 7.92% K  
 1.02% Ca  
 Volume 39Ar: 105.38 x 1E-10 cm<sup>3</sup> NTP  
 Integrated Age: 7.49 ± 0.09 Ma  
 Correlation Age: 6.47 ± 77.38 Ma (100.0% of 39Ar, steps marked by >)

Power	36Ar/40Ar	39Ar/40Ar	z	Ca/K	%40Ca	39Ar	40Ar-39K	Age
7000	0.00123339±0.0000430	0.351675±0.001532	0.002	0.17	35.70	24.20	1.813±0.038	7.66±0.16
7000	0.00114213 0.00000000	0.381669 0.00000000	0.002	0.08	32.96	35.77	1.743 0.028	7.16 0.12
7000	0.001233094 0.00000000	0.359619 0.00000000	0.003	0.15	35.61	40.03	1.776 0.027	7.50 0.12

Power	40Ar	39Ar	38Ar	37Ar	36Ar	Blank 40Ar	Atmos 40/36
7000	73.71±0.00	25.68±0.11	5.20±0.04	0.79±0.01	0.077±0.00	0.126±0.00	297.67±1.00
7000	100.46 0.00	37.95 0.16	9.41 0.07	0.534±0.01	0.121±0.00	0.126±0.00	297.67±1.00
7000	119.18 0.00	42.47 0.16	8.67 0.07	1.194±0.02	0.154±0.00	0.113±0.00	287.67±1.00



Measured volumes are x 1E-10 cm<sup>3</sup> NTP. All errors are ± x standard error.

# **FAR-216 Hornblende (60-100 mesh)**

Run date: 1995/10/04 Can/Pos: 141/5 J Value: 0.002347  
 Run: AS-12 & AS-105 Mass: 28.0 mg = 0.000014

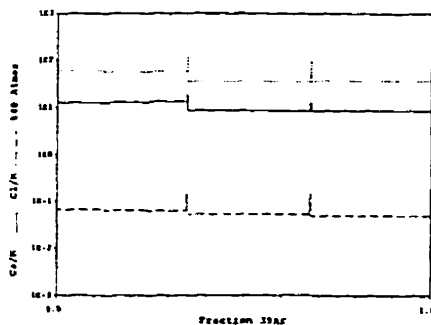
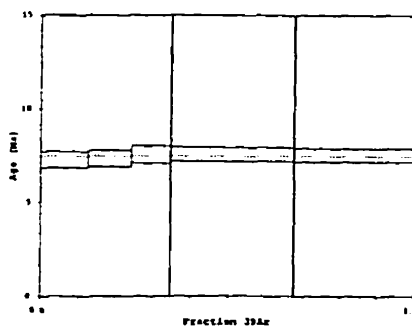
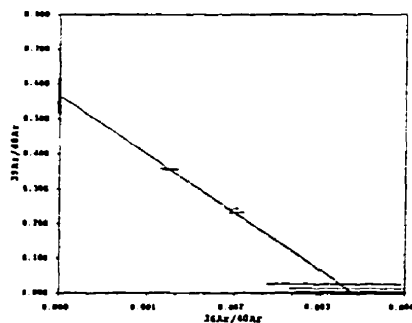
Volume 39Ar: 50.55 x 1E-10 cm3 NTP Approx. 1.09% K  
 Integrated Age: 7.45 ± 0.26 Ma 10.70% Ca

Initial 40/36: 296.67 ± 58.45 (MSWD = 0.64, isochron between 0.37 and 2.26)  
 Correlation Age: 7.47 ± 0.64 Ma (100.0% of 39Ar, steps marked by >)

Plateau Age: 7.50 ± 0.20 Ma ( 99.6% of 39Ar, steps marked by <)

Power	36Ar/40Ar	39Ar/40Ar	z	Ca/K	%40Ar	%39Ar	40Ar*/39K	Age
<7000	0.00204242±0.00007955	0.230758±0.001012	0.018	12.43	59.55	12.39	1.728±0.099	7.30±0.42
<7000	0.00196265±0.00006000	0.242627±0.000000	0.016	12.58	57.18	11.58	1.741±0.101	7.36±0.43
<7000	0.00199763±0.00000000	0.230201±0.000000	0.018	13.12	58.25	10.46	1.789±0.110	7.56±0.46
500	0.00399645±0.00069305	0.013620±0.000586	0.046	18.52	117.97	0.09	-13.240±9.861	-56.95±130.49
<7000	0.00123116±0.00000000	0.357931±0.000000	0.004	8.38	35.27	32.08	1.794±0.089	7.53±0.37
500	0.00316126±0.00000020	0.025857±0.000000	0.016	12.92	93.20	0.29	2.593±9.090	10.35±38.26
<7000	0.00126061±0.00000000	0.354945±0.000000	0.005	8.42	36.15	33.11	1.784±0.085	7.54±0.36

Power	40Ar	39Ar	38Ar	37Ar	36Ar	Blank 40Ar	Atmos 40/36
<7000	27.41±0.00	4.33±0.03	1.94±0.02	14.255±0.18	0.075±0.00	0.138±0.00	287.67±1.00
<7000	24.40±0.00	5.92±0.03	1.78±0.02	13.488±0.17	0.066±0.00	0.137±0.00	287.67±1.00
<7000	23.21±0.00	5.35±0.02	1.58±0.01	12.695±0.16	0.064±0.00	0.136±0.00	287.67±1.00
500	3.53±0.00	0.05±0.00	0.04±0.00	0.053±0.00	0.018±0.00	0.072±0.00	287.67±1.00
<7000	45.31±0.00	16.32±0.07	4.04±0.03	7.183±0.09	0.080±0.00	0.074±0.00	287.67±1.00
500	5.79±0.00	0.16±0.00	0.11±0.00	0.107±0.00	0.022±0.00	0.071±0.00	287.67±1.00
<7000	47.75±0.00	16.94±0.07	4.03±0.03	7.448±0.10	0.084±0.00	0.074±0.00	287.67±1.00



Measured volumes are x 1E-10 cm3 NTP. All errors are 2 x standard error.

# **FAR-224 Hornblende (60-100 mesh)**

Run date: 1995/10/05  
Run: AS-13 & AS-107

Can/Pos: 141/6  
Mass: 23.0 mg

J Value: 0.002348  
= 0.000014

Volume 39Ar: 38.06 x 1E-10 cm<sup>3</sup> NTP  
Integrated Age: 8.44 ± 0.52 Ma

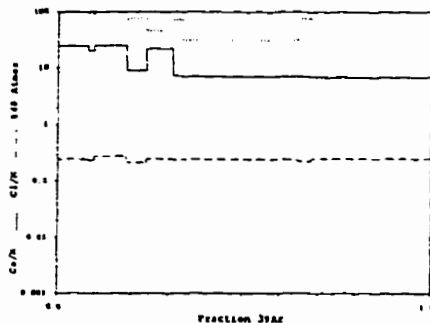
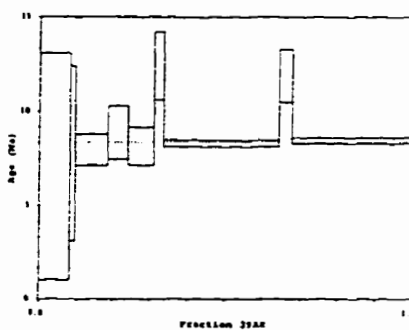
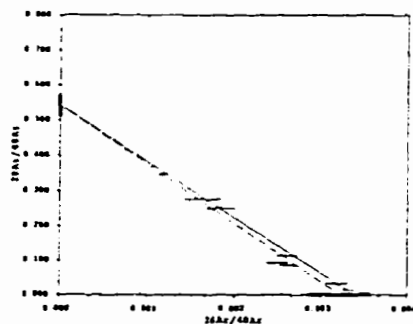
Approx. 0.99% K  
11.40% Ca

Initial 40/36: 311.07 ± 34.42 (MSWD = 6.20, isochron between 0.47 and 2.07)  
Correlation Age: 7.80 ± 0.40 Ma (100.0% of 39Ar, steps marked by >)

Plateau Age: 8.33 ± 0.18 Ma ( 84.58 of 39Ar, steps marked by <)

Power	36Ar/40Ar	39Ar/40Ar	ε	Ca/K	%40Ar	%39Ar	40Ar*/39K	Age
7000	0.00331431±0.00007492	0.012611±0.000128	0.543	25.08	97.84	8.05	1.671±1.428	7.07±6.03
750	0.00317619±0.00000000	0.034145±0.000000	0.132	19.97	93.41	1.42	1.833±1.098	7.75±4.63
<7000	0.00303284±0.00000000	0.248800±0.000000	0.030	25.56	52.59	8.68	1.884±0.196	7.96±0.83
< 750	0.00259504±0.00006437	0.113043±0.000250	0.011	9.09	75.96	5.28	2.095±0.335	8.85±1.41
<7000	0.00162568±0.00000000	0.275208±0.000000	0.016	22.32	46.45	7.06	1.927±0.235	8.14±0.99
300	0.00248222±0.00000003	0.093126±0.000000	0.010	7.45	72.37	2.56	2.937±0.427	12.40±1.80
<7000	0.00117001±0.00000000	0.347522±0.000000	0.008	7.18	31.44	10.55	1.960±0.038	8.28±0.16
300	0.00260202±0.00000000	0.084333±0.000000	0.014	7.15	76.02	3.23	2.812±0.335	11.87±1.41
<7000	0.00115754±0.00000000	0.344481±0.000000	0.008	7.01	30.90	12.98	1.993±0.036	8.42±0.15

Power	40Ar	39Ar	38Ar	37Ar	36Ar	Blank 40Ar	Atmos 40/36
7000	240.36±0.00	3.10±0.01	3.51±0.03	13.858±0.18	0.836±0.01	0.093±0.00	287.67±1.00
750	18.00±0.00	0.63±0.00	0.65±0.01	2.327±0.03	0.065±0.00	0.092±0.00	287.67±1.00
<7000	13.38±0.00	1.34±0.01	4.11±0.04	15.209±0.19	0.042±0.00	0.092±0.00	287.67±1.00
< 750	17.86±0.00	2.04±0.01	1.95±0.02	3.247±0.04	0.055±0.00	0.093±0.00	287.67±1.00
<7000	9.39±0.00	2.72±0.01	3.05±0.03	10.588±0.14	0.030±0.00	0.093±0.00	287.67±1.00
300	10.55±0.00	0.99±0.01	1.05±0.01	0.365±0.01	0.031±0.00	0.065±0.00	287.67±1.00
<7000	33.32±0.00	11.70±0.05	12.79±0.11	4.365±0.06	0.055±0.00	0.065±0.00	287.67±1.00
300	14.65±0.00	1.24±0.01	1.27±0.01	0.464±0.01	0.043±0.00	0.065±0.00	287.67±1.00
<7000	36.33±0.00	12.63±0.05	14.25±0.12	4.599±0.06	0.059±0.00	0.065±0.00	287.67±1.00



Measured volumes are x 1E-10 cm<sup>3</sup> NTP. All errors are 2 x standard error.

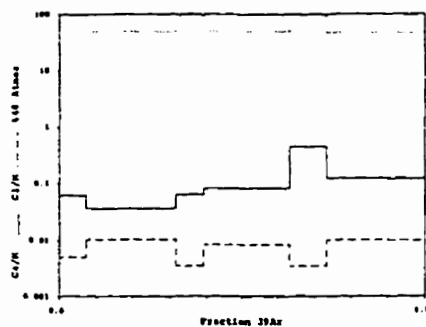
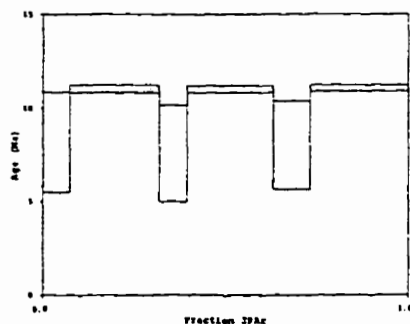
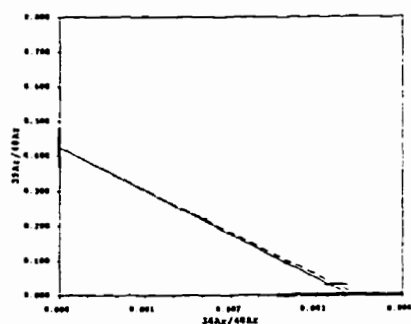
# **FAR-227 Whole Rock (60-80 mesh)**

Run date: 1996/10/23 Can/POS: 140/3 J Value: 0.002665  
Run: AS-201, Mass: 100.0 mg ± 0.000014

Volume 39Ar: 110.59 x 1E-10 cm<sup>3</sup> NTP  
Integrated Age: 10.25 ± 0.41 Ma Approx. 0.59% K  
Initial 40/36: 287.99 ± 75.76 (MSWD = 0.05, isochron between 0.29 and 2.41)  
Correlation Age: 11.26 ± 1.38 Ma (100.0% of 39Ar, steps marked by >)  
Plateau Age: 11.02 ± 0.13 Ma ( 75.0% of 39Ar, steps marked by <)

Power	36Ar/40Ar	39Ar/40Ar	r	Ca/K	%40Ar	%39Ar	40Ar*/39K	Age
500	0.00321888±0.00010319	0.028720±0.000255	0.765	0.06	94.99	7.22	1.704±0.557	8.17±2.66
<7000	0.00168454 0.00000000	0.219368 0.000000	0.046	0.04	49.15	24.07	2.298 0.041	11.01 0.20
500	0.00322559 0.00000000	0.029688 0.000000	0.866	0.06	95.19	7.71	1.580 0.539	7.58 2.58
<7000	0.00166799 0.00001866	0.221679 0.000446	0.046	0.08	48.69	23.80	2.294 0.041	11.00 0.19
500	0.00320324 0.00000000	0.032089 0.000000	0.768	0.44	94.52	10.10	1.668 0.496	8.00 2.37
<7000	0.00160311 0.00000001	0.226951 0.000000	0.036	0.12	46.74	27.11	2.307 0.038	11.06 0.18

Power	40Ar	39Ar	38Ar	37Ar	36Ar	Blank 40Ar	Atmos 40/36
500	278.67±0.00	8.05±0.03	0.46±0.01	0.004±0.01	0.932±0.01	0.330±0.00	294.57±1.00
<7000	122.78 0.00	26.82 0.11	1.63 0.02	0.004±0.01	0.215±0.00	0.345±0.00	294.57±1.00
500	287.74 0.00	8.59 0.03	0.43 0.01	0.004±0.01	0.964±0.02	0.338±0.00	284.57±1.00
<7000	120.16 0.00	26.52 0.10	1.39 0.02	0.006±0.01	0.209±0.00	0.337±0.00	284.57±1.00
500	348.73 0.00	11.25 0.04	0.55 0.01	0.009±0.01	1.161±0.02	0.333±0.00	294.57±1.00
<7000	132.55 0.00	30.21 0.12	1.78 0.02	0.008±0.01	0.221±0.00	0.340±0.00	294.57±1.00



Measured volumes are x 1E-10 cm<sup>3</sup> NTP. All errors are 2 x standard error.

# **FAR-228 Biotite (45-60 mesh)**

Run date: 1995/10/05  
Run: AS-14

Can/Pos: 141/8  
Mass: 15.0 mg

J Value: 0.002350  
± 0.000012

Volume 39Ar: 207.89 x 1E-10 cm<sup>3</sup> NTP  
Integrated Age: 0.54 ± 0.07 Ma

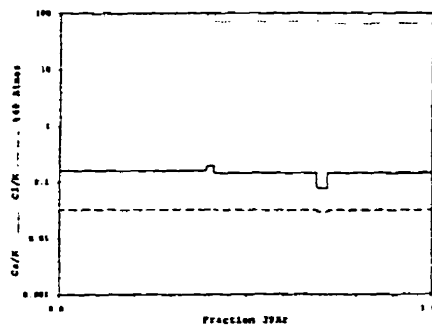
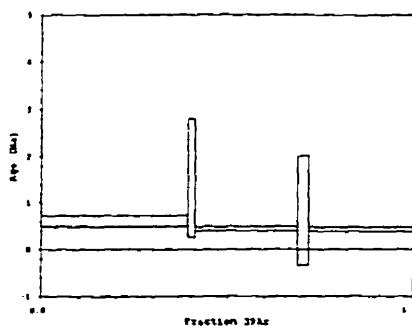
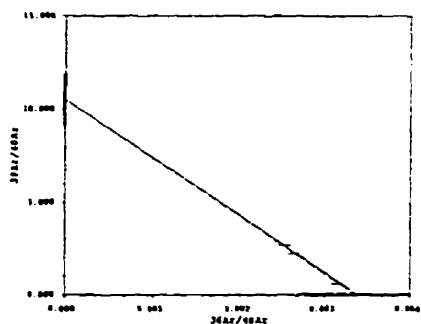
Approx. 8.32% K  
1.25% Ca

Initial 40/36: 258.00 ± 57.73 (MSWD = 1.77, isochron between 0.18 and 2.63)  
Correlation Age: 0.40 ± 0.05 Ma (100.0% of 39Ar, steps marked by >)

Plateau Age: 0.51 ± 0.06 Ma ( 95.1% of 39Ar, steps marked by <)

Power	36Ar/40Ar	39Ar/40Ar	r	Ca/K	%40Atm	%39Ar	40Ar*/39K	Age
<7000	0.00311478±0.00005668	0.572656±0.002517	0.006	0.16	89.62	38.88	0.144±0.030	0.61±0.13
750	0.00330537 0.00000000	0.065130 0.000000	0.001	0.20	97.38	1.93	0.362 0.299	1.53 1.27
<7000	0.00262852 0.00000000	2.227625 0.000000	0.014	0.15	70.10	27.80	0.105 0.010	0.44 0.04
750	0.00334021 0.00001103	0.067336 0.000146	0.001	0.08	98.40	2.92	0.197 0.277	0.83 1.17
<7000	0.00251490 0.00000000	2.669000 0.000000	0.014	0.15	65.72	28.46	0.101 0.010	0.43 0.04

Power	40Ar	39Ar	38Ar	37Ar	36Ar	Blank 40Ar	Atmos 40/36
<7000	144.62±0.00	81.37±0.35	12.69±0.11	2.322±0.03	0.460±0.01	0.101±0.00	237.67±1.00
750	62.00 0.00	4.06 0.02	0.67 0.01	0.152±0.00	0.216±0.00	0.099±0.00	287.67±1.00
<7000	28.45 0.00	58.18 0.25	3.85 0.08	1.504±0.02	0.078±0.00	0.099±0.00	237.67±1.00
750	30.58 0.00	6.13 0.03	0.93 0.01	0.095±0.00	0.316±0.01	0.099±0.00	287.67±1.00
<7000	24.73 0.00	59.56 0.25	3.14 0.08	1.551±0.02	0.065±0.00	0.098±0.00	287.67±1.00



Measured volumes are x 1E-10 cm<sup>3</sup> NTP. All errors are 2 x standard error.



# **FAR-229 Hornblende (60-100 mesh)**

Run date: 1995/10/05  
Run: AS-15 & AS-106

Can/Box: 141/9  
Mass: 31.0 mg

J Value: 0.002351  
± 0.000012

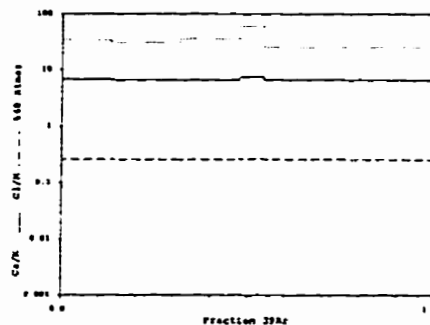
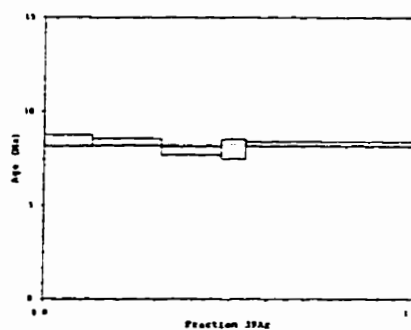
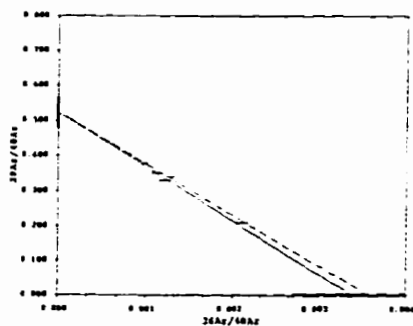
Volume 39Ar: 55.83 x 1E-10 cm<sup>3</sup> NTP  
Integrated Age: 8.24 ± 0.10 Ma

Approx. 1.08% K  
7.23% Ca

Initial 40/36: 279.92 ± 66.80 (MSWD = 7.33, isochron between 0.18 and 2.63)  
Correlation Age: 8.09 ± 0.63 Ma (100.0% of 39Ar, steps marked by >)

Power	36Ar/40Ar	39Ar/40Ar	z	Ca/K	%40Ar	%39Ar	40Ar*/39K	Age
7000	0.00119875±0.00008011	0.329803±0.001446	0.004	6.74	33.66	12.72	1.998±0.072	8.45±0.30
7000	0.00108771 0.00000000	0.350141 0.000000	0.006	6.69	30.32	18.41	1.977 0.046	8.37 0.19
7000	0.00127627 0.00000000	0.339731 0.000000	0.006	6.60	35.88	15.86	1.872 0.052	7.92 0.22
500	0.00210933 0.00004329	0.207942 0.000463	0.007	7.48	60.09	6.64	1.894 0.122	8.02 0.52
7000	0.00098796 0.00000000	0.378187 0.000000	0.009	6.64	25.70	46.37	1.954 0.027	9.27 0.12

Power	40Ar	39Ar	38Ar	37Ar	36Ar	Blank 40Ar	Atmos 40/36
7000	21.89±0.06	7.18±0.03	4.30±0.07	3.493±0.11	0.043±0.00	0.120±0.00	287.67±1.00
7000	29.83 0.00	10.37 0.04	11.25 0.10	12.185±0.16	0.052±0.00	0.117±0.00	287.67±1.00
7000	26.46 0.00	8.94 0.04	10.19 0.09	10.354±0.13	0.052±0.00	0.117±0.00	287.67±1.00
500	18.01 0.00	3.74 0.02	4.38 0.04	1.455±0.02	0.046±0.00	0.066±0.00	287.67±1.00
7000	27.47 0.00	26.05 0.11	30.12 1.06	8.991±0.12	0.098±0.00	0.090±0.00	287.67±1.00



Measured volumes are x 1E-10 cm<sup>3</sup> NTP. All errors are 2 x standard error.

# **FAR-238 Biotite (60-100 mesh)**

Run date: 1995/10/05  
 Run: AS-16 & AS-102

Can/Fos: 141/10  
 Mass: 4.0 mg

J Value: 0.002351  
 ± 0.000012

Volume 39Ar: 48.50 x 1E-10 cm<sup>3</sup> NTP  
 Integrated Age: 7.31 ± 0.20 Ma

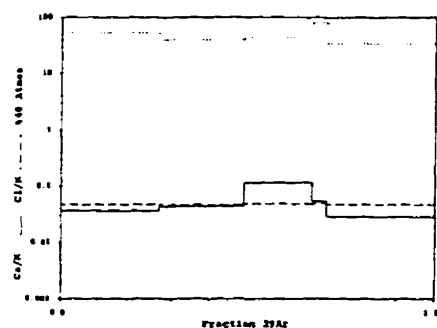
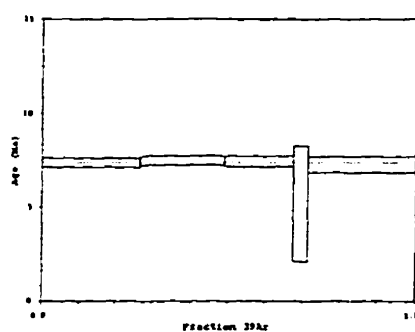
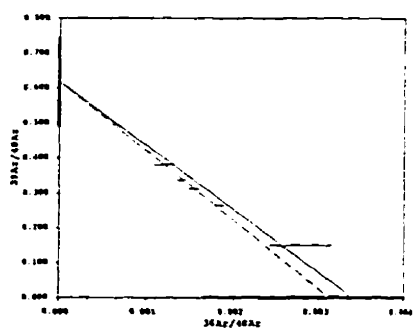
Approx. 7.27% K  
 0.37% Ca

Initial 40/36: 320.54 ± 148.60 (MSWD = 3.22, isochron between 0.18 and 2.63)  
 Correlation Age: 6.95 ± 1.38 Ma (100.0% of 39Ar, steps marked by >)

Plateau Age: 7.39 ± 0.17 Ma ( 96.2% of 39Ar, steps marked by <)

Power	36Ar/40Ar	39Ar/40Ar	ε	Ca/K	%40Ar	%39Ar	40Ar*/39K	Age
<7000	0.00183493±0.00005072	0.263350±0.001147	0.002	0.04	53.45	26.33	1.745±0.058	7.39±0.25
<7000	0.00139647 0.00000000	0.335418 0.000000	0.001	0.04	40.17	22.18	1.767 0.056	7.48 0.24
<7000	0.00152858 0.00000000	0.312944 0.000000	0.001	0.12	44.36	18.22	1.759 0.067	7.45 0.28
300	0.00276960 0.00018546	0.150138 0.000345	0.001	0.05	81.11	3.77	1.224 0.730	5.19 3.09
<7000	0.00118274 0.00000000	0.381226 0.000000	0.001	0.03	33.85	29.49	1.721 0.096	7.28 0.40

Power	40Ar	39Ar	38Ar	37Ar	36Ar	Blank 40Ar	Atmos 40/36
<7000	49.16±0.00	12.91±0.06	2.82±0.02	0.103±0.00	0.107±0.00	0.129±0.00	287.67±1.00
<7000	32.66 0.00	19.88 0.05	1.45 0.02	0.104±0.00	0.062±0.00	0.138±0.00	287.67±1.00
<7000	28.74 0.00	8.95 0.04	2.03 0.02	0.201±0.00	0.060±0.00	0.129±0.00	287.67±1.00
300	12.33 0.00	1.85 0.01	0.42 0.01	0.010±0.00	0.037±0.00	0.067±0.00	287.67±1.00
<7000	38.19 0.00	14.40 0.06	1.20 0.03	0.026±0.00	0.048±0.00	0.067±0.00	287.67±1.00



Measured volumes are x 1E-10 cm<sup>3</sup> NTP. All errors are 2 x standard error.

# **FAR-239 Sericite (60-80 mesh)**

Run date: 1995/10/23  
Run: AS-127

Can/Pos: 141/12  
Mass: 10.0 mg

J Value: 0.000353  
± 0.000012

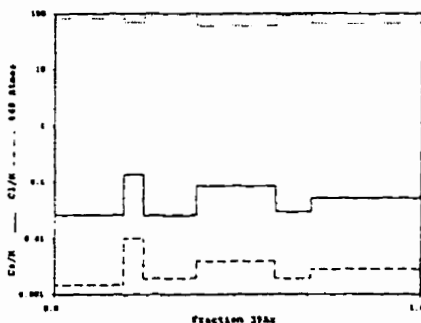
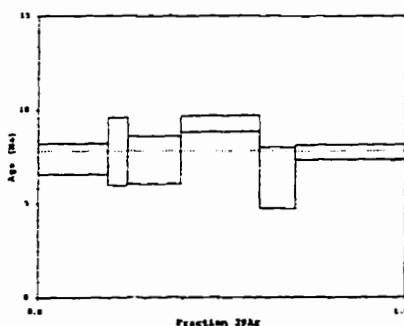
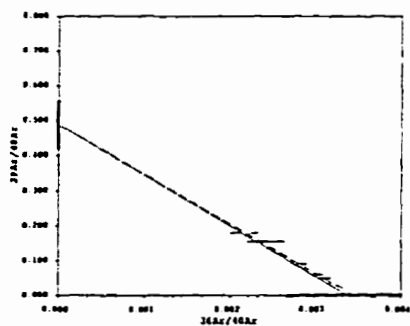
Volume 39Ar: 32.27 x 1E-10 cm3 NTP  
Integrated Age: 7.81 ± 0.36 Ma

Approx. 1.93% K  
0.10% Ca

Initial 40/36: 289.05 ± 64.67 (MSWD = 7.50, isochron between 0.29 and 2.41)  
Correlation Age: 8.68 ± 1.18 Ma (100.0% of 39Ar, steps marked by >)

Power	36Ar/40Ar	39Ar/40Ar	r	Ca/K	%40Atm	%39Ar	40Ar*/39K	Age
300	0.00285016±0.00005826	0.090425±0.000392	0.001	0.03	83.90	19.44	1.745±0.193	7.33±0.82
7000	0.00241823±0.00000000	0.155538±0.000000	0.001	0.14	70.95	5.16	1.838±0.427	7.75±1.80
100	0.00303730±0.00000000	0.059420±0.000000	0.001	0.03	89.53	14.43	1.725±0.301	7.31±1.27
7000	0.00205396±0.00000000	0.179792±0.000391	0.001	0.09	60.22	21.43	2.187±0.102	9.26±0.43
100	0.00313092±0.00000000	0.049794±0.000000	0.002	0.03	92.32	9.76	1.503±0.383	6.37±1.62
7000	0.00227919±0.00000001	0.178572±0.000000	0.001	0.05	66.94	29.78	1.829±0.091	7.75±0.39

Power	40Ar	39Ar	38Ar	37Ar	36Ar	Blank 40Ar	Atmos 40/36
300	69.70±0.00	6.32±0.03	0.17±0.00	0.017±0.00	0.210±0.00	0.072±0.00	287.67±1.00
7000	10.84±0.00	1.69±0.01	0.11±0.00	0.020±0.00	0.033±0.00	0.071±0.00	287.67±1.00
100	78.66±0.00	4.70±0.02	0.16±0.00	0.015±0.00	0.251±0.00	0.072±0.00	287.67±1.00
7000	38.24±0.00	6.97±0.03	0.24±0.00	0.037±0.00	0.088±0.00	0.072±0.00	287.67±1.00
100	63.49±0.00	3.18±0.01	0.12±0.00	0.014±0.00	0.210±0.00	0.071±0.00	287.67±1.00
7000	54.29±0.00	9.68±0.04	0.29±0.00	0.033±0.00	0.133±0.00	0.073±0.00	287.67±1.00



Measured volumes are x 1E-10 cm3 NTP. All errors are 2 x standard error.

# **FAR-239 Whole Rock (60-80 mesh)**

Run date: 1995/10/23  
Run: AS-202

Can/Pos: 140/4  
Mass: 100.0 mg

J Value: 0.002677  
= 0.000014

Volume 39Ar: 150.01 x 1E-10 cm3 NTP  
Integrated Age: 7.23 ± 0.30 Ma

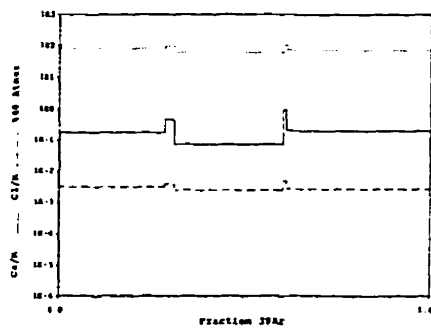
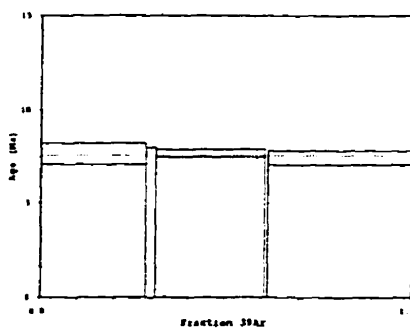
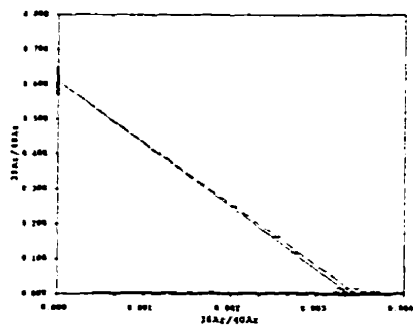
Approx. 0.79% K  
0.13% Ca

Initial 40/36: 289.62 ± 31.70 (MSWD = 0.83, isochron between 0.29 and 2.41)  
Correlation Age: 7.91 ± 0.48 Ma (100.0% of 39Ar, steps marked by >)

Plateau Age: 7.55 ± 0.24 Ma ( 96.48 of 39Ar, steps marked by <)

Power	36Ar/40Ar	39Ar/40Ar	r	Ca/K	%40Ar	%39Ar	40Ar*/39K	Age
100	0.00340725±0.00301649	0.005325±0.007731	0.998	0.00	100.66	0.06	-1.283±6.510	-6.21±31.55
<7000	0.00274677 0.00000000	0.118942 0.000000	0.022	0.17	80.74	28.33	1.586 0.116	7.64 0.56
300	0.00334749 0.00000000	0.016760 0.000000	0.911	0.44	98.84	2.61	0.648 1.002	3.13 4.83
<7000	0.00203987 0.00001798	0.250579 0.000503	0.007	0.07	59.61	29.17	1.587 0.043	7.65 0.21
300	0.00346970 0.00000000	0.008598 0.000000	0.975	0.92	102.49	0.90	-2.938 2.041	-14.24 9.94
<7000	0.00252828 0.00000001	0.164786 0.000000	0.010	0.20	74.17	38.94	1.537 0.077	7.41 0.37

Power	40Ar	39Ar	38Ar	37Ar	36Ar	Blank 40Ar	Atmos 40/36
100	15.83±0.11	0.09±0.00	0.02±0.00	0.007±0.00	0.061±0.00	0.224±0.00	284.57±1.00
<7000	359.24 0.00	42.81 0.17	1.38 0.01	0.017±0.00	1.024±0.00	0.226±0.00	284.57±1.00
300	233.93 0.00	3.95 0.02	0.28 0.00	0.010±0.00	0.818±0.00	0.230±0.00	284.57±1.00
<7000	176.67 0.00	44.09 0.17	1.16 0.01	0.012±0.00	0.376±0.00	0.231±0.00	284.57±1.00
300	157.48 0.00	1.37 0.01	0.16 0.00	0.010±0.00	0.572±0.00	0.233±0.00	284.57±1.00
<7000	357.10 0.00	58.85 0.23	1.48 0.01	0.022±0.00	0.938±0.00	0.226±0.00	284.57±1.00



Measured volumes are x 1E-10 cm3 NTP. All errors are 2 x standard error.

# **FAR-244 Hornblende (60-100 mesh)**

Run date: 1995/10/06  
Run: AS-20 & AS-108

Can/Pos: 141/13  
Mass: 25.0 mg

J Value: 0.002353  
± 0.000010

Volume 39Ar: 43.49 x 1E-10 cm<sup>3</sup> NTP  
Integrated Age: 6.72 ± 0.24 Ma

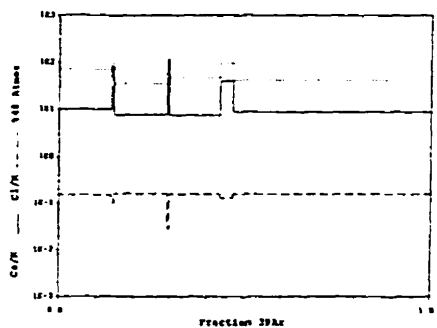
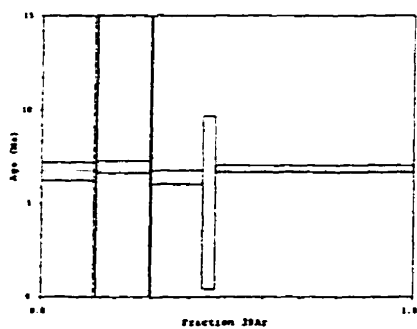
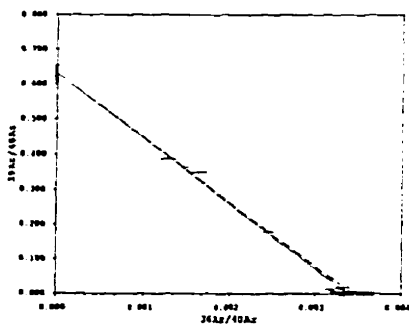
Approx. 1.04% K  
10.79% Ca

Initial 40/36: 290.73 ± 19.86 (MSWD = 1.27, isochron between 0.37 and 2.26)  
Correlation Age: 6.72 ± 0.23 Ma (100.0% of 39Ar, steps marked by >)

Plateau Age: 6.78 ± 0.15 Ma ( 95.68 of 39Ar, steps marked by <)

Power	36Ar/40Ar	39Ar/40Ar	r	Ca/K	%40Atm	%39Ar	40Ar*/39K	Age
<7000	0.00244761±0.00007117	0.176830±0.000774	0.017	10.01	71.40	14.00	1.588±0.116	6.73± 0.49
500	0.00328278 0.00000000	0.012125 0.000000	0.790	82.07	96.94	0.56	2.485 2.603	10.52 10.98
<7000	0.00125843 0.00000000	0.388523 0.000000	0.004	7.65	35.65	14.25	1.642 0.075	6.95 0.32
500	0.00338715 0.00011785	0.007980 0.000268	0.873	118.48	100.05	0.36	-0.109 4.166	-0.46 17.69
<7000	0.00161905 0.00000000	0.349786 0.000000	0.004	7.40	46.31	13.65	1.516 0.085	6.42 0.36
400	0.00331227 0.00000002	0.018474 0.000000	0.663	39.69	97.73	3.47	1.190 1.091	5.05 4.62
<7000	0.00145694 0.00000000	0.363773 0.000000	0.009	9.69	40.63	53.73	1.615 0.045	6.84 0.19

Power	40Ar	39Ar	38Ar	37Ar	36Ar	Blank 40Ar	Atmos 40/36
<7000	34.67±0.00	6.17±0.03	4.12±0.04	10.62±0.14	0.105±0.00	0.111±0.00	287.67±1.00
500	19.53 0.00	0.29 0.00	0.14 0.00	3.30±0.04	0.079±0.00	0.112±0.00	287.67±1.00
<7000	16.28 0.00	4.28 0.03	4.49 0.04	8.27±0.11	0.038±0.00	0.114±0.00	287.67±1.00
500	18.72 0.00	0.20 0.00	0.05 0.00	3.06±0.04	0.077±0.00	0.111±0.00	287.67±1.00
<7000	17.28 0.00	6.01 0.03	4.23 0.04	7.65±0.10	0.045±0.00	0.110±0.00	287.67±1.00
400	89.61 0.00	1.53 0.01	0.94 0.01	3.09±0.04	0.286±0.01	0.097±0.00	287.67±1.00
<7000	65.12 0.00	23.52 0.10	16.68 0.14	10.58±0.14	0.129±0.00	0.112±0.00	287.67±1.00



Measured volumes are x 1E-10 cm<sup>3</sup> NTP. All errors are 2 x standard error.

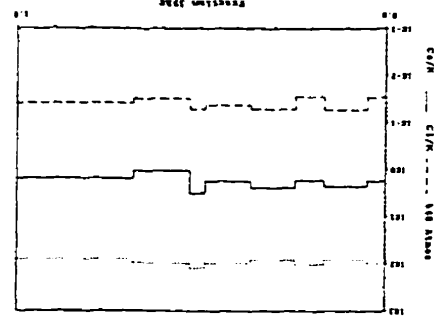
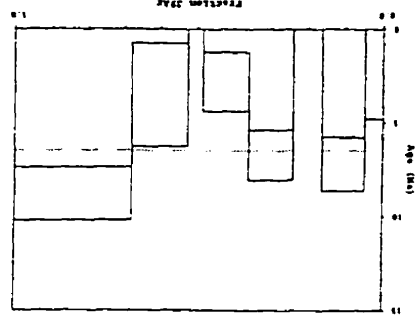
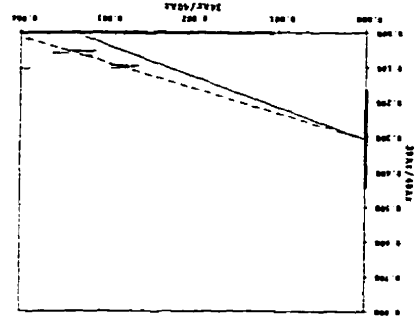
FAR-244 Biotite (60-100 mesh)

Run date: 1995/10/06  
Run: AS-21 & AS-103  
Can/Pos: 141/14  
Mass: 1.1 mg  
J Value: 0.002355  
± 0.000010

Volume 39Ar: 15.51 x 1E-10 cm<sup>3</sup> NTP  
Integrated Age: 4.93 ± 0.77 Ma  
Initial 40/36: 239.08 ± 178.20 (MSWD = 17.67, isochron between 0.42 and 2.15)  
Correlation Age: 13.91 ± 6.23 Ma (100.0% of 39Ar, steps marked by >)  
Plateau Age: 6.48 ± 0.85 Ma (84.3% of 39Ar, steps marked by <)

Power	36Ar/40Ar	39Ar/40Ar	r	Ca/K	40Ar/39Ar	40Ar/39Ar	Age
300	0.00332241±0.00013957	0.052743±0.000255	0.001	1.74	97.94	4.39	1.43±1.33
<500	0.00284587 0.00000000	0.094371 0.000000	0.002	2.28	83.69	11.19	7.13 1.42
500	0.00352912 0.00000000	0.060482 0.000000	0.001	1.70	104.00	7.51	-2.93 2.24
<7000	0.00283862 0.00005351	0.102331 0.000229	0.002	2.42	83.44	11.49	6.71 1.31
<750	0.00323756 0.00000000	0.065750 0.000000	0.002	1.75	95.36	12.04	2.82 1.57
7000	0.00421520 0.00000000	0.102749 0.000000	0.001	3.19	123.95	3.76	-10.15 4.21
<300	0.00323186 0.00000000	0.054938 0.000000	0.002	1.05	95.23	15.27	3.52 2.76
<7000	0.00270330 0.00000000	0.097671 0.000000	0.001	1.52	79.44	34.34	8.79 1.41

Power	40Ar	39Ar	38Ar	37Ar	36Ar	Blank 40Ar	Atmos 40/36
300	13.05±0.05	0.74±0.00	0.13±0.00	0.22±0.00	0.058±0.00	0.121±0.00	287.67±1.00
<7000	18.56 0.00	1.40 0.01	0.46 0.00	0.70±0.01	0.068±0.00	0.122±0.00	287.67±1.00
500	19.42 0.00	1.22 0.01	0.29 0.00	0.36±0.01	0.044±0.00	0.122±0.00	287.67±1.00
<7000	17.59 0.00	1.85 0.01	0.46 0.00	0.76±0.01	0.065±0.00	0.122±0.00	287.67±1.00
<750	28.58 0.00	1.93 0.01	0.43 0.00	0.58±0.01	0.108±0.00	0.122±0.00	287.67±1.00
7000	5.82 0.00	0.64 0.00	0.17 0.00	0.34±0.00	0.038±0.00	0.122±0.00	287.67±1.00
<300	43.26 0.00	2.39 0.01	0.39 0.01	0.137±0.00	0.146±0.01	0.063±0.00	287.67±1.00
<7000	54.79 0.00	5.35 0.02	1.04 0.01	0.435±0.01	0.156±0.01	0.081±0.00	287.67±1.00



Measured volumes are x 1E-10 cm<sup>3</sup> NTP. All errors are 2 x standard error.

# **FAR-254 Hornblende (60-100 mesh)**

Run date: 1995/10/06  
Run: AS-22 & AS-109

Can/Pos: 141/15  
Mass: 32.0 mg

J Value: 0.002355  
± 0.000010

Volume 39Ar: 56.24 x 1E-10 cm<sup>3</sup> NTP  
Integrated Age: 8.10 ± 0.13 Ma

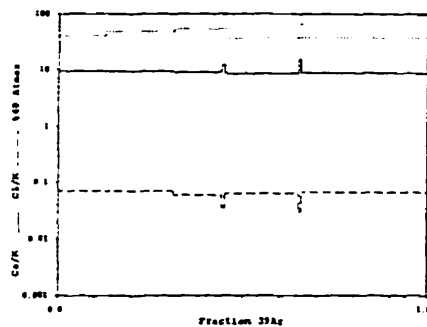
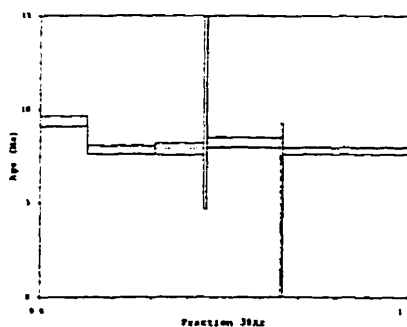
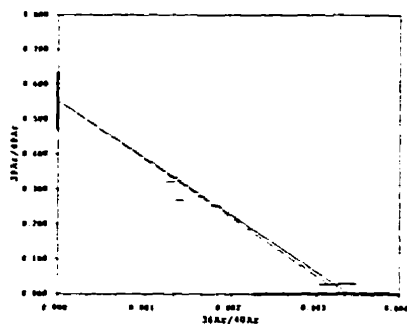
Approx. 1.05% K  
9.61% Ca

Initial 40/36: 303.25 ± 94.31 (MSWD = 24.07, isochron between 0.37 and 2.26)  
Correlation Age: 7.68 ± 1.10 Ma (100.0% of 39Ar, steps marked by >)

Plateau Age: 7.94 ± 0.12 Ma ( 85.8% of 39Ar, steps marked by <)

Power	36Ar/40Ar	39Ar/40Ar	z	Ca/K	40Ar	439Ar	40Ar*/39K	Age
7000	0.00139216±0.00005986	0.267189±0.001179	0.012	3.52	40.39	12.65	2.214±0.065	9.38±0.27
<7000	0.00164175 0.00000000	0.279619 0.000000	0.013	3.44	47.65	17.90	1.852 0.055	7.85 0.23
<7000	0.00180742 0.00000000	0.251180 0.000000	0.012	3.04	52.63	13.00	1.864 0.071	7.90 0.30
300	0.00314593 0.00006815	0.029125 0.000095	0.063	12.19	92.82	0.81	2.513 1.413	10.65 5.97
<7000	0.00129256 0.00000000	0.322363 0.000000	0.008	3.71	36.76	19.81	1.946 0.060	8.25 0.25
300	0.00331635 0.00000004	0.029638 0.000000	0.074	15.29	97.85	0.75	0.685 1.508	2.91 6.40
<7000	0.00132080 0.00000000	0.334675 0.000000	0.011	3.98	37.78	35.08	1.843 0.042	7.81 0.18

Power	40Ar	39Ar	38Ar	37Ar	36Ar	Blank 40Ar	Atmos 40/36
7000	26.96±0.00	7.25±0.03	1.40±0.02	11.77±0.15	0.067±0.00	0.128±0.00	287.67±1.00
<7000	36.43 0.00	10.22 0.04	3.30 0.03	16.507±0.21	0.394±0.00	0.129±0.00	287.67±1.00
<7000	29.46 0.00	7.45 0.03	1.07 0.02	11.491±0.15	0.084±0.00	0.132±0.00	287.67±1.00
300	16.23 0.00	0.47 0.00	0.05 0.00	0.236±0.00	0.058±0.00	0.084±0.00	287.67±1.00
<7000	35.00 0.00	11.22 0.05	1.31 0.03	5.055±0.06	0.064±0.00	0.085±0.00	287.67±1.00
300	14.30 0.00	0.43 0.00	0.07 0.00	0.343±0.00	0.054±0.00	0.085±0.00	287.67±1.00
<7000	59.67 0.00	19.86 0.08	4.27 0.05	3.207±0.12	0.110±0.00	0.086±0.00	287.67±1.00



Measured volumes are x 1E-10 cm<sup>3</sup> NTP. All errors are 2 x standard error.

# **FAR-262 Hornblende (45-80 mesh)**

Run date: 1995/10/06  
Run: AS-25 & AS-116

Can/Pos: 141/16  
Mass: 45.0 mg

J Value: 0.002356  
= 0.000010

Volume 39Ar: 77.24 x 1E-10 cm<sup>3</sup> NTP  
Integrated Age: 7.93 ± 0.22 Ma

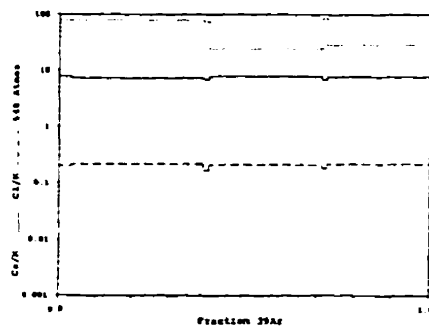
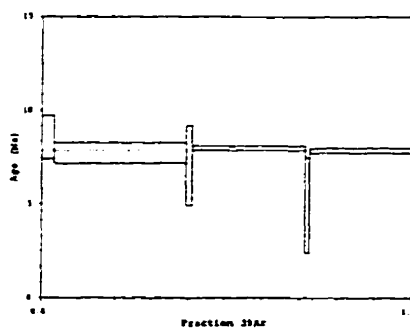
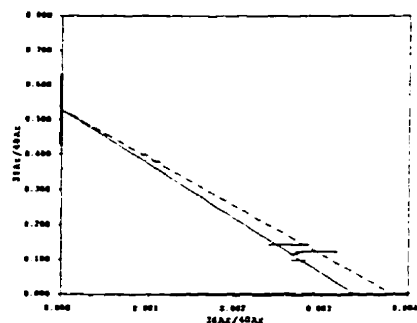
Approx. 1.03% K  
7.95% Ca

Initial 40/36: 261.47 ± 174.49 (MSWD = 51.38, isochron between 0.29 and 2.41)  
Correlation Age: 8.03 ± 1.52 Ma (100.0% of 39Ar, steps marked by >)

Plateau Age: 7.88 ± 0.22 Ma ( 97.38 of 39Ar, steps marked by <)

Power	36Ar/40Ar	39Ar/40Ar	z	Ca/K	%40Ar	%39Ar	40Ar*/39K	Age
< 500	0.00271607±0.00009252	0.099299±0.000440	0.014	8.04	79.60	3.27	2.022±0.274	8.57±1.16
<7000	0.00267021 0.00000000	0.118064 0.000000	0.019	7.35	78.09	35.91	1.823 0.128	7.73 0.54
400	0.00260157 0.00000000	0.143332 0.000000	0.004	7.07	75.68	1.42	1.665 0.503	7.06 2.13
<7000	0.00093384 0.00002155	0.398735 0.000875	0.009	8.01	24.55	30.16	1.882 0.032	7.98 0.13
400	0.00291815 0.00000000	0.124234 0.000000	0.004	6.87	85.08	1.28	1.166 0.602	4.95 2.55
<7000	0.00107889 0.00000001	0.381077 0.000000	0.003	7.83	28.85	27.96	1.855 0.035	7.87 0.15

Power	40Ar	39Ar	38Ar	37Ar	36Ar	Blank 40Ar	Atmos 40/36
< 500	25.59±0.00	2.56±0.01	2.27±0.02	3.147±0.04	0.078±0.00	0.089±0.00	287.67±1.00
<7000	235.57 0.00	27.93 0.12	26.69 0.23	31.492±0.40	0.676±0.01	0.099±0.00	287.67±1.00
400	7.79 0.00	1.12 0.00	0.93 0.01	0.406±0.01	0.029±0.00	0.116±0.00	287.67±1.00
<7000	59.34 0.00	23.45 0.10	22.02 0.19	9.543±0.10	0.030±0.00	0.118±0.00	287.67±1.00
400	8.07 0.00	1.01 0.00	0.82 0.01	0.356±0.00	0.032±0.00	0.116±0.00	287.67±1.00
<7000	57.54 0.00	21.74 0.09	20.48 0.18	9.650±0.11	0.094±0.00	0.117±0.00	287.67±1.00



Measured volumes are x 1E-10 cm<sup>3</sup> NTP. All errors are 1 x standard error.



# **FAR-262 Biotite (45-80 mesh)**

Run date: 1995/10/12 Can/Pos: 141/17 J Value: 0.001356  
Run: AS-26 & AS-128 Mass: 5.0 mg ± 0.000010

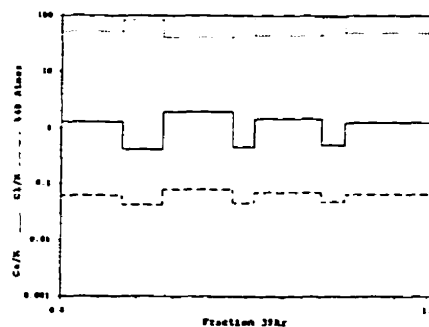
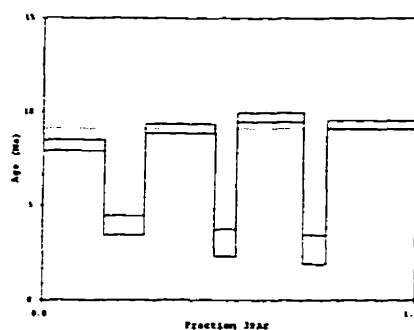
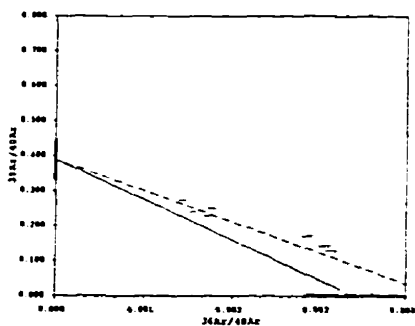
Volume 39Ar: 82.53 x 1E-10 cm<sup>3</sup> NTP Approx. 8.23% K  
Integrated Age: 7.83 ± 0.14 Ma 10.25% Ca

Initial 40/36: 228.74 ± 79.73 (MSWD = 62.56, isochron between 0.17 and 2.26)  
Correlation Age: 10.91 ± 1.54 Ma (100.0% of 39Ar, steps marked by >)

Plateau Age: 9.14 ± 0.13 Ma ( 77.3% of 39Ar, steps marked by <)

Power	36Ar/40Ar	39Ar/40Ar	r	Ca/K	40Ar	39Ar	40Ar*/39K	Age
<7000	0.00175820±0.00005669	0.248664±0.001081	0.002	1.29	51.16	16.07	1.943±0.068	8.24±0.29
300	0.00285439 0.00000000	0.163729 0.000000	0.001	0.42	83.63	10.74	0.929 0.121	3.95 0.52
<7000	0.00140744 0.00000000	0.272984 0.000000	0.002	1.92	40.76	19.00	2.153 0.056	9.13 0.24
300	0.00304644 0.00001992	0.143030 0.000310	0.001	0.45	89.28	5.82	0.712 0.166	3.03 0.71
<7000	0.00153484 0.00000000	0.240818 0.000000	0.002	1.49	44.36	18.08	2.292 0.057	9.72 0.24
300	0.00311953 0.00000002	0.127942 0.000000	0.001	0.51	91.49	6.13	0.627 0.182	2.66 0.77
<7000	0.00170451 0.00000000	0.227858 0.000000	0.002	1.27	49.41	24.17	2.199 0.055	9.32 0.23

Power	40Ar	39Ar	38Ar	37Ar	36Ar	Blank 40Ar	Atmos 40/36
<7000	53.99±0.06	13.37±0.06	1.92±0.03	2.663±0.03	0.106±0.00	0.117±0.00	287.67±1.00
300	52.70 0.00	8.94 0.04	1.83 0.02	0.588±0.01	0.160±0.00	0.116±0.00	287.67±1.00
<7000	58.16 0.00	15.80 0.07	5.70 0.05	4.667±0.06	0.094±0.00	0.117±0.00	287.67±1.00
300	33.87 0.00	4.85 0.02	1.07 0.01	0.113±0.00	0.111±0.00	0.100±0.00	287.67±1.00
<7000	62.65 0.00	15.03 0.06	4.91 0.04	1.060±0.01	0.107±0.00	0.112±0.00	287.67±1.00
300	39.86 0.00	5.11 0.02	1.18 0.01	0.132±0.00	0.134±0.00	0.113±0.00	287.67±1.00
<7000	88.45 0.00	20.08 0.09	6.09 0.05	1.207±0.02	0.164±0.00	0.120±0.00	287.67±1.00



Measured volumes are x 1E-10 cm<sup>3</sup> NTP. All errors are 2 x standard error.

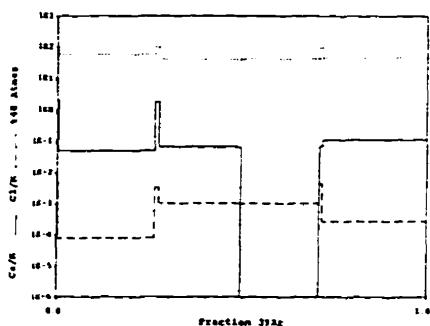
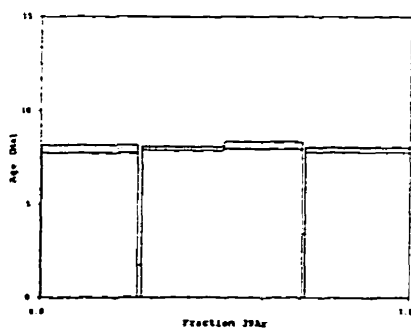
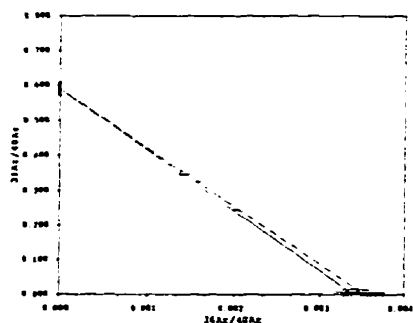
# **FAR-266 Whole Rock (45-60 mesh)**

Run date: 1996/10/24 Can/Pas: 140/6 J Value: 0.002691  
Run: AS-203 Mass: 100.0 mg ± 0.000016

Volume 39Ar: 290.84 x 1E-10 cm<sup>3</sup> NTP  
Integrated Age: 7.66 ± 0.15 Ma Approx. 0.76% K  
Initial 40/36: 264.43 ± 19.69 (MSWD = 0.87, isochron between 0.37 and 2.26)  
Correlation Age: 8.22 ± 0.23 Ma (100.0% of 39Ar, steps marked by >)  
Plateau Age: 8.01 ± 0.10 Ma ( 97.4% of 39Ar, steps marked by <)

Power	36Ar/40Ar	39Ar/40Ar	r	Cs/K	40Ar <sub>atm</sub>	439Ar	40Ar*/39K	Age
300	0.00348218±0.00031470	0.007123±0.000734	0.980	2.08	102.86	0.29	-4.065±2.506	-19.84±12.30
<7000	0.00202171 0.00000000	0.245019 0.000000	0.009	0.05	59.14	25.33	1.643 0.043	7.96 0.21
400	0.00342360 0.00000000	0.015440 0.000000	0.915	1.83	101.10	1.35	-0.753 1.105	-3.66 5.38
<7000	0.00139649 0.00001344	0.357153 0.000725	0.009	0.07	40.37	21.86	1.653 0.023	8.01 0.11
<7000	0.00141453 0.00000000	0.345647 0.000000	0.111	0.00	41.22	21.43	1.684 0.036	8.15 0.19
400	0.00341297 0.00000005	0.012602 0.000000	0.946	0.07	100.79	0.94	-0.671 1.379	-3.26 6.71
<7000	0.00158269 0.00000000	0.324790 0.000000	0.305	0.11	46.14	28.80	1.619 0.027	7.94 0.13

Power	40Ar	39Ar	38Ar	37Ar	36Ar	Blank 40Ar	Atmos 40/36
300	119.60±0.00	0.86±0.01	0.11±0.00	0.010±0.00	0.437±0.01	0.231±0.00	284.57±1.00
<7000	303.98 0.00	74.23 0.29	1.20 0.01	0.015±0.01	0.640±0.01	0.215±0.00	284.57±1.00
400	153.75 0.00	3.95 0.02	0.28 0.00	0.015±0.00	0.907±0.01	0.126±0.00	284.57±1.00
<7000	180.90 0.00	64.07 0.25	0.96 0.01	0.015±0.01	0.265±0.00	0.201±0.00	284.57±1.00
<7000	182.92 0.00	62.78 0.25	0.85 0.01	-0.035±0.04	0.266±0.01	0.027±0.00	284.57±1.00
400	216.35 0.00	2.75 0.01	0.24 0.00	0.011±0.00	0.775±0.01	0.161±0.00	284.57±1.00
<7000	261.59 0.00	84.39 0.33	1.38 0.01	0.022±0.00	0.435±0.01	0.161±0.00	284.57±1.00



Measured volumes are x 1E-10 cm<sup>3</sup> NTP. All errors are 2 x standard error.

# **FAR-266 Sericite (45-60 mesh)**

Run date: 1995/12/15  
Run: AS-125

Can/Pcs: 141/19  
Mass: 5.0 mg

J Value: 0.002357  
± 0.000010

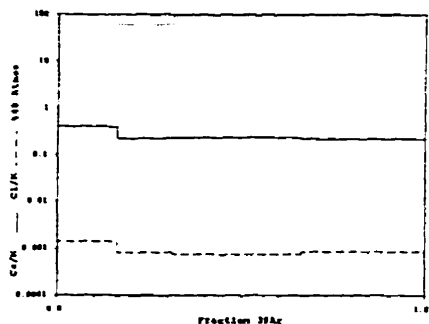
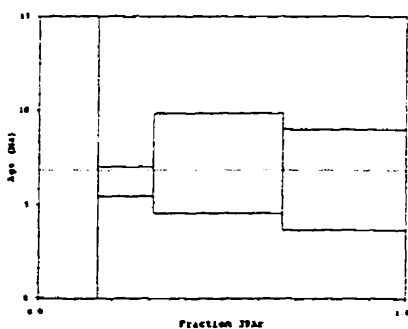
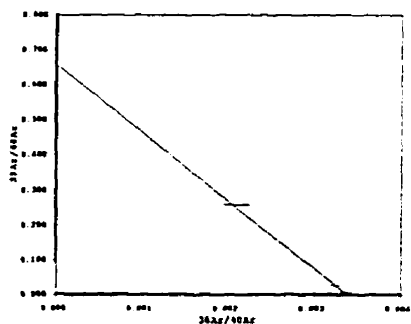
Volume 39Ar: 25.06 x 1E-10 cm<sup>3</sup> NTP  
Integrated Age: 6.82 ± 2.01 Ma

Approx. 3.00% K  
0.76% Ca

Initial 40/36: 296.15 ± 362.07 (MSWD = 0.29, isochron between 0.00 and 3.00)  
Correlation Age: 6.45 ± 5.49 Ma (100.0% of 39Ar, steps marked by >)

Power	36Ar/40Ar	39Ar/40Ar	ε	Ca/K	%40Ar	%39Ar	40Ar*/39K	Age
400	0.00331402±0.00005907	0.008348±0.000037	0.008	0.40	98.49	15.96	1.773±2.129	7.52±9.02
7000	0.00209240±0.00000000	0.259569±0.000000	0.001	0.22	61.16	14.63	1.471±0.184	6.24±0.78
7000	0.00322381±0.00000000	0.027826±0.000000	0.000	0.23	95.15	34.84	1.702±0.622	7.22±2.64
7000	0.00324320±0.00002894	0.027907±0.000060	0.000	0.22	95.72	34.57	1.492±0.625	6.33±2.65

Power	40Ar	39Ar	38Ar	37Ar	36Ar	Blank 40Ar	Atmos 40/36
400	479.44±0.00	4.05±0.02	0.40±0.00	0.094±0.00	1.652±0.03	0.102±0.00	297.67±1.00
7000	14.38±0.00	3.72±0.02	0.08±0.00	0.055±0.00	0.042±0.00	0.105±0.00	297.67±1.00
7000	314.19±0.00	8.81±0.04	0.36±0.00	0.116±0.00	1.051±0.02	0.103±0.00	297.67±1.00
7000	310.84±0.00	8.74±0.04	0.36±0.00	0.107±0.00	1.046±0.02	0.105±0.00	297.67±1.00



Measured volumes are x 1E-10 cm<sup>3</sup> NTP. All errors are 2 x standard error.

# **FAR-271 Hornblende (45-80 mesh)**

Run date: 1995/10/06 Can/Pos: 141/20 J Value: 0.002357  
Run: AS-23 & AS-115 Mass: 45.0 mg ± 0.000010

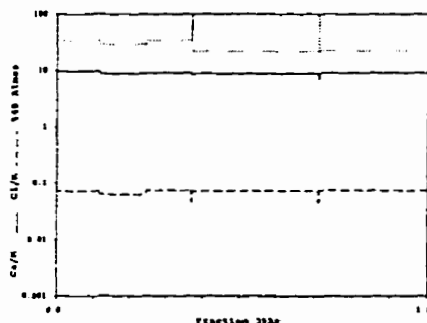
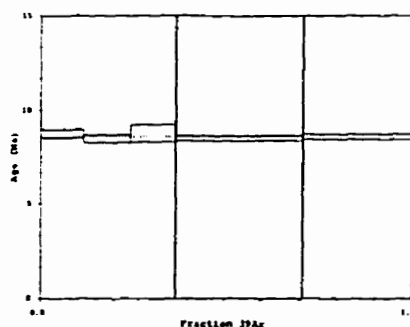
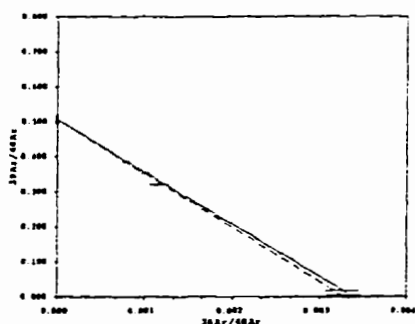
Volume 39Ar: 81.85 x 1E-10 cm<sup>3</sup> NTP Approx. 1.09% K  
Integrated Age: 8.60 ± 0.11 Ma 9.82% Ca

Initial 40/36: 304.86 ± 17.03 (MSWD = 1.02, isochron between 0.37 and 2.26)  
Correlation Age: 8.37 ± 0.15 Ma (100.0% of 39Ar, steps marked by >)

Plateau Age: 8.59 ± 0.10 Ma ( 99.48 of 39Ar, steps marked by <)

Power	36Ar/40Ar	39Ar/40Ar	z	Ca/K	%40Ar	%39Ar	40Ar*/39K	Age
<7000	0.00116275±0.00005754	0.320578±0.001416	0.012	9.96	33.55	11.53	2.059±0.052	8.73±0.22
<7000	0.00100412 0.00000000	0.352915 0.000000	0.008	8.76	28.91	12.46	2.002 0.048	8.49 0.20
<7000	0.00116389 0.00000000	0.318929 0.000000	0.005	9.03	33.56	12.25	2.069 0.110	8.78 0.47
400	0.00323296 0.00008327	0.016521 0.000099	0.090	8.42	35.44	0.27	2.717 3.138	11.52 13.26
<7000	0.00078502 0.00000000	0.386941 0.000000	0.011	8.91	21.39	33.52	2.007 0.033	8.51 0.14
400	0.00326765 0.00000004	0.017101 0.000000	0.076	7.01	96.47	0.28	2.026 1.025	8.59 12.80
<7000	0.00078726 0.00000000	0.383609 0.000000	0.011	9.02	22.03	29.69	2.023 0.033	8.58 0.14

Power	40Ar	39Ar	38Ar	37Ar	36Ar	Blank 40Ar	Atmos 40/36
<7000	29.86±0.00	9.61±0.04	3.17±0.03	16.307±0.21	0.071±0.00	0.145±0.00	287.67±1.00
<7000	29.38 0.00	10.37 0.04	3.00 0.03	15.513±0.20	0.065±0.00	0.144±0.00	287.67±1.00
<7000	31.33 0.00	10.10 0.04	3.36 0.03	14.020±0.19	0.054±0.00	0.073±0.00	287.67±1.00
400	13.57 0.00	0.23 0.00	0.06 0.01	0.105±0.00	0.051±0.00	0.079±0.00	287.67±1.00
<7000	71.91 0.00	27.61 0.12	8.95 0.08	12.514±0.16	0.098±0.00	0.087±0.00	287.67±1.00
400	13.60 0.00	0.24 0.00	0.06 0.01	0.092±0.00	0.051±0.00	0.077±0.00	287.67±1.00
<7000	64.23 0.00	24.45 0.10	8.19 0.07	11.213±0.14	0.088±0.00	0.078±0.00	287.67±1.00



Measured volumes are x 1E-10 cm<sup>3</sup> NTP. All errors are 2 x standard error.

# **FAR-284 Hornblende (45-60 mesh)**

Run date: 1995/10/05  
Run: AS-17 & AS-136

Can/Pos: 141/21  
Mass: 50.0 mg

J Value: 0.002358  
± 0.000010

Volume 39Ar: 93.70 x 1E-10 cm3 NTP  
Integrated Age: 6.70 ± 0.09 Ma

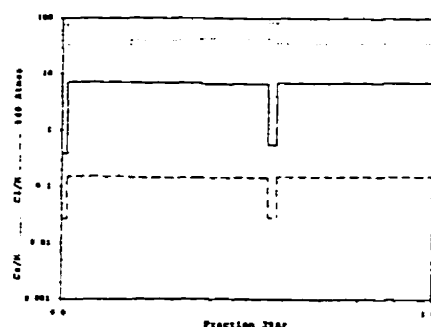
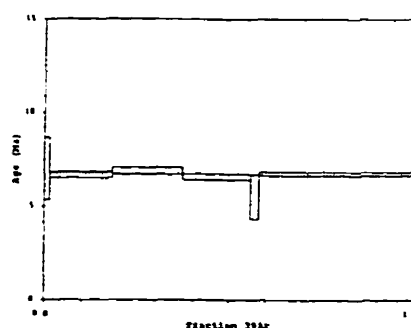
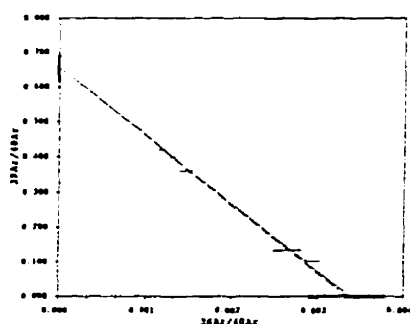
Approx. 1.00% K  
6.68% Ca

Initial 40/36: 299.51 ± 39.62 (MSWD = 3.41, isochron between 0.29 and 2.41)  
Correlation Age: 6.48 ± 0.35 Ma (100.0% of 39Ar, steps marked by >)

Plateau Age: 6.72 ± 0.08 Ma ( 96.5% of 39Ar, steps marked by <)

Power	36Ar/40Ar	39Ar/40Ar	z	Ca/K	40Ar <sub>atm</sub>	43Ar	40Ar <sub>ex</sub> /39K	Age
500	0.00264321±0.00017467	0.132944±0.000608	0.000	0.39	77.62	1.26	1.651±0.339	7.01±1.65
<7000	0.00117509 0.00000000	0.421131 0.000000	0.007	7.10	33.16	16.84	1.573 0.035	6.68 0.15
<7000	0.00143482 0.00000000	0.360446 0.000000	0.006	6.91	40.99	18.49	1.620 0.045	6.88 0.19
<7000	0.00152156 0.00002238	0.361788 0.000792	0.008	6.68	43.40	18.52	1.546 0.036	6.57 0.15
400	0.00293200 0.00000000	0.103505 0.000000	0.001	0.57	86.17	2.23	1.300 0.277	5.52 1.18
<7000	0.00130923 0.00000001	0.399279 0.000000	0.009	6.94	36.10	42.68	1.585 0.028	6.73 0.12

Power	40Ar	39Ar	38Ar	37Ar	36Ar	Blank 40Ar	Atmos 40/36
500	6.07±0.00	1.11±0.00	0.17±0.00	0.09±0.00	0.03±0.00	0.127±0.00	297.67±1.00
<7000	34.03 0.00	14.23 0.00	2.56 0.00	17.68±0.23	0.069±0.00	0.127±0.00	297.67±1.00
<7000	43.64 0.00	15.65 0.07	10.25 0.03	18.900±0.24	0.098±0.00	0.170±0.00	297.67±1.00
<7000	43.53 0.00	15.64 0.07	10.13 0.03	15.41±0.20	0.093±0.00	0.143±0.00	297.67±1.00
400	16.24 0.00	1.91 0.01	0.28 0.00	0.068±0.00	0.069±0.00	0.149±0.00	297.67±1.00
<7000	30.86 0.00	15.97 0.15	24.45 0.21	11.478±0.15	0.171±0.00	0.153±0.00	297.67±1.00



Measured volumes are x 1E-10 cm3 NTP. All errors are 2 x standard error.

# **FAR-285 Hornblende (60-80 mesh)**

Run date: 1995/10/05 Can/Pcs: 141/23 J Value: 0.002359  
Run: AS-19 & AS-114 Mass: 35.0 mg ± 0.000010

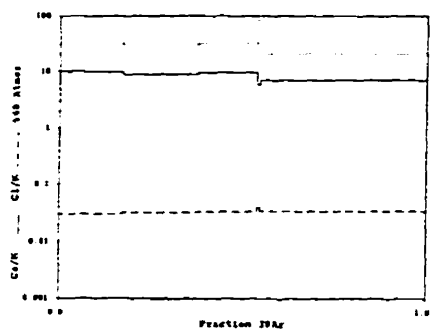
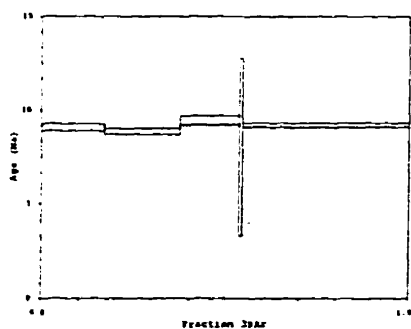
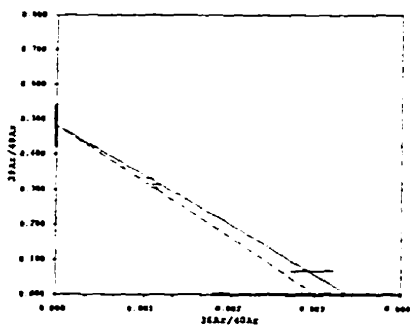
Volume 39Ar: 61.85 x 1E-10 cm3 NTP Approx. 1.06% K  
Integrated Age: 9.13 ± 0.10 Ma 8.91% Ca

Initial 40/36: 333.94 ± 133.42 (MSWD = 13.68, isochron between 0.18 and 2.63)  
Correlation Age: 8.80 ± 1.05 Ma (100.0% of 39Ar, steps marked by >)

Plateau Age: 9.14 ± 0.09 Ma ( 99.0% of 39Ar, steps marked by <)

Power	36Ar/40Ar	39Ar/40Ar	z	Ca/K	%40Ar	%39Ar	40Ar*/39K	Age
<7000	0.00112992±0.00005027	0.311737±0.001377	0.014	10.02	32.82	16.65	2.141±0.046	9.09±0.19
<7000	0.00106396 0.00000000	0.329834 0.000000	0.012	9.12	30.86	20.10	2.093 0.039	8.85 0.17
<7000	0.00110663 0.00000000	0.302610 0.000000	0.013	9.82	32.15	15.82	2.229 0.049	9.46 0.21
400	0.00294548 0.00013061	0.069991 0.000191	0.007	6.03	86.70	3.96	1.894 1.119	8.04 4.74
<7000	0.00074219 0.00000000	0.362578 0.000000	0.009	7.20	21.22	46.48	2.164 0.029	9.19 0.12

Power	40Ar	39Ar	38Ar	37Ar	36Ar	Blank 40Ar	Atmos 40/36
<7000	33.49±0.00	10.49±0.04	1.57±0.01	12.19±0.23	0.07±0.00	0.148±0.00	287.67±1.00
<7000	18.22 0.00	12.43 0.05	1.39 0.02	20.010±0.26	0.080±0.00	0.146±0.00	287.67±1.00
<7000	12.79 0.00	9.99 0.04	1.62 0.01	16.946±0.22	0.077±0.00	0.163±0.00	287.67±1.00
400	8.69 0.00	0.61 0.00	0.12 0.01	0.132±0.00	0.032±0.00	0.074±0.00	287.67±1.00
<7000	80.35 0.00	28.33 0.12	4.74 0.04	10.549±0.14	0.095±0.00	0.078±0.00	287.67±1.00



Measured volumes are x 1E-10 cm3 NTP. All errors are 2 x standard error.

# **FAR-288 Biotite (45-60 mesh)**

Run date: 1995/10/10  
Run: AS-27

Can/Pos: 141/24  
Mass: 8.5 mg

J Value: 0.000159  
= 0.000010

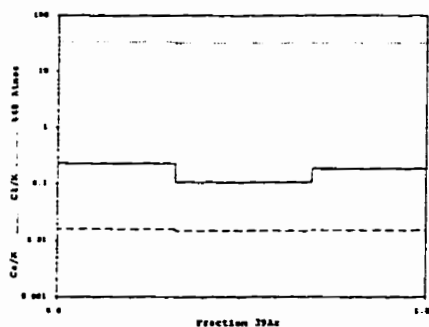
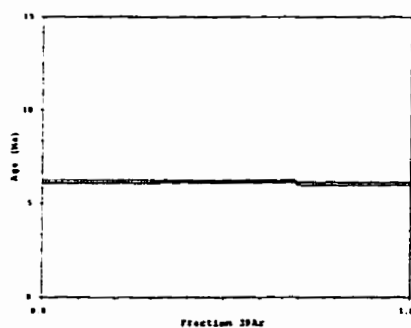
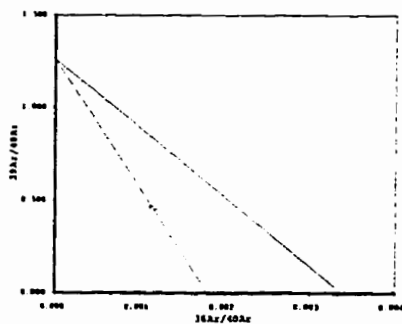
Volume  $^{39}\text{Ar}$ :  $118.83 \times 10^{-10} \text{ cm}^3 \text{ NTP}$   
Integrated Age:  $6.14 \pm 0.05 \text{ Ma}$

Approx.  $8.36\% \text{ K}$   
 $1.42\% \text{ Ca}$

Correlation Age:  $3.17 \pm 225.74 \text{ Ma}$  (100.0% of  $^{39}\text{Ar}$ , steps marked by >)

Power	$^{36}\text{Ar}/^{40}\text{Ar}$	$^{39}\text{Ar}/^{40}\text{Ar}$	$\alpha$	Ca/K	% $^{40}\text{Ar}$	% $^{39}\text{Ar}$	$^{40}\text{Ar}^*/^{39}\text{K}$	Age
7000	0.00117514 $\pm$ 0.00002652	0.450788 $\pm$ 0.001974	0.004	0.23	33.97	32.05	1.451 $\pm$ 0.019	6.16 $\pm$ 0.08
7000	0.00111189 0.00000000	0.461838 0.00000000	0.004	0.11	32.12	36.95	1.456 0.018	6.13 0.08
7000	0.00112963 0.00000000	0.468800 0.00000000	0.004	0.19	32.62	31.10	1.424 0.018	6.25 0.08

Power	$^{40}\text{Ar}$	$^{39}\text{Ar}$	$^{38}\text{Ar}$	$^{37}\text{Ar}$	$^{36}\text{Ar}$	Blank $^{40}\text{Ar}$	Atmos $^{40}/^{36}$
7000	46.21 $\pm$ 0.00	39.33 $\pm$ 0.16	3.06 $\pm$ 0.03	1.379 $\pm$ 0.02	0.120 $\pm$ 0.00	0.142 $\pm$ 0.00	297.67 $\pm$ 1.00
7000	46.78 0.00	44.13 0.19	3.50 0.03	0.739 $\pm$ 0.01	0.126 $\pm$ 0.00	0.142 $\pm$ 0.00	297.67 $\pm$ 1.00
7000	80.51 0.00	37.25 0.16	3.03 0.03	1.081 $\pm$ 0.01	0.109 $\pm$ 0.00	0.142 $\pm$ 0.00	297.67 $\pm$ 1.00



Measured volumes are  $\times 10^{-10} \text{ cm}^3 \text{ NTP}$ . All errors are 2  $\times$  standard error.

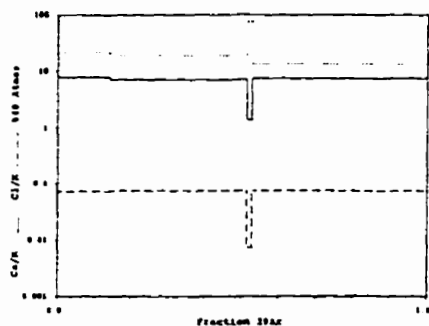
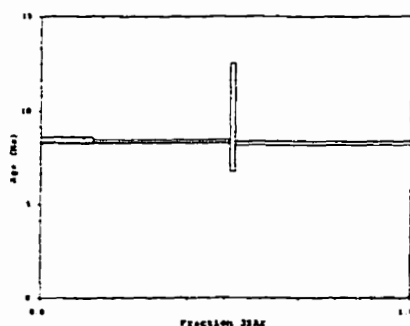
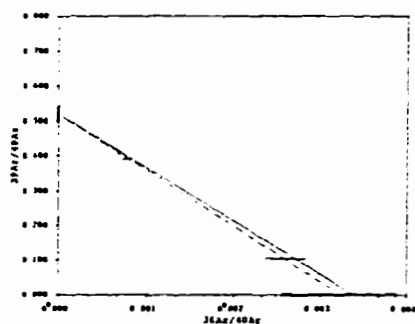
# **FAR-296 Hornblende (60-80 mesh)**

Run date: 1995/10/12      Can/Pes: 141/25      J Value: 0.002359  
 Run: AS-28 & AS-113      Mass: 45.0 mg      ± 0.000010

Volume <sup>39</sup>Ar: 76.13 x 1E-10 cm<sup>3</sup> NTP      Approx. 1.01% K  
 Integrated Age: 8.39 ± 0.09 Ma      7.46% Ca  
 Initial 40/36: 309.95 ± 62.36 (MSWD = 2.89, isochron between 0.00 and 3.00)  
 Correlation Age: 9.15 ± 0.33 Ma (100.0% of <sup>39</sup>Ar, steps marked by >)  
 Plateau Age: 8.37 ± 0.08 Ma ( 98.6% of <sup>39</sup>Ar, steps marked by <)

Power	<sup>36</sup> Ar/ <sup>40</sup> Ar	<sup>39</sup> Ar/ <sup>40</sup> Ar	z	Ca/K	%40Atm	% <sup>39</sup> Ar	<sup>40</sup> Ar*/ <sup>39</sup> K	Age
<7000	0.00075784±0.00005155	0.391805±0.001724	0.007	8.02	21.55	14.21	1.993±0.039	8.46±0.16
<7000	0.00067628 0.00000000	0.407095 0.000000	0.010	7.24	19.14	36.67	1.978 0.022	8.40 0.09
400	0.00258347 0.00000000	0.104022 0.000000	0.001	1.38	75.99	1.40	2.277 0.676	9.66 2.86
<7000	0.00050341 0.00001913	0.433754 0.000964	0.008	7.51	13.58	47.72	1.960 0.026	8.32 0.11

Power	<sup>40</sup> Ar	<sup>39</sup> Ar	<sup>38</sup> Ar	<sup>37</sup> Ar	<sup>36</sup> Ar	Blank <sup>40</sup> Ar	Atmos 40/36
<7000	29.14±0.00	10.36±0.05	3.71±0.03	13.36±0.17	0.050±0.00	0.159±0.00	287.67±1.00
<7000	49.71 0.00	28.16 0.12	4.63 0.18	31.11±0.40	0.092±0.00	0.160±0.00	287.67±1.00
400	10.43 0.00	1.09 0.00	0.04 0.00	0.08±0.00	0.037±0.00	0.114±0.00	287.67±1.00
<7000	84.04 0.00	36.57 0.16	12.74 0.11	14.15±0.18	0.092±0.00	0.136±0.00	287.67±1.00



Measured volumes are x 1E-10 cm<sup>3</sup> NTP. All errors are 2 x standard error.



# **FAR-297 Hornblende (60-100 mesh)**

Run date: 1995/10/12 Can/Pos: 141/26 J Value: 0.002360  
Run: AS-29 & AS-112 Mass: 30.0 mg = 0.000010

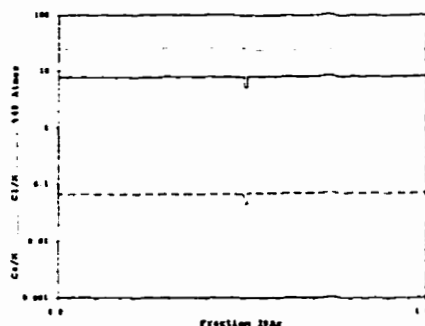
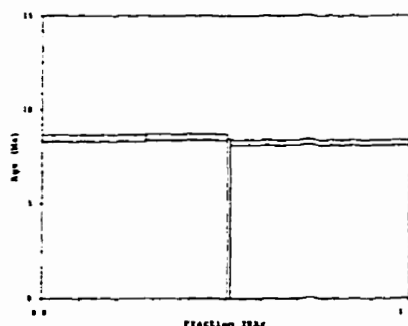
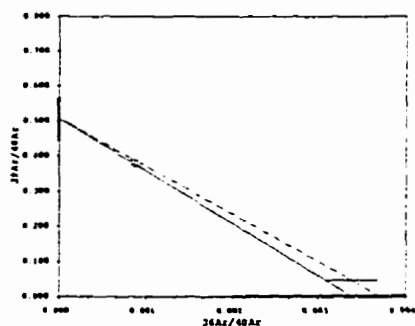
Volume 39Ar: 48.08 x 1E-10 cm3 NTP  
Integrated Age: 9.30 ± 0.12 Ma Approx. 0.96% K  
7.64% Ca

Initial 40/36: 269.10 ± 122.80 (MSWD = 12.73, isochron between 0.00 and 3.00)  
Correlation Age: 9.40 ± 0.99 Ma (100.0% of 39Ar, steps marked by >)

Plateau Age: 8.37 ± 0.11 Ma ( 99.2% of 39Ar, steps marked by <)

Power	36Ar/40Ar	39Ar/40Ar	z	Ca/K	%40Atm	%39Ar	40Ar*/39K	Age
<7000	0.00086773±0.00005894	0.375648±0.001652	0.006	7.79	24.83	27.68	1.991±0.046	8.46±0.20
<7000	0.00088712±0.00000000	0.369917±0.000000	0.008	7.99	25.40	22.23	2.006±0.041	8.52±0.17
400	0.00337691±0.00000000	0.047038±0.000000	0.013	5.28	39.52	0.78	0.060±1.922	0.25±8.19
<7000	0.00086602±0.00002291	0.387682±0.000847	0.009	9.18	24.35	49.31	1.941±0.034	8.25±0.15

Power	40Ar	39Ar	38Ar	37Ar	36Ar	Blank 40Ar	Atmos 40/36
<7000	36.06±0.00	13.47±0.06	4.13±0.03	15.47±0.21	0.064±0.00	0.172±0.00	287.67±1.00
<7000	29.42±0.00	10.84±0.05	3.23±0.03	12.923±0.17	0.058±0.00	0.165±0.00	287.67±1.00
400	5.04±0.00	0.39±0.00	0.14±0.00	0.114±0.00	0.037±0.00	0.113±0.00	287.67±1.00
<7000	42.08±0.00	23.87±0.10	7.14±0.07	15.566±0.13	0.091±0.00	0.117±0.00	287.67±1.00



Measured volumes are x 1E-10 cm3 NTP. All errors are 2 x standard error.

# **FAR-297 Biotite (60-100 mesh)**

Run date: 1995/10/13  
Run: AS-31 & AS-130

Can/Pos: 141/27  
Mass: 9.5 mg

J Value: 0.001360  
± 0.000010

Volume 39Ar: 129.84 x 1E-10 cm<sup>3</sup> NTP  
Integrated Age: 9.59 ± 0.08 Ma

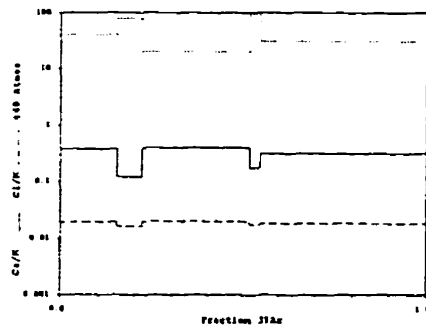
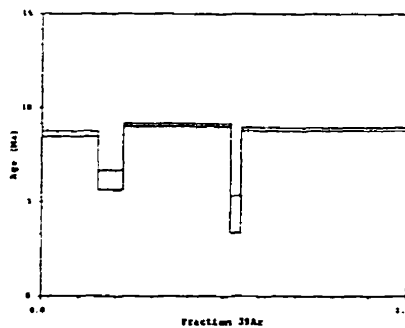
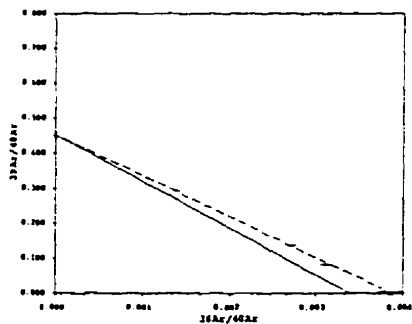
Approx. 8.17% K  
2.71% Ca

Initial 40/36: 258.95 ± 9.72 (MSWD = 1.69, isochron between 0.18 and 2.63)  
Correlation Age: 9.38 ± 0.10 Ma (100.0% of 39Ar, steps marked by >)

Plateau Age: 8.91 ± 0.07 Ma ( 90.3% of 39Ar, steps marked by <)

Power	36Ar/40Ar	39Ar/40Ar	z	Ca/K	%40Ar	%39Ar	40Ar*/39K	Age
<7000	0.00138193±0.00003379	0.291975±0.001270	0.002	0.37	40.25	15.04	2.030±0.036	8.62±0.15
300	0.00271956 0.00000000	0.135851 0.000000	0.001	0.12	79.87	6.68	1.448 0.119	6.16 0.51
<7000	0.00069469 0.00000000	0.371296 0.000000	0.002	0.40	20.09	29.58	2.144 0.018	9.11 0.08
300	0.00310256 0.00003120	0.081913 0.000179	0.001	0.18	91.32	3.01	1.021 0.229	4.94 0.97
<7000	0.00104575 0.00000000	0.331232 0.000000	0.003	0.32	30.29	45.69	2.092 0.021	8.88 0.09

Power	40Ar	39Ar	38Ar	37Ar	36Ar	Blank 40Ar	Atmos 40/36
<7000	47.84±0.00	13.67±0.02	1.94±0.02	1.120±0.01	0.105±0.00	0.123±0.00	287.67±1.00
300	64.29 0.00	5.75 0.04	0.77 0.01	3.175±0.00	0.187±0.00	0.129±0.00	287.67±1.00
<7000	105.15 0.00	13.48 0.16	3.89 0.03	2.340±0.03	0.085±0.00	0.130±0.00	287.67±1.00
300	48.07 0.00	3.98 0.02	0.39 0.00	0.051±0.00	0.167±0.00	0.139±0.00	287.67±1.00
<7000	161.70 0.00	59.72 0.25	5.61 0.05	0.905±0.01	0.211±0.00	0.150±0.00	287.67±1.00



Measured volumes are x 1E-10 cm<sup>3</sup> NTP. All errors are 2 x standard error.

# **FAR-299 Hornblende (45-60 mesh)**

Run date: 1995/10/13 Can/Pos: 141/28 J Value: 0.002360  
Run: AS-32 & AS-111 Mass: 45.0 mg ± 0.000010

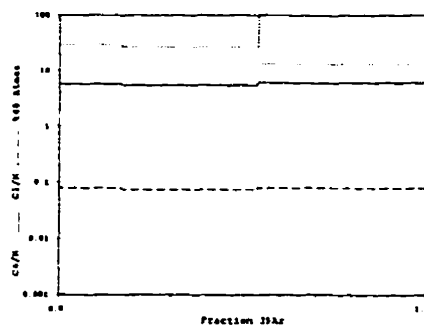
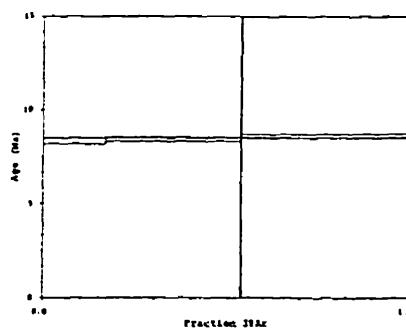
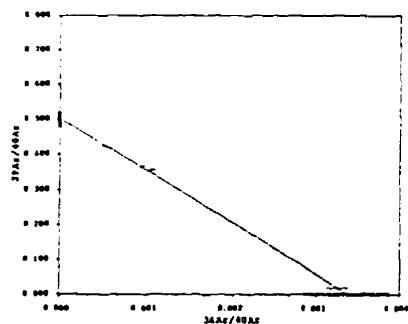
Volume 39Ar: 85.61 x 1E-10 cm3 NTP Approx. 1.144 K  
Integrated Age: 8.48 ± 0.08 Ma 5.64% Ca

Initial 40/36: 296.43 ± 44.50 (MSWD = 7.48, isochron between 0.00 and 3.00)  
Correlation Age: 8.49 ± 0.33 Ma (100.0% of 39Ar, steps marked by >)

Plateau Age: 8.48 ± 0.08 Ma ( 99.6% of 39Ar, steps marked by <)

Power	36Ar/40Ar	39Ar/40Ar	r	Ca/K	%40Ar	%39Ar	40Ar*/39K	Age
<7000	0.00104531±0.00004616	0.355162±0.001555	0.006	5.85	29.96	16.59	1.960±0.039	8.32±0.16
<7000	0.0009364±0.00000000	0.368090±0.000000	0.007	5.57	26.78	36.56	1.978±0.026	8.40±0.11
400	0.00325180±0.00000000	0.017926±0.000000	0.090	6.26	95.97	0.37	2.207±2.301	9.37±9.75
<7000	0.0005052±0.00001561	0.425484±0.000952	0.007	6.07	13.61	46.48	2.025±0.022	9.60±0.09

Power	40Ar	39Ar	38Ar	37Ar	36Ar	Blank 40Ar	Atmos 40/36
<7000	40.65±0.00	14.34±0.06	5.31±0.05	12.615±0.16	0.067±0.00	0.147±0.00	287.67±1.00
<7000	36.31±0.00	31.54±0.13	10.34±0.09	24.406±0.34	0.119±0.00	0.147±0.00	287.67±1.00
400	17.81±0.00	0.34±0.00	0.14±0.00	0.115±0.00	0.069±0.00	0.116±0.00	287.67±1.00
<7000	95.10±0.00	40.05±0.17	14.81±0.13	12.554±0.16	0.092±0.00	0.121±0.00	287.67±1.00



Measured volumes are x 1E-10 cm3 NTP. All errors are 2 x standard error.

# **FAR-299 Biotite (45-60 mesh)**

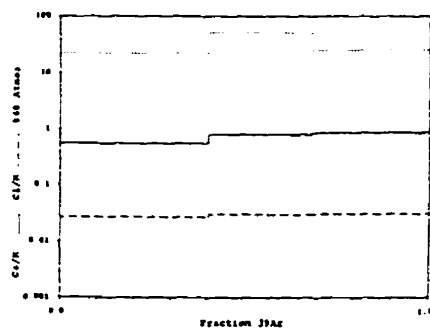
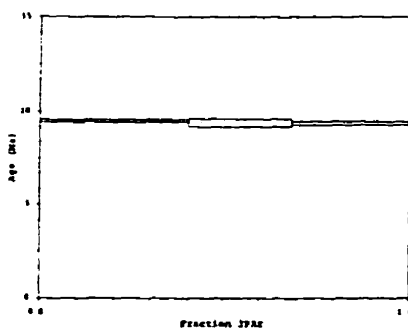
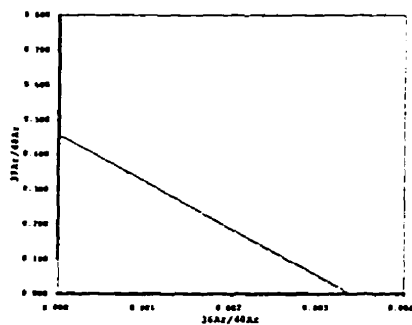
Run date: 1995/10/13 Can/Pos: 141/29 J Value: 0.002360  
Run: AS-33 Mass: 8.0 mg ± 0.000010

Volume 39Ar: 109.25 x 1E-10 cm3 NTP Approx. 8.16% K  
Integrated Age: 9.41 ± 0.09 Ma 5.98% Ca

Initial 40/36: 298.14 ± 919.95 (MSWD = 8.90, isochron between -0.41 and 3.83)  
Correlation Age: 9.31 ± 7.22 Ma (100.0% of 39Ar, steps marked by >)

Power	36Ar/40Ar	39Ar/40Ar	z	Ca/K	%40Ar	%39Ar	40Ar*/39K	Age
7000	0.00077182±0.00001825	0.346500±0.001511	0.003	0.56	22.38	40.03	2.211±0.019	9.47±0.08
7000	0.00179451 0.00000000	0.213137 0.000000	0.002	0.82	52.45	27.98	2.209 0.050	9.38 0.21
7000	0.00087207 0.00000000	0.317431 0.000000	0.003	0.88	25.23	31.98	2.205 0.021	9.36 0.09

Power	40Ar	39Ar	38Ar	37Ar	36Ar	Blank 40Ar	Atmos 40/36
7000	128.10±0.00	44.08±0.19	5.82±0.05	3.722±0.05	0.121±0.00	0.172±0.00	297.67±1.00
7000	144.85 0.00	30.83 0.13	4.53 0.14	3.817±0.05	0.286±0.00	0.174±0.00	297.67±1.00
7000	105.14 0.00	35.22 0.15	5.14 0.05	4.680±0.06	0.115±0.00	0.171±0.00	297.67±1.00



Measured volumes are x 1E-10 cm3 NTP. All errors are 2 x standard error.

# **Far-301 Hornblende (60-80 mesh)**

Run date: 1995/10/13  
Run: AS-34 & AS-117

Can/Fos: 141/30  
Mass: 50.0 mg

J Value: 0.000361  
± 0.000010

Volume 39Ar: 94.58 x 1E-10 cm<sup>3</sup> NTP  
Integrated Age: 7.55 ± 0.08 Ma

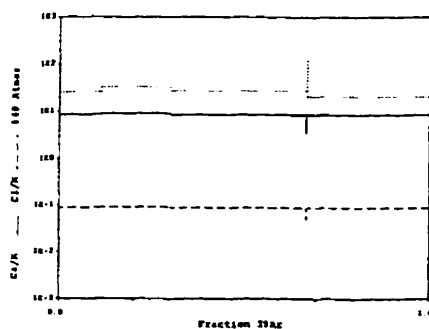
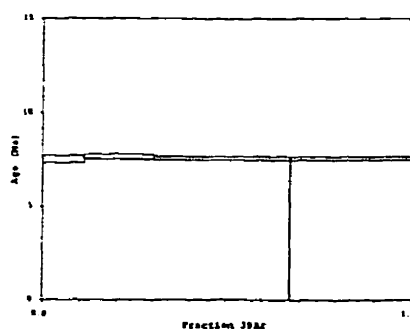
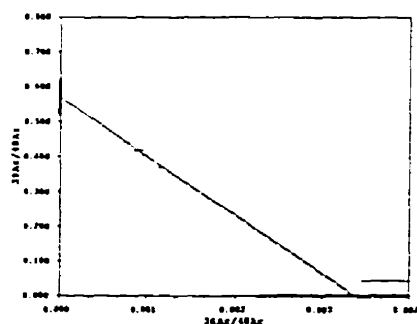
Approx. 1.13% K  
9.65% Ca

Initial 40/36: 297.37 ± 96.10 (MSWD = 3.85, isochron between 0.18 and 2.63)  
Correlation Age: 7.45 ± 0.62 Ma (100.0% of 39Ar, steps marked by >)

Plateau Age: 7.59 ± 0.08 Ma (99.8% of 39Ar, steps marked by <)

Power	36Ar/40Ar	39Ar/40Ar	r	Ca/K	%40Ar	%39Ar	40Ar*/39K	Age
<7000	0.00089651±0.00006182	0.418489±0.001848	0.007	8.42	25.41	10.98	1.772±0.043	7.55±0.18
<7000	0.00114585 0.00000000	0.370751 0.000000	0.012	8.93	32.76	18.93	1.800 0.033	7.65±0.14
<7000	0.00097288 0.00000000	0.405260 0.000000	0.011	8.49	27.17	16.84	1.786 0.028	7.53±0.12
400	0.00407511 0.00001180	0.043700 0.000199	0.014	3.55	120.13	0.17	-4.657 4.292	-19.3±18.48
<7000	0.00075297 0.00000000	0.442658 0.000000	0.010	8.54	20.64	33.08	1.784 0.027	7.55±0.11

Power	40Ar	39Ar	38Ar	37Ar	36Ar	Blank 40Ar	Atmos 40/36
<7000	25.33±0.00	10.53±0.04	4.22±0.04	13.224±0.17	0.055±0.00	0.166±0.00	287.6±1.00
<7000	49.04 0.00	19.13 0.08	7.66 0.07	24.115±0.31	0.100±0.00	0.148±0.00	287.6±1.00
<7000	87.30 0.00	35.07 0.15	14.07 0.12	15.102±0.19	0.136±0.00	0.133±0.00	287.6±1.00
400	3.75 0.00	0.18 0.00	0.05 0.00	0.039±0.00	0.023±0.00	0.116±0.00	287.6±1.00
<7000	71.90 0.00	31.49 0.13	12.71 0.11	13.629±0.17	0.101±0.00	0.127±0.00	287.6±1.00



Measured volumes are x 1E-10 cm<sup>3</sup> NTP. All errors are 2 x standard error.

# **FAR-303 Sericite (45-80 mesh)**

Run date: 1995/11/22 Can/Pos: 141/32 J Value: 0.002361  
 Run: AS-75 & AS-123 Mass: 12.5 mg ± 0.000010

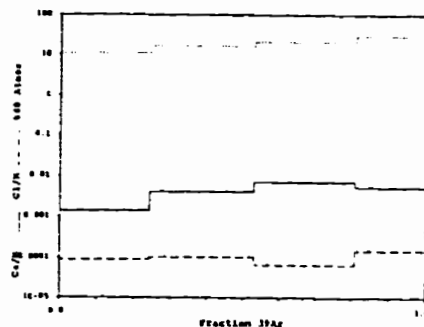
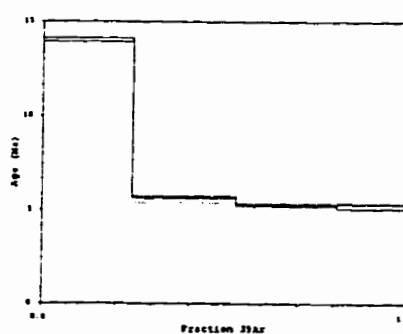
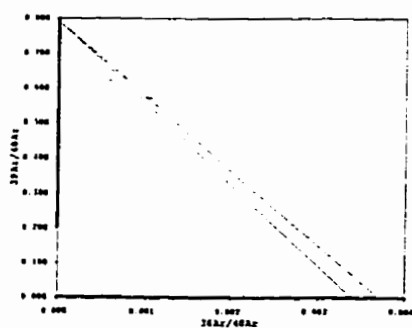
Volume 39Ar: 168.46 x 1E-10 cm3 NTP  
 Integrated Age: 7.50 ± 0.05 Ma Approx. 8.05% K  
 0.04% Ca

Initial 40/36: 270.76 ± 942.06 (MSWD = 289.14, isochron between -0.41 and 3.83)  
 Correlation Age: 5.39 ± 3.98 Ma ( 75.6% of 39Ar, steps marked by > )

Plateau Age: 5.41 ± 0.05 Ma ( 75.88 of 39Ar, steps marked by < )

Power	36Ar/40Ar	39Ar/40Ar	ε	Ca/K	%40Ar	%39Ar	40Ar*/39K	Age
7000	0.00037466±0.00001346	0.269137±0.001171	0.001	0.00	10.95	24.21	3.304±0.021	14.02±0.09
<7000>	0.00056746 ± 0.00000000	0.621739 ± 0.000000	0.003	0.00	16.34	28.17	1.339 ± 0.012	5.69 ± 0.05
<7000>	0.00073656 ± 0.00000000	0.631951 ± 0.000000	0.004	0.01	21.21	27.90	1.238 ± 0.012	5.27 ± 0.05
<7000>	0.00101670 ± 0.00002411	0.572093 ± 0.001258	0.002	0.01	29.34	19.72	1.223 ± 0.026	5.20 ± 0.11

Power	40Ar	39Ar	38Ar	37Ar	36Ar	Blank 40Ar	Atmos 40/36
7000	153.43±0.00	41.13±0.18	0.64±0.01	3.035±0.00	0.088±0.00	0.177±0.00	287.67±1.00
<7000>	78.46 ± 0.00	47.83 ± 0.20	0.74 ± 0.01	0.041±0.00	0.070±0.00	0.155±0.00	287.67±1.00
<7000>	76.47 ± 0.00	47.16 ± 0.20	0.72 ± 0.01	0.047±0.00	0.079±0.00	0.136±0.00	287.67±1.00
<7000>	59.55 ± 0.00	33.44 ± 0.14	0.52 ± 0.00	0.023±0.00	0.072±0.00	0.106±0.00	287.67±1.00



Measured volumes are x 1E-10 cm3 NTP. All errors are 2 x standard error.

# **FAR-303 Whole Rock (45-80 mesh)**

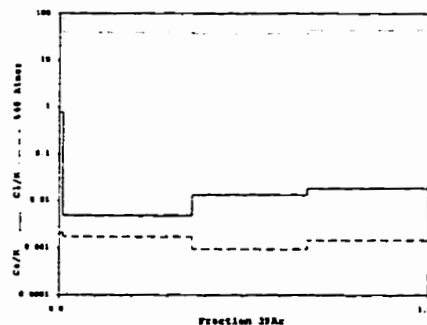
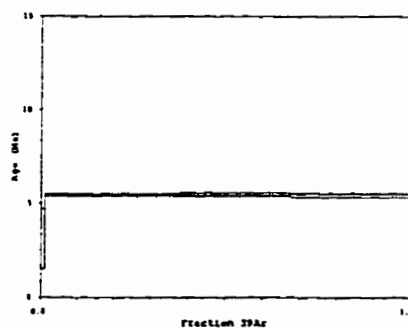
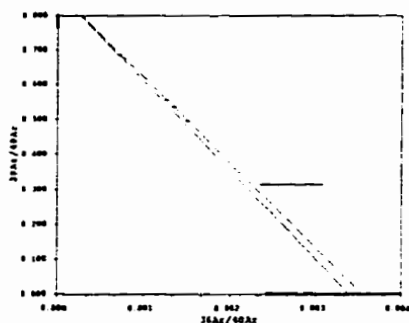
Run date: 1996/10/24 Can/Pos: 140/7 J Value: 0.000691  
 Run: AS-204 Mass: 100.0 mg ± 0.000014

Volume 39Ar: 253.08 x 1E-10 cm<sup>3</sup> NTP  
 Integrated Age: 5.43 ± 0.06 Ma Approx. 1.33% K  
 0.03% Ca

Initial 40/36: 282.96 ± 97.55 (MSWD = 2.97, isochron between 0.00 and 3.00)  
 Correlation Age: 5.61 ± 0.63 Ma (100.0% of 39Ar, steps marked by >)  
 Plateau Age: 5.45 ± 0.06 Ma ( 99.0% of 39Ar, steps marked by <)

Power	36Ar/40Ar	39Ar/40Ar	ε	Ca/K	%40Atm	%39Ar	40Ar*/39K	Age
400	0.00270365±0.00037176	0.314082±0.001381	0.092	0.76	78.81	0.96	0.642±0.326	3.11±1.58
<7000	0.00134004 0.00000000	0.536935 0.000000	0.005	0.00	38.66	35.38	1.12±0.016	5.46 0.08
<7000	0.00125716 0.00000000	0.556936 0.000000	0.005	0.01	36.26	30.46	1.129 0.016	5.47 0.08
<7000	0.00150938 0.00001474	0.495232 0.001004	0.005	0.02	43.64	33.20	1.120 0.018	5.43 0.09

Power	40Ar	39Ar	38Ar	37Ar	36Ar	Blank 40Ar	Atmos 40/36
400	7.39±0.00	2.46±0.01	0.07±0.00	0.012±0.00	0.031±0.00	0.154±0.00	284.57±1.00
<7000	170.63 0.00	93.20 0.36	2.01 0.02	0.011±0.00	0.242±0.00	0.161±0.00	284.57±1.00
<7000	141.79 0.00	77.67 0.31	1.46 0.01	0.012±0.00	0.190±0.00	0.160±0.00	284.57±1.00
<7000	173.34 0.00	94.66 0.33	1.81 0.01	0.012±0.00	0.276±0.00	0.160±0.00	284.57±1.00



Measured volumes are x 1E-10 cm<sup>3</sup> NTP. All errors are 2 x standard error.

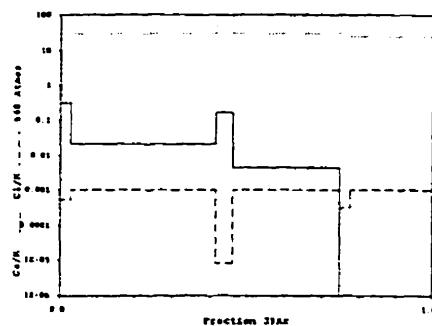
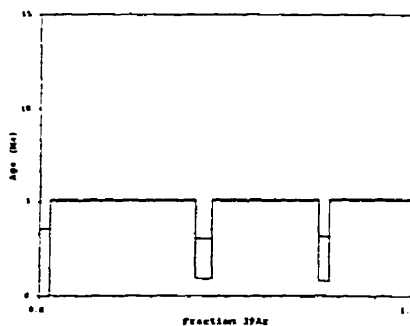
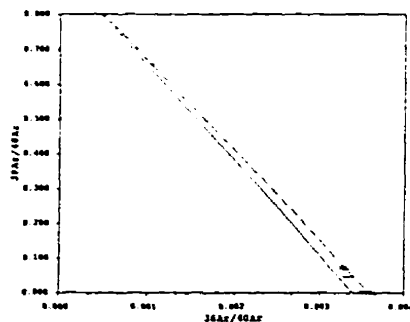
# **FAR-304 Whole Rock (45-60 mesh)**

Run date: 1996/10/24 Can/Fcs: 140/8 J Value: 0.002687  
Run: AS-205 Mass: 200.0 mg ± 0.000014

Volume 39Ar: 408.49 x 1E-10 cm3 NTP Approx. 1.07% K  
Integrated Age: 4.79 ± 0.09 Ma 0.03% Ca  
Initial 40/36: 279.99 ± 6.75 (MSWD = 1.29, isochron between 0.29 and 2.41)  
Correlation Age: 5.22 ± 0.05 Ma (100.0% of 39Ar, steps marked by >)  
Plateau Age: 5.11 ± 0.04 Ma ( 90.0% of 39Ar, steps marked by <)

Power	36Ar/40Ar	39Ar/40Ar	z	Ca/K	40Ar	39Ar	40Ar=39K	Age
400	0.00332690±0.00006432	0.045961±0.000201	0.203	0.31	98.12	2.85	0.368±0.367	1.77±1.78
<7000	0.00102597 0.00000000	0.659561 0.000000	0.006	0.02	29.52	38.43	1.056 0.010	5.11 0.05
400	0.00327699 0.00000000	0.076326 0.000000	0.088	0.17	96.53	4.35	0.415 0.218	2.22 1.06
<7000	0.00104423 0.00001055	0.657636 0.001342	0.006	0.00	30.04	38.46	1.051 0.011	5.09 0.05
400	0.00328954 0.00000000	0.068794 0.000000	0.143	0.00	96.93	2.84	0.406 0.244	1.97 1.18
<7000	0.00086464 0.00000000	0.702189 0.000001	0.006	0.00	24.84	23.08	1.060 0.009	5.13 0.05

Power	40Ar	39Ar	38Ar	37Ar	36Ar	Blank 40Ar	Atmos 40/36
400	254.40±0.00	11.77±0.05	0.37±0.00	0.017±0.00	0.892±0.01	0.253±0.00	284.57±1.00
<7000	244.79 0.00	158.15 0.62	2.14 0.01	0.017±0.00	0.270±0.00	0.259±0.00	284.57±1.00
400	233.73 0.00	17.92 0.07	0.41 0.00	0.017±0.00	0.808±0.01	0.257±0.00	284.57±1.00
<7000	181.88 0.00	117.14 0.46	1.60 0.01	0.014±0.00	0.207±0.00	0.259±0.00	284.57±1.00
400	169.16 0.00	11.69 0.05	0.30 0.00	0.011±0.00	0.588±0.01	0.190±0.00	284.57±1.00
<7000	138.36 0.00	94.98 0.37	1.27 0.01	0.011±0.00	0.133±0.00	0.185±0.00	284.57±1.00



Measured volumes are x 1E-10 cm3 NTP. All errors are 1 x standard error.



# **FAR-304 Sericite (45-60 mesh)**

Run date: 1995/11/22 Can/Pas: 141/34 J Value: 0.002361  
Run: AS-74 & AS-124 Mass: 14.0 mg ± 0.000010

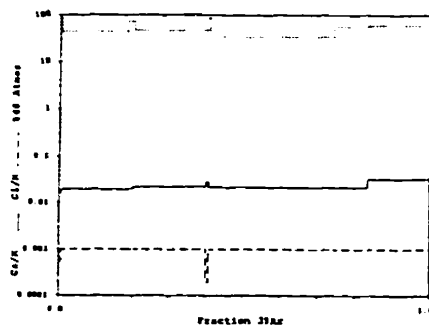
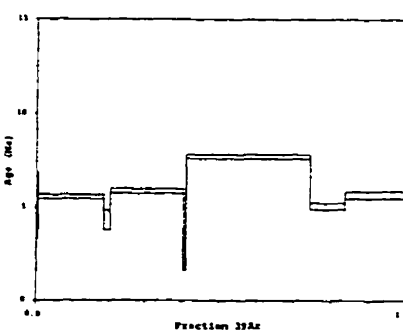
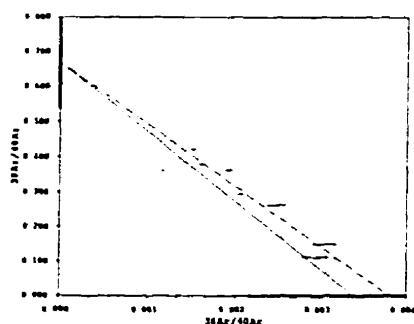
Volume 39Ar: 256.59 x 1E-10 cm3 NTP Approx. 11.03% K  
Integrated Age: 6.28 ± 0.07 Ma 0.26% Ca

Initial 40/36: 262.36 ± 113.08 (MSWD = 26.65, isochron between 0.37 and 2.26)  
Correlation Age: 6.36 ± 1.21 Ma ( 67.0% of 39Ar, steps marked by > )

Plateau Age: 5.73 ± 0.08 Ma ( 54.9% of 39Ar, steps marked by < )

Power	36Ar/40Ar	39Ar/40Ar	r	Ca/K	%40Atm	%39Ar	40Ar*/39K	Age
300>	0.00292935±0.00015712	0.112099±0.000506	0.001	0.02	96.16	0.49	1.199±0.415	5.10±1.76
<7000>	0.00150838 0.00000000	0.422462 0.000000	0.004	0.02	43.80	17.83	1.312 0.024	5.58 0.10
300>	0.00247480 0.00000000	0.264461 0.000000	0.001	0.02	72.33	1.65	1.016 0.124	4.32 0.53
<7000>	0.00160076 0.00001585	0.380235 0.000829	0.003	0.02	46.57	19.95	1.386 0.026	5.89 0.11
300>	0.00303517 0.00000000	0.149127 0.000000	0.001	0.03	89.13	0.71	0.691 0.308	2.94 1.31
7000	0.00115648 0.00000001	0.362130 0.000000	0.003	0.02	33.67	32.97	1.818 0.021	7.73 0.09
300>	0.00191661 0.00000000	0.363397 0.000000	0.003	0.02	55.79	9.30	1.193 0.040	5.08 0.17
<7000>	0.00205571 0.00000000	0.293752 0.000000	0.003	0.03	60.01	17.10	1.336 0.042	5.68 0.18

Power	40Ar	39Ar	38Ar	37Ar	36Ar	Blank 40Ar	Atmos 40/36
300>	11.50±0.00	1.32±0.01	0.04±0.00	0.016±0.00	0.047±0.00	0.110±0.00	287.67±1.00
<7000>	111.15 0.00	44.42 0.20	0.63 0.01	0.078±0.00	0.183±0.00	0.117±0.00	287.67±1.00
300>	16.44 0.00	4.34 0.02	0.08 0.00	0.021±0.00	0.054±0.00	0.112±0.00	287.67±1.00
<7000>	137.93 0.00	51.94 0.22	0.70 0.01	0.094±0.00	0.237±0.00	0.115±0.00	287.67±1.00
300>	12.44 0.00	1.39 0.01	0.05 0.00	0.019±0.00	0.052±0.00	0.114±0.00	287.67±1.00
7000	239.16 0.00	55.83 0.37	1.15 0.01	0.145±0.00	0.298±0.01	0.147±0.00	287.67±1.00
300>	67.23 0.00	24.22 0.10	0.35 0.00	0.040±0.00	0.142±0.00	0.104±0.00	287.67±1.00
<7000>	152.52 0.00	44.52 0.19	0.67 0.01	0.086±0.00	0.330±0.01	0.106±0.00	287.67±1.00



Measured volumes are x 1E-10 cm3 NTP. All errors are 1 x standard error.

# **FAR-307 Whole-Rock (60-80 mesh)**

Run date: 1995/11/20  
Run: AS-65

Can/Pos: 141/37  
Mass: 100.0 mg

J Value: 0.002361  
= 0.000010

Volume 39Ar: 72.68 x 1E-10 cm3 NTP  
Integrated Age: 7.99 ± 0.11 Ma

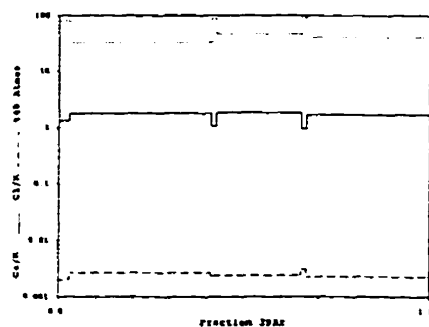
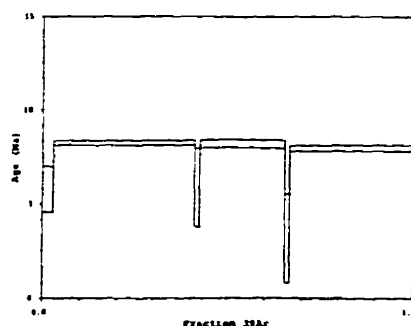
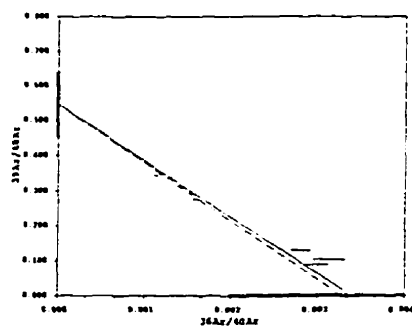
Approx. 0.43% K  
0.75% Ca

Initial 40/36: 305.90 ± 117.50 (MSWD = 21.37, isochron between 0.29 and 2.41)  
Correlation Age: 7.77 ± 1.32 Ma (100.0% of 39Ar, steps marked by >)

Plateau Age: 8.15 ± 0.10 Ma ( 94.5% of 39Ar, steps marked by <)

Power	36Ar/40Ar	39Ar/40Ar	τ	Ca/K	%40Ar	%39Ar	40Ar*/39Ar	Age
300	0.00278985±0.00012511	0.128921±0.000573	0.001	1.33	81.99	2.72	1.363±0.288	5.79±1.22
<7000	0.00112367 0.00000000	0.344034 0.000000	0.003	1.78	32.71	38.08	1.942 0.030	8.25 0.13
300	0.00297010 0.00000000	0.088530 0.000000	0.001	1.04	87.44	1.45	1.383 0.495	5.88 2.10
<7000	0.00158339 0.00002204	0.275100 0.000538	0.002	1.82	46.24	22.58	1.935 0.049	8.22 0.21
300	0.00312177 0.00000000	0.103241 0.000000	0.001	0.95	91.84	1.35	0.752 0.554	3.20 2.36
<7000	0.00139655 0.00000001	0.312477 0.000000	0.003	1.68	40.72	33.82	1.880 0.036	7.99 0.15

Power	40Ar	39Ar	38Ar	37Ar	36Ar	Blank 40Ar	Atmos 40/36
300	15.52±0.00	2.01±0.01	0.06±0.00	0.200±0.00	0.053±0.00	0.083±0.00	287.67±1.00
<7000	81.64 0.00	27.87 0.12	0.75 0.01	1.538±0.05	0.110±0.00	0.097±0.00	287.67±1.00
300	12.03 0.00	1.08 0.00	0.04 0.00	0.090±0.00	0.045±0.00	0.082±0.00	287.67±1.00
<7000	60.37 0.00	16.53 0.07	0.43 0.00	2.154±0.03	0.111±0.00	0.087±0.00	287.67±1.00
300	9.64 0.00	1.01 0.00	0.04 0.00	0.079±0.00	0.040±0.00	0.083±0.00	287.67±1.00
<7000	79.73 0.00	24.75 0.11	0.63 0.01	2.972±0.04	0.129±0.00	0.097±0.00	287.67±1.00



Measured volumes are x 1E-10 cm3 NTP. All errors are 2 x standard error.

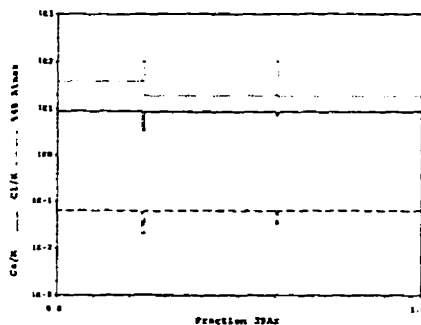
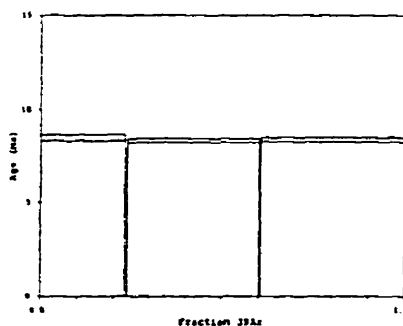
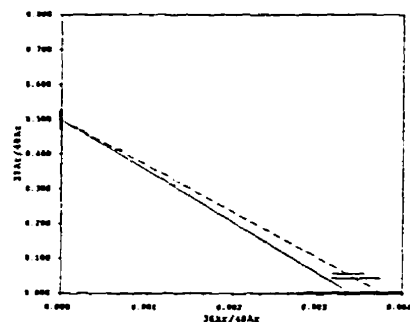
# **FAR-311 Hornblende (45-60 mesh)**

Run date: 1995/10/13 Can/Pcs: 141/36 J Value: 0.002361  
Run: AS-35 & AS-110 Mass: 40.0 mg = 0.000010

Volume 39Ar: 70.81 x 1E-10 cm3 NTP Approx. 1.06% K  
Integrated Age: 8.32 ± 0.09 Ma 9.05% Ca  
Initial 40/36: 255.56 ± 69.67 (MSWD = 10.53, isochron between 0.18 and 2.63)  
Correlation Age: 8.52 ± 0.45 Ma (100.0% of 39Ar, steps marked by >)  
Plateau Age: 8.41 ± 0.08 Ma ( 99.0% of 39Ar, steps marked by <)

Power	36Ar/40Ar	39Ar/40Ar	z	Ca/K	%40Ar	%39Ar	40Ar*/39K	Age
<7000	0.00128274±0.00004264	0.312604±0.001373	0.013	8.85	37.08	22.91	1.997±0.039	8.49±0.17
400	0.00335482 0.00000000	0.054688 0.000000	0.003	3.27	98.89	0.55	0.162 1.078	0.69 4.59
<7000	0.00066016 0.00000000	0.411610 0.000000	0.012	8.53	18.74	35.87	1.966 0.024	9.36 0.10
400	0.00344710 0.00011760	0.041710 0.000170	0.012	7.02	101.64	0.43	-0.436 2.088	-1.86 8.90
<7000	0.00064125 0.00000000	0.413858 0.000000	0.010	8.57	17.83	40.24	1.978 0.027	6.41 0.12

Power	40Ar	39Ar	38Ar	37Ar	36Ar	Blank 40Ar	Atmos 40/36
<7000	52.56±0.00	16.44±0.07	4.76±0.34	21.66±0.28	0.109±0.00	0.150±0.00	287.67±1.00
400	7.30 0.00	3.50 0.00	0.09 0.30	3.22±0.00	0.046±0.00	0.149±0.00	287.67±1.00
<7000	62.73 0.00	25.67 0.11	7.43 0.06	32.66±0.42	0.093±0.00	0.150±0.00	287.67±1.00
400	7.36 0.00	3.31 0.00	0.06 0.00	0.118±0.00	0.031±0.00	0.083±0.00	287.67±1.00
<7000	69.91 0.00	28.67 0.12	8.27 0.07	12.68±0.16	0.085±0.00	0.086±0.00	287.67±1.00



Measured volumes are x 1E-10 cm3 NTP. All errors are 2 x standard error.

# **FAR-312 Biotite (45-80 mesh)**

Run date: 1995/10/13  
Run: AS-36 & AS-112

Can/Pos: 141/39  
Mass: 10.0 mg

J Value: 0.002360  
= 0.000010

Volume 39Ar: 135.21 x 1E-10 cm3 NTP  
Integrated Age: 8.64 ± 0.08 Ma

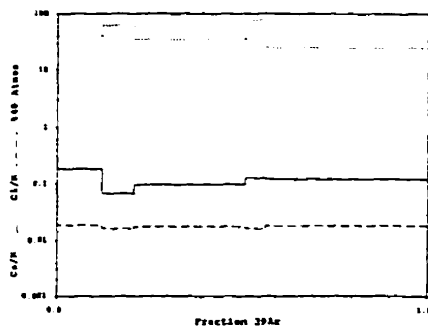
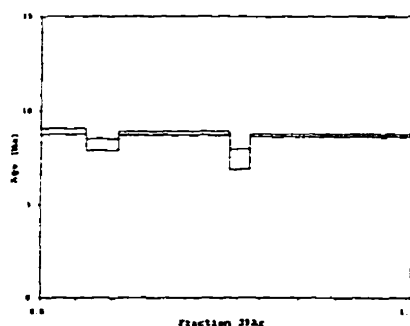
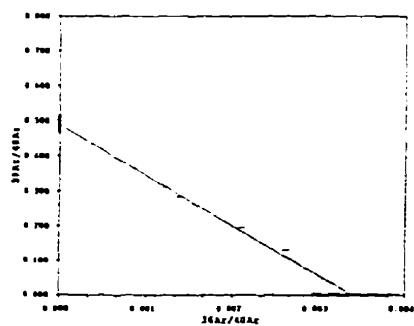
Approx. 8.08% K  
0.95% Ca

Initial 40/36: 294.82 ± 38.92 (MSWD = 14.80, isochron between 0.18 and 2.63)  
Correlation Age: 8.66 ± 0.39 Ma (100.0% of 39Ar, steps marked by >)

Plateau Age: 8.75 ± 0.07 Ma ( 86.1% of 39Ar, steps marked by <)

Power	36Ar/40Ar	39Ar/40Ar	z	Ca/K	%40Ar	%39Ar	40Ar*/39K	Age
<7000	0.00137060±0.00003511	0.284251±0.001244	0.002	0.18	39.92	12.58	2.097±0.038	8.91±0.16
300	0.00139980±0.00003000	0.194958±0.000000	0.002	0.07	61.79	8.68	1.934±0.073	8.22±0.31
<7000	0.00129157±0.00000000	0.312038±0.000000	0.003	0.10	75.01	29.89	2.068±0.026	8.78±0.11
300	0.00261351±0.00002645	0.130502±0.000282	0.001	0.13	76.74	5.22	1.750±0.122	7.44±0.52
<7000	0.00085382±0.00000000	0.365986±0.000000	0.003	0.12	24.81	43.64	2.044±0.017	8.68±0.07

Power	40Ar	39Ar	38Ar	37Ar	36Ar	Blank 40Ar	Atmos 40/36
<7000	60.73±0.00	17.25±0.07	1.70±0.01	0.517±0.01	0.109±0.00	0.211±0.00	287.67±1.00
300	60.87±0.00	11.94±0.05	1.09±0.01	0.163±0.00	0.155±0.00	0.211±0.00	287.67±1.00
<7000	131.42±0.00	40.91±0.17	3.79±0.03	1.645±0.01	0.185±0.00	0.212±0.00	287.67±1.00
300	54.45±0.00	7.11±0.03	0.64±0.01	0.052±0.00	0.152±0.00	0.077±0.00	287.67±1.00
<7000	163.75±0.00	59.37±0.25	5.57±0.05	0.340±0.00	0.150±0.00	0.079±0.00	287.67±1.00



Measured volumes are x 1E-10 cm3 NTP. All errors are 2 x standard error.

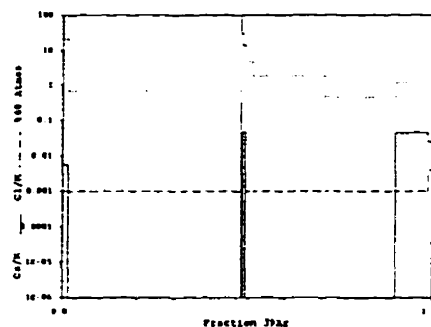
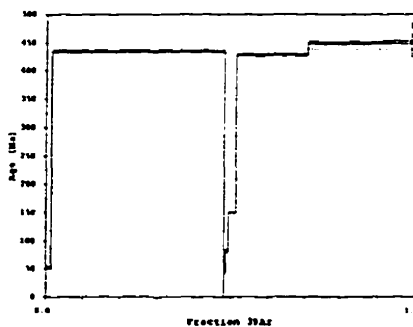
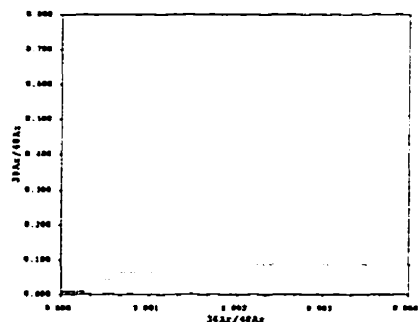
# **FAR-316 Sericite (60-80 mesh)**

Run date: 1995/11/22 Can/Pos: 141/42 J Value: 0.002360  
Run: AS-72 Mass: 10.0 mg ± 0.000010

Volume 39Ar: 124.26 x 1E-10 cm<sup>3</sup> NTP  
Integrated Age: 424.58 ± 1.99 Ma  
Approx. 7.42% K  
0.04% Ca  
Initial 40/36: Linear regression has positive slope.  
Correlation Age:  
Plateau Age: 437.93 ± 2.06 Ma ( 95.78 of 39Ar, steps marked by < )

Power	36Ar/40Ar	39Ar/40Ar	r	Ca/K	%40Atm	%39Ar	40Ar*/39K	Age
300	0.00071580±0.00012190	0.062677±0.000280	0.001	0.01	21.10	1.28	12.580±0.578	52.78± 2.39
<7000	0.00002383 0.00000000	0.008622 0.000000	0.080	0.00	0.70	46.43	115.171 0.508	433.77 1.70
100	0.00339226 0.00000000	0.086654 0.000000	0.003	0.35	99.96	0.07	-0.026 5.231	-0.11 22.27
200	0.00097982 0.00010241	0.062051 0.000165	0.002	0.00	28.88	0.39	11.450 0.977	48.10 4.05
300	0.00046743 0.00000000	0.043880 0.000000	0.005	0.05	13.79	0.69	19.642 0.646	91.75 2.63
500	0.00015488 0.00000000	0.026016 0.000000	0.004	0.00	4.57	1.87	36.679 0.279	149.77 1.09
<1000	0.00006244 0.00000000	0.008633 0.000000	0.075	0.00	1.84	19.46	113.693 0.507	429.82 1.70
<2000	0.00001549 0.00000000	0.008302 0.000000	0.029	0.00	0.46	19.14	119.900 0.649	449.53 2.15
<4000	0.00003994 0.00000000	0.008212 0.000000	0.184	0.05	1.18	8.68	120.332 0.678	450.96 2.25
<7000	0.00000764 0.00002071	0.008213 0.000016	0.289	0.03	0.22	1.99	121.477 9.210	454.76 30.47

Power	40Ar	39Ar	38Ar	37Ar	36Ar	Blank 40Ar	Atmos 40/36
300	25.63±0.00	1.63±0.01	0.04±0.00	0.012±0.00	0.028±0.00	0.130±0.00	287.67±1.00
<7000	4693.50 0.00	59.05 0.25	0.76 0.01	-0.027±0.04	0.170±0.01	0.092±0.00	287.67±1.00
100	1.26 0.00	0.13 0.00	0.02 0.00	0.017±0.00	0.016±0.00	0.248±0.00	287.67±1.00
200	8.10 0.00	0.53 0.00	0.03 0.00	0.016±0.00	0.021±0.00	0.260±0.00	287.67±1.00
300	19.71 0.00	0.90 0.00	0.03 0.00	0.019±0.00	0.023±0.00	0.256±0.00	287.67±1.00
500	89.86 0.00	2.39 0.01	0.05 0.00	0.017±0.00	0.029±0.00	0.270±0.00	287.67±1.00
<1000	2801.46 0.00	24.35 0.10	0.36 0.01	-0.056±0.02	0.187±0.01	0.150±0.00	287.67±1.00
<2000	2565.07 0.00	23.97 0.10	0.27 0.01	-0.063±0.02	0.053±0.03	0.263±0.00	287.67±1.00
<4000	1314.62 0.00	10.90 0.05	0.14 0.01	0.049±0.03	0.068±0.02	0.262±0.00	287.67±1.00
<7000	301.46 0.00	2.53 0.01	0.09 0.01	0.020±0.09	0.016±0.08	0.255±0.00	287.67±1.00



Measured volumes are x 1E-10 cm<sup>3</sup> NTP. All errors are 2 x standard error.

# **FAR-318 K-Spar (45-100 mesh)**

Run date: 1995/11/21  
Run: AS-70

Can/Pos: 141/43  
Mass: 9.0 mg

J Value: 0.002359  
= 0.000010

Volume 39Ar: 161.29 x 1E-10 cm3 NTP  
Integrated Age: 5.33 ± 0.06 Ma

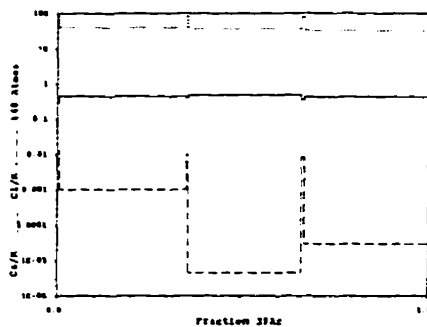
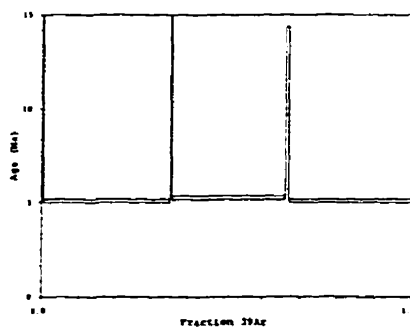
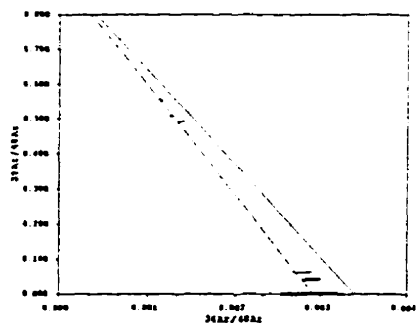
Approx. 10.71% K  
4.72% Ca

Initial 40/36: 344.11 ± 41.27 (MSWD = 5.21, isochron between 0.29 and 2.41)  
Correlation Age: 4.70 ± 0.24 Ma (100.0% of 39Ar, steps marked by >)

Plateau Age: 5.16 ± 0.05 Ma ( 98.18 of 39Ar, steps marked by <)

Power	36Ar/40Ar	39Ar/40Ar	r	Ca/K	%40Ar	%39Ar	40Ar*/39K	Age
300	0.00287573±0.00010060	0.038064±0.000175	0.003	0.28	84.83	0.56	3.950±0.785	16.73±3.31
<7000	0.00137556 0.00000000	0.493319 0.000000	0.004	0.43	39.83	34.49	1.203 0.021	5.11 0.09
300	0.00288281 0.00000000	0.045169 0.000000	0.002	0.38	85.01	0.56	3.282 0.775	13.91 3.27
<7000	0.00125272 0.00001641	0.507632 0.001113	0.003	0.48	36.25	30.12	1.241 0.020	5.27 0.09
300	0.00277653 0.00000000	0.063412 0.000000	0.001	0.34	81.82	0.76	2.834 0.552	12.02 2.34
<7000	0.00113203 0.00000001	0.553803 0.000001	0.004	0.43	32.70	33.51	1.202 0.017	5.11 0.07

Power	40Ar	39Ar	38Ar	37Ar	36Ar	Blank 40Ar	Atmos 40/36
300	23.82±0.00	1.95±0.00	0.02±0.00	0.033±0.00	0.082±0.00	0.101±0.00	287.67±1.00
<7000	115.20 0.00	56.02 0.24	0.83 0.01	1.693±0.02	0.177±0.00	0.120±0.00	287.67±1.00
300	19.98 0.00	0.34 0.00	0.08 0.00	0.039±0.00	0.071±0.00	0.102±0.00	287.67±1.00
<7000	97.82 0.00	49.82 0.21	0.73 0.01	1.639±0.02	0.139±0.00	0.106±0.00	287.67±1.00
300	19.46 0.00	1.27 0.01	0.09 0.00	0.044±0.00	0.067±0.00	0.100±0.00	287.67±1.00
<7000	99.94 0.00	54.42 0.23	0.81 0.01	1.626±0.02	0.129±0.00	0.103±0.00	287.67±1.00



Measured volumes are x 1E-10 cm3 NTP. All errors are 2 x standard error.

# **FAR-322 Whole Rock (60-80 mesh)**

Run date: 1996/10/25 Can/Pos: 142/1 J Value: 0.002303  
 Run: AS-208 Mass: 100.0 mg ± 0.000010

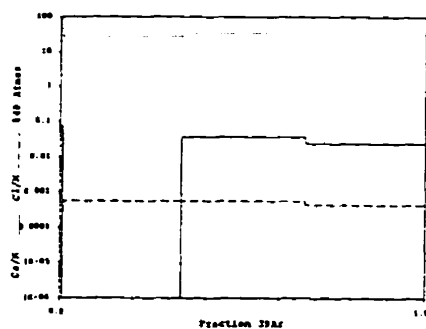
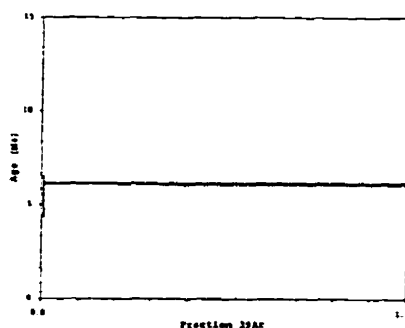
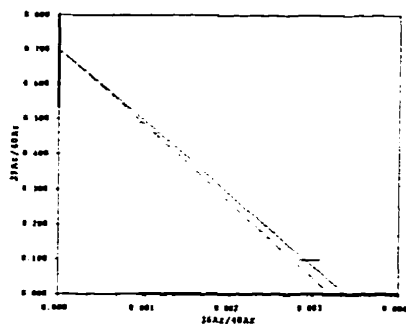
Volume 39Ar: 341.14 x 1E-10 cm<sup>3</sup> NTP Approx. 2.09% K  
 Integrated Age: 6.12 ± 0.05 Ma 0.04% Ca

Initial 40/36: 312.40 ± 220.99 (MSWD = 7.64, isochron between 0.00 and 3.00)  
 Correlation Age: 5.94 ± 1.38 Ma (100.0% of 39Ar, steps marked by >)

Plateau Age: 6.12 ± 0.05 Ma ( 99.38 of 39Ar, steps marked by <)

Power	36Ar/40Ar	39Ar/40Ar	ε	Ca/K	%40Atm	%39Ar	40Ar*/39K	Age
400	0.00295354±0.00012965	0.097250±0.000449	0.406	0.07	86.92	0.72	1.309±0.261	5.43±1.08
<7000	0.00092424±0.00006000	0.490974±0.000000	0.005	0.00	26.74	32.28	1.481±0.013	6.14±0.05
<7000	0.00113472±0.00006000	0.450655±0.000000	0.005	0.04	32.89	33.60	1.475±0.016	6.12±0.07
<7000	0.00109237±0.00001029	0.459909±0.000931	0.004	0.02	31.66	33.40	1.473±0.015	6.11±0.06

Power	40Ar	39Ar	38Ar	37Ar	36Ar	Blank 40Ar	Atmos 40/36
400	25.80±0.00	2.51±0.01	0.07±0.00	0.014±0.00	0.099±0.00	0.359±0.00	284.57±1.00
<7000	229.29±0.00	110.96±0.44	1.90±0.01	0.013±0.00	0.239±0.00	0.410±0.00	284.57±1.00
<7000	259.57±0.00	115.50±0.46	1.90±0.02	0.023±0.00	0.327±0.01	0.449±0.00	284.57±1.00
<7000	252.89±0.00	114.81±0.45	1.91±0.02	0.019±0.00	0.305±0.01	0.406±0.00	284.57±1.00



Measured volumes are x 1E-10 cm<sup>3</sup> NTP. All errors are 2 x standard error.

# **FAR-322 Whole Rock (60-80 mesh)**

Run date: 1997/05/06  
Run: AS-208, JG-079 & JG-080

Can/Pos: 142/1  
Mass: 100.0 mg

J Value: 0.002303  
± 0.000010

Volume 39Ar: 689.56 x 1E-10 cm<sup>3</sup> NTP  
Integrated Age: 5.99 ± 0.05 Ma

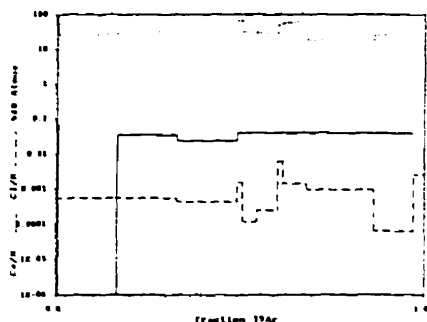
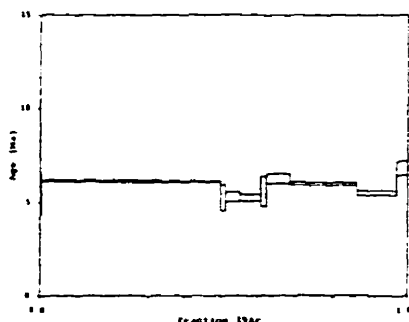
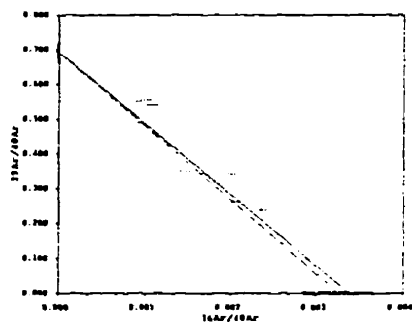
Approx. 4.22% K  
0.13% Ca

Initial 40/36: 306.78 ± 37.10 (MSWD = 1.99, isochron between 0.00 and 3.00)  
Correlation Age: 6.00 ± 0.22 Ma ( 67.0% of 39Ar, steps marked by > )

Plateau Age: 6.10 ± 0.04 Ma ( 67.0% of 39Ar, steps marked by < )

Power	36Ar/40Ar	39Ar/40Ar	r	Ca/K	%40Ar	%39Ar	40Ar*/39K	Age
400	0.00235354±0.00012985	0.097250±0.000463	0.406	0.07	86.92	0.16	1.309±0.261	5.43±1.08
<7000>	0.00092425 0.00000000	0.490974 0.000000	0.005	0.00	26.74	15.97	1.481 0.013	6.14 0.05
<7000>	0.00113472 0.00000000	0.450855 0.000000	0.005	0.04	32.89	16.62	1.475 0.016	6.12 0.07
<7000>	0.00109237 0.00001028	0.459909 0.000931	0.004	0.02	31.66	16.52	1.473 0.015	6.11 0.06
1000	0.00235914 0.00000000	0.238264 0.000000	0.015	0.04	68.98	1.47	1.273 0.165	5.23 0.68
2000	0.00103690 0.00000003	0.540679 0.000001	0.010	0.04	29.36	3.92	1.283 0.064	5.27 0.26
6000	0.00099796 0.00000000	0.554409 0.000000	0.013	0.04	28.80	5.64	1.272 0.043	5.23 0.18
8000	0.00182926 0.00000000	0.342424 0.000000	0.016	0.04	53.01	1.28	1.350 0.197	5.55 0.81
1000	0.00203904 0.00000000	0.261571 0.000000	0.020	0.04	59.56	6.19	1.521 0.063	6.25 0.26
<2000>	0.00062262 0.00000194	0.559362 0.000000	0.024	0.04	17.98	17.90	1.459 0.018	4.00 0.07
4500	0.00090180 0.00000522	0.550052 0.000176	0.018	0.04	26.05	10.35	1.334 0.028	5.48 0.11
7000	0.00142020 0.00001510	0.350235 0.000262	0.024	0.04	41.24	3.79	1.460 0.093	6.82 0.38

Power	40Ar	39Ar	38Ar	37Ar	36Ar	Blank 40Ar	Atmos 40/36
400	25.82±0.00	2.51±0.01	0.07±0.00	0.014±0.00	0.033±0.00	0.353±0.00	234.57±1.00
<7000>	229.29 0.00	110.95 0.44	1.30 0.01	0.013±0.00	0.233±0.00	0.410±0.00	234.57±1.00
<7000>	259.57 0.00	115.50 0.46	2.00 0.02	0.023±0.00	0.127±0.01	0.449±0.00	234.57±1.00
<7000>	252.89 0.00	114.81 0.45	1.31 0.02	0.019±0.00	0.105±0.01	0.406±0.00	234.57±1.00
1000	43.62 0.10	10.30 0.07	0.28 0.01	0.032±0.00	0.153±0.01	0.664±0.02	233.80±1.00
2000	51.81 0.11	27.33 0.10	0.46 0.01	0.033±0.00	0.103±0.01	0.661±0.02	233.80±1.00
6000	72.44 0.13	39.26 0.11	0.67 0.02	0.034±0.00	0.124±0.01	0.674±0.02	233.80±1.00
8000	26.81 0.11	8.99 0.06	0.44 0.02	0.035±0.00	0.103±0.01	0.703±0.02	233.80±1.00
1000	165.59 0.23	43.10 0.15	1.00 0.02	0.041±0.00	0.403±0.01	0.666±0.04	233.80±1.00
<2000>	226.43 0.32	124.39 0.31	1.81 0.03	0.044±0.00	0.205±0.01	0.684±0.03	233.80±1.00
4500	133.38 0.23	71.39 0.18	1.13 0.02	0.044±0.00	0.185±0.01	0.636±0.03	233.80±1.00
7000	76.43 0.21	26.48 0.12	0.79 0.02	0.052±0.00	0.183±0.01	0.804±0.04	233.80±1.00



Measured volumes are x 1E-10 cm<sup>3</sup> NTP. All errors are 2 x standard error.



# **FAR-322 Whole Rock (60-80 mesh)**

Run date: 1997/05/06 Can/Pos: 142/1 J Value: 0.002303  
Run: JG-079 & JG-080 Mass: 100.0 mg ± 0.000010

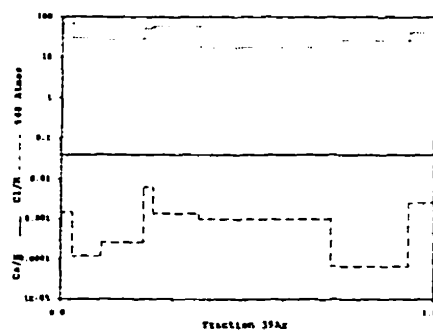
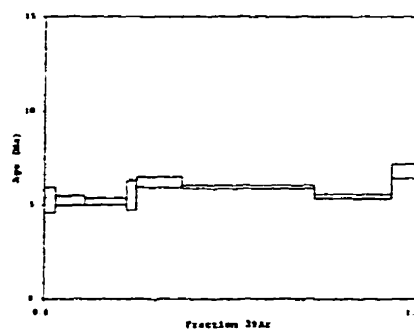
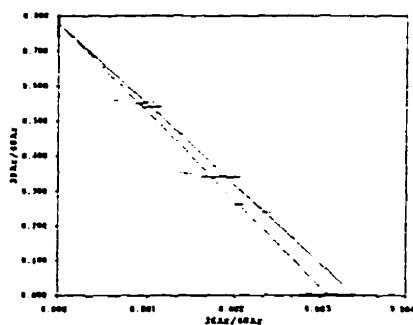
Volume 39Ar: 348.41 x 1E-10 cm3 NTP Approx. 2.13% K  
Integrated Age: 5.86 ± 0.07 Ma 0.09% Ca

Initial 40/36: 324.81 ± 32.29 (MSWD = 1.83, isochron between 0.00 and 3.00)  
Correlation Age: 5.33 ± 0.24 Ma ( 43.0% of 39Ar, steps marked by > )

Plateau Age: 5.42 ± 0.11 Ma ( 44.8% of 39Ar, steps marked by < )

Power	36Ar/40Ar	39Ar/40Ar	F	Ca/K	%40Ar	%39Ar	40Ar*/39K	Age
<1000	0.00235914±0.00013274	0.238264±0.001825	0.015	0.04	68.98	2.91	1.273±0.165	5.23±0.69
<2000>	0.00103690 0.00000000	0.540679 0.000000	0.010	0.04	29.96	7.76	1.293 0.064	5.27 0.26
<6000	0.00099796 0.00000000	0.554409 0.000000	0.013	0.04	28.80	11.16	1.272 0.043	5.23 0.18
<8000>	0.00182926 0.00011389	0.342424 0.001413	0.016	0.04	53.01	2.53	1.350 0.197	5.55 0.81
1000>	0.00203904 0.00000000	0.261571 0.000000	0.020	0.04	59.56	12.25	1.521 0.063	6.25 0.26
2000	0.00062262 0.00000001	0.559362 0.000000	0.024	0.04	17.98	35.42	1.459 0.018	6.03 0.07
<4500>	0.00090180 0.00000000	0.550052 0.000000	0.018	0.04	26.05	20.48	1.334 0.028	5.48 0.11
7000	0.00142020 0.00000000	0.350235 0.000000	0.024	0.04	41.24	7.49	1.660 0.093	6.82 0.38

Power	40Ar	39Ar	38Ar	37Ar	36Ar	Blank 40Ar	Atmos 40/36
<1000	43.62±0.10	10.30±0.07	0.28±0.01	0.032±0.00	0.153±0.01	0.664±0.02	293.80±1.00
<2000>	51.81 0.11	27.33 0.10	0.46 0.01	0.033±0.00	0.103±0.01	0.661±0.02	293.80±1.00
<6000	72.44 0.13	39.26 0.11	0.67 0.02	0.034±0.00	0.124±0.01	0.674±0.02	293.80±1.00
<8000>	26.81 0.11	8.99 0.06	0.44 0.02	0.035±0.00	0.103±0.01	0.703±0.02	293.80±1.00
1000>	165.59 0.23	43.10 0.15	1.00 0.02	0.041±0.00	0.403±0.01	0.666±0.04	293.80±1.00
2000	226.43 0.32	124.39 0.31	1.81 0.03	0.044±0.00	0.205±0.01	0.684±0.03	293.80±1.00
<4500>	133.38 0.23	71.99 0.18	1.13 0.02	0.044±0.00	0.185±0.01	0.696±0.03	293.80±1.00
7000	76.43 0.21	26.48 0.12	0.78 0.02	0.052±0.00	0.183±0.01	0.804±0.04	293.80±1.00



Measured volumes are x 1E-10 cm3 NTP. All errors are 2 x standard error.

# **FAR-324 Biotite (80-100 mesh)**

Run date: 1995/10/14  
Run: AS-40

Can/Pos: 141/45  
Mass: 7.0 mg

J Value: 0.002358  
= 0.000010

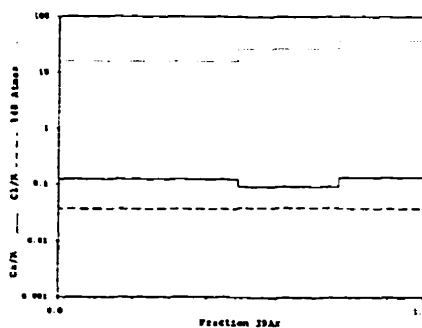
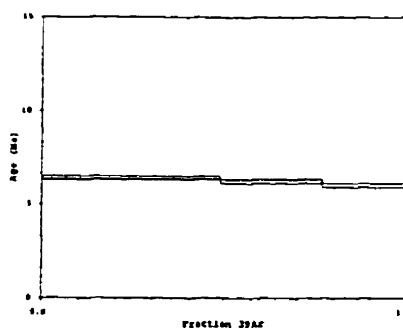
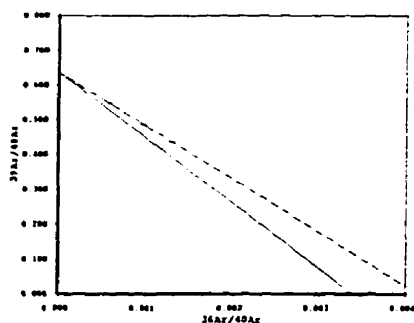
Volume 39Ar: 92.03 x 1E-10 cm3 NTP  
Integrated Age: 6.28 ± 0.06 Ma

Approx. 7.86% K  
0.92% Ca

Initial 40/36: 241.58 ± 1395.30 (MSWD = 0.30, isochron between -0.41 and 3.83)  
Correlation Age: 6.66 ± 11.46 Ma (100.0% of 39Ar, steps marked by >)

Power	36Ar/40Ar	39Ar/40Ar	ε	Ca/K	%40Ar	%39Ar	40Ar*/39K	Age
7000	0.00057945±0.00002828	0.549620±0.002414	0.002	0.12	16.38	48.57	1.515±0.017	6.43±0.07
7000	0.00096917 0.00000000	0.487313 0.000000	0.002	0.09	27.73	27.69	1.471 0.029	6.25 0.12
7000	0.00129593 0.00000000	0.438138 0.000000	0.003	0.13	37.31	23.74	1.415 0.027	6.01 0.11

Power	40Ar	39Ar	38Ar	37Ar	36Ar	Blank 40Ar	Atmos 40/36
7000	43.28±0.00	45.00±0.12	7.34±0.07	0.801±0.01	0.055±0.00	0.085±0.00	287.67±1.00
7000	53.44 0.00	25.66 0.11	4.75 0.04	0.348±0.00	0.058±0.00	0.085±0.00	287.67±1.00
7000	50.91 0.00	22.05 0.09	4.03 0.03	0.442±0.01	0.086±0.00	0.143±0.00	287.67±1.00



Measured volumes are x 1E-10 cm3 NTP. All errors are 2 x standard error.

# **FAR-324 Biotite (80-100 mesh)**

Run date: 1997/05/06 Can/Pos: 141/45 J Value: 0.002358  
 Run: JG-069 & JG-070 Mass: 400.0 mg = 0.000020

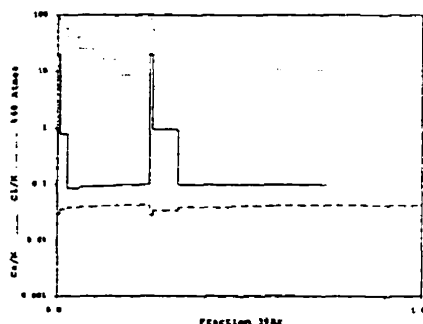
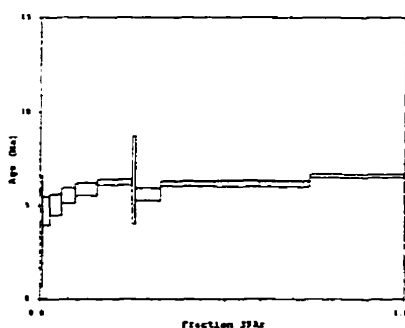
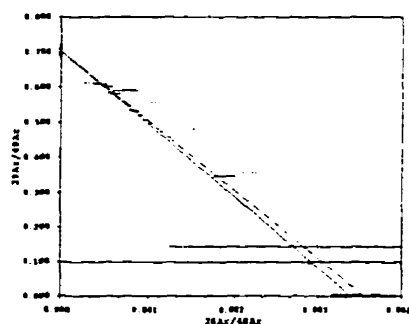
Volume 39Ar: 326.46 x 1E-10 cm3 NTP Approx. 0.49% K  
 Integrated Age: 6.24 ± 0.09 Ma 0.22% Ca

Initial 40/36: 281.99 ± 29.79 (MSWD = 0.99, isochron between 0.42 and 2.15)  
 Correlation Age: 6.04 ± 0.14 Ma ( 64.0% of 39Ar, steps marked by > )

Plateau Age: 6.30 ± 0.10 Ma ( 50.0% of 39Ar, steps marked by < )

Power	36Ar/40Ar	39Ar/40Ar	r	Ca/K	%40Atm	%39Ar	40Ar*/39K	Age
1000>	0.00299327±0.00176781	0.143146±0.005004	0.873	20.07	87.23	0.59	0.856±0.698	3.64±2.96
2000	0.00209984 0.00000000	0.355876 0.000000	0.029	0.79	59.05	2.07	1.126 0.187	4.73 0.78
3000	0.00151925 0.00000000	0.480437 0.000000	0.013	0.09	41.30	3.04	1.211 0.136	5.08 0.57
4000	0.00100934 0.00000196	0.556007 0.002045	0.010	0.09	25.54	3.77	1.329 0.096	5.57 0.41
6000>	0.00070750 0.00000000	0.590798 0.000000	0.007	0.09	16.47	5.58	1.407 0.078	5.90 0.33
<8000>	0.00044198 0.00000002	0.609479 0.000001	0.008	0.10	8.61	9.41	1.496 0.039	6.27 0.16
10000	0.00289345 0.00000000	0.098131 0.000000	0.992	19.96	84.71	0.89	1.523 0.566	6.39 2.38
2500>	0.00187702 0.00000000	0.345938 0.000000	0.104	0.94	52.72	6.30	1.345 0.090	5.64 0.33
<4000>	0.00081969 0.00000000	0.534745 0.000000	0.016	0.10	20.29	14.55	1.482 0.035	6.22 0.15
<5500>	0.00059150 0.00000979	0.583728 0.000367	0.012	0.10	13.18	12.17	1.482 0.044	6.22 0.18
<7000>	0.00051690 0.00000749	0.602213 0.000339	0.008	0.10	10.76	13.89	1.477 0.035	6.20 0.15

Power	40Ar	39Ar	38Ar	37Ar	36Ar	Blank 40Ar	Atmos 40/36
1000>	13.84±0.07	2.00±0.03	0.31±0.01	0.018±0.00	0.078±0.00	0.354±0.02	294.57±1.00
2000	19.65 0.07	6.86 0.06	1.21 0.02	0.018±0.00	0.074±0.00	0.355±0.02	294.57±1.00
3000	21.45 0.08	10.05 0.06	1.87 0.02	0.018±0.00	0.065±0.00	0.351±0.02	294.57±1.00
4000	22.99 0.08	12.41 0.08	2.34 0.03	0.018±0.00	0.057±0.00	0.357±0.02	294.57±1.00
6000>	31.96 0.10	19.37 0.11	3.62 0.04	0.018±0.00	0.057±0.00	0.358±0.02	294.57±1.00
<8000>	52.03 0.12	30.93 0.16	6.18 0.07	0.018±0.00	0.056±0.00	0.352±0.02	294.57±1.00
10000	29.52 0.09	2.95 0.03	0.44 0.01	0.026±0.00	0.132±0.01	0.365±0.02	294.57±1.00
2500>	66.38 0.17	22.70 0.12	3.83 0.04	0.027±0.00	0.169±0.01	0.367±0.02	294.57±1.00
<4000>	91.17 0.13	47.81 0.23	8.99 0.09	0.027±0.00	0.119±0.01	0.383±0.02	294.57±1.00
<5500>	70.11 0.18	40.01 0.19	7.85 0.08	0.030±0.00	0.097±0.01	0.403±0.02	294.57±1.00
<7000>	77.60 0.15	45.66 0.22	9.24 0.09	0.031±0.00	0.086±0.01	0.417±0.02	294.57±1.00



Measured volumes are x 1E-10 cm3 NTP. All errors are 2 x standard error.

# FAR-324 Biotite (80-100 mesh)

Run date: 1997/05/06  
Run: AS-40, JG-069 & JG-070

Can/Pes: 141/45  
Mass: 300.0 mg

J Value: 0.002358  
± 0.000010

Volume 39Ar: 418.50 x 1E-10 cm3 NTP  
Integrated Age: 6.25 ± 0.06 Ma

Approx. 0.83% K  
0.32% Ca

Initial 40/36: 291.84 ± 89.20 (MSWD = 18.90, isochron between 0.53 and 1.94)  
Correlation Age: 6.01 ± 0.53 Ma ( 71.9% of 39Ar, steps marked by > )

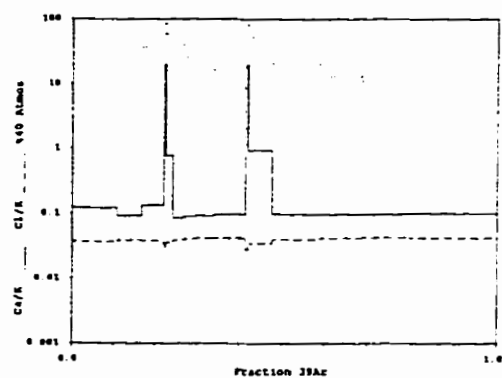
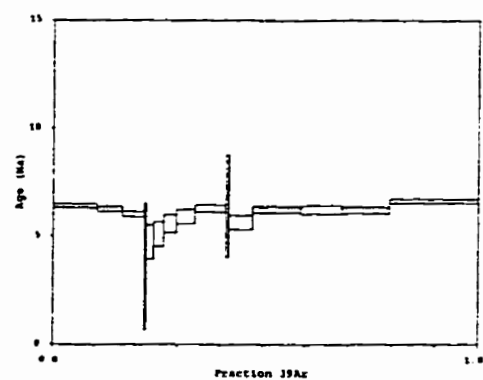
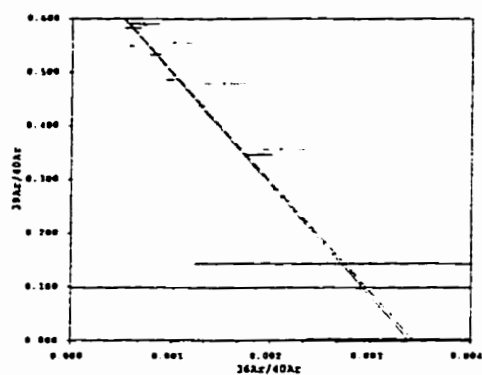
Plateau Age: 6.29 ± 0.06 Ma ( 61.0% of 39Ar, steps marked by < )

Power	36Ar/40Ar	39Ar/40Ar	r	Ca/K	%40Ar	%39Ar	40Ar*/39K	Age
<7000>	0.00057945±0.00002828	0.549620±0.002414	0.092	0.12	16.38	10.68	1.515±0.017	6.43±0.0
<7000>	0.00096917 0.00000000	0.487313 0.000000	0.092	0.09	27.73	6.09	1.471 0.028	6.25 0.1
<7000>	0.00129593 0.00000000	0.438138 0.000000	0.003	0.13	37.31	5.22	1.415 0.027	6.01 0.1
1000>	0.00299327 0.00088391	0.143146 0.002502	0.879	20.07	87.23	0.46	0.956 0.698	3.59 2.9
2000	0.00209984 0.00000000	0.355876 0.000000	0.029	0.79	59.05	1.62	1.126 0.187	4.73 0.7
3000	0.00151926 0.00000005	0.480437 0.000001	0.013	0.09	41.00	2.38	1.211 0.136	5.09 0.5
4000	0.00100934 0.00000000	0.556007 0.000000	0.010	0.09	25.54	2.94	1.329 0.098	5.57 0.4
6000>	0.00070750 0.00000000	0.590798 0.000000	0.007	0.09	16.47	4.35	1.407 0.078	5.90 0.3
<8000>	0.00044198 0.00000000	0.609479 0.000000	0.008	0.10	8.61	7.34	1.496 0.029	6.27 0.1
1000>	0.00289365 0.00020515	0.098131 0.000531	0.992	19.96	84.71	0.69	1.523 0.568	6.39 2.3
2500>	0.00187702 0.00000787	0.345938 0.000125	0.104	0.94	52.72	5.38	1.345 0.080	5.64 0.3
<4000>	0.00081969 0.00000308	0.534745 0.000140	0.016	0.10	20.29	11.35	1.482 0.035	6.22 0.1
<5500>	0.00059150 0.00000979	0.583728 0.000367	0.012	0.10	13.18	9.49	1.452 0.044	6.22 0.1
<7000>	0.00051690 0.00000749	0.602213 0.000339	0.008	0.10	10.76	10.83	1.477 0.035	6.20 0.1
8000	0.00026919 0.00001468	0.611330 0.000374	0.093	0.10	3.59	21.18	1.575 0.023	6.61 0.1

Power	40Ar	39Ar	38Ar	37Ar	36Ar	Blank 40Ar	Atmos 40/3
<7000>	83.28±0.00	45.00±0.19	7.94±0.07	0.801±0.01	0.055±0.00	0.085±0.00	287.67±1.0
<7000>	53.44 0.00	25.66 0.11	4.75 0.04	0.348±0.00	0.056±0.00	0.085±0.00	287.67±1.0
<7000>	50.91 0.00	22.05 0.09	4.03 0.03	0.442±0.01	0.086±0.00	0.143±0.00	287.67±1.0
1000>	13.84 0.07	2.00 0.03	0.31 0.01	0.018±0.00	0.078±0.00	0.354±0.02	284.57±1.0
2000	19.65 0.07	6.66 0.06	1.21 0.02	0.018±0.00	0.074±0.00	0.355±0.02	284.57±1.0
3000	21.45 0.08	10.05 0.06	1.87 0.03	0.018±0.00	0.065±0.00	0.351±0.02	284.57±1.0
4000	22.98 0.08	12.41 0.08	2.39 0.03	0.018±0.00	0.057±0.00	0.357±0.02	284.57±1.0
6000>	31.96 0.10	19.37 0.11	3.62 0.04	0.018±0.00	0.057±0.00	0.358±0.02	284.57±1.0
<8000>	52.03 0.12	30.93 0.16	6.18 0.07	0.018±0.00	0.056±0.00	0.352±0.02	284.57±1.0
1000>	29.52 0.09	2.95 0.03	0.44 0.01	0.026±0.00	0.132±0.01	0.365±0.02	284.57±1.0
2500>	66.38 0.17	22.70 0.12	3.83 0.04	0.027±0.00	0.169±0.01	0.367±0.02	284.57±1.0
<4000>	91.17 0.19	47.81 0.23	8.99 0.09	0.028±0.00	0.119±0.01	0.383±0.02	284.57±1.0
<5500>	70.11 0.18	40.01 0.19	7.85 0.06	0.030±0.00	0.087±0.01	0.403±0.02	284.57±1.0
<7000>	77.60 0.15	45.66 0.22	9.24 0.09	0.031±0.00	0.086±0.01	0.417±0.02	284.57±1.0
8000	149.16 0.32	89.20 0.42	17.78 0.16	0.036±0.00	0.092±0.01	0.463±0.03	284.57±1.0

Measured volumes are x 1E-10 cm3 NTP. All errors are 2 x standard error.

# FAR-324 Biotite (80-100 mesh)



Measured volumes are x 1E-10 cm<sup>3</sup> NTP. All errors are 2 x standard error.

# **FAR-325 Alunite (45-60 mesh)**

Run date: 1996/10/24 Can/Pos: 142/4 J Value: 0.002345  
Run: AS-207 Mass: 100.0 mg ± 0.000012

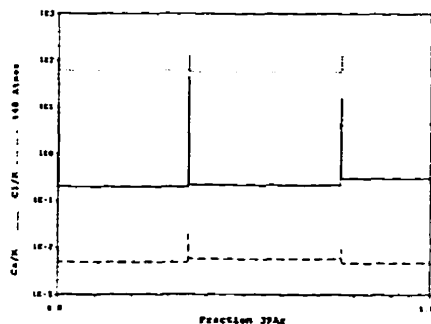
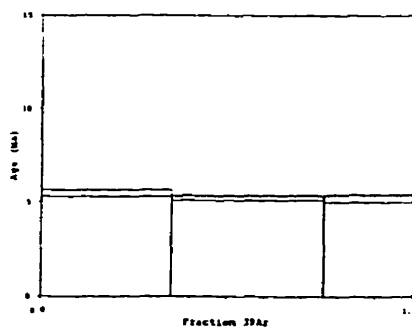
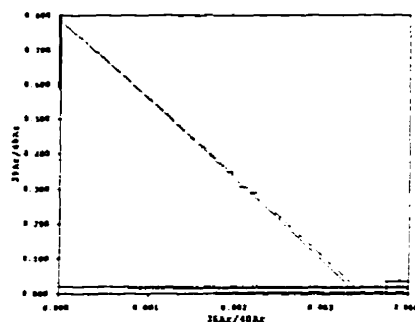
Volume 39Ar: 81.60 x 1E-10 cm3 NTP Approx. 0.49% K  
Integrated Age: 5.01 ± 0.12 Ma 0.18% Ca

Initial 40/36: 289.53 ± 141.25 (MSWD = 5.34, isochron between 0.29 and 2.41)  
Correlation Age: 5.36 ± 1.33 Ma (100.0% of 39Ar, steps marked by >)

Plateau Age: 5.34 ± 0.10 Ma ( 99.38 of 39Ar, steps marked by <)

Power	36Ar/40Ar	39Ar/40Ar	z	Ca/K	40Ar	39Ar	40Ar/39K	Age
400	0.00373480±0.00589097	0.019830±0.015053	0.995	11.29	110.26	0.10	-5.219±8.142	-22.22±34.87
<7000	0.00204212 0.00000000	0.105113 0.000000	0.008	0.20	59.47	14.74	1.304 0.040	5.51 0.17
500	0.00438504 0.00000000	0.014072 0.000000	0.996	44.86	129.48	0.12	-21.003 5.970	-91.12 26.57
<7000	0.00191579 0.00001943	0.149535 0.000705	0.007	0.21	55.64	40.49	1.246 0.033	5.26 0.14
500	0.00439698 0.00000000	0.035480 0.000000	0.752	15.95	129.71	0.47	-8.428 1.587	-36.01 6.85
<7000	0.00218356 0.00000001	0.298190 0.000000	0.007	0.30	63.65	24.07	1.235 0.048	5.22 0.20

Power	40Ar	39Ar	38Ar	37Ar	36Ar	Blank 40Ar	Atmos 40/36
400	4.31±0.00	0.09±0.00	0.01±0.00	0.008±0.00	0.022±0.00	0.132±0.00	294.57±1.00
<7000	94.22 0.00	23.56 0.11	1.07 0.01	0.013±0.00	0.204±0.00	0.137±0.00	294.57±1.00
500	7.00 0.00	0.10 0.00	0.02 0.00	0.012±0.00	0.038±0.00	0.132±0.00	294.57±1.00
<7000	96.04 0.00	33.29 0.13	1.34 0.01	0.015±0.00	0.195±0.00	0.137±0.00	294.57±1.00
500	11.00 0.00	0.40 0.00	0.03 0.01	0.014±0.00	0.054±0.00	0.133±0.00	294.57±1.00
<7000	69.10 0.00	12.79 0.08	0.73 0.01	0.014±0.00	0.162±0.00	0.136±0.00	294.57±1.00



Measured volumes are x 1E-10 cm3 NTP. All errors are 2 x standard error.

# **FAR-325 Alunite (45-60 mesh)**

Run date: 1997/05/06 Can/Pos: 142/4 J Value: 0.002345  
 Run: JG-071 & JG-072 Mass: 2008.0 mg ± 0.000014

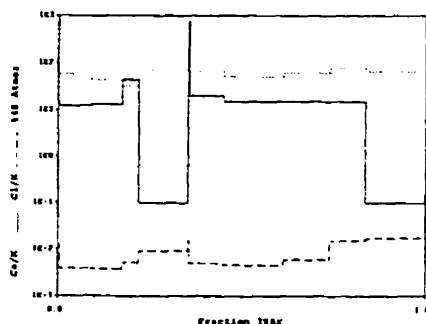
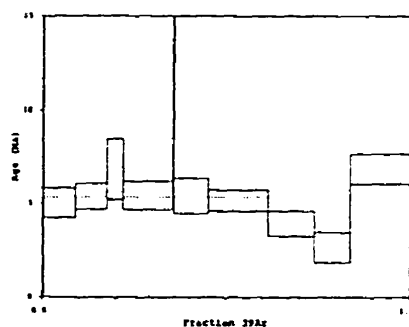
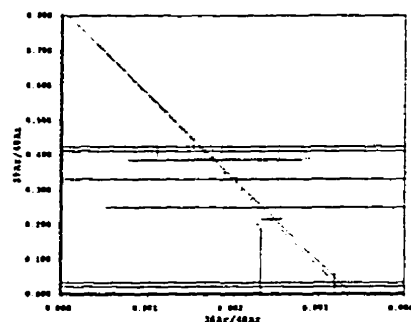
Volume 39Ar: 77.99 x 1E-10 cm<sup>3</sup> NTP Approx. 0.02% K  
 Integrated Age: 5.41 ± 0.29 Ma 0.31% Ca

Initial 40/36: 301.61 ± 7028.89 (MSWD = 0.01, isochron between 0.42 and 2.15)  
 Correlation Age: 5.18 ± 71.14 Ma ( 60.6% of 39Ar, steps marked by >)

Plateau Age: 5.37 ± 0.34 Ma ( 55.78 of 39Ar, steps marked by <)

Power	36Ar/40Ar	39Ar/40Ar	r	Ca/K	%40Ar	%39Ar	40Ar*/39K	Age
500>	0.0031833±0.01146189	0.032645±0.029436	0.996	15.03	93.88	0.28	1.834±5.399	7.74±22.75
<1000>	0.00202836 0.00000000	0.331413 0.000000	0.942	11.85	58.95	8.62	1.214 0.192	5.05 0.80
<1500>	0.00152701 0.00000000	0.424772 0.000000	0.891	13.31	44.13	8.42	1.297 0.163	5.33 0.68
2000>	0.00109581 0.00330639	0.412023 0.008978	0.954	44.22	31.56	4.36	1.648 0.393	6.25 1.63
<7500>	0.00243744 0.00000000	0.216113 0.000000	0.014	0.10	71.13	13.28	1.306 0.183	5.43 0.76
500>	0.00232153 0.00001653	0.022018 0.000042	1.000	787.91	68.49	0.26	14.281 8.015	58.46 32.30
<1000>	0.00228864 0.00000000	0.249636 0.000000	0.909	20.04	66.77	9.20	1.303 0.228	5.42 0.95
<1700>	0.00174952 0.00000000	0.385648 0.000000	0.674	15.11	51.24	16.17	1.243 0.136	5.17 0.56
3000	0.00213970 0.00000000	0.390973 0.000000	0.527	15.00	61.91	12.47	0.948 0.160	3.94 0.66
6000	0.00268838 0.00006655	0.331721 0.000330	0.473	14.95	77.71	9.73	0.640 0.196	3.66 0.81
8000	0.00228480 0.00001421	0.199288 0.000177	0.026	0.10	66.51	17.21	1.653 0.194	6.57 0.81

Power	40Ar	39Ar	38Ar	37Ar	36Ar	Blank 40Ar	Atmos 40/36
500>	6.92±0.01	0.24±0.01	0.03±0.01	0.012±0.00	0.040±0.00	0.290±0.02	284.57±1.00
<1000>	20.78 0.08	6.79 0.05	0.23 0.01	0.014±0.00	0.371±0.00	0.293±0.02	284.57±1.00
<1500>	15.97 0.07	6.63 0.06	0.22 0.01	0.014±0.00	0.055±0.00	0.305±0.02	284.57±1.00
2000>	8.57 0.05	3.45 0.04	0.15 0.01	0.019±0.00	0.053±0.00	0.312±0.02	284.57±1.00
<7500>	48.69 0.16	10.45 0.30	0.60 0.02	0.016±0.00	0.148±0.01	0.346±0.02	284.57±1.00
500>	7.41 0.06	0.24 0.03	0.04 0.01	0.019±0.00	0.061±0.00	0.351±0.02	284.57±1.00
<1000>	29.21 0.10	7.26 0.05	0.30 0.01	0.020±0.00	0.115±0.01	0.363±0.02	284.57±1.00
<1700>	33.42 0.11	12.73 0.08	0.47 0.01	0.023±0.00	0.116±0.01	0.363±0.02	284.57±1.00
3000	25.54 0.07	9.84 0.06	0.44 0.01	0.023±0.00	0.110±0.01	0.369±0.02	284.57±1.00
6000	23.49 0.07	7.70 0.06	0.66 0.01	0.025±0.00	0.117±0.00	0.420±0.02	284.57±1.00
8000	68.45 0.22	13.58 0.10	1.23 0.03	0.028±0.00	0.202±0.01	0.541±0.04	284.57±1.00



Measured volumes are x 1E-10 cm<sup>3</sup> NTP. All errors are 2 x standard error.

# **FAR-325 Alunite (45-60 mesh)**

Run date: 1997/05/06  
Run: AS-207, JG-071 & JG-072

Can/Pos: 142/4  
Mass: 500.0 mg

J Value: 0.002345  
: 0.000012

Volume 39Ar: 159.59 x 1E-10 cm3 NTP  
Integrated Age: 5.20 ± 0.16 Ma

Approx. 0.19% K  
1.28% Ca

Initial 40/36: 300.22 ± 66.97 (MSWD = 1.00, isochron between 0.53 and 1.94)  
Correlation Age: 5.11 ± 0.60 Ma ( 80.4% of 39Ar, steps marked by > )

Plateau Age: 5.35 ± 0.14 Ma ( 78.0% of 39Ar, steps marked by < )

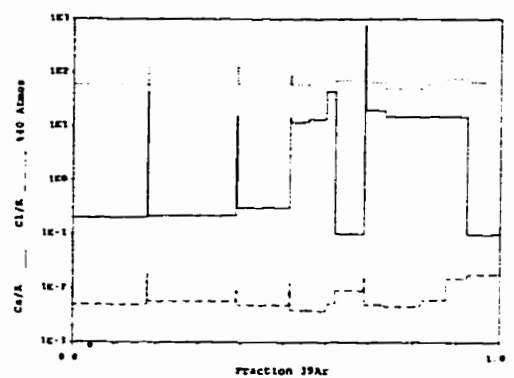
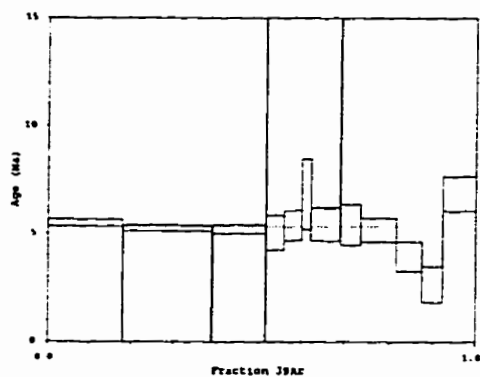
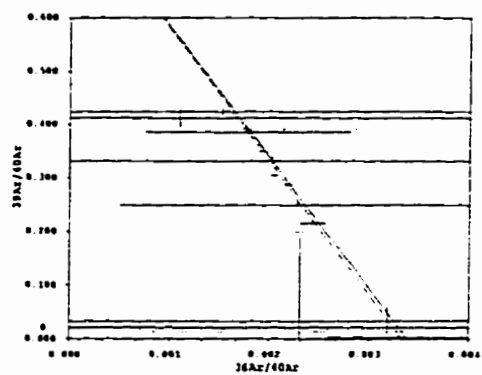
Power	36Ar/40Ar	39Ar/40Ar	r	Ca/K	%40Atm	%39Ar	40Ar*/39K	Age
400	0.00373480±0.00589097	0.019830±0.015053	0.995	11.29	110.26	0.05	-5.219±8.142	-22.22±34.8
<7000>	0.00204212 0.00000000	0.105113 0.000000	0.008	9.20	59.47	17.76	1.304 0.040	5.51 0.1
500	0.00438504 0.00000000	0.014072 0.000000	0.996	44.86	129.48	0.06	-21.003 5.570	-91.12 26.5
<7000>	0.00191579 0.00001943	0.349535 0.000705	0.007	0.21	55.64	20.70	1.246 0.033	5.26 0.1
500	0.00439696 0.00000000	0.035480 0.000000	0.952	15.95	129.71	0.24	-8.428 1.567	-36.01 6.8
<7000>	0.00218356 0.00000001	0.288199 0.000000	0.009	0.30	63.65	12.31	1.235 0.048	5.22 0.2
500	0.00318331 0.00000000	0.032645 0.000000	0.996	15.03	93.88	0.14	1.834 5.399	7.62 22.3
<1000>	0.00202836 0.00000000	0.331413 0.000000	0.942	11.85	56.95	4.21	1.214 0.192	5.05 0.8
<1500>	0.00152701 0.00000000	0.424772 0.000000	0.891	13.31	44.13	4.12	1.297 0.163	5.39 1.6
2000	0.00109583 0.00037693	0.412023 0.001023	0.954	44.22	31.56	2.13	1.648 0.393	6.85 1.6
<7500>	0.00243744 0.00001222	0.216113 0.000591	0.014	0.10	71.13	6.49	1.306 0.183	5.43 0.7
500	0.00232153 0.00320755	0.022018 0.008223	1.000	787.91	68.49	0.12	14.281 6.015	58.46 32.3
<1000>	0.00228664 0.00016041	0.249636 0.000452	0.909	20.04	66.77	4.50	1.303 0.228	5.42 0.9
<1700>	0.00176952 0.00005307	0.385648 0.000200	0.674	15.11	51.24	7.90	1.243 0.136	5.17 0.5
3000	0.00213970 0.00005890	0.390973 0.000270	1.527	15.00	61.91	6.10	0.948 0.160	3.94 0.6
6000	0.00268838 0.00006655	0.331721 0.000330	0.473	14.95	77.71	4.75	0.640 0.190	2.66 0.8
8000	0.00228480 0.00001421	0.199288 0.000177	0.026	0.10	66.51	8.41	1.653 0.194	6.87 0.8

Power	40Ar	39Ar	38Ar	37Ar	36Ar	Blank 40Ar	Atmos 40/3
400	4.31±0.00	0.09±0.00	0.01±0.00	0.008±0.00	0.022±0.00	0.132±0.00	284.57±1.0
<7000>	94.22 0.00	28.56 0.11	1.07 0.01	0.013±0.00	0.204±0.00	0.137±0.00	284.57±1.0
500	7.00 0.00	0.10 0.00	0.02 0.00	0.012±0.00	0.038±0.00	0.132±0.00	284.57±1.0
<7000>	96.04 0.00	33.29 0.13	1.34 0.01	0.015±0.00	0.195±0.00	0.137±0.00	284.57±1.0
500	11.00 0.00	0.40 0.00	0.02 0.01	0.014±0.00	0.056±0.00	0.133±0.00	284.57±1.0
<7000>	69.10 0.00	19.79 0.09	0.73 0.01	0.014±0.00	0.162±0.00	0.136±0.00	284.57±1.0
500	6.92 0.07	0.24 0.01	0.03 0.01	0.012±0.00	0.040±0.00	0.290±0.02	284.57±1.0
<1000>	20.78 0.08	6.79 0.05	0.23 0.01	0.014±0.00	0.071±0.00	0.293±0.02	284.57±1.0
<1500>	15.97 0.07	6.63 0.06	0.22 0.01	0.014±0.00	0.055±0.00	0.305±0.02	284.57±1.0
2000	8.57 0.05	3.45 0.04	0.15 0.01	0.019±0.00	0.053±0.00	0.312±0.02	284.57±1.0
<7500>	48.69 0.16	10.45 0.30	0.60 0.02	0.016±0.00	0.148±0.01	0.346±0.02	284.57±1.0
500	7.41 0.06	0.24 0.03	0.04 0.01	0.019±0.00	0.061±0.00	0.351±0.02	284.57±1.0
<1000>	29.21 0.10	7.26 0.05	0.30 0.01	0.020±0.00	0.115±0.01	0.363±0.02	284.57±1.0
<1700>	13.42 0.11	12.73 0.08	0.47 0.01	0.023±0.00	0.116±0.01	0.363±0.02	284.57±1.0
3000	25.54 0.07	9.84 0.06	0.44 0.01	0.023±0.00	0.110±0.01	0.389±0.02	284.57±1.0
6000	23.49 0.07	7.70 0.06	0.66 0.01	0.025±0.00	0.117±0.00	0.420±0.02	284.57±1.0
8000	66.45 0.22	13.58 0.10	1.29 0.03	0.028±0.00	0.202±0.01	0.541±0.04	284.57±1.0

Measured volumes are x 1E-10 cm3 NTP. All errors are 2 x standard error.



**FAR-325 Alunite (45-60 mesh)**



Measured volumes are  $\times 10^{-10}$  cm<sup>3</sup> NTP. All errors are 2 x standard error.

# **FAR-327 Biotite (45-80 mesh)**

Run date: 1995/10/16  
Run: AS-41 & AS-133

Can/Eos: 141/47  
Mass: 5.4 mg

J Value: 0.002357  
± 0.000010

Volume 39Ar: 72.09 x 1E-10 cm<sup>3</sup> NTP  
Integrated Age: 12.21 ± 0.18 Ma

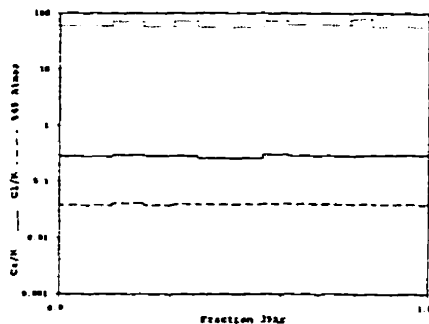
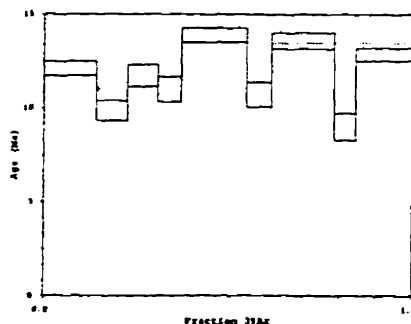
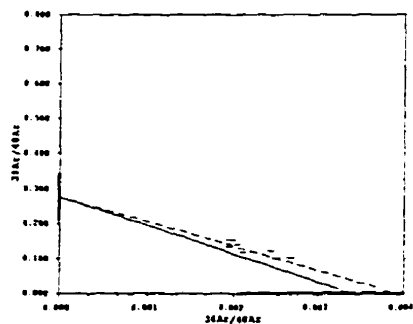
Approx. 7.99% K  
2.28% Ca

Initial 40/36: 555.50 ± 120.87 (MSWD = 40.26, isochron between 0.47 and 2.07)  
Correlation Age: 15.35 ± 3.52 Ma (100.0% of 39Ar, steps marked by >)

Plateau Age: 13.44 ± 0.24 Ma ( 50.78 of 39Ar, steps marked by <)

Power	36Ar/40Ar	39Ar/40Ar	r	Ca/K	%40Ar	%39Ar	40Ar*/39K	Age
7000	0.00201987±0.00004106	0.139531±0.000604	0.001	0.28	59.84	13.96	2.854±0.090	12.09±0.38
300	0.00242396 0.00000000	0.122790 0.000000	0.001	0.29	71.17	8.32	2.318 0.125	9.83 0.53
7000	0.00196067 0.00000000	0.152682 0.000000	0.001	0.29	57.47	8.13	2.762 0.137	11.71 0.58
300	0.00249311 0.00002679	0.102254 0.000221	0.001	0.29	73.23	6.36	2.588 0.158	10.97 0.67
<7000	0.00191931 0.00000000	0.132688 0.000000	0.001	0.26	56.23	17.39	3.275 0.087	13.87 0.37
300	0.00250303 0.00000001	0.103761 0.000000	0.001	0.30	73.51	6.61	2.522 0.155	10.69 0.66
<7000	0.00210259 0.00000000	0.118633 0.000000	0.001	0.29	61.67	17.05	3.205 0.102	13.58 0.43
300	0.00266243 0.00000000	0.101045 0.000000	0.001	0.29	78.21	5.97	2.123 0.169	9.01 0.72
<7000	0.00194048 0.00000000	0.141393 0.000000	0.001	0.29	56.83	16.22	3.030 0.083	12.84 0.35

Power	40Ar	39Ar	38Ar	37Ar	36Ar	Blank 40Ar	Atmos 40/36
7000	72.62±0.00	10.15±0.04	1.86±0.02	0.423±0.01	0.160±0.00	0.105±0.00	287.67±1.00
300	49.19 0.00	6.06 0.03	1.20 0.01	0.266±0.00	0.130±0.00	0.104±0.00	287.67±1.00
7000	38.84 0.00	5.95 0.03	1.11 0.01	0.265±0.00	0.094±0.00	0.201±0.00	287.67±1.00
300	45.08 0.00	4.63 0.02	0.89 0.01	0.072±0.00	0.122±0.00	0.078±0.00	287.67±1.00
<7000	95.09 0.00	12.63 0.05	2.39 0.02	0.164±0.00	0.195±0.00	0.091±0.00	287.67±1.00
300	46.18 0.00	4.81 0.02	0.95 0.01	0.077±0.00	0.125±0.00	0.078±0.00	287.67±1.00
<7000	104.17 0.00	12.38 0.05	2.41 0.02	0.174±0.00	0.231±0.00	0.079±0.00	287.67±1.00
300	42.83 0.00	4.34 0.02	0.84 0.01	0.068±0.00	0.123±0.00	0.078±0.00	287.67±1.00
<7000	81.27 0.00	11.78 0.05	2.22 0.02	0.170±0.00	0.172±0.00	0.077±0.00	287.67±1.00



Measured volumes are x 1E-10 cm<sup>3</sup> NTP. All errors are 2 x standard error.

# **FAR-327 Biotite (45-80 mesh)**

Run date: 1997/05/06  
Run: JG-065 & JG-066

Can/Pos: 141/47  
Mass: 15.0 mg

J Value: 0.002357  
± 0.000020

Volume 39Ar: 70.53 x 1E-10 cm<sup>3</sup> NTP  
Integrated Age: 9.87 ± 0.42 Ma

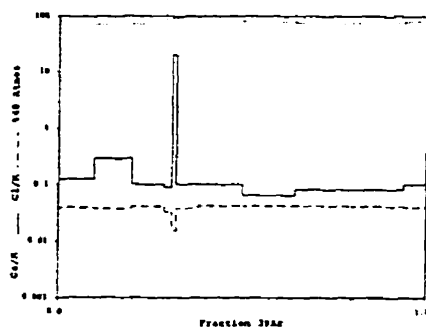
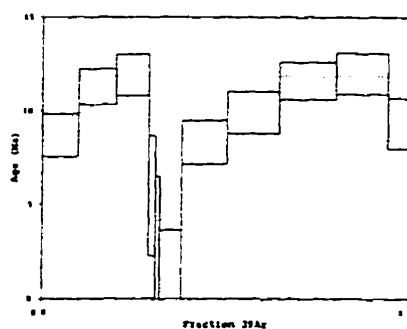
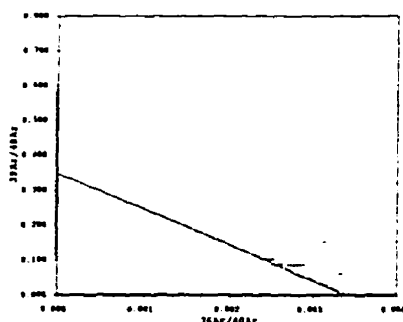
Approx. 2.81% K  
0.95% Ca

Initial 40/36: 290.98 ± 337.33 (MSWD = 0.84, isochron between 0.00 and 3.00)  
Correlation Age: 12.20 ± 8.35 Ma (49.1% of 39Ar, steps marked by >)

Plateau Age: 11.84 ± 0.56 Ma (48.1% of 39Ar, steps marked by <)

Power	36Ar/40Ar	39Ar/40Ar	ε	Ca/K	%40Ar	%39Ar	40Ar*/39K	Age
1000	0.00277633±0.00008014	0.088589±0.000737	0.044	0.12	81.55	9.63	2.049±0.270	8.69±1.14
<2000>	0.00245680 0.00000000	0.103925 0.000000	0.042	0.29	71.70	9.96	2.693 0.226	11.29 0.94
<3000>	0.00243357 0.00000000	0.100902 0.000000	0.018	0.10	71.00	8.76	2.844 0.267	11.91 1.11
4000	0.00301061 0.00011383	0.087810 0.000782	0.017	0.09	88.21	1.94	1.306 0.766	5.48 3.21
7000	0.00312520 0.00000000	0.151397 0.000000	0.951	20.07	91.44	1.14	0.528 1.029	2.22 4.32
500	0.00331792 0.00000003	0.061774 0.000000	0.023	0.10	97.44	5.82	0.374 0.498	1.57 2.09
1000	0.00281107 0.00000000	0.088505 0.000000	0.043	0.10	82.16	12.20	1.982 0.278	8.31 1.16
1700	0.00271057 0.00000000	0.086718 0.000000	0.031	0.07	79.22	14.21	2.363 0.266	9.90 1.11
<2500>	0.00255571 0.00000000	0.090577 0.000000	0.028	0.08	74.61	15.47	2.772 0.240	11.61 1.00
<3500>	0.00255645 0.00001162	0.087582 0.000106	0.020	0.08	74.67	13.96	2.861 0.261	11.98 1.09
8000	0.00276982 0.00001200	0.084006 0.000093	0.036	0.10	81.02	6.91	2.226 0.322	9.33 1.35

Power	40Ar	39Ar	38Ar	37Ar	36Ar	Blank 40Ar	Atmos 40/36
1000	77.16±0.24	6.86±0.05	1.33±0.02	0.017±0.00	0.231±0.01	0.192±0.01	284.57±1.00
<2000>	88.05 0.15	7.08 0.05	1.33 0.02	0.013±0.00	0.187±0.01	0.197±0.01	284.57±1.00
<3000>	61.69 0.13	6.23 0.05	1.24 0.02	0.013±0.00	0.172±0.01	0.206±0.01	284.57±1.00
4000	15.89 0.07	1.40 0.02	0.24 0.01	0.014±0.00	0.068±0.00	0.213±0.01	284.57±1.00
7000	5.52 0.03	0.83 0.01	0.03 0.01	0.013±0.00	0.038±0.00	0.203±0.01	284.57±1.00
500	66.85 0.12	4.15 0.04	0.81 0.02	0.013±0.00	0.247±0.01	0.238±0.02	284.57±1.00
1000	37.79 0.12	8.67 0.07	1.19 0.03	0.014±0.00	0.306±0.01	0.246±0.02	284.57±1.00
1700	116.22 0.31	10.10 0.06	1.07 0.03	0.016±0.00	0.352±0.01	0.269±0.02	284.57±1.00
<2500>	121.22 0.23	11.01 0.08	1.28 0.03	0.018±0.00	0.349±0.01	0.300±0.02	284.57±1.00
<3500>	113.15 0.23	9.34 0.04	2.03 0.03	0.019±0.00	0.330±0.01	0.314±0.02	284.57±1.00
8000	58.57 0.12	4.95 0.04	0.35 0.02	0.019±0.00	0.199±0.01	0.327±0.02	284.57±1.00



Measured volumes are x 1E-10 cm<sup>3</sup> NTP. All errors are 2 x standard error.

# FAR-327 Biotite (45-80 mesh)

Run date: 1995/01/31 Can/Pos: 141/47 J Value: 0.002357  
 Run: AS-41, JS-133, JG-065 & JG-066 Mass: 10.0 mg ± 0.000010

Volume 39Ar: 142.62 x 1E-10 cm3 NTP Approx. 8.53% K  
 Integrated Age: 11.05 ± 0.24 Ma 2.65% Ca

Initial 40/36: 279.47 ± 79.32 (MSWD = 8.58, isochron between 0.37 and 2.26)  
 Correlation Age: 14.19 ± 2.05 Ma ( 49.4% of 39Ar, steps marked by > )

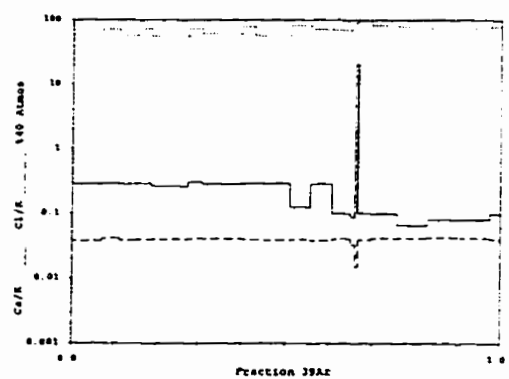
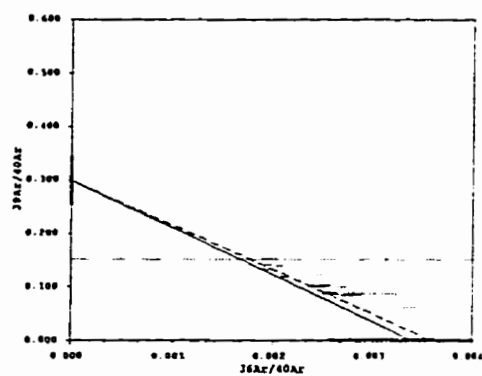
Plateau Age: 12.67 ± 0.30 Ma ( 49.4% of 39Ar, steps marked by < )

Power	36Ar/40Ar	39Ar/40Ar	F	Ca/K	40Ar <sub>atm</sub>	39Ar	40Ar*/39K	Age
7000	0.00203987±0.00004106	0.139531±0.0000604	0.001	0.23	59.84	7.05	2.854±0.090	12.09±0.3
300	0.00242396 0.00000000	0.122790 0.0000000	0.001	0.23	71.17	4.20	2.318 0.125	9.83 0.5
7000	0.00196067 0.00000000	0.152682 0.0000000	0.001	0.29	57.47	4.11	2.762 0.137	11.71 0.5
300	0.00249311 0.00002679	0.102254 0.000221	0.001	0.29	73.23	3.21	2.588 0.158	10.97 0.6
<7000>	0.00191931 0.00000000	0.132688 0.0000000	0.001	0.26	56.23	6.79	3.275 0.087	13.87 0.3
300	0.00250303 0.00000001	0.103761 0.0000000	0.001	0.30	73.51	3.34	2.522 0.155	10.69 0.6
<7000>	0.00210259 0.00000000	0.118633 0.0000000	0.001	0.29	61.67	8.62	3.205 0.102	11.58 0.4
300	0.00266243 0.00000000	0.101045 0.0000000	0.001	0.29	78.21	3.02	2.123 0.169	9.01 0.7
<7000>	0.00194048 0.00000000	0.141393 0.0000000	0.001	0.29	56.83	8.20	3.030 0.083	12.84 0.3
1000	0.00277633 0.00000593	0.089589 0.0000055	0.044	0.12	81.55	4.76	2.049 0.270	8.59 1.1
<2000>	0.00245680 0.00000506	0.103925 0.000048	0.042	0.23	71.70	4.92	2.693 0.226	11.28 0.9
<3000>	0.00243357 0.00000607	0.100902 0.000061	0.018	0.10	71.30	4.33	2.844 0.267	11.91 1.1
4000	0.00301061 0.00001366	0.087810 0.000094	0.017	0.09	88.21	0.96	1.306 0.766	5.48 3.2
7000	0.00312520 0.00003560	0.151397 0.0000949	0.951	20.37	91.44	0.56	0.528 1.029	2.22 4.3
500	0.00331792 0.00000636	0.061774 0.000042	0.023	0.10	97.44	2.68	0.374 0.498	1.57 2.0
1000	0.00281107 0.00000847	0.088505 0.000079	0.043	0.10	82.16	6.03	1.982 0.278	8.31 1.1
1700	0.00271057 0.00009466	0.086718 0.000044	0.031	0.07	79.22	7.03	2.363 0.266	9.90 1.1
<2500>	0.00255571 0.00000575	0.090577 0.000053	0.028	0.06	74.61	7.65	2.772 0.240	11.61 1.0
<3500>	0.00255645 0.00001162	0.087582 0.000106	0.020	0.08	74.67	6.90	2.861 0.261	11.98 1.0
8000	0.00276982 0.00001200	0.084006 0.000093	0.036	0.10	81.92	3.42	2.226 0.322	9.33 1.3

Power	40Ar	39Ar	38Ar	37Ar	36Ar	Blank 40Ar	Atmos 40/3
7000	72.62±0.00	10.15±0.04	1.86±0.02	0.423±0.01	0.160±0.00	0.105±0.00	287.67±1.0
300	49.19 0.00	6.06 0.03	1.20 0.01	0.266±0.00	0.136±0.00	0.104±0.00	287.67±1.0
7000	38.94 0.00	5.95 0.03	1.11 0.01	0.265±0.00	0.094±0.00	0.201±0.00	287.67±1.0
300	45.08 0.00	4.63 0.02	0.89 0.01	0.072±0.00	0.122±0.00	0.078±0.00	287.67±1.0
<7000>	95.09 0.00	12.63 0.05	2.39 0.02	0.164±0.00	0.195±0.00	0.091±0.00	287.67±1.0
300	46.18 0.00	4.81 0.02	0.95 0.01	0.077±0.00	0.125±0.00	0.078±0.00	287.67±1.0
<7000>	104.17 0.00	12.38 0.05	2.41 0.02	0.174±0.00	0.231±0.00	0.079±0.00	287.67±1.0
300	42.83 0.00	4.34 0.02	0.84 0.01	0.068±0.00	0.123±0.00	0.078±0.00	287.67±1.0
<7000>	83.27 0.00	11.78 0.05	2.22 0.02	0.170±0.00	0.172±0.00	0.077±0.00	287.67±1.0
1000	77.16 0.24	6.86 0.05	1.33 0.02	0.017±0.00	0.231±0.01	0.192±0.01	284.57±1.0
<2000>	68.05 0.15	7.08 0.05	1.33 0.02	0.013±0.00	0.187±0.01	0.197±0.01	284.57±1.0
<3000>	61.69 0.13	6.22 0.05	1.24 0.02	0.013±0.00	0.172±0.01	0.206±0.01	284.57±1.0
4000	15.36 0.07	1.40 0.02	0.24 0.01	0.014±0.00	0.068±0.00	0.213±0.01	284.57±1.0
7000	5.52 0.03	0.83 0.01	0.08 0.01	0.013±0.00	0.038±0.00	0.203±0.01	284.57±1.0
500	66.85 0.18	4.15 0.04	0.81 0.02	0.013±0.00	0.247±0.01	0.236±0.02	284.57±1.0
1000	97.79 0.32	8.67 0.07	1.79 0.03	0.014±0.00	0.306±0.01	0.246±0.02	284.57±1.0
1700	116.22 0.31	10.10 0.08	2.07 0.03	0.016±0.00	0.392±0.01	0.269±0.02	284.57±1.0
<2500>	121.22 0.29	11.01 0.08	2.28 0.03	0.018±0.00	0.349±0.01	0.300±0.02	284.57±1.0
<3500>	113.15 0.23	9.94 0.06	2.03 0.03	0.019±0.00	0.330±0.01	0.314±0.02	284.57±1.0
8000	58.57 0.18	4.95 0.04	0.98 0.02	0.019±0.00	0.199±0.01	0.327±0.02	284.57±1.0

Measured volumes are x 1E-10 cm3 NTP. All errors are 2 x standard error.

**FAR-327 Biotite (45-80 mesh)**



Measured volumes are  $\times 10^{-10}$  cm<sup>3</sup> NTP. All errors are 2  $\times$  standard error.

# **FAR-329 Sericite (45-60 mesh)**

Run date: 1995/11/22  
Run: AS-71

Can/Pos: 141/48  
Mass: 15.0 mg

J Value: 0.002357  
= 0.000010

Volume 39Ar: 176.77 x 1E-10 cm3 NTP  
Integrated Age: 339.38 ± 1.50 Ma

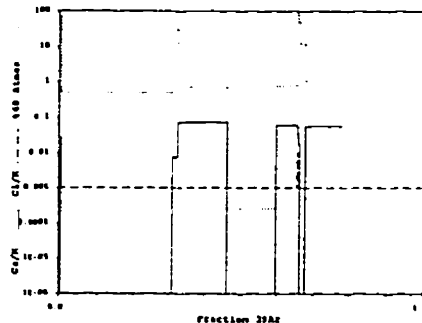
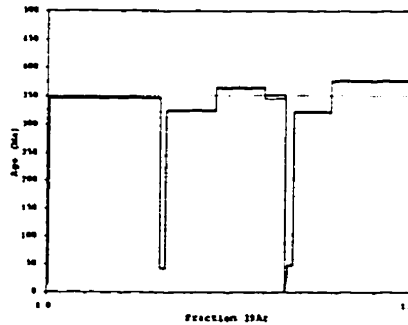
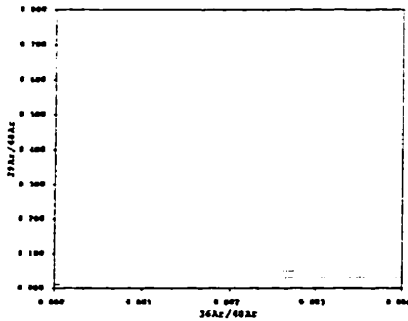
Approx. 7.05% K  
0.17% Ca

Initial 40/36: Linear regression has positive slope.  
Correlation Age:

Plateau Age: 351.13 ± 1.56 Ma ( 95.9% of 39Ar, steps marked by < )

Power	36Ar/40Ar	39Ar/40Ar	r	Ca/K	40Ar <sub>atm</sub>	39Ar	40Ar*/39K	Age
300	0.00231195±0.00020755	0.069214±0.000376	0.002	0.03	68.12	0.47	4.577±0.887	19.36± 3.73
<7000	0.00001642 0.00000000	0.011052 0.000000	0.627	0.00	0.49	30.33	90.040 0.402	347.21 1.41
500	0.00103478 0.00000000	0.066363 0.000000	0.001	0.01	30.49	1.60	10.461 0.205	43.94 0.85
<1000	0.00002492 0.00000527	0.011863 0.000026	0.004	0.07	0.74	13.60	83.677 0.451	324.75 1.60
<2000	0.00000000 0.00000000	0.010537 0.000000	0.158	0.00	0.00	13.42	94.900 0.452	364.18 1.57
<7000	0.00002687 0.00000001	0.010954 0.000000	0.036	0.06	0.79	5.84	90.568 0.988	349.06 3.46
100	0.00323018 0.00000000	0.031851 0.000000	0.040	0.05	95.32	0.03	1.431 6.913	6.07 23.30
200	0.00264548 0.00000000	0.049822 0.000000	0.014	0.03	78.01	0.21	4.381 0.858	18.53 3.61
300	0.00156832 0.00000000	0.097494 0.000000	0.002	0.02	46.16	0.36	5.503 0.638	23.25 2.68
500	0.00038856 0.00000239	0.074933 0.000020	0.001	0.00	11.45	1.39	11.813 0.161	49.54 0.67
<1000	0.00003519 0.00000363	0.011915 0.000018	0.043	0.06	1.04	10.19	83.054 0.443	322.54 1.58
<7000	-0.00000002 0.00000039	0.010124 0.000002	0.016	0.02	0.00	22.54	98.771 0.493	377.59 1.70

Power	40Ar	39Ar	38Ar	37Ar	36Ar	Blank 40Ar	Atmos 40/36
300	12.05±0.00	0.85±0.00	0.02±0.00	0.010±0.00	0.035±0.00	0.058±0.00	287.67±1.00
<7000	4852.71 0.00	53.93 0.23	0.72 0.01	-0.003±0.40	0.082±0.01	0.005±0.00	287.67±1.00
500	42.86 0.00	2.87 0.01	0.06 0.00	0.012±0.00	0.053±0.00	0.064±0.00	287.67±1.00
<1000	2027.17 0.00	24.20 0.10	0.33 0.01	0.130±0.01	0.059±0.02	0.042±0.00	287.67±1.00
<2000	2252.06 0.00	23.88 0.10	0.25 0.01	-0.029±0.05	-0.095±0.01	0.064±0.00	287.67±1.00
<7000	343.26 0.00	10.42 0.04	0.10 0.01	0.056±0.02	0.036±0.03	0.081±0.00	287.67±1.00
100	1.96 0.00	0.08 0.00	0.02 0.00	0.013±0.00	0.016±0.00	0.075±0.00	287.67±1.00
200	7.72 0.00	0.41 0.00	0.02 0.00	0.014±0.00	0.031±0.00	0.078±0.00	287.67±1.00
300	7.05 0.00	0.71 0.00	0.02 0.00	0.014±0.00	0.021±0.00	0.077±0.00	287.67±1.00
500	32.44 0.00	2.50 0.01	0.05 0.00	0.013±0.00	0.023±0.00	0.080±0.00	287.67±1.00
<1000	1512.32 0.00	18.13 0.08	0.21 0.01	0.077±0.03	0.060±0.02	0.044±0.00	287.67±1.00
<7000	3936.37 0.00	40.10 0.17	0.52 0.01	0.060±0.03	-0.055±0.03	0.083±0.00	287.67±1.00



Measured volumes are x 1E-10 cm3 NTP. All errors are 2 x standard error.

# **FAR-333 Whole Rock (60-80 mesh)**

Run date: 1996/10/24  
Run: AS-206

Can/Pos: 142/8  
Mass: 100.0 mg

J Value: 0.002371  
= 0.000014

Volume 39Ar: 255.80 x 1E-10 cm<sup>3</sup> NTP  
Integrated Age: 6.38 ± 0.12 Ma

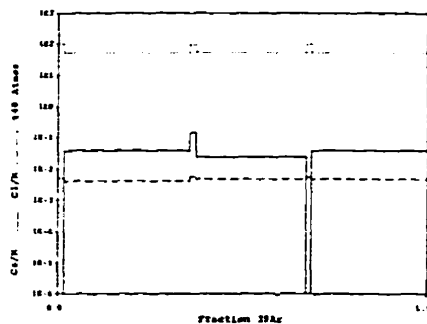
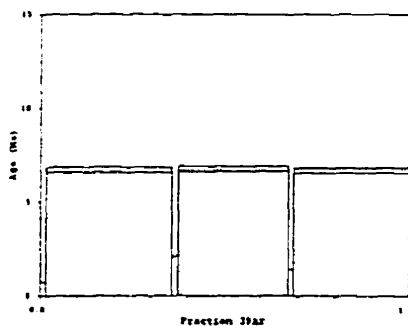
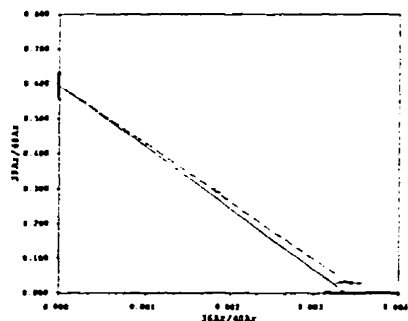
Approx. 1.52% K  
0.05% Ca

Initial 40/36: 278.68 ± 34.76 (MSWD = 0.22, isochron between 0.29 and 2.41)  
Correlation Age: 7.18 ± 0.44 Ma (100.0% of 39Ar, steps marked by >)

Plateau Age: 6.73 ± 0.09 Ma ( 95.58 of 39Ar, steps marked by <)

Power	36Ar/40Ar	39Ar/40Ar	z	Ca/K	%40Ar	%39Ar	40Ar*/39K	Age
400	0.00342758±0.00010180	0.029142±0.000144	0.719	0.00	101.15	1.47	-0.437±0.605	-1.87±2.59
<7000	0.00179550 0.00000000	0.298997 0.000000	0.005	0.04	52.30	34.13	1.573 0.032	6.72 0.14
400	0.00338749 0.00000000	0.033085 0.000000	0.623	0.15	89.95	1.77	-0.026 0.525	-0.11 2.25
<7000	0.00182605 0.00001711	0.290884 0.000585	0.016	0.02	53.20	29.76	1.587 0.033	6.77 0.14
400	0.00341123 0.00000000	0.029926 0.000000	0.890	0.00	100.66	1.30	-0.263 0.595	-1.13 2.55
<7000	0.00185295 0.00000001	0.288806 0.000000	0.005	0.04	53.99	31.57	1.571 0.034	6.71 0.14

Power	40Ar	39Ar	38Ar	37Ar	36Ar	Blank 40Ar	Atmos 40/36
400	129.64±0.10	3.41±0.02	0.22±0.00	0.009±0.00	0.472±0.01	0.181±0.00	284.57±1.00
<7000	295.78 0.00	87.96 0.35	3.32 0.02	0.015±0.00	0.557±0.01	0.181±0.00	284.57±1.00
400	137.22 0.10	4.58 0.02	0.29 0.00	0.012±0.00	0.494±0.01	0.184±0.00	284.57±1.00
<7000	265.00 0.00	76.63 0.30	2.95 0.02	0.009±0.01	0.503±0.01	0.135±0.00	284.57±1.00
400	111.39 0.00	3.36 0.01	0.21 0.00	0.007±0.00	0.400±0.01	0.141±0.00	284.57±1.00
<7000	283.13 0.00	81.36 0.32	3.01 0.02	0.011±0.00	0.545±0.01	0.135±0.00	284.57±1.00



Measured volumes are x 1E-10 cm<sup>3</sup> NTP. All errors are 1 x standard error.

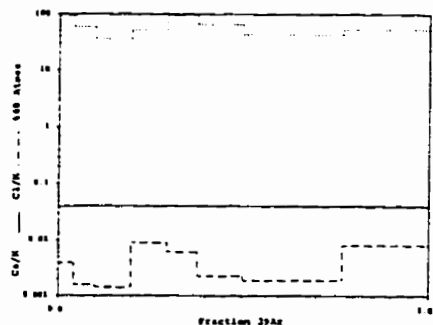
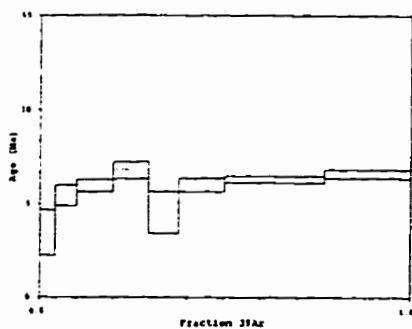
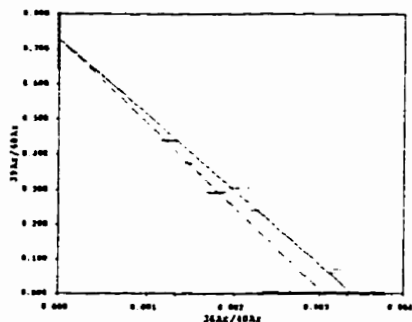
# **FAR-333 Whole Rock (60-80 mesh)**

Run date: 1997/05/06 Can/Pos: 142/8 J Value: 0.000371  
 Run: JG-077 & JG-078 Mass: 100.0 mg ± 0.000016

Volume 39Ar: 217.21 x 1E-10 cm<sup>3</sup> NTP  
 Integrated Age: 6.20 ± 0.16 Ma Approx. 1.29 ± 0.05 Ma  
 Initial 40/36: 329.75 ± 80.29 (MSWD = 0.58, isochron between 0.00 and 3.00)  
 Correlation Age: 5.86 ± 0.67 Ma ( 69.6% of 39Ar, steps marked by > )  
 Plateau Age: 6.83 ± 0.22 Ma ( 33.2% of 39Ar, steps marked by < )

Power	36Ar/40Ar	39Ar/40Ar	r	Ca/K	40Ar/40Ar	39Ar	40Ar*/39K	Age
1000	0.00318910±0.00006746	0.070719±0.000466	0.025	0.04	93.33	4.21	0.820±0.286	2.51±1.22
2000	0.00203735 0.00000000	0.304946 0.000000	0.022	0.04	59.39	5.69	1.307 0.133	5.45 0.55
6000>	0.00124372 0.00000000	0.440562 0.000000	0.016	0.04	36.01	9.80	1.438 0.075	6.07 0.31
<8000>	0.00178691 0.00005521	0.291516 0.000797	0.032	0.04	51.83	9.47	1.431 0.110	6.27 0.46
1000	0.00316986 0.00000000	0.058409 0.000000	0.099	0.04	93.40	8.27	1.092 0.271	4.56 1.13
2000	0.00221789 0.00000002	0.239347 0.000000	0.037	0.04	64.82	12.23	1.443 0.086	6.02 0.36
6000>	0.00146709 0.00000000	0.374264 0.000000	0.027	0.04	42.59	26.62	1.516 0.040	6.32 0.16
<7000>	0.00182059 0.00000000	0.292979 0.000000	0.029	0.04	52.84	23.71	1.588 0.054	6.42 0.22

Power	40Ar	39Ar	38Ar	37Ar	36Ar	Blank 40Ar	Atmos 40/36
1000	130.87±0.23	9.28±0.06	0.40±0.01	0.023±0.00	0.463±0.01	1.103±0.05	283.81±1.00
2000	42.15 0.12	12.51 0.06	0.31 0.01	0.024±0.00	0.129±0.01	1.110±0.05	283.81±1.00
6000>	50.30 0.14	21.49 0.08	0.49 0.01	0.025±0.00	0.108±0.01	1.123±0.05	283.81±1.00
<8000>	72.83 0.20	20.80 0.09	1.17 0.02	0.028±0.00	0.183±0.01	1.419±0.07	283.81±1.00
1000	308.82 0.48	19.16 0.08	0.96 0.02	0.027±0.00	1.055±0.02	0.607±0.02	283.81±1.00
2000	112.70 0.24	26.23 0.09	0.74 0.02	0.028±0.00	0.300±0.01	0.615±0.02	283.81±1.00
6000>	157.57 0.29	58.31 0.20	1.40 0.02	0.031±0.00	0.287±0.01	0.654±0.02	283.81±1.00
<7000>	179.64 0.30	51.96 0.17	2.68 0.03	0.034±0.00	0.387±0.01	0.690±0.02	283.81±1.00



Measured volumes are x 1E-10 cm<sup>3</sup> NTP. All errors are 2 x standard error.



# **FAR-333 Whole Rock (60-80 mesh)**

Run date: 1997/05/06  
Run: AS-206, JG-077 & JG-078

Can./Pos: 142/8  
Mass: 100.0 mg

J Value: 0.002371  
± 0.000014

Volume 39Ar: 473.01 x 1E-10 cm3 NTP  
Integrated Age: 6.30 ± 0.11 Ma

Approx. 2.81% K  
0.11% Ca

Initial 40/36: 323.19 ± 63.98 (MSWD = 0.49, isochron between 0.37 and 2.26)  
Correlation Age: 5.98 ± 0.59 Ma ( 83.6% of 39Ar, steps marked by > )

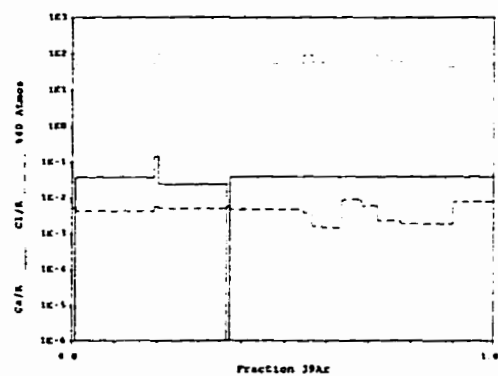
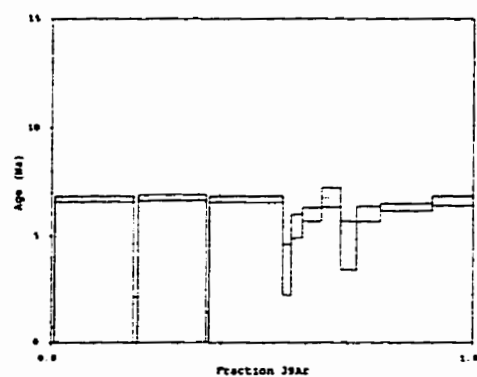
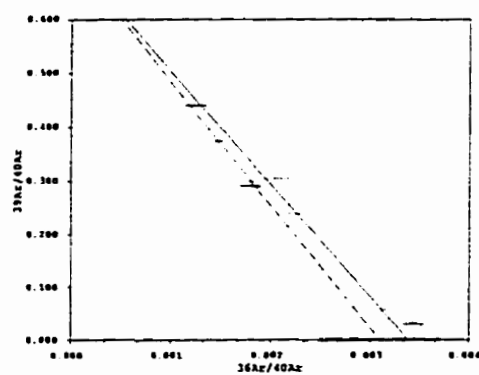
Plateau Age: 6.75 ± 0.09 Ma ( 66.9% of 39Ar, steps marked by < )

Power	36Ar/40Ar	39Ar/40Ar	r	Ca/K	%40Atm	%39Ar	40Ar*/39K	Age
400	0.00342758±0.00010180	0.029142±0.000244	0.719	0.00	101.15	0.80	-0.437±0.605	-1.87±2.5
<7000>	0.00179550 0.00000000	0.298997 0.000000	0.005	0.04	52.30	18.46	1.573 0.032	6.72 0.1
400	0.00338749 0.00000000	0.033085 0.000000	0.623	0.15	99.95	0.96	-0.026 0.525	-0.11 2.2
<7000>	0.00182605 0.00001711	0.290884 0.000585	0.016	0.02	53.20	16.09	1.587 0.033	6.77 0.1
400	0.00341123 0.00000000	0.029926 0.000000	0.890	0.00	100.66	0.70	-0.263 0.595	-1.13 2.5
<7000>	0.00185295 0.00000001	0.288806 0.000000	0.005	0.04	53.99	17.07	1.571 0.034	6.71 0.1
1000	0.00318910 0.00000000	0.070719 0.000000	0.025	0.04	93.93	1.93	0.920 0.286	3.42 1.1
2000	0.00203735 0.00000000	0.304946 0.000000	0.022	0.04	59.39	2.61	1.307 0.133	5.45 0.5
6000>	0.00124372 0.00000000	0.440562 0.000000	0.016	0.04	36.01	4.50	1.438 0.075	6.00 0.3
<8000>	0.00178691 0.00002087	0.291516 0.000301	0.032	0.04	51.83	4.35	1.631 0.110	6.80 0.4
1000	0.00316986 0.00001250	0.058409 0.000064	0.099	0.04	93.40	3.80	1.092 0.271	4.56 1.1
2000	0.00221789 0.00001161	0.239367 0.000198	0.037	0.04	64.82	5.62	1.442 0.096	6.02 0.3
6000>	0.00146709 0.00000591	0.374264 0.000302	0.027	0.04	42.59	12.23	1.516 0.040	6.32 0.1
<7000>	0.00182059 0.00000859	0.292978 0.000191	0.029	0.04	52.84	16.89	1.589 0.054	6.62 0.2

Power	40Ar	39Ar	38Ar	37Ar	36Ar	Blank 40Ar	Atmos 40/3
400	129.64±0.00	3.81±0.02	0.23±0.00	0.009±0.00	0.472±0.01	0.181±0.00	284.57±1.0
<7000>	295.78 0.00	87.96 0.35	3.02 0.02	0.015±0.00	0.557±0.01	0.181±0.00	284.57±1.0
400	137.22 0.00	4.58 0.02	0.28 0.00	0.012±0.00	0.494±0.01	0.184±0.00	284.57±1.0
<7000>	265.00 0.00	76.69 0.30	2.85 0.02	0.009±0.01	0.503±0.01	0.135±0.00	284.57±1.0
400	111.39 0.00	3.36 0.01	0.21 0.00	0.007±0.00	0.400±0.01	0.141±0.00	284.57±1.0
<7000>	283.13 0.00	81.36 0.32	3.01 0.02	0.011±0.00	0.545±0.01	0.135±0.00	284.57±1.0
1000	130.87 0.23	8.28 0.06	0.40 0.01	0.023±0.00	0.469±0.01	1.103±0.05	283.80±1.0
2000	42.15 0.12	12.51 0.06	0.31 0.01	0.024±0.00	0.129±0.01	1.110±0.05	283.80±1.0
6000>	50.20 0.14	21.49 0.08	0.49 0.01	0.025±0.00	0.108±0.01	1.123±0.05	283.80±1.0
<8000>	72.83 0.20	20.80 0.09	1.17 0.02	0.029±0.00	0.183±0.01	1.418±0.07	283.80±1.0
1000	308.82 0.48	18.16 0.08	0.96 0.02	0.027±0.00	1.055±0.02	0.607±0.02	283.80±1.0
2000	112.70 0.24	26.83 0.09	0.74 0.02	0.029±0.00	0.300±0.01	0.615±0.02	283.80±1.0
6000>	157.57 0.28	58.31 0.20	1.40 0.02	0.031±0.00	0.287±0.01	0.654±0.02	283.80±1.0
<7000>	178.64 0.30	51.96 0.17	2.68 0.03	0.034±0.00	0.387±0.01	0.690±0.02	283.80±1.0

Measured volumes are x 1E-10 cm3 NTP. All errors are 2 x standard error.

# **FAR-333 Whole Rock (60-80 mesh)**



Measured volumes are  $\times 1\text{E}-10$  cm<sup>3</sup> NTP. All errors are 2 x standard error.

# **FAR-334 Biotite (25-60 mesh)**

Run date: 1996/10/27  
Run: AS-211

Can/Bos: 142/9  
Mass: 100.0 mg

J Value: 0.002372  
= 0.000012

Volume 39Ar: 28.62 x 1E-10 cm<sup>3</sup> NTP  
Integrated Age: 5.63 ± 0.54 Ma

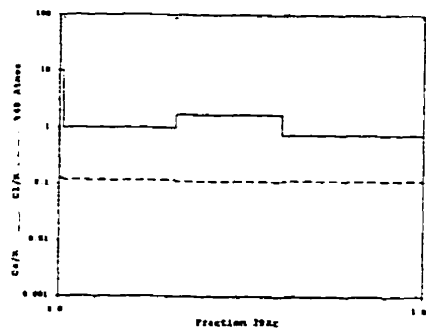
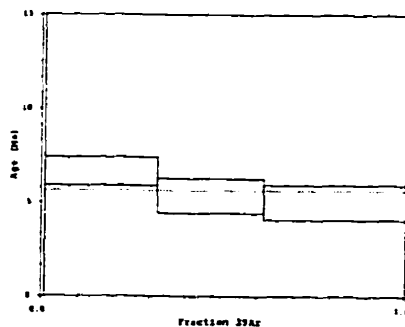
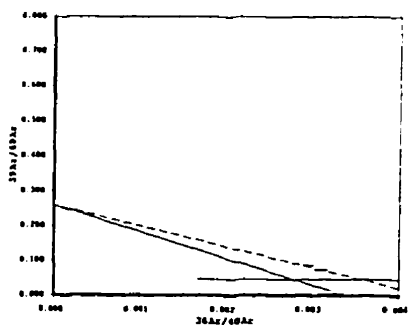
Approx. 0.17% K  
0.20% Ca

Initial 40/36: 230.21 ± 910.53 (MSWD = 2.45, isochron between 0.00 and 3.00)  
Correlation Age: 16.43 ± 37.59 Ma (100.0% of 39Ar, steps marked by >)

Plateau Age: 5.63 ± 0.53 Ma ( 99.18 of 39Ar, steps marked by <)

Power	36Ar/40Ar	39Ar/40Ar	ε	Ca/K	%40Ar	%39Ar	40Ar*/39K	Age
500	0.00317810±0.00152321	0.046921±0.003838	0.967	10.25	93.25	0.93	1.400±2.155	5.98±9.19
<7000	0.00295138 0.00000000	0.087635 0.000000	0.129	0.99	86.05	30.80	1.556 0.177	6.65 0.76
<7000	0.00308960 0.00000000	0.074661 0.000000	0.253	1.67	90.34	29.50	1.257 0.215	5.17 0.92
<7000	0.00311606 0.00003356	0.073320 0.000156	0.210	0.75	91.11	38.78	1.175 0.217	5.02 0.93

Power	40Ar	39Ar	38Ar	37Ar	36Ar	Blank 40Ar	Atmos 40/36
500	5.91±0.00	0.28±0.00	0.16±0.00	0.011±0.00	0.023±0.00	0.226±0.00	284.57±1.00
<7000	101.83 0.00	8.95 0.04	4.68 0.04	0.018±0.00	0.321±0.01	0.233±0.00	284.57±1.00
<7000	114.38 0.00	8.58 0.03	4.40 0.03	0.024±0.00	0.376±0.01	0.227±0.00	284.57±1.00
<7000	153.06 0.00	11.27 0.04	5.39 0.05	0.017±0.00	0.504±0.01	0.235±0.00	284.57±1.00



Measured volumes are x 1E-10 cm<sup>3</sup> NTP. All errors are 2 x standard error.

# **FAR-334 Biotite (25-60 mesh)**

Run date: 1997/05/06 Can/Pos: 142/9 J Value: 0.000870  
 Run: JG-067 & JG-068 Mass: 1006.0 mg ± 0.000014

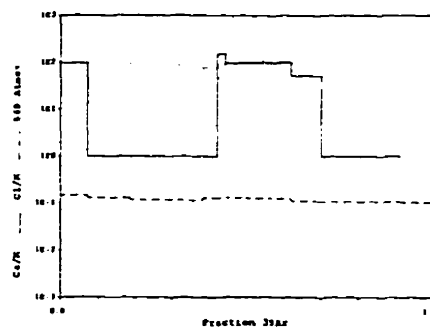
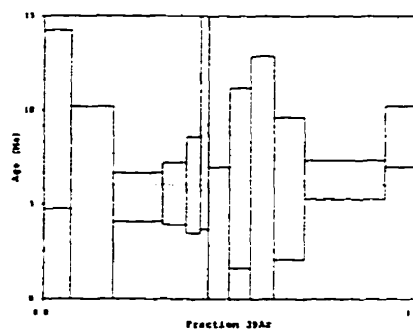
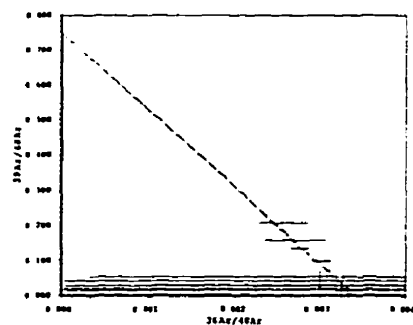
Volume 39Ar: 36.56 × 1E-10 cm<sup>3</sup> NTP Approx. 0.024 K  
 Integrated Age: 6.46 ± 1.07 Ma 0.66% Ca

Initial 40/36: 292.22 ± 460.64 (MSWD = 0.15, isochron between 0.53 and 1.94)  
 Correlation Age: 5.72 ± 5.79 Ma ( 90.0% of 39Ar, steps marked by > )

Plateau Age: 6.05 ± 0.72 Ma ( 44.6% of 39Ar, steps marked by < )

Power	36Ar/40Ar	39Ar/40Ar	r	Ca/K	%40Atm	%39Ar	40Ar*/39K	Age
1000>	0.00124615±0.00648037	0.020044±0.016618	1.000	96.41	95.46	7.02	1.127±1.111	9.50±4.73
2000>	0.00133000 0.00000000	0.016323 0.000000	0.806	1.00	98.06	11.39	1.149 1.286	4.79 5.39
<3000>	0.00201144 0.00000000	0.097249 0.000000	0.102	0.98	97.13	13.32	1.287 0.309	5.37 1.29
<4000>	0.00255451 0.00015333	0.207184 0.001535	0.064	0.99	71.74	6.24	1.334 0.396	6.56 1.65
<8000>	0.00270714 0.00000000	0.157252 0.000000	0.086	0.97	76.81	3.80	1.443 0.614	6.01 2.56
600>	0.00300123 0.00000280	0.043030 0.000007	0.999	151.68	87.80	2.00	2.798 1.921	11.64 7.97
1000>	0.00326827 0.00000000	0.052867 0.000000	0.333	98.16	95.46	5.29	0.213 0.853	3.41 3.55
1400>	0.00325202 0.00000000	0.028464 0.000000	0.999	101.78	95.51	5.59	1.538 1.149	6.41 4.78
1800>	0.00331579 0.00000000	0.015240 0.000000	1.000	101.78	97.67	6.16	1.489 1.602	6.20 6.66
2400>	0.00325630 0.00051450	0.029985 0.001321	0.397	50.73	95.46	8.01	1.407 0.902	5.66 3.75
<5000>	0.00275600 0.00005355	0.135093 0.000478	0.057	0.97	79.10	21.20	1.514 0.246	6.31 1.02

Power	40Ar	39Ar	38Ar	37Ar	36Ar	Blank 40Ar	Atmos 40/36
1000>	124.17±0.21	2.53±0.03	1.75±0.03	0.014±0.00	0.460±0.01	0.134±0.01	284.57±1.00
2000>	255.49±0.33	4.20±0.05	2.62±0.04	0.012±0.00	0.496±0.02	0.130±0.01	284.57±1.00
<3000>	50.49±0.13	4.42±0.04	2.65±0.04	0.012±0.00	0.174±0.01	0.202±0.01	284.57±1.00
<4000>	11.31±0.06	2.31±0.03	1.21±0.02	0.013±0.00	0.048±0.00	0.216±0.01	284.57±1.00
<8000>	3.10±0.05	1.41±0.02	0.83±0.02	0.012±0.00	0.043±0.00	0.208±0.01	284.57±1.00
600>	16.44±0.09	0.78±0.02	0.43±0.01	0.016±0.00	0.088±0.00	0.258±0.02	284.57±1.00
1000>	35.71±0.11	1.39±0.03	1.15±0.02	0.018±0.00	0.171±0.01	0.261±0.02	284.57±1.00
1400>	63.67±0.16	2.11±0.03	1.21±0.03	0.021±0.00	0.294±0.01	0.281±0.02	284.57±1.00
1800>	142.13±0.21	2.32±0.03	1.36±0.03	0.023±0.00	0.556±0.01	0.306±0.02	284.57±1.00
2400>	56.42±0.17	3.02±0.03	1.57±0.03	0.023±0.00	0.382±0.01	0.330±0.02	284.57±1.00
<5000>	59.07±0.15	7.27±0.06	3.84±0.04	0.021±0.00	0.203±0.01	0.356±0.02	284.57±1.00



Measured volumes are × 1E-10 cm<sup>3</sup> NTP. All errors are 2 × standard error.

# FAR-334 Biotite (25-60 mesh)

Run date: 1997/05/06  
Run: AS-211, JG-067 & JG-068

Can/Pos: 142/9  
Mass: 500.0 mg

J Value: 0.002372  
± 0.000012

Volume 39Ar: 65.39 x 1E-10 cm3 NTP  
Integrated Age: 6.09 ± 0.66 Ma

Approx. 0.08% K  
1.37% Ca

Initial 40/36: 289.77 ± 135.24 (MSWD = 0.60, isochron between 0.59 and 1.82)  
Correlation Age: 5.92 ± 1.83 Ma ( 94.0% of 39Ar, steps marked by > )

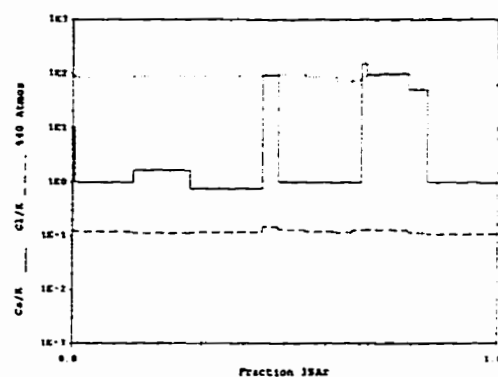
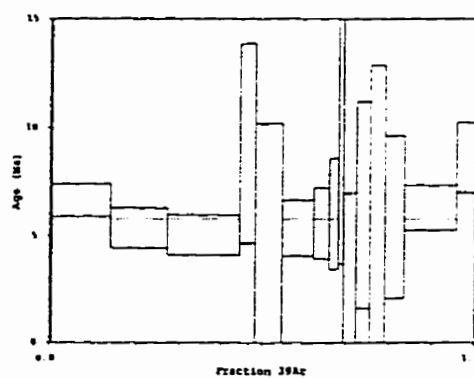
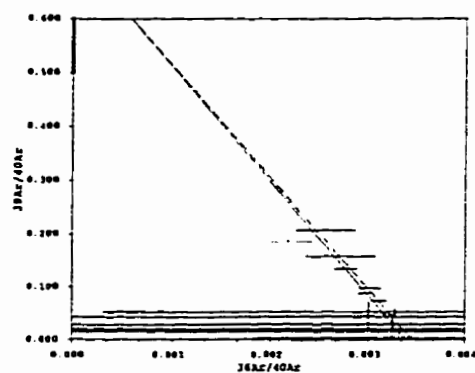
Plateau Age: 5.78 ± 0.44 Ma ( 68.6% of 39Ar, steps marked by < )

Power	36Ar/40Ar	39Ar/40Ar	r	Ca/K	%40Ar	%39Ar	40Ar*/39K	Age
500	0.00317810±0.00152321	0.046921±0.003838	0.967	10.25	93.25	0.41	1.400±2.155	5.98±9.1
<7000>	0.00295138 0.00000000	0.087635 0.000000	0.209	0.99	86.05	13.57	1.556 0.177	6.65 0.7
<7000>	0.00308960 0.00000000	0.074661 0.000000	0.253	1.67	90.34	13.00	1.257 0.215	5.37 0.9
<7000>	0.00311606 0.00003356	0.073320 0.000156	0.212	0.75	91.11	17.09	1.175 0.217	5.02 0.9
1000>	0.00324615 0.00000000	0.020044 0.000000	1.000	96.41	95.46	3.93	2.227 1.111	9.27 4.6
2000>	0.00333000 0.00000004	0.016329 0.000000	0.806	1.00	98.06	6.37	1.148 1.296	4.79 5.3
<3000>	0.00301144 0.00000000	0.097269 0.000000	0.102	0.98	87.13	7.45	1.287 0.309	5.37 1.2
<4000>	0.00255451 0.00000000	0.207184 0.000000	0.064	0.98	71.74	3.49	1.334 0.396	5.56 1.6
<8000>	0.00270714 0.00000000	0.157252 0.000000	0.088	0.97	76.81	2.13	1.443 0.614	6.01 2.5
600>	0.00300123 0.00054264	0.043030 0.001394	0.999	151.68	87.90	1.12	2.798 1.921	11.64 7.9
1000>	0.00326927 0.00038583	0.052867 0.000396	0.993	99.16	95.46	2.96	0.919 0.353	3.41 3.5
1400>	0.00325202 0.00071470	0.029464 0.001834	0.999	101.78	95.51	3.13	1.538 1.149	6.41 4.7
1800>	0.00331579 0.00095832	0.015240 0.002457	1.000	101.78	97.67	3.45	1.499 1.600	6.20 6.6
2400>	0.00325630 0.00051450	0.029985 0.001321	0.997	50.73	95.66	4.48	1.407 0.902	5.86 3.7
<5000>	0.00275600 0.00005355	0.135093 0.000478	0.057	0.97	79.10	11.66	1.514 0.246	6.31 1.0
8000	0.00217251 0.00003097	0.185605 0.000242	0.019	0.94	61.15	5.57	2.068 0.387	8.61 1.6

Power	40Ar	39Ar	38Ar	37Ar	36Ar	Blank 40Ar	Atmos 40/3
500	5.91±0.06	0.28±0.00	0.16±0.00	0.011±0.00	0.028±0.00	0.226±0.00	284.57±1.0
<7000>	101.83 0.00	8.95 0.04	4.89 0.04	0.018±0.00	0.321±0.01	0.233±0.00	284.57±1.0
<7000>	114.38 0.00	8.58 0.02	4.40 0.03	0.024±0.00	0.376±0.01	0.227±0.00	284.57±1.0
<7000>	153.06 0.00	11.27 0.04	5.99 0.05	0.017±0.00	0.504±0.01	0.235±0.00	284.57±1.0
1000>	124.17 0.21	2.59 0.03	1.75 0.03	0.014±0.00	0.460±0.01	0.184±0.01	284.57±1.0
2000>	255.49 0.33	4.20 0.05	2.62 0.04	0.012±0.00	0.896±0.02	0.190±0.01	284.57±1.0
<3000>	50.49 0.13	4.92 0.04	2.65 0.04	0.012±0.00	0.174±0.01	0.202±0.01	284.57±1.0
<4000>	11.31 0.06	2.31 0.03	1.21 0.02	0.013±0.00	0.048±0.00	0.216±0.01	284.57±1.0
<8000>	9.10 0.05	1.41 0.02	0.83 0.02	0.012±0.00	0.043±0.00	0.208±0.01	284.57±1.0
600>	16.44 0.08	0.78 0.02	0.43 0.01	0.016±0.00	0.088±0.00	0.258±0.02	284.57±1.0
1000>	35.71 0.11	1.99 0.03	1.15 0.02	0.018±0.00	0.171±0.01	0.261±0.02	284.57±1.0
1400>	69.67 0.16	2.11 0.03	1.21 0.03	0.021±0.00	0.294±0.01	0.281±0.02	284.57±1.0
1800>	143.13 0.21	2.32 0.03	1.36 0.03	0.023±0.00	0.556±0.01	0.306±0.02	284.57±1.0
2400>	96.42 0.17	3.01 0.03	1.57 0.03	0.023±0.00	0.382±0.01	0.330±0.02	284.57±1.0
<5000>	58.07 0.15	7.87 0.06	3.84 0.04	0.021±0.00	0.203±0.01	0.356±0.02	284.57±1.0
8000	20.16 0.06	3.74 0.04	1.79 0.02	0.022±0.00	0.084±0.00	0.377±0.02	284.57±1.0

Measured volumes are x 1E-10 cm3 NTP. All errors are 2 x standard error.

# **FAR-334 Biotite (25-60 mesh)**



Measured volumes are x 1E-10 cm<sup>3</sup> NTP. All errors are 2 x standard error.

# **FAR-336 Biotite (25-80 mesh)**

Run date: 1995/11/13  
Run: AS-44

Can/Pos: 141/52  
Mass: 7.2 mg

J Value: 0.002354  
± 0.000010

Volume 39Ar: 96.32 x 1E-10 cm<sup>3</sup> NTP  
Integrated Age: 6.93 ± 0.12 Ma

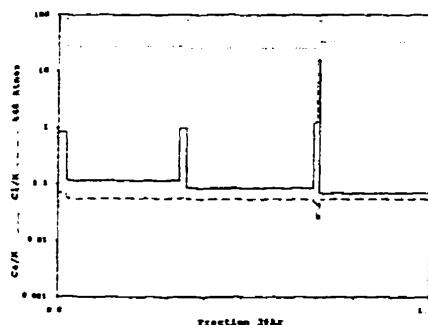
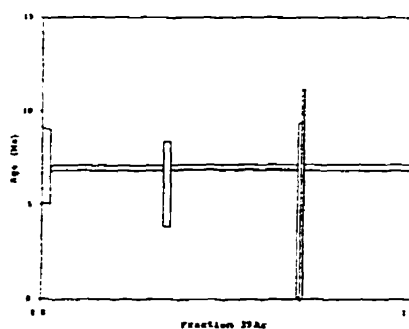
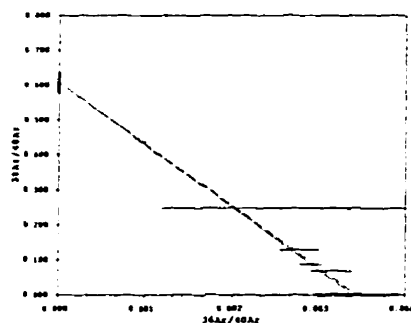
Approx. 8.01% K  
1.82% Ca

Initial 40/36: 291.02 ± 39.81 (MSWD = 0.38, isochron between 0.37 and 2.26)  
Correlation Age: 6.98 ± 0.31 Ma (100.0% of 39Ar, steps marked by >)

Plateau Age: 6.99 ± 0.09 Ma ( 94.4% of 39Ar, steps marked by <)

Power	36Ar/40Ar	39Ar/40Ar	z	Ca/K	%40Ar	%39Ar	40Ar*/39K	Age
300	0.00289441±0.00013932	0.087497±0.000395	0.001	0.82	85.07	2.19	1.671±0.472	7.08±2.00
<7000	0.00096421±0.00000000	0.438186±0.000000	0.001	0.11	27.40	30.79	1.645±0.035	6.97±0.15
7000	0.00275327±0.00000000	0.129011±0.000000	0.000	0.99	80.92	1.90	1.445±0.535	6.13±2.26
<7000	0.00090234±0.00002241	0.447350±0.000979	0.002	0.08	25.59	33.94	1.651±0.011	7.00±0.13
300	0.00312752±0.00000000	0.068507±0.000000	0.001	1.25	92.07	0.88	1.118±1.091	4.74±4.62
1000	0.00270780±0.00000038	0.248029±0.000000	0.001	16.10	79.05	0.60	0.812±1.825	3.44±7.73
<7000	0.00114416±0.00000000	0.404413±0.000000	0.002	0.07	32.72	29.70	1.650±0.036	6.99±0.15

Power	40Ar	39Ar	38Ar	37Ar	36Ar	Blank 40Ar	Atmos 40/36
300	24.36±0.09	1.13±0.01	1.63±0.01	1.14±0.00	0.074±0.00	0.145±0.00	287.67±1.00
<7000	69.06±0.00	29.94±0.13	7.55±0.07	3.25±0.00	0.070±0.00	0.147±0.00	287.67±1.00
7000	14.37±0.00	1.84±0.01	3.47±0.01	3.15±0.00	0.043±0.00	0.145±0.00	287.67±1.00
<7000	74.44±0.00	32.89±0.14	8.13±0.07	1.231±0.00	0.070±0.00	0.145±0.00	287.67±1.00
300	12.61±0.00	0.86±0.00	0.20±0.00	1.092±0.00	0.043±0.00	0.143±0.00	287.67±1.00
1000	2.48±0.00	0.58±0.00	0.07±0.01	0.763±0.01	0.010±0.00	0.143±0.00	287.67±1.00
<7000	72.07±0.00	29.79±0.12	7.18±0.06	0.165±0.00	0.086±0.00	0.144±0.00	287.67±1.00



Measured volumes are x 1E-10 cm<sup>3</sup> NTP. All errors are 2 x standard error.

# **FAR-336 Biotite (25-80 mesh)**

Run date: 1997/05/06  
Run: JG-063 & JG-064

Can/Pos: 142/10  
Mass: 200.0 mg

J Value: 0.002354  
= 0.000014

Volume 39Ar: 207.44 x 1E-10 cm<sup>3</sup> NTP  
Integrated Age: 6.77 ± 0.10 Ma

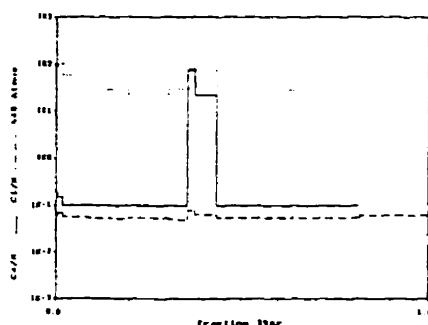
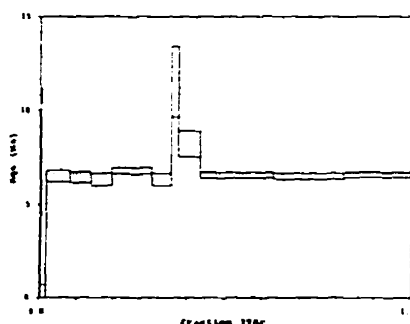
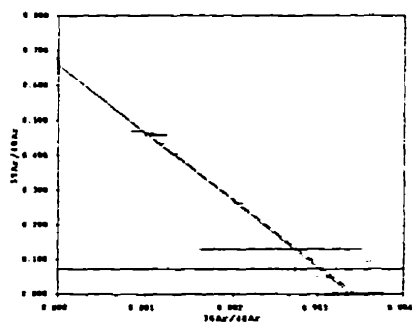
Approx. 0.62% K  
1.70% Ca

Initial 40/36: 290.72 ± 27.57 (MSWD = 1.59, isochron between 0.50 and 1.00)  
Correlation Age: 6.45 ± 0.22 Ma ( 98.3% of 39Ar, steps marked by > )

Plateau Age: 6.68 ± 0.08 Ma ( 90.6% of 39Ar, steps marked by < )

Power	36Ar/40Ar	39Ar/40Ar	z	Ca/K	%40Ar	%39Ar	40Ar*/39K	Age
500	0.00302543±0.00008502	0.049870±0.000479	0.020	0.19	89.12	0.33	2.145±0.508	9.09±2.15
1000	0.00349804 0.00000000	0.093575 0.000000	0.047	0.15	102.75	1.39	-0.337 0.507	-1.41 2.12
<2000>	0.00204891 0.00000000	0.262929 0.000000	0.030	0.10	58.03	6.34	1.572 0.073	6.54 0.30
<3000>	0.00106822 0.00005227	0.459513 0.001720	0.018	0.10	27.86	5.59	1.558 0.068	6.49 0.28
<4000>	0.00110957 0.00000000	0.461769 0.000000	0.014	0.10	29.05	5.73	1.524 0.077	6.34 0.32
<6000>	0.00088264 0.00000002	0.470547 0.000001	0.017	0.10	22.17	10.78	1.540 0.043	6.83 0.19
<8000>	0.00111939 0.00000000	0.457864 0.000000	0.013	0.10	29.58	5.21	1.526 0.080	6.35 0.33
10000	0.00273290 0.00000000	0.071969 0.000000	0.997	75.51	79.77	1.34	2.777 0.453	11.54 1.88
20000	0.00254339 0.00000000	0.130568 0.000000	0.958	21.36	73.70	5.70	1.994 0.166	8.25 0.69
<40000>	0.00131431 0.00000149	0.404667 0.000063	0.019	0.10	35.38	19.47	1.562 0.038	6.59 0.16
<60000>	0.00104010 0.00000697	0.463802 0.000324	0.018	0.10	26.93	19.60	1.554 0.037	6.51 0.15
<80000>	0.00116621 0.00000406	0.435406 0.000173	0.027	0.10	30.42	18.33	1.585 0.031	6.60 0.13

Power	40Ar	39Ar	38Ar	37Ar	36Ar	Blank 40Ar	Atmos 40/36
500	13.73±0.03	3.69±0.01	0.12±0.00	0.005±0.00	3.043±0.00	0.007±0.00	284.57±1.00
1000	31.04 0.18	2.31 0.04	0.31 0.02	0.025±0.00	0.115±0.00	0.200±0.01	284.57±1.00
<2000>	50.67 0.11	13.23 0.07	3.43 0.03	0.012±0.00	0.114±0.00	0.142±0.01	284.57±1.00
<3000>	25.31 0.09	11.48 0.08	2.92 0.04	0.013±0.00	0.038±0.00	0.189±0.01	284.57±1.00
<4000>	26.41 0.08	11.37 0.07	2.99 0.04	0.013±0.00	0.041±0.00	0.193±0.01	284.57±1.00
<6000>	48.64 0.12	22.51 0.12	5.46 0.06	0.012±0.00	0.056±0.00	0.139±0.01	284.57±1.00
<8000>	24.26 0.07	10.89 0.07	2.54 0.03	0.012±0.00	0.040±0.00	0.204±0.01	284.57±1.00
10000	54.31 0.13	4.07 0.05	1.50 0.03	0.020±0.00	0.208±0.01	0.223±0.01	284.57±1.00
20000	90.49 0.12	11.91 0.06	3.49 0.04	0.020±0.00	0.288±0.01	0.173±0.01	284.57±1.00
<40000>	101.75 0.18	40.66 0.20	10.41 0.10	0.014±0.00	0.154±0.01	0.250±0.01	284.57±1.00
<60000>	85.07 0.18	38.35 0.20	3.34 0.09	0.014±0.00	0.110±0.00	0.260±0.01	284.57±1.00
<80000>	92.07 0.13	39.53 0.18	11.37 0.10	0.013±0.00	0.127±0.00	0.246±0.01	284.57±1.00



Measured volumes are x 1E-10 cm<sup>3</sup> NTP. All errors are 1 x standard error.



# FAR-336 Biotite (25-80 mesh)

Run date: 1997/05/06

Can/Pos: 141/52

J Value: 0.002354

Run: AS-44, JG-063 & JG-064

Mass: 200.0 mg

= 0.000010

Volume 39Ar: 303.76 x 1E-10 cm<sup>3</sup> NTP

Approx. 0.314 K

Integrated Age: 6.82 ± 0.08 Ma

1.764 Ga

Initial 40/36: 295.66 ± 63.65 (MSWD = 10.22, isochron between 0.57 and 1.85)

Correlation Age: 6.58 ± 0.48 Ma ( 97.1% of 39Ar, steps marked by > )

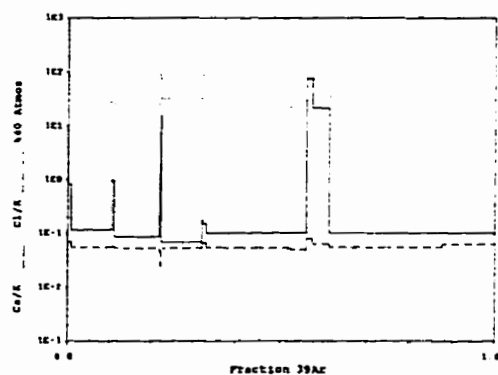
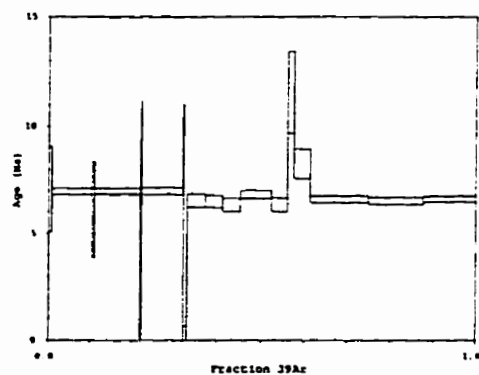
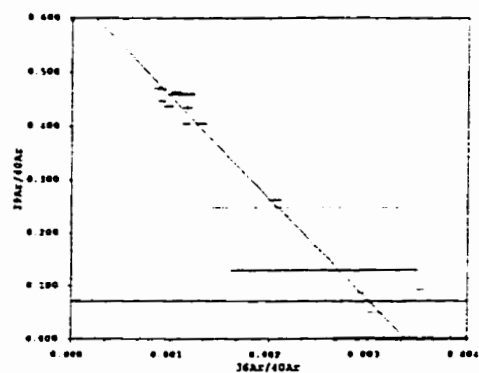
Plateau Age: 6.83 ± 0.07 Ma ( 76.2% of 39Ar, steps marked by < )

Power	36Ar/40Ar	39Ar/40Ar	r	Ca/K	%40Ar	%39Ar	40Ar*/39K	Age
300	0.09289441±0.00012932	0.087497±0.000395	0.001	0.82	85.07	0.70	1.671±0.472	7.08±2.0
<7000>	0.00096421 0.00000000	0.432186 0.000000	0.001	0.11	27.40	9.76	1.645 0.035	6.97 0.1
7000	0.00275927 0.00000000	0.129011 0.000000	0.000	0.99	80.92	0.60	1.445 0.535	6.13 2.2
<7000>	0.00090234 0.00002261	0.447880 0.000979	0.002	0.08	25.59	10.76	1.651 0.031	7.00 0.1
300	0.00312752 0.00000000	0.068507 0.000000	0.001	1.25	92.07	0.26	1.115 1.091	4.74 4.6
1000	0.00270780 0.00000039	0.248929 0.000000	0.001	16.10	79.05	0.19	0.212 1.325	3.44 7.7
<7000>	0.00114416 0.00000000	0.404413 0.000000	0.002	0.07	32.72	9.42	1.650 0.036	6.99 0.1
500	0.00302543 0.00000000	0.049870 0.000000	0.020	0.19	89.12	0.22	2.145 0.508	8.92 2.1
1000	0.00349804 0.00000000	0.093575 0.000000	0.047	0.15	102.75	0.95	-0.337 0.507	-1.41 2.1
2000>	0.00204891 0.00000540	0.262929 0.000128	0.030	0.10	58.03	4.23	1.572 0.073	6.54 0.3
3000>	0.00106822 0.00000894	0.459513 0.000294	0.016	0.10	27.86	3.82	1.558 0.065	6.49 0.2
4000>	0.00110957 0.00000990	0.461769 0.000267	0.014	0.10	29.05	3.91	1.524 0.077	6.34 0.2
<6000>	0.00085264 0.00000560	0.470547 0.000232	0.017	0.10	22.37	7.36	1.640 0.343	6.83 0.1
8000>	0.00111939 0.00000962	0.457864 0.000259	0.013	0.10	29.58	3.56	1.526 0.080	6.35 0.2
1000>	0.00273290 0.00038406	0.071969 0.000990	0.997	75.51	79.77	1.32	2.777 0.453	11.54 1.8
2000>	0.00254339 0.00008140	0.130568 0.000218	0.958	21.36	73.70	3.89	1.994 0.166	8.25 0.6
<4000>	0.00131431 0.00000149	0.404667 0.000063	0.019	0.10	35.38	13.30	1.592 0.038	6.58 0.1
<6000>	0.00104010 0.00000697	0.463802 0.000324	0.018	0.10	26.93	12.70	1.564 0.037	6.51 0.1
<8000>	0.00116621 0.00000406	0.435406 0.000173	0.027	0.10	30.42	12.93	1.535 0.031	6.60 0.1

Power	40Ar	39Ar	38Ar	37Ar	36Ar	Blank 40Ar	Atmos 40/3
300	24.36±0.00	2.13±0.01	0.69±0.01	0.148±0.00	0.074±0.00	0.145±0.00	287.67±1.0
<7000>	69.06 0.00	29.84 0.13	7.55 0.07	0.285±0.00	0.070±0.00	0.147±0.00	287.67±1.0
7000	14.37 0.00	1.84 0.01	0.49 0.01	0.154±0.00	0.043±0.00	0.145±0.00	287.67±1.0
<7000>	74.49 0.00	32.89 0.14	8.13 0.07	0.231±0.00	0.070±0.00	0.145±0.00	287.67±1.0
300	12.61 0.00	0.66 0.00	0.20 0.01	0.092±0.00	0.043±0.00	0.143±0.00	287.67±1.0
1000	2.48 0.00	0.58 0.00	0.07 0.01	0.763±0.01	0.010±0.00	0.143±0.00	287.67±1.0
<7000>	72.07 0.00	26.79 0.12	7.15 0.06	0.165±0.00	0.086±0.00	0.144±0.00	287.67±1.0
500	13.73 0.03	0.69 0.01	0.19 0.00	0.005±0.00	0.043±0.00	0.007±0.00	284.57±1.0
1000	31.04 0.18	2.91 0.04	0.91 0.02	0.025±0.00	0.115±0.00	0.200±0.01	284.57±1.0
2000>	50.67 0.11	13.23 0.07	3.43 0.03	0.012±0.00	0.114±0.00	0.142±0.01	284.57±1.0
3000>	25.91 0.09	11.68 0.08	2.92 0.04	0.013±0.00	0.038±0.00	0.189±0.01	284.57±1.0
4000>	26.41 0.08	11.97 0.07	2.99 0.04	0.013±0.00	0.041±0.00	0.193±0.01	284.57±1.0
<6000>	48.64 0.12	22.51 0.12	5.66 0.06	0.012±0.00	0.056±0.00	0.199±0.01	284.57±1.0
8000>	24.26 0.07	10.89 0.07	2.54 0.03	0.012±0.00	0.040±0.00	0.234±0.01	284.57±1.0
1000>	54.91 0.13	4.07 0.05	1.50 0.03	0.020±0.00	0.208±0.01	0.223±0.01	284.57±1.0
2000>	90.49 0.12	11.91 0.06	3.49 0.04	0.020±0.00	0.298±0.01	0.173±0.01	284.57±1.0
<4000>	101.75 0.18	40.66 0.20	10.41 0.10	0.014±0.00	0.154±0.01	0.250±0.01	284.57±1.0
<6000>	85.67 0.18	38.85 0.20	9.94 0.09	0.014±0.00	0.110±0.00	0.260±0.01	284.57±1.0
<8000>	92.07 0.13	39.53 0.19	11.37 0.10	0.013±0.00	0.127±0.00	0.246±0.01	284.57±1.0

Measured volumes are x 1E-10 cm<sup>3</sup> NTP. All errors are 2 x standard error.

# **FAR-336 Biotite (25-80 mesh)**



Measured volumes are  $\times 1E-10$  cm<sup>3</sup> NTP. All errors are 2 x standard error.

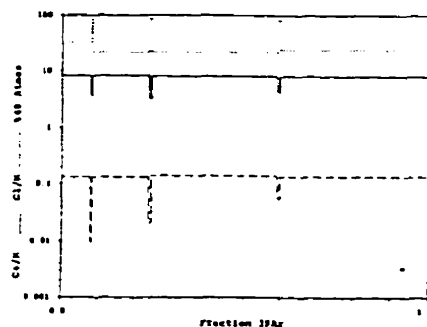
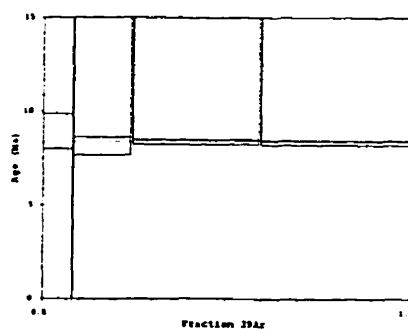
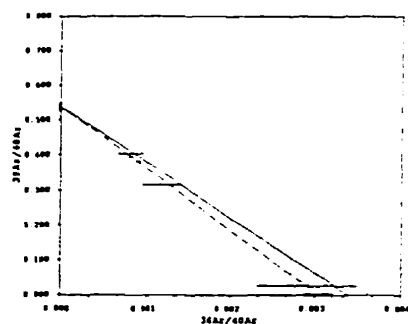
# **FAR-338 Hornblende (60-80 mesh)**

Run date: 1995/11/13 Can Pos: 141/53 J Value: 0.002353  
 Run: AS-45 & AS-118 Mass: 50.0 mg ± 0.000010

Volume 39Ar: 88.55 x 1E-10 cm<sup>3</sup> NTP  
 Integrated Age: 8.60 ± 0.15 Ma Approx. 1.06% K  
 Initial 40/36: 329.70 ± 16.51 (MSWD = 0.80, isochron between 0.37 and 2.26)  
 Correlation Age: 7.56 ± 0.15 Ma (100.0% of 39Ar, steps marked by >)  
 Plateau Age: 8.36 ± 0.13 Ma ( 98.58 of 39Ar, steps marked by <)

Power	36Ar/40Ar	39Ar/40Ar	r	Ca/K	%40Atm	%39Ar	40Ar*/39K	Age
<7000	0.00115967±0.00023512	0.316701±0.001337	0.002	8.52	32.77	7.38	2.109±0.219	8.93± 0.93
300	0.00290094 0.00000000	0.026506 0.000000	0.003	3.58	85.62	0.26	5.389 6.696	22.73 28.07
<7000	0.00079801 0.00000000	0.404448 0.000000	0.003	8.44	21.83	15.43	1.924 0.113	8.15 0.48
400	0.00294361 0.00005496	0.323521 0.000053	0.021	3.25	87.06	0.56	5.465 1.432	23.05 6.00
<7000	0.00080356 0.00000000	0.394778 0.000000	0.010	8.29	21.62	34.34	1.376 0.029	8.37 0.12
400	0.00279796 0.00000003	0.028206 0.000000	0.025	4.38	82.53	0.67	6.158 1.247	25.95 5.22
<7000	0.00088351 0.00000000	0.383278 0.000000	0.011	6.14	24.22	40.76	1.967 0.028	8.33 0.12

Power	40Ar	39Ar	38Ar	37Ar	36Ar	Blank 40Ar	Atmos 40/36
<7000	22.64±0.00	7.12±0.03	4.23±0.04	4.935±0.06	0.038±0.01	0.096±0.00	287.67±1.00
300	8.83 0.00	0.24 0.00	0.02 0.00	0.074±0.00	0.023±0.01	0.095±0.00	287.67±1.00
<7000	34.34 0.00	13.75 0.06	8.39 0.07	9.438±0.12	0.047±0.01	0.095±0.00	287.67±1.00
400	21.13 0.00	0.53 0.00	0.08 0.00	0.038±0.00	0.079±0.00	0.137±0.00	287.67±1.00
<7000	76.20 0.00	20.63 0.13	19.45 0.17	12.860±0.16	0.115±0.00	0.145±0.00	287.67±1.00
400	21.03 0.00	0.61 0.00	0.17 0.00	0.140±0.00	0.067±0.00	0.071±0.00	287.67±1.00
<7000	95.48 0.00	36.33 0.15	22.54 0.13	14.752±0.13	0.134±0.00	0.072±0.00	287.67±1.00



Measured volumes are x 1E-10 cm<sup>3</sup> NTP. All errors are 1 x standard error.

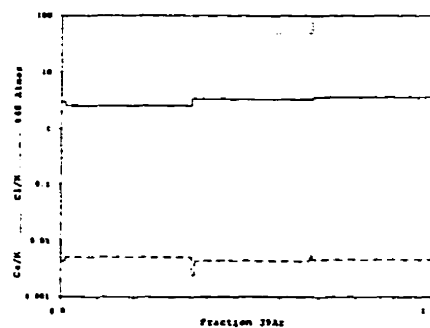
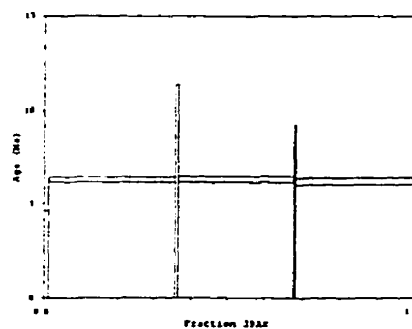
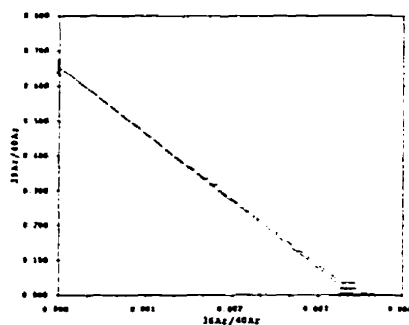
# **JC-30 Whole Rock (40-60 mesh)**

Run date: 1995/11/20      Gas/Pass: 141/76      J Value: 0.002128  
 Run: AS-67      Mass: 25.0 mg      ± 0.000018

Volume 39Ar: 92.87 × 1E-10 cm<sup>3</sup> NTP  
 Integrated Age: 6.22 ± 0.13 Ma      Approx. 3.01% K  
 Initial 40/36: 290.50 ± 16.90 (MSWD = 1.41, isochron between 0.29 and 2.41)  
 Correlation Age: 6.42 ± 0.20 Ma (100.0% of 39Ar, steps marked by >)  
 Plateau Age: 6.30 ± 0.11 Ma ( 97.5% of 39Ar, steps marked by <)

Power	36Ar/40Ar	39Ar/40Ar	r	Ca/K	%40Ar	%39Ar	40Ar*/39K	Age
300	0.0033403120.00008719	0.03506620.000169	0.007	3.05	98.58	1.15	0.365±0.739	1.53±3.10
<7000	0.00151412 0.00000000	0.366227 0.000000	0.003	2.59	44.02	34.30	1.510 0.033	6.13 0.14
300	0.00330807 0.00000000	0.017136 0.000000	0.022	3.45	97.68	0.70	1.312 1.406	5.50 5.99
<7000	0.00167352 0.00000004	0.334166 0.0000730	0.004	3.36	48.71	30.74	1.514 0.037	6.25 0.16
300	0.00334654 0.00000000	0.018131 0.000000	0.033	3.34	99.91	0.60	0.614 1.609	2.58 6.75
<7000	0.00176549 0.00000001	0.317994 0.000000	0.004	3.67	52.03	32.51	1.487 1.344	6.23 0.13

Power	40Ar	39Ar	38Ar	37Ar	36Ar	Blank 40Ar	Atmos 40/36
300	27.34±0.00	1.04±0.00	0.03±0.00	0.23±0.00	0.114±0.00	0.156±0.00	287.67±1.00
<7000	79.90 0.00	39.69 0.12	1.10 0.01	5.27±0.00	0.154±0.00	0.178±0.00	287.67±1.00
300	34.12 0.00	0.46 0.00	0.06 0.00	0.167±0.00	0.135±0.00	0.152±0.00	287.67±1.00
<7000	77.37 0.00	15.71 0.11	0.41 0.01	6.10±0.00	0.163±0.00	0.154±0.00	287.67±1.00
300	27.43 0.00	0.52 0.00	0.04 0.00	0.125±0.00	0.100±0.00	0.060±0.00	287.67±1.00
<7000	65.81 0.00	27.12 0.12	0.47 0.01	6.36±0.00	0.176±0.00	0.072±0.00	287.67±1.00



Measured volumes are × 1E-10 cm<sup>3</sup> NTP. All errors are 2 × standard error.

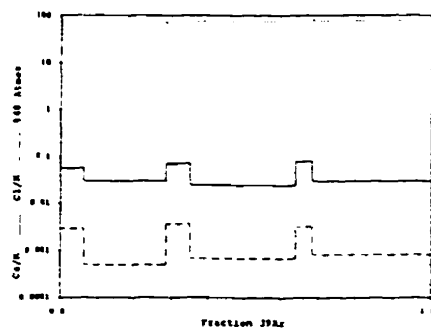
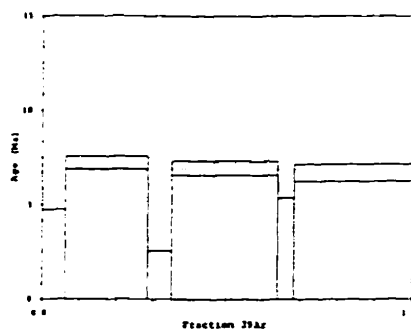
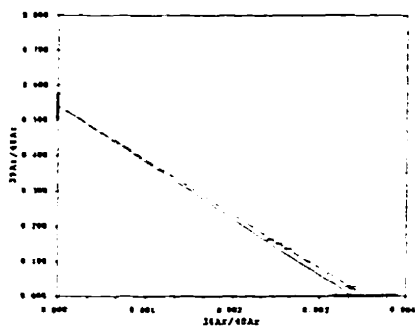
# **JC-31a Whole Rock (40-60 mesh)**

Run date: 1995/11/00 Gas Spd: 141.75 J Value: 0.000009  
Run: AS-66 Mass: 30.0 mg  $\pm$  0.000018

Volume 39Ar: 247.97  $\times$  1E-10 cm<sup>3</sup> NTP  
Integrated Age: 5.91  $\pm$  0.39 Ma  
Initial 40/36: 293.43  $\pm$  29.71 (MSWD = 1.42, isochron between 0.29 and 0.41)  
Correlation Age: 7.74  $\pm$  0.50 Ma (100.0% of 39Ar, steps marked by >)  
Plateau Age: 6.91  $\pm$  0.25 Ma ( 82.7% of 39Ar, steps marked by <)

Power	36Ar/40Ar	39Ar/40Ar	r	Ca/K	%40Ar	%39Ar	40Ar*/39K	Age
300	0.0033402 $\pm$ 0.00005 $\pm$ 5	0.027111 $\pm$ 0.000117	0.000	0.06	98.59	6.40	0.478 $\pm$ 0.656	2.01 $\pm$ 2.75
<7000	0.00243685	0.00000000	0.162860	0.000000	0.002	0.03	71.52	21.97
300	0.00335794	0.00000000	0.027557	0.000000	0.000	0.07	100.00	6.47
<7000	0.00253334	0.00002265	0.152237	0.000323	0.002	0.02	74.39	28.81
300	0.00335933	0.00000000	0.019721	0.000000	0.001	0.08	99.18	4.39
<7000	0.00265248	0.00000001	0.135327	0.000000	0.001	0.03	77.94	31.95

Power	40Ar	39Ar	38Ar	37Ar	36Ar	Blank 40Ar	Atmos 40/36
300	562.04 $\pm$ 0.10	16.00 $\pm$ 0.07	0.92 $\pm$ 0.11	0.173 $\pm$ 0.00	2.020 $\pm$ 0.03	0.113 $\pm$ 0.00	287.67 $\pm$ 1.00
<7000	537.31	54.87	1.07	0.136 $\pm$ 0.00	0.953 $\pm$ 0.01	0.154 $\pm$ 0.00	287.67 $\pm$ 1.00
300	543.35	16.19	0.88	0.135 $\pm$ 0.00	2.040 $\pm$ 0.03	0.120 $\pm$ 0.00	287.67 $\pm$ 1.00
<7000	472.40	71.93	1.48	0.151 $\pm$ 0.00	1.240 $\pm$ 0.02	0.185 $\pm$ 0.00	287.67 $\pm$ 1.00
300	562.55	10.97	0.85	0.166 $\pm$ 0.00	1.911 $\pm$ 0.03	0.053 $\pm$ 0.00	287.67 $\pm$ 1.00
<7000	544.53	73.74	1.72	0.175 $\pm$ 0.01	1.604 $\pm$ 0.03	0.060 $\pm$ 0.00	287.67 $\pm$ 1.00



Measured volumes are  $\times$  1E-10 cm<sup>3</sup> NTP. All errors are 2  $\times$  standard error.

## JC-33 Hornblende

Run date: 1995/11/17  
Run: AS-57 & AS-122

Can/Pos: 141/67  
Mass: 32.0 mg

J Value: 0.002337  
± 0.000014

Volume 39Ar: 56.93 x 1E-10 cm<sup>3</sup> NTP  
Integrated Age: 12.28 ± 0.22 Ma

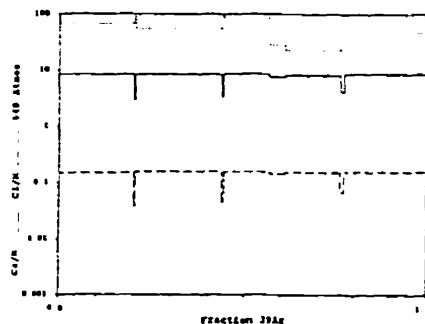
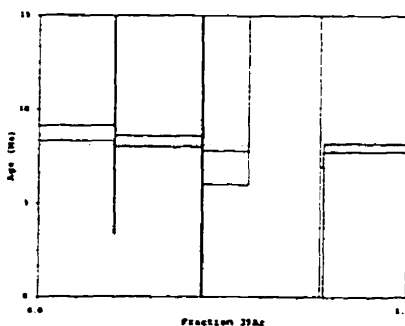
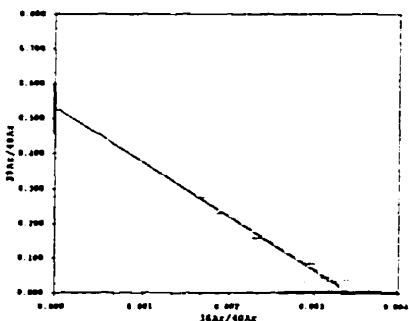
Approx. 1.071 K  
0.921 Ca

Initial 40/36: 291.85 ± 70.81 (MSWD = 11.34, isochron between 0.00 and 3.00)  
Correlation Age: 7.94 ± 1.03 Ma ( 78.54 of 39Ar, steps marked by > )

Plateau Age: 8.09 ± 0.22 Ma ( 78.58 of 39Ar, steps marked by < )

Power	36Ar/40Ar	39Ar/40Ar	z	Ca/K	%40Ar	%39Ar	40Ar*/39K	Age
<7000>	0.00229899±0.00005417	0.157414±0.000684	0.017	8.36	66.88	19.63	2.076±0.100	8.73± 0.42
500	0.00305730 0.00000000	0.031021 0.000000	0.009	2.89	90.20	0.49	3.123 2.335	13.12 9.77
<7000>	0.00188504 0.00000000	0.229577 0.000000	0.012	8.39	54.23	23.05	1.971 0.071	8.29 0.30
500	0.00322056 0.00019905	0.043161 0.000175	0.005	3.33	94.94	0.42	1.132 2.724	4.77 11.46
<7000>	0.00293513 0.00000000	0.083030 0.000000	0.030	8.66	86.10	12.49	1.639 0.212	6.90 0.89
400	0.00097546 0.00000001	0.038764 0.000000	0.079	7.48	28.60	4.26	18.407 0.264	75.99 1.07
7000	0.00081471 0.00000000	0.194868 0.000000	0.016	3.29	22.95	15.21	3.945 0.068	16.55 0.28
400	0.00328727 0.00000000	0.037547 0.000000	0.010	4.12	96.91	1.10	0.784 0.880	3.30 3.70
<7000>	0.00166138 0.00000000	0.275294 0.000000	0.012	8.66	47.19	23.34	1.899 0.056	7.99 0.23

Power	40Ar	39Ar	38Ar	37Ar	36Ar	Blank 40Ar	Atmos 40/36
<7000>	71.32±0.00	11.26±0.05	7.55±0.06	7.111±0.09	0.187±0.00	0.060±0.00	287.67±1.00
500	8.97 0.00	3.29 0.00	0.06 0.00	0.069±0.00	0.024±0.00	0.058±0.00	287.67±1.00
<7000>	57.60 0.00	13.22 0.06	9.42 0.08	8.365±0.11	0.173±0.00	0.062±0.00	287.67±1.00
500	5.55 0.00	0.25 0.00	0.06 0.00	0.068±0.00	0.024±0.00	0.057±0.00	287.67±1.00
<7000>	85.75 0.00	7.17 0.03	5.06 0.04	4.684±0.06	0.272±0.01	0.059±0.00	287.67±1.00
400	62.65 0.00	2.46 0.01	1.62 0.01	0.921±0.01	0.073±0.00	0.108±0.00	287.67±1.00
7000	44.79 0.00	3.73 0.04	5.96 0.05	3.601±0.05	0.055±0.00	0.138±0.00	287.67±1.00
400	16.86 0.00	0.65 0.00	0.22 0.00	0.142±0.00	0.065±0.00	0.138±0.00	287.67±1.00
<7000>	49.79 0.00	13.39 0.06	9.36 0.08	5.763±0.07	0.106±0.00	0.112±0.00	287.67±1.00



Measured volumes are x 1E-10 cm<sup>3</sup> NTP. All errors are 2 x standard error.

# JC-41 Biotite (20-60 mesh)

Run date: 1995/11/17  
Run: AS-60

Can/Pos: 141/71  
Mass: 17.9 mg

J Value: 0.002333  
= 0.000016

Volume 39Ar: 236.78 x 1E-10 cm3 NTP  
Integrated Age: 6.91 ± 0.12 Ma

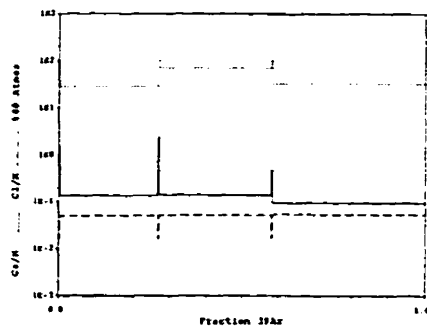
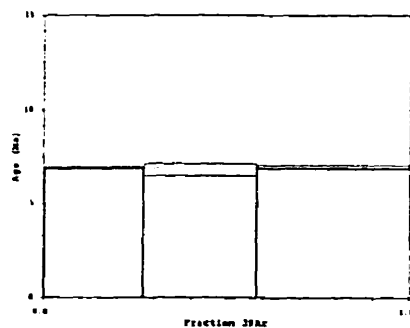
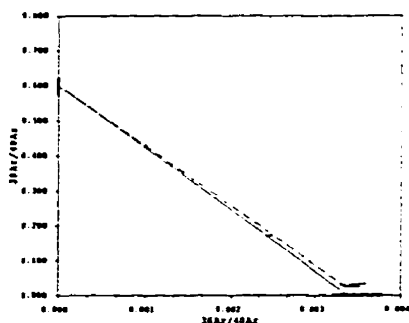
Approx. 7.99% K  
1.06% Ca

Initial 40/36: 295.53 ± 22.83 (MSWD = 6.75, isochron between 0.29 and 2.41)  
Correlation Age: 7.00 ± 0.26 Ma (100.0% of 39Ar, steps marked by >)

Plateau Age: 6.90 ± 0.12 Ma ( 99.0% of 39Ar, steps marked by <)

Power	36Ar/40Ar	39Ar/40Ar	r	Ca/K	%40Ar	%39Ar	40Ar*/39K	Age
300	0.00339465±0.00011212	0.029938±0.000173	0.005	1.56	100.17	0.24	-0.100±1.111	-0.42±4.68
<7000	0.00099787 0.00000000	0.431698 0.000000	0.004	0.14	28.40	26.33	1.647 0.017	6.92 0.07
300	0.00350733 0.00000000	0.033263 0.000000	0.006	2.42	103.48	0.31	-1.091 0.887	-4.60 3.74
<7000	0.00244321 0.00002171	0.172713 0.000373	0.002	0.14	71.45	30.75	1.623 0.076	6.82 0.32
300	0.00343407 0.00000000	0.026701 0.000000	0.004	0.51	101.35	0.41	-0.549 1.251	-2.31 5.27
<7000	0.00115841 0.00000001	0.401273 0.000000	0.003	0.09	33.09	41.96	1.654 0.020	6.95 0.08

Power	40Ar	39Ar	38Ar	37Ar	36Ar	Blank 40Ar	Atmos 40/36
300	19.40±0.00	3.60±0.00	3.07±0.00	3.07±0.00	3.07±0.00	0.060±0.00	287.67±1.00
<7000	147.08 0.00	62.74 0.27	15.05 0.13	0.655±0.01	0.159±0.00	0.031±0.00	287.67±1.00
300	22.32 0.00	0.76 0.00	0.09 0.00	0.146±0.00	0.030±0.00	0.060±0.00	287.67±1.00
<7000	424.64 0.00	73.27 0.31	18.09 0.15	0.783±0.01	1.068±0.02	0.079±0.00	287.67±1.00
300	36.39 0.00	0.99 0.01	0.11 0.00	0.042±0.00	0.132±0.00	0.057±0.00	287.67±1.00
<7000	251.79 0.00	99.96 0.43	25.23 0.22	0.692±0.01	0.300±0.01	0.057±0.00	287.67±1.00



Measured volumes are x 1E-10 cm3 NTP. All errors are 2 x standard error.

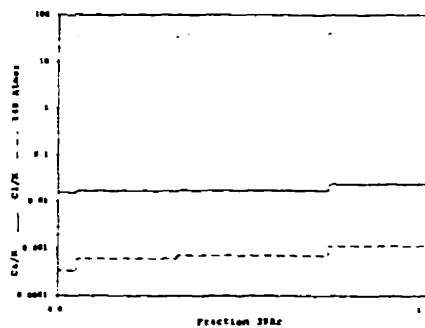
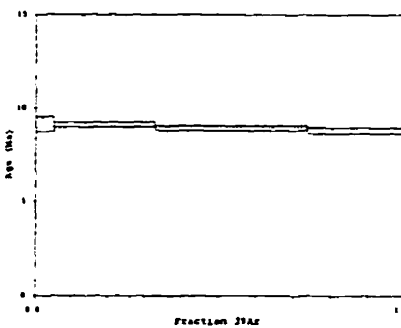
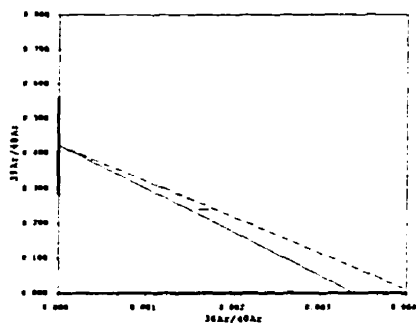
# **JC-42a Whole Rock (40-60 mesh)**

Run date: 1995/11/19      Calc Poz: 141.74      J Value: 0.000330  
 Run: AS-63      Mass: 25.0 mg      = 0.000016

Volume  $^{39}\text{Ar}$ :  $118.96 \times 10^{-10} \text{ cm}^3 \text{ NTP}$       Approx. 3.36% K  
 Integrated Age:  $9.95 \pm 0.10 \text{ Ma}$       0.064 Ca  
 Initial  $^{40}\text{Ar}/^{36}\text{Ar}$ :  $245.02 \pm 245.31$  (MSWD = 7.62, isochron between 3.00 and 3.00)  
 Correlation Age:  $9.93 \pm 3.21 \text{ Ma}$  (100.0% of  $^{39}\text{Ar}$ , steps marked by >)

Power	$^{36}\text{Ar}/^{40}\text{Ar}$	$^{39}\text{Ar}/^{40}\text{Ar}$	$\tau$	Ca/K	$^{40}\text{Ar}_{\text{atm}}$	$^{43}\text{Ar}$	$^{40}\text{Ar}^*/^{39}\text{K}$	Age
300	$0.00163253 \pm 0.00007534$	$0.238128 \pm 0.001033$	0.001	0.02	47.76	5.30	$2.174 \pm 0.034$	$9.11 \pm 0.39$
7000	$0.00115116 \pm 0.00000000$	$0.303866 \pm 0.000000$	0.001	0.02	33.59	27.52	$2.172 \pm 0.030$	$9.11 \pm 0.13$
7000	$0.00133937 \pm 0.00000000$	$0.283688 \pm 0.000000$	0.002	0.02	39.13	40.54	$2.129 \pm 0.031$	$8.93 \pm 0.13$
7000	$0.00146929 \pm 0.00001567$	$0.270245 \pm 0.000597$	0.002	0.02	42.94	26.94	$2.093 \pm 0.036$	$8.78 \pm 0.15$

Power	$^{40}\text{Ar}$	$^{39}\text{Ar}$	$^{38}\text{Ar}$	$^{37}\text{Ar}$	$^{36}\text{Ar}$	Blank $^{40}\text{Ar}$	Atmos $^{40}/^{36}$
300	$29.60 \pm 0.00$	$7.02 \pm 0.03$	$0.13 \pm 0.00$	$0.021 \pm 0.00$	$0.358 \pm 0.00$	$0.110 \pm 0.00$	$287.67 \pm 1.00$
7000	$127.58 \pm 0.00$	$38.50 \pm 0.16$	$0.69 \pm 0.01$	$0.062 \pm 0.00$	$0.161 \pm 0.00$	$0.141 \pm 0.00$	$287.67 \pm 1.00$
7000	$201.05 \pm 0.00$	$56.70 \pm 0.24$	$1.34 \pm 0.01$	$0.089 \pm 0.00$	$0.285 \pm 0.01$	$0.145 \pm 0.00$	$287.67 \pm 1.00$
7000	$140.20 \pm 0.00$	$37.68 \pm 0.16$	$0.77 \pm 0.01$	$0.179 \pm 0.00$	$0.220 \pm 0.00$	$0.129 \pm 0.00$	$287.67 \pm 1.00$



Measured volumes are  $\times 10^{-10} \text{ cm}^3 \text{ NTP}$ . All errors are 2 x standard error.



# JC-47b Biotite (60-100 mesh)

Run date: 1995/11/19 Can/Pos: 141/72 J Value: 0.002332  
Run: AS-61 Mass: 10.0 mg z 0.000016

Volume 39Ar: 133.88 x 1E-10 cm3 NTP Approx. 8.09% K  
Integrated Age: 8.36 ± 0.12 Ma 0.62% Ca

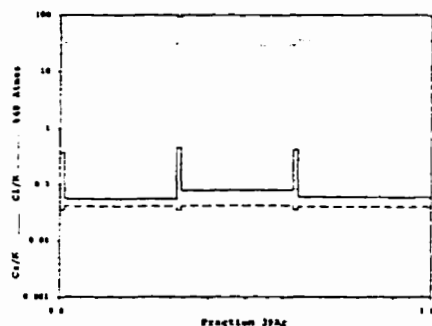
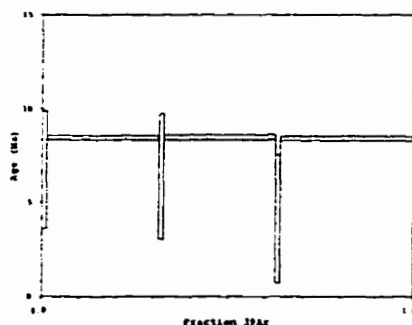
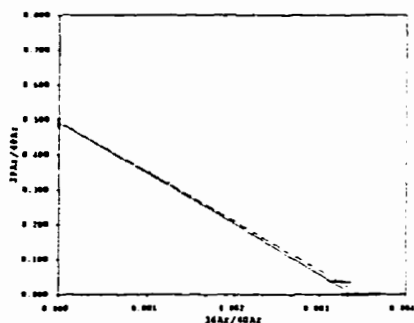
Initial 40/36: 286.86 ± 17.24 (MSWD = 0.35, isochron between 0.29 and 2.41)

Correlation Age: 8.53 ± 0.21 Ma (100.0% of 39Ar, steps marked by >)

Plateau Age: 8.46 ± 0.10 Ma ( 96.48 of 39Ar, steps marked by <)

Power	36Ar/40Ar	39Ar/40Ar	r	Ca/K	%40Ar	%39Ar	40Ar*/39K	Age
300	0.00317785±0.00009613	0.038105±0.000191	0.002	3.37	93.72	1.24	1.603±0.750	6.76±3.14
<7000	0.00110342 0.00000000	0.035962 0.000000	0.002	3.06	31.79	30.03	2.017 0.033	8.47 0.14
300	0.00319657 0.00000000	0.036527 0.000000	0.002	3.47	94.28	1.18	1.526 0.795	6.41 3.33
<7000	0.00099950 0.00001318	0.030463 0.000763	0.002	3.08	28.71	29.75	2.022 0.034	8.49 0.14
300	0.00327074 0.00000000	0.034271 0.000000	0.002	3.41	96.48	1.15	0.987 0.813	4.15 3.41
<7000	0.00122780 0.00000001	0.018962 0.000000	0.002	3.06	35.46	36.65	2.009 0.031	8.43 0.13

Power	40Ar	39Ar	38Ar	37Ar	36Ar	Blank 40Ar	Atmos 40/36
300	43.84±0.00	1.63±0.01	3.31±0.01	0.051±0.00	0.147±0.00	0.056±0.00	287.67±1.00
<7000	121.41 0.00	40.46 0.17	7.89 1.07	0.16±0.00	0.140±0.00	0.058±0.00	287.67±1.00
300	43.34 0.00	1.60 0.01	3.30 0.00	0.060±0.00	0.146±0.00	0.057±0.00	287.67±1.00
<7000	115.36 0.00	40.08 0.17	8.08 1.07	0.23±0.00	0.122±0.00	0.064±0.00	287.67±1.00
300	44.98 0.00	1.54 0.01	3.29 0.00	0.052±0.00	0.155±0.00	0.055±0.00	287.67±1.00
<7000	155.93 0.00	49.37 0.21	9.49 1.08	0.21±0.00	0.199±0.00	0.058±0.00	287.67±1.00



Measured volumes are x 1E-10 cm3 NTP. All errors are 2 x standard error.

# **JC-77a Whole Rock (40-80 mesh)**

Run date: 1995/11/01 Can/Pos: 141.77 J Value: 0.000327  
 Run: AS-69 Mass: 30.0 mg = 0.000320

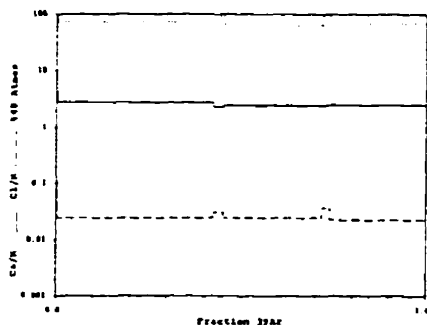
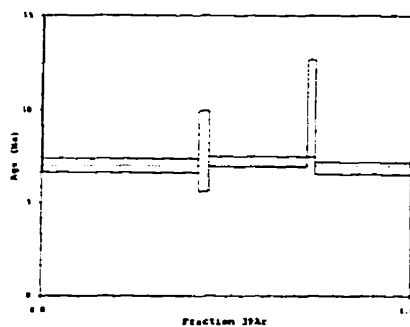
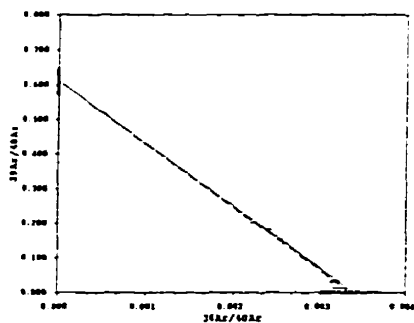
Volume 39Ar: 109.20 x 1E-10 cm3 NTP Approx. 2.214 K  
 Integrated Age: 7.13 ± 0.23 Ma 5.734 Ga

Initial 40/36: 299.78 ± 28.86 (MSWD = 1.83, isochron between 0.29 and 2.41)  
 Correlation Age: 6.88 ± 0.42 Ma (100.0% of 39Ar, steps marked by >)

Plateau Age: 7.02 ± 0.22 Ma ( 94.9% of 39Ar, steps marked by <)

Power	36Ar/40Ar	39Ar/40Ar	r	Ca/K	%40Atm	%39Ar	40Ar*/39K	Age
300	0.00321497±0.00003614	0.013504±0.000080	0.053	4.37	94.91	0.27	3.731±2.100	15.59±5.74
<7000	0.00251465 0.00000000	0.154169 0.000000	0.004	2.76	73.79	41.74	1.669 0.091	4.39 0.38
500	0.0016433 0.00000000	0.035004 0.000000	0.006	2.30	93.34	2.70	1.864 0.516	7.81 2.16
<7000	0.00221251 0.00002156	0.201609 0.000437	0.003	2.45	64.70	26.54	1.724 0.065	7.22 0.27
500	0.0015105 0.00000000	0.028759 0.000000	0.008	2.46	92.97	2.16	2.404 0.626	10.07 2.61
<7000	0.00238819 0.00000001	0.180462 0.000000	0.003	2.53	69.93	26.60	1.637 0.076	6.56 0.32

Power	40Ar	39Ar	38Ar	37Ar	36Ar	Blank 40Ar	Atmos 40/36
300	21.51±0.00	0.32±0.00	0.17±0.00	0.102±0.00	0.062±0.00	0.095±0.00	287.67±1.00
<7000	297.35 0.00	45.88 0.20	5.63 0.05	8.619±0.11	0.792±0.11	0.097±0.00	287.67±1.00
500	84.46 0.00	3.00 0.01	0.61 0.00	0.400±0.01	0.286±0.01	0.097±0.00	287.67±1.00
<7000	144.94 0.00	29.19 0.12	3.59 0.03	4.996±0.06	0.349±0.01	0.112±0.00	287.67±1.00
500	82.00 0.00	2.40 0.01	0.47 0.00	0.419±0.01	0.276±0.00	0.095±0.00	287.67±1.00
<7000	162.14 0.00	29.26 0.12	3.39 0.03	5.161±0.07	0.419±0.01	0.112±0.00	287.67±1.00



Measured volumes are x 1E-10 cm3 NTP. All errors are 1 x standard error.

# **JC-191 Biotite (45-60 mesh)**

Run date: 1995/11/19 Can/Pos: 141/73 J Value: 0.002331  
Run: AS-62 Mass: 6.6 mg ± 0.000016

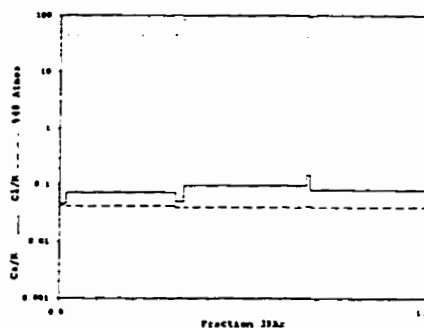
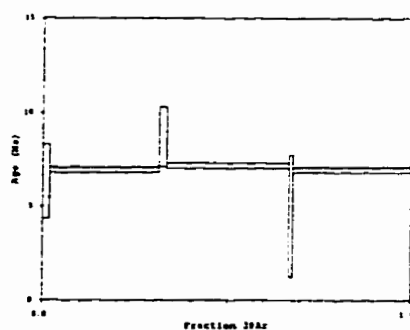
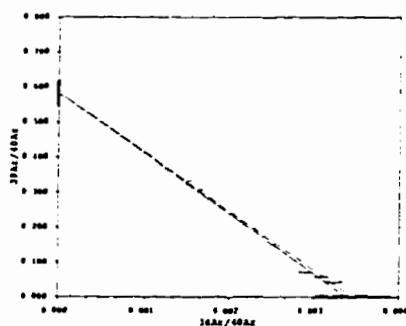
Volume 39Ar: 87.21 x 1E-10 cm<sup>3</sup> NTP Approx. 7.99% K  
Integrated Age: 7.04 ± 0.11 Ma 0.67% Ca

Initial 40/36: 288.90 ± 35.69 (MSWD = 5.36, isochron between 0.29 and 2.41)  
Correlation Age: 7.20 ± 0.41 Ma (100.0% of 39Ar, steps marked by >)

Plateau Age: 7.03 ± 0.10 Ma ( 95.1% of 39Ar, steps marked by <)

Power	36Ar/40Ar	39Ar/40Ar	r	Ca/K	%40Ar	%39Ar	40Ar*/39K	Age
300	0.00309242±0.00009052	0.057497±0.000257	0.002	0.05	91.09	1.78	1.511±0.468	6.34±1.96
<7000	0.00153351 0.00000000	0.331967 0.000000	0.002	0.07	44.33	29.12	1.659 0.035	6.96 0.15
300	0.00288941 0.00000000	0.070663 0.000000	0.001	0.05	85.06	2.22	2.079 0.375	8.72 1.57
<7000	0.00144422 0.00001746	0.337650 0.000735	0.003	0.10	41.73	33.49	1.708 0.032	7.17 0.13
300	0.00323330 0.00000000	0.042101 0.000000	0.005	0.15	95.33	0.90	1.070 0.778	4.49 3.27
<7000	0.00167106 0.00000001	0.307256 0.000000	0.003	0.08	48.43	32.48	1.658 0.036	6.96 0.15

Power	40Ar	39Ar	38Ar	37Ar	36Ar	Blank 40Ar	Atmos 40/36
300	27.13±0.00	1.58±0.01	0.35±0.00	0.318±0.00	0.095±0.00	0.091±0.00	287.67±1.00
<7000	27.45 0.00	25.58 0.11	5.11 1.14	0.150±0.00	0.131±0.00	0.085±0.00	287.67±1.00
300	27.61 0.00	1.39 0.01	1.32 1.00	0.321±0.00	0.091±0.00	0.084±0.00	287.67±1.00
<7000	27.79 0.00	29.41 0.13	5.59 1.05	0.222±0.00	0.138±0.00	0.082±0.00	287.67±1.00
300	18.77 0.00	0.80 0.00	0.17 0.00	0.017±0.00	0.068±0.00	0.058±0.00	287.67±1.00
<7000	33.43 0.00	28.51 0.12	5.47 0.05	0.176±0.00	0.165±0.00	0.060±0.00	287.67±1.00



Measured volumes are x 1E-10 cm<sup>3</sup> NTP. All errors are 2 x standard error.